Effects of Fault Segmentation, Mechanical Interaction, and Structural Complexity on Earthquake-Generated Deformation

by

David Elias Haddad

A Dissertation Presented in Partial Fulfillment
of the Requirements for the Degree
Doctor of Philosophy

Approved April 2014 by the
Graduate Supervisory Committee:

J Ramón Arrowsmith, Chair
Stephen Reynolds
Steven Semken
Manoochehr Shirzaei
Kelin Whipple
Olaf Zielke

ARIZONA STATE UNIVERSITY

May 2014

ABSTRACT

Earth's topographic surface forms an interface across which the geodynamic and geomorphic engines interact. This interaction is best observed along crustal margins where topography is created by active faulting and sculpted by geomorphic processes. Crustal deformation manifests as earthquakes at centennial to millennial timescales. Given that nearly half of Earth's human population lives along active fault zones, a quantitative understanding of the mechanics of earthquakes and faulting is necessary to build accurate earthquake forecasts. My research relies on the quantitative documentation of the geomorphic expression of large earthquakes and the physical processes that control their spatiotemporal distributions. The first part of my research uses high-resolution topographic lidar data to quantitatively document the geomorphic expression of historic and prehistoric large earthquakes. Lidar data allow for enhanced visualization and reconstruction of structures and stratigraphy exposed by paleoseismic trenches. Lidar surveys of fault scarps formed by the 1992 Landers earthquake document the centimeter-scale erosional landforms developed by repeated winter storm-driven erosion. The second part of my research employs a quasi-static numerical earthquake simulator to explore the effects of fault roughness, friction, and structural complexities on earthquake-generated deformation. My experiments show that fault roughness plays a critical role in determining fault-to-fault rupture jumping probabilities. These results corroborate the accepted 3-5 km rupture jumping distance for smooth faults. However, my simulations show that the rupture jumping threshold distance is highly variable for rough faults due to heterogeneous elastic strain energies. Furthermore, fault roughness controls spatiotemporal variations in slip rates such that rough faults exhibit lower slip rates

relative to their smooth counterparts. The central implication of these results lies in guiding the interpretation of paleoseismically derived slip rates that are used to form earthquake forecasts. The final part of my research evaluates a set of Earth science-themed lesson plans that I designed for elementary-level learning-disabled students. My findings show that a combination of concept delivery techniques is most effective for learning-disabled students and should incorporate interactive slide presentations, tactile manipulatives, teacher-assisted concept sketches, and student-led teaching to help learning-disabled students grasp Earth science concepts.

DEDICATION

I dedicate this dissertation to my family and especially to my mother. Her countless sacrifices have shaped me into the man I am today.

ACKNOWLEDGMENTS

I owe my scientific intellect to my advisor and mentor Ramón Arrowsmith. Ramón's always-positive attitude and relentless drive are contagious. He has shown me that I can do pretty much anything with MATLAB (except maybe fry an egg). Ramón's encouragement to pursue a research project during my undergraduate days opened up endless opportunities that have allowed me to grow professionally and personally. Now, 10 years and one PhD degree later, my scientific thinking is still influenced by my interactions with Ramón. And I am sure it will continue to be so for a long time. Ramón, it has been an honor and a pleasure to work with you these past 10 years. You have set the bar pretty high for other advisors. Thank you for everything!

I am grateful to the members of my dissertation committee for their support during my PhD progress. I am especially thankful to Olaf Zielke's support in developing the FIMoz and FIMozFric modeling environments of which this dissertation made extensive use. Thank you Olaf for letting me peek under the hood of your earthquake engine and break things as I tailored it to my research needs. I thank Stephen Reynolds for his interest in my project and for being a superb supporter of my goal to become an applied geoscientist. Kelin Whipple provided tremendously helpful insights into the broader aspects of my research. Manoochehr Shirzaei's excellent guidance only makes me wish he joined ASU sooner so that I could have had a longer interaction with his genius. I thank Steven Semken for being an inspirational teacher and for one particular conversation we shared in the field that ultimately sealed my decision to pursue the PhD degree.

A huge thank you to my colleagues Nathan Toké, Barrett Salisbury, Gayatri

Marlyani, and Tsurue Sato of the ASU Active Tectonics group for fruitful discussions in our seminars. I especially thank you for your support during the hot field days of trenching in the Carrizo Plain (and for showing me that there actually is a method to the madness of interpreting paleoseismic trenches!).

Many thanks go to the ASU Graduate & Professional Student Association, the ASU Office of the Vice President for Research and Economic Affairs, and the ASU Graduate College for granting me research funds and travel support to six conferences. I am grateful to the ASU Advanced Computing Center for the high-performance computing environment in which I ran many hundreds of earthquake simulations.

Extra special thanks go to Steve and Katie Turner and the Turner Steakhouse for many Sundays of hearty Texan food and unbeatable Southern hospitality. Last, but certainly not least, I thank my wonderful wife Amanda Haddad for her tremendous support during the past four years and for being the best wife that I could have ever asked for.

TABLE OF CONTENTS

Page

CHAPTER Page

CHAPTER Page

APPENDIX Page

LIST OF TABLES

Table Page

LIST OF FIGURES

Figure Page

Figure Page

Figure Page

Figure Page

Figure Page

Chapter 1

INTRODUCTION

OVERVIEW

Nearly half of Earth's human population lives on active plate boundaries with a 10% exceedance probability of 0.4 *g* for earthquake-induced peak ground accelerations in the next fifty years (Giardini et al., 1999). As population densities along plate boundaries continue to rise, our understanding of earthquake processes and the mechanical behavior of seismogenic faults will become increasingly critical to guiding seismic hazard analyses and ensuring societal and economic security (Jordan et al., 2011). Therefore, a sound understanding of the mechanics of earthquakes and how they manifest in Earth's topography is needed.

Geologic datasets feed the fundamental building blocks of earthquake forecasts. Take the latest iteration of the Uniform California Earthquake Forecast (UCERF3) as an example (e.g., Field et al., 2013). Three of the four UCERF3 components rely on data obtained by geologic means, such as fault models (spatial geometry of fault systems), deformation models (fault slip rates used to compute seismic moment release), and earthquake-rate models (earthquake-recurrence behavior). Of particular importance to the above are earthquake-recurrence models that aid the interpretation of paleoseismically derived slip rates. Conceptual models of earthquake behavior were first developed by studies along the San Andreas fault (SAF) and Wasatch fault (Schwartz and Coppersmith, 1984; Sieh and Jahns, 1984). These resulted in the formulation of the characteristic and uniform-slip earthquake-recurrence models. Both models describe the magnitude of coseismic slip and the potential length of ruptures generated by large

earthquakes. The characteristic earthquake model posits that coseismic slip magnitude does not change at a point and that fault slip rate can vary along strike. The uniform-slip model describes constant slip magnitude during earthquakes and thus a constant slip rate along strike. Both models are attractive options for earthquake forecasts due to their simple description of earthquake recurrence (e.g., Field et al., 2013). But what really controls the shape of earthquake slip distributions and are the above models appropriate idealizations of surface slip in earthquake forecasts? We know that coseismic slip distributions are controlled by many factors. For example, structural and frictional complexities along faults may result in highly variable slip distributions for large earthquakes. These complexities may also control the long-term clustering of earthquakes in space and time. Therefore, slip rates determined at individual points along faults have the potential to vary significantly in space and time.

Earthquake ruptures along crustal faults originate in the middle to lower depths of the seismogenic layer and transmit deformation to Earth's surface by driving slip along faults (Fig. 1.1; e.g., Scholz, 2002; Titus et al., 2011). This process is evident in Earth's topography via localized (e.g., fault scarps and fractures) or distributed (e.g., off-fault folding and warping) deformation (e.g., Oskin et al., 2012; Quigley et al., 2012). The extent to which these surficial features represent seismic moment release at depth is poorly understood, but is generally thought to be controlled by the geometrical complexity of faults and the spatiotemporal strength variations of the upper lithosphere (Sibson, 1977, 1982, 1986; Scholz, 1988, 2002). Because this manifestation is commonly expressed in the topography of fault zones as displaced geomorphic markers (e.g., Hilley and Arrowsmith, 2008; Arrowsmith and Zielke, 2009; Hilley et al., 2010; Zielke et al.,

2010), their accurate characterization is important to test their fidelity in recording the magnitude of coseismic slip-per-event and the representation of coseismic slip at depth. Documenting the surface record of faulting relative to the seismic moment released at depth is therefore necessary to build an understanding of how fault systems operate through space and time. Site-specific paleoseismic studies provide detailed information about the rupture history of individual fault segments where strains are highly localized (e.g., Sibson, 2003; Rockwell and Ben-Zion, 2007; McCalpin, 2009). However, interpretations derived from these studies are unable to constrain overall fault behavior, especially when coseismic deformation is distributed across multiple fault strands that act as broad shear zones (Johnson et al., 1997) or has been modified post-seismically via after slip (Marone and Richardson, 2010). Similarly, coseismic slip histories derived from such studies ignore the detailed structure of fault zones by not accounting for strain partitioning along mechanically interacting faults or heterogeneities in crustal strength properties, despite their proven implications for rupture dynamics (e.g., Shi and Ben-Zion, 2006).

With the exception of very limited observations of active faults at depth (e.g., the San Andreas Fault Observatory at Depth), faults cannot be directly accessed in the seismogenic layer. However, advances in light detection and ranging (lidar) and numerical earthquake simulators allow for high-resolution and physically based analyses of surface manifestations of deep faulting processes (e.g., Haugerud et al., 2003; Sherrod et al., 2004; Bevis et al., 2005; Kondo et al., 2008; Zielke and Arrowsmith, 2008; Cochran et al., 2009; Cooke and Dair, 2011; Frankel et al., 2011; Nissen et al., 2012; Oskin et al., 2012; Tullis et al., 2012). This is done by allowing for the quantitative

documentation of coseismic deformation within 10s to a few 1000s of meters from fault ruptures. Such datasets help us interpret fracture patterns observed in the paleoseismic record (Lawson, 1908; Wallace and Schulz, 1983; Wallace, 1991; McCalpin, 2009) and enable surface ruptures to be interrogated for their fidelity in representing coseismic processes at depth (e.g., Nissen et al., 2012; Oskin et al., 2012). These datasets also provide important controls for measuring coseismic slip in the most recent event and slip accumulated over multiple earthquakes (e.g., Arrowsmith et al., 2011; Haddad et al., 2011; Madden et al., 2011), thereby improving the understanding of fault system behavior and interactions through space and time.

DISSERTATION CHAPTER OUTLINE

My dissertation is divided into seven chapters. The order of the chapters is organized such that geologic/paleoseismic data and their applications are presented first (Chapters 2 and 3) followed by numerical explorations in an earthquake simulator (Chapter 4) and its application in various seismotectonic settings (Chapter 5). The final chapter is a side project in which I took charge to develop Earth science lesson plans for elementary-school students with learning disabilities (Chapter 6). The following paragraphs provide an overview of the rationale and importance of each chapter.

In Chapter 2, I evaluate various research applications of airborne and terrestrial lidar. I investigate lidar applications in paleoseismic trenching, fault scarp degradation monitoring, and imaging of precariously balanced rocks. Terrestrial lidar enables the rapid production of high-resolution 3D orthophotographs of stratigraphic and fault relationships in paleoseismic trenches. I then show how repeat topographic surveys using lidar can be used to quantify fault scarp degradation rates. The last case study that I

present in this chapter shows how both airborne and terrestrial lidar datasets can be used to document the 3D shape and geomorphic setting of precariously balanced rocks. This chapter was published in the Geological Society of America journal *Geosphere*. My co-authors include Sinan Akçiz (University of California, Los Angeles), Ramón Arrowsmith (Arizona State University), Dallas Rhodes (Kennesaw State University), John Oldow (University of Texas at Dallas), Olaf Zielke (King Abdullah University of Science and Technology), Nathan Toké (Utah Valley University), Amanda Haddad (University of Southern California), Juergen Mauer (Z+F USA, Inc.), and Prabin Shilpakar (University of Texas at Dallas).

Chapter 3 presents an analysis on how structural complexities control coseismic displacement distributions along faults and geomechanically derives predictions of topographic deformation. This chapter also provides a preliminary analysis of the3D displacement field of a section of the 2010 El Mayor-Cucupah earthquake as a proof of concept. The latter analysis was done by co-author Edwin Nissen (Colorado School of Mines) during his postdoctoral research with Ramón Arrowsmith. The importance of Chapter 3 lies in delineating the first-order controls on the complexity of surface ruptures through bedrock versus sedimentary basins, and the fault mechanics responsible for the observed topographic deformation (i.e. where should we expect uplift/subsidence/warping to occur?). This chapter will be published in the book *Remote Sensing for Geoscientists: Integration and Analysis* by Gary Prost (ConocoPhillips). Gary invited me to contribute this chapter to his book after learning about my lidar research during my 2011 internship with ConocoPhillips. The book will come out in late 2014. My

co-authors on this chapter are Edwin Nissen (Colorado School of Mines) and Ramón Arrowsmith (Arizona State University).

In Chapter 4, I investigate the effects of fault structural and frictional complexities on earthquake-generated deformation using an earthquake simulator. The simulator was developed by Olaf Zielke as part of his PhD research with Ramón Arrowsmith at ASU. Olaf generously allowed me and helped me to modify the source code for his simulator to fit my experimental needs. I used the simulator to carry out numerical experiments with the goal of determining what effects fault structural complexities, frictional properties, and roughness have on individual and cumulative slip along seismogenic faults. I found that key relationships exist between the configuration of structural barriers, fault frictional properties, fault roughness, and the surface expression of coseismic deformation. Based on these relationships, I expanded upon our understanding of earthquake rupture processes (e.g., Wesnousky, 2008). The central implication of this chapter lies in guiding the interpretation of the surface manifestation of coseismic faulting, paleoseismic data, and the formulation of rupture jumping rules in future iterations of earthquake forecasts. I plan to submit this chapter to the *Journal of Geophysical Research*. My co-authors will include Olaf Zielke (King Abdullah University of Science and Technology) and Ramón Arrowsmith (Arizona State University).

In Chapter 5, I present the results from earthquake simulations on two iconic 3D structures in California: the Garlock fault and the Hayward-Calaveras fault system. I find that earthquake simulators have a place in the formulation of future iterations of the Uniform California Earthquake Forecast. This chapter discusses the implications that my

results have for interpreting paleoseismic datasets in the context of spatiotemporal earthquake clustering and regional fault interactions. I close this chapter by presenting various implications that go into modeling fault-related deformation at the single- and multi-earthquake scales in terms of fault zone evolution. I plan to submit this chapter to the *Bulletin of the Seismological Society of America* or the *Geophysical Journal International*. My co-authors will be Olaf Zielke (King Abdullah University of Science and Technology) and Ramón Arrowsmith (Arizona State University).

Chapter 6 presents a series of Earth science lesson plans that I designed to engage learning disabled (LD) students in the scientific method while helping them meet Arizona state-mandated Earth science curriculum standards. All lessons were developed with the sole purpose of adapting key Earth science concepts to the learning abilities of LD elementary school students. The two primary findings of this chapter are: (1) Earth science provides a highly engaging learning environment for LD students, and (2) hands-on, student-led learning activities are paramount to enhancing the retention of Earth science concepts by LD students. I plan to submit this chapter to the *Journal of Geoscience Education* as a curriculum contribution following additional classroom observations and data analysis. My co-authors will be Amanda Haddad (University of Southern California), Mary Turner (Challenger Middle School), HyunTae Kim (Pukyong National University), Tsurue Sato (Arizona State University), and Vicki Mills (Arizona State University).

I conclude my dissertation in Chapter 7 by presenting my thoughts on how my findings will serve as a framework upon which various avenues for future research can be constructed.

FIGURES

Figure 1.1. Synoptic overview of a fault zone as manifested in Earth's surface and interior. In Earth's interior, geologic and seismic properties of fault zones control how strain is transmitted through the seismogenic layer (outlined in red) to Earth's surface. On Earth's surface, the tectonic geomorphology of fault zones provides clues into the coseismic moment released at depth by preserving faulted geomorphic elements. The case shown here is for thick-skinned lithospheric deformation, although it may also occur in thin-skinned deformational settings. Derived from concepts that were developed by Vedder and Wallace (1970), Sylvester (1999), and Scholz (2002). Figure elements are not to scale.

Figure 1.1

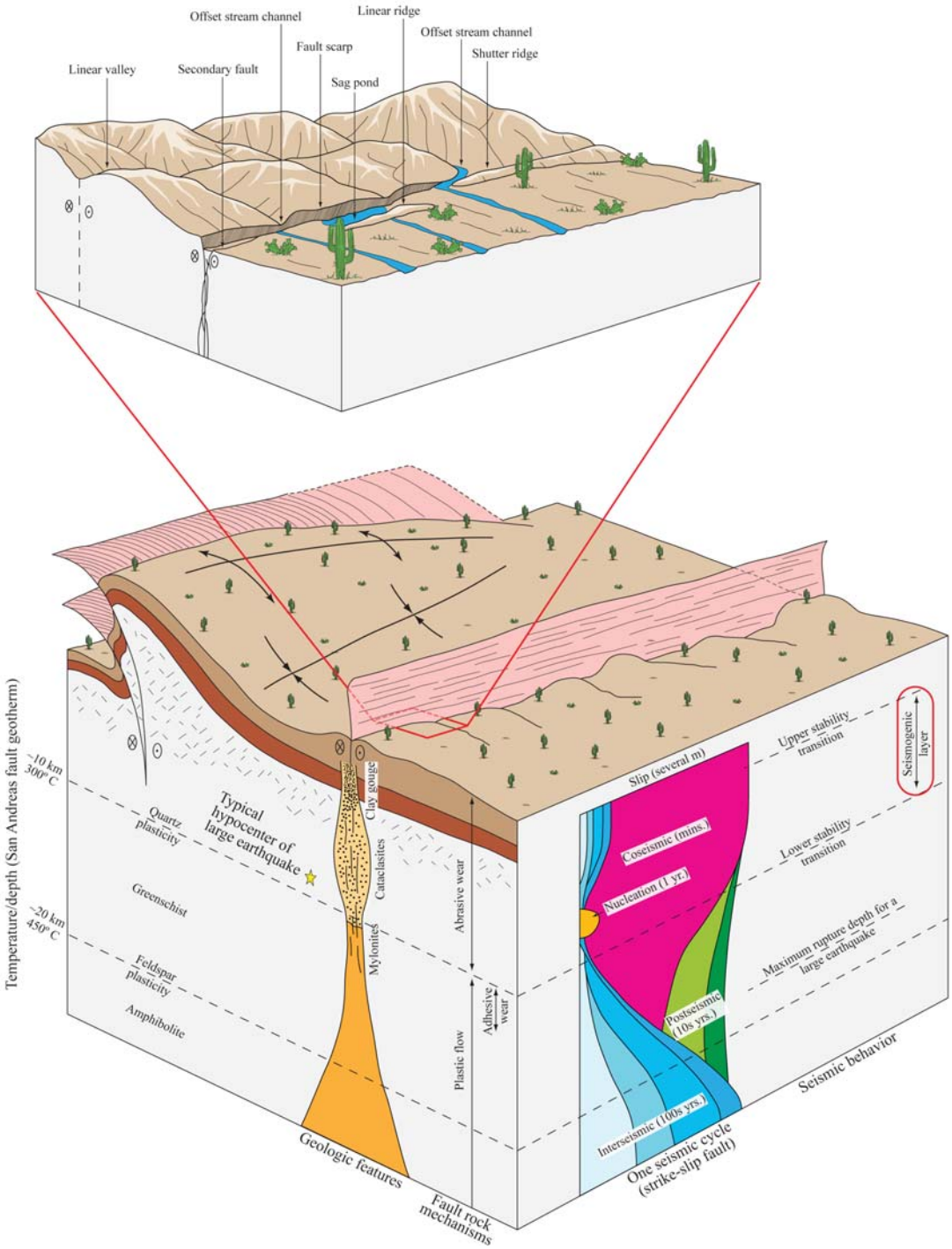
Offset stream channel
Linear ridge
Fault scarp
Offset stream channel
Shutter ridge
Linear valley
Secondary fault
Sag pond
Temperature/depth (San Andreas fault geotherm)
~10 km
300° C
~20 km
450° C
Quartz plasticity
Typical hypocenter of large earthquake
Greenschist
Feldspar plasticity
Amphibolite
Clay gouge
Cataclasites
Mylonites
Abrasive wear
Plastic flow
Adhesive wear
Geologic features
Fault rock mechanisms
Slip (several m)
Upper stability transition
Seismogenic layer
Coseismic (mins.)
Nucleation (1 yr.)
Lower stability transition
Maximum rupture depth for a large earthquake
Postseismic (10s yrs.)
Interseismic (100s yrs.)
Seismic behavior
One seismic cycle (strike-slip fault)

REFERENCES

Arrowsmith, J. R., Madden, C. M., Haddad, D. E., Salisbury, J. B., and Weldon, R. J., 2011, Compilation of slip in the last event data for high slip rate faults in California for input into slip-dependent rupture forecast: Eos Trans., no. AGU, S13B-06.

Arrowsmith, J. R., and Zielke, O., 2009, Tectonic geomorphology of the San Andreas Fault zone from high resolution topography: An example from the Cholame segment: Geomorphology, v. 113, no. 1-2, p. 70-81.

Bevis, M., Hudnut, K., Sanchez, R., Toth, C., Grejner-Brzezinska, D., Kendrick, E., Caccamise, D., Raleigh, D., Zhou, H., Shan, S., Shindle, W., Yong, A., Harvey, J., Borsa, A., Ayoub, F., Elliot, B., Shrestha, R., Carter, B., Sartori, M., Phillips, D., Coloma, F., and Stark, K., 2005, The B4 Project: scanning the San Andreas and San Jacinto fault zones: Eos Trans. AGU 86(52), Fall Meet. Suppl., Abstract H34B-01.

Cochran, E. S., Li, Y., Shearer, P. M., Barbot, S., Fialko, Y., and Vidale, J. E., 2009, Seismic and geodetic evidence for extensive, long-lived fault damage zones: Geology, v. 37, no. 4, p. 315-318.

Cooke, M. L., and Dair, L. C., 2011, Simulating the recent evolution of the southern big bend of the San Andreas fault, Southern California: Journal of Geophysical Research, v. 116, no. B04405, p. 20.

Field, E. H., Biasi, G. P., Bird, P., Dawson, T. E., Felzer, K. R., Jackson, D. D., Johnson, K. M., Jordan, T. H., Madden, C., Michael, A. J., Milner, K. R., Page, M. T., Parsons, T., Powers, P. M., Shaw, B. E., Thatcher, W. R., Weldon, R. J., and Zeng, Y., 2013, Uniform California Earthquake Rupture Forecast, Version 3 (UCERF3)—The Time-Independent Model: U.S. Geological Survey Open-File Report 2013-1165.

Frankel, K. L., Dolan, J. F., Owen, L. A., Ganev, P., and Finkel, R. C., 2011, Spatial and temporal constancy of seismic strain release along an evolving segment of the Pacific-North America plate boundary: Earth and Planetary Science Letters, v. 304, no. 3-4, p. 565-576.

Giardini, D., Grunthal, G., Shedlock, K., and Zhang, P., 1999, The Global Seismic Hazard Map.

Haddad, D. E., Madden, C. M., Salisbury, J. B., Arrowsmith, J. R., and Weldon, R. J., 2011, LiDAR-derived measurements of slip in the most recent ground-rupturing earthquakes along elements of the San Andreas fault system: SCEC Proceedings and Abstracts, v. 21.

Haugerud, R. A., Harding, D. J., Johnson, S. Y., Harless, J. L., Weaver, C. S., and Sherrod, B. L., 2003, High-resolution Lidar topography of the Puget Lowland, Washington—a bonanza for earth science: GSA Today, v. 13, no. 6, p. 4-10.

Hilley, G. E., and Arrowsmith, J. R., 2008, Geomorphic response to uplift along the Dragon's Back pressure ridge, Carrizo Plain, California: Geology, v. 36, no. 5, p. 367-370.

Hilley, G. E., DeLong, S., Prentice, C., Blisniuk, K., and Arrowsmith, J., 2010, Morphologic dating of fault scarps using airborne laser swath mapping (ALSM) data: Geophysical Research Letters, v. 37.

Johnson, A. M., Fleming, R. W., Cruikshank, K. M., Martosudarmo, S. Y., Johnson, N. A., Johnson, K. M., and Wei, W., 1997, Analecta of structures formed during the 28 June 1992 Landers-Big Bear, California earthquake sequence: U.S. Geological Survey.

Jordan, T. H., Chen, Y., Gasparini, P., Madariaga, R., Main, I., Marzocchi, W., Papadopoulos, G., Sobolev, G., Yamaoka, K., and Zschau, J., 2011, Operational earthquake forecasting: state of knowledge and guidelines for utilization: Annals of Geophysics, v. 54, no. 4, p. 316-391.

Kondo, H., Toda, S., Okamura, K., and Chiba, T., 2008, A fault scarp in an urban area identified by LiDAR survey: a Case study on the Itoigawa–Shizuoka Tectonic Line, central Japan: Geomorphology, v. 101, p. 731-739.

Lawson, A., 1908, Report of the Earthquake Investigation Commission upon the California Earthquake of April 18, 1906: Carnegie Institution.

Madden, C. M., Arrowsmith, J. R., Haddad, D. E., Salisbury, J. B., and Weldon, R. J., 2011, Compilation of slip in the last earthquake data for high slip rate faults in California for input into slip-dependent rupture forecast: SCEC Proceedings and Abstracts, v. 21.

Marone, C., and Richardson, E., 2010, Learning to read fault-slip behavior from fault-zone structure: Geology, v. 38, no. 8, p. 767-768.

McCalpin, J. P., 2009, Paleoseismology, International Geophysics Series: San Diego, Academic Press, p. 613.

Nissen, E., Krishnan, A. K., Arrowsmith, J. R., and Saripalli, S., 2012, Three-dimensional surface displacements and rotations from differencing pre- and post-earthquake LiDAR point clouds: Geophysical Research Letters, v. 39.

Oskin, M. E., Arrowsmith, J. R., Hinojosa, A. C., Elliott, A. J., Fletcher, J. M., Fielding, E. J., Gold, P. O., Garcia, J. J. G., Hudnut, K. W., Liu-Zheng, J., and Teran, O. J.,

2012, Near-field deformation from the El Mayor-Cucupah earthquake revealed by differential LiDAR: Science, v. 335, no. 702.

Quigley, M., Van Dissen, R., Litchfield, N., Duffy, B., Barrell, D., Furlong, K., Stahl, T., Bilderback, E., and Noble, D., 2012, Surface rupture during the 2010 Mw 7.1 Darfield (Canterbury) earthquake: implications for fault rupture dynamics and seismic-hazard analysis: Geology, v. 40, no. 1, p. 55-58.

Rockwell, T. K., and Ben-Zion, Y., 2007, High localization of primary slip zones in large earthquakes from paleoseismic trenches: Observations and implications for earthquake physics: Journal of Geophysical Research-Solid Earth, v. 112, no. B10.

Scholz, C. H., 1988, The brittle-plastic transition and the depth of seismic faulting: Geologische Rundschau, v. 77, no. 1, p. 319-328.

-, 2002, The mechanics of earthquakes and faulting, Cambridge, Cambridge Universiry Press, 496 p.

Schwartz, D. P., and Coppersmith, K. J., 1984, Fault behavior and characteristic earthquakes; examples from the Wasatch and San Andreas fault zones: Journal of Geophysical Research, v. 89, p. 5681-5698.

Sherrod, B. L., Brocher, T. M., Weaver, C. S., Bucknam, R. C., Blakely, R. J., Kelsey, H. M., Nelson, A. R., and Haugerud, R. A., 2004, Holocene fault scarps near Tacoma, Washington, USA: Geology, v. 32, p. 9-12.

Shi, Z. Q., and Ben-Zion, Y., 2006, Dynamic rupture on a bimaterial interface governed by slip-weakening friction: Geophysical Journal International, v. 165, no. 2, p. 469-484.

Sibson, R. H., 1977, Fault rocks and fault mechanisms: Journal of the Geological Society of London, v. 133, p. 191-213.

-, 1982, Fault zone models, heat flow, and the depth distribution of earthquakes in the continental crust of the United States: Bulletin of the Seismological Society of America, v. 72, no. 1, p. 151-163.

-, 1986, Earthquakes and rock deformation in crustal fault zones: Annual Reviews of Earth and Planetary Sciences, v. 14, p. 149-175.

-, 2003, Thickness of the seismic slip zone: Bulletin of the Seismological Society of America, v. 93, no. 3, p. 1169-1178.

Sieh, K. E., and Jahns, R. H., 1984, Holocene activity of the San Andreas fault at Wallace Creek, California: Geological Society of America Bulletin, v. 95, p. 883-896.

Sylvester, A. G., 1999, Rifting, transpression, and neotectonics in the Central Mecca Hills, Salton Trough, Santa Barbara, University of California, Santa Barbara, 52 p.

Titus, S. J., Dyson, M., DeMets, C., Tikoff, B., Rolandone, F., and Buergmann, R., 2011, Geologic versus geodetic deformation adjacent to the San Andreas fault, central California: Geological Society of America Bulletin, v. 123, no. 5-6, p. 794-820.

Tullis, T. E., Sachs, M. K., Turcotte, D. L., Ward, S. N., Yikilmaz, M. B., Richards-Dinger, K., Barall, M., Dieterich, J. H., Field, E. H., Heien, E. M., Kellogg, L. H., Pollitz, F. F., and Rundle, J. B., 2012, Generic Earthquake Simulator: Seismological Research Letters, v. 83, no. 6, p. 959-963.

Vedder, J. G., and Wallace, R. E., 1970, Recent active breaks along the San Andreas fault between Cholame Valley and Tejon Pass, California: U.S. Geological Survey Miscellaneous Geological Investigations Map I-741, scale 1:24,000, 3 sheets.

Wallace, R. E., 1991, The San Andreas Fault System, California: U.S. Geological Survey Open File Report.

Wallace, R. E., and Schulz, S. S., 1983, Aerial views in color of the San Andreas fault, California: U S Geological Survey Open File Report.

Wesnousky, S. G., 2008, Displacement and Geometrical Characteristics of Earthquake Surface Ruptures: Issues and Implications for Seismic-Hazard Analysis and the Process of Earthquake Rupture: Bulletin of the Seismological Society of America, v. 98, no. 4, p. 1609-1632.

Zielke, O., and Arrowsmith, J. R., 2008, Depth variation of coseismic stress drop explains bimodal earthquake magnitude-frequency distribution: Geophysical Research Letters, v. 35, no. 24.

Zielke, O., Arrowsmith, J. R., Ludwig, L. G., and Akciz, S. O., 2010, Slip in the 1857 and earlier large earthquakes along the Carrizo Plain, San Andreas Fault (vol 327, pg 1119, 2010): Science, v. 329, no. 5990, p. 390-390.

Chapter 2

APPLICATIONS OF AIRBORNE AND TERRESTRIAL LASER SCANNING TO PALEOSEISMOLOGY

ABSTRACT

Paleoseismic investigations aim to document past earthquake characteristics such as rupture location, frequency, distribution of slip, and ground shaking intensity – critical parameters for improved understanding of earthquake processes and refined earthquake forecasts. These investigations increasingly rely on high-resolution (<1 m) digital elevation models (DEMs) to measure earthquake-related ground deformation and perform process-oriented analyses. Three case studies demonstrate airborne and terrestrial laser scanning (ALS and TLS) for paleoseismic research: (1) Rapid production of accurate, high-resolution, and georeferenced three-dimensional (3D) orthophotographs of stratigraphic and fault relationships in trench exposures. TLS scans reduced the preparation time of the trench and provided 3D visualization and reconstruction of strata, contacts, and permanent digital archival of the trench. (2) Quantification of fault scarp degradation rates using repeat topographic surveys. The topographic surveys of the scarps formed in the 1992 Landers (California) earthquake documented the cm-scale erosional landforms developed by repeated winter storm-driven erosion, particularly in narrow channels crossing the surface rupture. Vertical and headward incision rates of channels reached up to ~6.25 cm/yr and ~62.5 cm/yr, respectively. (3) Characterization of the 3D shape and geomorphic setting of precariously balanced rocks (PBRs) that serve as negative indicators for strong ground motions. Landscape morphometry computed from ALS-derived DEMs showed that PBRs are preserved on hillslope angles between 10°-40°

and contributing areas (per unit contour length) between 5 m^2/m and 30 m^2/m. This situation refines interpretations of PBR exhumation rates and thus their effectiveness as paleoseismometers. In summary, given that earthquakes disrupt Earth's surface at cm to m scales and that depositional and erosional responses typically operate on similar scales, ALS and TLS provide the absolute measurement capability sufficient to characterize these changes in challenging geometric arrangements, and thus demonstrate their value as effective analytical tools in paleoseismology.

INTRODUCTION

Determining the location, magnitude, rupture frequency, and associated ground motions of past earthquakes is a necessary step toward the formulation of accurate earthquake forecasts (e.g., WGCEP, 2008). Earthquake ruptures disrupt Earth's topography and surface process responses (i.e. erosion and deposition) to this deformation operate at cm to m scales. The accurate measurement of earthquake-induced topographic deformation and the associated geomorphic process response rates in complex geometrical arrangements is a necessary step toward characterizing earthquakes and refining earthquake forecasts.

The detail and accuracy of digital topographic data collected by light detection and ranging (LiDAR) instruments provide an opportunity to quantitatively analyze earthquake-produced surface deformation. In paleoseismology, two primary LiDAR platforms are employed: airborne and terrestrial laser scanning (Fig. 2.1). Airborne laser scanning (ALS) employs an aircraft-mounted laser scanner that scans topography in side-to-side swaths perpendicular to the aircraft's flight path. Typical scan rates range from tens to several hundred kHz. The orientation (yaw, pitch, and roll) of the aircraft is monitored by an on-board inertial navigation measurement unit, and its location is determined by a high-precision kinematic global positioning system (GPS; El-Sheimy et al., 2005; Carter et al., 2007; Shan et al., 2007). Post processing places the LiDAR data in a global reference frame as a point cloud of the laser returns with typical shot densities >1 m^{-2} (Fig. 2.1). Recent ALS campaigns have yielded digital representations of topography at resolutions sufficient to make measurements of earthquake-related surface deformation (e.g., Hudnut et al., 2002; Bevis et al., 2005; Oskin et al., 2007; Prentice et al., 2009;

DeLong et al., 2010; Hilley et al., 2010; Oskin et al., 2010a; Oskin et al., 2010b; Oskin et al., 2012). For example, ALS effectively depicts fault trace geometries and stream channels that are offset by structures such as the San Andreas fault (SAF; e.g., Arrowsmith and Zielke, 2009; DeLong et al., 2010). Systematic analyses of these data reveal geomorphic observations that are barely perceivable in the field, but can fundamentally change our inferences about paleoseismic records and fault segmentation (e.g., Zielke et al., 2010). Airborne laser scanning also assists in characterizing paleoseismic study sites by defining the local tectonic geomorphology of paleoseismic trench data (e.g., offset alluvial fans, pressure ridges, sags; e.g., Akçiz et al., 2010; Toké et al., 2011) and aiding in the location of potential paleoseismic sites.

Terrestrial laser scanning (TLS) systems employ a tripod-mounted laser scanner operated from various user-selected and near-field positions to ensure complete scan coverage of the feature of interest. Reflective targets with known geographic coordinates placed around the feature are used to align the final point cloud and place it in a global reference frame (Fig. 2.1). Shot densities for TLS point clouds can be $>10^4$ m^{-2} and the acquisition geometry provides a true three-dimensional (3D) representation of the scanned feature. Additionally, TLS systems employ high-resolution digital color photography where point attributes such as red-green-blue (RGB) values acquired by a TLS-mounted digital camera are used to color the point clouds and produce photorealistic images.

The utility of ALS and TLS datasets for visualization and analysis is often demonstrated using gridded digital elevation models (DEMs) that are generated from the spatially heterogeneous point clouds (El-Sheimy et al., 2005). Where the point spacing is

less than the desired resolution of the DEM, a local binning algorithm is applied to compute values within a specified search radius, *r*, at each node and a predefined mathematical function (e.g., mean, minimum, maximum, inverse distance weighting; IDW; El-Sheimy et al., 2005). For the ALS and TLS analysis presented here, we used IDW ($1/r^2$) and appropriate search radii to generate our high-resolution DEMs.

In this paper, we present three case studies to demonstrate the utility of ALS and TLS in paleoseismic research (Fig. 2.2). The first case study employs TLS in a paleoseismic investigation of the SAF in the Carrizo Plain. Trenches excavated perpendicular to the SAF reveal fractures and coseismically disrupted strata, while fault-parallel trenches are excavated across stream channels and alluvial fans to provide information about the history of aggradation, degradation, and channel geometry. Datable samples from both types of trenches constrain the timing of earthquakes and incision events. Next, we explore the utility of TLS in monitoring the geomorphic evolution of part of the 1992 M_w 7.3 Landers, California, earthquake fault scarp. Coseismically generated fault scarps provide information about the timing, frequency, and extent of the earthquakes that produced them. By assessing the initial forms and tracking the subsequent morphologic modification of these landforms, information about the earthquake's timing and recurrence may be determined (e.g., Nash, 1980; Arrowsmith and Rhodes, 1994; Arrowsmith et al., 1996). Finally, we present ALS and TLS data that characterize the geomorphic setting and 3D form of precariously balanced rocks (PBRs). By serving as negative indicators for earthquake-induced strong ground motions, fragile geologic features such as PBRs provide information about past ground motions, their geographic extent, and intensity (Brune, 1993a, b, 1994, 1996; Brune and Whitney, 2000;

Brune et al., 2006). The geologic and geomorphic processes that operate in all of our case studies span spatiotemporal scales that range from cm to hundreds of m and decades to millennia. The case studies demonstrate TLS and ALS as promising technologies that provide a framework upon which the efficient and accurate characterization of earthquake processes may be constructed over a range of spatiotemporal scales.

BACKGROUND

Paleoseismic Trenches and Offset Geomorphic Markers

Conventional paleoseismic logging of structures, strata, and samples is typically conducted either manually (e.g., tape measure and pencil on mm-grid paper) or on digital photomosaics of trench walls (McCalpin, 2009). The latter method involves taking up to hundreds of digital photographs perpendicular to the trench walls and creating a digital photomosaic of the stratigraphy and structures exposed in the trench walls. The footprint of each photograph depends on the aperture angle of the lens and the distance between the wall and the camera. In conventional 1 m-wide trenches, this footprint is approximately 1 m x 0.5 m. The final mosaics are then used as base maps on which the trench walls are logged. This method has several time-consuming drawbacks. For example, lens distortion introduces mismatches between photograph edges that lead to spatial distortions in the photomosaic. Similarly, unwanted parallax effects resulting from large vertical and horizontal photograph spacing lead to further spatial distortions in the final photomosaic. These problems are exaggerated by trench walls that have large surface irregularities, thereby introducing more geometrical inaccuracies in the final photomosaics. Issues such as these cannot be rectified without extensive post processing of the photographs.

Paleoseismic investigations also include topographic surveys of paleoseismic sites for context or offset geomorphic markers (e.g., stream channels and terraces) that provide information about earthquake-generated vertical and lateral displacements. Conventional methods for measuring these features include performing dense total station surveys. Such surveys may consume many person hours to acquire a sufficiently large number of point measurements from which an adequate surface model of the offset marker can be made.

Fault Scarp Formation and Degradation

Surface-rupturing earthquakes often produce initially subvertical fault scarps that degrade to their angle of repose over time by diffusive processes (e.g., Wallace, 1977; Hanks et al., 1984; Pierce and Colman, 1986; Stewart and Hancock, 1990; Arrowsmith and Rhodes, 1994; Arrowsmith et al., 1998; Hanks, 2000). Stream channels crossing these scarps are steepened and the response is more vigorous than those portions of the landscape not dominated by surface runoff. Typical scarp modification occurs in three stages (Arrowsmith and Rhodes, 2000): (1) “set-up”: pre-earthquake drainage network upslope of the scarp is re-established and flow patterns are redefined, (2) “integration”: re-establishment of a connected drainage network via channel capture and multiple incisions that occurred across the scarp, and (3) “development”: establishment of the channel flow paths that extend headward into the drainage basin. The rate at which each stage modifies the fault scarp depends on climate, the complexity of the scarp’s initial form, and the geometry of the drainage basin. Post-earthquake monitoring of scarp degradation provides an essential step toward understanding the evolution of fault scarps. In addition, it helps evaluate the veracity of landscape evolution models to quantitatively

extract temporal information about the recurrence of earthquakes from landscape form (e.g., Gilbert, 1877; Davis, 1892, 1899; Gilbert, 1909; Hanks et al., 1984; Hilley and Arrowsmith, 2001, 2003).

Precariously Balanced Rocks

Fragile geologic features such as PBRs (Fig. 2.3) provide information about the timing of past ground motions, their geographic extent, and their intensity (Brune, 1993a, b, 1994, 1996; Brune and Whitney, 2000; Brune et al., 2006). The exposure time of a PBR's basal contact with its pedestal is a proxy for the time since the PBR has remained balanced following its exhumation to the ground surface. Knowing the exposure time of the PBR's pedestal aids in reconstructing its exhumation history using surface exposure dating methods (e.g., Bell et al., 1998; Stirling et al., 2002; Stirling and Anooshehpoor, 2006; Rood et al., 2008; Stirling, 2008; Rood et al., 2009). However, a number of geomorphic factors can affect the surface exposure ages of a PBR and its pedestal (Heimsath et al., 2001; Haddad, 2010), and therefore the time since the PBR has been balanced. For example, the rates of soil production from bedrock and downslope soil transport are controlled by geomorphic parameters such as hillslope gradient and upslope drainage area (Gilbert, 1877, 1909; Penck, 1953; Schumm, 1967; Kirkby, 1971). These parameters are typically not considered in cosmogenically determined exhumation histories of PBRs. Therefore, assessing the local geomorphic settings of PBRs is important to defining their utility as physical validators of past ground motions.

A PBR's 3D form and geometry control its static stability and survivability during earthquakes (Purvance, 2005; Purvance et al., 2008a). Furthermore, the PBR's stability provides information about the upper limits of past earthquake-induced ground motions

that have occurred since the exposure of the PBR's pedestal (e.g., Shi et al., 1996). Conventional methods for estimating the 3D form of a PBR involve photogrammetry (e.g., Anooshehpoor et al., 2007; Anooshehpoor et al., 2009). In this process, paper targets are attached to the PBR and up to hundreds of photographs are acquired from multiple viewpoints. Photogrammetric alignment techniques are then used to generate surface models of the PBR from which its 3D stability may be computed. A drawback to this method is its inability to accurately document the basal contact between the PBR and its pedestal. Because the geometry of the basal contact is integral to a PBR's rocking response to ground motions (Purvance, 2005; Purvance et al., 2008a; Purvance et al., 2008b), uncertainties can be introduced in applying measured seismic waveforms to documented PBRs (e.g., Hudnut et al., 2009a; Hudnut et al., 2009b).

METHODS

Case Study I: Carrizo Plain

Our first study site is located on the Bidart Fan in the Carrizo Plain section of the southern SAF (Figs. 2.2 and 2.4), which last ruptured in 1857. Data from over 20 trenches that have been excavated since the late 1980s (Grant and Sieh, 1994; Akçiz et al., 2009; Akçiz et al., 2010) suggest that earthquakes along the SAF that ruptured the Carrizo Plain section were on average about every 90 years and caused surface displacements that ranged between ~1 m and ~5.5 m, at least during the last 700 years (Grant Ludwig et al., 2010; Zielke et al., 2010). These results call into question whether or not earthquake recurrence along the SAF strictly follows the characteristic earthquake model (e.g., Schwartz and Coppersmith, 1984; Sieh and Jahns, 1984). The first goal of this case study is to demonstrate the utility of TLS at efficiently producing an accurate

base image of paleoseismic trench walls. The second goal of this case study is to demonstrate how TLS can aid in measuring very subtle geomorphic markers by scanning a low-relief channel that crosses the SAF.

We implemented two TLS setups at the Bidart Fan site in 2009. The first included scanning a 5 m wide section of the southwest wall of a 3.5 m deep fault-parallel trench that exposed the stratigraphy of an offset stream channel (BDT18 in Fig. 2.4). The second setup included scans of a stream channel that crosses the SAF (BDT19 in Fig. 2.4). Both setups employed the short-range Zoller+Fröhlich (Z+F) Imager 5006i terrestrial laser scanner. Trench BDT18 was scanned at three equally spaced depths at which sets of four scans were performed. All scans were aligned to a single point cloud in the Z+F LaserControl point cloud registration software. Scan alignments were aided by targets that were strategically placed in the trench so that at least four targets were visible from each scan viewpoint. Each scan also included the acquisition of high-resolution digital photographs of the trench walls. For BDT19, the scanner was mounted on a standard survey tripod and employed in ten scan positions. All scans were registered using the Z+F LaserControl software to a single point cloud that totaled over 21 million points. A 0.1 m DEM was generated from the point cloud using IDW binning and a 1 m search radius. We also employed a low-altitude (~200 m above ground level) camera lofted by balloon to provide high-resolution color photographs of the channel.

Case Study II: Landers Earthquake Fault Scarp

This case study presents our observations of the initial form and subsequent geomorphic modification of the Landers fault scarp with the goal of evaluating the TLS method for measuring the scarp's erosion rates, upstream drainage network evolution,

and knickzone migration rates nearly two decades following the 28 June 1992 Landers, California, earthquake (M_w 7.3; Figs. 2.2 and 2.5). Repeat surveys of the scarp were begun three days following the earthquake, followed by surveys in late 1992, mid 1993, mid 1994, mid 1995, mid 1997, late 1998, and early 2000 using conventional fault scarp measurement techniques (e.g., morphologic mapping, ground stereo photography, topographic, and channel profile surveys with an optical total station; Arrowsmith and Rhodes, 1994, 2000). In mid 2008, we repeated our monitoring efforts using TLS scans of the scarp.

In 1992, we established a control network and over the years focused on several channels that crossed the scarp (Fig. 2.5). In 2008, we used a Reigl LPM 321 terrestrial laser scanner to scan the study site. Eleven scan positions were tied together with as many as 18 control points and a total of 8.8 million points were collected. Shot densities varied from ~1 to 3.8 $x10^4$ m^{-2} (Fig. 2.5). Given the absolute GPS control from 2008, we rotated and translated the prior survey data into the 2008 UTM Zone 11 NAD83 coordinate system using least squares (<10 cm error in the network adjustments). Despite the numerous advantages of the TLS system for topographic survey (e.g., scanning in a few seconds what normally takes an entire day to do manually), the TLS could not illuminate the walls or floors of the narrow (few dm-wide), incised, and tortuous knick channels in the most rapidly eroding portions of the scarps. We augmented the scans in the knickpoint channels with kinematic GPS measures of points (~1 cm accuracy) using a plumb pole. Our study focuses on Gully 6 (Fig. 2.5) which has the greatest erosion signal and highest quality network adjustment of pre-2008 survey points. We extracted 416 thousand points from the point cloud (TLS and GPS) and compared them with the 100

points measured at Gully 6 in the summer of 1993 (after modest winter erosion of the fault scarp). These comparisons were made in both projected cross sections of the points with knowledge that the GPS points indicated the local minima along the knick channels and by subtracting 5 cm DEMs with the same grid node positions to produce a 1993 to 2008 erosion map.

Case Study III: Precariously Balanced Rocks

Our PBR study site is located in the Granite Dells precarious rock zone (GDPRZ), central Arizona (Fig. 2.2 and 2.6). The primary PBR-forming rock unit is the Proterozoic Dells Granite (1.110 Ga – 1.395 Ga; Dewitt et al., 2008; outlined in Fig. 2.6). With the exception of local compositional variations, the Dells Granite is as a massive, medium- to coarse-grained locally porphyritic granite. It forms a prominent pediment surface that is dissected by angular, joint-controlled drainage networks. A large population of PBRs resides in the GDPRZ on bedrock hillslopes that flank these drainages (Haddad, 2010). The first goal of this case study is to use ALS-generated DEMs to document the geomorphic setting of PBRs. The second goal of this case study is to demonstrate the effectiveness of TLS in illuminating the PBR's basal contact.

Landscape Morphometry

Airborne laser scanning data for this site were collected by the National Center for Airborne Laser Mapping (NCALM) and covered the entirety of the GDPRZ. The average aircraft elevation was 850 m above ground level. Over 350 million laser returns were collected, covering ~35 km^2 and an average point density of 11.4 m^{-2}. A 0.25 m DEM was then generated from the ALS data using the IDW algorithm and a 1 m search radius (Fig. 2.6; El-Sheimy et al., 2005). Finally, ground examinations were performed

on 261 PBRs and were located using a hand-held GPS unit (+/-2 m horizontal accuracy). The resolution of the DEM was fine enough to locate only large (>1 m diameter) PBRs. However, small PBRs were severely smoothed out by the DEM algorithm and thus not recognizable without the aid of high-resolution color aerial photographs.

Local hillslope angles were computing from the DEM by fitting a plane to a 3 x 3 pixel computation window around each DEM and calculating the maximum slope value of the plane and assigning it to the node. The computation window then moves to the adjacent central cell and this process is repeated (DeMers, 2002). Stream channels were defined as grid cells using an upslope contributing area >100 m^2 and the D∞ flow routing algorithm (Tarboton, 1997). The local hillslope angle and contributing area of each PBR *x-y* coordinate were then extracted from the gradient and contributing area rasters and plotted.

PBR Basal Contact Imaging

We used TLS to scan one of the surveyed PBRs in the GDPRZ (Fig. 2.7). This provided a preliminary assessment of the PBR's 3D static stability and tested the effectiveness of TLS in capturing the PBR's basal contact. We used a tripod-mounted Riegl LPM 321 terrestrial laser scanner and scanned the PBR from six positions. All scans were aligned using the Riegl RiProfile software and the aid of six reflective targets. The final point cloud totaled ~3.4 million points.

RESULTS AND DISCUSSION

Case Study I: Carrizo Plain

Trench BDT18 Scans

The final point cloud of our BDT18 trench scans totaled over 129 million points and was used to produce seamless color orthorectified base images of the trench walls (Fig. 2.8). Even though the scanner used a 5 MP digital camera compared to our 8 MP point-and-shoot camera with which we compared the results, overall image quality at 1:10-scale image printouts were not noticeably different (Fig. 2.8). While the TLS-produced images did not provide new insight or help to automate the identification of individual stratigraphic units, the efficiency and ease of orthomosaic production was greatly appreciated by the trench loggers. For example, the need for setting up reference grids was eliminated because the orthomosaics were automatically scaled by the scanner. Also, the subjectivity that is normally present when logging continuous contact traces that cross multiple mismatched photographs (by as much as 1-3 mm at the 1:10 scale) was significantly reduced (Fig. 2.8). Furthermore, total station surveys of contacts and locations of important features such as samples were not needed because the TLS-generated base image was locally georeferenced by the scanner. The paleoseismic logs, contacts, and sample locations can be placed in a global coordinate system such that a complete integration of these data with other paleoseismic datasets is possible. This high-accuracy geometric control is important for the 3D reconstruction of deformed features by retrodeforming offset channels and measuring vertical and horizontal components of displacement.

Trench BDT19 Scans

A 0.1-m DEM was prepared using the point cloud data obtained from the combined BDT19 scans (Fig. 2.9). The TLS-generated DEM is superior to the ALS-generated DEM in the clarity with which the stream channel is shown (compare Figs. 2.4 and 2.9). A ~5 m dextral bend in the channel is observable from the TLS-generated DEM as it crosses the SAF. However, whether this bend is a result of the most recent earthquake to rupture this section of the SAF or a deflection that occurred after this earthquake is inconclusive. Our TLS-generated DEM will aid in planning future 3D excavations across this channel to investigate its stratigraphy and relationship with past earthquakes in greater detail. Unlike the setup inside the trenches described above, our TLS scans of the channel could not automatically assign an RGB value for each scan point to generate a photomosaic of the offset channel. Our inability to keep the camera in the shade at all times caused sharp contrasts in the digital images during 360° scans and did not provide enough RGB data points to be locally referenced. However, the TLS-generated DEM provided a detailed topographic surface to which our low-altitude balloon aerial photographs were georeferenced and draped (Fig. 2.10).

Case Study II: Landers Earthquake Fault Scarp

The 2008 topographic survey provides a spectacular view of the original forms and initial modifications of the 16 year-old fault scarps produced in the Landers earthquake (Arrowsmith and Rhodes, 1994; Fig. 2.5). The discontinuous main and secondary scarps and the erosional responses to the ~1 m uplift of the northeastern block are well illustrated by the TLS data. Where runoff is poorly channelized, the scarps have begun to fail by block- and grain-scale diffusive processes. The largest changes are

evident in the channels that cross the scarp. Gully 6 is representative of that response (Fig. 2.11); the knick channels are ~10-20 cm wide and have incised ~1 m into the displaced block, resulting in a vertical incision rate of ~6.25 cm/yr of the knickpoint formed in Gully 6. The long profiles of the gully thalwegs now approach their pre-seismic forms. At Gully 6, the vertical displacement of the channel across the fault created a knickpoint that has moved upslope about 10 m from the scarp, which corresponds to a headward incision rate of ~62.5 cm/yr. The thalweg profile remains irregular with the upslope knickpoint accommodating most of the relief change. Above the knickpoint, an erosional zone of a few 10s of cm communicates the knickpoint erosion headward (e.g., Gardner, 1983).

Case Study III: Precariously Balanced Rocks

Geomorphic Characterization of PBRs

We plotted the values of local hillslope angle versus upslope contributing area for all of the surveyed PBRs (Fig. 2.12). Only slope-area values that were extracted from the PBR locations are plotted (green dots). The remaining slope-area values are binned into a 2-dimensional histogram to reduce clutter, and the density of the slope-area values is plotted as a color map. The surveyed PBRs are clustered in the bottom-right corner of slope-area space. Contributing areas per unit contour length for PBRs range between 5 m^2/m and 30 m^2/m. Local hillslope angles on which PBRs are situated range between 10° and 40°.

The stark difference between the slope-area plot of the PBR landscape and that of a soil-mantled landscape likely reflects the differences in the geomorphic processes that operate in either setting. Slope-area plots for soil-mantled landscapes exhibit a

boomerang pattern that capture convexo-concave hillslopes bounded by stream channel elements. This pattern consists of slope values that vary inversely with contributing area for convergent parts of the landscape, and vice versa for divergent landscape elements (Dietrich et al., 1992; Roering et al., 1999). However, the wide range of slope-area values that we extracted from our DEM is indicative of the etched topographic nature of the GDPRZ, which is dominated by joint-controlled angular drainage networks and hillslope gradients that range between near vertical and near horizontal (e.g., Twidale, 1982). Therefore, our application of the slope-area threshold approach (e.g., Dietrich et al., 1992) must be made with caution because it assumes that the landscape is in dynamic denudational equilibrium. As a result, present-day geomorphic processes bounded by the landform process thresholds may not apply to our PBRs because they are preserved in pre-existing etched landscapes. However, the slope-area approach allows us to extract fundamental information about the present-day geomorphic situation, preservation, and exhumation histories of PBRs on a first-order basis.

The preservation potential of PBRs appears to be controlled by their location in a drainage basin. Most of the PBRs in the GDPRZ are located in the upper reaches of catchments near drainage divides. This may indicate that the geomorphic conditions in the upper reaches of a drainage basin are conducive to forming and preserving PBRs. Because spatially variable soil production and transport rates affect the subsurface formation of corestones from bedrock (e.g., Heimsath et al., 2001), geomorphic rates in the upper reaches of catchments may be ideal for PBRs to survive subsurface chemical attack and their subsequent exhumation. After exhumation, the survival of the PBRs is controlled by the local geomorphology (e.g., hillslope gradient and upslope drainage

area) during the evolution of the catchment. These geomorphic complexities illustrate that caution should be taken when PBR exhumation histories are reconstructed from surface exposure ages because these histories do not account for the overall geomorphic setting of the PBRs in a drainage basin, and thus do not provide a complete understanding of the processes that act to exhume the PBRs.

PBR Basal Contact Assessment

The PBR's 3D form is captured with great detail that shows the intricacies of the PBR's basal contact (Fig. 2.13). Closer examination of this contact shows that a significant overhang exists between the PBR's width and its basal contact. Detailed inspection of this contact would not have been possible with the use of conventional photogrammetry. Therefore, an overestimation in the width of the PBR's basal contact, and thus its stability, may have likely resulted from photogrammetric methods. Our scans, however, show that careful documentation of this contact is made possible using TLS and that uncertainty in the PBR's 3D stability can be significantly reduced.

CASE STUDY CONCLUSIONS

Our TLS work in the Carrizo Plain demonstrates that, with careful consideration to the scanner setup and lighting conditions, TLS is an effective tool for imaging subtle paleoseismic features. TLS-generated images produce superior base maps (in both functionality and geometric accuracy) on which trenches can be logged when compared to their photomosaicked counterparts. For both sets of scans, TLS proved to be an efficient alternative to conventional surveying techniques and base image production from mosaicked photographs. In addition to its analytical value, a significant potential for TLS lies in its utility as a digital archival and educational tool in paleoseismic research.

Digital archives of trench records will facilitate reviews of paleoseismic interpretations by other members of the paleoseismological community. Furthermore, digital records of the trenches provide valuable educational tools for students who are engaged in paleoseismic trench interpretations and exercises.

Our results from the Landers fault scarp demonstrate that TLS is an effective tool for the rapid and detailed characterization of the original forms and evolution of earthquake-produced surface ruptures. Initially steep fault scarps begin to fail by block- and grain-scale diffusive processes. Vertical and headward incision rates of knickpoints in stream channels that cut across fault scarps can reach up to several cm/year and several dm/yr, respectively. This underlines the importance of rapidly documenting surface ruptures using TLS prior to their complete geomorphic degradation. Recent scans of the El Mayor-Cucupah M_w 7.2 earthquake in northern Baja California (Oskin et al., 2010a; Oskin et al., 2010b; Gold et al., 2012) alone and nested within ALS (Oskin et al., 2010a) have shown the exquisitely fine original character of the brittle deformation along the surface rupture. Repeat scans with TLS can also be used to measure the surface process response to the change in base level of local stream channels and postseismic surface deformation. Unlike our study, in which the original forms of scarps were represented crudely with manual surveys and roughly matched to dm-accuracy network adjustments, cm-accurate ultrahigh-resolution repeat TLS will measure those changes in an unprecedented manner. Not only can the original forms and initial geomorphic modifications be measured, but also postseismic changes can be measured in future high-resolution surface rupture studies with TLS (e.g., Wilkinson et al., 2010).

The ALS-derived DEMs allowed us to characterize PBRs geomorphically at the drainage basin scale. They showed that PBRs are preserved in the upper reaches of drainage basins on moderately steep hillslope gradients. Gentle hillslopes may not promote sufficient soil production rates to form the corestones prior to their exhumation as PBRs. Conversely, steep hillslopes may drive transport rates too high for the PBRs to remain preserved in a landscape. At a finer scale, surface and volumetric analyses from TLS may be used to validate the accuracy of 2-dimensional (2D) static stability estimators (e.g., Haddad, 2010) versus their 3D implementations (e.g., Purvance, 2005; Anooshehpoor et al., 2007; Anooshehpoor et al., 2009). Because the stability and survivability of PBRs during ground motion events are controlled by the geometry of a PBR's basal contact, TLS scans of PBRs provide valuable views into the complexity of the PBR's basal contact. Therefore, high-resolution TLS-derived surface models of PBRs can refine simulations of coseismic ground motions (e.g., Hudnut et al., 2009a; Hudnut et al., 2009b).

SUMMARY

Paleoseismic research is significantly enhanced by the use of airborne and terrestrial LiDAR data. Our three case studies include examples of these data at different spatial scales. A nested combination of ALS and TLS will become an integral paleoseismic tool to study m- and cm-scale fault-related deformation. In addition, ALS and TLS can refine our understanding of the geologic and geomorphic processes that act within the earthquake cycle by allowing us to study these processes at multiple spatiotemporal scales and at the appropriately fine (cm to dm) scales at which the

relevant surface and deformational processes operate. The work presented here should aid paleoseismologists in planning ALS and/or TLS campaigns for future investigations.

A challenging yet important task in using a nested LiDAR approach for paleoseismic research is the multiscale integration of DEM preparation and distribution capabilities. Facilities such as OpenTopography (http://www.opentopography.org – where most of the data discussed here are available) facilitate this task for ALS data and are spearheading the integration of TLS with ALS datasets to produce customized DEM products (e.g., Krishnan et al., 2011). The integration of these datasets with short-range photographic and multispectral imaging provides detailed material property information with excellent geometric control (e.g., Xu, 2000; Ragona et al., 2006). These integrated products enhance the interpretation and analysis of the 3D targets while allowing for their virtual reviews and digital archival. This integration will therefore be an important step toward the management of scientifically meaningful LiDAR datasets that have high resolution, accuracy, density, and spatial coverage. Such datasets will become important tools in paleoseismic efforts that aim to extract information about earthquakes from tectonically produced landscapes, thereby making ALS and TLS integral components of the paleoseismic toolbox. Finally, when coupled with powerful visualization tools (e.g., LiDAR Viewer (http://keckcaves.org/software/lidar/index.html), the educational value of these data becomes apparent. For example, bringing a surface rupture or an outcrop of the SAF into an educational setting in 3D significantly enhances student learning.

ACKNOWLEDGMENTS

We dedicate this paper to Kurt Frankel. Thank you to Kenneth Hudnut, an anonymous reviewer, and Carol Frost for providing constructive reviews that significantly benefitted this paper. We thank Carlos Aiken, Mohammed Al Farhan, and Lionel White from the University of Texas at Dallas Cybermapping Laboratory for their TLS support. David Phillips and UNAVCO provided technical and logistical support for our TLS campaigns. Special thanks to Susan Selkirk for generously providing her technical drafting expertise in Figure 2.1. Thank you to Lisa Grant Ludwig for making the trenching activities in the Carrizo Plain possible. We thank Kenneth Hudnut for spearheading the application of TLS in PBR research. Tariq Ahmed, Adam Gorecki, Derek Miller, and Benjamin Peterson provided valuable field assistance. Virginia Seaver generously provided access to the PBRs in Storm Ranch, Arizona. Major support for this work was provided by the National Science Foundation (NSF): Tectonics Program (EAR 0405900, EAR 0711518), Instrumentation and Facilities Program (INTERFACE; EAR 0651098), and OpenTopography (EAR 0930731, EAR 0930643). Additional support was provided by the U. S. Geological Survey (USGS) grant 07HQGR0092 and the Southern California Earthquake Center (SCEC). The SCEC is funded by NSF Cooperative Agreement EAR-0529922 and USGS Cooperative Agreement 07HQAG0008. This is SCEC contribution number 1631. Haddad was supported by a grant that was awarded jointly by the Arizona State University (ASU) Graduate & Professional Student Association, the ASU Office of the Vice President of Research & Economic Affairs, and the ASU Graduate College. The Granite Dells ALS data were collected by the NSF-funded National Center for Airborne Laser Mapping (NCALM) for a Seed Grant awarded

to Haddad. San Andreas fault ALS data were also collected by the NCALM for the B4 Project (Bevis et al., 2005).

FIGURES

Figure 2.1. Schematic illustration of LiDAR platforms and their applications in paleoseismic research. Airborne and terrestrial laser scanning (ALS and TLS) characterize earthquake-related deformation at scales that range from m to cm. ALS-derived digital topographic data illuminate m-scale fault-related structures (e.g., offset stream channels) and geomorphic elements of faulted topography (e.g., fault scarps). TLS-derived digital topographic data compliment ALS datasets by illuminating fault- and landscape-related components at cm to mm scales (e.g., paleoseismic trench walls, subtle geomorphic features, and fragile geologic features). Data from each platform are acquired in their local coordinate system (x_i, y_i, z_i). When combined in a global coordinate system (X, Y, Z), ALS and TLS form valuable additions to the paleoseismic toolbox because they allow for the accurate extraction of geometric and topographic information at multiple spatial scales. This nested approach also permits the analysis of geologic and geomorphic processes that operate during and after repeating earthquakes at appropriate measurement scales.

Figure 2.2. Seismotectonic settings of the studied paleoseismic sites. The Landers fault scarp (LFS) produced by the 1992 M_w 7.3 Landers (California) earthquake and the trenches and channels crossing the San Andreas fault (SAF) in the Carrizo Plain (CP) were scanned with TLS. Both ALS and TLS were used to scan precariously balanced rocks in the Granite Dells precarious rock zone (GDPRZ). Digital topographic data provide physiographic context and were accessed from the U.S. Geological Survey (USGS) Seamless Data Warehouse (http://seamless.usgs.gov/). Fault data were acquired

and modified from the USGS Quaternary Fault and Fold Database (http://earthquake.usgs.gov/hazards/qfaults/).

Figure 2.3. An example of a precariously balanced rock (PBR) in the Granite Dells precarious rock zone (Fig. 2.2). Scale is 0.2 m.

Figure 2.4. Hillshade of a 0.25 m ALS-derived DEM showing the location of our paleoseismic trenching activities in the Carrizo Plain (Fig. 2.2). The inset white corners correspond to the TLS-generated DEM in Fig. 2.5. Yellow boxes indicate excavations. BDT18 and BDT19 were the target of the TLS scans (Fig. 2.4 and Fig. 2.5). Solid white arrows delineate the SAF trace. White half arrows indicate dextral motion along the SAF. The DEM was prepared in the OpenTopography portal (http://www.opentopography.org). ALS data were collected by the NCALM for the B4 project (Bevis et al., 2005).

Figure 2.5. TLS scan (2008) of the Emerson fault zone surface rupture from the 1992 M_w 7.3 Landers, California, earthquake (Fig. 2.2). (A) Overview of a 0.1 m DEM and hillshade showing ~20 m local relief along the drainage basins whose lower ends were elevated about 1 m by the vertical component of offset in the earthquake. (B) Gully 2 shot density map overlain on hillshade from 0.1 m DEM showing high density of points on incising channel. (C) Gully 6 shot density map over hillshade from the 0.1 m DEM (see Fig. 2.11 for detailed analysis of erosion at this site). (D) 1998 balloon platform digital camera image georeferenced to the TLS DEM. Both C and D show the incising

and headward cutting knickpoints. The DEM was prepared in the OpenTopography portal (http://www.opentopography.org).

Figure 2.6. Color hillshade produced from an ALS-derived 0.25 m DEM of the Granite Dells precarious rock zone (GDPRZ). The GDPRZ is located in a prominent pediment that is formed in the Proterozoic Dells Granite pluton (outlined by a dashed white line). Yellow star indicates location of a PBR that was scanned using TLS (see Fig. 2.7 for location). Red dots indicate locations of the studied PBRs. The ALS data were collected by the NCALM (Haddad, 2010). The DEM was prepared in the OpenTopography portal (http://www.opentopography.org).

Figure 2.7. (A) Location map of the TLS-scanned PBR. It was scanned from six positions to fully capture its 3D form. The underlying hillshade was prepared from a 0.25 m ALS-generated DEM. (B) photographs of the TLS setup used for this PBR. Six 1.5 m-long polyvinyl chloride pipes with reflective tape attached to their tops were used as targets.

Figure 2.8. TLS scans of BDT18 (see Fig. 2.4 for location). Comparison between the base images generated by conventional photomosaicking (A) and TLS scans of a portion of BDT18's southeastern wall (B). Yellow stars indicate features common to both images and the trench log. The nearly seamless TLS-generated base image is geometrically superior to the photomosaic. Photograph edge mismatch is significantly reduced while continuous sedimentary units are easily demarcated in the TLS-generated image. (C) The

TLS setup used to scan the walls of BDT18. A Z+F laser scanner was operated from twelve positions in this trench (shown here on the trench floor). Fourteen targets (black and white checker-board patterns) were placed within the trench to aid in scan alignment. Plywood sheets were placed over the trench to provide even lighting conditions for the scanner's digital camera. (D) The paleoseismic log of the BDT18 offset channel.

Figure 2.9. Comparison between ALS- and TLS-generated digital elevation models (DEMs) of BDT19 (see Fig. 2.4 for location). (A) A hillshade prepared from a 0.25 m ALS-generated DEM of BDT19. Dashed white arrows show the trace of the SAF. White half arrows indicate dextral motion along the SAF. (B) A color hillshade of a 0.1 m TLS-generated DEM of the same area shown in A. Linear local highs around BDT19's box trenches are spoil piles that were excavated from the trench. Other features are vehicles and people. The white dashed lines outline a bend in a channel that crosses the SAF. Solid white arrows indicate the directions of the oblique viewpoints in Figure 2.10.

Figure 2.10. (A) Oblique views of a low-altitude aerial photograph of BDT19. The photograph was taken from a balloon-mounted digital camera and draped over the 0.1 m TLS-generated DEM to provide topographic context. The SAF is shown as a narrow zone of deformation (red polygon). (B) Comparison between an oblique view of the aerial photograph and a photograph that was taken at ground level from the same viewing direction. Such 3D representations of paleoseismic sites can be beneficial for peer reviews of paleoseismic interpretations, digital archival of trenches, and virtual field trips for educational activities.

Figure 2.11. Point cloud map and repeat topographic survey at Gully 6 (see Fig. 2.5 for location). (A) Points extracted from the 2008 TLS scan (black dots) were combined with kinematic GPS measurements from the tortuous and narrow knick channels (blue dots) to represent the 2008 topographic surface and compared to the 1993 survey points (red dots). (B) A narrow swath of the point cloud data were extracted and projected to a common reference plane. The kinematic GPS points (blue dots) indicate the minimum elevations along the channel profile within the swath and show the erosion in 15 years relative to the red points (1993 survey) and the black points showing relatively uneroded channel margins. (C) The 2008 DEM computed from the extracted TLS and GPS points (white dots) was subtracted from the 1993 survey points to produce an erosion map (5 cm/pixel). Maximum erosion in the 10-20 cm-wide knick channels is about 1 m and they have cut >10 m upstream between 1993 and 2008.

Figure 2.12. Hillslope angle versus upslope contributing area per unit contour length of landscape elements containing PBRs. Black dots are slope-area values for the landscapes plotted every 25^{th} point. Green dots are slope-area values for each PBR computed from a 5 m ALS-derived DEM. Most of the surveyed PBRs are located in contributing areas between 5 m/m^2-30 m/m^2 and local hillslope angles between 10° and 40° (indicted by dashed blue lines).

Figure 2.13. Oblique views of the point cloud representing the PBR scanned using TLS. Total point count shown is ~3.4 million. TLS illuminates the 3D complexities of the PBR's form and its basal contact (outlined in white at right).

Figure 2.1

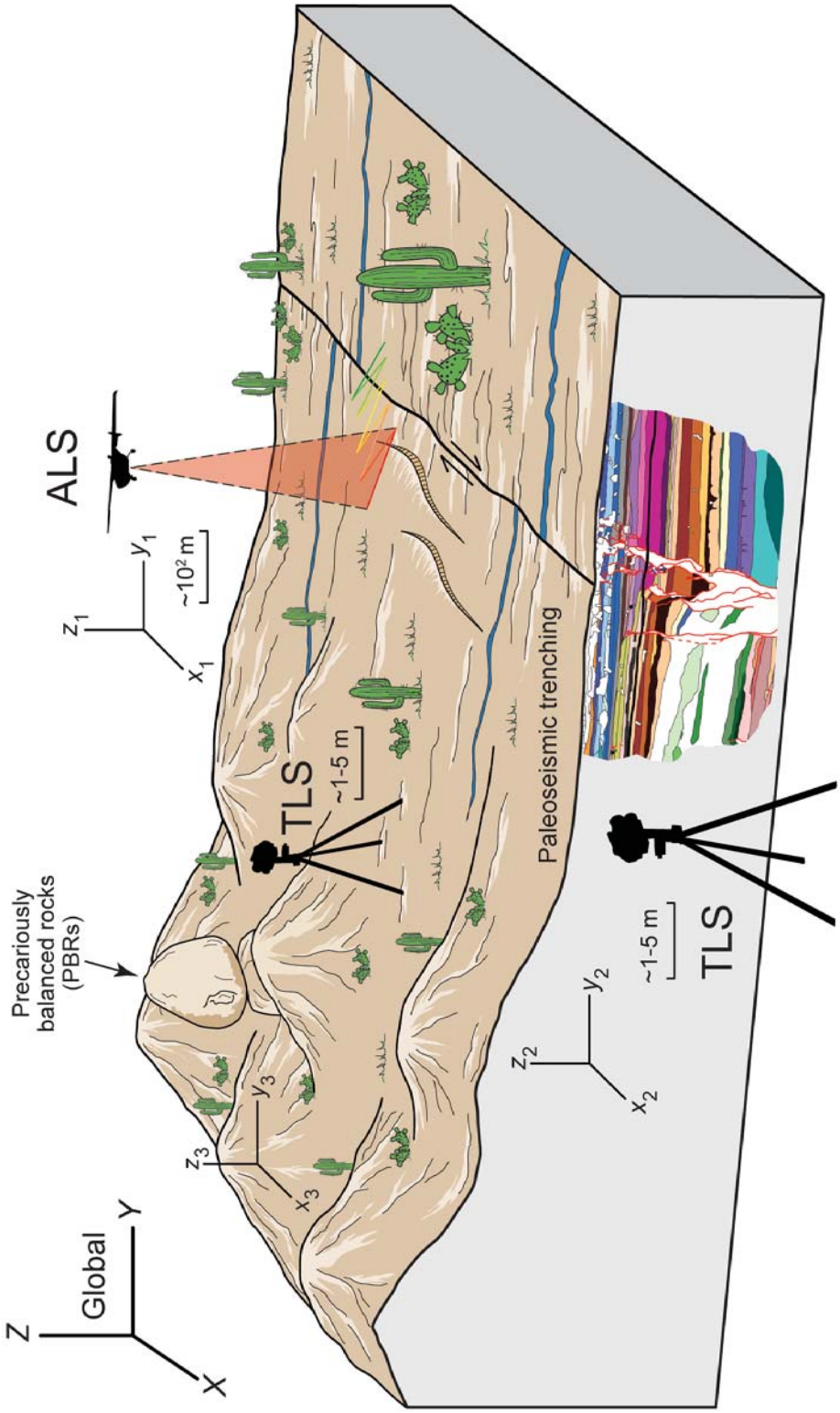
ALS
TLS
TLS
Paleoseismic trenching
Precariously balanced rocks (PBRs)
~10² m
~1-5 m
~1-5 m
Global
Z
Y
X
z_1
y_1
x_1
z_2
y_2
x_2
z_3
y_3
x_3

Figure 2.2

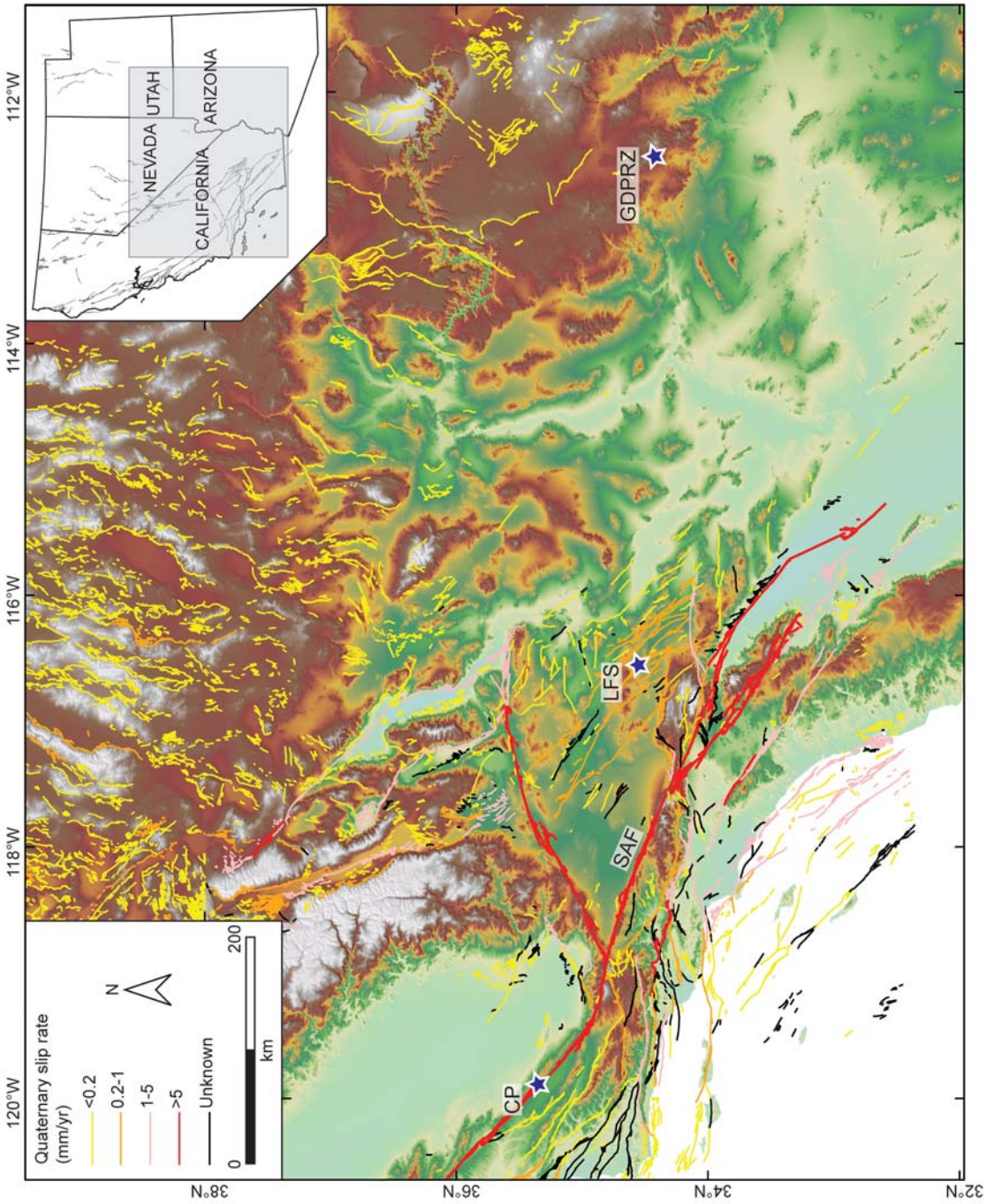
NEVADA
UTAH
ARIZONA
CALIFORNIA
GDPRZ
LFS
SAF
CP
Quaternary slip rate (mm/yr)
<0.2
0.2-1
1-5
>5
Unknown
N
0
200
km
112°W
114°W
116°W
118°W
120°W
38°N
36°N
34°N
32°N

Figure 2.3

Figure 2.4

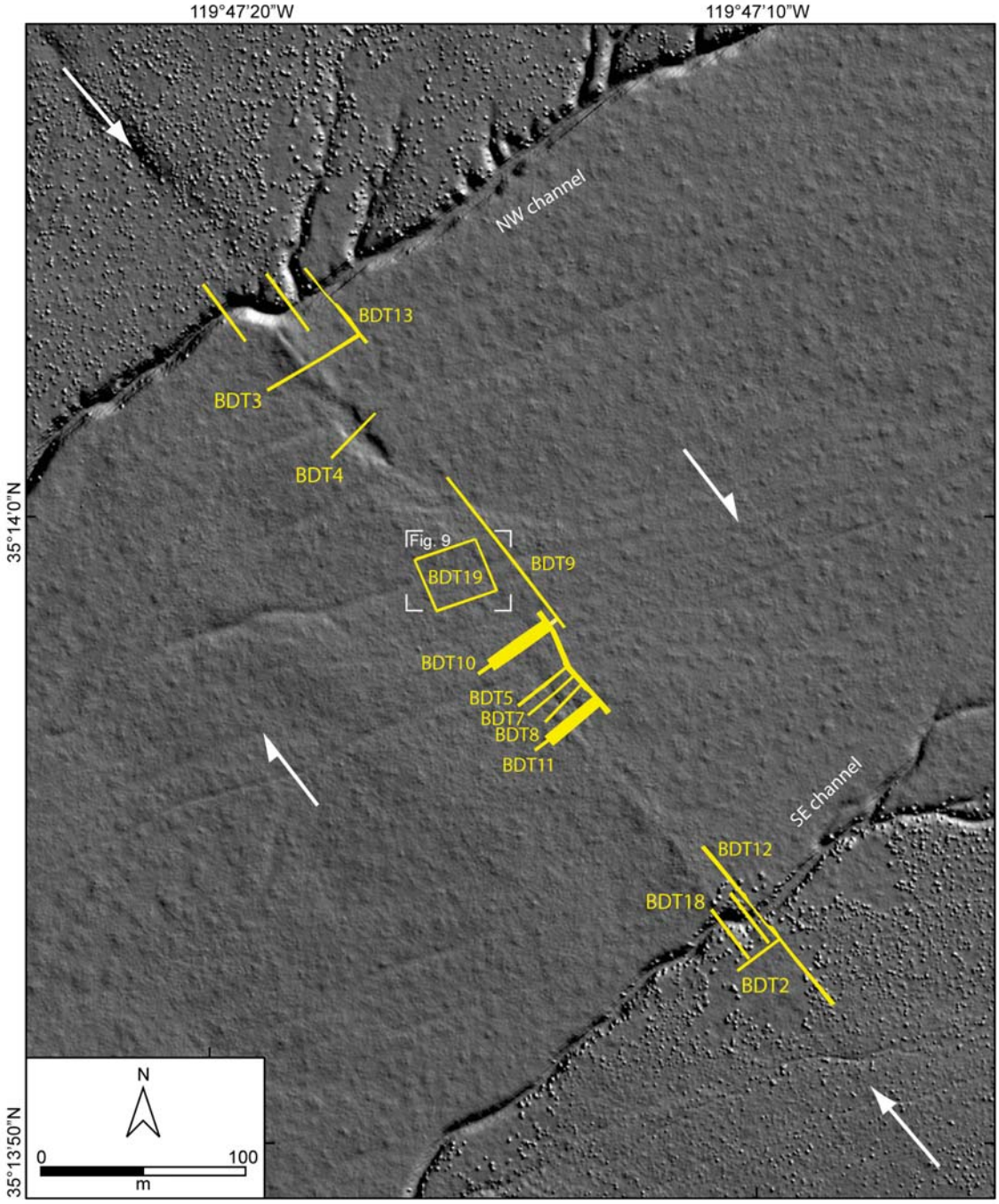
119°47'20"W
119°47'10"W
35°14'0"N
35°13'50"N
NW channel
SE channel
BDT13
BDT3
BDT4
Fig. 9
BDT19
BDT9
BDT10
BDT5
BDT7
BDT8
BDT11
BDT12
BDT18
BDT2
N
0
100
m

Figure 2.5

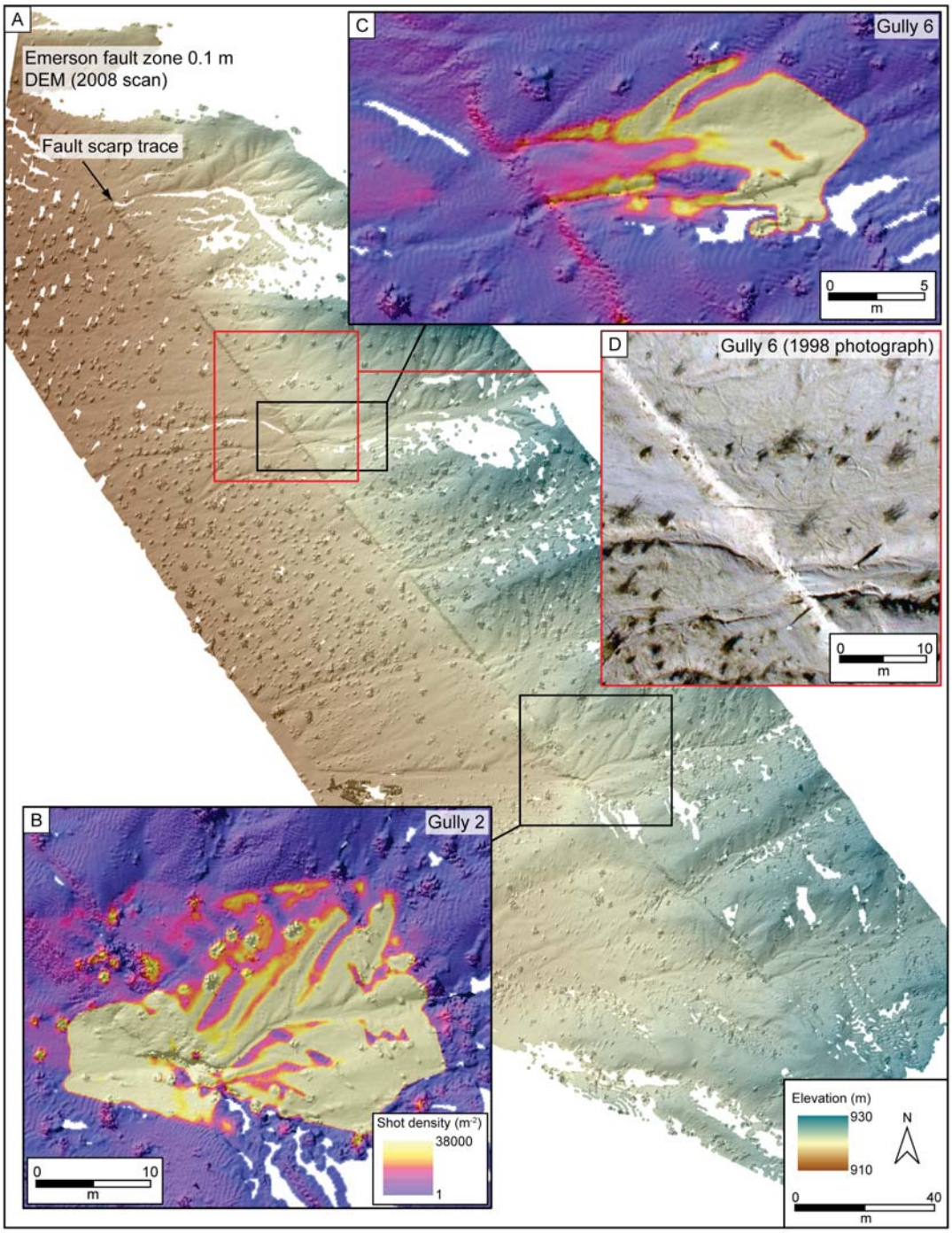
A
Emerson fault zone 0.1 m
DEM (2008 scan)
Fault scarp trace
C
Gully 6
0
5
m
D
Gully 6 (1998 photograph)
0
10
m
B
Gully 2
Shot density (m-2)
38000
1
0
10
m
Elevation (m)
930
910
N
0
40
m

Figure 2.6

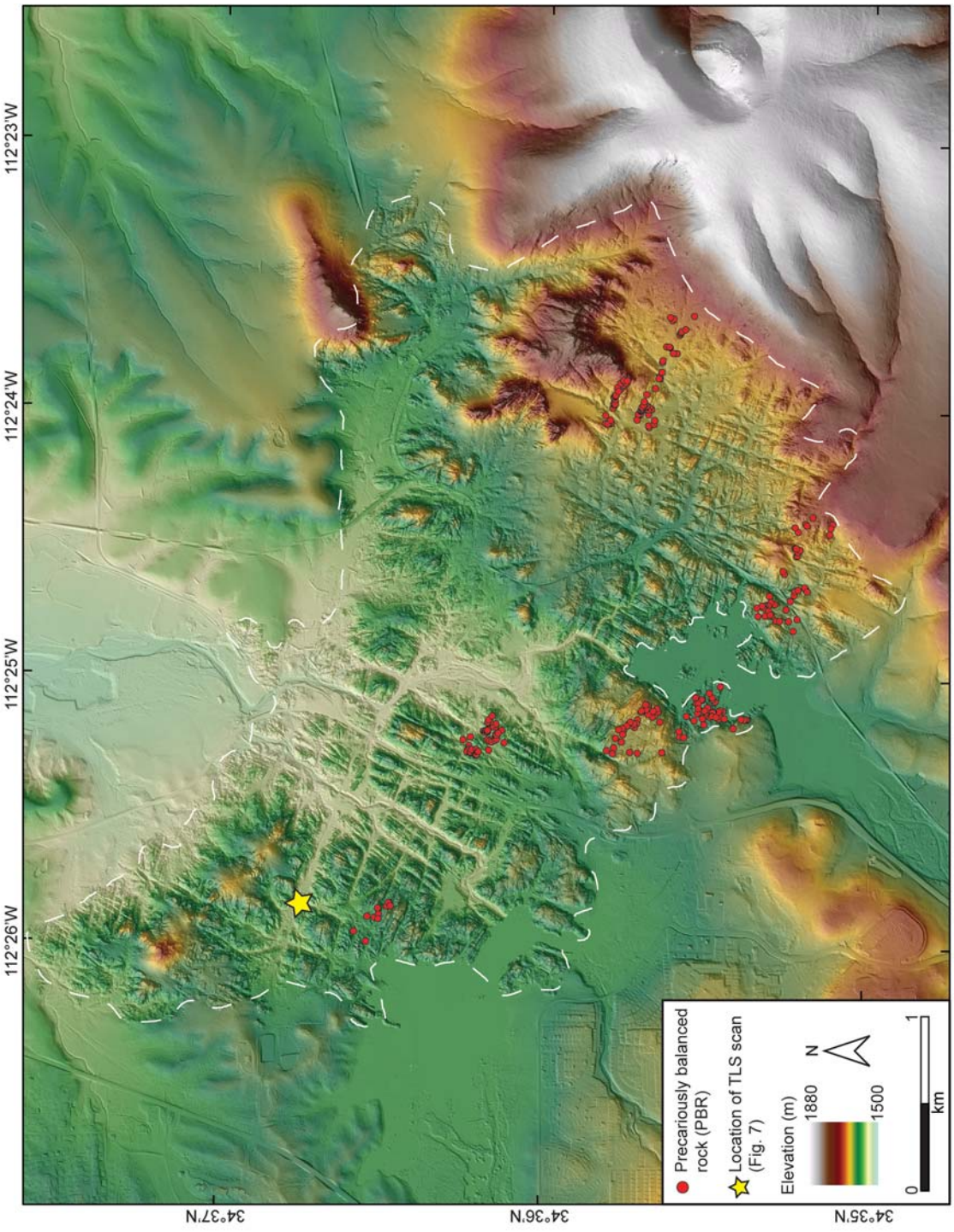
112°26'W
112°25'W
112°24'W
112°23'W
34°37'N
34°36'N
34°35'N
Precariously balanced rock (PBR)
Location of TLS scan (Fig. 7)
Elevation (m)
1880
1500
N
0
1
km

Figure 2.7

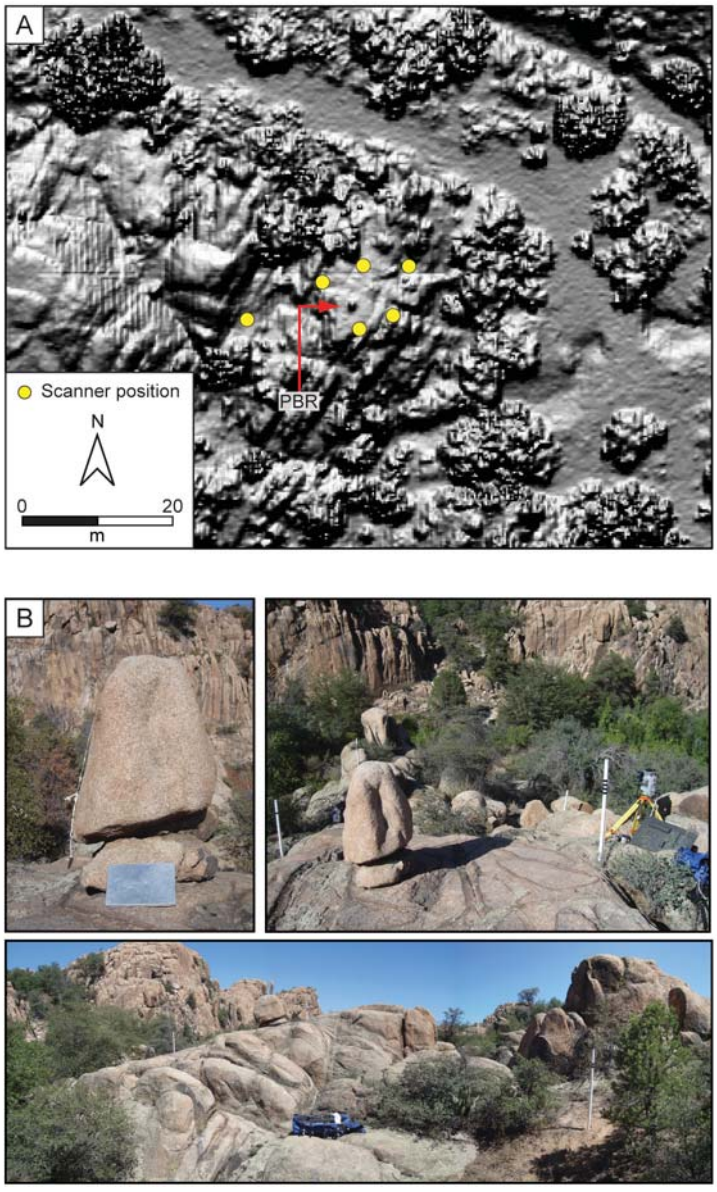

Figure 2.8

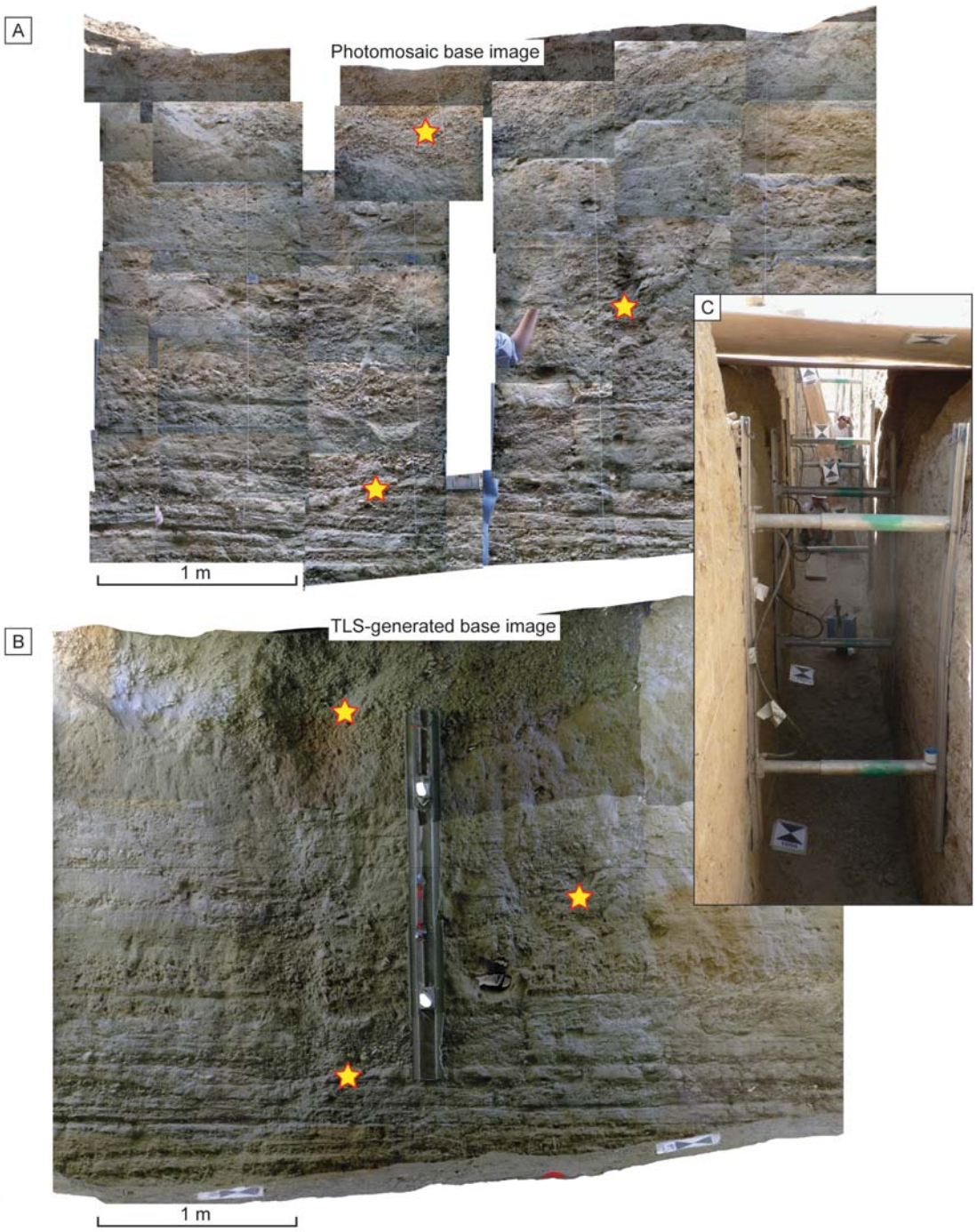

Figure 2.8 continued

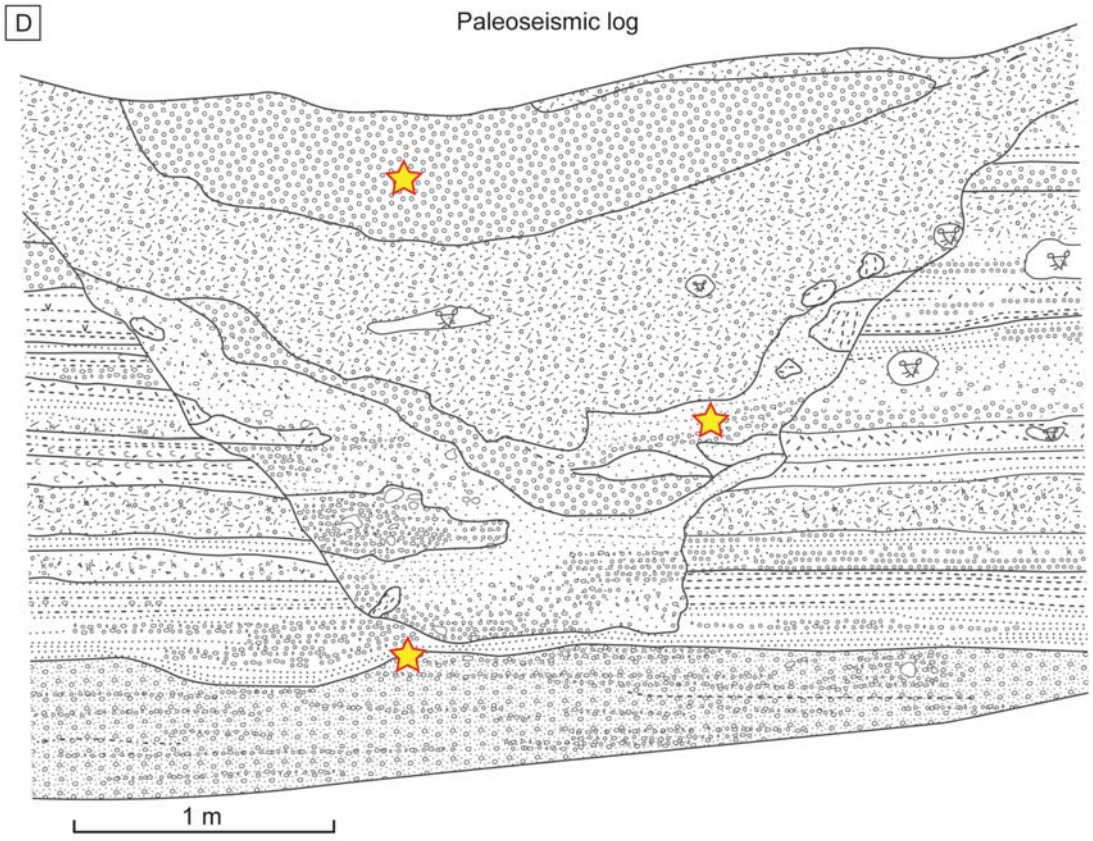

Figure 2.9

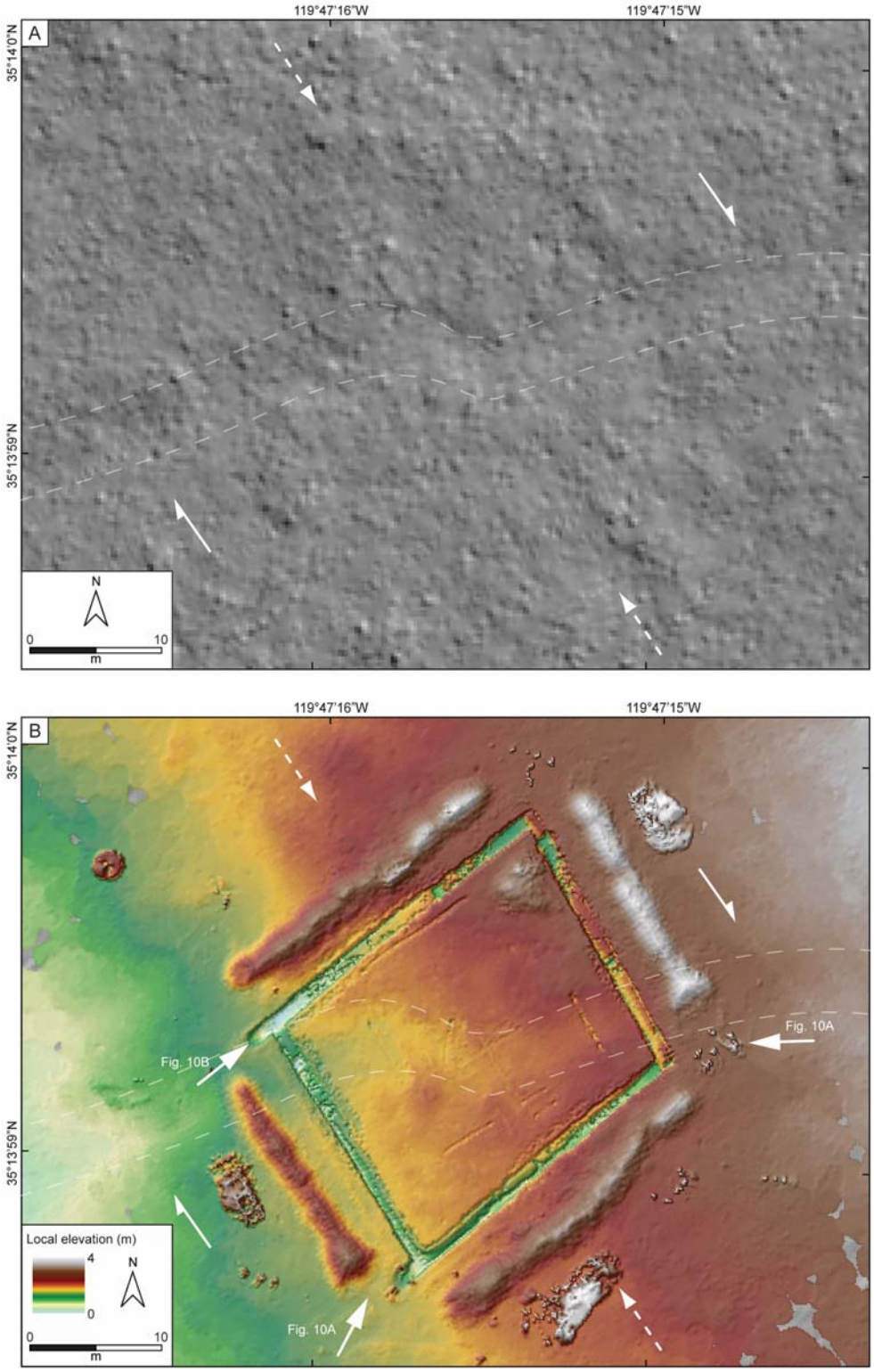
A
119°47'16"W
119°47'15"W
35°14'0"N
35°13'59"N
N
0
10
m
B
119°47'16"W
119°47'15"W
35°14'0"N
35°13'59"N
Fig. 10B
Fig. 10A
Fig. 10A
Local elevation (m)
4
0
N
0
10
m

Figure 2.10

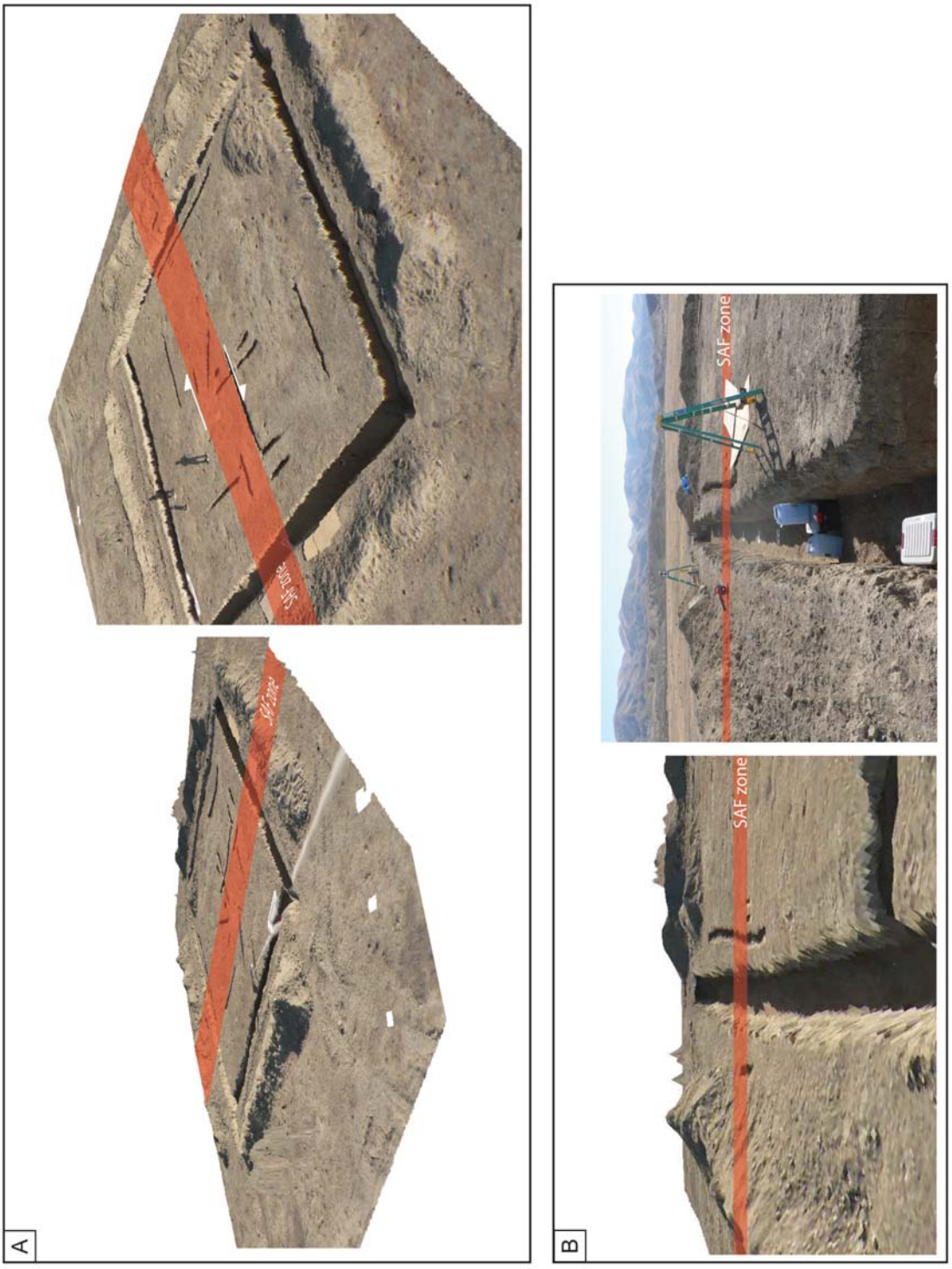

Figure 2.11

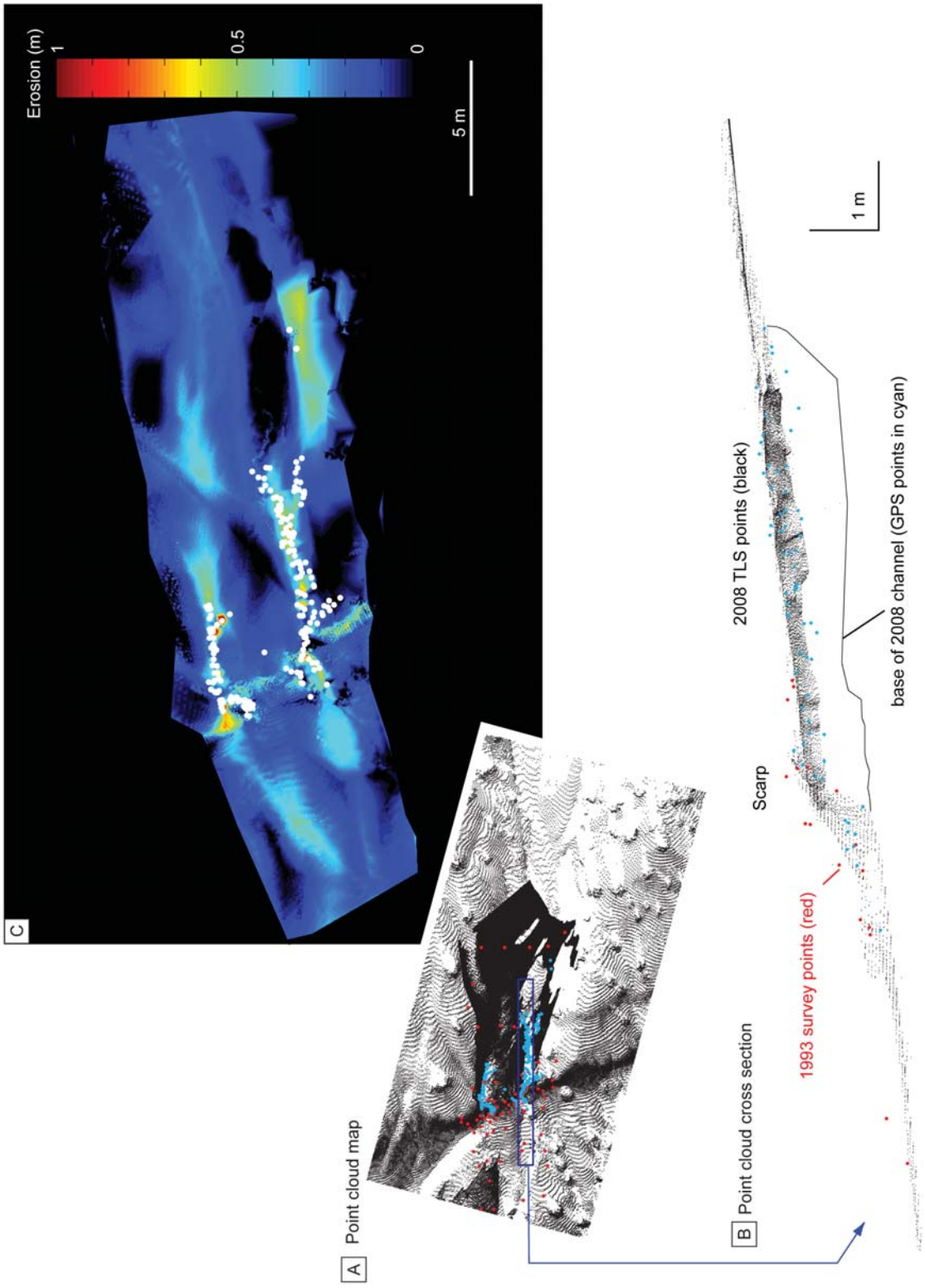
C
Erosion (m)
1
0.5
0
5 m
A Point cloud map
B Point cloud cross section
2008 TLS points (black)
Scarp
1993 survey points (red)
base of 2008 channel (GPS points in cyan)
1 m

Figure 2.12

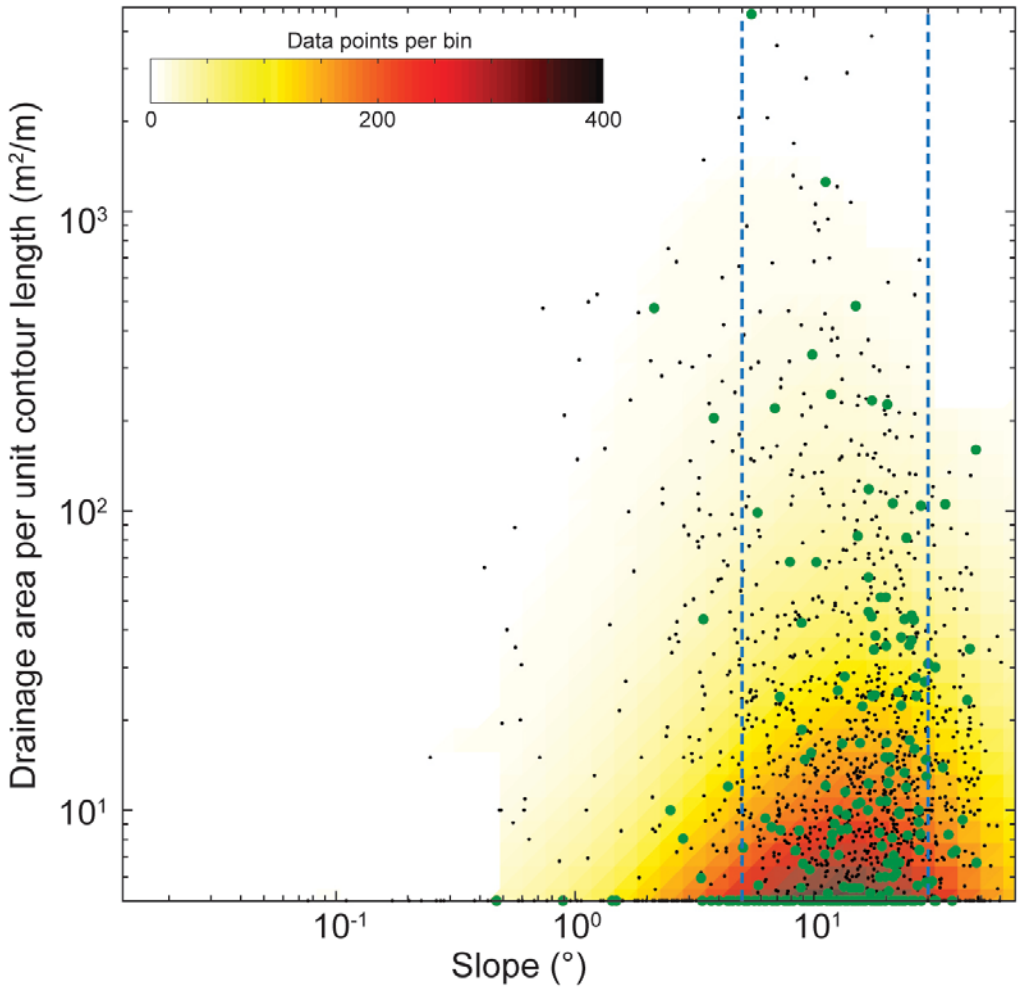
Data points per bin
0
200
400
Drainage area per unit contour length (m²/m)
10³
10²
10¹
10⁻¹
10⁰
10¹
Slope (°)

Figure 2.13

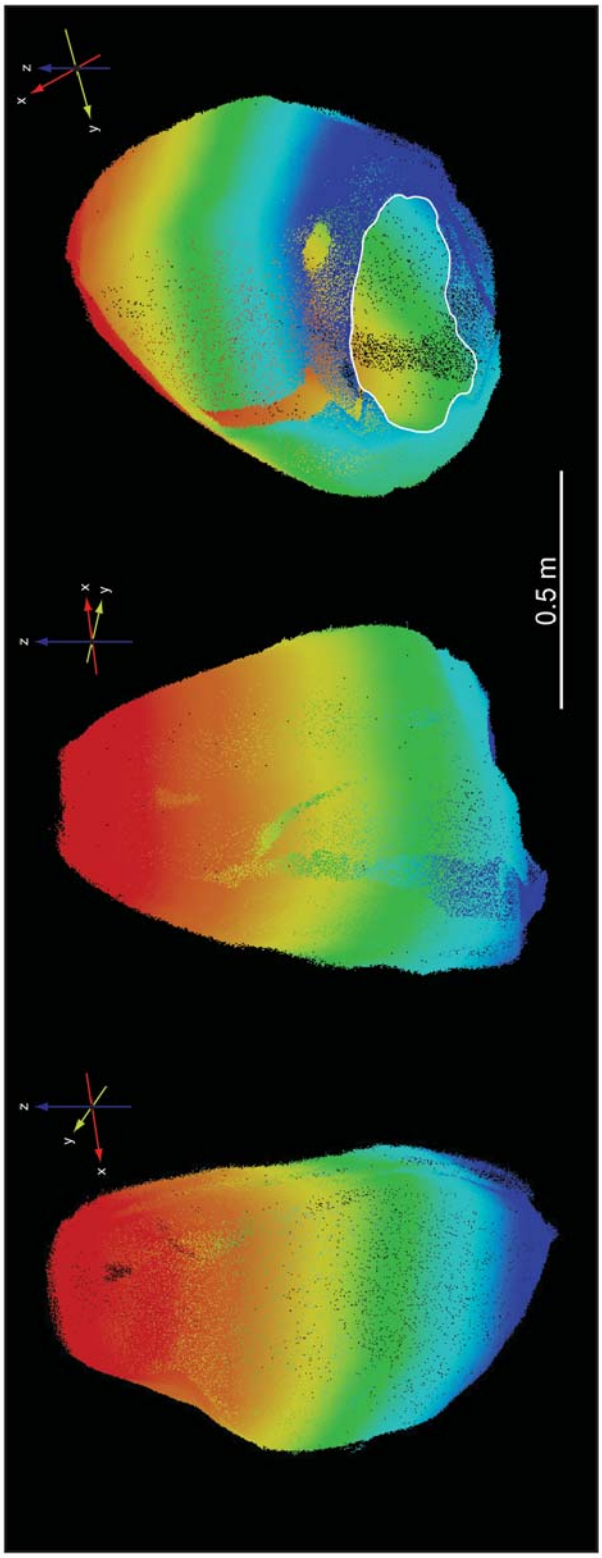

REFERENCES

Akçiz, S. O., Grant Ludwig, L., and Arrowsmith, J. R., 2009, Revised dates of large earthquakes along the Carrizo section of the San Andreas fault, California, since A.D. 1310 ± 30: Journal of Geophysical Research, v. 114, no. B01313.

Akçiz, S. O., Grant Ludwig, L., Arrowsmith, J. R., and Zielke, O., 2010, Century-long average time intervals between earthquake ruptures of the San Andreas fault in the Carrizo Plain, California: Geology, v. 38, no. 9, p. 787-790.

Anooshehpoor, A., Brune, J. N., and Purvance, M. D., 2009, Field-test of precariously balanced rocks near Yucca Valley, California: seismic hazard ramifications (proceedings and abstracts): SCEC Annual Meeting, Palm Springs, California, September 12-16, 2009, 19.

Anooshehpoor, A., Purvance, M., Brune, J., and Rennie, T., 2007, Reduction in the uncertainties in the ground motion constraints by improved field testing techniques of precariously balanced rocks (proceedings and abstracts): SCEC Annual Meeting, Palm Springs, California, September 9-12, 2007, 17.

Arrowsmith, J. R., Pollard, D. D., and Rhodes, D. D., 1996, Hillslope development in areas of active tectonics: Journal of Geophysical Research, v. 101, p. 6255-6275.

Arrowsmith, J. R., and Rhodes, D. D., 1994, Original forms and initial modifications of the Galway Lake Road scarp formed along the Emerson Fault during the 28 June 1992 Landers, California, Earthquake: Bulletin of the Seismological Society of America, v. 84, no. 3, p. 511-527.

-, 2000, A 3-stage model for erosional modification of the Emerson fault (Landers, California earthquake) scarp, June 1992-January 2000: GSA Abstracts with Programs, v. 7, no. A-366.

Arrowsmith, J. R., Rhodes, D. D., and Pollard, D. D., 1998, Morphologic dating of scarps formed by repeated slip events along the San Andreas fault, Carrizo Plain, California: Journal of Geophysical Research, v. 103, p. 10141-10160.

Arrowsmith, J. R., and Zielke, O., 2009, Tectonic geomorphology of the San Andreas Fault zone from high resolution topography: An example from the Cholame segment: Geomorphology, v. 113, p. 70-81.

Bell, J. W., Brune, J. N., Liu, T., Zreda, M., and Yount, J. C., 1998, Dating precariously balanced rocks in seismically active parts of California and Nevada: Geology, v. 26, no. 6, p. 495-498.

Bevis, M., Hudnut, K., Sanchez, R., Toth, C., Grejner-Brzezinska, D., Kendrick, E., Caccamise, D., Raleigh, D., Zhou, H., Shan, S., Shindle, W., Yong, A., Harvey, J., Borsa, A., Ayoub, F., Elliot, B., Shrestha, R., Carter, B., Sartori, M., Phillips,

D., Coloma, F., and Stark, K., 2005, The B4 Project: scanning the San Andreas and San Jacinto fault zones: Eos Trans. AGU 86(52), Fall Meet. Suppl., Abstract H34B-01.

Brune, J. N., 1993a, Distribution of precariously balanced rocks in Nevada and California - correlation with probability maps for strong ground motion: Eos, v. 73, no. 43, p. 351.

-, 1993b, Precariously balanced rocks in Nevada and California - implications for earthquake hazard in Nevada, particularly at Yucca Mountain: Geological Society of America Abstracts with Programs, v. 25, no. 5, p. 15.

-, 1994, Constraints on ground motion from great earthquakes provided by groups of precarious rocks: Seismological Research Letters, v. 65, no. 1, p. 64.

-, 1996, Precariously balanced rocks and ground-motion maps for Southern California: Bulletin of the Seismological Society of America, v. 86, no. 1A, p. 43-54.

Brune, J. N., Anooshehpoor, A., Purvance, M. D., and Brune, R. J., 2006, Band of precariously balanced rocks between the Elsinore and San Jacinto, California, fault zones: Constraints on ground motion for large earthquakes: Geology, v. 34, no. 3, p. 137-140.

Brune, J. N., and Whitney, J. W., 2000, Precarious rocks and seismic shaking at Yucca Mountain, Nevada: US Geological Survey Digital Data Series 058, p. 1-19.

Carter, W. E., Shrestha, R. L., and Slatton, K. C., 2007, Geodetic laser scanning: Physics Today, v. 60, no. 12, p. 41-47.

Davis, W. M., 1892, The convex profile of badland divides: Science, v. 20, p. 245.

-, 1899, The geographical cycle: The Geographical Journal, v. 14, p. 481-504.

DeLong, S. B., Hilley, G. E., Rymer, M. J., and Prentice, C., 2010, Fault zone structure from topography: Signatures of en echelon fault slip at Mustang Ridge on the San Andreas Fault, Monterey County, California: Tectonics, v. 29, no. TC5003, doi: 10.1029/2010TC002673.

DeMers, 2002, Fundamentals of Geographic Information Systems, Hoboken, John Wiley & Sons, 480 p.

DeWitt, E., Langenheim, V., Force, E., Vance, R. K., Lindberg, P. A., and Driscoll, R. L., 2008, Geologic map of the Prescott National Forest and the headwaters of the Verde River, Yavapai and Coconino Counties, Arizona: US Geological Survey Scientific Investigations Map 2996, scale 1:100,000, p. 100.

Dietrich, W. E., Wilson, C. J., Montgomery, D. R., McKean, J., and Bauer, R., 1992, Erosion thresholds and land surface morphology: Geology, v. 20, p. 675-679.

El-Sheimy, N., Valeo, C., and Habib, A., 2005, Digital terrain modeling: acquisition, manipulation, and applications, Boston, MA, Artech House, 257 p.

Gardner, T. W., 1983, Experimental study of knickpoint and longitudinal profile evolution in cohesive, homogenous material: Geological Society of America Bulletin, v. 94, p. 664-672.

Gilbert, G. K., 1877, Report on the geology of the Henry Mountains (Utah), Washington, D.C., U.S. Geographical and Geological Survey of the Rocky Mountain Region, Government Printing Office, 160 p.

-, 1909, The convexity of hilltops: Journal of Geology, v. 17, p. 344-350.

Gold, P. O., Cowgill, E., Kreylos, O., and Gold, R. D., 2012, A terrestrial lidar-based workflow for determining three-dimensional slip vectors and associated uncertainties: Geosphere, v. 8, no. 2, p. 431-442.

Grant, L. B., and Sieh, K., 1994, Paleoseismic evidence of clustered earthquakes on the San Andreas fault in the Carrizo Plain, California: Journal of Geophysical Research, v. 99, no. B4, p. 6819-6841.

Grant Ludwig, L., Akçiz, S. O., Noriega, G. R., Zielke, O., and Arrowsmith, J. R., 2010, Climate-modulated channel incision and rupture history of the San Andreas fault in the Carrizo Plain: Science, v. 327, p. 1117-1119.

Haddad, D. E., 2010, Geologic and geomorphic characterization of precariously balanced rocks, MS Thesis: Arizona State University, 207 p.

Hanks, T. C., 2000, The age of scarplike landforms from diffusion-equation analysis, in Noller, J. S., Sowers, J. M., and Lettis, W. R., eds., Quaternary Geochronology, AGU Reference Shelf, p. 313-338.

Hanks, T. C., Bucknam, R. C., Lajoie, K. R., and Wallace, R. E., 1984, Modification of wave-cut and faulting-controlled landforms: Journal of Geophysical Research, v. 89, no. B7, p. 5771-5790.

Heimsath, A. M., Chappell, J., Dietrich, W. E., Nishiizumi, K., and Finkel, R., 2001, Late Quaternary erosion in southeastern Australia: a field example using cosmogenic nuclides: Quaternary International, v. 83-85, p. 169-185.

Hilley, G. E., and Arrowsmith, J. R., 2001, Penck1D: Transport- and production-limited fault scarp simulation software: GSA Special Short Course Manual, p. 44.

-, 2003, Scarp dater software: Scarp diffusion exercise from the International Quality Network Workshop: Potsdam, Germany, Potsdam University.

Hilley, G. E., DeLong, S., Prentice, C., Blisniuk, K., and Arrowsmith, J. R., 2010, Morphologic dating of fault scarps using airborne laser swath mapping (ALSM) data: Geophysical Research Letters, v. 37, no. L04301, doi: 10.1029/2009GL042044.

Hudnut, K., Amidon, W., Bawden, G., Brune, J., Bond, S., Graves, R., Haddad, D. E., Limaye, A., Lynch, D. K., Phillips, D. A., Pounders, E., Rood, D., and Weiser, D., 2009a, The Echo Cliffs precariously balanced rock; discovery and description by terrestrial laser scanning (proceedings and abstracts): Southern California Earthquake Center Annual Meeting, Palm Springs, California, September 12-16, 2009, 19.

Hudnut, K., Amidon, W., Bawden, G., Brune, J., Graves, R., Haddad, D. E., Limaye, A., Lynch, D. K., Phillips, D. A., Pounders, E., and Rood, D., 2009b, The Echo Cliffs precariously balanced rock: discovery and description by terrestrial laser scanning: Eos Trans. AGU 90(52), Fall Meet. Suppl., Abstract G51B-0657.

Hudnut, K. W., Borsa, A., Glennie, C., and Minster, J.-B., 2002, High-resolution topography along surface rupture of the 16 October 1999 Hector Mine, California, earthquake (Mw 7.1) from airborne laser swath mapping: Bulletin of the Seismological Society of America, v. 92, no. 4, p. 1570-1576.

Kirkby, M. J., 1971, Hillslope process-response models based on the continuity equation: Institute of British Geographers, Special Publication, v. 3, p. 15-30.

Krishnan, S., Crosby, C., Nandigam, V., Phan, M., Cowart, C., Baru, C., Arrowsmith, J. R., and OpenTopography, 2011, A services oriented architechture for community access to LiDAR topogaphy: Proceedings of the 2nd International Conference on Computing for Geospatial Research and Applications.

McCalpin, J. P., 2009, Paleoseismology, International Geophysics Series: San Diego, Academic Press, p. 613.

Nash, D. B., 1980, Morphologic dating of degraded normal fault scarps: Journal of Geology, v. 88, p. 353-360.

Oskin, M., Arrowsmith, R., Hinojosa, A., Gonzalez, J., Gonzalez, A., Sartori, M., Fernandez, J., Fialko, Y., Floyd, M., Galetzka, J., and Sandwell, D., 2010a, Airborne lidar survey of the 4 April 2010 El Mayor-Cucupah earthquake rupture: (proceedings and abstracts): Southern California Earthquake Center Annual Meeting, Palm Springs, California, September 12-16, 2009, 19.

Oskin, M. E., Arrowsmith, J. R., Hinojosa, A. C., Elliott, A. J., Fletcher, J. M., Fielding, E. J., Gold, P. O., Garcia, J. J. G., Hudnut, K. W., Liu-Zheng, J., and Teran, O. J.,

2012, Near-field deformation from the El Mayor-Cucupah earthquake revealed by differential LiDAR: Science, v. 335, no. 702.

Oskin, M. E., Gold, P. O., Hinojosa, A., Arrowsmith, J. R., Elliott, A. J., Taylor, M. H., Herrs, A. J., Sartori, M., Gonzalez-Garcia, J. J., Gonzalez, A., Kreylos, O., and Cowgill, E., 2010b, Airborne and terrestrial lidar imaging and analysis of the 4 April 2010 El Mayor-Cucupah earthquake rupture: Abstract T35B-2135 presented at 2010 Fall Meeting, AGU, San Francisco, Calif. 13-17 Dec.

Oskin, M. E., Le, K., and Strane, M. D., 2007, Quantifying fault-zone activity in arid environments with high-resolution topography: Geophysical Research Letters, v. 34, no. L23S05, doi: 10.1029/2007GL031295.

Penck, W., 1953, Morphological analysis of land forms, London, MacMillan and Co., Limited.

Pierce, K. L., and Colman, S. M., 1986, Effect of height and orientation (microclimate) on geomorphic degradation rates and processes, late-glacial terrace scarps in central Idaho: Geological Society of America Bulletin, v. 97, p. 869-885.

Prentice, C. S., Crosby, C. J., Whitehill, C. S., Arrowsmith, J. R., Furlong, K. P., and Phillips, D. A., 2009, Illuminating northern California's active faults: Eos, v. 90, no. 7, p. 55-56.

Purvance, M., 2005, Overturning of slender blocks: numerical investigation and application to precariously balanced rocks in southern California, PhD Dissertation: University of Nevada, Reno, 233 p.

Purvance, M. D., Abdolrasool, A., and Brune, J. N., 2008a, Freestanding block overturning fragilities: Numerical simulation and experimental validation: Earthquake Engineering and Structural Dynamics, v. 37, p. 791-808.

Purvance, M. D., Brune, J. N., Abrahamson, N. A., and Anderson, J. G., 2008b, Consistency of precariously balanced rocks with probabilistic seismic hazard estimates in Southern California: Bulletin of the Seismological Society of America, v. 98, no. 6, p. 2629-2640.

Ragona, D., Minster, B., Rockwell, T., and Jussila, J., 2006, Field imaging spectroscopy: A new methodology to assist the description, interpretation, and archiving of paleoseismological information from faulted exposures: Journal of Geophysical Research, v. 111, no. B10309, doi: 10.1029/2006JB004267.

Roering, J. J., Kirchner, J. W., and Dietrich, W. E., 1999, Evidence for nonlinear, diffusive sediment transport on hillslopes and implications for landscape morphology: Water Resources Research, v. 35, no. 3, p. 853-870.

Rood, D., Brune, J., Kendrick, K., Purvance, M., Anooshehpoor, R., Grant-Ludwig, L., and Balco, G., 2008, How do we date a PBR?: testing geomorphic models using surface-exposure dating and numerical methods: ExGM Workshop, SCEC Annual Meeting, Palm Springs, California, September 6-11, 2009, 18.

Rood, D. H., Balco, G. A., Purvance, M. D., Anooshehpoor, A., Brune, J. N., Grant-Ludwig, L. B., and Kendrick, K., 2009, How do we date a PBR?: a robust method using BE-10 surface exposure dating with numerical models: SCEC Annual Meeting, Palm Springs, California, September 12-16, 2009, 19.

Schumm, S. A., 1967, Rates of surficial rock creep on hillslopes in western Colorado: Science, v. 155, no. 3762, p. 560-562.

Schwartz, D. P., and Coppersmith, K. J., 1984, Fault behavior and characteristic earthquakes; examples from the Wasatch and San Andreas fault zones: Journal of Geophysical Research, v. 89, p. 5681-5698.

Shan, S., Bevis, M., Kendrick, E., Mader, G. L., Raleigh, D., Hudnut, K., Sartori, M., and Phillips, D., 2007, Kinematic GPS solutions for aircraft trajectories: Identifying and minimizing systematic height errors associated with atmospheric propagation delays: Geophysical Research Letters, v. 34, no. 23.

Shi, B., Abdolrasool, A., Zeng, Y., and and Brune, J. N., 1996, Rocking and overturning of precariously balanced rocks by earthquakes: Bulletin of the Seismological Society of America, v. 86, no. 5, p. 1364-1371.

Sieh, K. E., and Jahns, R. H., 1984, Holocene activity of the San Andreas fault at Wallace Creek, California: Geological Society of America Bulletin, v. 95, p. 883-896.

Stewart, I. S., and Hancock, P. L., 1990, What is a fault scarp?: Episodes, v. 13, no. 4, p. 256-263.

Stirling, M., 2008, Cosmogenic and soil age constraints on PBRs in New Zealand: ExGM Workshop, SCEC Annual Meeting, Palm Springs, California, September 6-11, 2009, 18.

Stirling, M. W., Anooshehpoor, A., Brune, J. N., Biasi, G. P., and Wesnousky, G., 2002, Assessment of the site conditions of precariously balanced rocks in the Mojave Desert, Southern California: Bulletin of the Seismological Society of America, v. 92, p. 2139-2144.

Stirling, M. W., and Anooshehpoor, R., 2006, Constraints on probabilistic seismic-hazard models from unstable landform features in New Zealand: Bulletin of the Seismological Society of America, v. 96, no. 2, p. 404-414.

Tarboton, D. G., 1997, A new method for the determination of flow directions and upslope areas in grid digital elevation models: Water Resources Research, v. 33, no. 2, p. 309-319.

Toké, N. A., Arrowsmith, J. R., Rymer, M. J., Landgraf, A., Haddad, D. E., Busch, M., Coyan, J., and Hannah, A., 2011, Late Holocene slip rate of the San Andreas fault and its accommodation by creep and moderate-magnitude earthquakes at Parkfield, California: Geology, v. 39, no. 3, p. 243-246.

Twidale, C. R., 1982, Granitic Landforms, Amsterdam, Elsevier, 372 p.

Wallace, R. E., 1977, Profiles and ages of young fault scarps, north-central Nevada: Geological Society of America Bulletin, v. 88, p. 1267-1281.

WGCEP, 2008, The uniform California earthquake rupture forecast, Version 2 (UCERF 2): U.S. Geological Survey Open File Report 2007-1437, p. 104.

Wilkinson, M., McCaffrey, K. J. W., Roberts, G., Cowie, P. A., Phillips, R. J., Michetti, A. M., Vittori, E., Guerrieri, L., Blumetti, A. M., Bubeck, A., Yates, A., and Sileo, G., 2010, Partitioned postseismic deformation associated with the 2009 Mw 6.3 L'Aquila earthquake surface rupture measured using a terrestrial laser scanner: Geophysical Research Letters, v. 37, no. L10309, doi:10.1029/2010GL043099.

Xu, X., 2000, Three-dimensional virtual geology: photorealistic outcrops, and their acquisition, visualization and analysis: PhD Dissertation, University of Texas, Dallas, Dallas, TX.

Zielke, O., Arrowsmith, J. R., Ludwig, L. G., and Akciz, S. O., 2010, Slip in the 1857 and earlier large earthquakes along the Carrizo Plain, San Andreas Fault: Science, v. 327, p. 1119-1122.

Chapter 3

HIGH-RESOLUTION DIGITAL TOPOGRAPHY IN ACTIVE TECTONICS RESEARCH

INTRODUCTION

Earth's topographic surface forms an interface through which the geodynamic and geomorphic engines interact. This interaction is best observed along crustal margins where topography is created by tectonic processes and sculpted by geomorphic processes (e.g., Vedder and Wallace, 1970). The rates at which these processes operate dictate the preservation potential of tectonically deformed topography. At centennial to millennial rates, earthquakes are the primary driver for topographic deformation. Therefore, the topography of active fault zones holds a wealth of information about the record of past earthquakes and active faulting (Fig. 3.1). From a societal standpoint, fault zone topography provides crucial information about the recurrence of past earthquakes that may help forecast the likelihood of future earthquakes and prepare seismically sensitive infrastructures such as schools, hospitals, and nuclear power plants for strong ground motions (e.g., WGCEP, 2008). Quantitative documentation and characterization of fault zone topography is thus important.

Until the late 1990s, measurement of tectonically displaced features, such as offset stream channels, terraces, and topographic ridges, was made using total station surveys (e.g., Arrowsmith and Rhodes, 1994; Arrowsmith et al., 1998). In these surveys, thousands of measurements were made over multiple days such that a sufficient number of points were measured to depict the topography of displacement markers. Over the past decade, a significant expanse in the development of light detection and ranging (lidar)

instruments provided an opportunity to survey topography with unprecedented speed, accuracy, and resolution. Airborne lidar campaigns along active plate boundaries were quickly recognized as necessary to document the record of earthquake-generated deformation at appropriate spatiotemporal scales (Fig. 3.1). Such campaigns have yielded digital representations of topography at resolutions sufficient to make measurements of earthquake-related vertical and lateral topographic displacements (e.g., Hudnut et al., 2002; Bevis et al., 2005; Oskin et al., 2007; Prentice et al., 2009; DeLong et al., 2010; Hilley et al., 2010; Oskin et al., 2010a; Oskin et al., 2010b; Oskin et al., 2012). For example, fault trace geometries and stream channels that were offset by past earthquakes are clearly illuminated by lidar datasets (e.g., Arrowsmith and Zielke, 2009; DeLong et al., 2010; Haddad et al., 2012). Systematic analyses of these data reveals geomorphic observations that are barely perceivable in the field but may change the fundamentals of inferring earthquake recurrence and fault segmentation (e.g., Zielke et al., 2010).

In this chapter, we first describe the basics of airborne and terrestrial lidar platforms that are generally used in present-day active tectonic studies. We then present two applications of airborne lidar research along the tectonically active North American-Pacific plate boundary. Finally, we describe the future of lidar in active tectonics research and provide lidar data access and processing resources. The geologic and geomorphic processes that operate in both case studies span spatiotemporal scales that range from centimeters to hundreds of meters and years to millennia. Our case studies demonstrate that lidar is a promising technology that provides a framework upon which the efficient and accurate characterization of earthquake processes may be constructed over a range of spatiotemporal scales.

Lidar Data Acquisition and Processing

Two platforms are typically employed in research that uses lidar data. Airborne lidar systems use an aircraft-mounted laser scanner that scans topography in side-to-side swaths at rates that range between tens and several hundred kHz (Fig. 3.2A). The orientation (yaw, pitch, and roll) of the aircraft is monitored by an on-board inertial navigation measurement unit, and its location is determined by a high-precision kinematic global positioning system (GPS; El-Sheimy et al., 2005; Carter et al., 2007; Shan et al., 2007). Post processing places the lidar data in a global reference frame as a point cloud of the laser returns with typical shot densities >1 m^{-2}. Terrestrial lidar platforms employ a tripod-mounted laser scanner that can be operated from various near-field positions to ensure complete scan coverage of the feature of interest (Fig. 3.3B). Reflective targets with known geographic coordinates are needed to align point clouds from the different scan positions into a final point cloud within a global reference frame. Point cloud densities for terrestrial lidar can reach up to >10^4 m^{-2} depending on the scanning distance. Furthermore, acquisition geometry of terrestrial lidar systems provides a true three-dimensional (3D) representation of the scanned feature or outcrop. As a result, complete 3D representations of features scanned by terrestrial lidar can be accomplished, as opposed to airborne lidar platforms that scan topographic features in "2.5D".

The utility of airborne and terrestrial lidar datasets for the visualization and analysis of topographic data is often demonstrated by gridded digital elevation models (DEMs). These DEMS are generated from the spatially heterogeneous point clouds that were detected by the lidar scanner. Where the point spacing is less than the desired

resolution of the DEM, a local binning algorithm is applied to compute values within a specified search radius at each node and a predefined mathematical function (e.g., mean, minimum, maximum). For the case studies presented here, we used the following algorithm to generate submeter-resolution DEMs (El-Sheimy et al., 2005):

$$Z_{IDW} = \frac{\sum_{l=1}^{n} \frac{Z_l}{r_l^2}}{\sum_{l=1}^{n} \frac{1}{r_l^2}} , \qquad (3.1)$$

where Z_{IDW} is the interpolated distance-weighted elevation computed for each grid node, n is the total number of grid nodes, l is the grid node index, and r is the radius of the node-centered computational bin.

CASE STUDIES

Case Study I: Structure and Geomechanics of Active Fault Zones

Earthquake ruptures produced along crustal faults originate in the middle to lower depths of the seismogenic layer and transmit deformation to Earth's surface by driving slip along faults and block motions (Fig. 3.1; Scholz, 2002; Titus et al., 2011). This process is manifested in Earth's topography via fault scarps and fractures or off-fault folding and warping (e.g., Oskin et al., 2012; Quigley et al., 2012). The extent to which this surface manifestation represents earthquake processes at depth is generally thought to be controlled by the geometrical complexity of faults, faulting mechanisms, and the spatiotemporal strength variations of the upper lithosphere (Sibson, 1986; Scholz, 2002). With the exception of very limited direct observations of active faults at depth (e.g., the San Andreas Fault Observatory at Depth), we do not have direct access to faults embedded in the seismogenic layer. However, lidar allows for high-resolution analyses of

coseismic deformation of fault zone topography within 10s to a few 1000s of meters from fault ruptures. These datasets help us interpret fracture patterns observed in the paleoseismic record and enable surface rupture patterns to be interrogated for their fidelity in representing coseismic ruptures and seismic moment released at depth (e.g., Oskin et al., 2012). Furthermore, these datasets provide important controls for measuring coseismic slip in the most recent event and slip accumulated over multiple earthquakes (e.g., Arrowsmith et al., 2011; Haddad et al., 2011; Madden et al., 2011), thereby improving our understanding of fault system behavior and interactions through space and time. For this case study, we showcase the application of airborne lidar data for past surface ruptures along the Garlock fault, California (Fig. 3.4).

Fault Zone Mapping

We mapped the surface traces of past earthquake ruptures and faults along the Garlock fault, California, using high-resolution aerial photographs and submeter-resolution DEMs. Our maps revealed that along-strike fault trace patterns differ significantly between the western and eastern sections of the Garlock fault. The topographic expression of the western section is not well defined when compared to the ubiquitous fault scarps of the central and eastern sections. Similarly, few lateral displacements in stream channels and ridges are preserved along the western section in comparison to the central and eastern sections. This may be due to the high density of mass wasting that has obliterated fault scarps and surface manifestations of topographic displacements in the last few earthquakes along the western section of the Garlock fault. We attribute this to the along-strike climatic gradient where the wetter conditions of the

western section are not conducive to preserving fault scarps when compared to the central and eastern sections that reside in the Mojave Desert.

Fault Zone Complexity

Our lidar-derived fault trace maps for the Garlock fault were also used to calculate fault complexity parameters such as segmentation and length, where we correlated these metrics with fault zone geology to explore for lithologic controls on surface rupture breaks. Figure 3.5 presents the results from an analysis of a spatial correlation between fault segmentation, length, and rock type for a section of the central Garlock fault. Fault complexity was calculated using 300 m-wide bins that moved along strike of the fault zone and show that, in general, fault segmentation is greater in bedrock breaks than alluvial breaks. This is counter to the general intuition that unconsolidated media (e.g., Qal in Fig. 3.5) tend to distribute brittle deformation across broad fracture belts. However, we attribute the relatively simple Qal rupture patterns observed in our fault complexity analysis to be caused by the thin alluvial cover that overlies the shallow bedrock and thus have low confining stresses. As a result, the transmission of strain through the Qal cover and to the topography of the Garlock fault zone is via fewer fractures than if the bedrock depth were greater. Our analyses also showed that fault segment length appears to be controlled by rock type; segments are generally longer in granodiorite (Tg) than those breaking through alluvium or quartz-monzonite (Qal, Tgm in Fig. 3.5), indicating that rock type controls the local continuity and mechanics of earthquake ruptures.

Lateral Displacement of Geomorphic Markers

The lidar datasets for the Garlock fault provide important insights into the along-strike distribution of slip created by past earthquakes. For this component of the case study, we measured laterally displaced geomorphic markers such as offset ridges, stream channels, and terraces along the entire length of the Garlock Fault using a lateral offset calculator and submeter-resolution DEMs (e.g., Zielke and Arrowsmith, 2012). Figure 3.6 presents results from our displacement analysis of 431 offset features along the Garlock fault. To validate our lidar-derived measurements with those made in the field, we reoccupied 129 offsets that were measured in the field by McGill and Sieh (1991) using the lidar offset calculator. Our lidar-derived measurements compare well with those made in the field for the same offset features, attaining correlation coefficients R^2 of 0.9. This validation demonstrates that our lidar-derived offset measurements are reliable indicators of coseismic slip in the last few earthquakes and thus provide accurate representations of slip distributions for fault zones, especially where no field measurements of earthquake-related offsets are available, such as in the western section of the Garlock fault. For the western, central, and eastern sections of the Garlock fault, we calculated average surface slip in the last earthquake to be 3.6 m ±1.1 m, 3.8 m ±0.8 m, and 3.3 m ±0.9 m, respectively. McGill and Sieh (1991) report the average slip from field-derived displacement measurements for the central Garlock as nearly double our measured lidar-derived average slip, indicating that such inconsistencies between lidar- and field-derived slip measurements have important implications for how slip distributions are interpreted (e.g., Zielke et al., 2010).

Geomechanical Modeling

Our lidar-derived fault trace maps also allow us to constrain parameters for geomechanical models of the faulting processes that operate in the upper few kilometers of the Garlock fault. To build a deeper understanding of the subsurface structures responsible for the fault segments that we mapped using lidar, we used 3D geomechanical models with the goal of illuminating the factors that control the fidelity of our interpretations of faulting patterns in the topographic record of the Garlock fault zone.

In classical mechanics, the stability along an interface between two solids is controlled by the magnitude of shear (τ) and normal (σ_n) tractions and the coefficients of static (μ_s) and dynamic (μ_d) friction acting on the interface. Slip along this interface occurs when

$$\tau \geq \mu_s \sigma_n \tag{3.2}$$

When this condition is met and sliding initiates, the value of μ_s decreases to μ_d such that the shear stress drop associated with the sliding motion is

$$\Delta\tau = (\mu_s - \mu_d)\sigma_n \tag{3.3}$$

This approach can be applied to natural fault systems where coseismic stresses and strains due to displacements along source faults drive slip along receiver faults. The potential for receiver faults to fail is expressed in terms of Coulomb failure stress (*CFS*),

$$\Delta CFS = \Delta\tau + \mu'\Delta\sigma_n, \tag{3.4}$$

where $\Delta\tau$ and $\Delta\sigma_n$ are the changes in shear and normal stresses along the receiver faults, respectively, and μ' is the effective friction coefficient after accounting for change in pore fluid pressure. Failure along the receiver fault occurs when the ratio of τ to σ_n exceeds the coefficient of static friction μ_s; an increase in normal stresses relative to shear stresses

acting on receiver faults will reduce this ratio and inhibit conditions for slip. In terms of ΔCFS, failure along receiver faults is therefore encouraged if ΔCFS is positive, and vice versa.

We employed the above approach in a fault interaction modeling environment that was built on analytical descriptions of internal deformation due to slip along rectangular dislocations in an elastic half-space (Okada, 1992; Zielke and Arrowsmith, 2008). We used our lidar-derived fault trace maps and offset measurements to guide our fault models by providing kinematic parameters such as slip vectors, magnitudes, and the attitudes of receiver faults. Figure 3.7 presents the result of two model runs from the central and eastern parts of the Garlock fault. Figure 3.7A shows a fault configuration where a driving sinistral master fault is flanked by an obliquely oriented horst and graben system and a major SE-dipping driving normal fault. The orientations and rakes of receiver faults are identical to those of the horst and graben faults. Local positive ΔCFS lobes are present along the master strike-slip fault and are likely created by local segment irregularities along strike (e.g., small stepovers and fault bends). The region between the driving strike-slip and normal faults exhibits reduced ΔCFS along receiver faults, which is consistent with the presence of the horst and graben system as accommodating the deformation induced by the master strike-slip fault. This is corroborated by the vertical displacement calculations where sinistral slip on the master fault and down-to-the-southeast slip on the normal fault are consistent with our lidar-derived fault mapping and the topography. Figure 3.7B presents a system of three left-stepping and overlapping sinistral faults that form at least two releasing steps in an accommodation zone. The ΔCFS calculations show that the stepovers and releasing steps experience enhanced

ΔCFS on NE-striking receiver faults. This is consistent with the presence of NE-striking normal faults that bind the rhomboidal-shaped pull-apart basins, as evident in our lidar-derived fault maps and the vertical displacement calculations.

Case Study II: Measuring Earthquake Deformation Using Differential Lidar

In conjunction with advancing our understanding of the geomorphology and paleoseismology of active faults, lidar datasets offer a topographic baseline against which to compare repeat lidar surveys, such as could be undertaken in the aftermath of a future earthquake. The typically submeter lidar point spacing is finer than the scale of displacements caused by large earthquakes, making differential lidar analyses well suited for capturing 3D near-fault ground displacements. The development of these methods, some of which are described in this case study, provides further impetus to efforts at expanding the range of active faults mapped with lidar. In the future, differential lidar analyses will complement common satellite-based techniques such as interferometric synthetic aperture radar (InSAR) and subpixel optical matching, which map only certain components of the deformation field and which are often hindered by variable coherence close to surface faulting and in areas of dense vegetation.

The M_w 7.2 El Mayor-Cucapah, Mexico, earthquake of April 4th 2010 is currently the only complete rupture with both pre- and post-event lidar coverage, although the pre-event point density of ~0.013 m^{-2} is orders of magnitude sparser than most modern datasets. By differencing pre- and post-event lidar DEMs, Oskin et al. (2012) revealed a complex pattern of surface elevation changes that included slip on numerous fault strands and tilting and warping of the ground between these segments during the El Mayor-Cucupah earthquake. However, the measured elevation changes do not correspond

directly to the actual surface displacements, and a large horizontal displacement component results in apparent vertical motions that are governed by the local slope facing direction. Leprince et al. (2011) overcame this limitation by using image co-registration and subpixel correlation techniques to measure the horizontal offsets, which were then back-slipped and differenced to reveal the vertical deformation caused by the El Mayor-Cucupah earthquake. However, this two-step procedure still relies on gridding the original pre- and post-event point clouds into DEMs, which introduces biases and artifacts in the resulting displacement calculations.

A pair of recent studies by Borsa and Minster (in press) and Nissen et al. (in press) outline methods for capturing 3D earthquake displacements more directly by computing the translations that best align square windows of the pre- and post-earthquake topography. Both studies use simulated lidar datasets to test their methods. These datasets were generated by adding synthetic earthquakes with known displacements to real B4 lidar point clouds (Bevis et al., 2005). This approach enables a full exploration of displacement resolutions and accuracies at a range of input point cloud densities, but does not take into account the effects of ground shaking, erosion and deposition, vegetation growth or infrastructure development. However, as long as these processes occur on shorter length-scales than the window size they are unlikely to impact the results.

In Borsa and Minster's (in press) approach, a set of harmonic basis functions was used to produce a smoothed surface model of the pre-earthquake topography onto which square subsets of the post-earthquake points were translated using a least-squares minimization scheme. Their method also incorporated lidar intensity data as an additional, independent constraint on horizontal displacements. Nissen et al. (in press)

instead used an adaptation of the iterative closest point (ICP) algorithm to align pre-event (source) and post-event (target) point clouds. The ICP method was originally developed as a computer graphics and medical imaging tool, and works by iterating three steps: (1) identify the closest point in the target point cloud for each point in the source point cloud, (2) calculate the rigid body translation and rotation between all paired points from step 1 to minimize the mean square error in the points' 3D locations, and (3) apply the transformations in step 2 and update the mean square error between the source and target point clouds. These steps are iterated until a local minimum in closest point distances is reached, which is determined when the reduction in the mean square error falls below some threshold. In past geological applications, the ICP method was used to detect landslide displacements using repeat terrestrial lidar datasets (Terza et al., 2007). Its main advantage over other lidar differencing techniques is that it alleviates the need for any gridding or smoothing of either dataset. The method also works well when there are large mismatches in the density of the two point clouds, eliminating the need to downsample the denser dataset. A final, unique aspect of ICP is that it can measure rotations directly, thus providing important new kinematic data in areas of distributed faulting where block rotations may be important.

Figure 3.8 shows an example of an ICP analysis of simulated pre- and post-earthquake point clouds derived from B4 (Bevis et al., 2005) data on part of the southern San Andreas fault. To simulate a large earthquake with right-lateral slip, a synthetic fault was added to the post-event dataset. Points southwest of the fault were moved 2 m to the northwest, and points northeast of the fault were moved 2 m to the southeast and also raised by 1 m. The datasets were split into 50 m x 50 m windows, and the ICP algorithm

was applied separately to each window. The input displacements were reproduced with horizontal and vertical accuracies of ~20 cm and ~4 cm, respectively, to mimic errors in the original point height measurements. As expected, accuracies are highest in windows containing rugged topography but the method is mostly successful even in low-relief areas. Improved accuracies and finer resolutions should be achievable using higher point cloud densities and with further advances in survey georeferencing during the airborne lidar campaign.

SUMMARY

Research in active tectonics and earthquake geology is significantly enhanced by the use of airborne lidar datasets. Applications of such datasets will help refine our understanding of the geologic and geomorphic processes that act along fault zones by allowing us to study these processes at multiple spatiotemporal scales that are relevant to surface and deformational processes. For furture earthquakes, differential analyses that span repeat lidar datasets will provide a wealth of near-fault displacement data to complement existing geodetic or field-based observations. Such displacements will help constrain the slip distribution and rheology of the shallow depths of fault zones, which are crucial for interpreting paleoseismic and geomorphic offsets, and informing studies of long-term earthquake behavior. When coupled with satellite-based measurements such as InSAR, differential lidar analyses will also offer the means to explore relations between surface rupturing and deeper fault zone processes.

An added benefit from lidar datasets in active tectonics research is their educational value. With the increase in web-based 3D topographic visualization such as the ubiquitous Google Earth platform, lidar datasets can provide important teaching aids

in undergraduate- and graduate-level geoscience courses. Therefore, it will become important to the future of geoscience education to integrate lidar datasets as components in undergraduate- and graduate-level curricula by bringing virtual outcrops of faults to the classroom.

LIDAR RESOURCES

The following is a list of suggested web resources where publicly available lidar data and processing capabilities are available for airborne and terrestrial lidar datasets (see also Appendix E):

- http://lidar.asu.edu
- http://www.opentopography.org (airborne lidar datasets presented in this chapter can be downloaded from this website).
- http://www.ncalm.org/
- http://facility.unavco.org/project_support/tls/tls.html#interface/
- http://lidar.cr.usgs.gov/
- http://lvis.gsfc.nasa.gov/

ACKNOWLEDGMENTS

Major support for this work was provided by the National Science Foundation (NSF): Tectonics Program (EAR 0405900, EAR 0711518), Instrumentation and Facilities Program (INTERFACE; EAR 0651098), and OpenTopography (EAR 0930731, EAR 0930643). Additional support was provided by the U. S. Geological Survey (USGS) grant 07HQGR0092 and the Southern California Earthquake Center (SCEC). The SCEC is funded by NSF Cooperative Agreement EAR-0529922 and USGS Cooperative Agreement 07HQAG0008. This is SCEC contribution number 1631. Haddad was

supported by a grant that was awarded jointly by the Arizona State University (ASU) Graduate & Professional Student Association, the ASU Office of the Vice President of Research & Economic Affairs, and the ASU Graduate College. San Andreas fault airborne lidar data were collected by the NSF-funded National Center for Airborne Laser Mapping (NCALM) for the B4 Project (Bevis et al., 2005).

FIGURES

Figure 3.1. Synoptic overview of fault zone processes as manifested in Earth's surface and interior. In Earth's interior, geologic and seismic properties of fault zones control how strain is transmitted through the seismogenic layer (outlined in red) to Earth's surface. On Earth's surface, the tectonic geomorphology of fault zones provides clues into the coseismic moment released at depth by preserving faulted geomorphic elements. Derived from concepts that were developed by Vedder and Wallace (1970), Sylvester (1999), and Scholz (2002). Figure elements are not to scale.

Figure 3.2. (A) A typical setup of an airborne light detection and ranging (lidar) campaign. The aircraft-mounted laser scanner scans topography in side-to-side swaths. The orientation of the aircraft is monitored by an on-board inertial navigation measurement unit (IMU), and its location is determined by a high-precision kinematic global positioning system (GPS). (B) A lidar-equipped twin-engine Cessna Skymaster aircraft operated and managed by the National Center for Airborne Laser Mapping (NCALM; www.ncalm.org).

Figure 3.3. A tripod-mounted Riegl LPM 321 terrestrial laser scanner operating under the Interdisciplinary Alliance for Digital Field data Aquisition and Exploration collaboration (http://facility.unavco.org/project_support/tls/tls.html#interface).

Figure 3.4. Seismotectonic settings of the case studies presented in this chapter. The first case study uses airborne light detection and ranging (lidar) datasets to document

earthquake-related slip distributions along the Garlock fault (GF). The second case study uses airborne lidar data to compute three-dimensional topography displacements created by the April 4th 2010 El Mayor-Cucupah (EMC) earthquake rupture. Digital topographic data in this map were accessed from the U.S. Geological Survey (USGS) Seamless Data Warehouse (http://seamless.usgs.gov). Fault data were acquired and modified from the USGS Quaternary Fault and Fold Database (http://earthquake.usgs.gov/hazards/qfaults/).

Figure 3.5. Results from the fault complexity analyses using lidar-derived fault trace maps. The analyses were performed in the central Garlock fault, California, where past coseismic breaks ruptured through alluvium (Qal), quartz monzonite (Tqm), and granodiorite (Tg) rock units (for the area shown). Fault segment length and number of segments were computed in 300 m bins along strike. SAF – San Andreas fault, GF – Garlock fault. Geology from Ludington et al. (2007).

Figure 3.6. Results from our lidar-derived offset measurements. (A) Overview map of offset measurements compiled for major faults in California. (B) Lidar- vs. field-derived offset measurements for the Garlock fault. Garlock field measurements were made by McGill and Sieh (1991). (C) Slip distribution plots for the Garlock fault made from lidar- and field-derived offset measurements.

Figure 3.7. Examples of fault trace mapped using lidar-derived digital elevation models, their 3D model representation in an elastic halfspace, Coulomb failure stress (*CFS*) calculations, and vertical displacement calculations. (A) A sinistral master fault is flanked

by a horst and graben system, exhibiting distributed surface deformation >1.5 km across the main fault trace. (B) Three left-stepping and overlapping sinistral faults forming at least two releasing steps where extension is accommodated by a system of normal faults. *CFS* and vertical displacement calculations were performed using the elastic dislocation model by Zielke and Arrowsmith (2008). Both modeling scenarios are from the Garlock fault, California.

Figure 3.8. Results for a simulated earthquake experiment at Painted Canyon on the southern San Andreas fault. Shaded topography is a 1 m-resolution digital elevation model constructed from the B4 lidar dataset (Bevis et al., 2005) and illuminated from the NE. White patches show areas in which pre- and post-earthquake point cloud coverage is unavailable. The iterative closest point (ICP; see text) window size is 50 m. White and black arrows show input and output horizontal displacements, respectively, and colored circles show output vertical displacements. The synthetic fault is plotted in yellow. Adapted from Nissen et al. (in press).

Figure 3.1

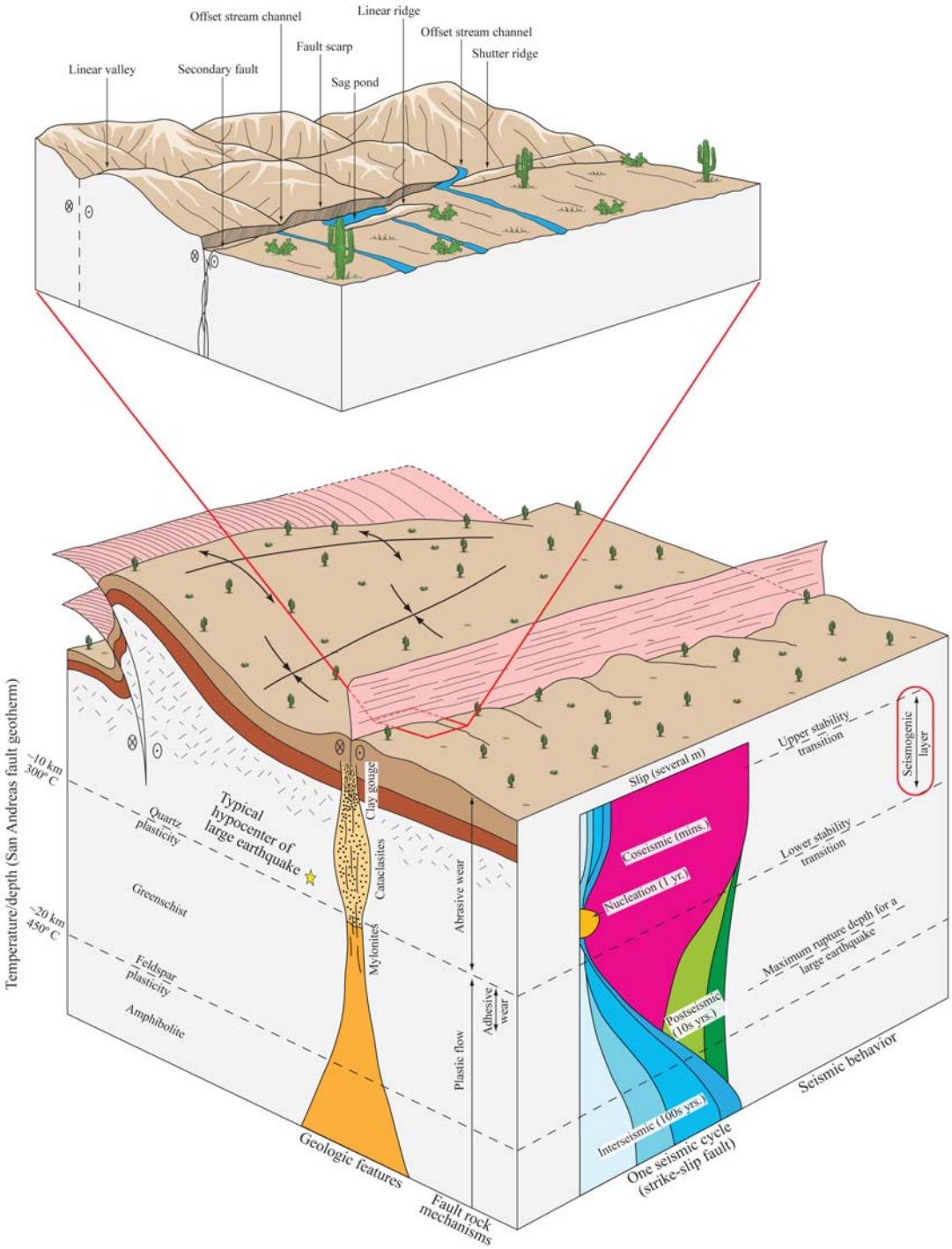
Offset stream channel
Linear ridge
Offset stream channel
Fault scarp
Shutter ridge
Linear valley
Secondary fault
Sag pond
Temperature/depth (San Andreas fault geotherm)
~10 km
300° C
~20 km
450° C
Quartz plasticity
Typical hypocenter of large earthquake
Clay gouge
Cataclasites
Greenschist
Mylonites
Abrasive wear
Feldspar plasticity
Amphibolite
Plastic flow
Adhesive wear
Geologic features
Fault rock mechanisms
Slip (several m)
Upper stability transition
Seismogenic layer
Coseismic (mins.)
Nucleation (1 yr.)
Lower stability transition
Maximum rupture depth for a large earthquake
Postseismic (10s yrs.)
Interseismic (100s yrs.)
Seismic behavior
One seismic cycle (strike-slip fault)

Figure 3.2

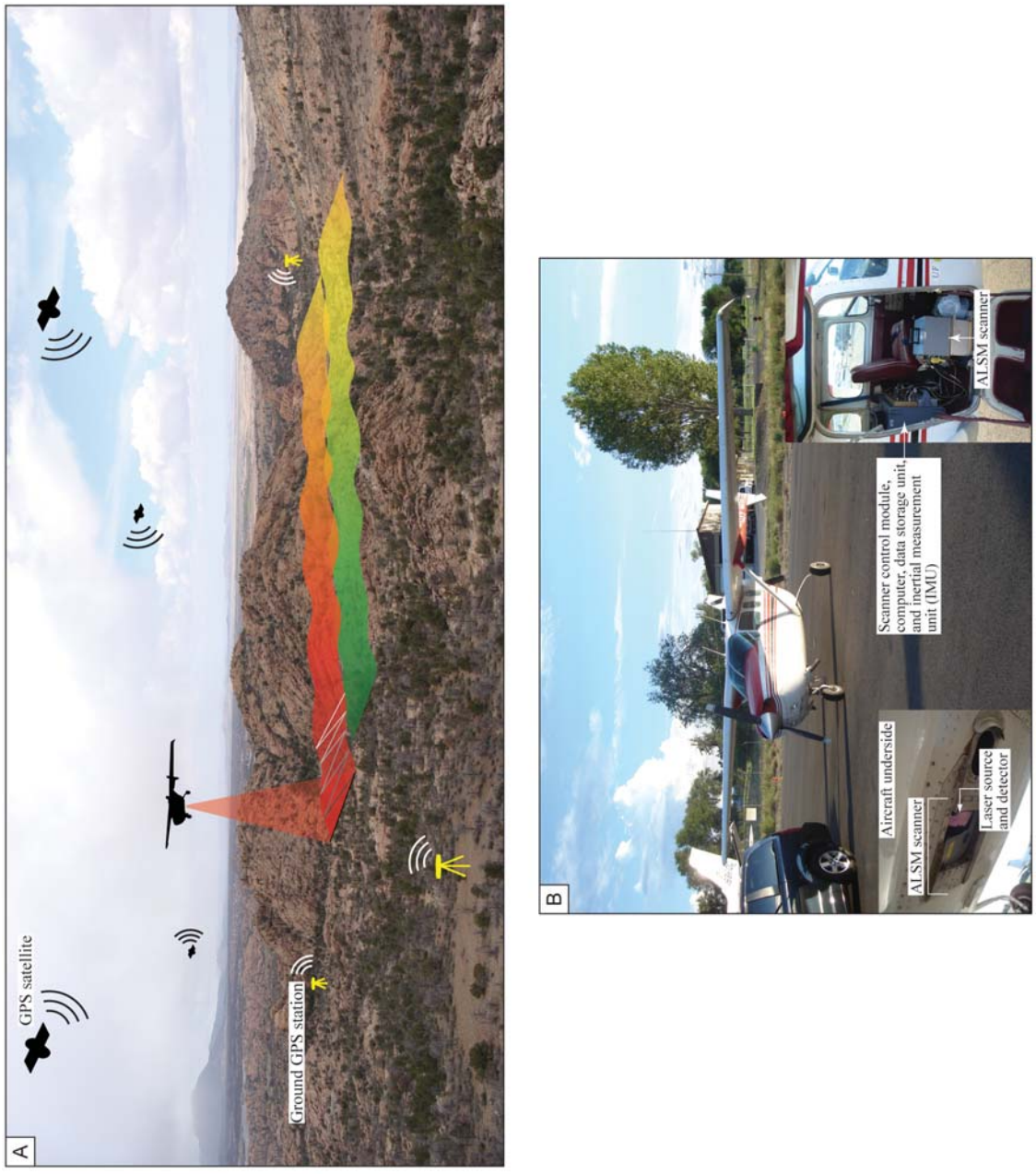
A
GPS satellite
Ground GPS station
B
Scanner control module, computer, data storage unit, and inertial measurement unit (IMU)
ALSM scanner
Aircraft underside
ALSM scanner
Laser source and detector

Figure 3.3

Figure 3.4

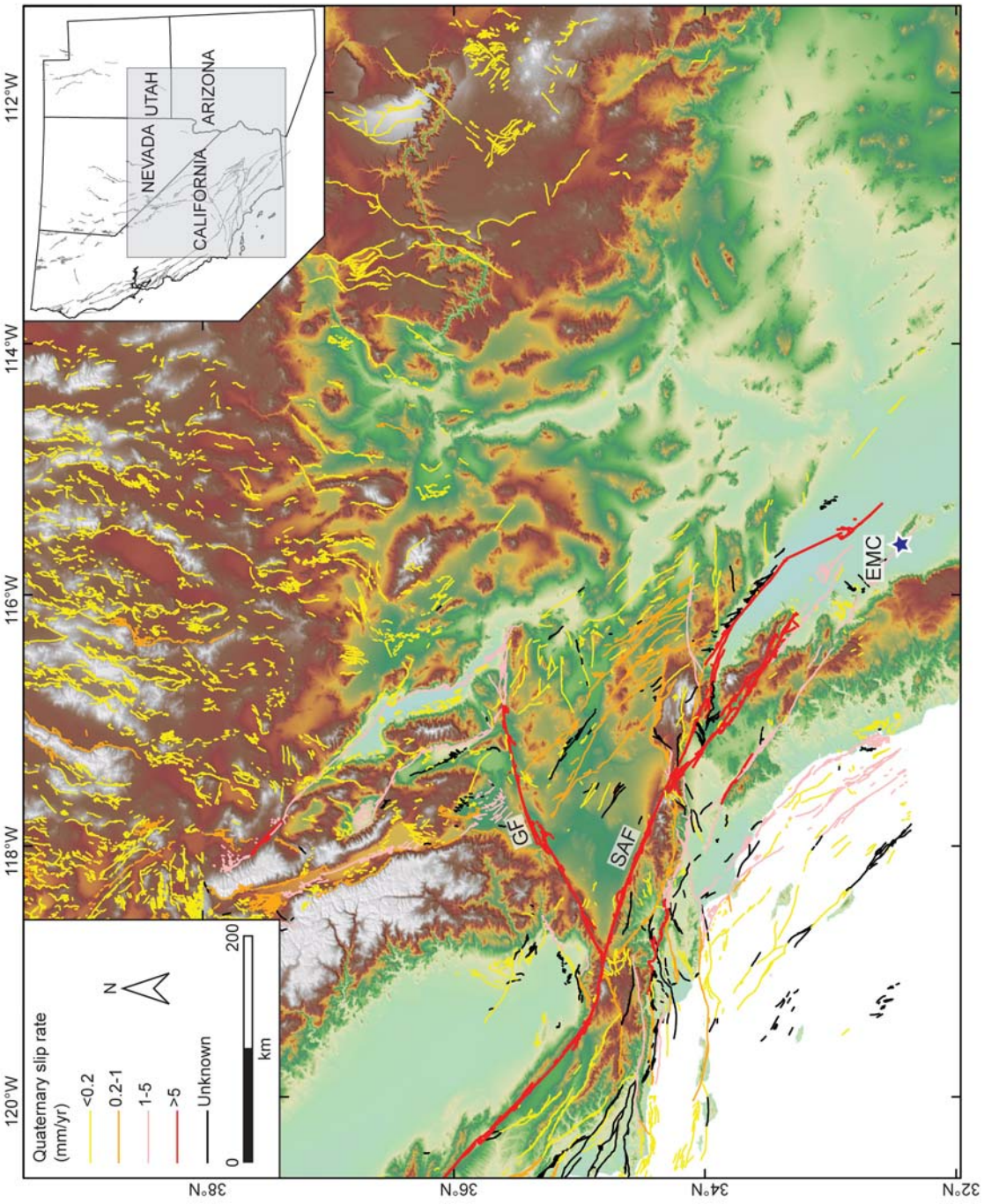
NEVADA
UTAH
ARIZONA
CALIFORNIA
112°W
114°W
116°W
118°W
120°W
38°N
36°N
34°N
32°N
EMC
GF
SAF
Quaternary slip rate
(mm/yr)
<0.2
0.2-1
1-5
>5
Unknown
N
200
km
0

Figure 3.5

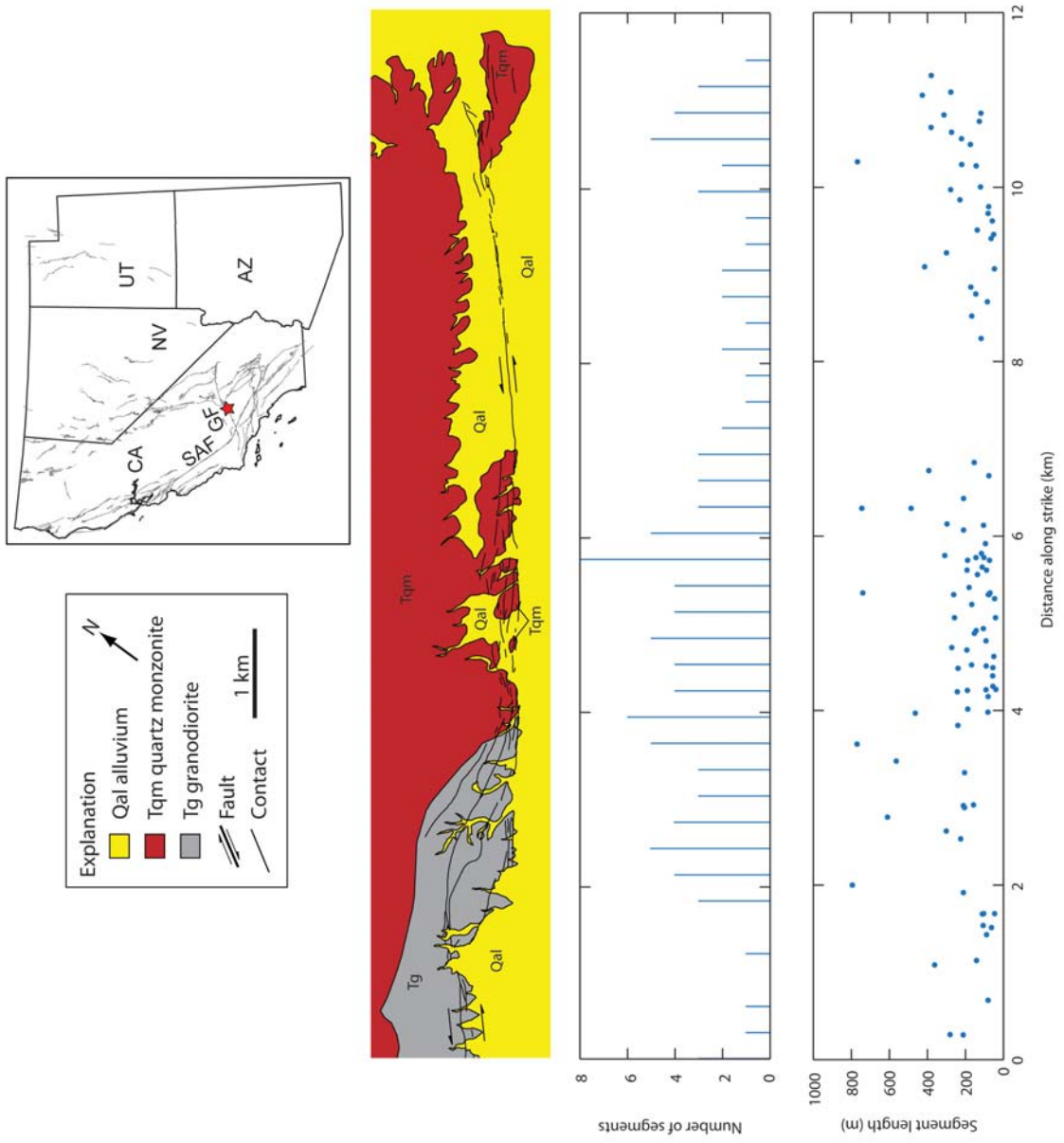
Explanation
Qal alluvium
Tqm quartz monzonite
Tg granodiorite
Fault
Contact
1 km
N
UT
AZ
NV
CA
SAF
GF
Tqm
Qal
Tg
Number of segments
Segment length (m)
Distance along strike (km)

Figure 3.6

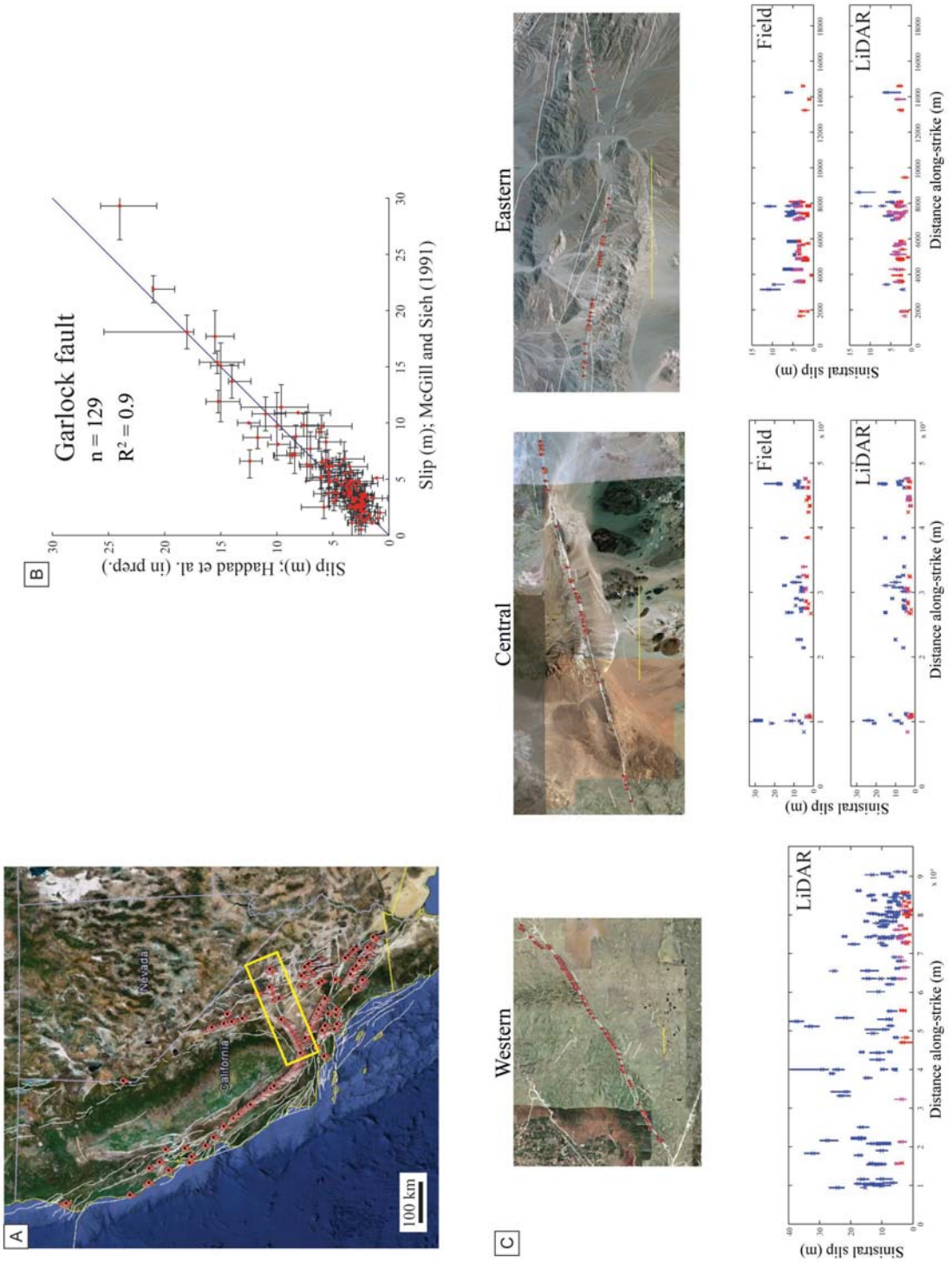
A
Nevada
California
100 km
B
Garlock fault
n = 129
R² = 0.9
Slip (m); Haddad et al. (in prep.)
Slip (m); McGill and Sieh (1991)
C
Western
Central
Eastern
LiDAR
Field
Sinistral slip (m)
Distance along-strike (m)

Figure 3.7

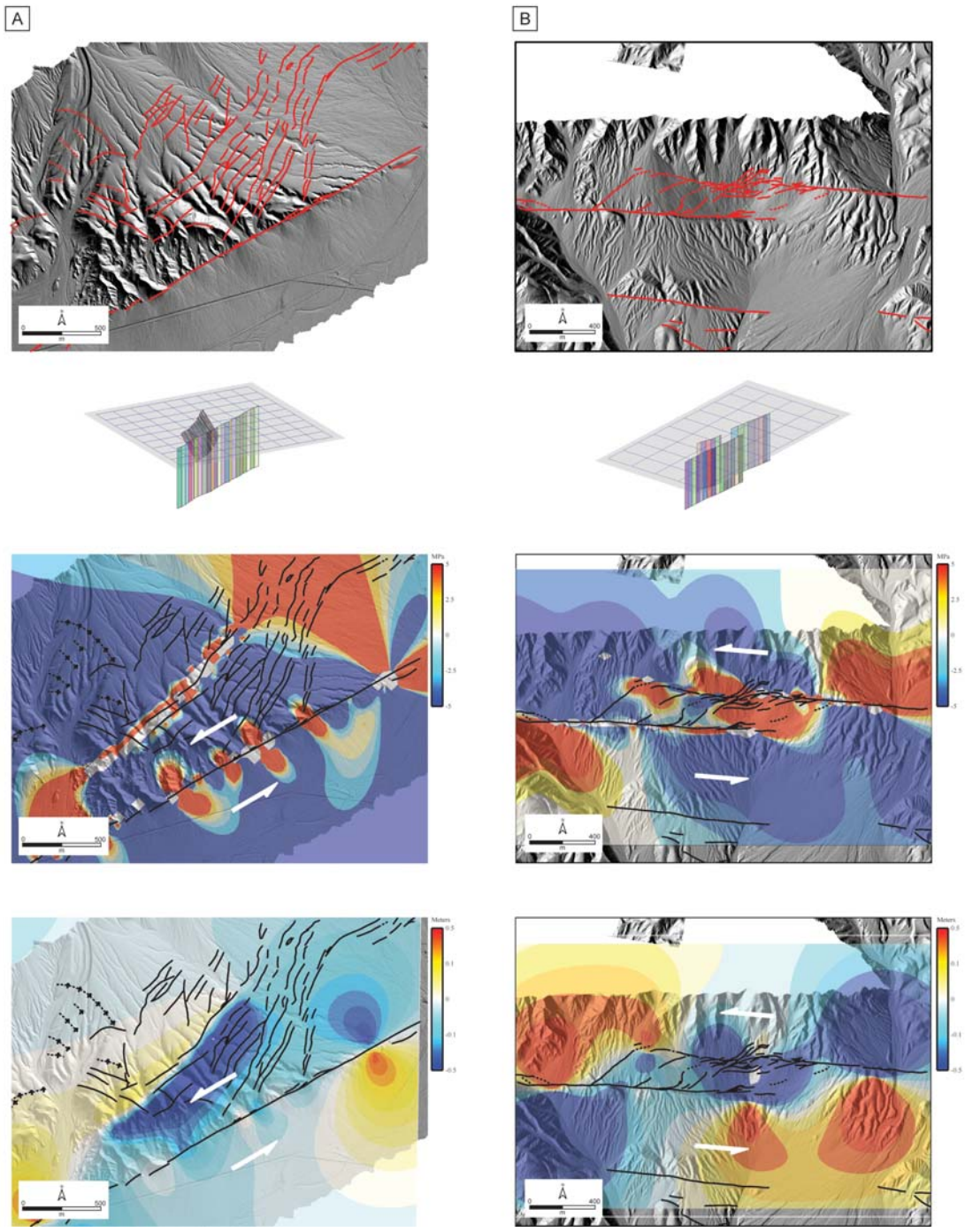

Figure 3.8

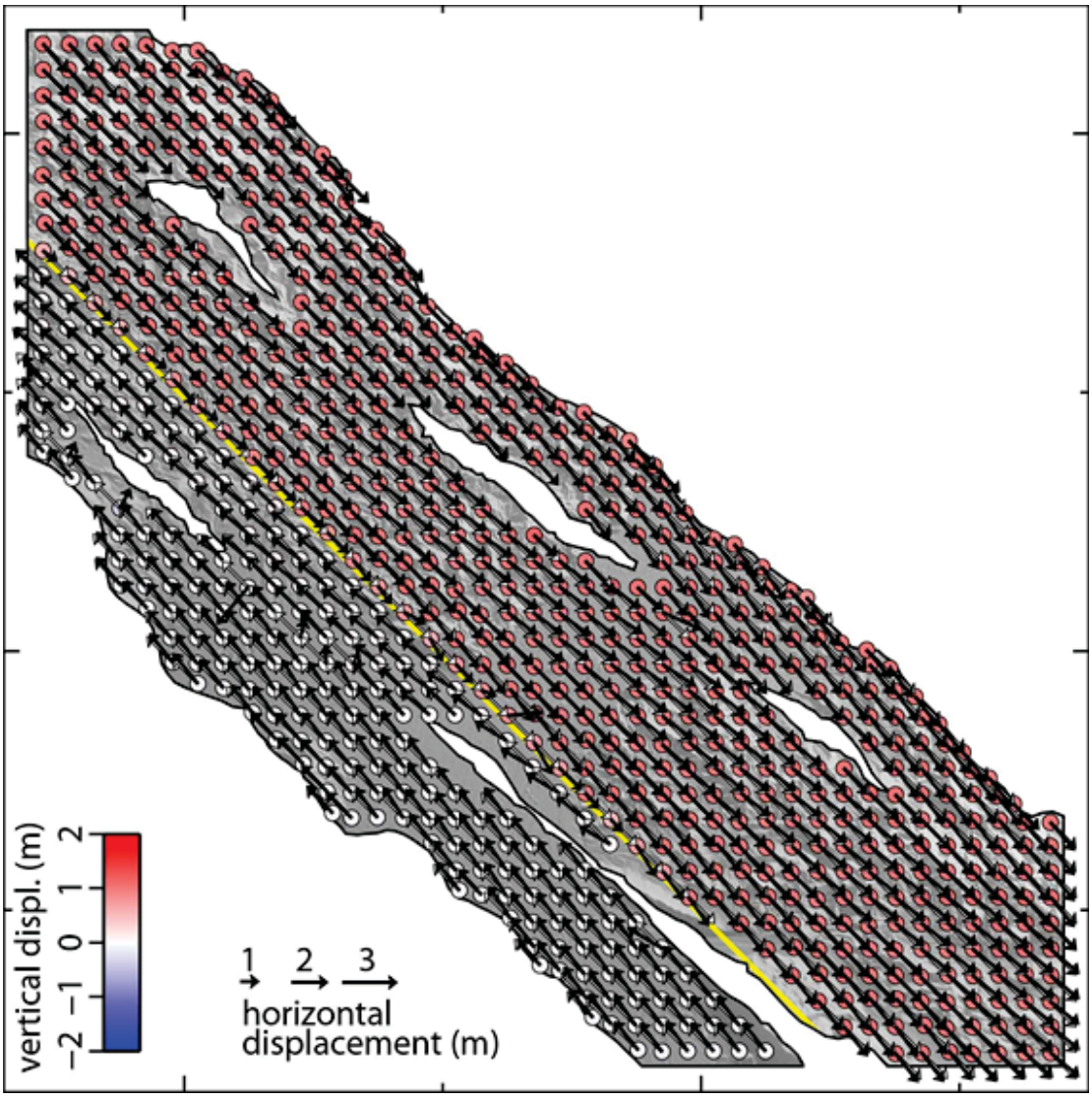

REFERENCES

Arrowsmith, J. R., Madden, C. M., Haddad, D. E., Salisbury, J. B., and Weldon, R. J., 2011, Compilation of slip in the last event data for high slip rate faults in California for input into slip-dependent rupture forecast: Eos Trans., no. AGU, S13B-06.

Arrowsmith, J. R., and Rhodes, D. D., 1994, Original forms and initial modifications of the Galway Lake Road scarp formed along the Emerson Fault during the 28 June 1992 Landers, California, Earthquake: Bulletin of the Seismological Society of America, v. 84, no. 3, p. 511-527.

Arrowsmith, J. R., Rhodes, D. D., and Pollard, D. D., 1998, Morphologic dating of scarps formed by repeated slip events along the San Andreas fault, Carrizo Plain, California: Journal of Geophysical Research, v. 103, no. B5, p. 10,141-110,160.

Arrowsmith, J. R., and Zielke, O., 2009, Tectonic geomorphology of the San Andreas Fault zone from high resolution topography: An example from the Cholame segment: Geomorphology, v. 113, p. 70-81.

Bevis, M., Hudnut, K., Sanchez, R., Toth, C., Grejner-Brzezinska, D., Kendrick, E., Caccamise, D., Raleigh, D., Zhou, H., Shan, S., Shindle, W., Yong, A., Harvey, J., Borsa, A., Ayoub, F., Elliot, B., Shrestha, R., Carter, B., Sartori, M., Phillips, D., Coloma, F., and Stark, K., 2005, The B4 Project: scanning the San Andreas and San Jacinto fault zones: Eos Trans. AGU 86(52), Fall Meet. Suppl., Abstract H34B-01.

Borsa, A., and Minster, J. B., in press, Rapid determination of near-fault earthquake deformation using differential LiDAR: Bulletin of the Seismological Society of America.

Carter, W. E., Shrestha, R. L., and Slatton, K. C., 2007, Geodetic laser scanning: Physics Today, v. 60, no. 12, p. 41-47.

DeLong, S. B., Hilley, G. E., Rymer, M. J., and Prentice, C., 2010, Fault zone structure from topography: Signatures of en echelon fault slip at Mustang Ridge on the San Andreas Fault, Monterey County, California: Tectonics, v. 29, no. TC5003, doi: 10.1029/2010TC002673.

El-Sheimy, N., Valeo, C., and Habib, A., 2005, Digital terrain modeling: acquisition, manipulation, and applications, Boston, MA, Artech House, 257 p.:

Haddad, D. E., Akciz, S. O., Arrowsmith, J. R., Rhodes, D. D., Oldow, J. S., Zielke, O., Toké, N. A., Haddad, A. G., Mauer, J., and Shilpakar, P., 2012, Applications of airborne and terrestrial laser scanning to paleoseismology: Geosphere, v. 8, no. 4, p. 771-786.

Haddad, D. E., Madden, C. M., Salisbury, J. B., Arrowsmith, J. R., and Weldon, R. J., 2011, LiDAR-derived measurements of slip in the most recent ground-rupturing earthquakes along elements of the San Andreas fault system: SCEC Proceedings and Abstracts, v. 21.

Hilley, G. E., DeLong, S., Prentice, C., Blisniuk, K., and Arrowsmith, J. R., 2010, Morphologic dating of fault scarps using airborne laser swath mapping (ALSM) data: Geophysical Research Letters, v. 37, no. L04301, doi: 10.1029/2009GL042044.

Hudnut, K. W., Borsa, A., Glennie, C., and Minster, J.-B., 2002, High-resolution topography along surface rupture of the 16 October 1999 Hector Mine, California, earthquake (Mw 7.1) from airborne laser swath mapping: Bulletin of the Seismological Society of America, v. 92, no. 4, p. 1570-1576.

Leprince, S., Hudnut, K. W., Akciz, S., Hinojosa-Corona, A., and Fletcher, J. M., 2011, Surface rupture and slip variation induced by the 2010 El Mayor-Cucupah earthquake, Baja California, quantified using COSI-Corr analysis on pre- and post-earthquake LiDAR acquitions: AGU Fall Meeting Abstracts, EP41A-0596.

Ludington, S., Moring, B. C., Miller, R. J., Stone, P. A., Bookstrom, A. A., Bedford, D. R., Evans, J. G., Haxel, G. A., Nutt, C. J., Flyn, K. S., and Hopkins, M. J., 2007, Preliminary integrated geologic map databases for the United States - Western States: California, Nevada, Arizona, Washington, Oregon, Idaho, and Utah: U.S. Geological Survey Open-File Report 2005-1305.

Madden, C. M., Arrowsmith, J. R., Haddad, D. E., Salisbury, J. B., and Weldon, R. J., 2011, Compilation of slip in the last earthquake data for high slip rate faults in California for input into slip-dependent rupture forecast: SCEC Proceedings and Abstracts, v. 21.

McGill, S. F., and Sieh, K., 1991, Surficial offsets on the central and eastern Garlock fault associated with prehistoric earthquakes: Journal of Geophysical Research, v. 96, no. B13, p. 21,597-521,621.

Nissen, E., Krishnan, A. K., Arrowsmith, J. R., and Saripalli, S., in press, Three-dimensional surface displacements and rotations from differencing pre- and post-earthquake LiDAR point clouds: Geophysical Research Letters.

Okada, Y., 1992, Internal deformation due to shear and tensile faults in a half-space: Bulletin of the Seismological Society of America, v. 82, no. 2, p. 1018-1040.

Oskin, M., Arrowsmith, R., Hinojosa, A., Gonzalez, J., Gonzalez, A., Sartori, M., Fernandez, J., Fialko, Y., Floyd, M., Galetzka, J., and Sandwell, D., 2010a, Airborne lidar survey of the 4 April 2010 El Mayor-Cucupah earthquake rupture: (proceedings and abstracts): Southern California Earthquake Center Annual Meeting, Palm Springs, California, September 12-16, 2009, 19.

Oskin, M. E., Arrowsmith, J. R., Hinojosa, A. C., Elliott, A. J., Fletcher, J. M., Fielding, E. J., Gold, P. O., Garcia, J. J. G., Hudnut, K. W., Liu-Zheng, J., and Teran, O. J., 2012, Near-field deformation from the El Mayor-Cucupah earthquake revealed by differential LiDAR: Science, v. 335, no. 702.

Oskin, M. E., Gold, P. O., Hinojosa, A., Arrowsmith, J. R., Elliott, A. J., Taylor, M. H., Herrs, A. J., Sartori, M., Gonzalez-Garcia, J. J., Gonzalez, A., Kreylos, O., and Cowgill, E., 2010b, Airborne and terrestrial lidar imaging and analysis of the 4 April 2010 El Mayor-Cucupah earthquake rupture: Abstract T35B-2135 presented at 2010 Fall Meeting, AGU, San Francisco, Calif. 13-17 Dec.

Oskin, M. E., Le, K., and Strane, M. D., 2007, Quantifying fault-zone activity in arid environments with high-resolution topography: Geophysical Research Letters, v. 34, no. L23S05, doi: 10.1029/2007GL031295.

Prentice, C. S., Crosby, C. J., Whitehill, C. S., Arrowsmith, J. R., Furlong, K. P., and Phillips, D. A., 2009, Illuminating northern California's active faults: Eos, v. 90, no. 7, p. 55-56.

Quigley, M., Van Dissen, R., Litchfield, N., Duffy, B., Barrell, D., Furlong, K., Stahl, T., Bilderback, E., and Noble, D., 2012, Surface rupture during the 2010 Mw 7.1 Darfield (Canterbury) earthquake: implications for fault rupture dynamics and seismic-hazard analysis: Geology, v. 40, no. 1, p. 55-58.

Scholz, C. H., 2002, The mechanics of earthquakes and faulting, Cambridge, Cambridge Universiry Press, 496 p.:

Shan, S., Bevis, M., Kendrick, E., Mader, G. L., Raleigh, D., Hudnut, K., Sartori, M., and Phillips, D., 2007, Kinematic GPS solutions for aircraft trajectories: Identifying and minimizing systematic height errors associated with atmospheric propagation delays: Geophysical Research Letters, v. 34, no. 23.

Sibson, R. H., 1986, Earthquakes and rock deformation in crustal fault zones: Annual Reviews of Earth and Planetary Sciences, v. 14, p. 149-175.

Sylvester, A. G., 1999, Rifting, transpression, and neotectonics in the Central Mecca Hills, Salton Trough, Santa Barbara, University of California, Santa Barbara, 52 p.:

Terza, G., Galgaro, A., Zaltron, N., and Genevois, R., 2007, Terrestrial laser scanner to detect landslide displacement fields: a new approach: International Journal of Remote Sensing, v. 28, no. 16, p. 3425-3446.

Titus, S. J., Dyson, M., DeMets, C., Tikoff, B., Rolandone, F., and Buergmann, R., 2011, Geologic versus geodetic deformation adjacent to the San Andreas fault, central California: Geological Society of America Bulletin, v. 123, no. 5-6, p. 794-820.

Vedder, J. G., and Wallace, R. E., 1970, Recent active breaks along the San Andreas fault between Cholame Valley and Tejon Pass, California: U.S. Geological Survey Miscellaneous Geological Investigations Map I-741, scale 1:24,000, 3 sheets.

WGCEP, 2008, The uniform California earthquake rupture forecast, Version 2 (UCERF 2): U.S. Geological Survey Open File Report 2007-1437, p. 104.

Zielke, O., and Arrowsmith, J. R., 2008, Depth variation of coseismic stress drop explains bimodal earthquake magnitude-frequency distribution: Geophysical Research Letters, v. 35, no. 24.

Zielke, O., and Arrowsmith, J. R., 2012, LaDiCaoz and LiDARimager - MATLAB GUIs for LiDAR data handling and lateral displacement measurement: Geosphere, v. 8, p. 206-221.

Zielke, O., Arrowsmith, J. R., Ludwig, L. G., and Akciz, S. O., 2010, Slip in the 1857 and earlier large earthquakes along the Carrizo Plain, San Andreas Fault: Science, v. 327, p. 1119-1122.

Chapter 4

EFFECTS OF FAULT STRUCTURAL COMPLEXITY, FRICTIONAL PROPERTIES, AND ROUGHNESS ON SURFACE SLIP AND RUPTURE JUMPING PROBABILITIES

ABSTRACT

The topographic manifestation of earthquakes takes on many forms which are exploited by geologists to infer rupture processes, interpret paleoseismic data, and construct earthquake recurrence models. These interpretations may be difficult to make because natural fault systems are arranged in complicated geometries that contain complex frictional properties. Here I use a quasi-static earthquake simulator to investigate the effect of fault structural complexity and frictional properties on how large earthquakes are recorded in topography. I also use long records of simulated earthquakes to investigate how these factors control rupture jumping probabilities. I model the following fault structural scenarios: a single fault with simple frictional behavior, two faults with a velocity-strengthening (stable sliding/creeping) sedimentary basin, a single fault with a creeping section, two faults in releasing/restraining stepovers, and three faults in releasing/restraining double bends. All modeled configurations changed the shapes of along-strike surface slip distributions and rupture jumping probabilities. In the scenario of a velocity-strengthening basin, I found that deep basins allow only the largest earthquakes to transit coseismic deformation to the ground surface. For the single fault with a creeping section scenario, only the long-term record of coseismic faulting was preserved in the ground surface when the degree of velocity-strengthening for the creeping section was increased. Whether the releasing or restraining steps/bends

controlled rupture jumping probabilities depended on fault roughness. Rough faults limited the lateral extent of ruptures because coseismic stresses due to slip were consumed by overcoming fault asperities. Therefore, rupture jumping probabilities for rough faults increased only when stepover distances were sufficiently small (2 km). I propose that the widely accepted 3 – 5 km radius of the rupture process zone (Wesnousky, 2008) varies as a function of fault roughness. These results have direct implications for guiding the interpretation of paleoseismic data and generating rupture propagation rules in earthquake forecasts.

INTRODUCTION

Faults in nature rarely exist as individual planar surfaces. Instead, they are organized into zones of discontinuities and behave as interacting systems. At crustal scales, these interactions are controlled by the mechanical properties of the lithosphere, tectonic loading rates along plate boundaries, and the structural and frictional complexities of fault segments (Scholz, 2002). All of these factors ultimately govern the behavior of fault systems and hence their seismic hazard potential.

Large-magnitude earthquakes originate in the middle to lower depths of the seismogenic zone and transmit deformation to Earth's surface (Fig. 4.1). The topographic record of such ruptures may be localized along fault scarps and offset geomorphic markers or distributed via off-fault folding and warping (e.g., Salyards et al., 1992; Oskin et al., 2012). This record forms the basis for along-strike surface slip distributions of ground-rupturing earthquakes, which is a fundamental dataset that forms the basis for reconstructing the seismic behavior of active faults. Surface slip distributions are documented using a combination of field measurements/mapping and instrumentation (e.g., lidar, InSAR). However, even for well-studied faults such as the southern San Andreas fault system, measurements of coseismic slip that extend beyond the timing of penultimate earthquakes are few and widely scattered. Given the importance of these datasets in earthquake forecasts (e.g., the Uniform California Earthquake Forecast – UCERF3: http://pubs.usgs.gov/of/2013/1165/), various attempts have been made to construct surface slip distributions for prehistoric earthquakes using few slip measurements (e.g., Chang and Smith, 2002). These estimates are probabilistic in nature in that they model slip distributions as elliptical probability distributions that are then

inverted for earthquake magnitude and surface rupture length to give slip measurements at a point (e.g., Biasi and Weldon, 2006).

UCERF3 employs a compilation of slip measurements and slip rates (e.g., Haddad et al., 2011; Madden et al., 2011) as geologic constraints to its deformation model (Field et al., 2013). Given the paucity of geologic slip rates and slip measurements for most of California's faults, the UCERF3 deformation model idealizes slip distributions for California faults using the above-mentioned probabilistic approach (Field et al., 2013). However, several factors control the surface slip distributions of earthquakes. Structural and frictional complexities along faults can be responsible for highly variable slip distributions for large earthquakes. These complexities also control the long-term clustering of earthquakes in space and time. Therefore, the spatiotemporal variations of slip rates determined at individual points along faults will vary. As a result, the mechanical characteristics of fault surfaces, structural geometry, and frictional properties will influence the surface slip distributions of large earthquakes (Scholz, 2002) and thus how paleoseismically determined slip rates are interpreted in UCERF3.

Extensive documentation of surface slip distributions and rupture maps from historic earthquakes by Wesnousky (2008), for example, showed the wide variability in surface slip distributions (Fig. 4.2). Consider the 1987 Superstition Hills earthquake (M_w 6.2) as an example (Fig. 4.2A). The surface rupture length for this earthquake was 27 km and propagated through several stepovers prior to stopping. What controlled the shape of the Superstition Hills earthquake's slip distribution? Why did the rupture break through the stepover regions and stop? This example, along with the many examples presented in Wesnousky's (2008) compilation, hints at the need to make mechanical sense of

coseismic slip distributions instead of simply using empirical methods to predict their shapes.

A major finding from empirical compilations of earthquake ruptures (e.g., Wesnousky, 1988, 2006; Wesnousky, 2008) is that there exists a critical stepover distance beyond which ruptures do not jump. These observations showed that rupture jumping is primarily controlled by the geometrical complexity of structural barriers such as stepovers and double bends. For strike-slip earthquakes, there exists a 3-4 km limit on the stepover distance through which recent and historic ruptures did not jump. The plausibility of multi-fault rupture and fault-to-fault rupture jumping that is implemented in UCERF3 is based on this critical distance (Field et al., 2013) despite the fact that rupture jumping probabilities are controlled by a multitude of factors that are not explained by empirical observations alone (Wesnousky, 2008).

In this chapter, I pursue two goals: (1) show how the mechanical, frictional, and structural complexities of faults affect the distribution of slip over single and thousands of earthquakes, and (2) present a physically based method for determining the likelihood of fault-to-fault rupture jumping. To meet these goals, I use an earthquake simulator to derive a basic understanding of the effects of rate- and state-friction on the slip distributions of ground-rupturing earthquakes. I then investigate the controls of the geometry of structural barriers, sedimentary basins, and fault creep on surface slip distributions and slip rates at a point. This is followed by a presentation of a new method to compute rupture jumping probabilities. My goals are formulated in response to the plan put forth by UCERF of implementing future improvements to its next iteration of

California's earthquake forecast model. As shown in this chapter, earthquake simulators will play a definitive role in improving future earthquake forecast.

METHODS

In this section, I provide a brief overview of earthquake simulators and the details of the earthquake simulator that I used. I then describe each modeling scenario and how I calculated rupture jumping probabilities. Figure 4.3 provides graphical definitions of fault stepovers and double bends that I used in this chapter.

Earthquake Simulators

Despite the availability of dense seismic records of recent earthquakes and seismic networks that record the complete earthquake cycle (interseismic – coseismic – post-seismic – interseismic) for small repeating earthquakes (e.g., along the creeping section of the San Andreas fault), a complete earthquake cycle for large (>M_w 7) earthquakes has yet to be documented. This forms the crux of the challenges faced by efforts to document the detailed processes of plate boundary evolution, the seismicity of faults, and the formulation of accurate earthquake forecasts. This has led to the development of earthquake simulators, which are numerical models that are designed to simulate long earthquake records using what we know about the mechanics of faults and the physics of earthquakes. Earthquake simulators provide us with opportunities to investigate earthquake phenomena that are otherwise not possible (e.g., Zielke and Arrowsmith, 2008).

Several flavors of earthquake simulators have been developed over the years (Tullis et al., 2012). The most recent of these include ALLCAL (Ward, 2012), Virtual California (Sachs et al., 2012), ViscoSim (Pollitz, 2012), and RSQSim (Richards-Dinger

and Dieterich, 2012). These simulators incorporate one form or another of the following components: tectonic loading mechanism, fault interaction, implementation of various friction laws, and elastodynamic effects. I refer the reader to the *Seismological Research Letters* focused issue (Tullis et al., 2012) on earthquake simulators for a complete description of these simulators, their strengths, and limitations.

FIMozFric Earthquake Simulator

In this chapter I use FIMozFric (Zielke and Arrowsmith, 2008; Zielke, 2009). FIMozFric is a quasi-static, physics-based earthquake simulator that incorporates fault interaction and enables the construction of fault frameworks that are governed by complex friction laws. FIMozFric employs the 3D boundary element method and numerically models the stresses and strains that result from slip along rectangular displacement discontinuities (faults). Faults are embedded in a mechanically homogeneous, isotropic, and linear-elastic halfspace (e.g., Okada, 1992; Densmore et al. 1998; Toda et al. 2011). FIMozFric was initially used by (Zielke and Arrowsmith, 2008) to generate long earthquake records and statistically interrogate the physical causes of the bimodality of earthquake magnitude-frequency distributions. Zielke and Arrowsmith (2008) found that bimodal magnitude-frequency distributions can be explained by the depth, and hence temperature, dependence of constitutive friction laws that govern depth-variable coseismic stress drops.

Friction Implementation

In FIMozFric, faults are discretized into1 km x 1 km discontinuities, henceforth referred to as patches, which are assigned varying strikes and dips to simulate non planar surfaces. Each patch is also assigned dynamic and static coefficients of friction. The

difference between these coefficients varies with depth in order to simulate laboratory-derived fault friction behavior. This is done by expanding upon the Coulomb friction law and implementing the depth/temperature dependency effects on fault friction. Laboratory friction experiments show that friction varies with slip velocity (rate dependence) and holding time (time since the last slip occurred on the slip interface) (e.g., Marone et al., 1990; Blanpied et al., 1991; Beeler et al., 1994; Dieterich and Kilgore, 1994). This resulted in the formulation of the rate- and state-friction law (Ruina, 1983),

$$\tau = \sigma_n \left[\mu_0 + a \ln \frac{V}{V_0} + b \ln \frac{V_0 \theta}{D_c}\right], \tag{4.1}$$

where τ is the shear stress, σ_n is the normal stress, μ_0 is the initial coefficient of friction, V is the sliding velocity, V_0 is the initial sliding velocity, θ is the state variable, D_c is the critical slip distance, and a, b are experimentally determined constants. Velocity-weakening frictional behavior occurs when $[a - b] < 0$ and promotes unstable sliding (earthquakes) whereas velocity-strengthening behavior promotes stable sliding (creep) and occurs when $[a - b] > 0$.

In FIMozFric, each fault patch is assigned a $[a - b]$ value to determine its frictional behavior during simulations (Zielke and Arrowsmith, 2008; Zielke, 2009). FIMozFric also allows the distribution of velocity-strengthening and velocity-weakening patches to be customized so that the effects of realistic fault properties can be investigated (e.g., a creeping section in an otherwise locked fault, sedimentary basins, etc.).

Seismic Cycle Implementation

FIMozFric divides the seismic cycle into interseismic and coseismic stages by iteratively evaluating the current state of stress along all patches given their friction

coefficients and the tectonic loading rate (Zielke and Arrowsmith, 2008; Zielke, 2009). During the interseismic stage, the tectonic loading mechanism incrementally increases shear tractions until they exceed the static friction strength of a patch (see Chapter 3 for a formulation of this criterion). The shear traction and friction strength of each patch is calculated at every interseismic time increment. FIMozFric enteres the coseismic stage if shear tractions exceed the frictional strength of at least one patch. When this happens, the tectonic loading mechanism is halted and the static friction coefficients of all patches that failed are converted to dynamic friction coefficients. Shear tractions are then relieved via in-plane slip. Displacements due to slip along patches are calculated using Okada's (1992)formulations, which alter the local stresses in the volume surrounding the failed patches. These altered stresses may induce further coseismic stresses on neighboring patches and may cause them to fail too. Thus an earthquake is born and propagates along the fault until all shear tractions are released and fall below the dynamic strength of activated patches. Once this happens, FIMozFric enters the interseismic stage where static friction coefficients are reapplied to all patches and the tectonic loading mechanism is resumed. The above process is done quasi-statically such that no time component is included (i.e. the simulations are not dynamic) except to move the stress and resulting strain calculations forward.

Coulomb Failure Stress Analysis: the FIMoz Model

To help provide mechanical explanations for the results presented in this chapter, I employed the Coulomb failure stress (CFS) analysis in FIMoz. As with FIMozFric, FIMoz is a separate program that divides fault segments into 1 km x 1 km patches. Coulomb failure stress calculations are made using a stress boundary condition with σ_1

and σ_3 oriented to encourage right-lateral slip on fixed receiver faults. All receiver faults have the same orientation as the main faults in each model scenario. For some scenarios, I selected representative earthquakes from the FIMozFric earthquake catalogs to calculate CFS and illustrate the intricate details of how the mechanics of the rupturing process explain my results. All CFS calculations presented in this chapter are displayed at a depth of 8.5 km (half the seismogenic width).

Fault Roughness

FIMozFric allows for the simulation of earthquakes along faults that are either smooth or rough. I define fault roughness as the deviation from a planar surface. This deviation is described in FIMozFric by the random mid-point displacement algorithm (e.g., Zielke, 2009). Faults are discretized into 1 km by 1 km patches where the midpoint of each patch is displaced from a central fault plane. The strike and dip of each patch are varied along strike and with depth so that a continuous self-similar fault surface is constructed (e.g., Power and Tullis, 1991). Figure 4.4 illustrates the difference between a smooth and a rough fault. In some of the experiments presented in this chapter, I investigate the controls that fault roughness have on the mechanics of simulated earthquakes and the surface manifestation of coseismic faulting.

Calculating Surface Slip Distributions and Slip at a Point for a Single Fault

To help build a basic understanding of the surface manifestations of earthquakes at the paleoseismic and microgeomorphic spatiotemporal scales, I start simple by simulating earthquakes along a single, vertically dipping strike-slip fault with a simple down-dip and along-strike rate- and state-dependent friction distribution. The fault is 100 km long and 17 km wide with a 30 mm/yr tectonic loading rate applied using the self-

induced strain formulation (Zielke, personal communication). The elastic halfspace is assigned a Young's modulus of 40 GPa, Poisson's ratio of 0.25, shear modulus of 16 GPa, and a density of 2700 kg/m^3. These parameters were used in this experiment and all experiments presented in the remainder of this chapter.

Control of Stepover and Underlap/Overlap Distance on Surface Slip Distributions and Slip at a Point

It has long been known that the particular framework of structural barriers such as underlap/overlap regions, stepovers, and double bends controls displacement distributions along faults at spatiotemporal scales of single earthquakes (e.g., Wesnousky, 1988, 2006; Wesnousky, 2008) and over geologic time (e.g., Ferrill and Morris, 2001). Analytical (e.g., Segall and Pollard, 1980) and numerical (Segall, 2010) expressions provide us with insights into the mechanics of this relationship. However, analyses of individual earthquakes allow for very focused but short-term views of the surface manifestation and the mechanics of single earthquakes, thereby making them too fault-specific and not useful at helping us make generalizations about the overall coseismic behavior of faults. On the other hand, analyses into the cumulative displacements accommodated by faults over long (>10,000 years) timescales allow us to make fairly good generalizations about relationships (e.g., displacement-length scaling) but are too coarse to give us sufficient insight into the timescales in which paleoseismic and microgeomorphic analyses (several 1000s of years) are used to guide earthquake forecasts. This is where FIMozFric earthquake simulator comes in handy by providing us with the sufficient spatiotemporal scales of investigation.

In this set of experiments, I use FIMozFric to simulate earthquakes rupturing through releasing steps with variable stepover distances (7 km, 5 km, and 2 km). These simulations were done on two fault systems; one with a 20 km underlap and the other with a 50 km overlap. I used the same model parameters as those described in Figure 4.5 (i.e. tectonic loading rate of 30 mm/yr, Coulomb failure with a simple [$a - b$] friction profile, etc.).

Effect of Sedimentary Basin Depth on Surface Slip Distributions and Slip at a Point

Earthquake ruptures that propagate through unconsolidated to poorly consolidated sediments are manifest by complex and sometimes obscured topographic expressions (e.g., Oskin et al., 2012; Moss et al., 2013). As a result, preservation of displaced features and their measurement by geologists in the field and remotely via lidar may not be representative of subsurface faulting behavior. In this set of experiments, I add another level of complexity to the above structural settings by including a sedimentary basin in the stepover regions. Consider the geometry of two right-stepping, right-lateral vertical strike-slip faults. This geometry creates a releasing step that is manifest as a topographic depression. The creation of accommodation space in the stepover region lends hand to the formation of thick sedimentary basins if given sufficient space and time (Burbank and Anderson, 2001).

The portions of faults that are embedded in thick, poorly consolidated sediments exhibit velocity-strengthening frictional behavior (e.g., Chang et al., 2013). In this set of experiments, I simulate the presence of a sedimentary basin by assigning a region of velocity-strengthening friction to the faults in the overlapping section. InSAR datasets of recent earthquakes have determined [$a - b$] values that are in the range of 0.004 to 0.007

(unitless) at depths ranging from 0 to 7 km in fault regions where coseismic ruptures occurred in unconsolidated to poorly consolidated sediments (Chang et al., 2013; Kaneko et al., 2013; Gualandi et al., 2014). These values were corroborated by recent laboratory experiments for velocity-strengthening fault rocks (e.g., Chang et al., 2013). Given this wide range of published [$a - b$] friction values for sediments, I selected a [$a - b$] of 0.005 for rate- and state-dependent friction in the sedimentary basins. Whether this is the correct number is not the point; the patterns of surface slip and slip at a point observed in this set of experiments is what matters and provides important insights into the control of sedimentary basins in accommodation zones on the surface expression of coseismic faulting. For each simulation, I varied the overall down-dip extent of the velocity-strengthening basin from 1 km, 2 km, and 3 km to explore the effect of varying the depth of the sedimentary basin on the slip distributions and magnitudes of slip-at-a-point. I used the same model parameters as those described in Figure 4.5 (i.e. tectonic loading rate of 30 mm/yr, Coulomb failure with a simple [$a - b$] friction profile, etc.).

Effect of Fault Creep on Surface Slip Distributions and Slip at a Point

In this set of experiments, I vary the [$a - b$] frictional strength of a shallow creeping section from 0.002 to 0.008 to span the range of observed [$a - b$] values from laboratory friction experiments and geodetic data (Chang et al., 2013; Kaneko et al., 2013; Gualandi et al., 2014). The simulated earthquakes ruptured through a 100 km-long and 17 km-wide vertically dipping fault. The shallow creeping section spanned 40 km in length and had a down-dip extent of 6 km. The remainder of the fault followed a regular [$a - b$] frictional profile and the same model parameters described in Figure 4.5 (i.e.

tectonic loading rate of 30 mm/yr, Coulomb failure with a simple [$a - b$] friction profile, etc.).

To Jump or Not to Jump? Rupture Jumping Probabilities

Determining the probabilities of multi-fault ruptures or rupture jumping has been a subject of research for many years. The first computational studies that investigated what controls rupture jumping were by Harris et al. (1991) and Harris and Day (1993). These studies simulated earthquakes along parallel faults and found that ruptures can jump through structural barriers that are up to 5 km wide for releasing steps and up to ~2 km wide for restraining steps (e.g., Oglesby et al., 2003; Oglesby, 2008; Lozos et al., 2012). Work by Aochi et al. (2002), Kame et al. (2003), Kase and Day (2006), and Duan and Oglesby (2006) used dynamic rupture models to show that rupture jumping depends on the geometries of faults and the structural barriers.

Here I expand on this work by incorporating probability calculations for rupture jumping given various structural arrangements in FIMozFric. I carry out experiments on various long earthquake records of different structural and frictional configurations. Given a particular structural configuration, what is the probability that a fault segment will rupture as a result of rupture occurring on a neighboring fault? The following section describes how I calculate the conditional probability of a rupture jumping from one fault to another for various structural configurations. I remind the reader that my numerical experiments do not include processes and effects that are inherent to rupture dynamics because FIMozFric simulates earthquakes in a quasi-static manner.

Calculating Rupture Jumping Probabilities

Earthquake catalogs generated by FIMozFric provide an efficient and statistically robust dataset from which the probability of ruptures jumping from fault to fault across structural complexities can be calculated. This section describes how I compute rupture jumping probabilities. I then provide a worked example that demonstrates how this calculation is done.

Calculating the probability of a rupture jumping from one fault to another is best expressed as a conditional probability. For example, consider a two-fault system consisting of Segments 1 and 2. If a rupture initiates on Segment 1, what is its probability of jumping to Segment 2? In other words, what is the probability of Segment 2 rupturing as a resulting of rupture occurring on Segment 1? In this question, the probability of a rupture jumping to Segment 2 is ***conditioned*** on Segment 1 rupturing. Using this formulation, I report rupture-jumping probabilities as ***conditional probabilities***. Similarly, in a three-fault system that contains hypothetical fault Segments 1, 2, and 3, one can compute the probability of a rupture jumping by conditioning it on any segment of choice. For example, what is the probability of Segments 2 and 3 failing as a result of rupture occurring on Segment 1 (i.e. ***conditioned*** on Segment 1)?

Two pieces of information are needed to calculate the conditional rupture jumping probabilities: (1) the percentage of patches in each fault segment that were activated during every earthquake in the catalog, and (2) the minimum number of failed patches needed to trigger a rupture jump from one fault to another, henceforth termed the "***minimum patch participation level***." Given that the number of fault patches that failed during each event is known in an earthquake catalog, the number of patches that failed in

each segment during each event can easily be computed as a percentage of the total number of patches for both segments (e.g., 20% of Segment 1's patches failed during an arbitrary earthquake). However, determining the appropriate minimum number of activated patches that is necessary to trigger rupture jumping is not as straightforward and requires a sweep through the minimum patch participation level. For example, suppose Event ID 2134 was a M7.6 earthquake in a hypothetical earthquake catalog for a two-fault system, and that 23% of the patches in Segment 1 and 5% of the patches in Segment 2 were activated. FIMozFric first searches the catalog for events that occurred on Segments 1 and 2 where at least *x*% of the patches in Segment 1 failed. For both segments, the participation probabilities are normalized to Segment 1's participation probability and reported as rupture jumping probabilities conditioned on Segment 1. But what value for *x* should be used as the minimum patch participation level?

Table 4.1 shows a worked example of how I calculate conditional rupture jumping probabilities. Note that the worked example is hypothetical. In this example, every time a rupture occurs along Segment 1 which activates at least 70% of its patches, Segment 2 has a 46% chance of participating in that rupture. Conversely, if the rupture jumping probability were conditioned on Segment 2, then every time a rupture occurs on Segment 2 that activates at least 70% of its patches, Segment 1 has a 48% chance of participating in that rupture. In this example, the 70% parameter is the minimum patch participation level.

Determining the Minimum Patch Participation Level

With the above in mind, which value should be used to set the minimum patch participation level (e.g., 70% in the example presented in Table 4.1) that is best suited to

determine the probability of fault-to-fault rupture jumping? Does any threshold exist for the least number of patches needed to fail so that a rupture can jump from one fault to another? The following section describes a parameter sweep that I did for the minimum patch participation level to determine this.

I systematically swept through the minimum patch participation level from 0-100% using the following structural barrier configurations (Fig. 4.6):

- Releasing step (two fault segments)
    - 20 km underlap: 7 km, 5 km, and 2 km stepover distances.
    - 50 km overlap: 7 km, 5 km, and 2 km stepover distances.
- Restraining step (two fault segments)
    - 20 km underlap: 7 km, 5 km, and 2 km stepover distances.
    - 50 km overlap: 7 km, 5 km, and 2 km stepover distances.
- Releasing double bend (three fault segments)
    - 20 km underlap between Segments 1 and 2: 7 km, 5 km, and 2 km stepover distances.
- Restraining double bend (three fault segments)
    - 20 km underlap between Segments 1 and 2: 7 km, 5 km, and 2 km stepover distances.

In the releasing and restraining step scenarios, fault segments were 17 km-wide, vertically dipping right-lateral faults. Segments 1 and 2 were 100 km long and 17 km wide. In the releasing and restraining double-bend scenarios, the length of Segment 3 varied as a function of the stepover distance, but in most cases was approximately 20 km long and 17 km wide. Segments 1 and 2 served as primary faults while Segment 3 was an

intermediary fault that connected Segments 1 and 2. The goals of the restraining and releasing double-bend experiments were to determine (1) if the intermediary fault (Segment 3) promoted/inhibited rupture propagation from Segment 1 to Segment 2, and (2) if the vergence direction (releasing/restraining) of Segments 1 and 2 controlled rupture jumping probabilities.

For each experiment, I swept through the minimum patch participation level parameter from 0% (no patches ruptured) to 100% (all patches ruptured) for all segments such that the conditional probabilities of rupture jumping were computed for each fault (i.e. conditioned on Segments 1, 2, and 3 individually). Furthermore, all experiments were performed on smooth and rough fault topologies to determine if fault roughness controlled rupture jumping probabilities. I used the same model parameters as those described in Figure 4.5 (i.e. tectonic loading rate of 30 mm/yr, Coulomb failure with a simple [$a - b$] friction profile, etc.).

Relative Rupture Time

Although the above simulations were quasi-static in nature (as opposed to fully dynamic simulations of rupture propagation), the iterative mechanical interaction between individual patches allows for the tracking of when patches fail relative to each other. Therefore, although FIMozFric cannot dynamically simulate individual ruptures, the relative timing of when patches fail in each earthquake can be interrogated to statically illustrate the order in which patches failed and hence serve as a proxy for rupture time. Figure 4.7 is an example of the relative rupture time for a single earthquake. Red patches are patches that ruptured first, followed by yellow, green, blue, and finally purple patches that failed last. In this example (Fig. 4.7), the rupture initiated in the center

of the fault and propagated outward from this nucleation site. The utility of this feature in FIMozFric is that one can quasi-statically investigate the path along which earthquake ruptures pass around local asperities (in rough faults, for example) and whether ruptures initiate at these asperities or within structural barrier zones.

Fault Topologic Effects on Rupture Jumping Probabilities

The nature of smooth faults generated in FIMozFric is such that the variability in their surface morphology is low. As a result, rupture jumping probabilities for smooth faults are not expected to be controlled by the minor differences in the strikes and dips of patches that make up smooth faults. On the other hand, asperities along rough faults may influence rupture jumping probabilities. To investigate this, I ran two sets of simulations on rough faults. The first set of simulations was run on two vertical strike-slip faults with a 50 km overlap and 7 km stepover distance. The second set of simulations was done on two vertical strike-slip faults with a 50 km overlap and 2 km stepover distance. Both sets of simulations were repeated 10 times with different topologies, where each run swept through the minimum patch participation level from 0-100% for both fault segments. I used the same model parameters as those described in Figure 4.5 (i.e. tectonic loading rate of 30 mm/yr, Coulomb failure with a simple [$a - b$] friction profile, etc.).

Effect of Structural Barrier Geometry and Fault Roughness on Rupture Jumping

The final set of experiments includes varying the underlap and overlap distances between two faults in order to determine their effects on the probabilities of rupture jumping. This set of experiments was done on smooth and rough right-stepping faults. Stepover distances ranged from 2 km to 4 km at 1 km increments. Underlap and overlap distances ranged from -5 km (underlap) to 5 km (overlap) using. Each structural

configuration was simulated 5 times. All rupture jumping probabilities were computed using the 80% minimum patch participation level.

RESULTS

Surface Slip Distributions and Slip at a Point

Single Fault with Simple Friction

Simulations of earthquakes along a single fault with a simple [$a - b$] friction profile (Fig. 4.5) resulted in surface slip distributions that were relatively simple. Along-strike slip distributions for the first 10 earthquakes were elliptical and tapered to zero at both fault ends (Fig. 4.5A). The location of slip maxima for individual earthquakes varied around the center of the fault along strike. However, the longer records of slip distributions for 50 and 100 earthquakes showed that there was no predictable variation in the location of slip maxima along strike. In fact, the cumulative surface slip reached a steady-state shape that flattened along the majority of the fault length and tapered to zero at the fault ends. Similarly, the slip histories of individual patches showed behavior that was expected from a simple fault with relatively simple frictional and roughness properties (Fig. 4.5B). Deep patches (patch # 263, 858, and 1453) had slipped by the same magnitude during every earthquake at a relatively uniform slip rate. Surface patches exhibited the same slip histories but with smaller slip magnitudes per event.

Two Faults with Simple Friction

Simulations of earthquakes in two-fault systems with varying overlap/underlap and stepover distances showed interesting results. Faults that were far apart (Fig. 4.8) exhibited single patch slip histories and surface slip distributions that were similar to those simulated along a single fault. However, when the two fault segments were in close

proximity to each other (Fig. 4.11, Fig. 4.12, and Fig. 4.13), the slip histories of individual patches near the stepover region were irregular in magnitude and timing (e.g., patches 1445 and 1972 in Fig. 4.13). Patches in the overlap region followed an unpredictable behavior such that slip and slip magnitude at a point clustered along strike and temporally. Furthermore, when considering the surface slip distributions for two faults in close proximity to each other, significant steepening of the along-strike slip gradient occurs such that the locations of displacement maxima were skewed toward the stepover region (Fig. 4.13A), as has been seen before (e.g., Burgmann et al., 1994; Willemse et al., 1996)

Sedimentary Basin

Slip histories for shallow patches in the overlapping region that contained the simulated velocity-strengthening basin (patch # 1445 and 1972) showed different behaviors as the depth of the sedimentary basin increased from 1 km to 3 km (Fig. 4.14A, Fig. 4.15A, and Fig. 4.16A, respectively). As the depth of the sedimentary basin increased, surface-rupturing earthquakes became more sporadic in time. The absolute magnitude of slip per earthquake in the overlap region varied sporadically; periods of relatively consistent slip-at-a-point were punctuated by episodic large surface slip. Surface slip distributions in all three scenarios (Figs 4.14B, 4.14B, and 4.14B) showed slip deficits in the overlap region. This deficit is especially pronounced in the long-term record of surface slip distributions (the 100-event record in Figs. 4.14B, 4.14B, and 4.14B).

Creeping Section

Using a [$a - b$] value of 0.002 (Fig. 4.17A), the slip history of a single point located in the middle of the creeping section (patch # 850 in Fig. 4.17A) exhibited sporadic slip behavior with a hint of clustering of low-magnitude slip events that were punctuated by large slip events. Increasing the [$a - b$] value to 0.004 through 0.006 (Figs. 4.18A, 4.18A, and 4.18A) resulted in more regular surface slip histories and surface records of coseismic events that had relatively larger slip magnitudes. In terms of surface slip distributions, the creeping section showed low cumulative slip relative to the remainder of the fault that did not creep. On the scale of a few earthquakes (e.g., plots of 10 events in Figs. 4.17B, 4.18B, 4.19B, and 4.20B), the presence of small slip magnitudes was not as obvious as that displayed in the long-term record of slip distributions (e.g., plots of 100 events in Figs. 4.17B, 4.18B, 4.19B, and 4.20B).

Rupture Jumping Probabilities

Minimum Patch Participation Level

I designed this set of experiments to constrain the most appropriate minimum patch participation level to use in my rupture jumping probability calculations. I compared the conditional rupture jumping probabilities using 0-100% minimum patch participation levels of for different configurations of structural barriers that contained smooth and rough faults. Figures 4.21 through 4.24 show these results. To help keep things organized, I report the results of each structural configuration separately.

Releasing step, 20 km underlap and 50 km overlap

Figure 4.21 presents the results from this set of experiments for smooth and rough faults. In general, smooth faults had slightly higher rupture jumping probabilities than

their rough counterparts given a large stepover distance of 7 km (Fig. 4.21A). However, decreasing the stepover distance increased the conditional rupture jumping probabilities to a little over 10% for smooth and rough faults in all minimum patch participation levels (Figs. 4.21E and 4.21I). For simulated stepover distances of 7 km and 5 km where the overlap was 50 km, rupture jumping probabilities had a slight increase to 15% in most minimum patch participation levels (Fig. 4.21C and 4.21G). However, when the two fault segments were in close proximity to each other (50 km overlap with a 2 km stepover distance; Fig. 4.21K), rupture jumping probabilities increased to 45% for smooth and rough fault segments, especially in the 50-80% minimum patch participation levels.

Restraining step, 20 km underlap and 50 km overlap

Figure 4.22 presents the results from this set of experiments for smooth and rough faults. In the underlapping cases, rupture jumping probabilities were uniform in all minimum patch participation levels and hovered around 10% (Fig. 4.22A, 4.22E, and 4.22I). Conversely, the rupture jumping probabilities increased systematically from ~15% in the 7 km stepover case to 35% in the 2 km stepover case for smooth faults. Rough faults, however, had higher rupture jumping probabilities of up to 45% in the 2 km stepover case and significantly increased to 90% for minimum patch participation levels >60% (Fig. 4.22C, 4.22G, and 4.22K).

Releasing and restraining double bends, with 20 km underlap

Figures 4.23 and 4.24 present results from the set of experiments I carried out on releasing and restraining double bends, respectively. In both cases, there was a marked difference between the rupture jumping probabilities along smooth faults versus rough faults. In almost all structural geometries for smooth faults, jumping probabilities

exceeded 70% in all minimum patch participation levels on all three segments. Furthermore, in all minimum patch participation levels for smooth faults, the conditional rupture jumping probabilities of Segment 3 were significantly higher than for Segments 1 and 2. Rough faults, on the other hand, had lower rupture jumping probabilities (between 30% and 50%).

Fault Topologic Effects

Cases where the rupture jumping probabilities were anomalously high, (e.g., rough faults in Fig. 4.22A) suggested that rupture jumping probabilities may be influenced by the topology of the fault segments. However, there is no topologic control on rupture jumping probabilities based on simulations for 10 different fault roughness cases (Fig. 4.25). In both stepover distances (Fig. 4.25B and 4.25D), the calculated rupture jumping probabilities for all minimum patch participation levels ranged within a few percent. However, using 10 simulations may not be enough to determine the full effects of fault topology on rupture jumping, which calls for a more rigorous statistical approach (see Discussion).

Effect of Structural Barrier Geometry and Fault Roughness on Rupture Jumping

I ran this set of experiments on two right-stepping faults where several relationships emerged between rupture jumping probabilities, the geometry of structural barriers, and fault roughness. In the case of the 4 km stepover distance for smooth faults (Fig. 4.26A top plots), rupture jumping probabilities ranged between 10% and 25% for all underlap/overlap distances. For the case of rough faults at the 4 km stepover distance (Fig. 4.26A bottom plots), rupture jumping probabilities were less than 10% for underlap distances <-3km, then increased to 10-25% from an underlap distance of -3 km to an

overlap distance of 2 km. The rupture jumping probabilities then decreased to ~10% for overlap distances >2 km. In the case of the 3 km stepover distance (Fig. 4.26B), both rough and smooth fault sets had rupture jumping probabilities that ranged between 10-30% and increased to >30% at overlap distances >3 km. For the smooth faults with a 2 km stepover distance (Fig. 4.26C), the range of rupture jumping probabilities increased to 20-50%. This range remained constant for underlap/overlap distances between -5 km and 3 km but decreased to <30 % for stepover distances >3 km (Fig. 4.26C top panels). Conversely, the rupture jumping probabilities for rough faults increased from 10-20% up to ~40% for underlap/overlap distances between -5 km to ~1 km (Fig. 4.26C bottom panels). These probabilities then showed a marked increase to 70% for overlap distances >2 km.

DISCUSSION

Surface Slip Distributions and Slip at a Point

Single Fault with Simple Friction

The intended purpose of this simulation was to check the modeled behavior of earthquakes with what is known about earthquake behavior along faults with simple geometries and frictional properties. Results from this simulation are as expected and in fact widely observed in models of slip distributions for crack-like dislocations (Burgmann et al., 1994). The slip histories of deep and shallow patches are expected for a simple fault geometry and the given [$a - b$] friction profile, which led to an earthquake record that lacked spatiotemporal clustering of slip events. The overall characteristic behavior of slip histories of deep patches is consistent with episodic events that occur with some regularity at the base of the seismogenic zone. This observation agrees with

many strike-slip and dip-slip earthquakes and is common to all deep slip histories simulated in this chapter.

Two Faults with Simple Friction

The spatiotemporal clustering of earthquakes in the stepover region of two closely spaced faults can be explained in terms of mechanical interaction. It has long been shown that the stress field due to slip along a single fault mechanically interacts with the stress field of a nearby fault (Segall and Pollard, 1980). When considering this principle in terms of coseismic stress transfer between two faults, the propagation of a rupture along a fault may trigger failure along nearby faults if they are critically stressed; that is, if the receiving fault is optimally oriented and stressed to the point of failure. This has been shown to occur in terms of static Coulomb stress transfer (e.g., Toda et al., 2011) and stress transfers due to dynamic rupture processes (e.g., Harris et al., 1991; Oglesby, 2008; Lozos et al., 2012). From the observed time-intermittent coseismic slip near fault ends, I infer that the stress transfer between one fault to another does not occur at a constant rate between earthquakes. This explains the observed spatiotemporal clustering of earthquakes within my modeled stepover regions (e.g., Fig. 4.13) and points toward earthquake synchrony. Scholz (2010)suggested the synchronization of earthquakes along mechanically interaction faults by analyzing paleoseismic data from some of the major fault systems in southern California. Although the spatial scale of Scholz' (2010) analysis is at least an order of magnitude greater than that of my simulations, the synchronous transfer of stress, and hence earthquakes, from one fault to another is clear along structural barriers. Similarly, the steepening of along-strike slip gradients near the overlap regions of two faults (Fig. 4.11, 4.12, and 4.13) can be explained by mechanical

interaction. This interaction is expected and has been shown to be controlled by the increased CFS in the stepover region (Willemse et al., 1996; Willemse, 1997).

Sedimentary Basin

Overall, significant spatiotemporal clustering of surface-rupturing events was present in the overlapping faults scenario with a thick sedimentary basin. This was due to the velocity-strengthening sedimentary basin that acted to impede the propagation of ruptures from the base of the seismogenic zone to the ground surface. I interpret this as the cause for the episodic nature of slip histories of the surface patches (patch # 1445 and 1972). A clear relationship exists between the thickness of the sedimentary basin and the episodic nature of surface slip histories; as the thickness of the sediment basin increased, slip histories at a point in the overlapping region were increasingly regular with infrequent large-slip magnitude events punctuating frequent small-slip magnitude events. Similarly, the coseismic slip deficit in the overlap region increased with the depth of the sedimentary basin.

Results from this set of simulations may play a critical role in implications related to the accuracy of paleoseismic data interpretations of the timing and magnitude of earthquakes that rupture through faults embedded in thick sedimentary basins. Thick velocity-strenghtening basins may act as rupture barriers by absorbing the rupture's energy. Therefore, during the interseismic period, stress build-up is concentrated along the lower edges of sedimentary basins that are then released as very large-magnitude (>M 7) coseismic events that are able to penetrate the velocity-strengthening basin. The surface record of coseismic faulting would therefore be clustered in space and time. I posit that there exists a relationship between the overall thickness of the sedimentary

basin and the degree of spatiotemporal clustering of earthquakes. In cases where the basin was shallow (e.g., the 1 km basin in Fig. 4.14), strain accumulation along the lower edges was low and thus large ruptures were able to punch through the basin. In cases where the basin was deep (e.g., the 3 km basin in Fig. 4.16), large strain accumulation likely existed at the lower edges of the basin and resulted in a large updip strain gradient from the base of the seismogenic zone through the basin. Only the largest of earthquakes were able to propagate through the basin and make it to the ground surface. Given enough time as shown in the earthquake catalog, this resulted in a large temporal clustering of earthquakes through the thick sedimentary basin.

Creeping Section

Increasing the velocity-strengthening friction behavior of the creeping section led to increasing the impedance of coseismic ruptures such that only very large earthquakes penetrated through the creeping section. This in essence mirrors the effects of the velocity-strengthening base of the seismogenic zone, where only large earthquakes are able to penetrate it (Sibson, 1984).

With respect to the record of surface slip distributions, the fact that coseismic slip distributions in the creeping section exhibited smaller magnitudes of cumulative slip implies that a significant slip deficit existed in the creeping section. This is especially apparent in the highly velocity-strengthening creeping section scenario (Fig. 4.20B). However, this behavior is only clearly visible in the long-term record of coseismic faulting. The short-term record does not include a clear signal of coseismic ruptures, suggesting that large coseismic events may not have a clear geomorphic expression in

creeping sections. Instead, only the long-term geomorphic record of coseismic ruptures is preserved in creeping sections.

Rupture Jumping Probabilities

Minimum Patch Participation Level

Stepovers

A common observation from all of my experiments to determine the most appropriate minimum patch participation level was that when fault segments were far apart, the rupture jumping probabilities were low, and vice versa for when the two fault segments were close and overlapping. This relationship is expected and can be explained using CFS analyses for individual earthquakes given stress boundary conditions that promote right-lateral strike-slip faulting. For faults that were far apart (e.g., Fig. 4.21B and 4.21F), the computed CFS lobes around the ends of the segments that ruptured placed the ends of the faults that did not rupture in stress shadows (negative CFS regions in Fig. 4.21B, 4.21F, and 4.21J). This mechanical setting was not conducive for ruptures to jump from the activated segments to the others. This explains the low rupture jumping probabilities for faults that were far apart in a releasing step geometry. Considering cases where faults were close to each other (e.g., Figs. 4.21L and 4.21M), faults that did not participate in the main ruptures were optimally oriented and within regions of positive CFS. As a result, they were more likely to participate in ruptures that originated in the segments on which the rupture jumping probabilities were conditioned. As with the underlapping geometries, when considering the entire earthquake record for overlapping faults with short stepover distances, the rupture jumping probabilities were markedly high regardless of onto which fault the probabilities were conditioned.

Double bends

Similar to the above discussion about fault steps, the interesting observation that smooth faults in a double-bend system have much higher rupture jumping probabilities than their rough counterparts can be explained by the mechanics of the fault system. The relative rupture time for an example earthquake (Event ID 2508; M7.71) is plotted in Figure 4.23B and shows this phenomenon well. The rupture originated on Segment 2, propagated through Segment 3, and continued along Segment 1 even though the underlap and stepover distances were relatively large (20 km and 7 km, respectively). Segment 3 was optimally located in the positive CFS region of Segment 2, thereby allowing the rupture to propagate through the double bend. In another earthquake (Event ID 3677; M7.69; Fig. 4.23F), the rupture originated in the bend region along Segment 3 and propagated bilaterally to Segments 1 and 2 (see relative rupture time plot in Fig. 4.23F). In this case, Segments 1 and 2 were optimally located in the positive CFS lobes of Segment 3, which enhanced the rupture's propagation along these segments. There were significant differences in the computed single-earthquake CFS for these smooth faults compared to their rough counterparts. Figures 4.23C and 4.23L (Event IDs 1174 and 1400, respectively) are good examples of such differences and show ruptures that originated along Segment 1, propagated through and terminated at Segment 3. Regions of positive CFS were much smaller and irregular than those computed for the smooth faults, indicating that the majority of the rupture energy was consumed by overcoming local asperities along the rough fault surfaces. This limited the extent of the ruptures along strike and hence lowered its jumping probability. This also explains the high rupture jumping probabilities along Segment 3 when conditioned on either Segments 1 or 2;

ruptures that originated in either Segments 1 or 2 had high probabilities of involving Segment 3 whether the rupture jumped from Segment 1 to Segment 2 or vice versa.

Effect of Structural Barrier Geometry and Fault Roughness on Rupture Jumping

Interestingly, the jumping probabilities were consistently higher for ruptures that occurred along smooth faults than rough faults in geometries where faults were farther apart. This relationship reversed when the faults were closer to each other; rough faults had higher rupture jumping probabilities than smooth faults within the same structural barrier geometry. I postulate that the cause of the reversal in rupture jumping probabilities is the mechanics of rough faults. Ruptures that occur on smooth faults are not faced with the local asperities that are found in rough faults. I will explain this in terms of elastic strain energy as follows (Jaeger et al., 2007). Consider a three dimensional linear-elastic solid that is made of cubic elements and is subjected to external compressional forces. Using the convention of tension is positive, each face of this element is subjected to normal (σ_{ij}) and shear (τ_{ij}) tractions as follows (Pollard and Fletcher, 2005):

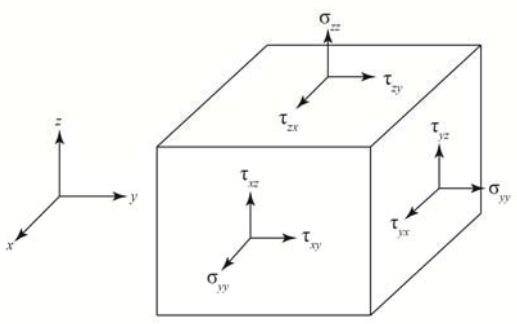

Deformational forces that are applied to an elastic volume dV result in normal strains (ε_{ij}) and shear strains (γ_{ij}) along each face of this cubic element. Thus, the incremental strain energy dU stored in this volume is

$$dU = \frac{1}{2}\{\sigma_{xx}\varepsilon_{xx} + \sigma_{yy}\varepsilon_{yy} + \sigma_{zz}\varepsilon_{zz} + \tau_{xy}\gamma_{xy} + \tau_{xz}\gamma_{xz} + \tau_{yz}\gamma_{yz}\}dV. \quad (4.2)$$

The total elastic strain energy U can be determined by integrating dU over the entire volume V,

$$U = \frac{1}{2}\int_V \{\sigma_{xx}\varepsilon_{xx} + \sigma_{yy}\varepsilon_{yy} + \sigma_{zz}\varepsilon_{zz} + \tau_{xy}\gamma_{xy} + \tau_{xz}\gamma_{xz} + \tau_{yz}\gamma_{yz}\}\, dV. \quad (4.3)$$

This expression can then be simplified by vectorizing the stresses and strains as follows:

$$\vec{\sigma} = \sigma_{xx}\ \sigma_{yy}\ \sigma_{zz}\ \tau_{xx}\ \tau_{yy}\ \tau_{zz}, \quad (4.4)$$

$$\vec{\varepsilon} = \varepsilon_{xx}\ \varepsilon_{yy}\ \varepsilon_{zz}\ \gamma_{xx}\ \gamma_{yy}\ \gamma_{zz}, \quad (4.5)$$

$$U = \frac{1}{2}\int_V\ \vec{\sigma}\ \vec{\varepsilon}\, dV. \quad (4.6)$$

Following the principle of conservation of energy, work that is stored in the deformed body takes the general form of elastic strain energy U, which is potentially available to cause slip along dislocations in the surrounding volume. The elastic strain energies that are produced and stored in the elastic halfspace during ruptures along smooth faults are expended on propagating the rupture along the faults. On the other hand, ruptures along rough faults consume a significant proportion of the elastic strain energy so that they can overcome asperities in the fault surface. The extent of the rupture, and hence the volumetric extent of positive CFS regions, is limited along rough faults. As a result, for ruptures to jump from one rough fault to another requires both faults to be close to each other. This explanation can also be applied to cases where earthquakes ruptured through rough faults in double-bend geometries (Figs. 4.23C, 4.23G, 4.23L, 4.23C, 4.23F, and 4.23I).

Implications for the Rupture Process Zone

Taking into consideration the effects of variable fault roughness as illustrated in my topology analysis and my choice of using the 80% minimum patch participation level in computing rupture jumping probabilities, the relationships that emerged above provide physical insights into the rupture process zone. The rupture jumping probabilities for a long stepover distance (Fig. 4.26A) compared to a short stepover distance (Fig. 4.26C) for smooth faults showed a noticeable decline in the rupture jumping probabilities for overlaps that exceeded 3 km. This implies that a threshold exists for rupture jumping probabilities beyond which they decrease with increasing overlap distances for smooth faults. Empirical analyses of rupture jumping occurrences from recent and historic earthquakes by Wesnousky (2008) led him to postulate that there exists a 3-4 km distance beyond which strike-slip earthquakes do not propagate. He attributed this to a vertical cylindrical process zone with a 3-4 km radius that operates at the rupture front and remains largely invariable during the rupture (Fig. 4.27). This process zone places an upper limit on the crustal volume that is affected by stress changes at the rupture front, which in turn affects the triggering potential of faults that are encountered by the process zone (Wesnousky, 2008). This conceptual model explains the results derived from my earthquake simulations along smooth faults. However, my results for rough faults (Fig. 4.26C) imply that there is a degree of control that rough faults have on rupture jumping probabilities (e.g., Saucier et al., 1992; Dieterich and Smith, 2009; Dunham et al., 2011). Consider the following from the perspective of coseismic shear stress concentrations. Figure 4.28 shows conceptual plots of coseismic shear stress plotted as a function of fault strike for smooth and rough faults. Shear stress along a smooth fault that is subjected to a

uniform slip distribution is concentrated at the fault tips (Fig. 4.28A). In the case of a rough fault with a non-uniform along-strike slip distribution, shear stress concentrations are invariable due to local fault topologic complexities (Fig. 4.28B). This results in large stress fluctuations along strike that are comparable in magnitude to the high stress concentrations at the fault tips (Burgmann et al., 1994). Therefore, I posit that the geometric complexity of faults, and in particular fault roughness, affects rupture propagation such that elastic strain energies are consumed by overcoming fault asperities and thus are unavailable to be expended for coseismic slip. The variability in stress concentrations along rough faults and the increase in rupture jumping probabilities between rough faults leads me to conclude that the radius of the process zone changes in lateral and vertical extent as the rupture propagates through rough faults or through rough regions of otherwise smooth faults (Fig. 4.29). I postulate that the radius of the rupture process zone increases with increased fault roughness such that the volume that is affected by stress change at the rupture front is variable. Therefore, the forcing of ruptures through structural complexities will depend on the size of the process zone and hence the roughness of the faults near the structural complexity (Fig. 4.29).

Implications for Future UCERF Iterations

A central implication of my modeled spatiotemporal clustering of surface-rupturing earthquakes concerns paleoseismic interpretations of earthquakes near fault ends. Even though my modeled spatiotemporal clustering of earthquakes near stepover regions is non-unique, it indicates that correlation of individual ruptures from one fault segment to another is not as straightforward as one would like it to be, especially given the long-term (>1,000 year scale) irregularity of slip at a point near fault ends in stepover

regions. Paleoseismic datasets provide detailed records of only those coseismic strains that are localized along faults. However, interpretations derived from these studies cannot constrain the overall coseismic behavior of a fault if deformation is distributed across multiple fault strands, especially where ruptures are able to jump across structural barriers. So the need to create rules for whether a rupture will jump a structural barrier is high.

Faults in the UCERF3 fault model have varying attitudes but are composed of planar elements (Field et al., 2013). As seen from the above analyses, rupture jumping probabilities have strong ties with fault roughness and thus need to be implemented into future UCERF iterations. This may be difficult to do given how little is known about actual fault roughness for California's faults. However, using simple rules such as total fault displacement as a proxy for age, and hence fault roughness (i.e. the younger the fault, the rougher it is), may provide a first-order approximation for fault roughness in future UCERF implementations. Lidar-derived roughness measurements of exposed faults (e.g., Bistacchi et al., 2011) can provide further insights into the nature of fault roughness.

The computed rupture jumping probabilities highlight the importance of structural barrier geometry in determining the likelihood for a rupture to jump. At present, UCERF3 invokes a 3-5 km fault-to-fault distance rule to determine the plausibility of rupture jumps (Field et al., 2013). Future iterations of UCERF can and should improve upon this by including the use of earthquake simulators in simulating on-fault seismicity. I envision this being implement as a more sophisticated and mechanically based plausibility scheme for rupture jumping than what UCERF currently employs. For

example, FIMozFric can be used to simulate thousands of earthquakes given the variety of fault junctions and structural barriers that are present in the current UCERF fault model. Simulations need not be performed statewide in one go. They can be carried out piecewise for every fault junction given the available geologically derived slip rates. The plausibilities for rupture jumping across UCERF's statewide fault model can then be ranked by the computed rupture jumping probabilities and included in the UCERF Grand Inversion. Such an approach is certainly possible using present-day computing capabilities (e.g., the average time to complete one simulation using 1 km x 1 km fault patches was 20 minutes using a 16 Gb RAM, 8 core computing node on the ASU Advanced Computing Center – a time that can be cut by more than half if FIMozFric were parallelized!). This would be an improvement to UCERF's current ranking system for rupture jumping, which at present analyzes rupture jumping probabilities for all fault junctions/stepovers statically and then ranks them once for single earthquakes (Parsons et al., 2012). The statistically significant number of simulated earthquakes (e.g., >1000 earthquakes per simulation per fault junction) would provide a more robust analysis of rupture jumping probabilities on a junction by junction basis. Therefore, it is clear that earthquake simulators can play an important role in the next iteration of UCERF.

Assumptions and Other Ponderings

It is interesting to note that the locations of rupture nucleation in all simulated structural geometries are independent of fault roughness. This indicates that asperities along rough faults do not control where ruptures are likely to initiate in my models. However, a systematic analysis is needed to investigate whether such a relationship exists. Future work should involve using the Monte Carlo method to generate thousands

of earthquake simulations using faults with randomly assigned roughness. Locations of rupture nucleation can then be compared with asperities along those faults. A related element that I did not explore in this chapter is rupture directivity. Figures 4.23B and 4.23F show how ruptures can propagate either unilaterally or bilaterally away from their nucleation sites. What controls this and is it predictable? Is it related to fault roughness, fault friction, or fault structural complexity? Future work may employ FIMozFric to answer these questions and perhaps add another set of rules to the UCERF decision tree of where ruptures will likely initiate given different fault scenarios.

My chosen 80% minimum patch participation level to compute rupture jumping probabilities renders them non-unique. It is likely that different rupture jumping probabilities can be calculated for the same fault geometries but with different degrees of roughness and minimum patch participation levels. A more robust approach would be to perform the same parameter sweep that I did for the minimum patch participation level thousands of times using different fault roughness values so that a deeper understanding of the topologic effect on rupture jumping probabilities can be achieved.

It is important to note that all deformation considered in this chapter is coseismic. Given the quasi-static nature of FIMozFric and its assumption of a linear-elastic halfspace, it is not possible to account for the effects of time-dependent afterslip caused by viscoelastic relaxation following large earthquakes. We know from geodetic observations that postseismic deformation is a phenomenon that occurs hours to months after large earthquakes (Segall, 2010). This secondary deformation may significantly add to the total magnitude of slip preserved in the earthquake record of fault zones. Therefore, all of my simulated along-strike slip distributions and on-fault slip should be considered

minima and non-unique because they neglect postseismic secondary deformation. With the exception of ViscoSim (Pollitz, 2012), the assumption of linear elasticity in current earthquake simulators limits the extent of interpretations of rupture processes to phenomena that occur in the seismogenic zone alone. Therefore, I cannot use my results to explain complex interactions between the deep lithosphere and the seismogenic zone.

One thing to keep in mind here is that, given the elastic nature of the simulator's formulation, no plastic deformation (e.g., folding, warping) is allowed. As a result, the model does not allow for new faults to form in areas where the elastic strength of the halfspace is exceeded. The model likely does not represent that deformation accurately in the sedimentary basin because I expect plastic deformation to occur in the form of off-fault warping (e.g., Oskin et al., 2012). Ideally, the simulator would incorporate the principles of damage mechanics to allow for the formation of new faults and/or plastic deformation in the simulated sedimentary basin.

One major assumption in this model, which is related to its limitation of being quasi-static in formulation, is that the transition of [$a - b$] from creep to stick-slip behavior is fixed along strike and downdip. It has been shown by dynamic earthquake models that the depth and along-strike extent of creeping sections can vary during interseismic periods of the earthquake cycle (e.g., Kaneko et al., 2013). Therefore, a significant complication arises in interpreting my results in that the distribution of [$a - b$] can vary in space and time, making it nearly impossible to come up with a generalized set of rules for interpreting surface slip measurements or histories (from paleoseismology) of creeping sections. My simulation results for a creeping section in a fault are non-unique and should be used with caution.

As with other earthquake simulators, FIMozFric does not allow for the topographic degradation of displaced geomorphic markers in the computed along-strike slip distributions. When considering the length of earthquake records generated in my simulations (between 5,000 and 10,000 years long), the modeled along-strike slip distributions and surface patch slip histories should be considered maximum values because they are not allowed to geomorphically degrade over the simulation time. We know that this is unrealistic (see Chapter 2 for a quantification of fault scarp degradation, for example). Future iterations of earthquake simulators could consider incorporating some geomorphic degradation law to allow the modeled topographic expressions of coseismic faulting to degrade (e.g., Densmore et al., 1998). Of course, this means that additional geomorphic parameters such as climatic conditions and forcing rates must be known.

In all of my simulations, the loading mechanism and rate were held constant at 30 mm/yr. Therefore, all model scenarios that exhibit spatiotemporal clustering of earthquakes (whether in simulations of creeping fault sections or in structural barriers) should be attributed to mechanical processes in the seismogenic zone. Although this serves my needs here, my results could significantly vary if I assume a different loading mechanism or rate. Future work should investigate the effects (if any) that loading mechanisms and rates have on the surface slip distributions and rupture jumping probabilities for the scenarios that I explored here.

CONCLUSIONS

In this chapter, I investigated the effects of fault structural and frictional complexities on earthquake-generated deformation. I used the FIMozFric earthquake

simulator to model these effects by setting up various scenarios of fault structural/geometrical configurations and frictional complexities. Although my results are non-unique and may be limited by the assumptions of linear elasticity and lack of rupture dynamics, I found that key relationships exist between the configuration of structural barriers, fault frictional properties, fault roughness, and the surface expression of coseismic deformation. Based on these relationships, I expanded upon the concept of a fixed-radius rupture process zone that controls multi-fault ruptures and fault-to-fault rupture jumping probabilities. I proposed that the size of this process zone is not fixed but in fact varies as a function of fault roughness. This variation occurs in three dimensions. The central implication of my results lies in guiding the interpretation of the surface manifestation of coseismic faulting, paleoseismic data, and the formulation of rupture jumping rules in future iterations of earthquake forecasts. Earthquake simulators such as FIMozFric offer several opportunities for advancements in future implementations of earthquake forecasts such as the Uniform California Earthquake Rupture Forecast.

ACKNOWLEDGMENTS

I thank Terry Tullis for discussions regarding the determination of appropriate [$a - b$] friction values for poorly consolidated sediments and Manoochehr Shirzaei for his insights into geodetically derived fault friction properties. I am grateful to Olaf Zielke for making his code for FIMoz and FIMozFric available to me and especially for his technical support in running his code. I thank the Arizona State University Advanced Computing Center for allowing me to use their high-performance computing environment to run the hundreds of earthquake simulations presented in this chapter.

FIGURES

Figure 4.1. Synoptic overview of fault zone processes that take place in the upper lithosphere and as manifested in the topography of fault zones. Geologic and seismic properties of the seismogenic zone (outlined in red) determine the lateral and vertical extents of interseismic, coseismic, and post-seismic strains, and how they are transmitted to Earth's surface. The prehistoric and historic record of coseismic faulting is recorded in the topography of fault zones as fault scarps and displaced geomorphic markers. Derived from concepts that were developed by Vedder and Wallace (1970), Sylvester (1999) and Scholz (2002). Figure elements are not to scale.

Figure 4.2. Examples of the complexities surface rupture traces and slip distributions of recent earthquakes for (A) the 1987 Superstition Hills earthquake in California, (B) the 1968 Borrego Mountain earthquake in California, and (C) the 1887 Pitaycachi earthquake in Sonora, Mexico. Modified from Wesnousky (2008).

Figure 4.3. Definitions of structural barrier geometries used in simulations. (A) Map views of a releasing step, a restraining step, a releasing double bend, and a restraining double bend. (B) Map views of an underlap and an overlap.

Figure 4.4. Examples of a smooth and a rough fault. Faults are discretized into 1 km by 1 km patches. Strikes and dips of patches in smooth faults have little deviation from each other. Conversely, patches in rough faults have variable strikes and dips, which results in an overall rougher fault geometry.

Figure 4.5. Model configuration for a single vertical fault with a simple [$a - b$] friction profile. (A) Top panel illustrates the fault geometry and modeled friction. The fault is 17 km wide and 100 km long with an applied right-lateral slip rate of 30 mm/yr. Lower panels show computed surface slip distributions (right-lateral) for the first 10, 50, and 100 earthquakes in the earthquake record generated by this simulation. (B) Patch slip histories for six selected patches. Selected patches are numbered and indicated in the 3D block model.

Figure 4.6. Matrix showing the various model setups and fault configurations on which earthquakes were simulated. The structural setting in the first column is for two vertical strike-slip, right-lateral faults with 20 km of underlap and variable stepover distances. The second column illustrates the same two faults with 50 km overlap and varying stepover distances.

Figure 4.7. Relative rupture time for patches that failed during an example earthquake on a smooth fault. The rupture nucleated at a depth of ~10 km toward the center of the fault along strike. Black arrows point in the direction of rupture propagation, indicating a bidirectional rupture propagation from the nucleation zone.

Figure 4.8. Patch slip histories for six selected patches in two right-stepping faults with a 20 km underlap and 7 km stepover. (A) Selected patches are numbered and indicated in the 3D block model for Segments 1 and 2. (B) Computed surface slip distributions (right-

lateral) for the first 10, 50, and 100 earthquakes in the earthquake record generated by this simulation.

Figure 4.9. Patch slip histories for six selected patches in two right-stepping faults with a 20 km underlap and 5 km stepover. (A) Selected patches are numbered and indicated in the 3D block model for Segments 1 and 2. (B) Computed surface slip distributions (right-lateral) for the first 10, 50, and 100 earthquakes in the earthquake record generated by this simulation.

Figure 4.10. Patch slip histories for six selected patches in two right-stepping faults with a 20 km underlap and 2 km stepover. (A) Selected patches are numbered and indicated in the 3D block model for Segments 1 and 2. (B) Computed surface slip distributions (right-lateral) for the first 10, 50, and 100 earthquakes in the earthquake record generated by this simulation.

Figure 4.11. Patch slip histories for six selected patches in two right-stepping faults with a 50 km overlap and 7 km stepover. (A) Selected patches are numbered and indicated in the 3D block model for Segments 1 and 2. (B) Computed surface slip distributions (right-lateral) for the first 10, 50, and 100 earthquakes in the earthquake record generated by this simulation.

Figure 4.12. Patch slip histories for six selected patches in two right-stepping faults with a 50 km overlap and 5 km stepover. (A) Selected patches are numbered and indicated in

the 3D block model for Segments 1 and 2. (B) Computed surface slip distributions (right-lateral) for the first 10, 50, and 100 earthquakes in the earthquake record generated by this simulation.

Figure 4.13. Patch slip histories for six selected patches in two right-stepping faults with a 50 km overlap and 2 km stepover. (A) Selected patches are numbered and indicated in the 3D block model for Segments 1 and 2. (B) Computed surface slip distributions (right-lateral) for the first 10, 50, and 100 earthquakes in the earthquake record generated by this simulation.

Figure 4.14. Patch slip histories for six selected patches in two right-stepping faults with a 50 km overlap and 5 km stepover. This structural configuration forms a 1 km deep pull-apart basin that contains sedimentary infill. This is modeled by velocity-strengthening friction in the overlap region. (A) Selected patches are numbered and indicated in the 3D block model for Segments 1 and 2. (B) Computed surface slip distributions (right-lateral) for the first 10, 50, and 100 earthquakes in the earthquake record generated by this simulation.

Figure 4.15. Patch slip histories for six selected patches in two right-stepping faults with a 50 km overlap and 5 km stepover. This structural configuration forms a 2 km deep pull-apart basin that contains sedimentary infill. This is modeled by velocity-strengthening friction in the overlap region. (A) Selected patches are numbered and indicated in the 3D block model for Segments 1 and 2. (B) Computed surface slip distributions (right-lateral)

for the first 10, 50, and 100 earthquakes in the earthquake record generated by this simulation.

Figure 4.16. Patch slip histories for six selected patches in two right-stepping faults with a 50 km overlap and 5 km stepover. This structural configuration forms a 3 km deep pull-apart basin that contains sedimentary infill. This is modeled by velocity-strengthening friction in the overlap region. (A) Selected patches are numbered and indicated in the 3D block model for Segments 1 and 2. (B) Computed surface slip distributions (right-lateral) for the first 10, 50, and 100 earthquakes in the earthquake record generated by this simulation.

Figure 4.17. Configuration for a single vertical fault with a region of velocity-strengthening friction [$a - b$] of 0.002 in the central part of the fault. (A) Patch slip histories for six selected patches. Selected patches are numbered and indicated in the 3D block model. (B) Computed surface slip distributions (right-lateral) for the first 10, 50, and 100 earthquakes in the earthquake record generated by this simulation.

Figure 4.18. Configuration for a single vertical fault with a region of velocity-strengthening friction [$a - b$] of 0.004 in the central part of the fault. (A) Patch slip histories for six selected patches. Selected patches are numbered and indicated in the 3D block model. (B) Computed surface slip distributions (right-lateral) for the first 10, 50, and 100 earthquakes in the earthquake record generated by this simulation.

Figure 4.19. Configuration for a single vertical fault with a region of velocity-strengthening friction [$a - b$] of 0.006 in the central part of the fault. (A) Patch slip histories for six selected patches. Selected patches are numbered and indicated in the 3D block model. (B) Computed surface slip distributions (right-lateral) for the first 10, 50, and 100 earthquakes in the earthquake record generated by this simulation.

Figure 4.20. Configuration for a single vertical fault with a region of velocity-strengthening friction [$a - b$] of 0.008 in the central part of the fault. (A) Patch slip histories for six selected patches. Selected patches are numbered and indicated in the 3D block model. (B) Computed surface slip distributions (right-lateral) for the first 10, 50, and 100 earthquakes in the earthquake record generated by this simulation.

Figure 4.21. Parameter sweep to investigate the effect of varying activated patch participation level on rupture jumping probabilities in a releasing step. (A) Top panel shows the structural configuration for which this parameter sweep was performed (underlap 20 km, stepover 7 km). Lower panels are plots of conditional rupture probabilities for Segments 1 and 2 on smooth and rough faults. (B) Top panel is a map view of the Coulomb failure stress computed at a depth of 8.5 km using the indicated stress boundary condition. Lower panels are 3D views of (from top to bottom) fault roughness, total right-lateral displacement, and relative rupture time for Event ID 3869. (C) Top panel shows the structural configuration for which this parameter sweep was performed (overlap 50 km, stepover 7 km). Lower panels are plots of conditional rupture probabilities for Segments 1 and 2 on smooth and rough faults. (D) Top panel is a map

view of the Coulomb failure stress computed at a depth of 8.5 km using the indicated stress boundary condition. Lower panels are 3D views of (from top to bottom) fault roughness, total right-lateral displacement, and relative rupture time for Event ID 4797. (E) Top panel shows the structural configuration for which this parameter sweep was performed (underlap 20 km, stepover 5 km). Lower panels are plots of conditional rupture probabilities for Segments 1 and 2 on smooth and rough faults. (F) Top panel is a map view of the Coulomb failure stress computed at a depth of 8.5 km using the indicated stress boundary condition. Lower panels are 3D views of (from top to bottom) fault roughness, total right-lateral displacement, and relative rupture time for Event ID 3737. (G) Top panel shows the structural configuration for which this parameter sweep was performed (overlap 50 km, stepover 5 km). Lower panels are plots of conditional rupture probabilities for Segments 1 and 2 on smooth and rough faults. (H) Top panel is a map view of the Coulomb failure stress computed at a depth of 8.5 km using the indicated stress boundary condition. Lower panels are 3D views of (from top to bottom) fault roughness, total right-lateral displacement, and relative rupture time for Event ID 2973. (I) Top panel shows the structural configuration for which this parameter sweep was performed (underlap 20 km, stepover 2 km). Lower panels are plots of conditional rupture probabilities for Segments 1 and 2 on smooth and rough faults. (J) Top panel is a map view of the Coulomb failure stress computed at a depth of 8.5 km using the indicated stress boundary condition. Lower panels are 3D views of (from top to bottom) fault roughness, total right-lateral displacement, and relative rupture time for Event ID 1331. (K) Top panel shows the structural configuration for which this parameter sweep was performed (overlap 50 km, stepover 2 km). Lower panels are plots of conditional

rupture probabilities for Segments 1 and 2 on smooth and rough faults. (L) Top panel is a map view of the Coulomb failure stress computed at a depth of 8.5 km using the indicated stress boundary condition. Lower panels are 3D views of (from top to bottom) fault roughness, total right-lateral displacement, and relative rupture time for Event ID 1869 and (M) Event ID 4719.

Figure 4.22. Parameter sweep to investigate the effect of varying activated patch participation level on rupture jumping probabilities in a restraining step. (A) Top panel shows the structural configuration for which this parameter sweep was performed (underlap 20 km, stepover 7 km). Lower panels are plots of conditional rupture probabilities for Segments 1 and 2 on smooth and rough faults. (B) Top panel is a map view of the Coulomb failure stress computed at a depth of 8.5 km using the indicated stress boundary condition. Lower panels are 3D views of (from top to bottom) fault roughness, total right-lateral displacement, and relative rupture time for Event ID 941. (C) Top panel shows the structural configuration for which this parameter sweep was performed (overlap 50 km, stepover 7 km). Lower panels are plots of conditional rupture probabilities for Segments 1 and 2 on smooth and rough faults. (D) Top panel is a map view of the Coulomb failure stress computed at a depth of 8.5 km using the indicated stress boundary condition. Lower panels are 3D views of (from top to bottom) fault roughness, total right-lateral displacement, and relative rupture time for Event ID 3157. (E) Top panel shows the structural configuration for which this parameter sweep was performed (underlap 20 km, stepover 5 km). Lower panels are plots of conditional rupture probabilities for Segments 1 and 2 on smooth and rough faults. (F) Top panel is a

map view of the Coulomb failure stress computed at a depth of 8.5 km using the indicated stress boundary condition. Lower panels are 3D views of (from top to bottom) fault roughness, total right-lateral displacement, and relative rupture time for Event ID 2348. (G) Top panel shows the structural configuration for which this parameter sweep was performed (overlap 50 km, stepover 5 km). Lower panels are plots of conditional rupture probabilities for Segments 1 and 2 on smooth and rough faults. (H) Top panel is a map view of the Coulomb failure stress computed at a depth of 8.5 km using the indicated stress boundary condition. Lower panels are 3D views of (from top to bottom) fault roughness, total right-lateral displacement, and relative rupture time for Event ID 4745. (I) Top panel shows the structural configuration for which this parameter sweep was performed (underlap 20 km, stepover 2 km). Lower panels are plots of conditional rupture probabilities for Segments 1 and 2 on smooth and rough faults. (J) Top panel is a map view of the Coulomb failure stress computed at a depth of 8.5 km using the indicated stress boundary condition. Lower panels are 3D views of (from top to bottom) fault roughness, total right-lateral displacement, and relative rupture time for Event ID 3942. (K) Top panel shows the structural configuration for which this parameter sweep was performed (overlap 50 km, stepover 2 km). Lower panels are plots of conditional rupture probabilities for Segments 1 and 2 on smooth and rough faults. (L) Top panel is a map view of the Coulomb failure stress computed at a depth of 8.5 km using the indicated stress boundary condition. Lower panels are 3D views of (from top to bottom) fault roughness, total right-lateral displacement, and relative rupture time for Event ID 2158.

Figure 4.23. Parameter sweep to investigate the effect of varying activated patch participation level on rupture jumping probabilities in a releasing double bend. (A) Top panel shows the structural configuration for which this parameter sweep was performed (underlap 20 km, stepover 7 km). Lower panels are plots of conditional rupture probabilities for Segments 1 and 2 on smooth and rough faults. (B) Top panel is a map view of the Coulomb failure stress computed at a depth of 8.5 km using the indicated stress boundary condition. Lower panels are 3D views of (from top to bottom) fault roughness, total right-lateral displacement, and relative rupture time for Event ID 2508, (C) Event ID 1174, and (D) Event ID 4476. (E) Top panel shows the structural configuration for which this parameter sweep was performed (underlap 20 km, stepover 5 km). Lower panels are plots of conditional rupture probabilities for Segments 1 and 2 on smooth and rough faults. (F) Top panel is a map view of the Coulomb failure stress computed at a depth of 8.5 km using the indicated stress boundary condition. Lower panels are 3D views of (from top to bottom) fault roughness, total right-lateral displacement, and relative rupture time for Event ID 3677, (G) Event ID 1447, (H) Event ID 4800, and (I) 2493. (J) Top panel shows the structural configuration for which this parameter sweep was performed (underlap 20 km, stepover 2 km). Lower panels are plots of conditional rupture probabilities for Segments 1 and 2 on smooth and rough faults. (K) Top panel is a map view of the Coulomb failure stress computed at a depth of 8.5 km using the indicated stress boundary condition. Lower panels are 3D views of (from top to bottom) fault roughness, total right-lateral displacement, and relative rupture time for Event ID 2563, (L) Event ID 1400, and (M) Event ID 3139.

Figure 4.24. Parameter sweep to investigate the effect of varying activated patch participation level on rupture jumping probabilities in a restraining double bend. (A) Top panel shows the structural configuration for which this parameter sweep was performed (underlap 20 km, stepover 7 km). Lower panels are plots of conditional rupture probabilities for Segments 1 and 2 on smooth and rough faults. (B) Top panel is a map view of the Coulomb failure stress computed at a depth of 8.5 km using the indicated stress boundary condition. Lower panels are 3D views of (from top to bottom) fault roughness, total right-lateral displacement, and relative rupture time for Event ID 4872, and (C) Event ID 2591. (D) Top panel shows the structural configuration for which this parameter sweep was performed (underlap 20 km, stepover 5 km). Lower panels are plots of conditional rupture probabilities for Segments 1 and 2 on smooth and rough faults. (E) Top panel is a map view of the Coulomb failure stress computed at a depth of 8.5 km using the indicated stress boundary condition. Lower panels are 3D views of (from top to bottom) fault roughness, total right-lateral displacement, and relative rupture time for Event ID 3837, and (F) Event ID 418. (G) Top panel shows the structural configuration for which this parameter sweep was performed (underlap 20 km, stepover 2 km). Lower panels are plots of conditional rupture probabilities for Segments 1 and 2 on smooth and rough faults. (H) Top panel is a map view of the Coulomb failure stress computed at a depth of 8.5 km using the indicated stress boundary condition. Lower panels are 3D views of (from top to bottom) fault roughness, total right-lateral displacement, and relative rupture time for Event ID 3103, and (I) Event ID 1856.

Figure 4.25. Exploring the effect of variable fault topology on rupture jumping probabilities. Three-dimensional views of ten different fault roughness configurations for a restraining step that is made up of two vertical, right-lateral strike-slip faults with a (A) 50 km overlap and 7 km stepover and (C). The structural configurations for both sets of model runs is shown in the upper panels of (B) and (D), while the lower panels are plots of conditional rupture probabilities as a function of segment participation level for each of the 10 runs.

Figure 4.26. Computed rupture jumping probabilities for different underlap (negative *x*-axis) and overlap (positive *x*-axis) distances between two smooth faults and two rough faults. Stepover distances ranged from 2 km to 4 km at 1 km increments. Underlap and overlap distances ranged from -5 km (underlap) to 5 km (overlap) at 1 km increments using. Each structural configuration was simulated 5 times. All rupture jumping probabilities were computed using the 80% minimum patch participation level.

Figure 4.27. Wesnousky's (2008) rupture process zone as it propagates with the leading edge of a large rupture. It is based on Wesnousky's (2008) compilation of empirical observations that correlate fault trace complexity with rupture jumping. The radius of the process zone cylinder ranges from 3-4 km and contains a volume where stress change magnitudes are invariable at the front of the rupture. From Wesnousky (2008).

Figure 4.28. Plots of total slip distribution and static stress drop for a hypothetical vertically striking fault. (A) Displacement along a smooth fault follows an elliptical shape

and results in a uniform stress drop along strike. High stress concentrations are localized at the fault ends. (B) Displacement along a rough fault results in an irregular slip distribution and non-uniform stress drop. Local asperities along the fault surface create localized high and low stress regions such that the surrounding volume experiences non-uniform stress drops. In some locations, stresses are enhanced to levels comparable to the high stresses near fault ends.

Figure 4.29. Conceptual model of the process zone for a rupture propagating along a rough fault. Local asperities inherent to rough faults cause the shape and size of the rupture process zone to change along strike and down dip. The size of the rupture process zone may increase with increasing fault roughness, but rapidly decreases as the rupture propagates along the fault.

Figure 4.1

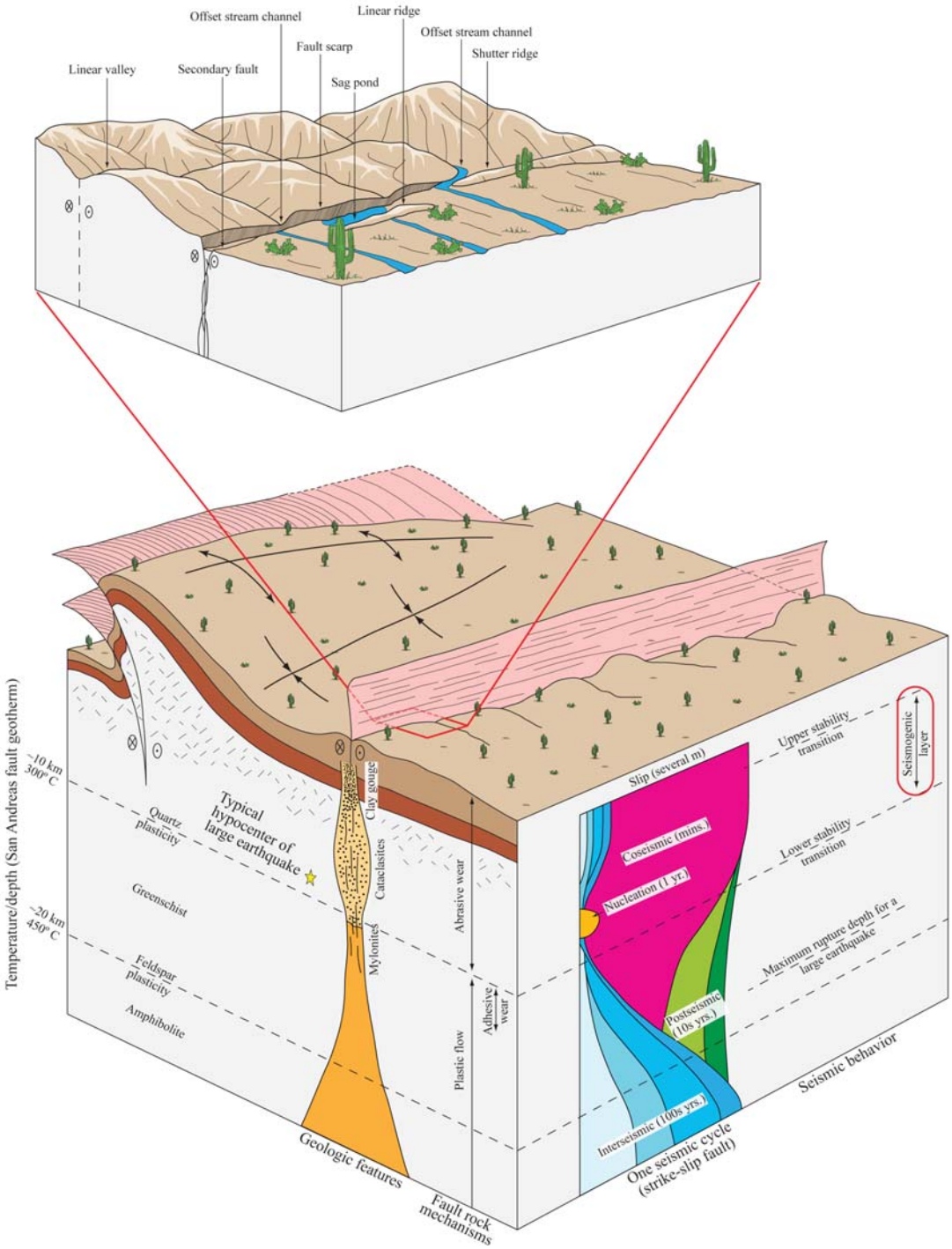
Offset stream channel
Linear ridge
Offset stream channel
Fault scarp
Shutter ridge
Linear valley
Secondary fault
Sag pond
Temperature/depth (San Andreas fault geotherm)
~10 km
300° C
~20 km
450° C
Quartz plasticity
Typical hypocenter of large earthquake
Greenschist
Feldspar plasticity
Amphibolite
Clay gouge
Cataclasites
Mylonites
Abrasive wear
Plastic flow
Adhesive wear
Geologic features
Fault rock mechanisms
Slip (several m)
Upper stability transition
Seismogenic layer
Coseismic (mins.)
Nucleation (1 yr.)
Lower stability transition
Maximum rupture depth for a large earthquake
Postseismic (10s yrs.)
Interseismic (100s yrs.)
Seismic behavior
One seismic cycle (strike-slip fault)

Figure 4.2

(A) 1987 Superstition Hills earthquake, California

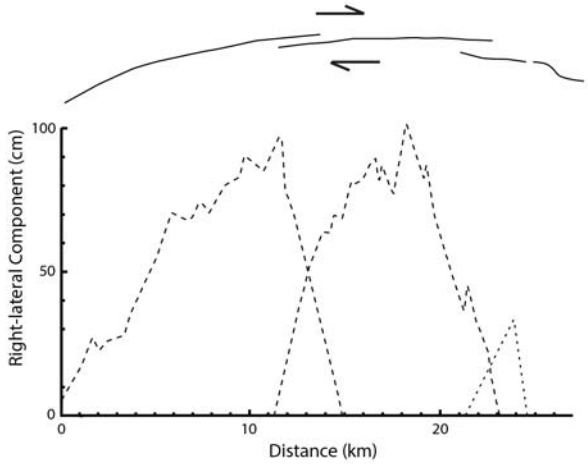

(B) 1968 Borrego Mountain earthquake, California

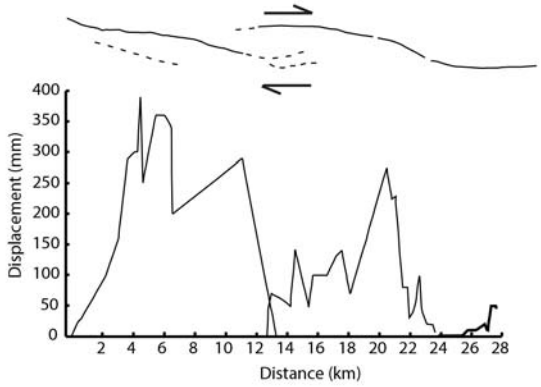

(C) 1887 Pitaycachi earthquake, Sonora, Mexico

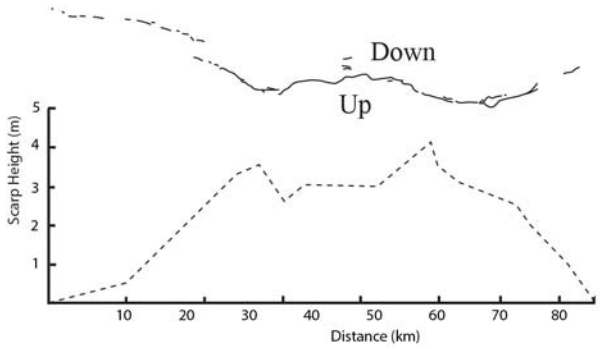

Figure 4.3A

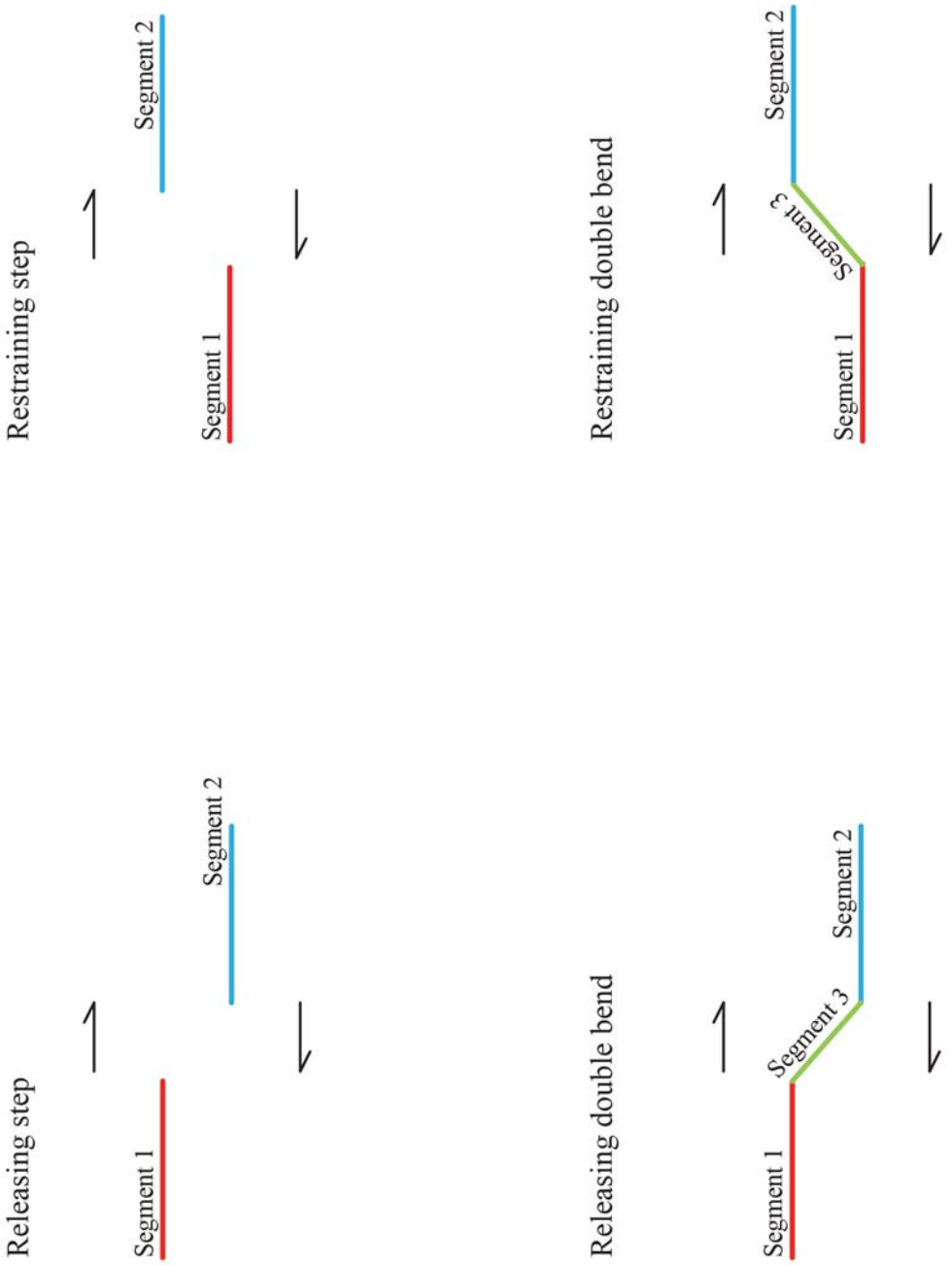
Restraining step
Segment 2
Segment 1
Restraining double bend
Segment 2
Segment 3
Segment 1
Releasing step
Segment 2
Segment 1
Releasing double bend
Segment 2
Segment 3
Segment 1

Figure 4.3B

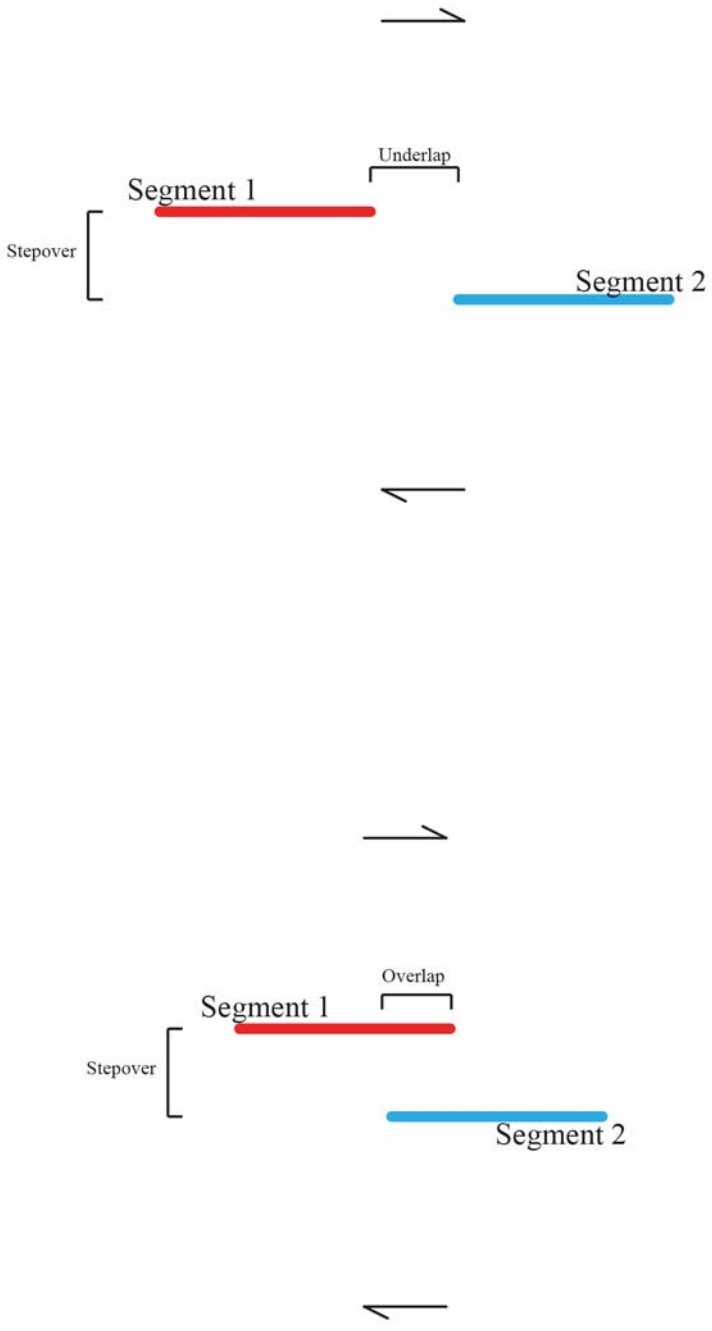
Underlap
Segment 1
Stepover
Segment 2
Overlap
Segment 1
Stepover
Segment 2

Figure 4.4

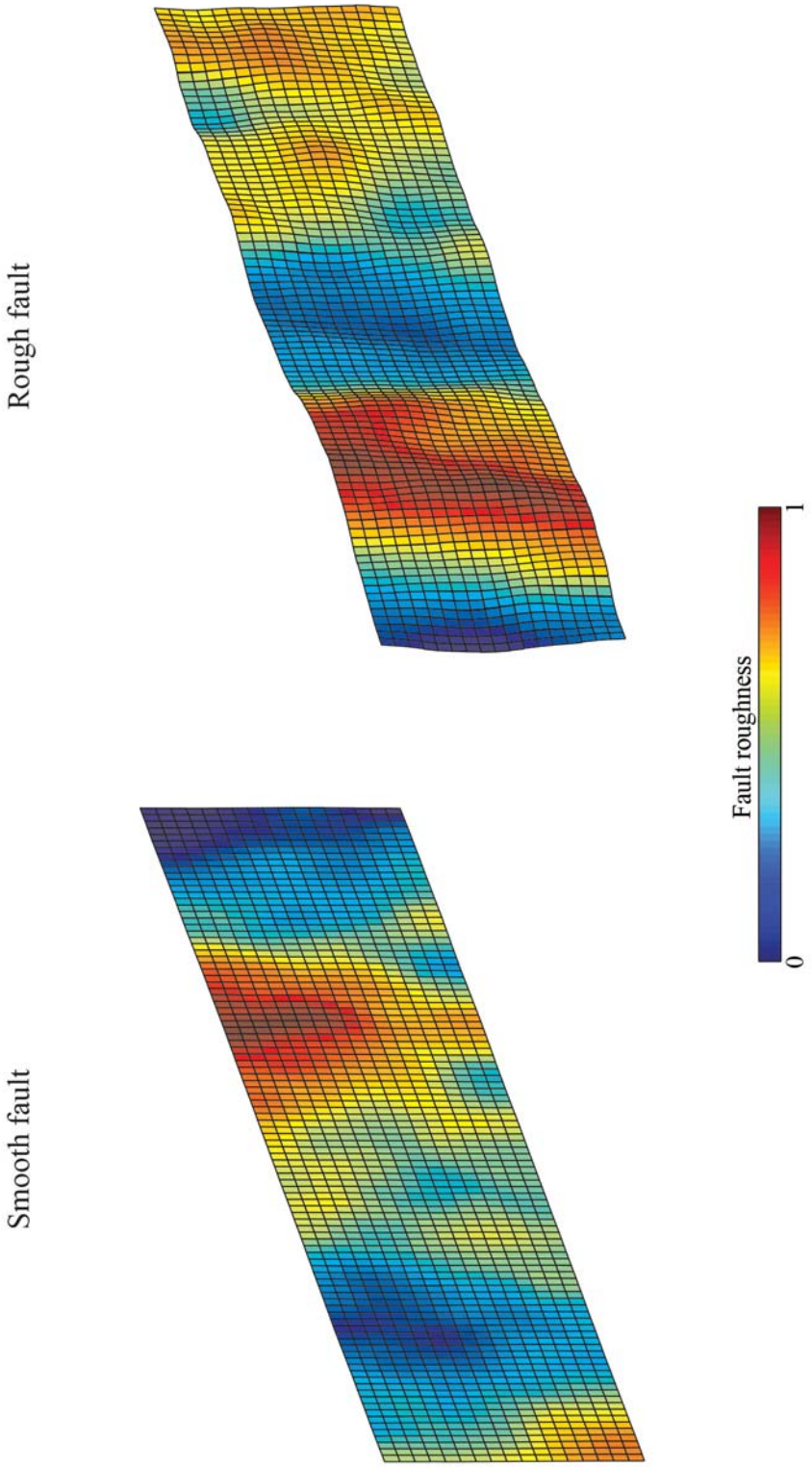

Figure 4.5A

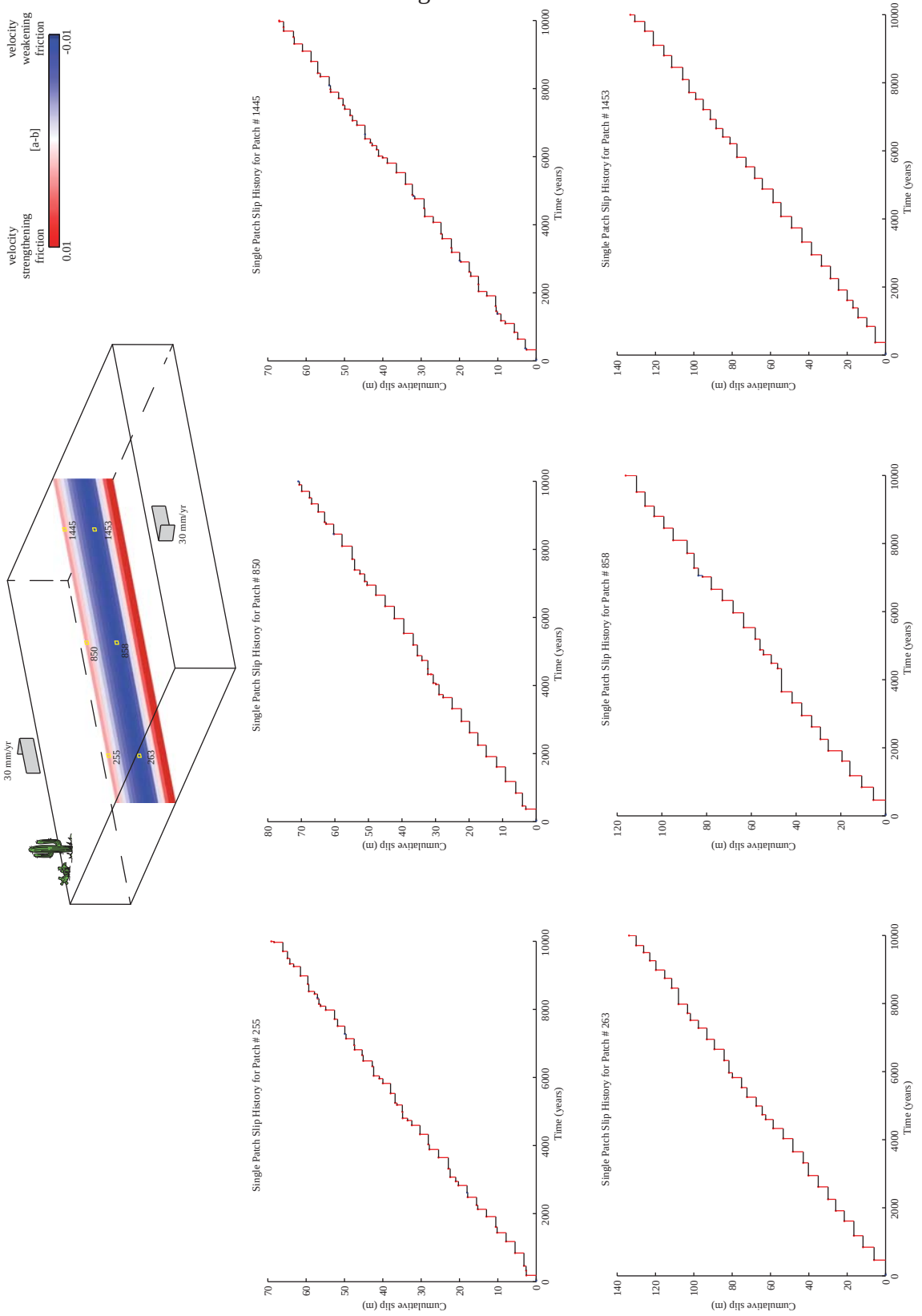
velocity weakening friction
-0.01
[a-b]
velocity strengthening friction
0.01
30 mm/yr
30 mm/yr
1445
1453
850
858
255
263
Single Patch Slip History for Patch # 1445
Single Patch Slip History for Patch # 1453
Single Patch Slip History for Patch # 850
Single Patch Slip History for Patch # 858
Single Patch Slip History for Patch # 255
Single Patch Slip History for Patch # 263
Cumulative slip (m)
Time (years)

Figure 4.5B

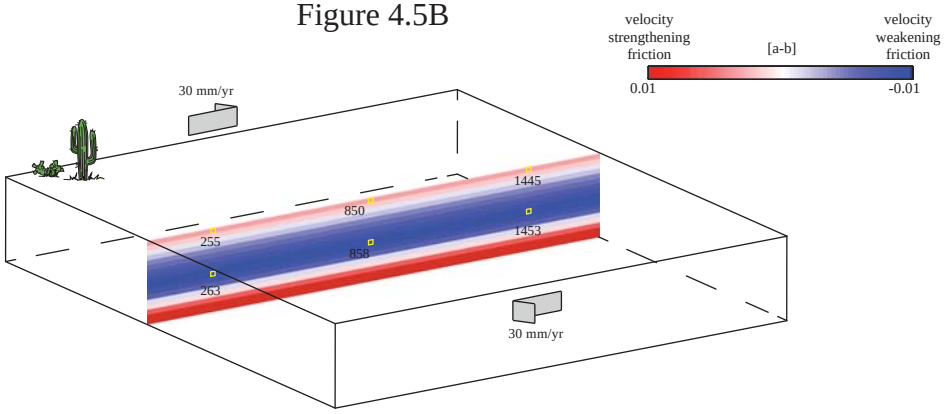
velocity strengthening friction
[a-b]
velocity weakening friction
0.01
-0.01
30 mm/yr
1445
850
1453
255
858
263
30 mm/yr

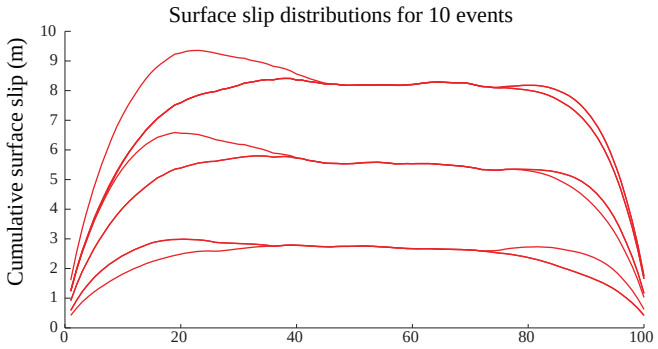
Surface slip distributions for 10 events
Cumulative surface slip (m)
0
1
2
3
4
5
6
7
8
9
10
0
20
40
60
80
100

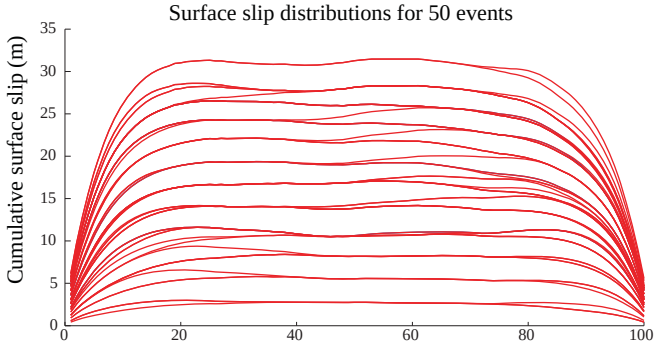
Surface slip distributions for 50 events
Cumulative surface slip (m)
0
5
10
15
20
25
30
35
0
20
40
60
80
100

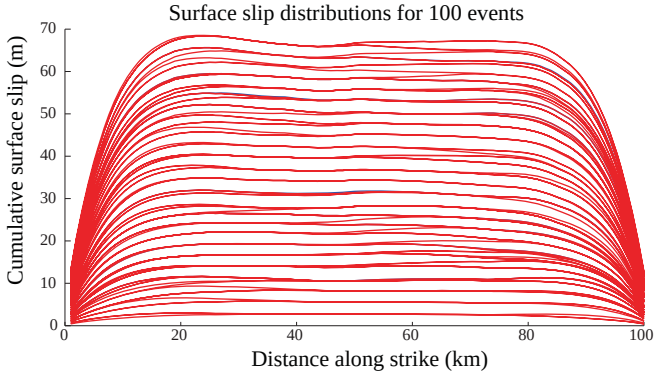
Surface slip distributions for 100 events
Cumulative surface slip (m)
0
10
20
30
40
50
60
70
0
20
40
60
80
100
Distance along strike (km)

Figure 4.6

Overlap: 50 km
Stepover: 7 km
Overlap: 50 km
Stepover: 5 km
Overlap: 50 km
Stepover: 2 km
Underlap: 20 km
Stepover: 7 km
Underlap: 20 km
Stepover: 5 km
Underlap: 20 km
Stepover: 2 km
30 mm/yr
Segment 1
Segment 2

Figure 4.7

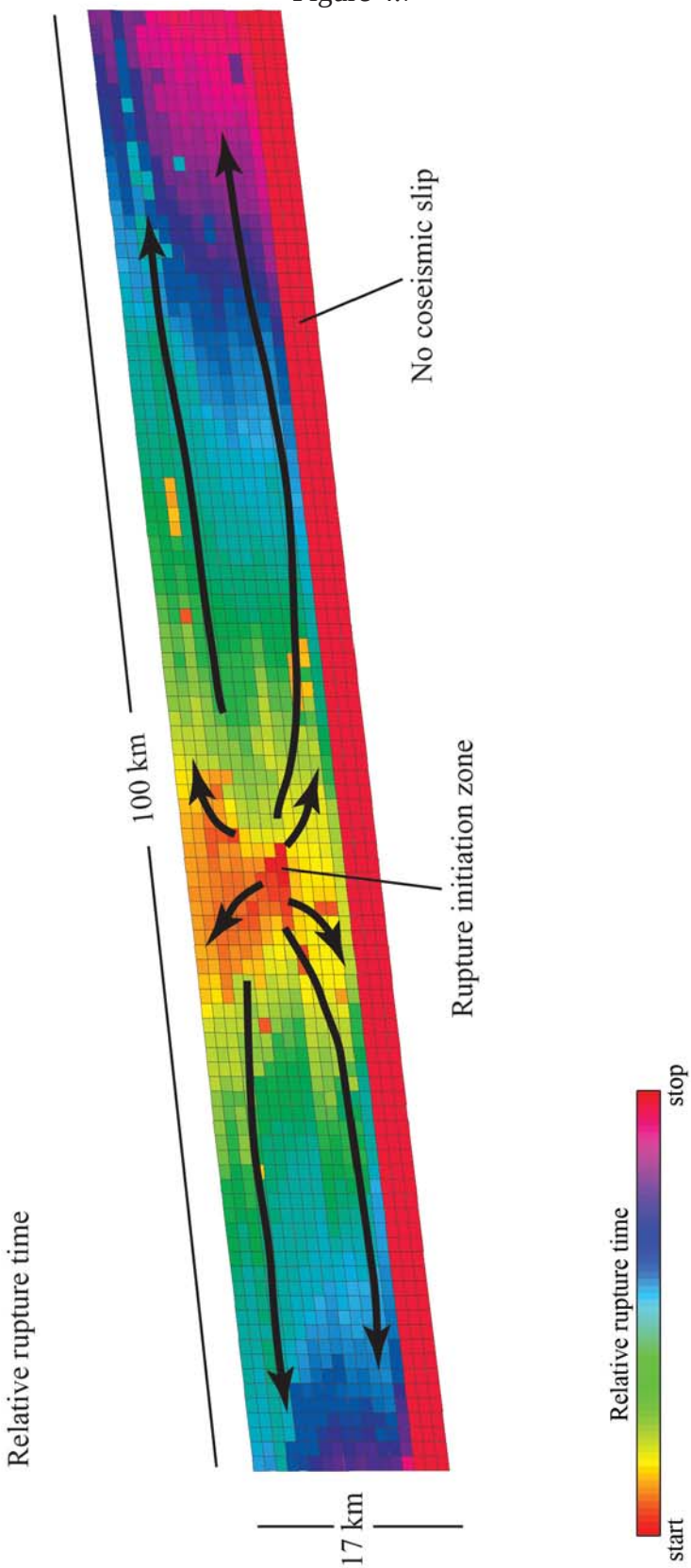
No coseismic slip
100 km
Rupture initiation zone
Relative rupture time
17 km
Relative rupture time
stop
start

Figure 4.8A - Segment 1

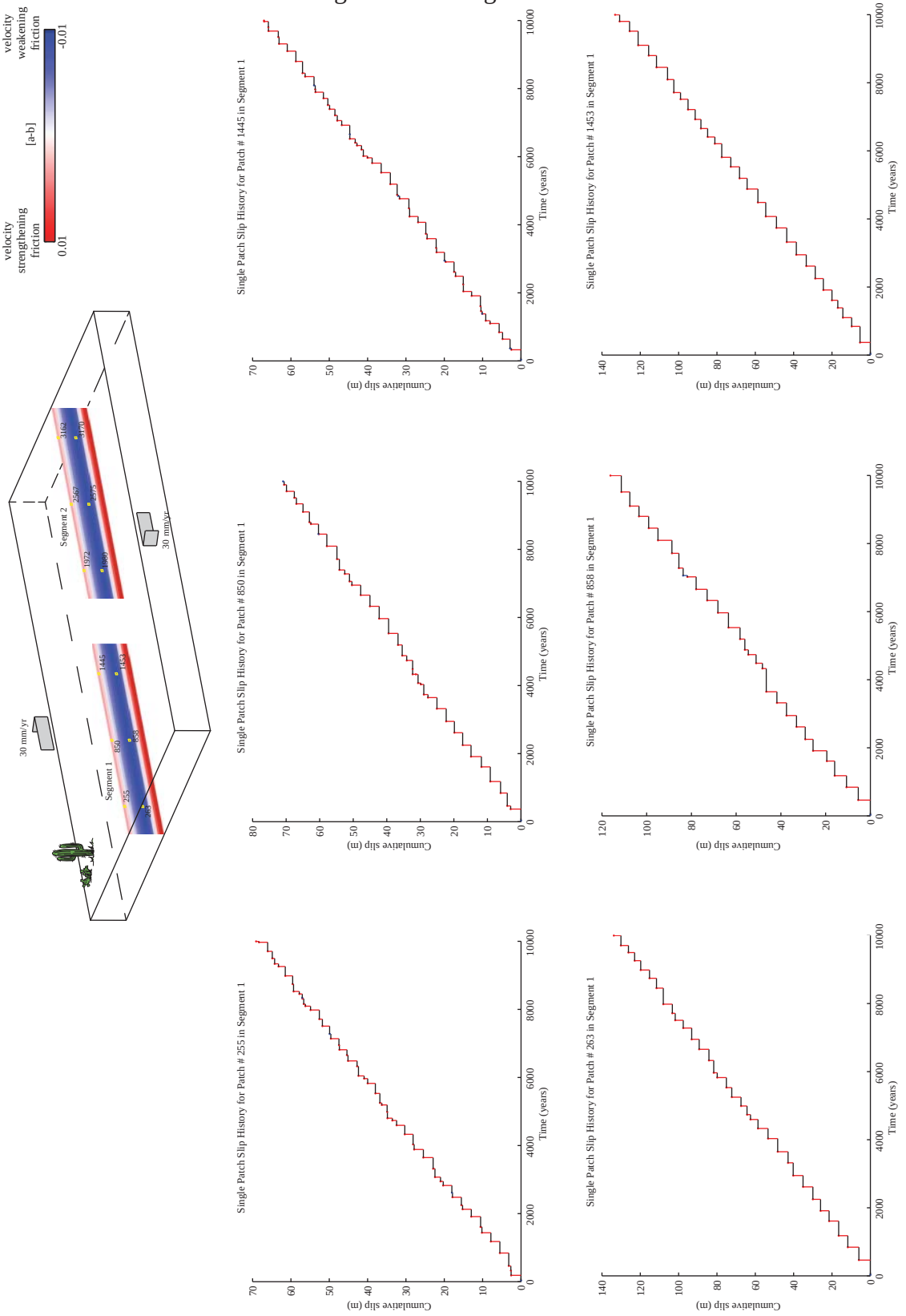

Figure 4.8A - Segment 2

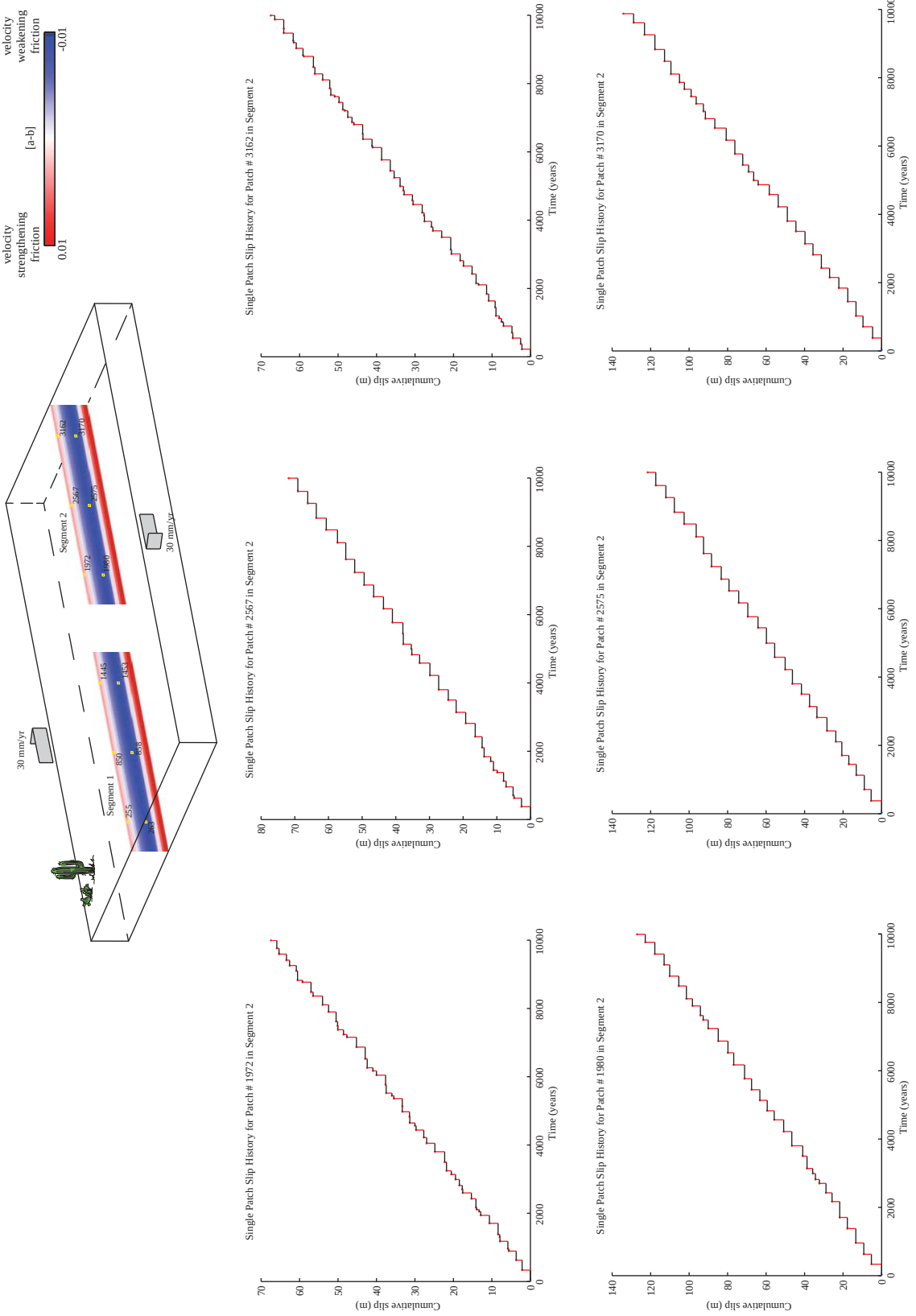

Figure 4.8B

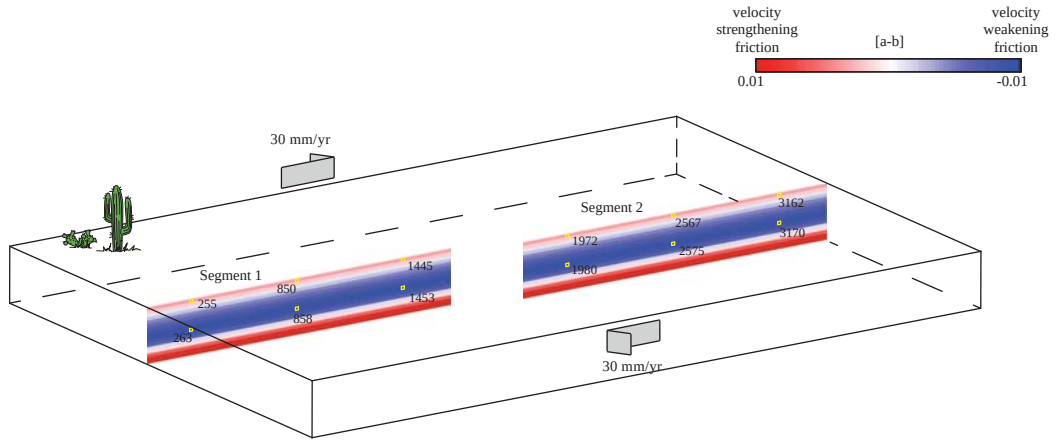

Segment 1 | Segment 2

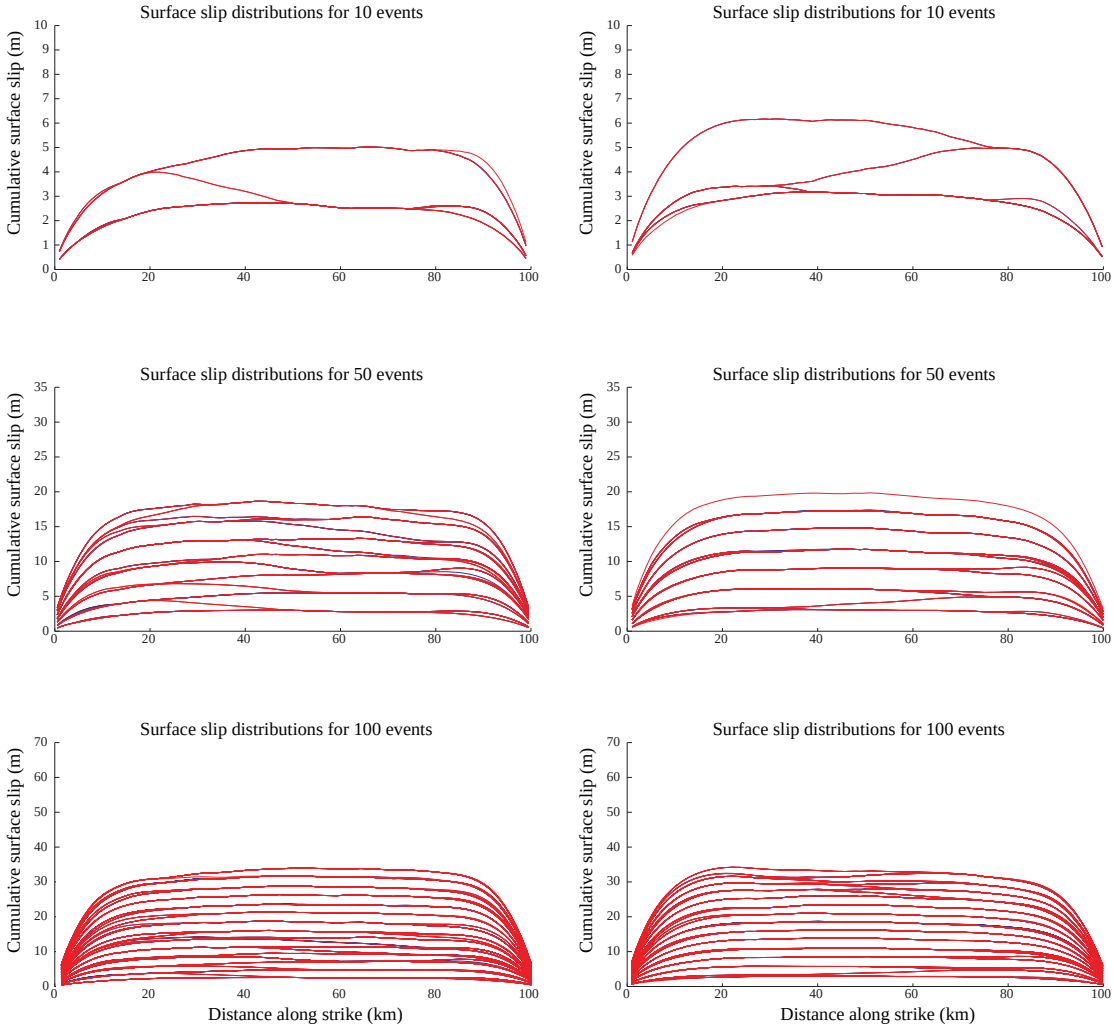

Figure 4.9A - Segment 1

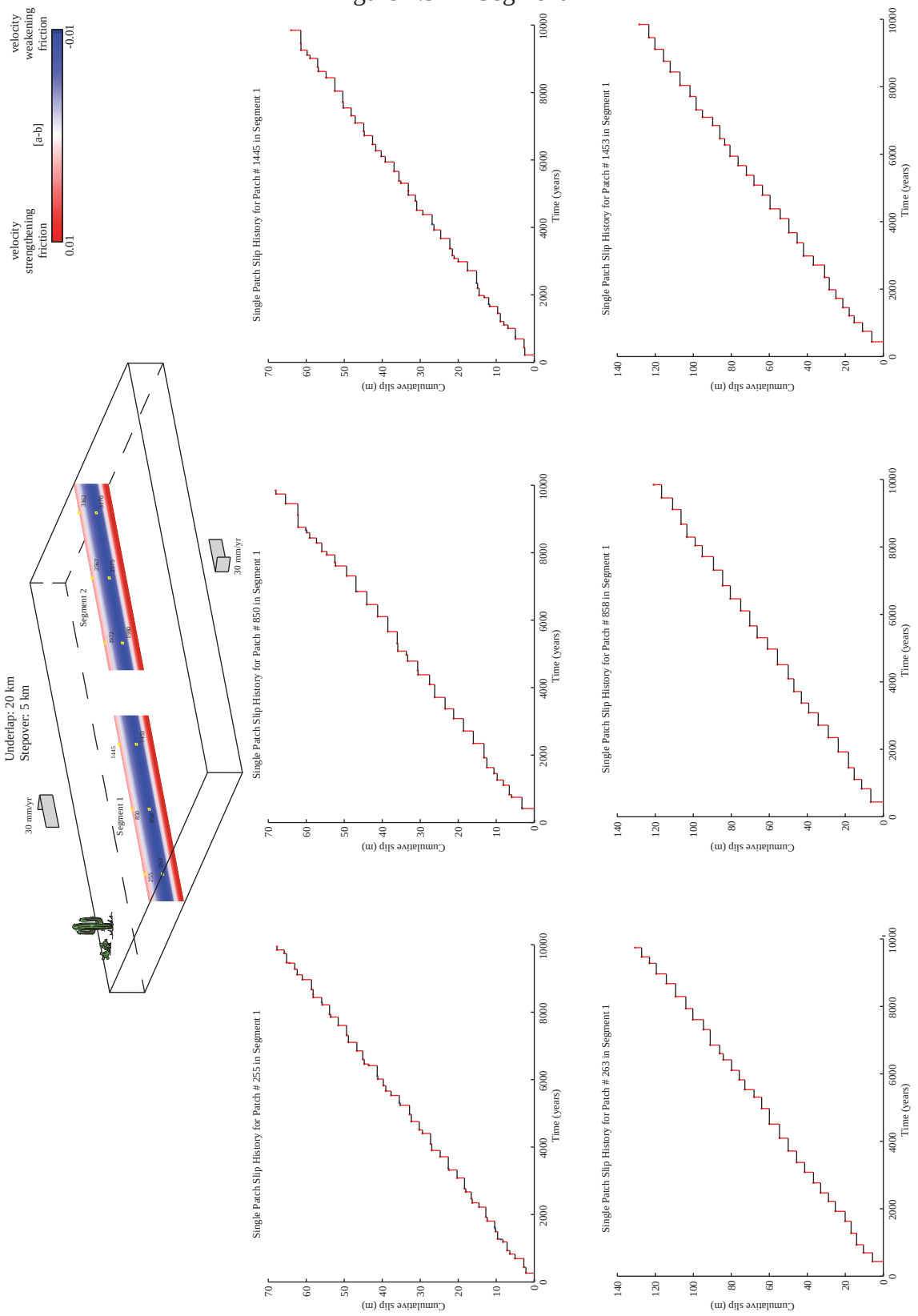

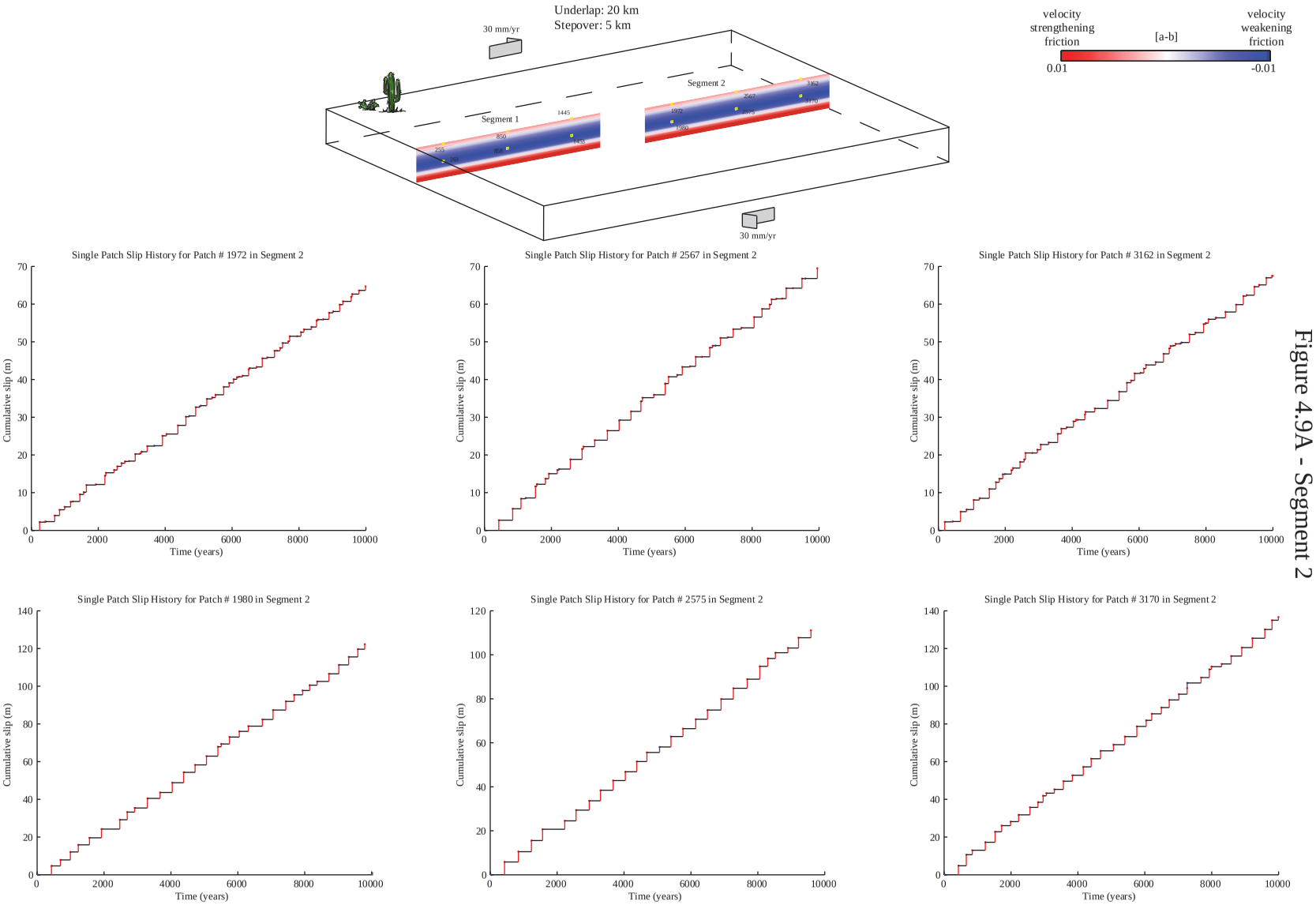

Figure 4.9A - Segment 2

Figure 4.9B

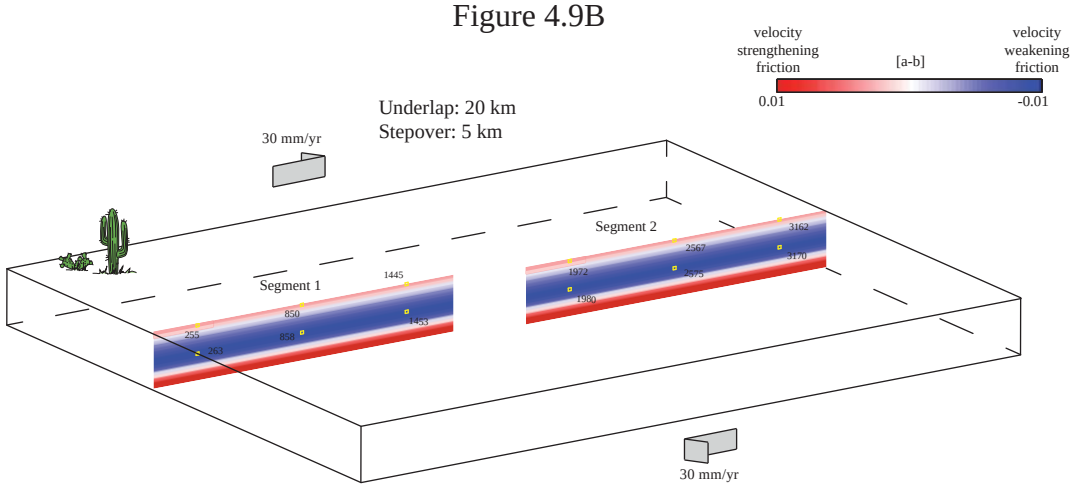

Segment 1 | Segment 2

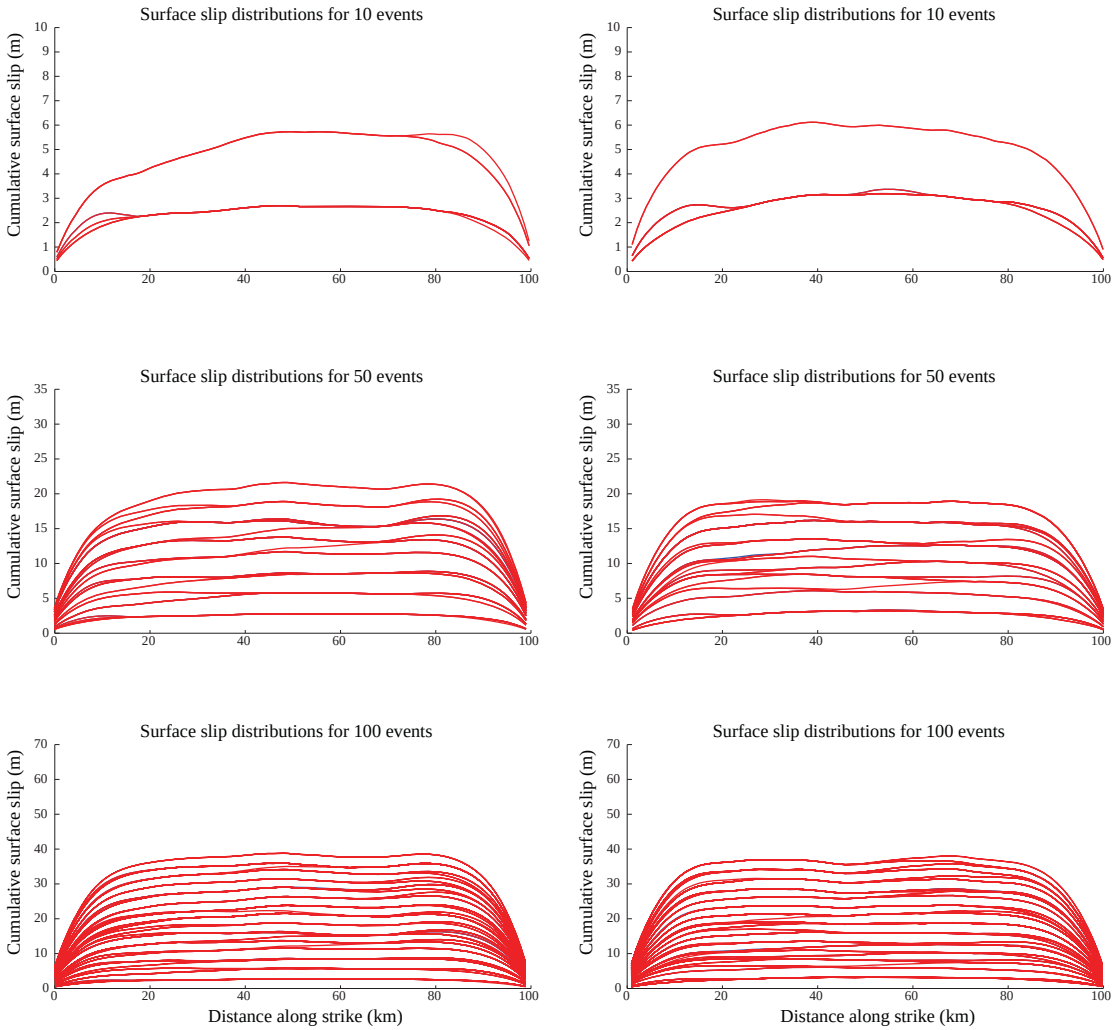

Figure 4.10A - Segment 1

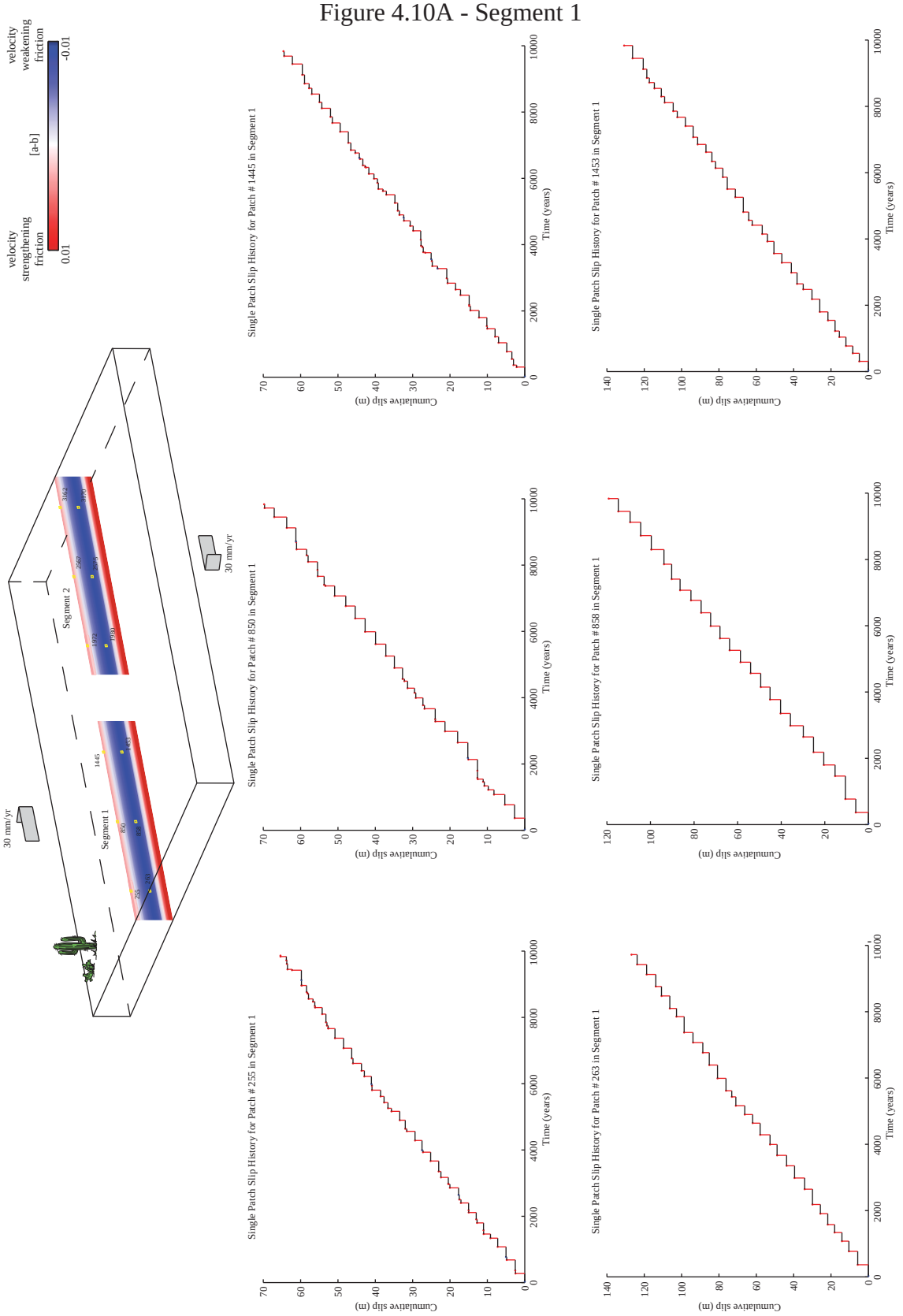

Figure 4.10A - Segment 2

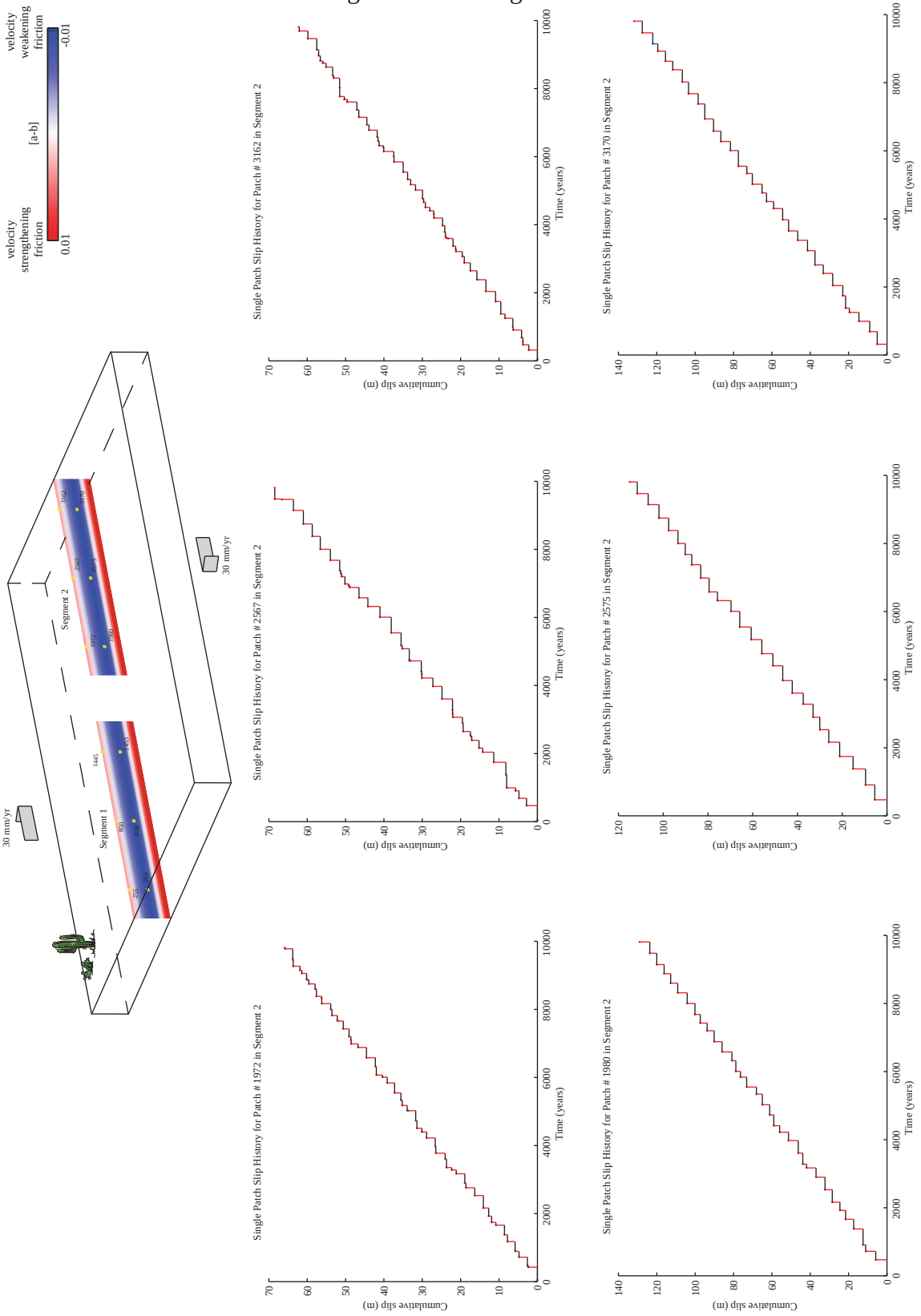

Figure 4.10B

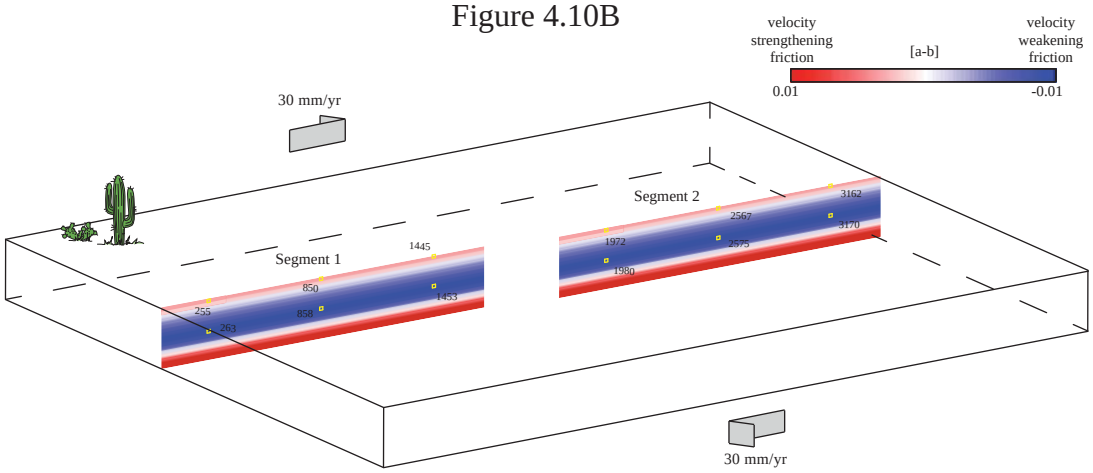

Segment 1 | Segment 2

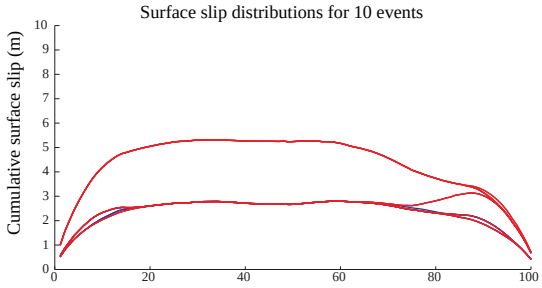

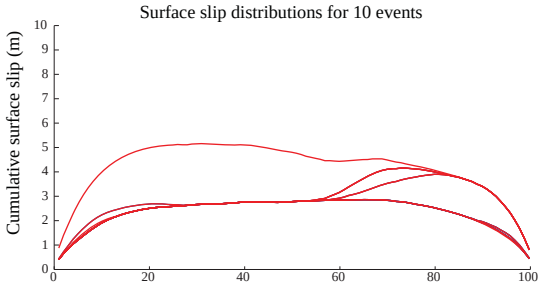

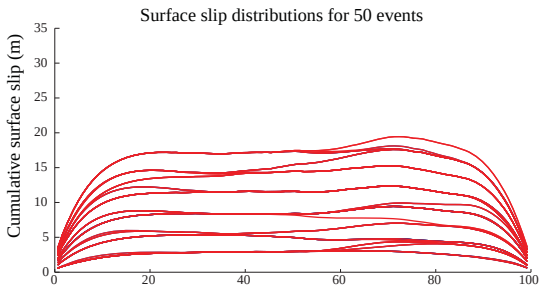

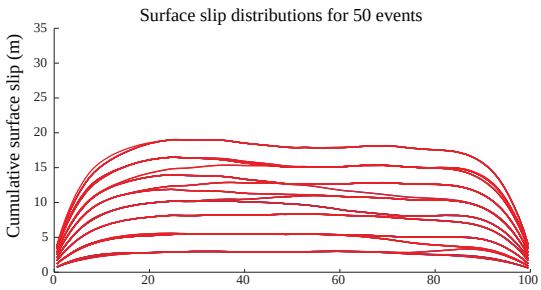

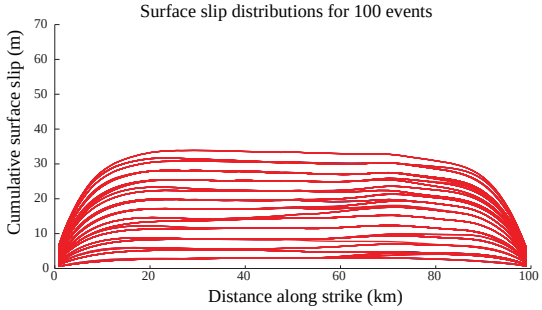

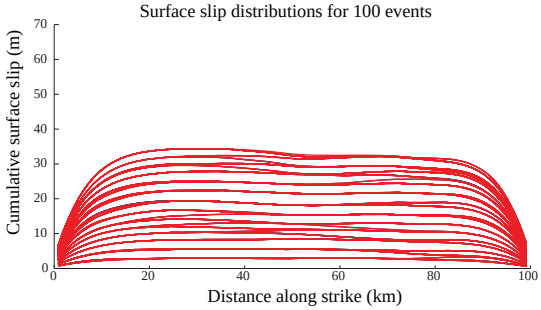

Figure 4.11A - Segment 1

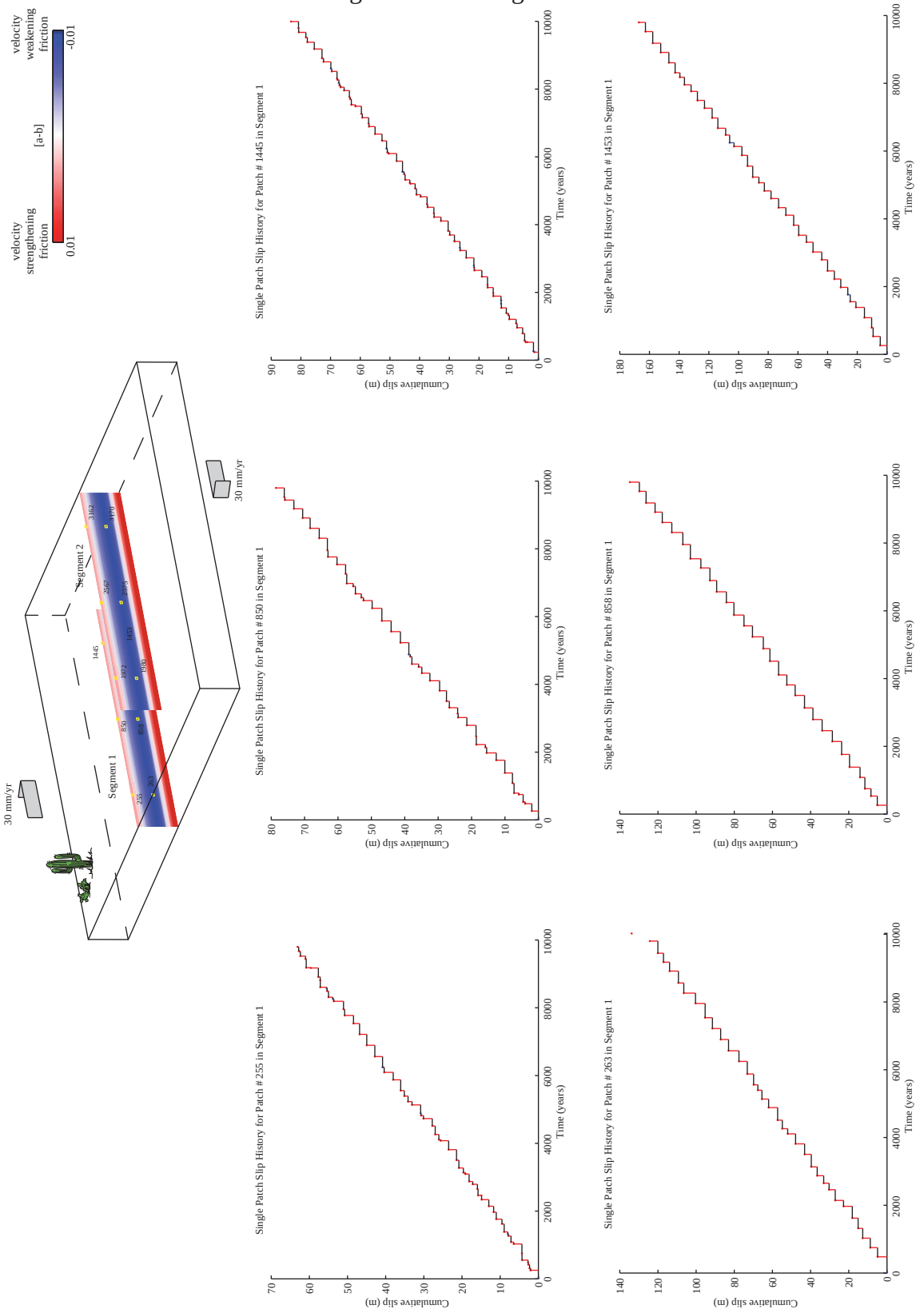

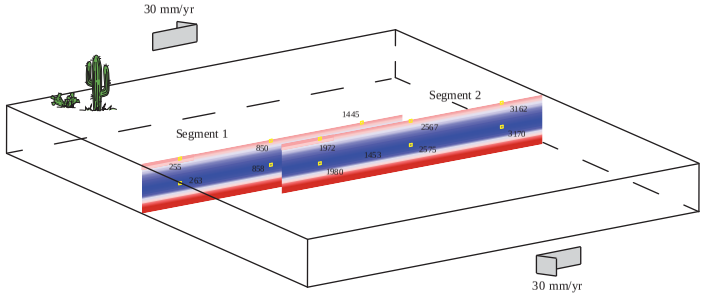

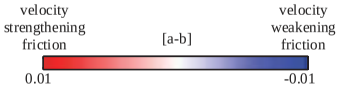

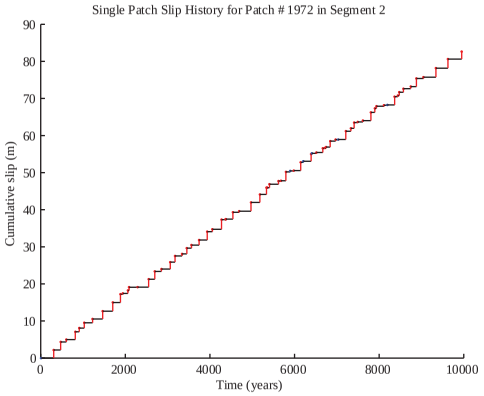

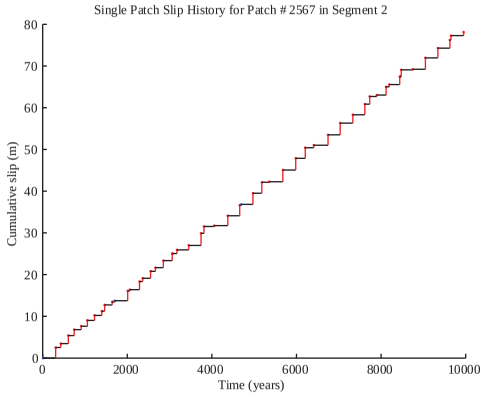

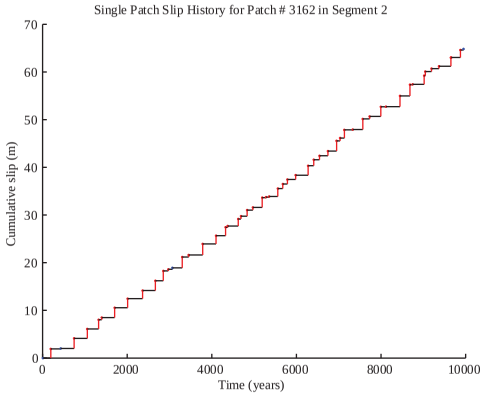

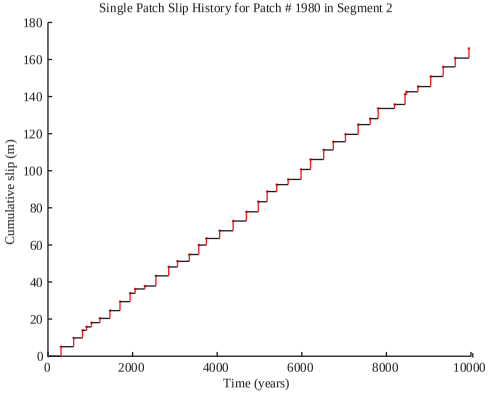

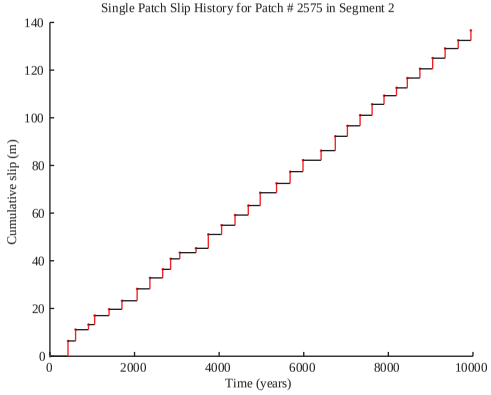

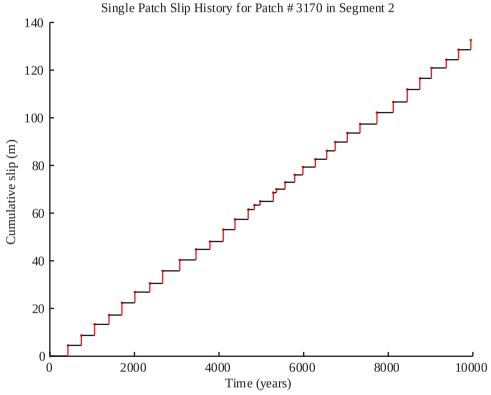

Figure 4.11A - Segment 2

Figure 4.11B

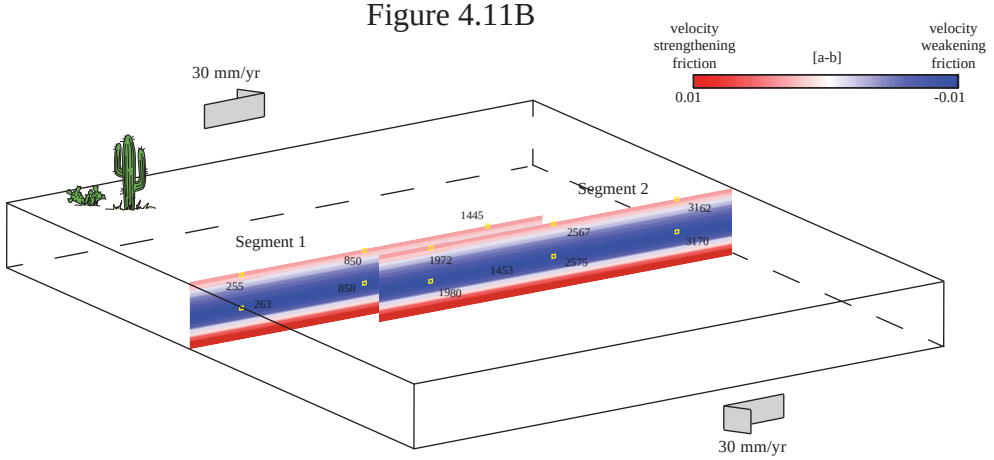

Segment 1 | Segment 2

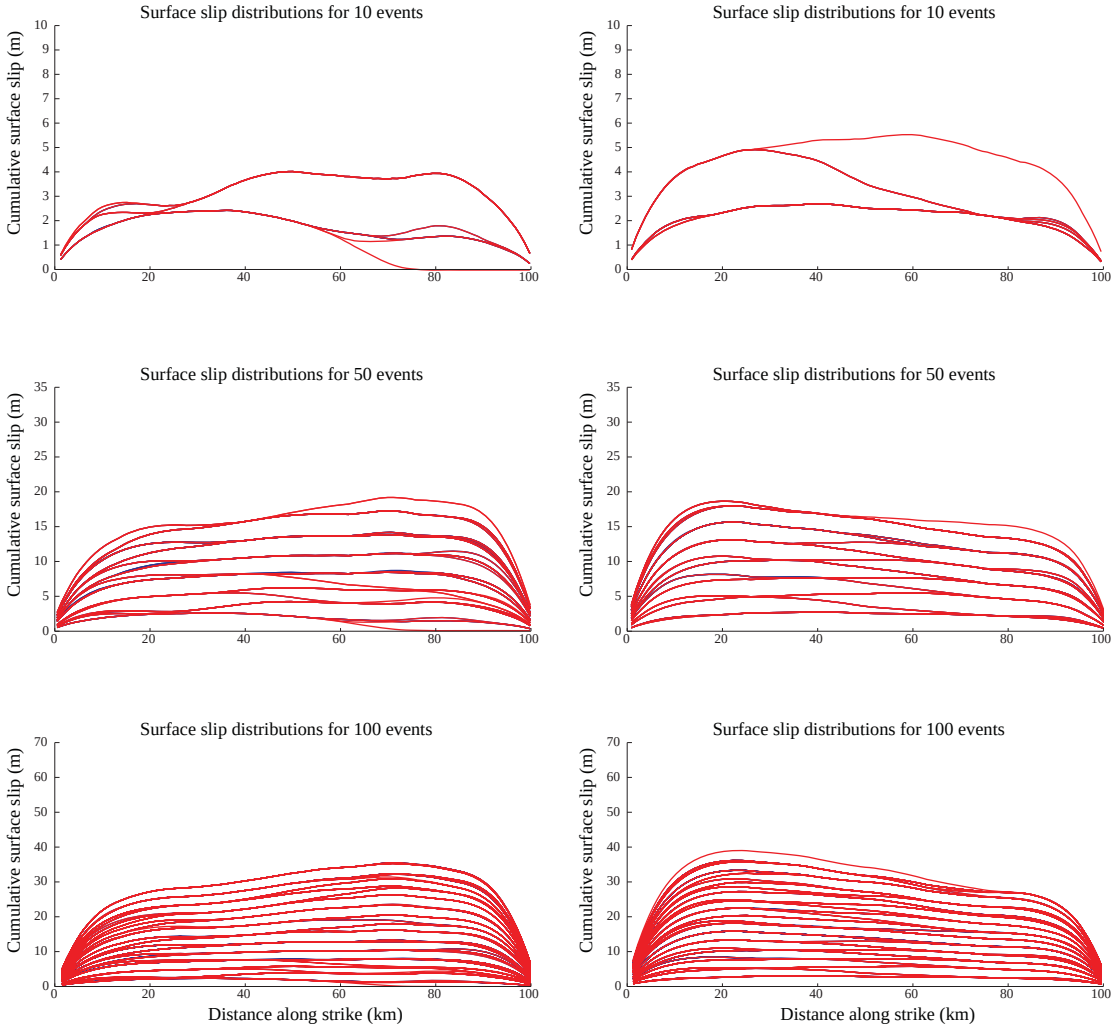

Figure 4.12A - Segment 1

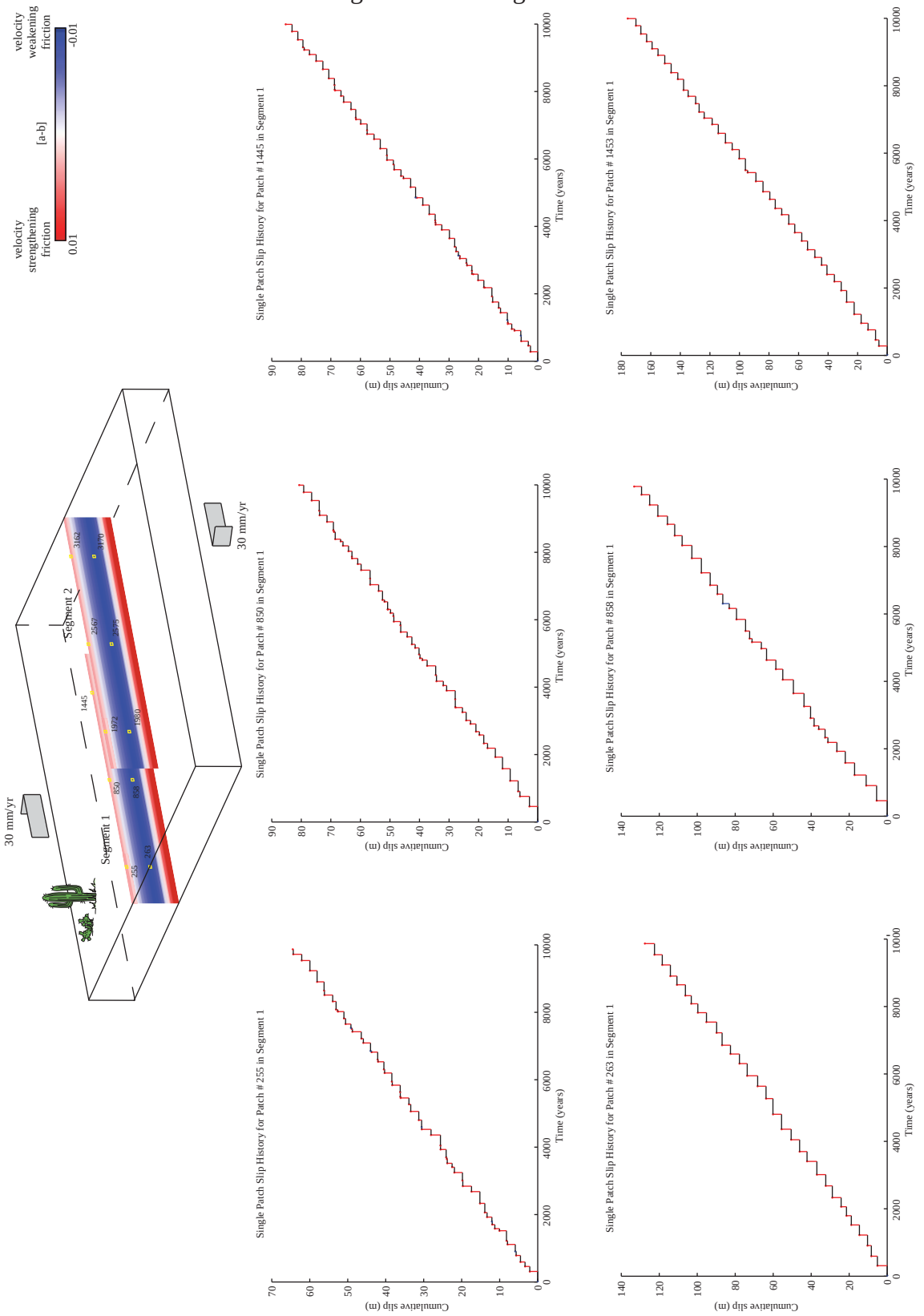

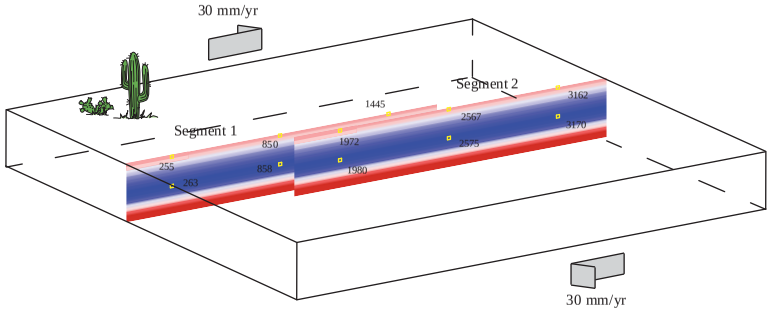

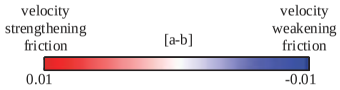

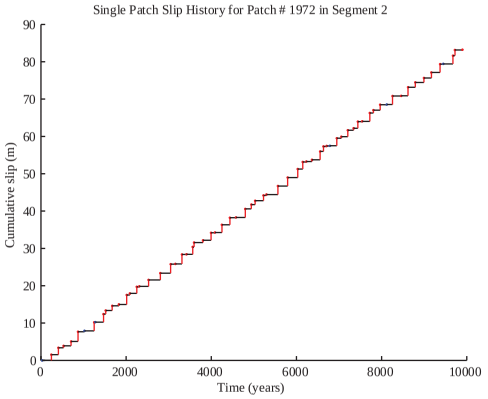

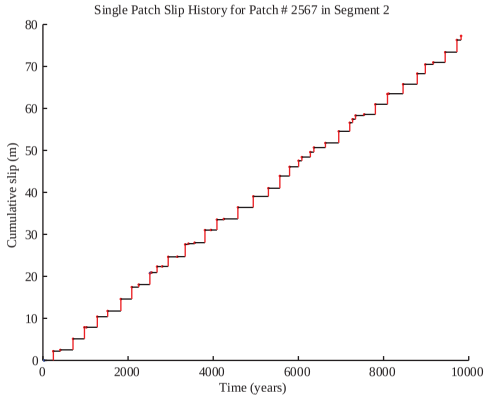

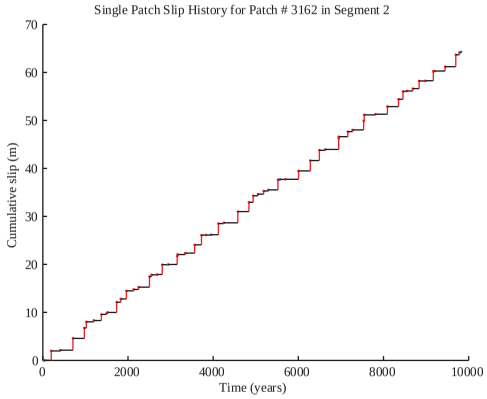

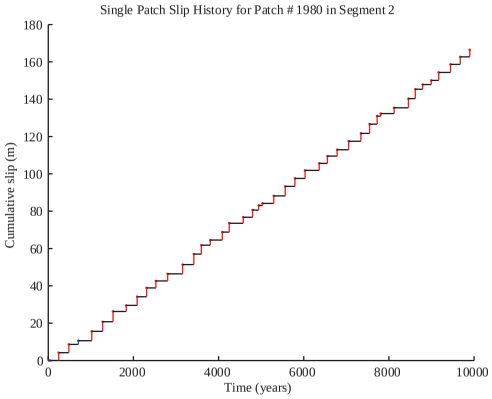

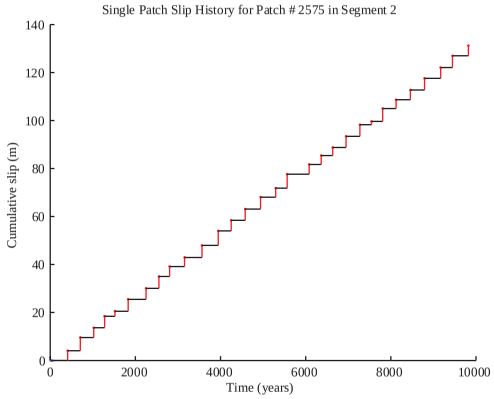

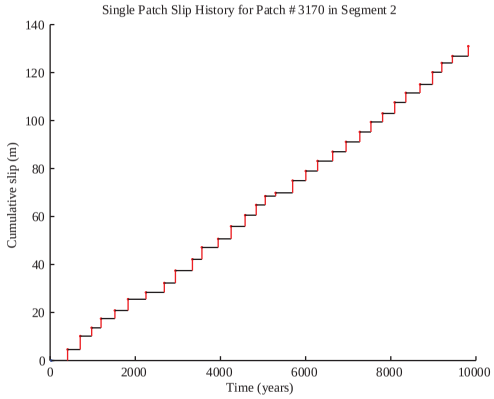

Figure 4.12A - Segment 2

Figure 4.12B

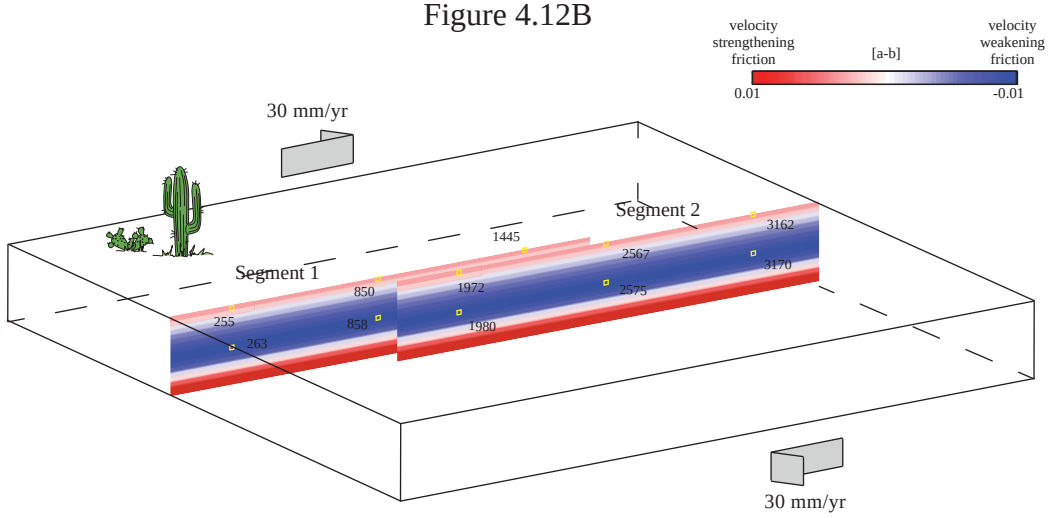

Segment 1 | Segment 2

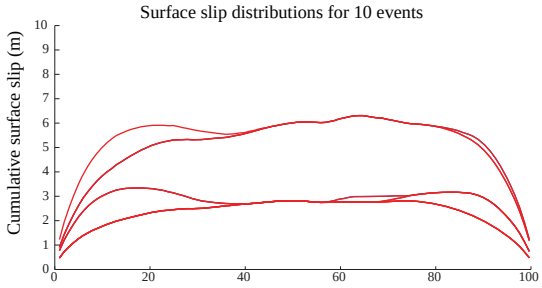

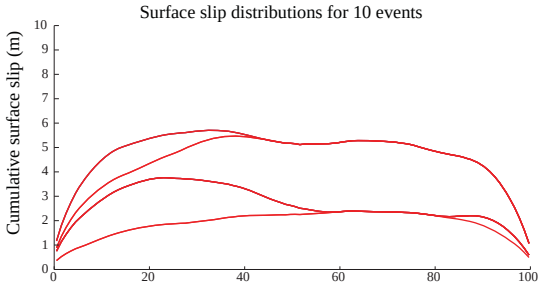

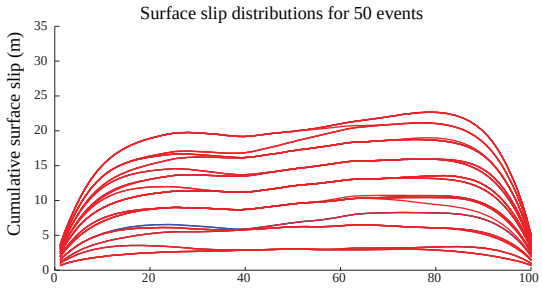

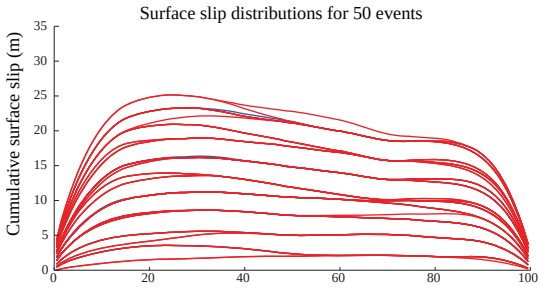

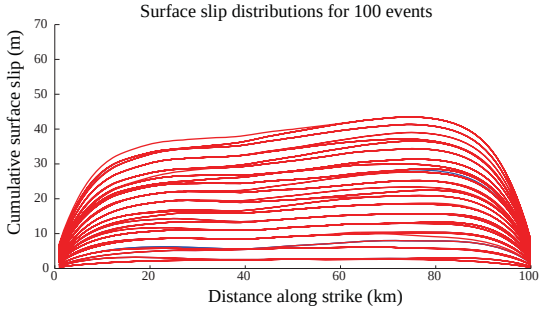

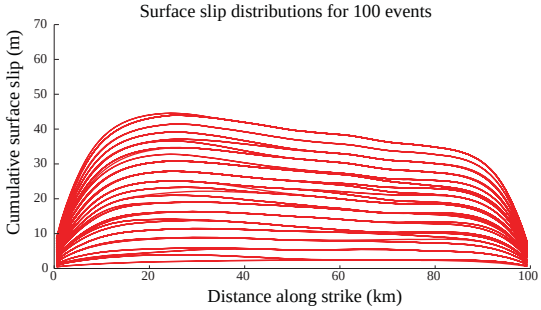

Figure 4.13A - Segment 1

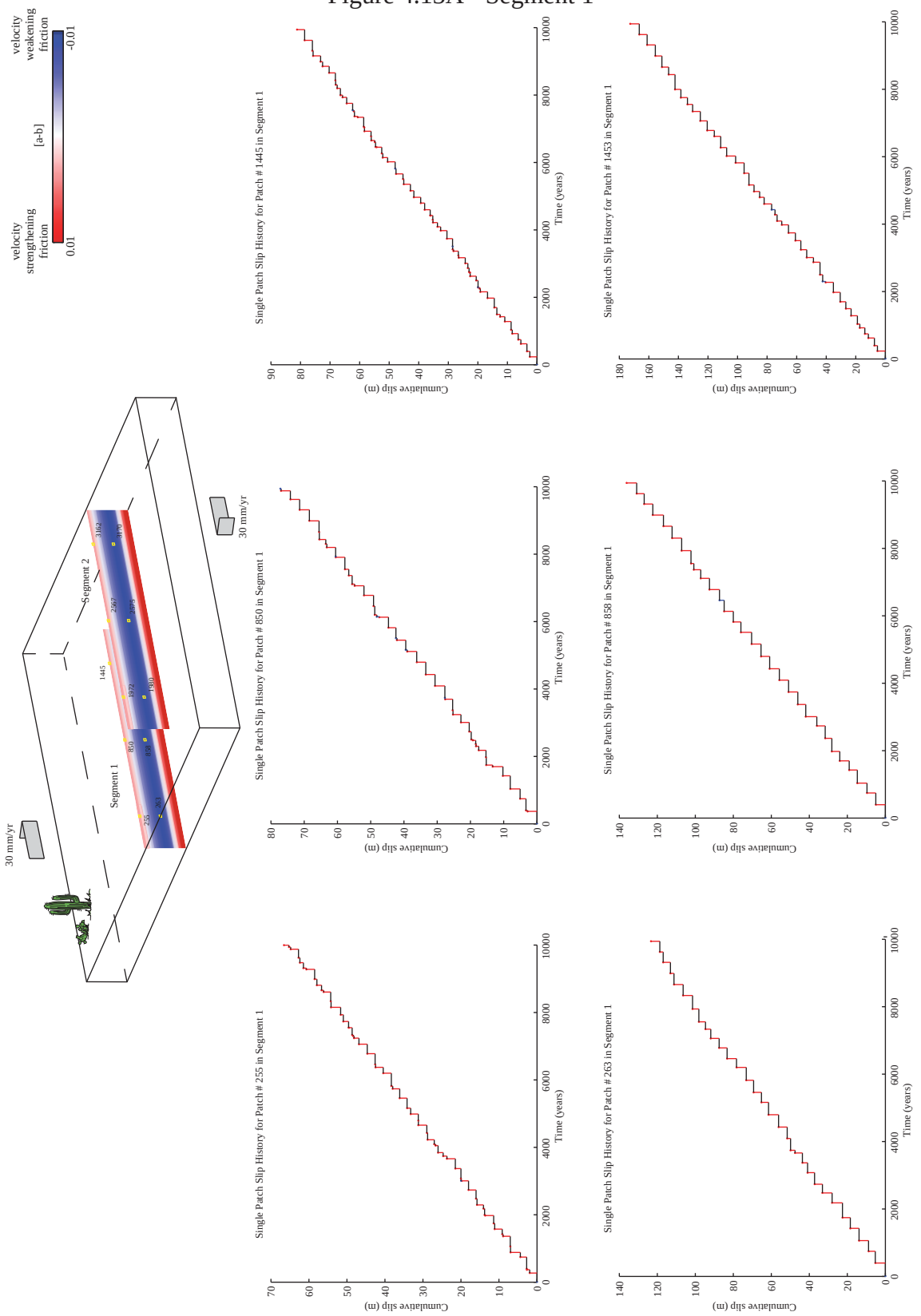

Figure 4.13A - Segment 2

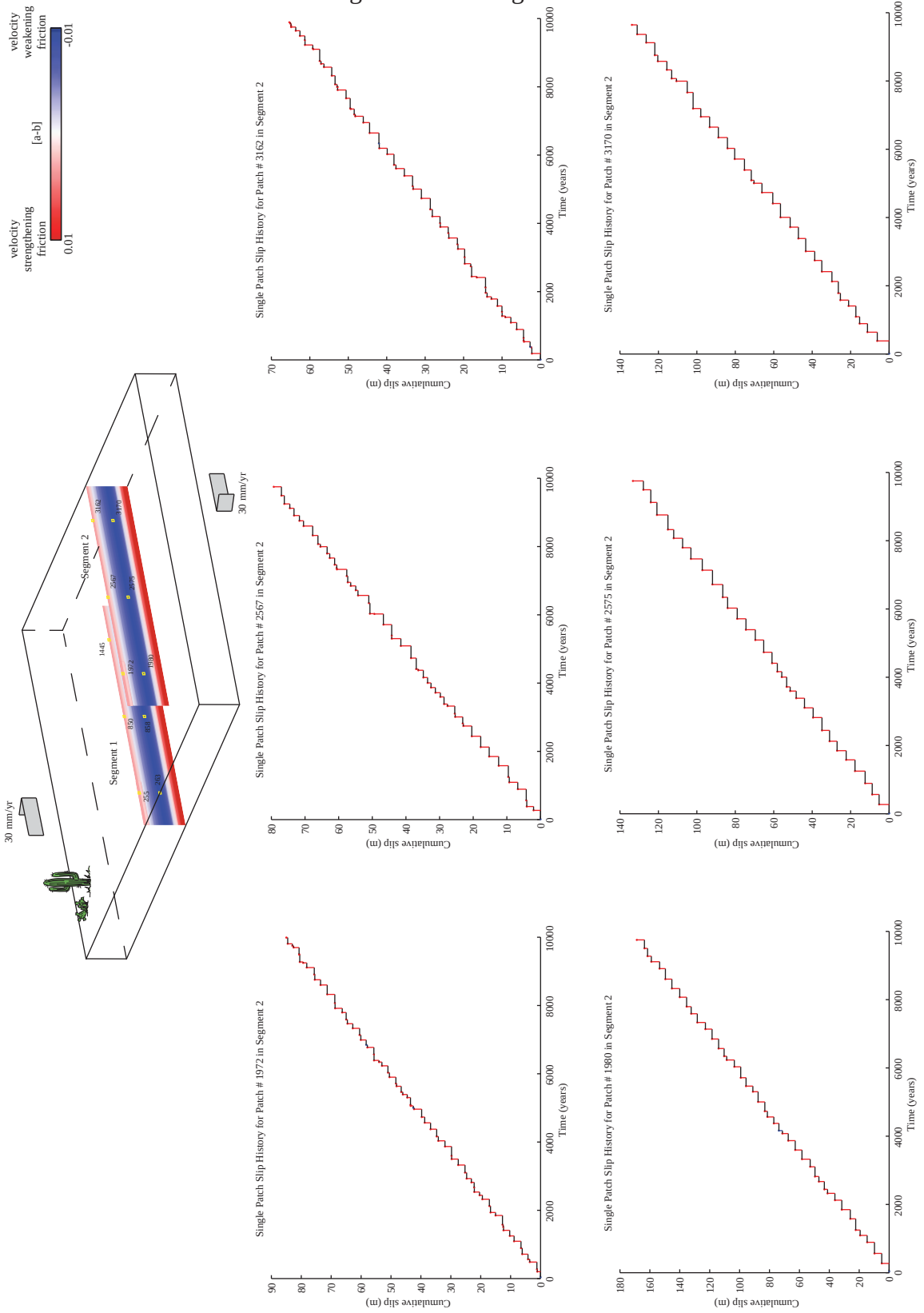

Figure 4.13B

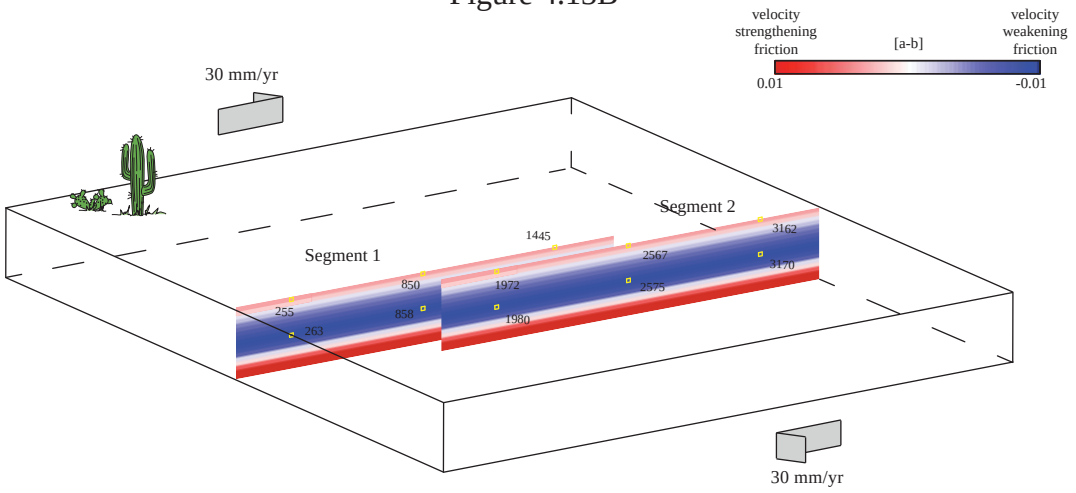

Segment 1 | Segment 2

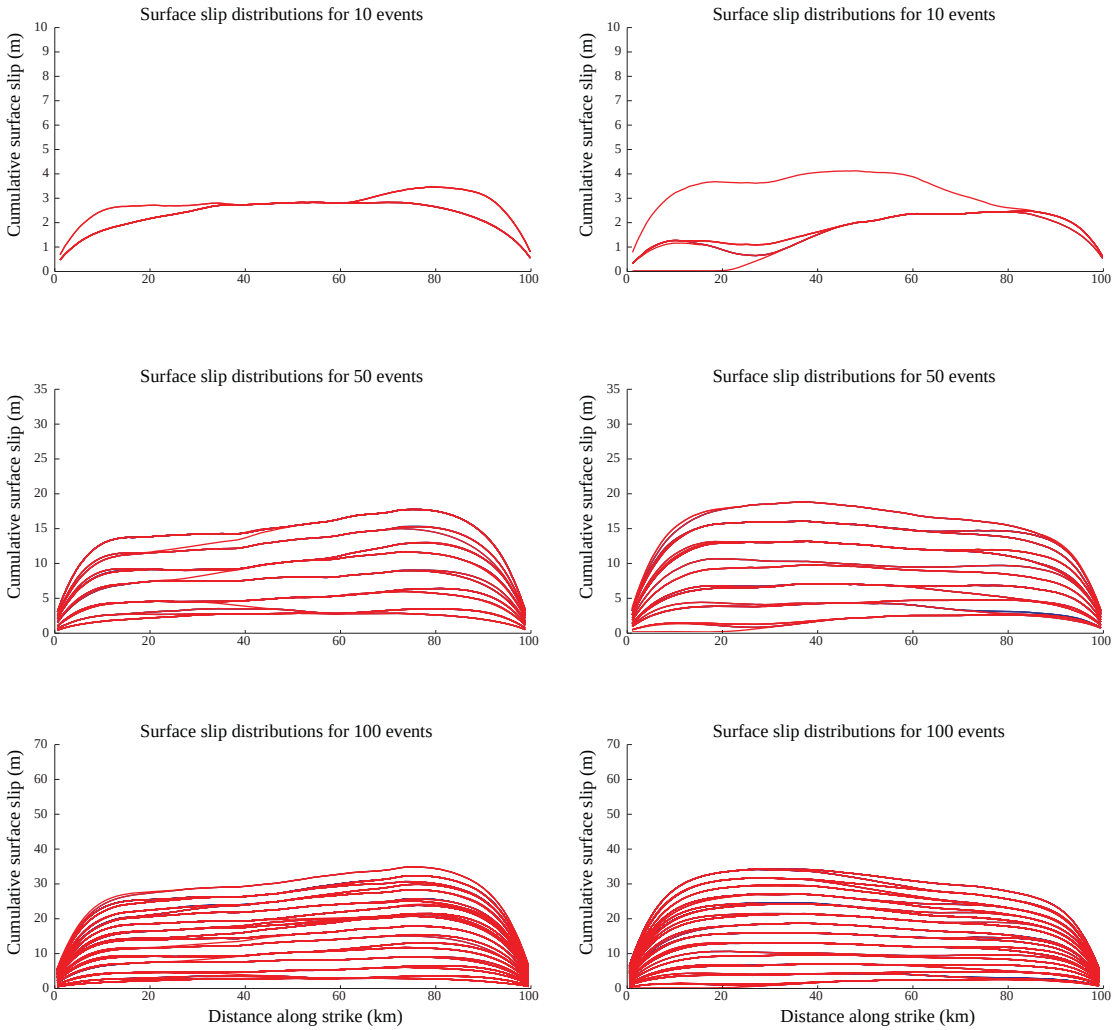

Figure 4.14A - Segment 1

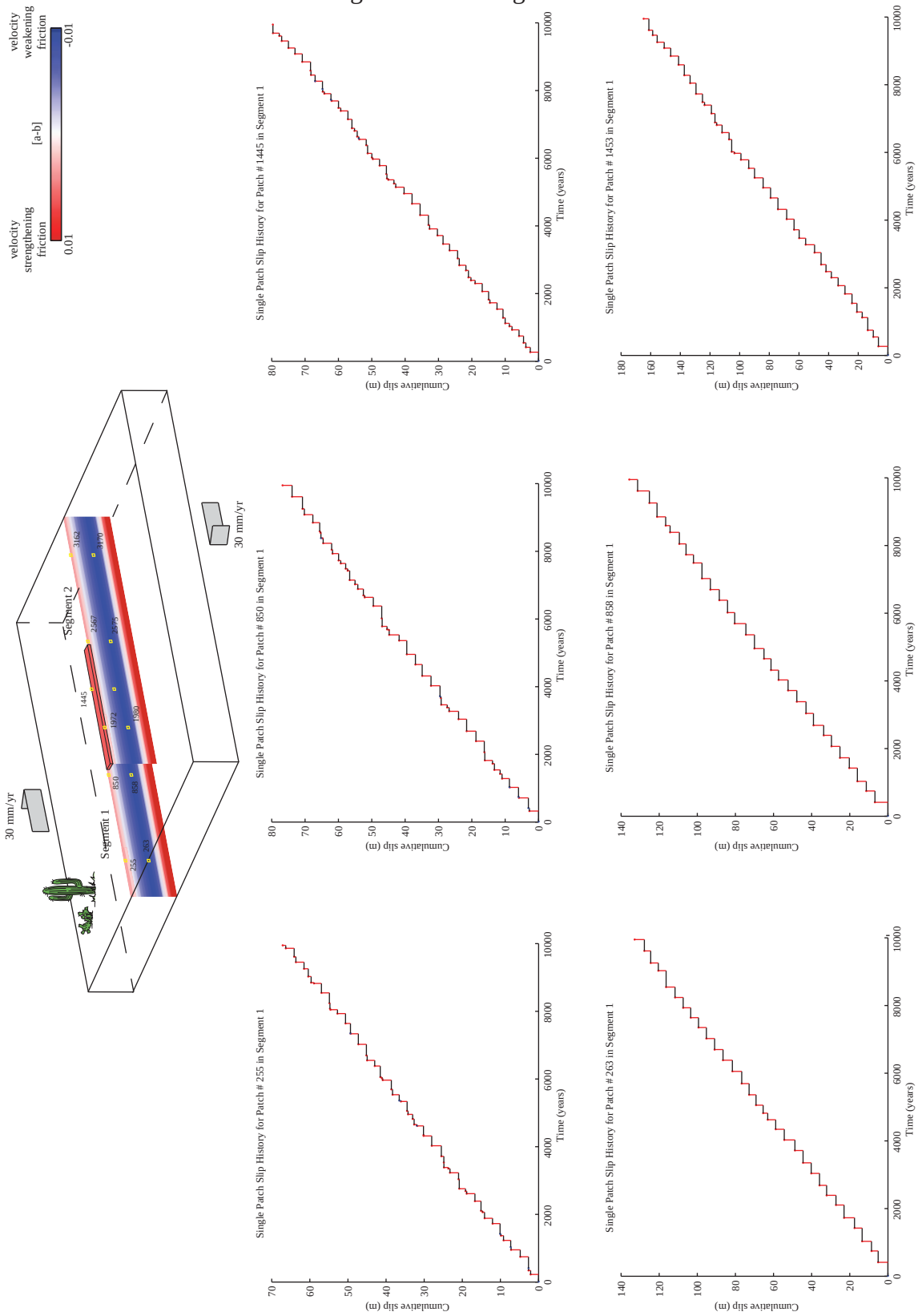

Figure 4.14A - Segment 2

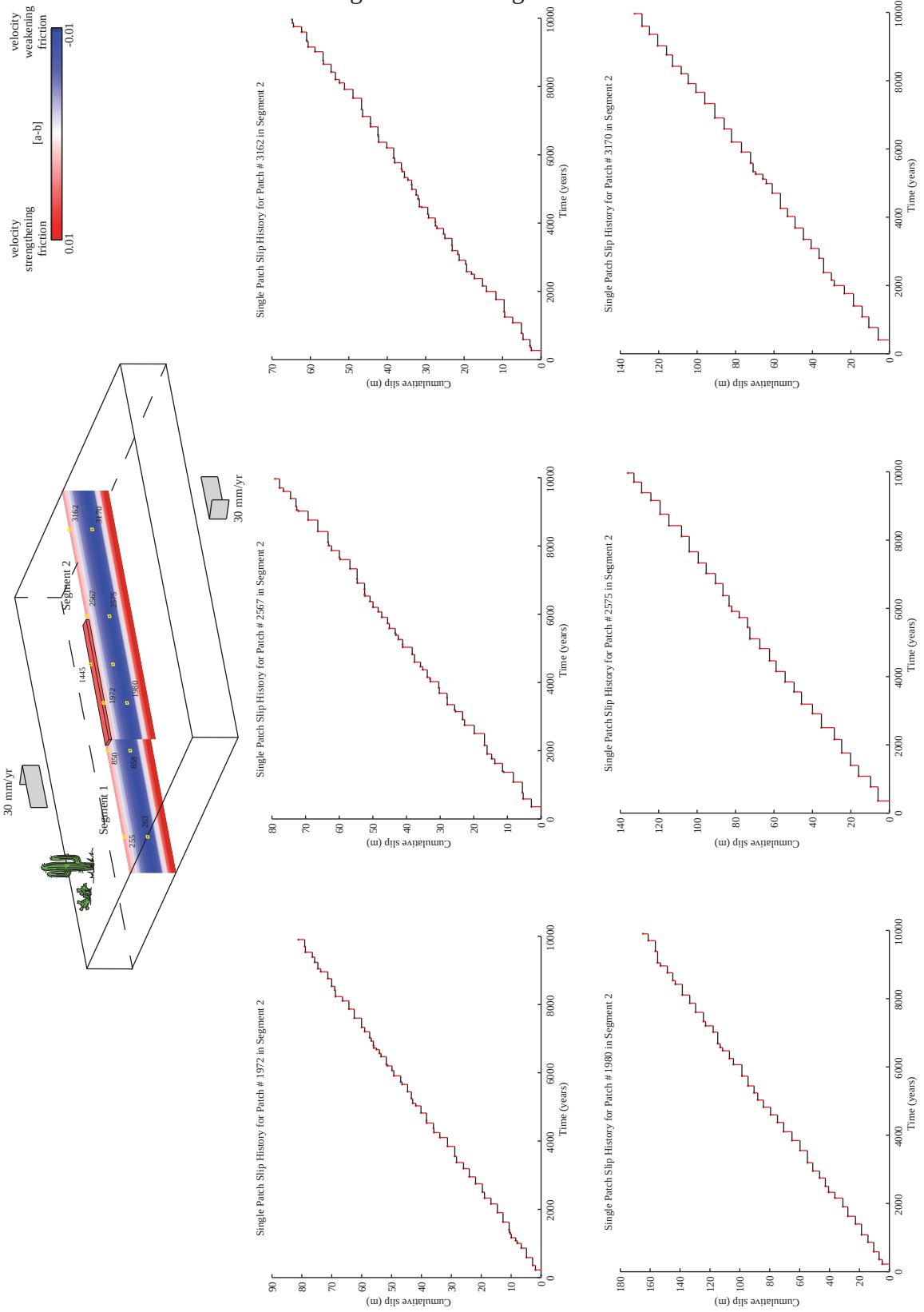

Figure 4.14B

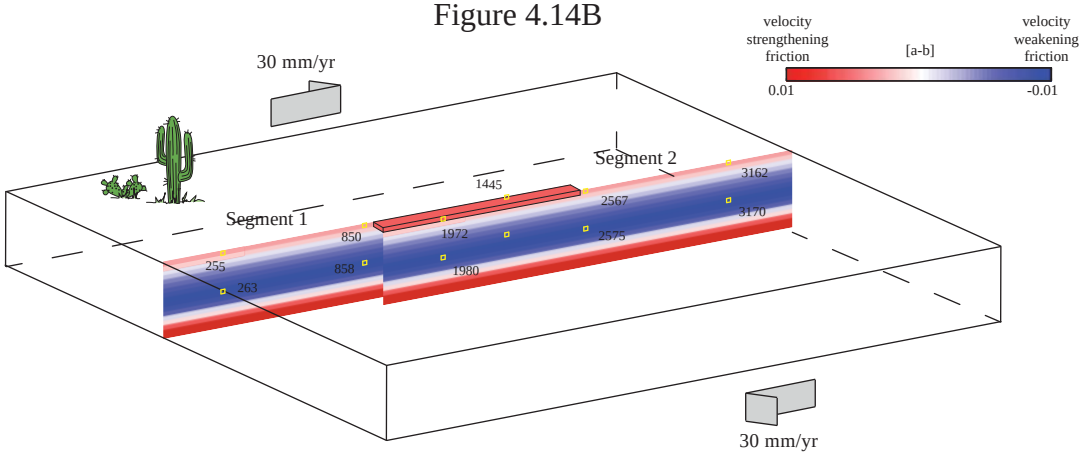

Segment 1 Segment 2

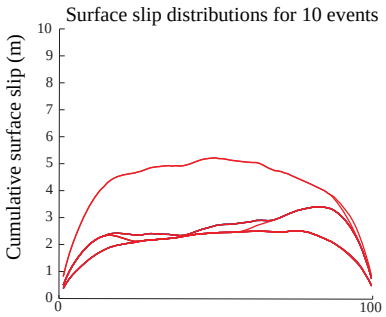

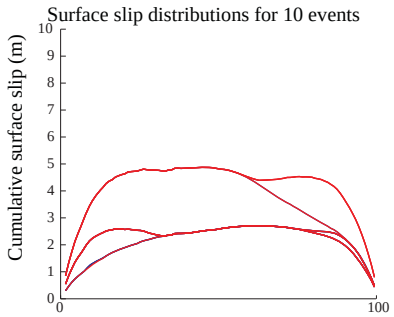

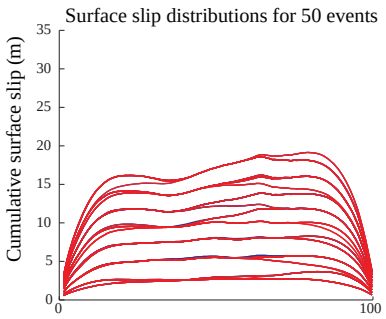

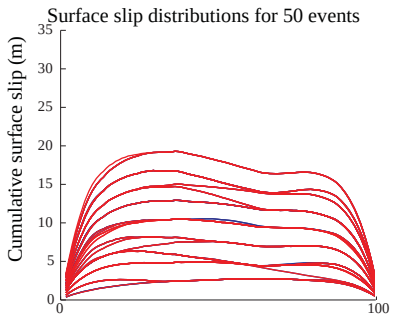

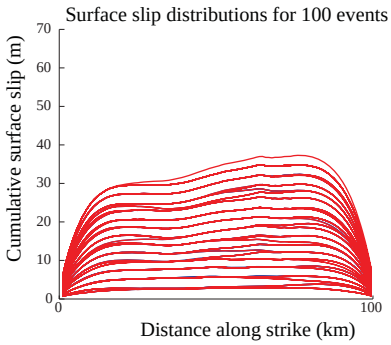

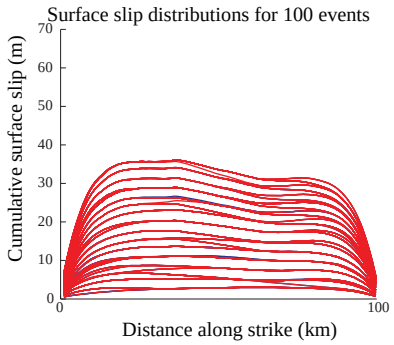

Figure 4.15A - Segment 1

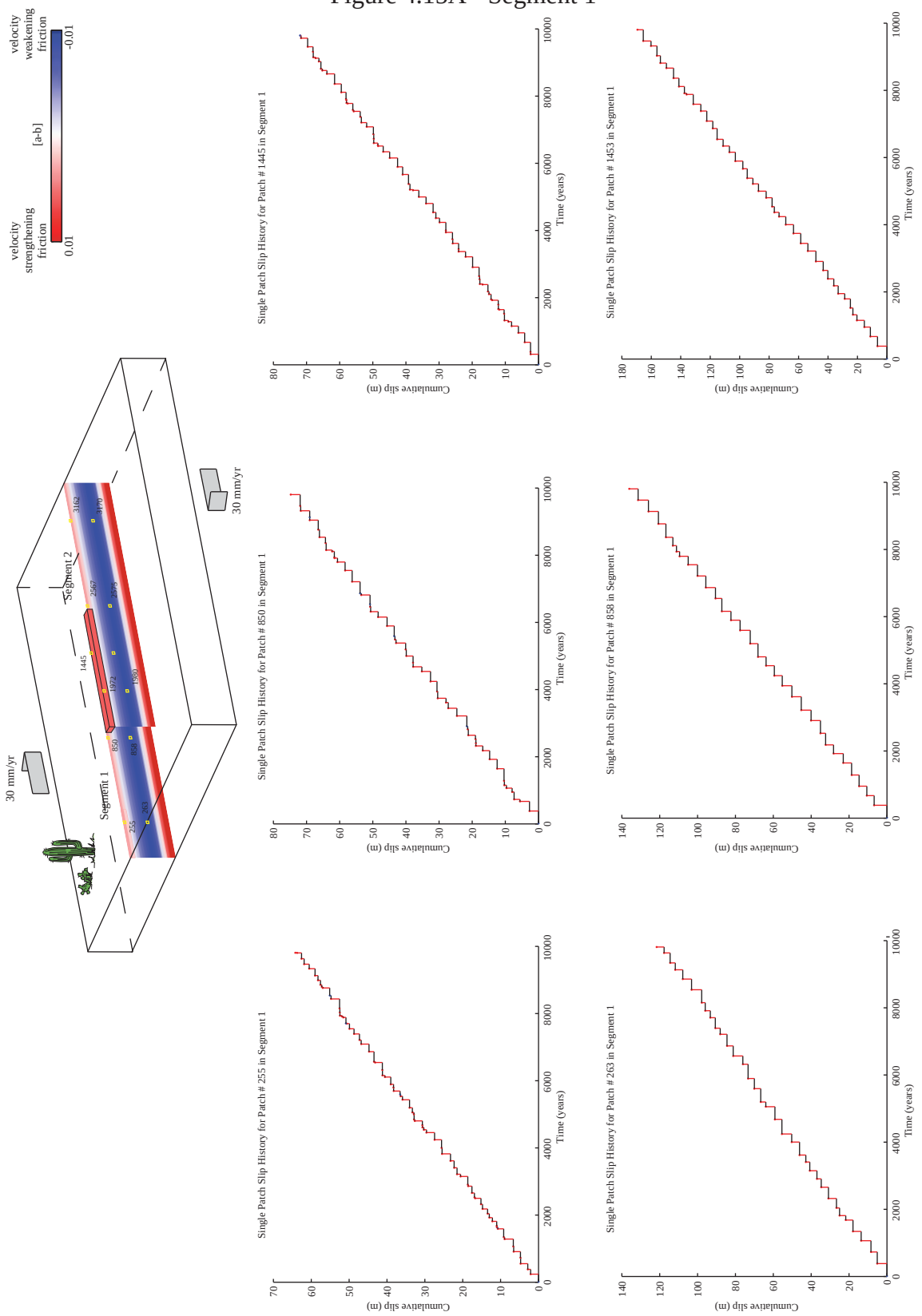

Figure 4.15A - Segment 2

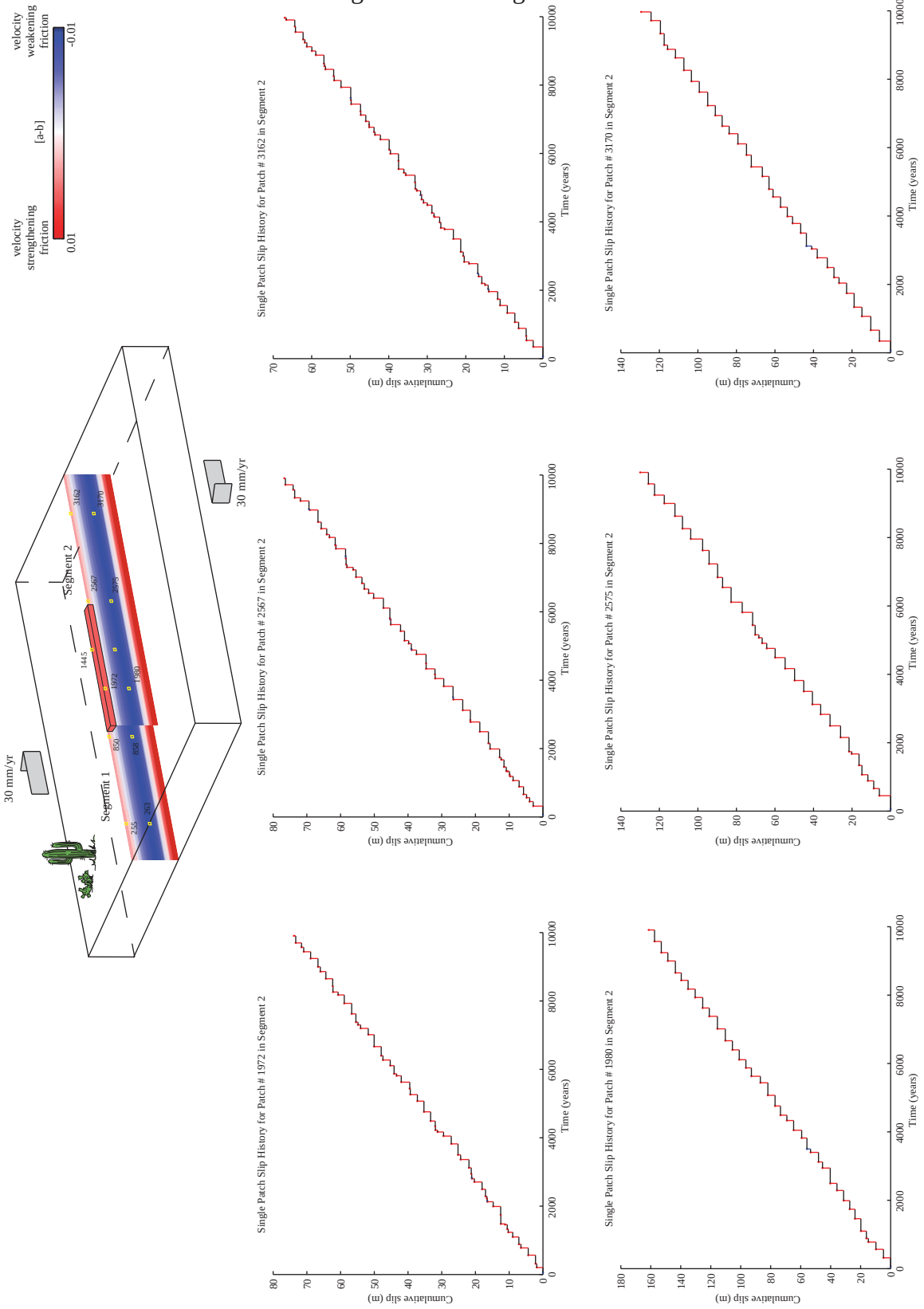

Figure 4.15B

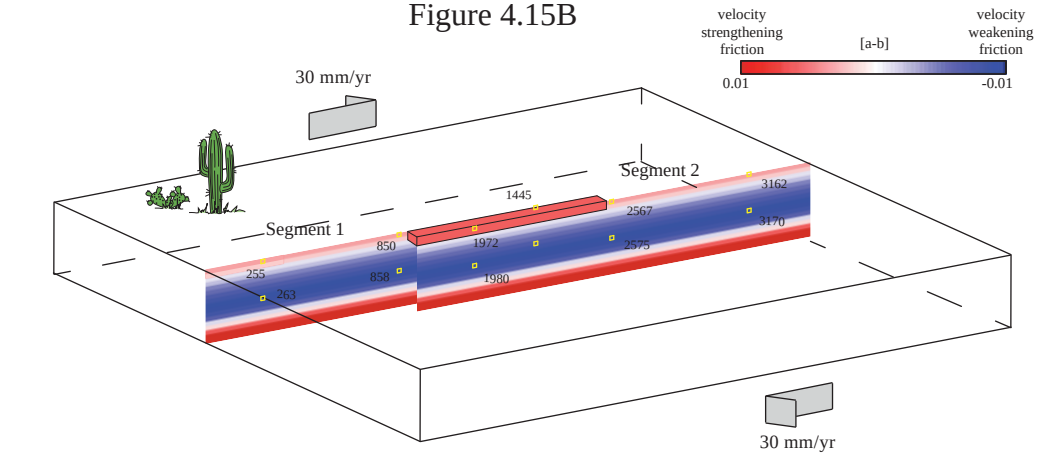

Segment 1 Segment 2

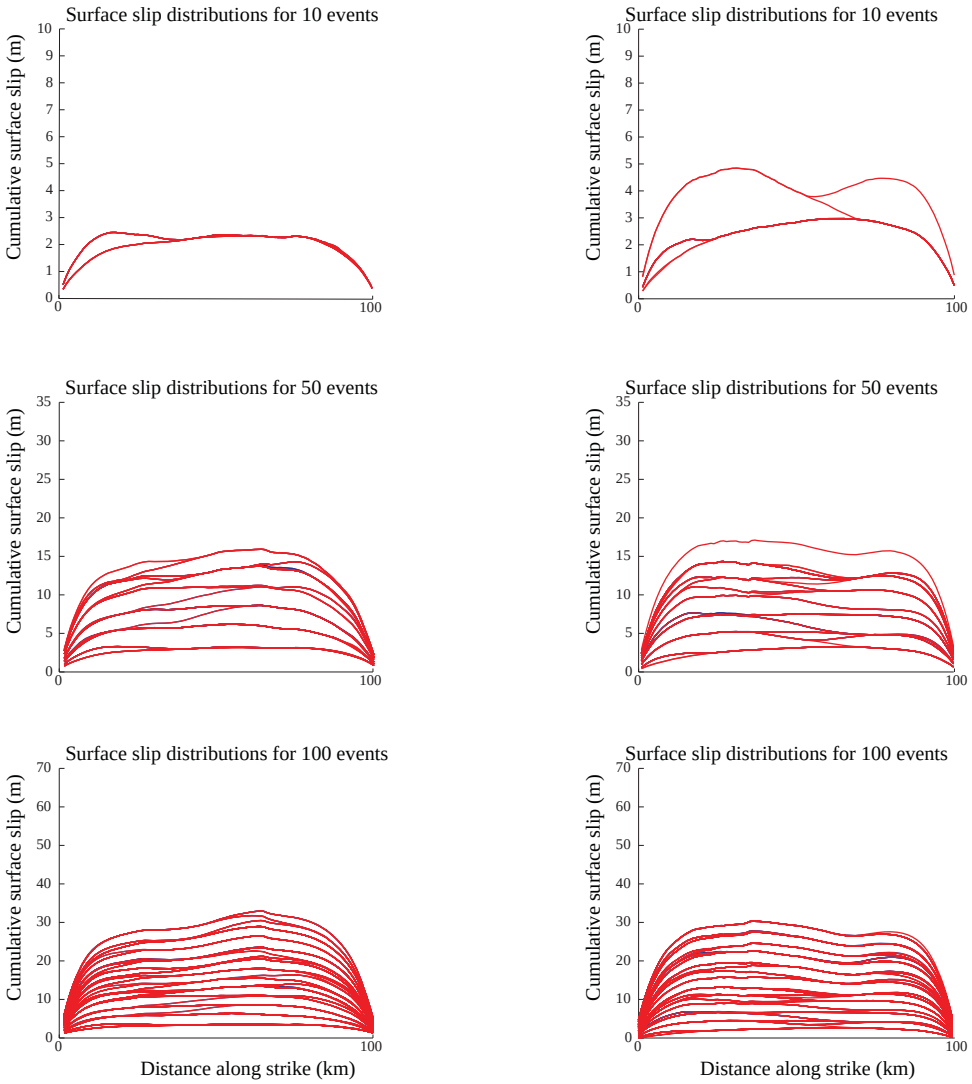

Figure 4.16A - Segment 1

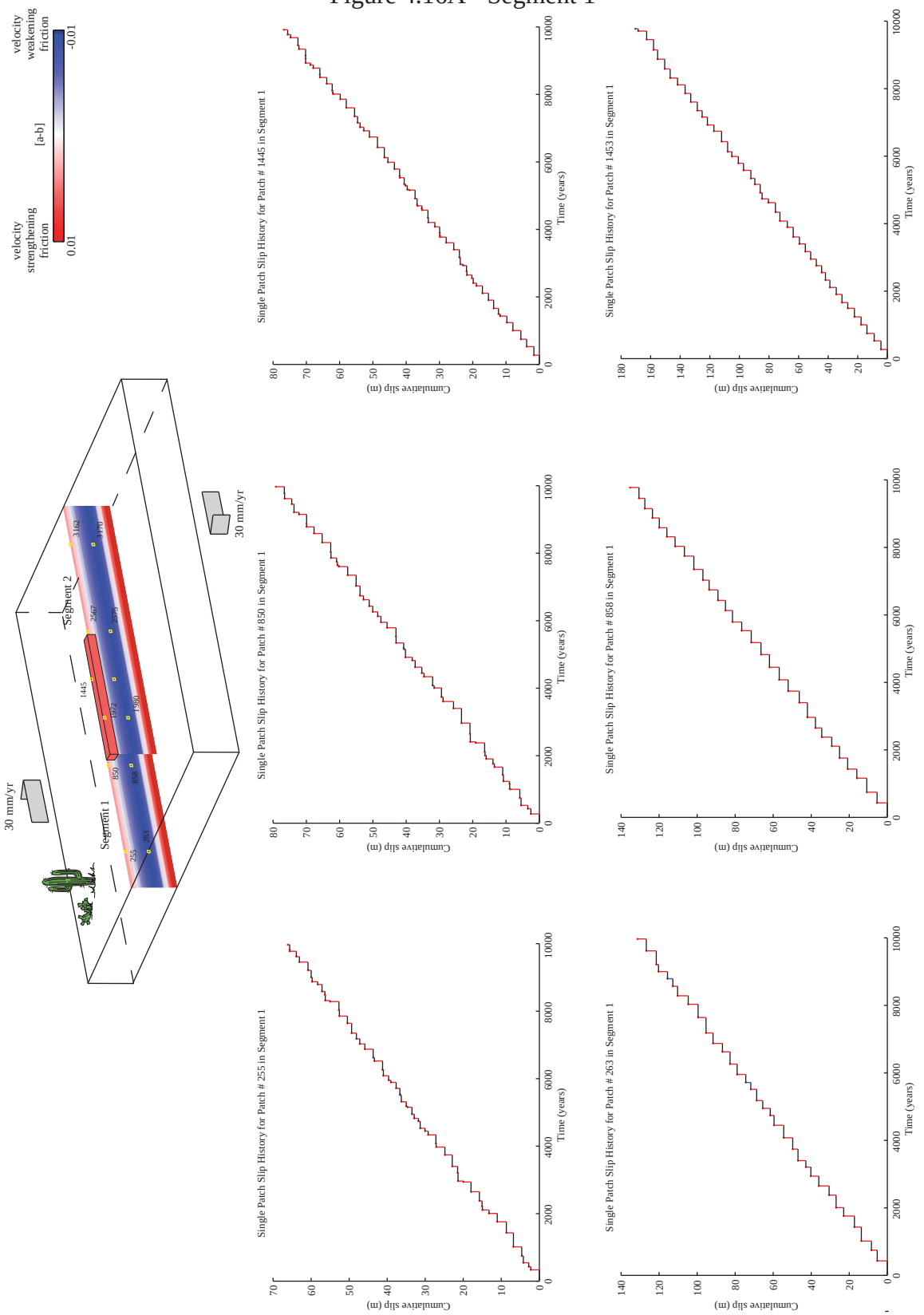

Figure 4.16A - Segment 2

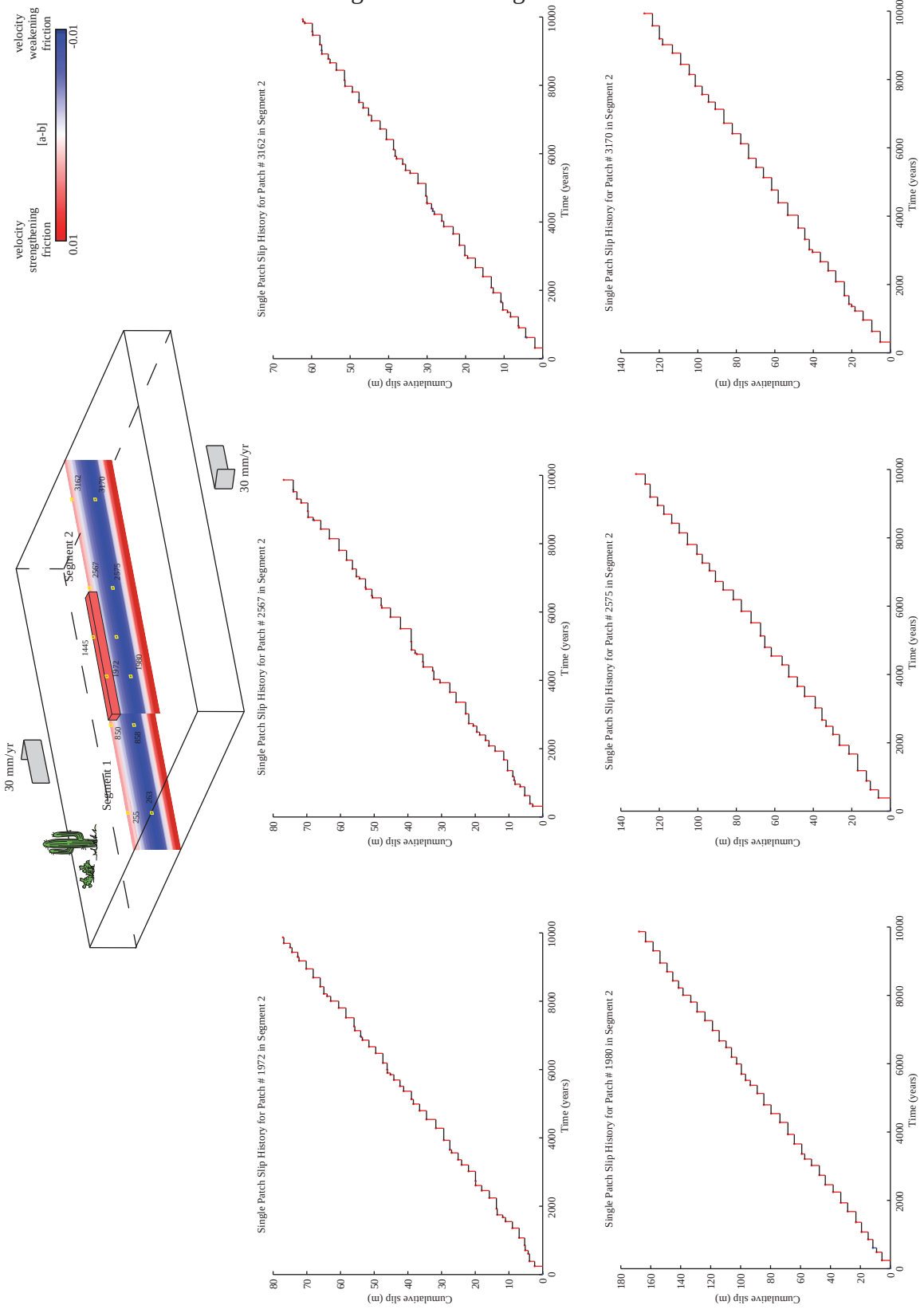

Figure 4.16B

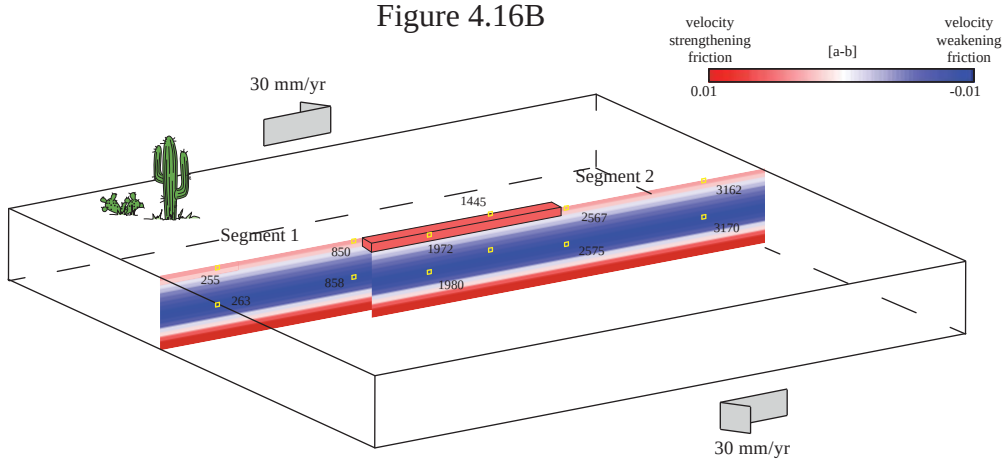

Segment 1 Segment 2

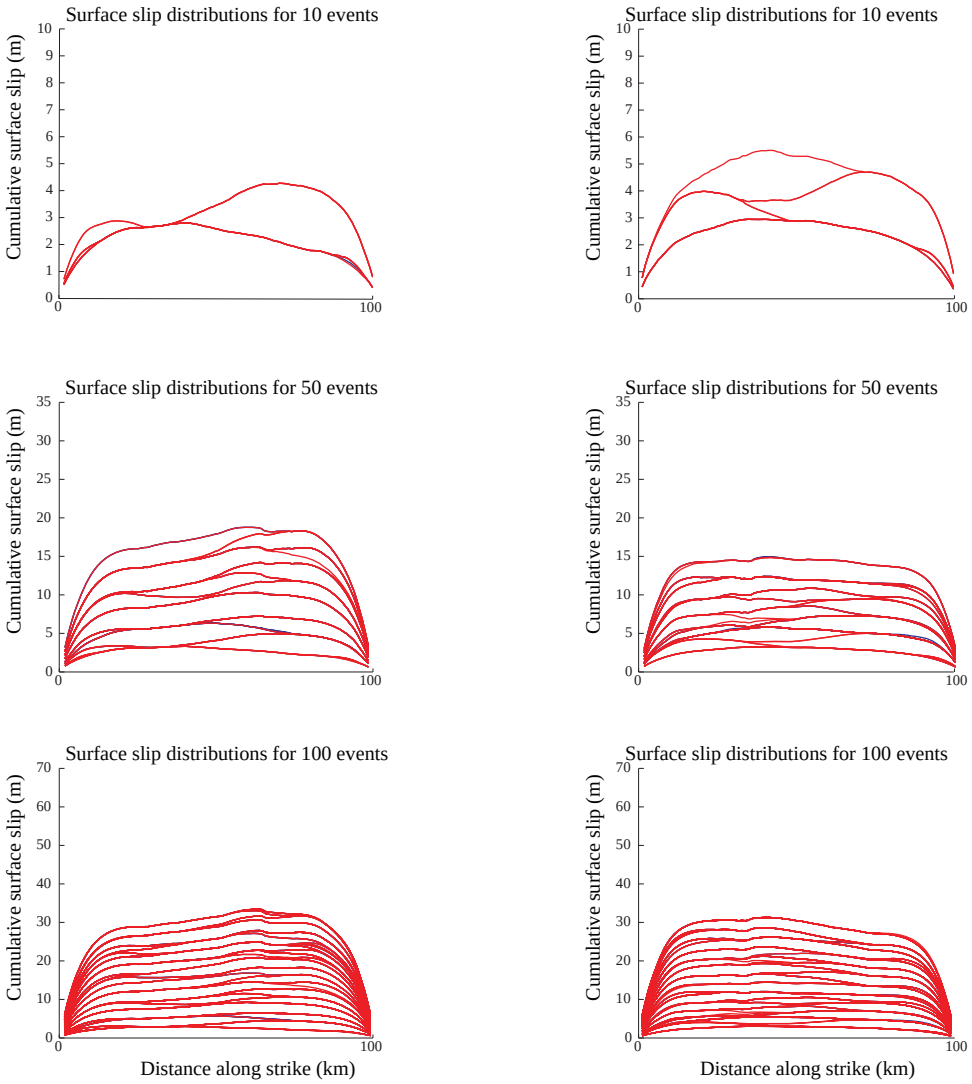

Figure 4.17A

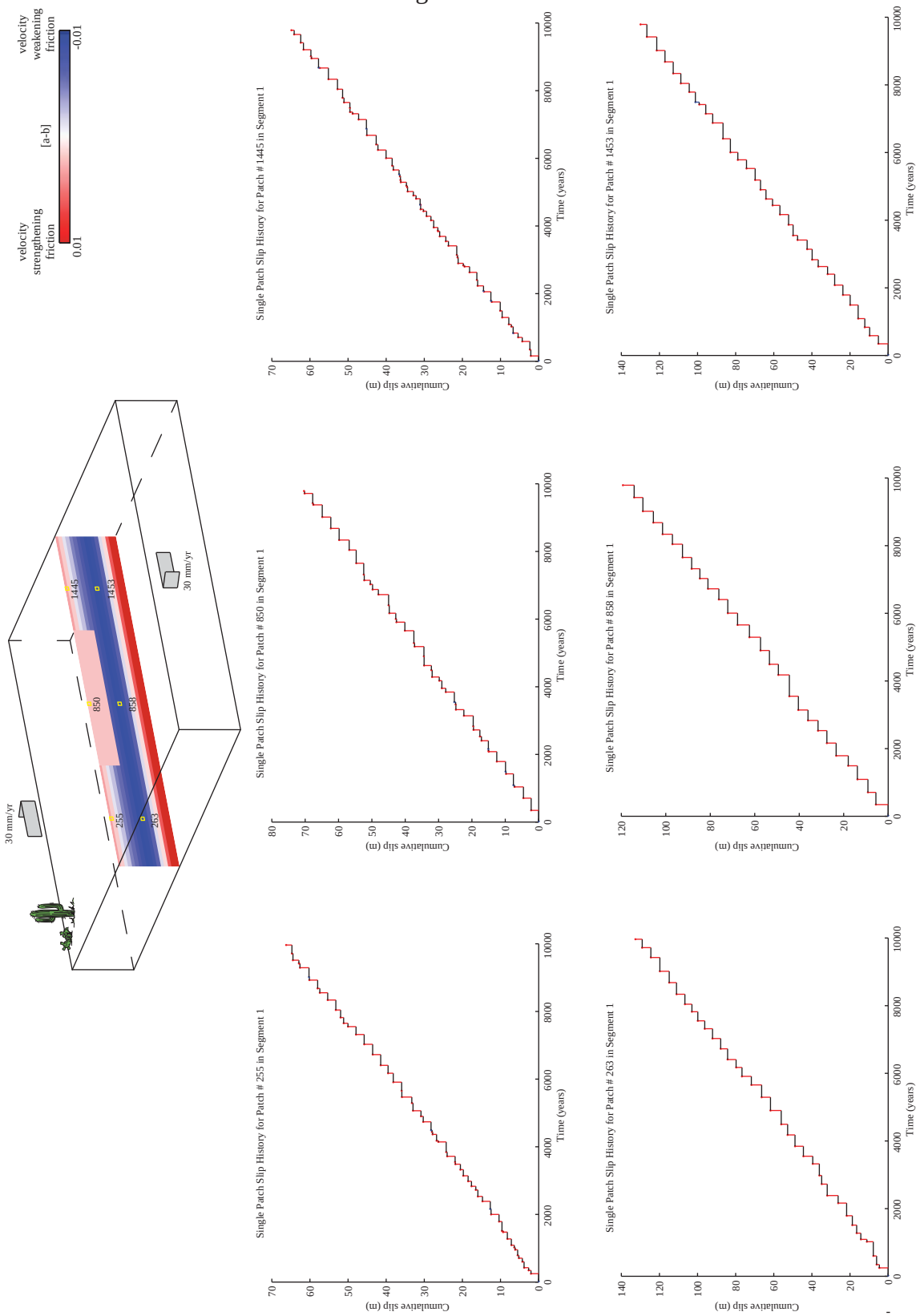
velocity weakening friction
[a-b]
-0.01
0.01
velocity strengthening friction
30 mm/yr
30 mm/yr
1445
1453
850
858
255
263
Single Patch Slip History for Patch # 1445 in Segment 1
Single Patch Slip History for Patch # 1453 in Segment 1
Single Patch Slip History for Patch # 850 in Segment 1
Single Patch Slip History for Patch # 858 in Segment 1
Single Patch Slip History for Patch # 255 in Segment 1
Single Patch Slip History for Patch # 263 in Segment 1
Cumulative Slip (m)
Time (years)

Figure 4.17B

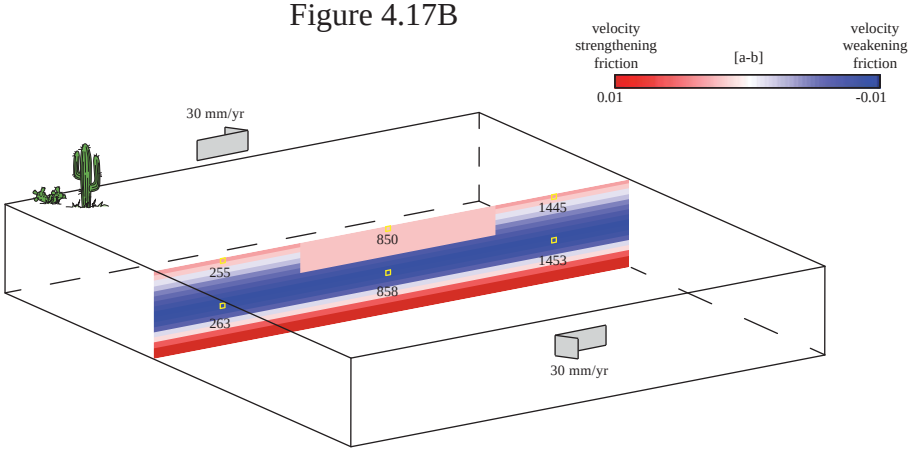
velocity
strengthening
friction
[a-b]
velocity
weakening
friction
0.01
-0.01
30 mm/yr
1445
850
1453
255
858
263
30 mm/yr

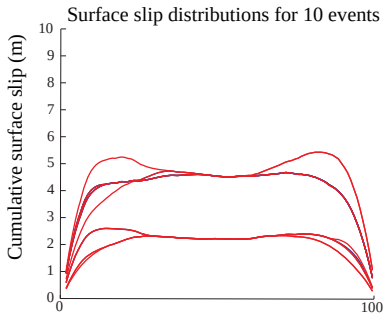
Surface slip distributions for 10 events
Cumulative surface slip (m)
0
1
2
3
4
5
6
7
8
9
10
0
100

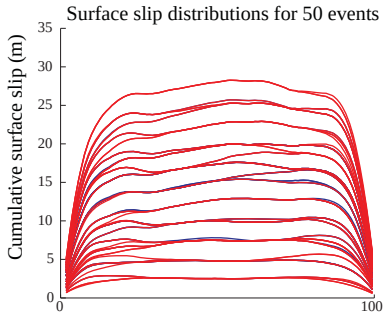
Surface slip distributions for 50 events
Cumulative surface slip (m)
0
5
10
15
20
25
30
35
0
100

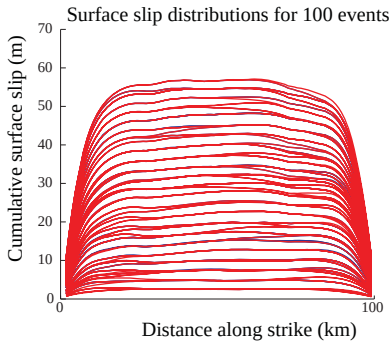
Surface slip distributions for 100 events
Cumulative surface slip (m)
0
10
20
30
40
50
60
70
0
100
Distance along strike (km)

Figure 4.18A

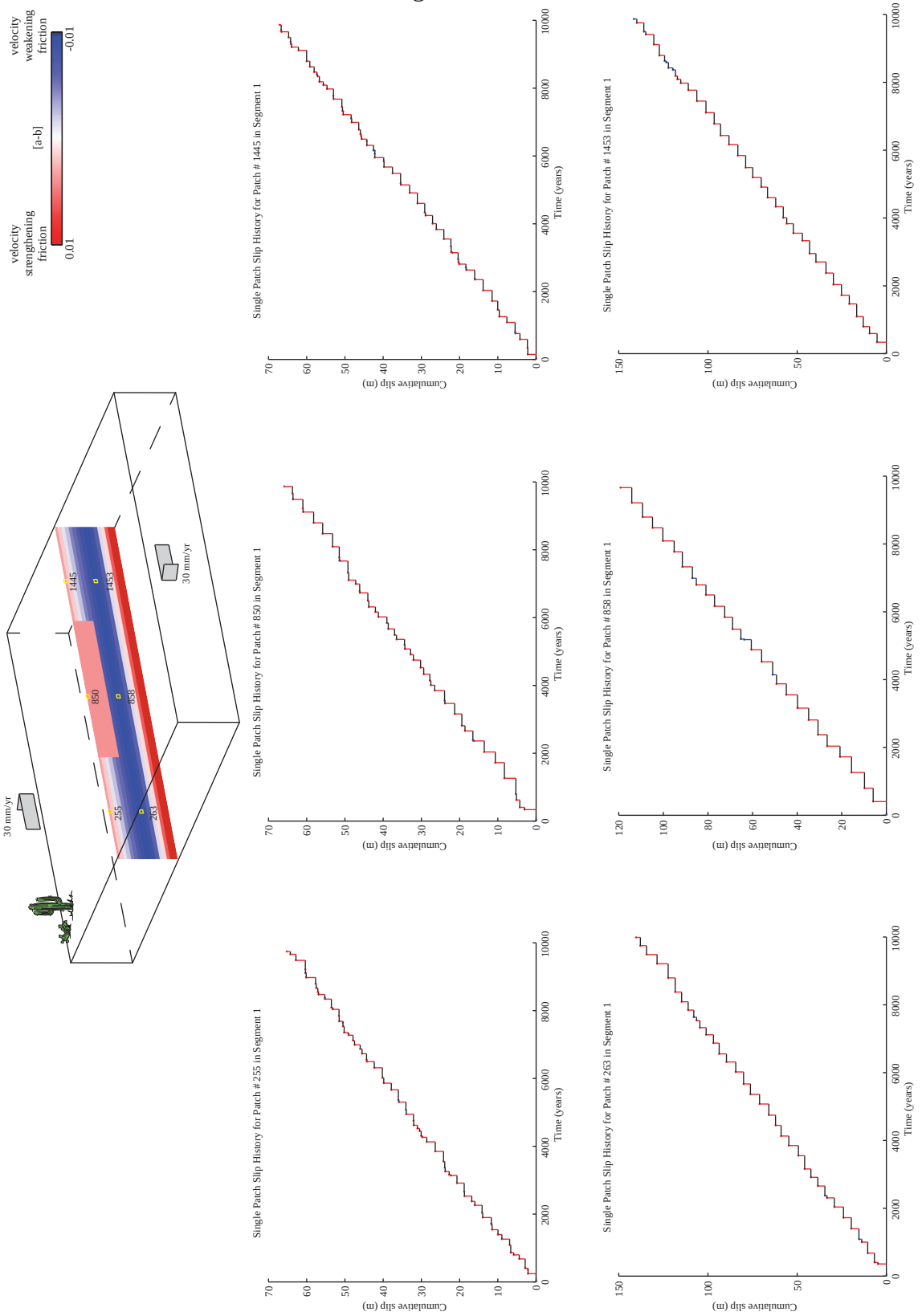
velocity weakening friction
[a-b]
velocity strengthening friction
-0.01
0.01
30 mm/yr
30 mm/yr
1445
1453
850
858
255
263
Single Patch Slip History for Patch # 1445 in Segment 1
Single Patch Slip History for Patch # 1453 in Segment 1
Single Patch Slip History for Patch # 850 in Segment 1
Single Patch Slip History for Patch # 858 in Segment 1
Single Patch Slip History for Patch # 255 in Segment 1
Single Patch Slip History for Patch # 263 in Segment 1
Cumulative Slip (m)
Time (years)

Figure 4.18B

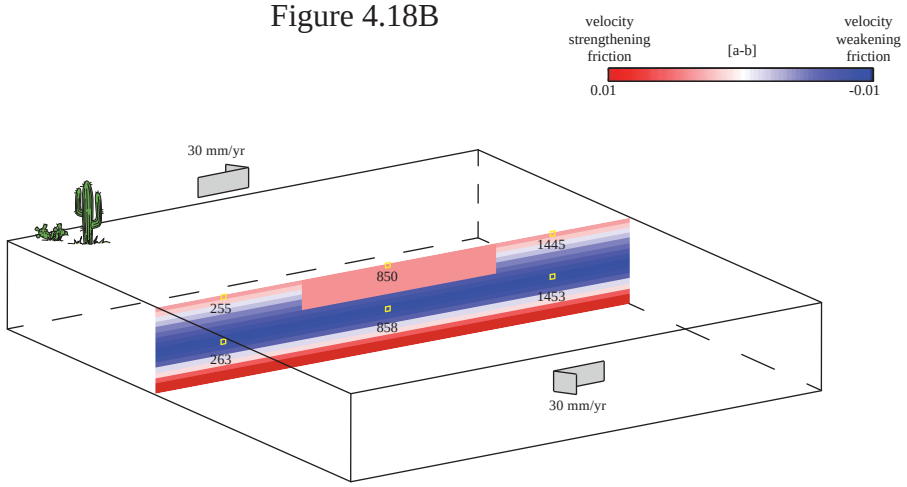
velocity strengthening friction
[a-b]
velocity weakening friction
0.01
-0.01
30 mm/yr
1445
850
1453
255
858
263
30 mm/yr

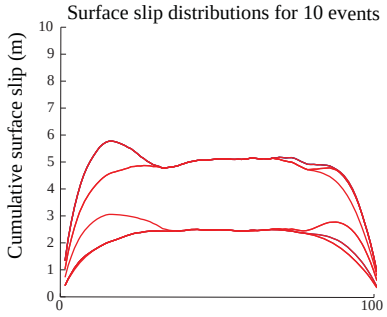
Surface slip distributions for 10 events
Cumulative surface slip (m)
0
1
2
3
4
5
6
7
8
9
10
0
100

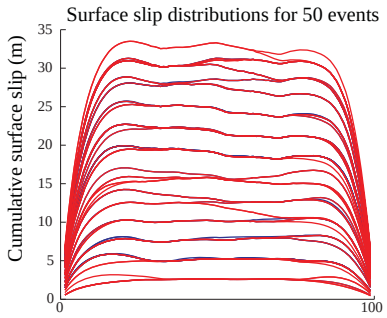
Surface slip distributions for 50 events
Cumulative surface slip (m)
0
5
10
15
20
25
30
35
0
100

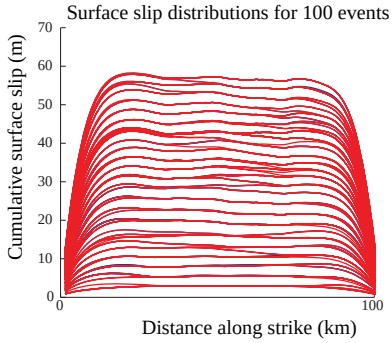
Surface slip distributions for 100 events
Cumulative surface slip (m)
0
10
20
30
40
50
60
70
0
100
Distance along strike (km)

Figure 4.19A

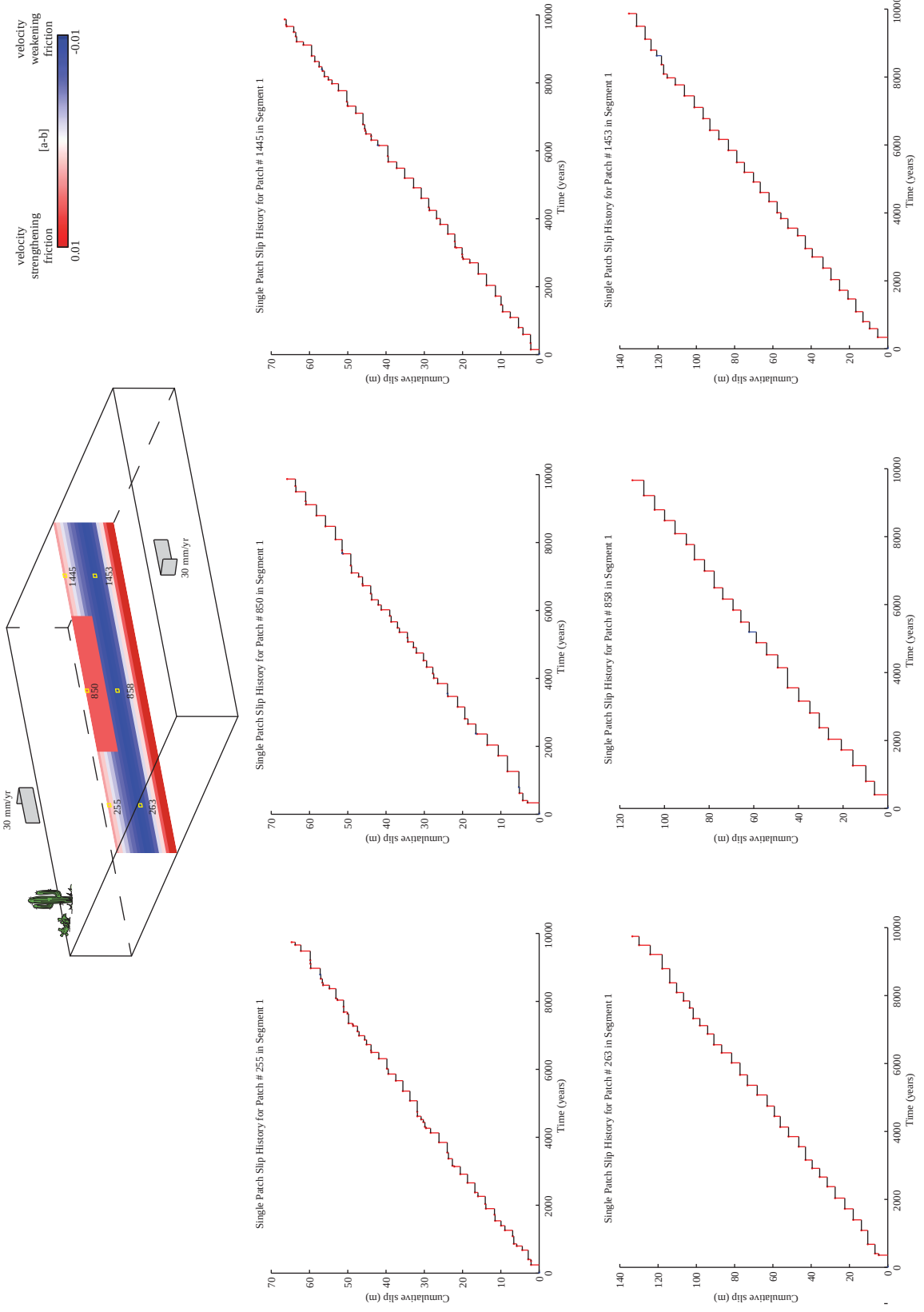
velocity weakening friction
[a-b]
-0.01
0.01
velocity strengthening friction
30 mm/yr
30 mm/yr
1445
1453
850
858
255
263
Single Patch Slip History for Patch # 1445 in Segment 1
Single Patch Slip History for Patch # 1453 in Segment 1
Single Patch Slip History for Patch # 850 in Segment 1
Single Patch Slip History for Patch # 858 in Segment 1
Single Patch Slip History for Patch # 255 in Segment 1
Single Patch Slip History for Patch # 263 in Segment 1
Cumulative slip (m)
Time (years)

Figure 4.19B

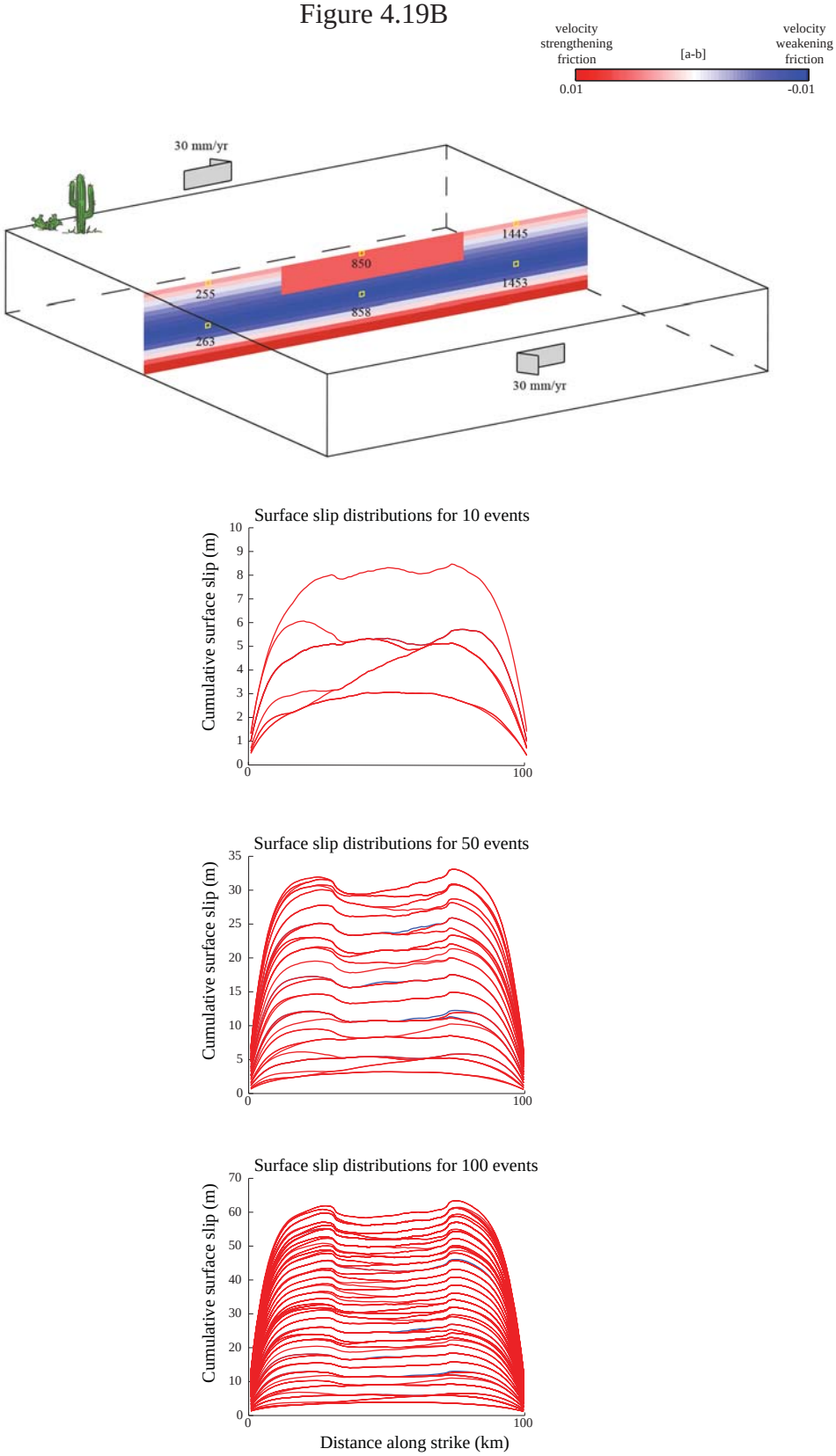
velocity strengthening friction
[a-b]
velocity weakening friction
0.01
-0.01
30 mm/yr
1445
850
1453
255
858
263
30 mm/yr
Surface slip distributions for 10 events
Cumulative surface slip (m)
Surface slip distributions for 50 events
Cumulative surface slip (m)
Surface slip distributions for 100 events
Cumulative surface slip (m)
Distance along strike (km)

Figure 4.20A

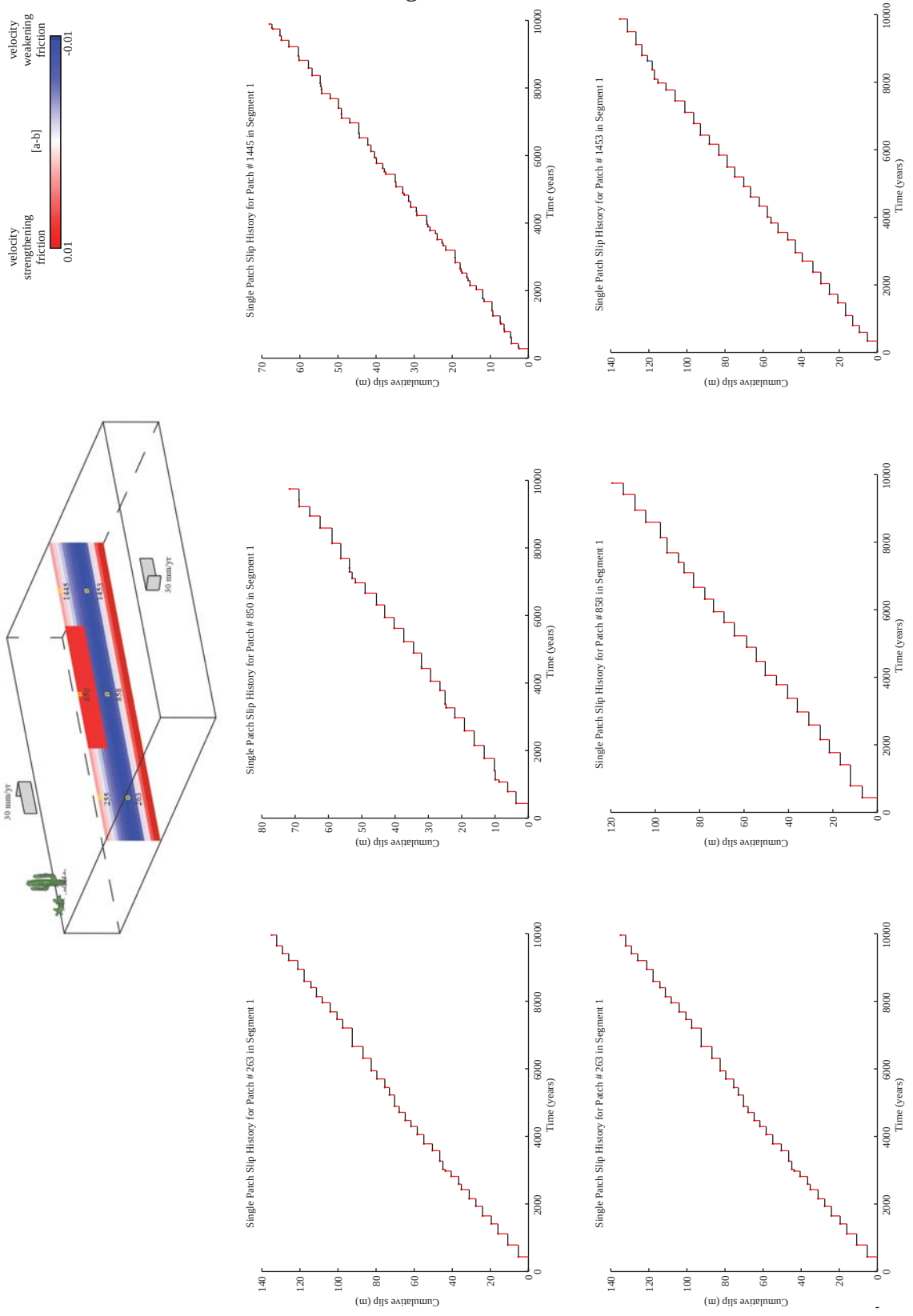
velocity weakening friction
[a-b]
-0.01
0.01
velocity strengthening friction
30 mm/yr
30 mm/yr
1415
1453
858
263
Single Patch Slip History for Patch # 1445 in Segment 1
Single Patch Slip History for Patch # 1453 in Segment 1
Single Patch Slip History for Patch # 850 in Segment 1
Single Patch Slip History for Patch # 858 in Segment 1
Single Patch Slip History for Patch # 263 in Segment 1
Single Patch Slip History for Patch # 263 in Segment 1
Cumulative Slip (m)
Time (years)

Figure 4.20B

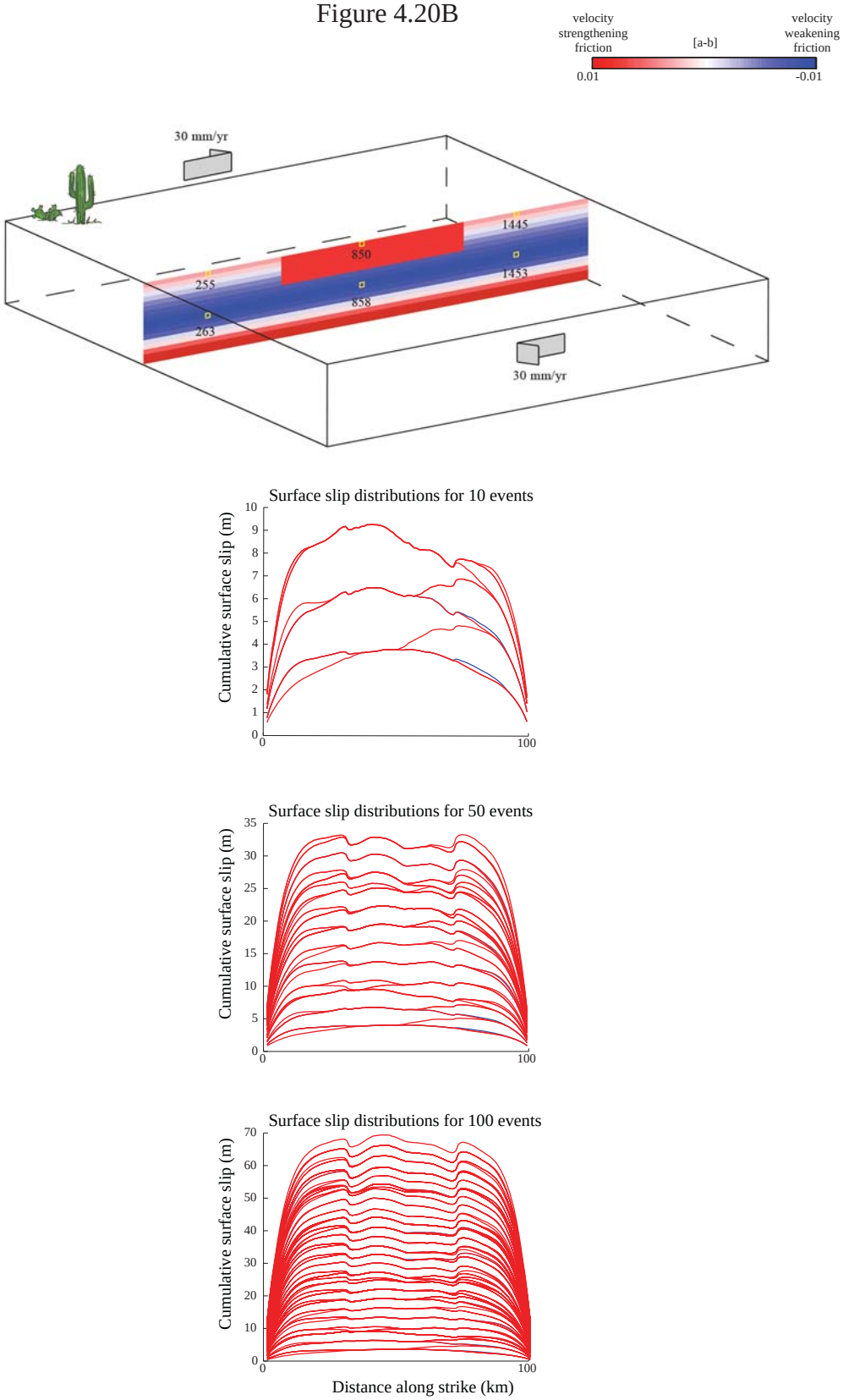
velocity strengthening friction
[a-b]
velocity weakening friction
0.01
-0.01
30 mm/yr
1445
850
1453
255
858
263
30 mm/yr
Surface slip distributions for 10 events
Cumulative surface slip (m)
Surface slip distributions for 50 events
Cumulative surface slip (m)
Surface slip distributions for 100 events
Cumulative surface slip (m)
Distance along strike (km)

Figure 4.21A

20 km underlap, 7 km stepover

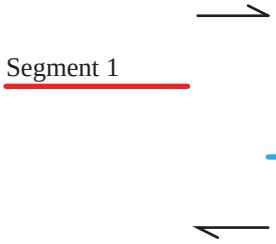

Smooth faults

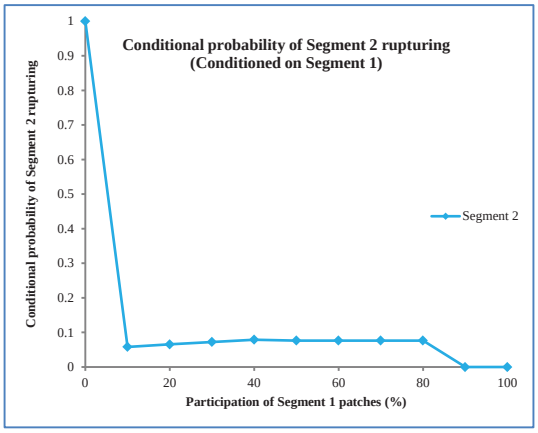

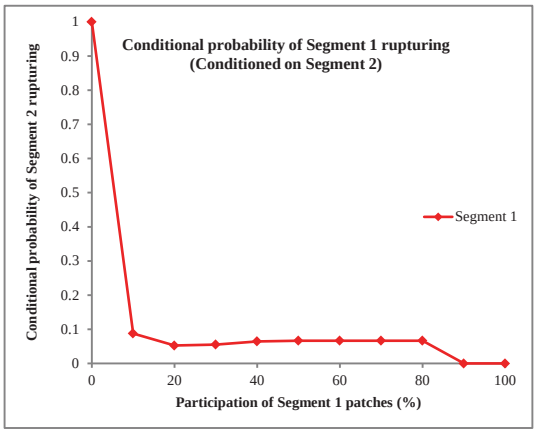

Rough faults

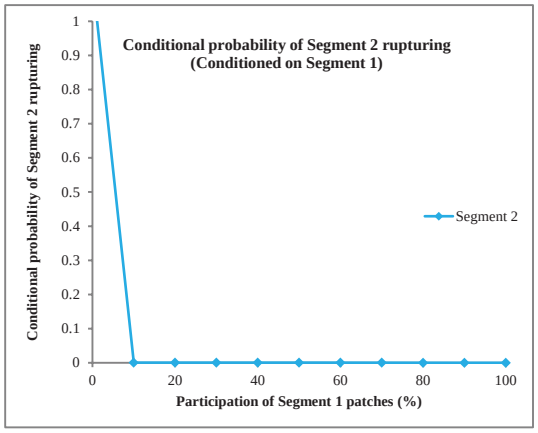

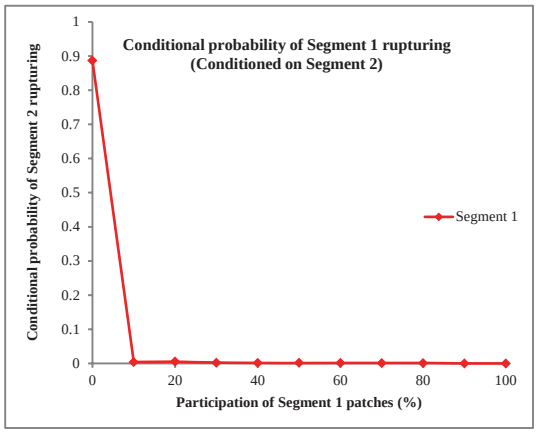

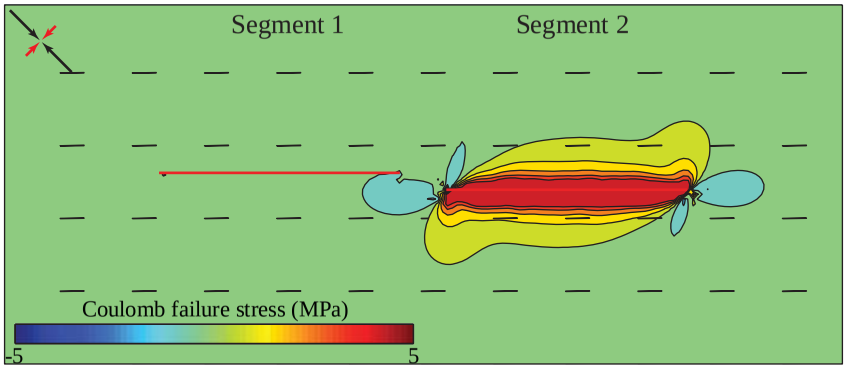

Event ID 3869 (M 7.48)

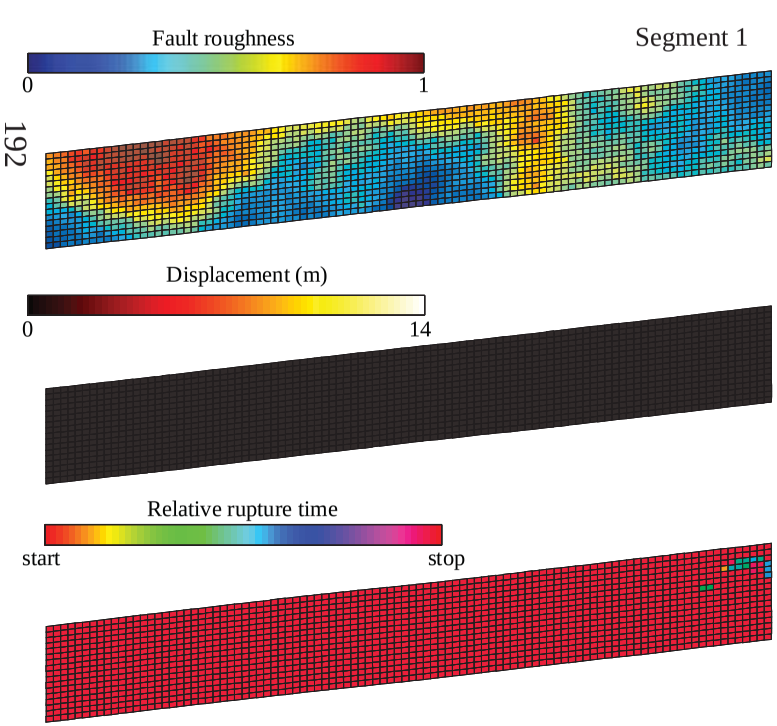

Segment 1

Segment 2

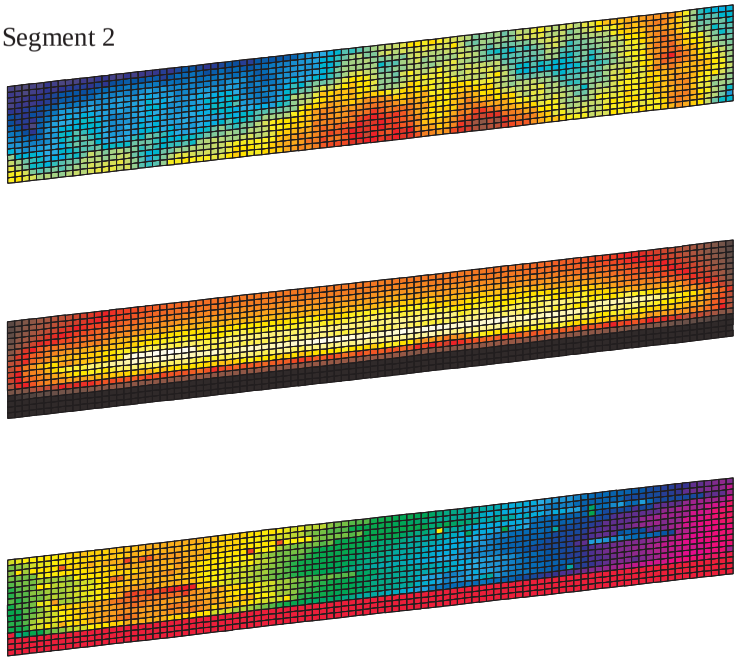

Figure 4.21B

Figure 4.21C

50 km overlap, 7 km stepover

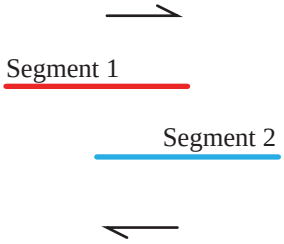

Smooth faults

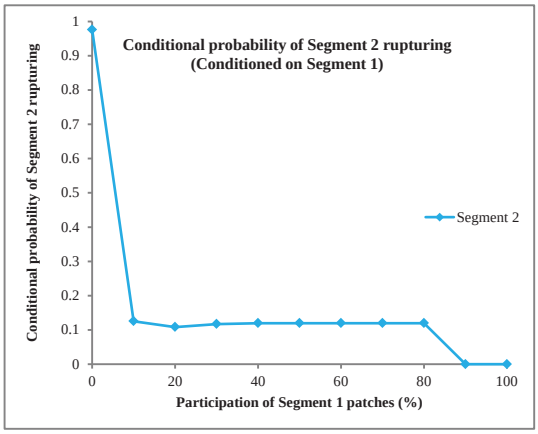

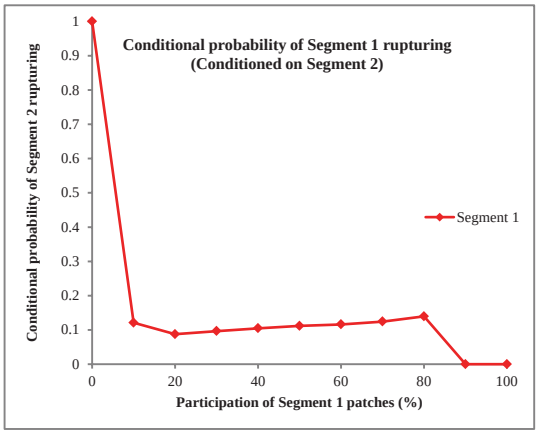

Rough faults

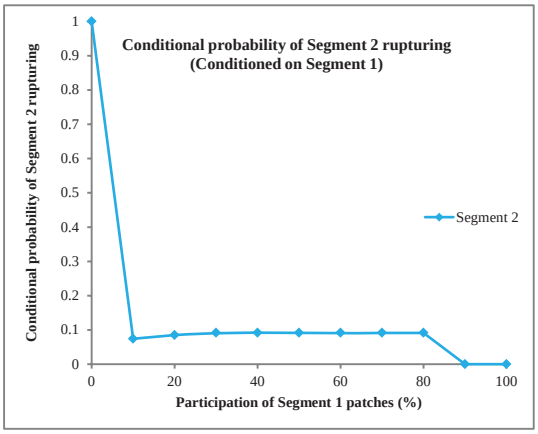

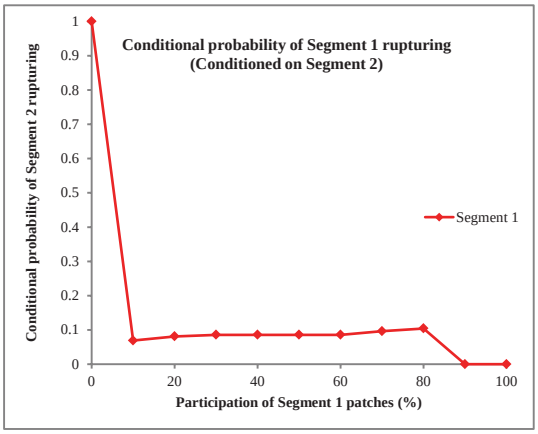

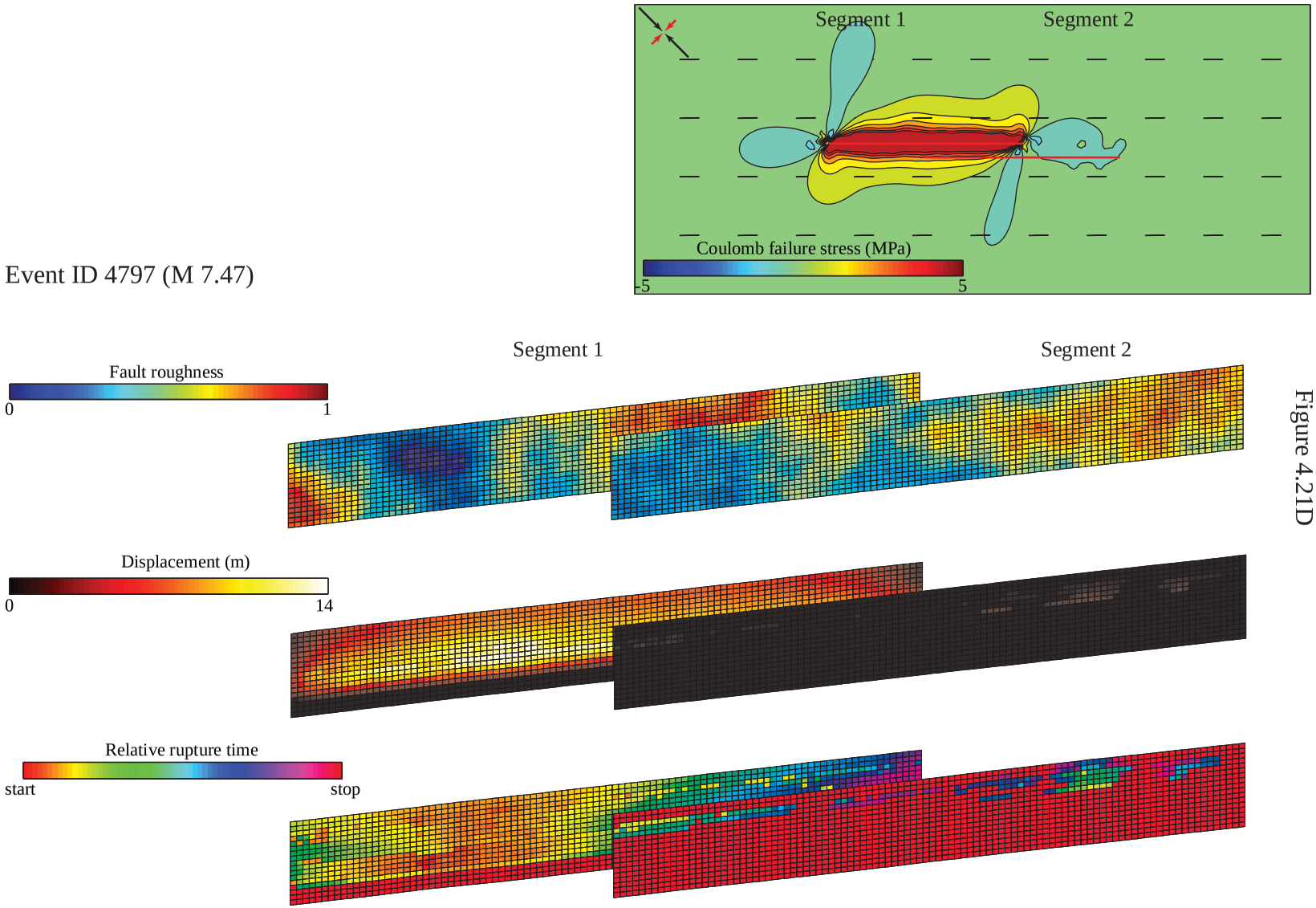
Segment 1
Segment 2
Coulomb failure stress (MPa)
-5
5
Event ID 4797 (M 7.47)
Segment 1
Segment 2
Fault roughness
0
1
Displacement (m)
0
14
Relative rupture time
start
stop

Figure 4.21D

Figure 4.21E

20 km underlap, 5 km stepover

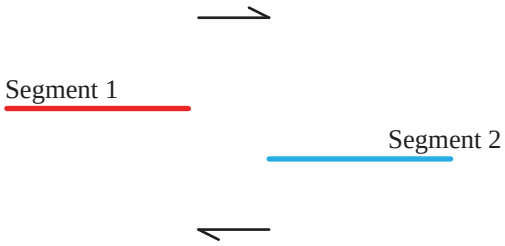

Smooth faults

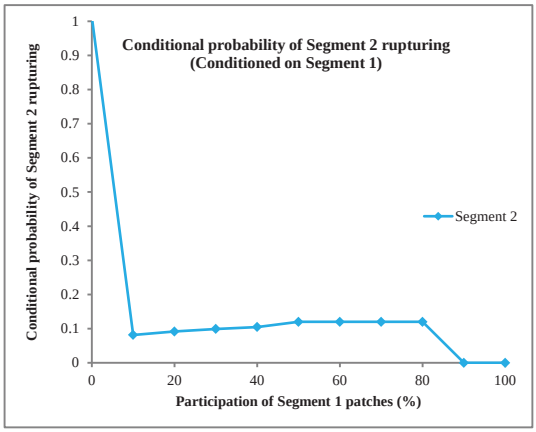

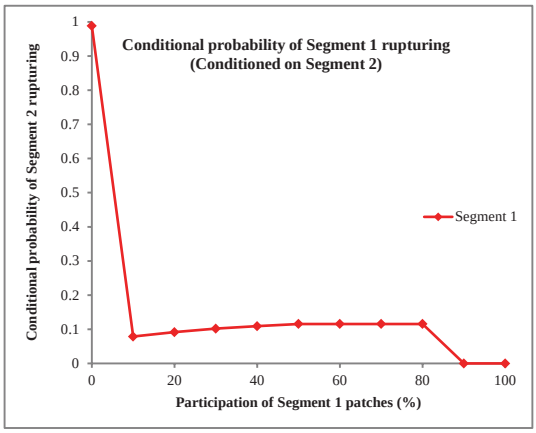

Rough faults

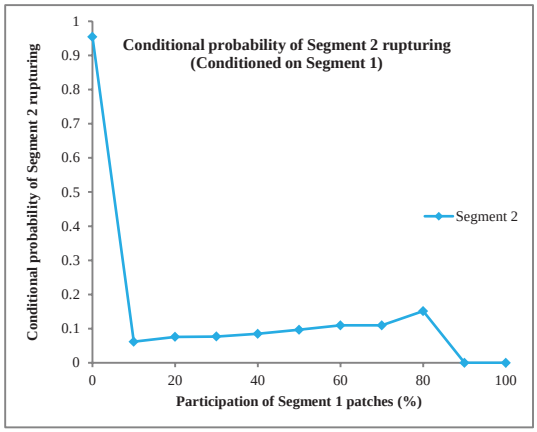

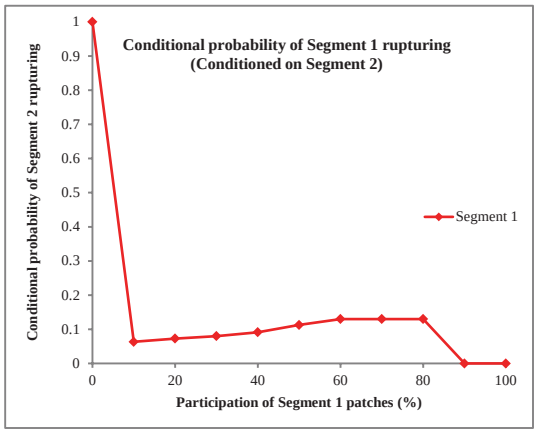

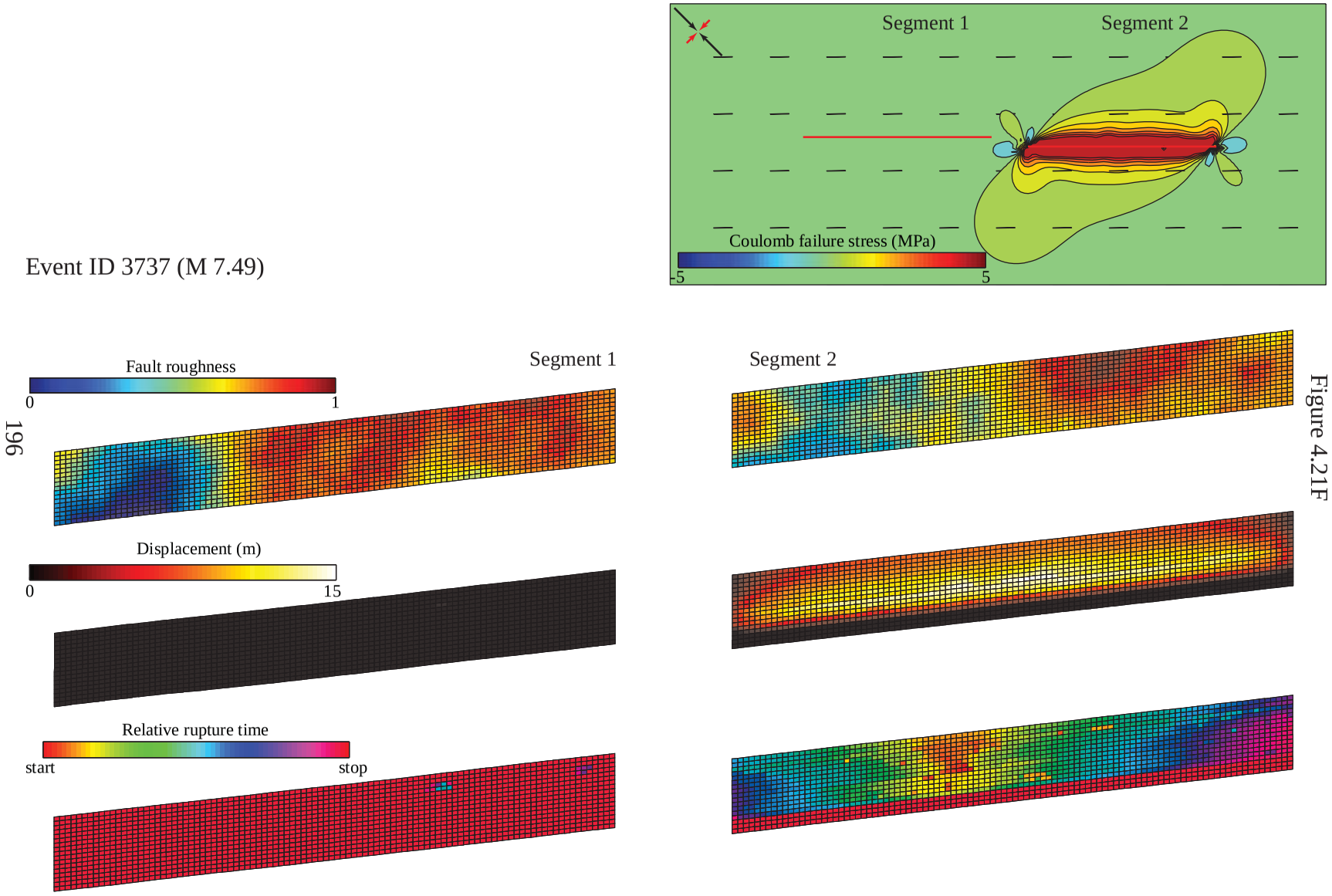
Segment 1
Segment 2
Coulomb failure stress (MPa)
-5
5
Event ID 3737 (M 7.49)
Fault roughness
0
1
Segment 1
Segment 2
Displacement (m)
0
15
Relative rupture time
start
stop

Figure 4.21F

Figure 4.21G

50 km overlap, 5 km stepover

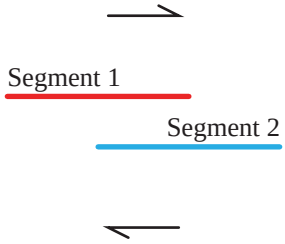

Smooth faults

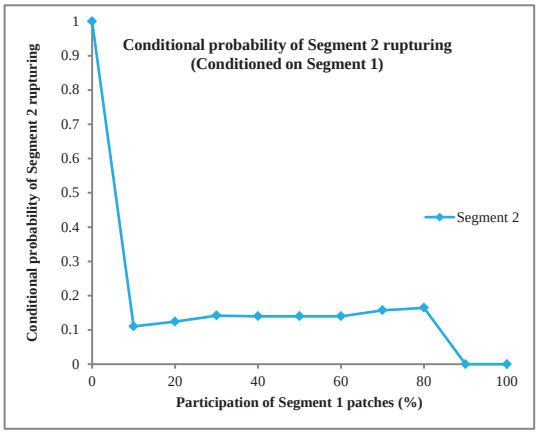

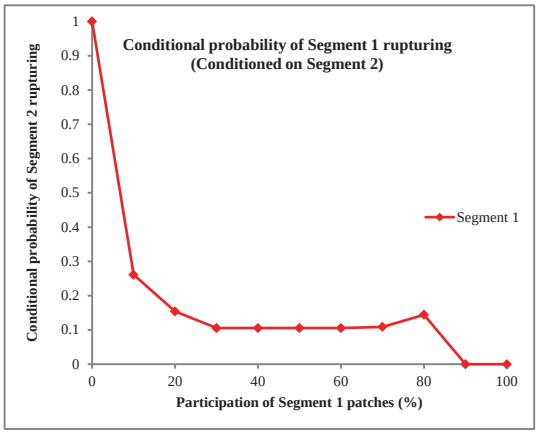

Rough faults

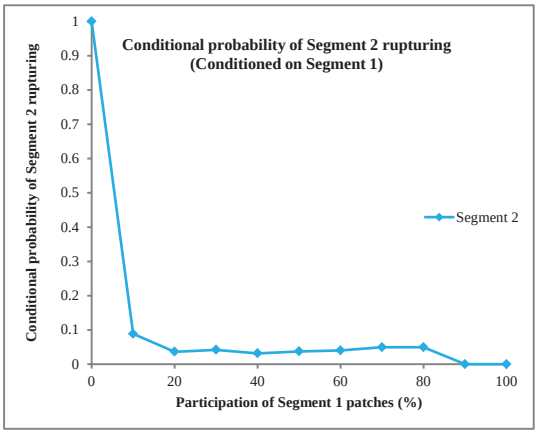

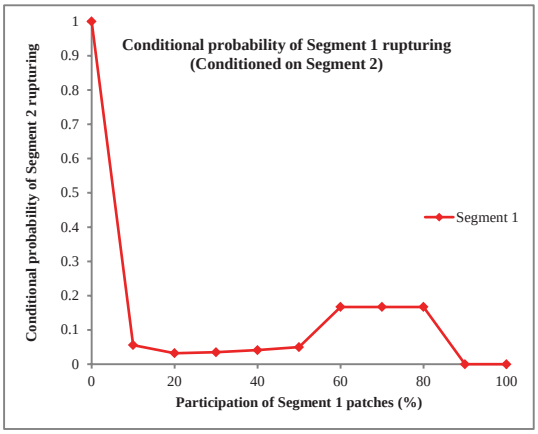

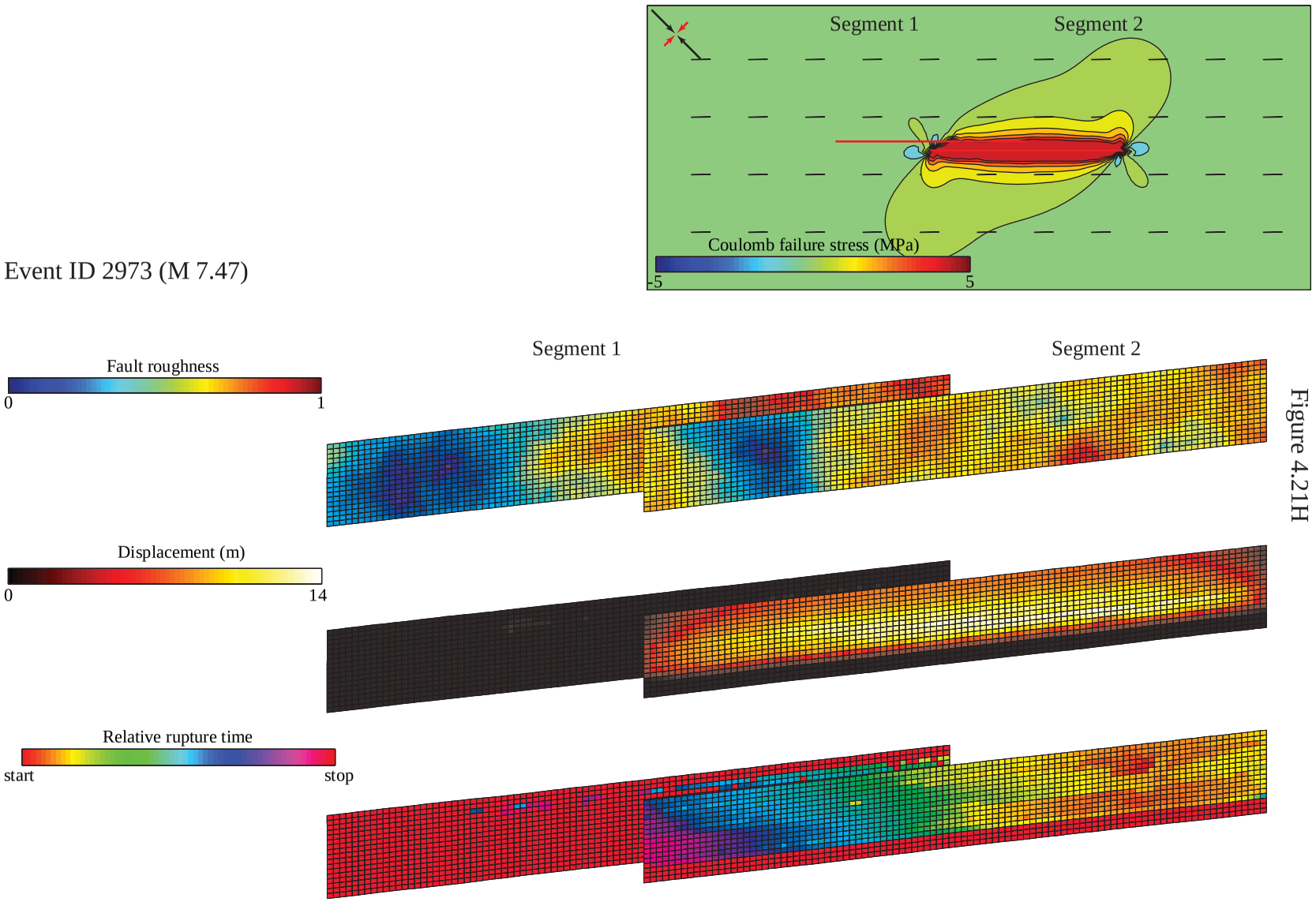
Segment 1
Segment 2
Coulomb failure stress (MPa)
-5
5
Event ID 2973 (M 7.47)
Segment 1
Segment 2
Fault roughness
0
1
Displacement (m)
0
14
Relative rupture time
start
stop

Figure 4.21H

Figure 4.21I

20 km underlap, 2 km stepover

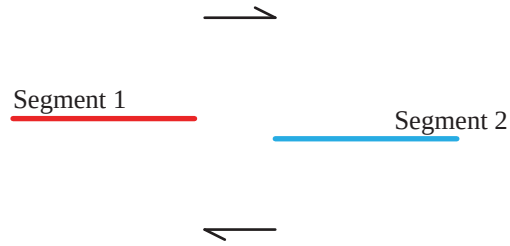

Smooth faults

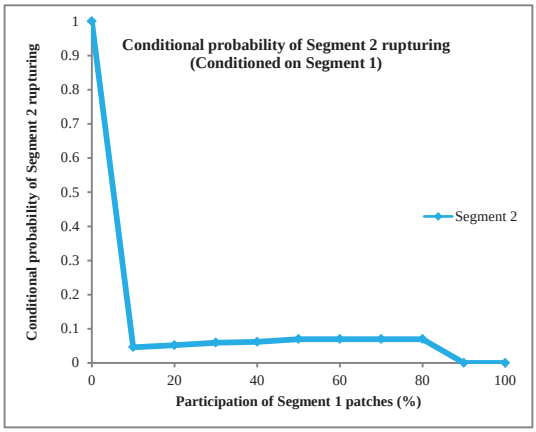

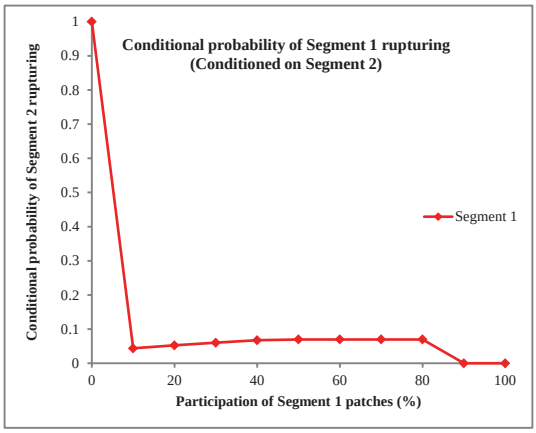

Rough faults

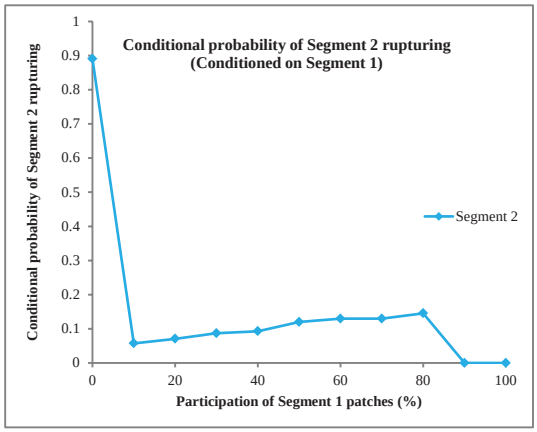

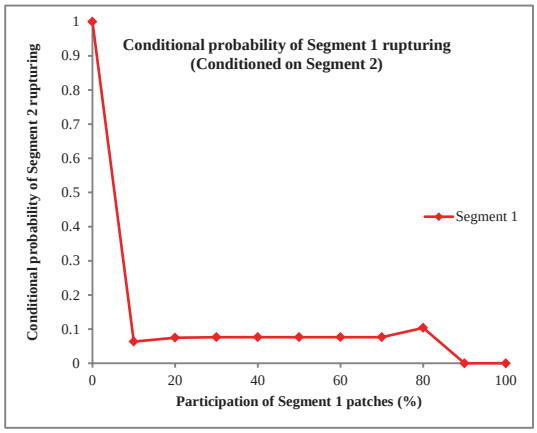

Figure 4.21J

Segment 1
Segment 2
Coulomb failure stress (MPa)
5
-5
Segment 2
Segment 1
Fault roughness
1
0
Displacement (m)
14
0
Relative rupture time
stop
start
Event ID 1311 (M 7.48)

Figure 4.21K

50 km underlap, 2 km stepover

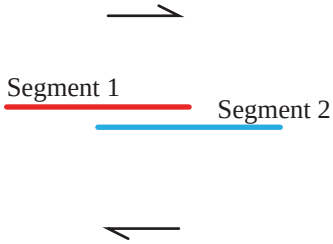

Smooth faults

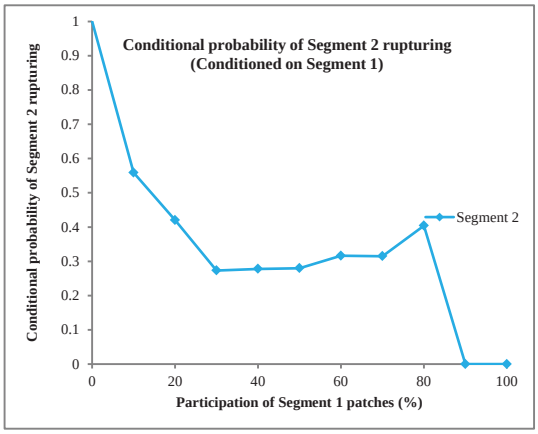

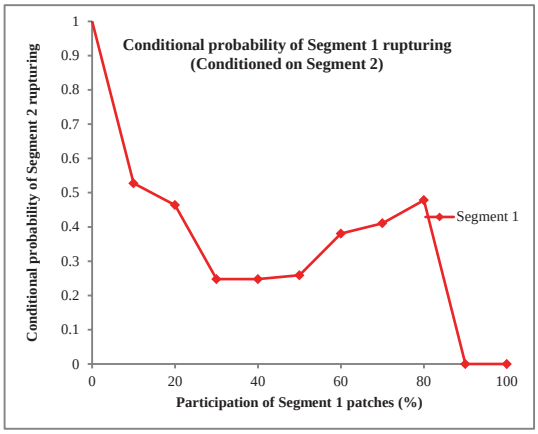

Rough faults

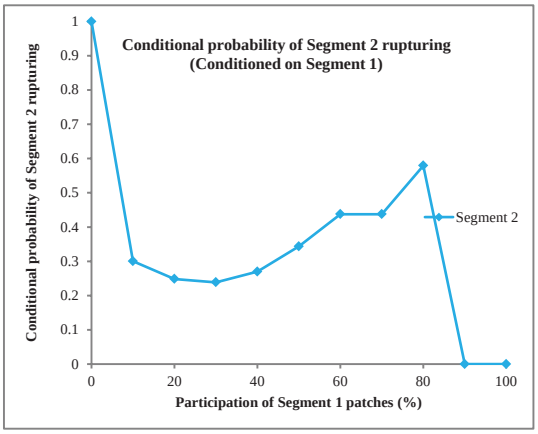

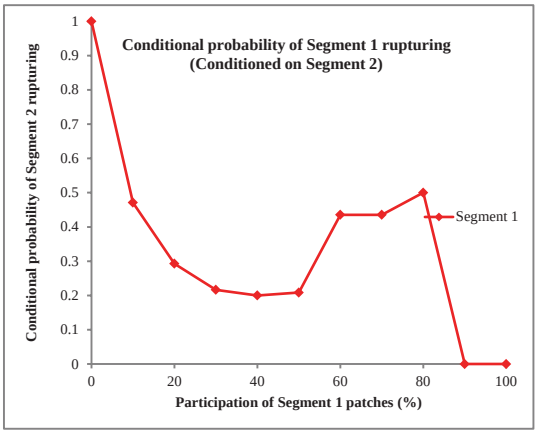

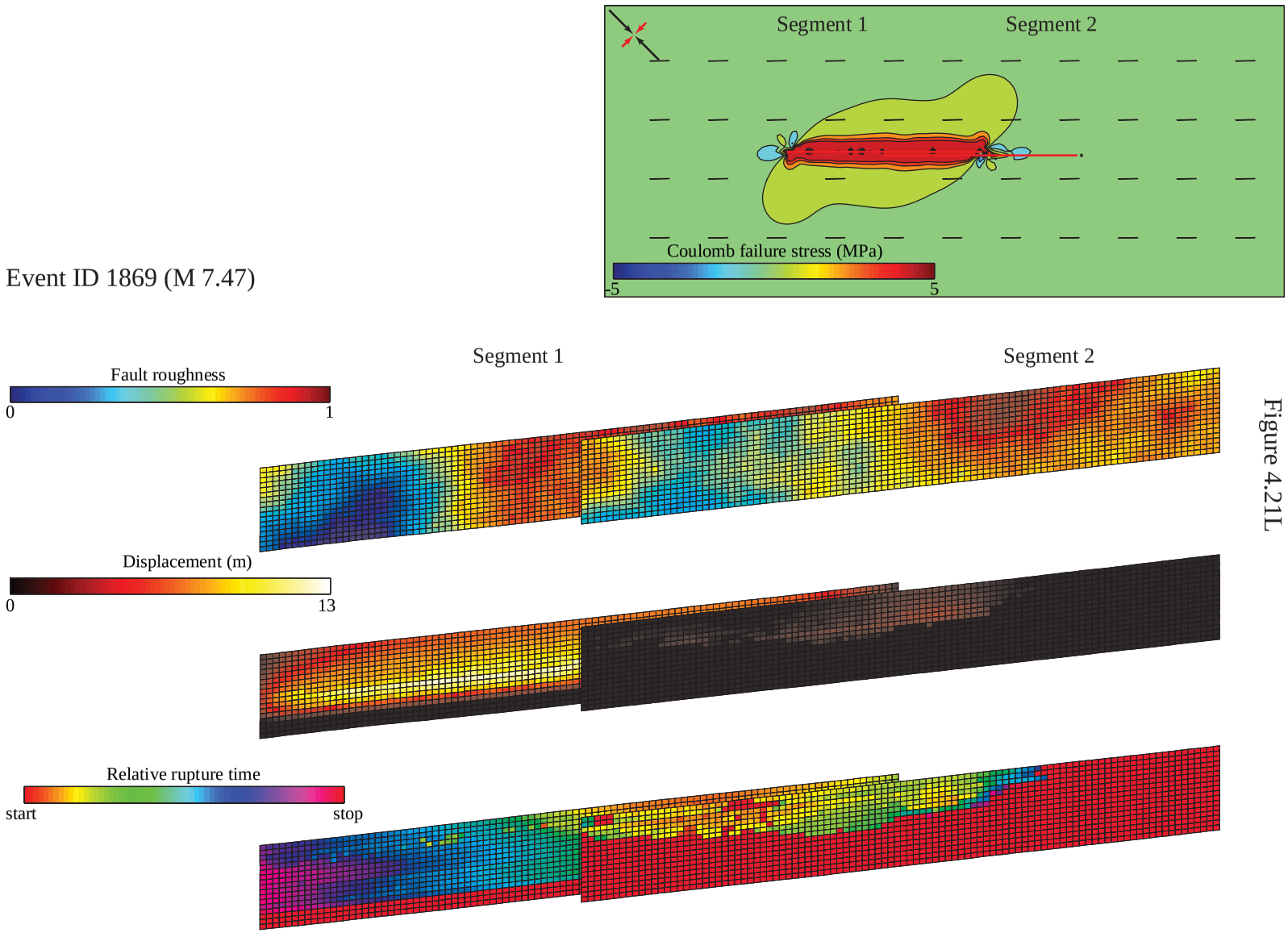
Segment 1
Segment 2
Coulomb failure stress (MPa)
-5
5
Event ID 1869 (M 7.47)
Segment 1
Segment 2
Fault roughness
0
1
Displacement (m)
0
13
Relative rupture time
start
stop

Figure 4.21L

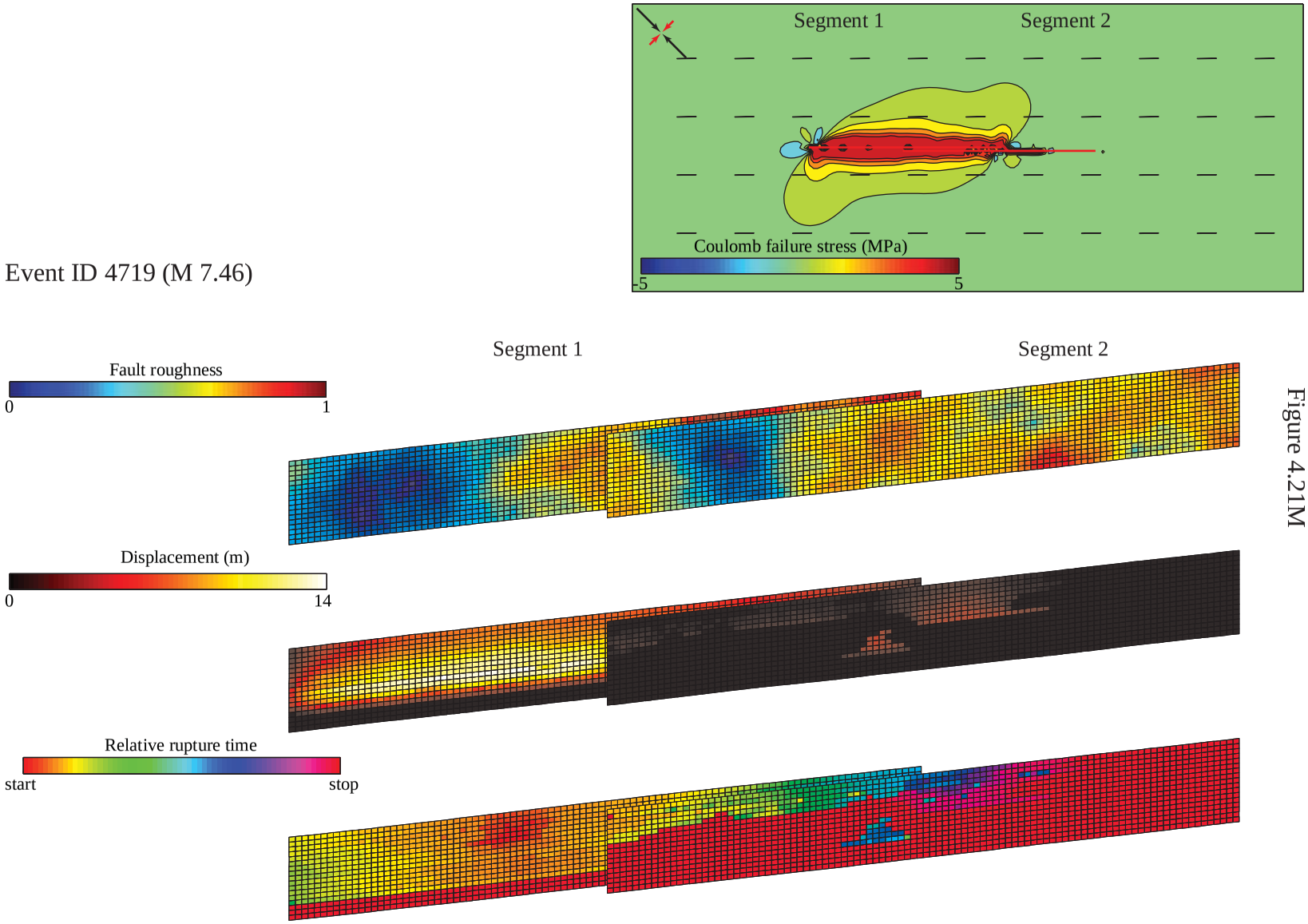
Segment 1
Segment 2
Coulomb failure stress (MPa)
-5
5
Event ID 4719 (M 7.46)
Segment 1
Segment 2
Fault roughness
0
1
Displacement (m)
0
14
Relative rupture time
start
stop

Figure 4.21M

Figure 4.22A

20 km underlap, 7 km stepover

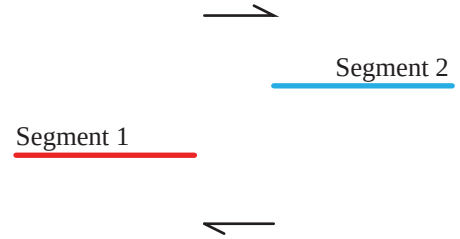

Smooth faults

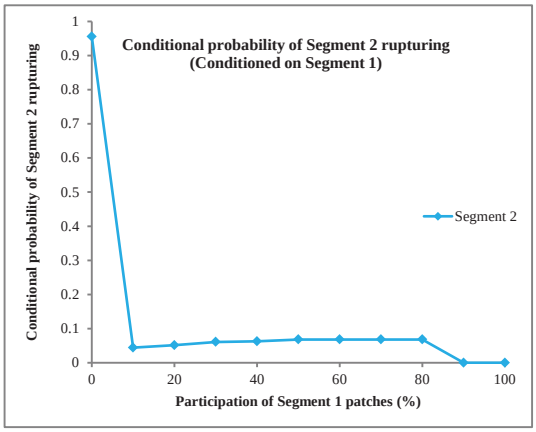

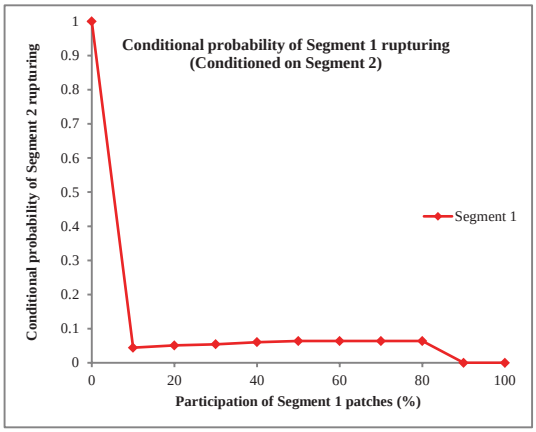

Rough faults

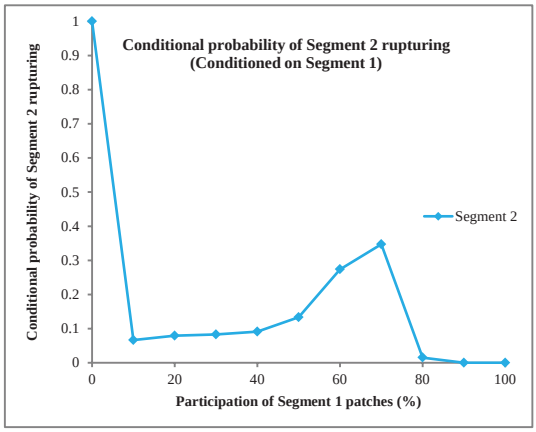

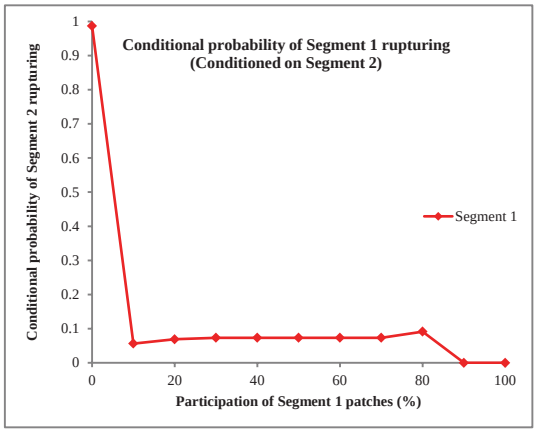

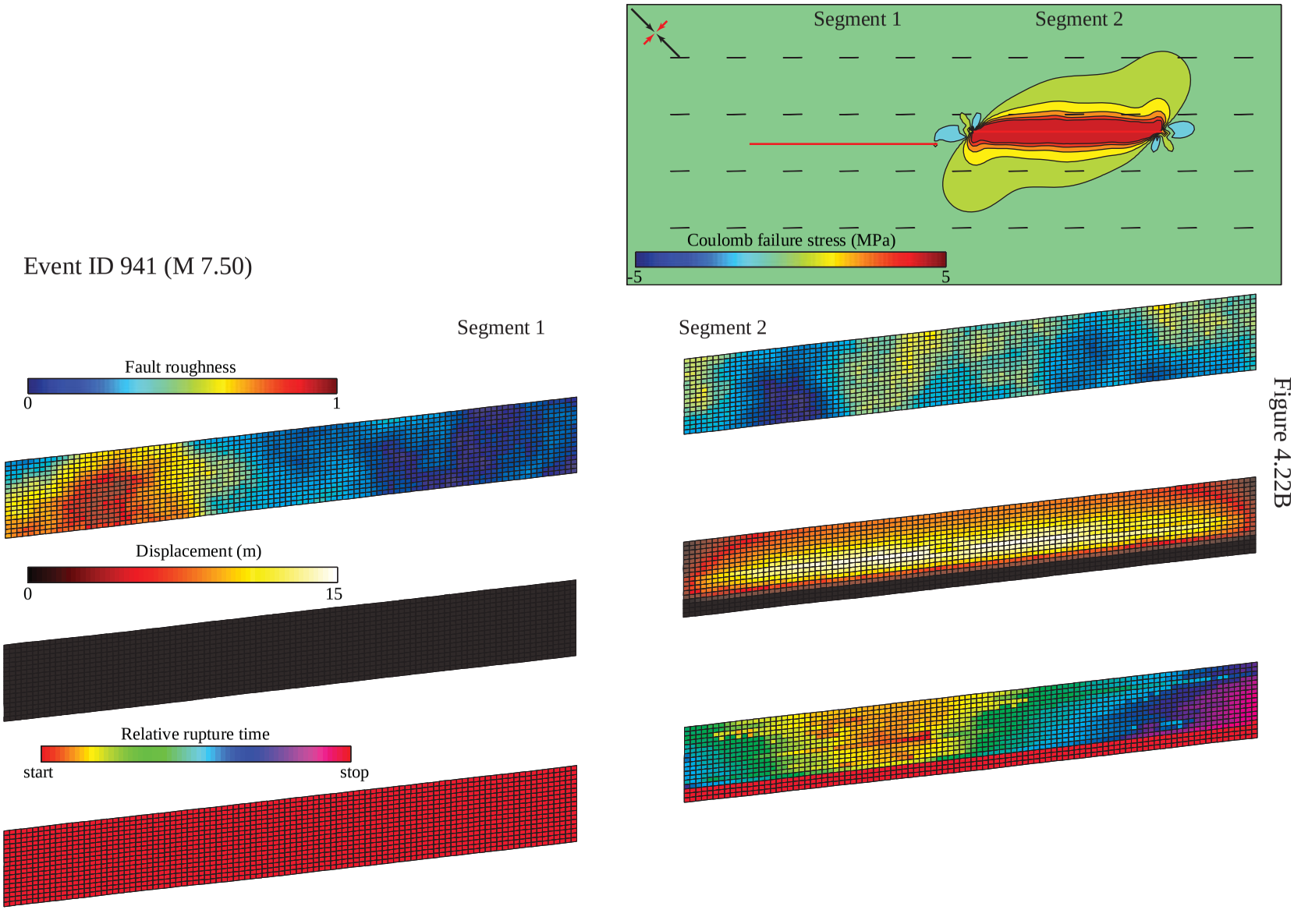
Segment 1
Segment 2
Coulomb failure stress (MPa)
-5
5
Event ID 941 (M 7.50)
Segment 1
Segment 2
Fault roughness
0
1
Displacement (m)
0
15
Relative rupture time
start
stop

Figure 4.22B

Figure 4.22C

50 km overlap, 7 km stepover

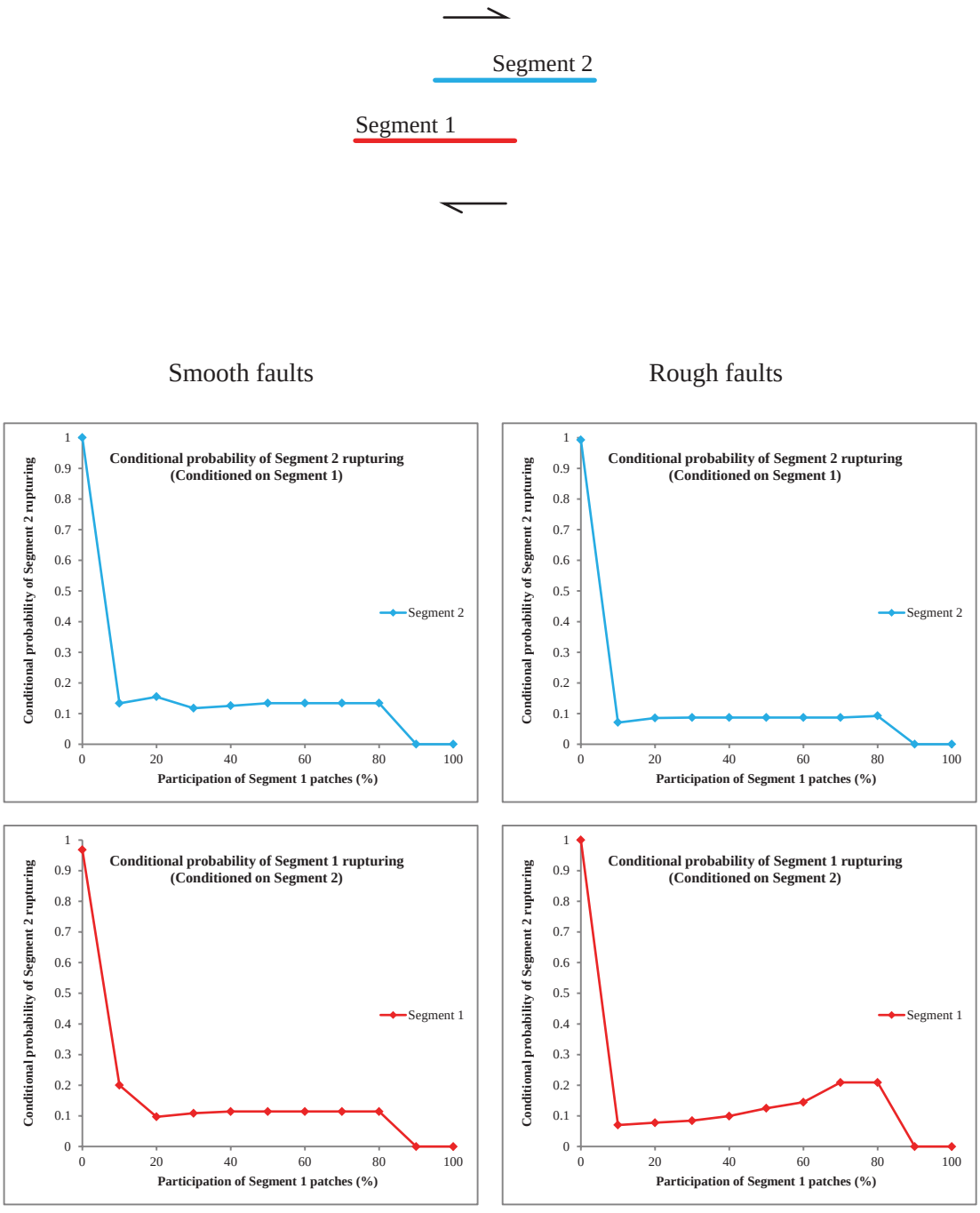

Figure 4.22D

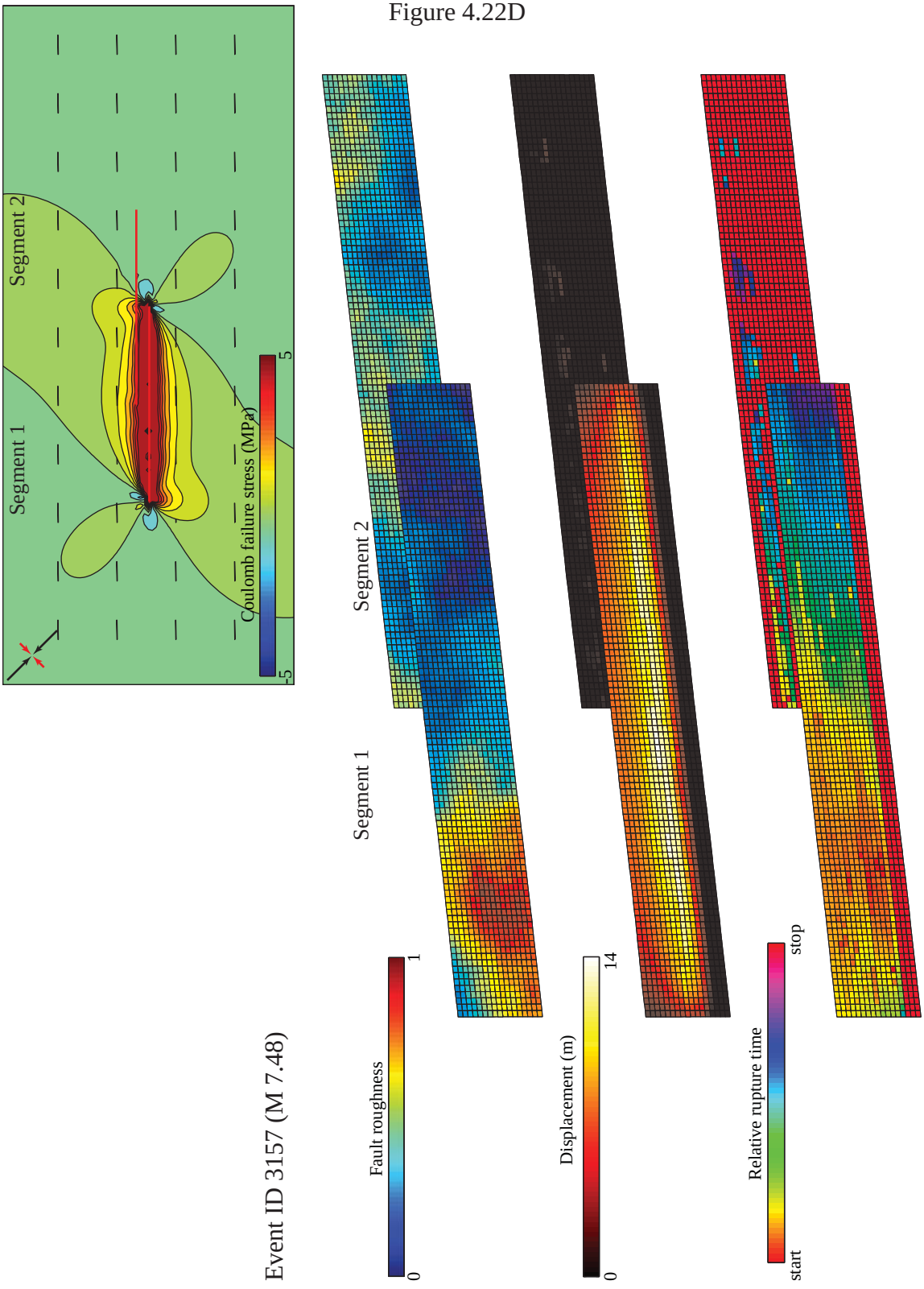

Event ID 3157 (M 7.48)

Figure 4.22E

20 km underlap, 5 km stepover

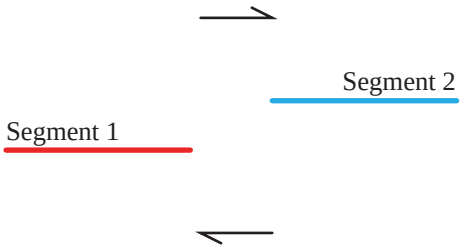

Smooth faults

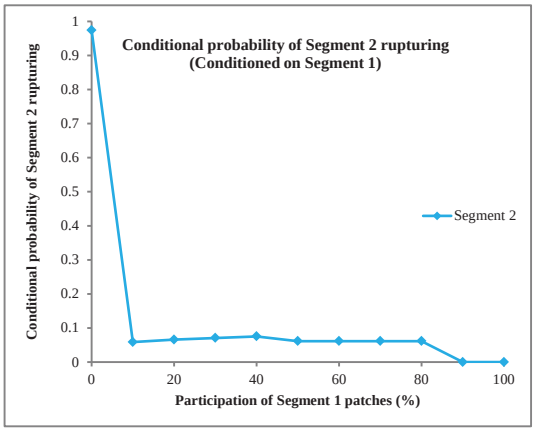

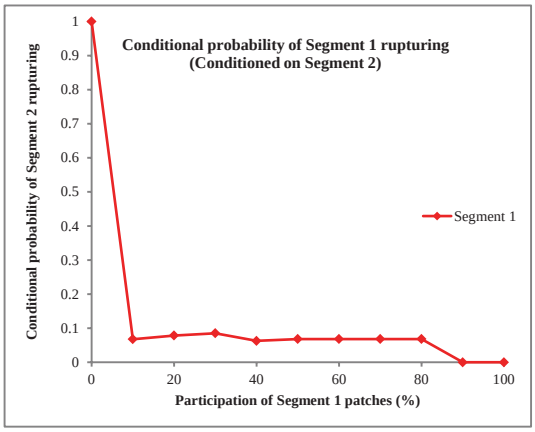

Rough faults

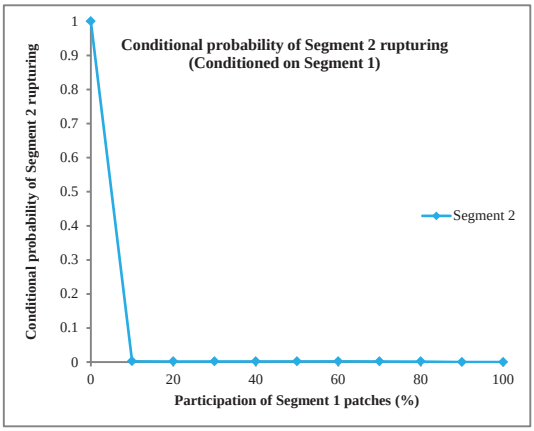

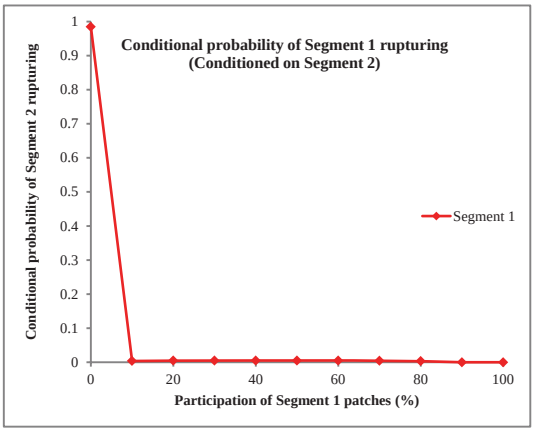

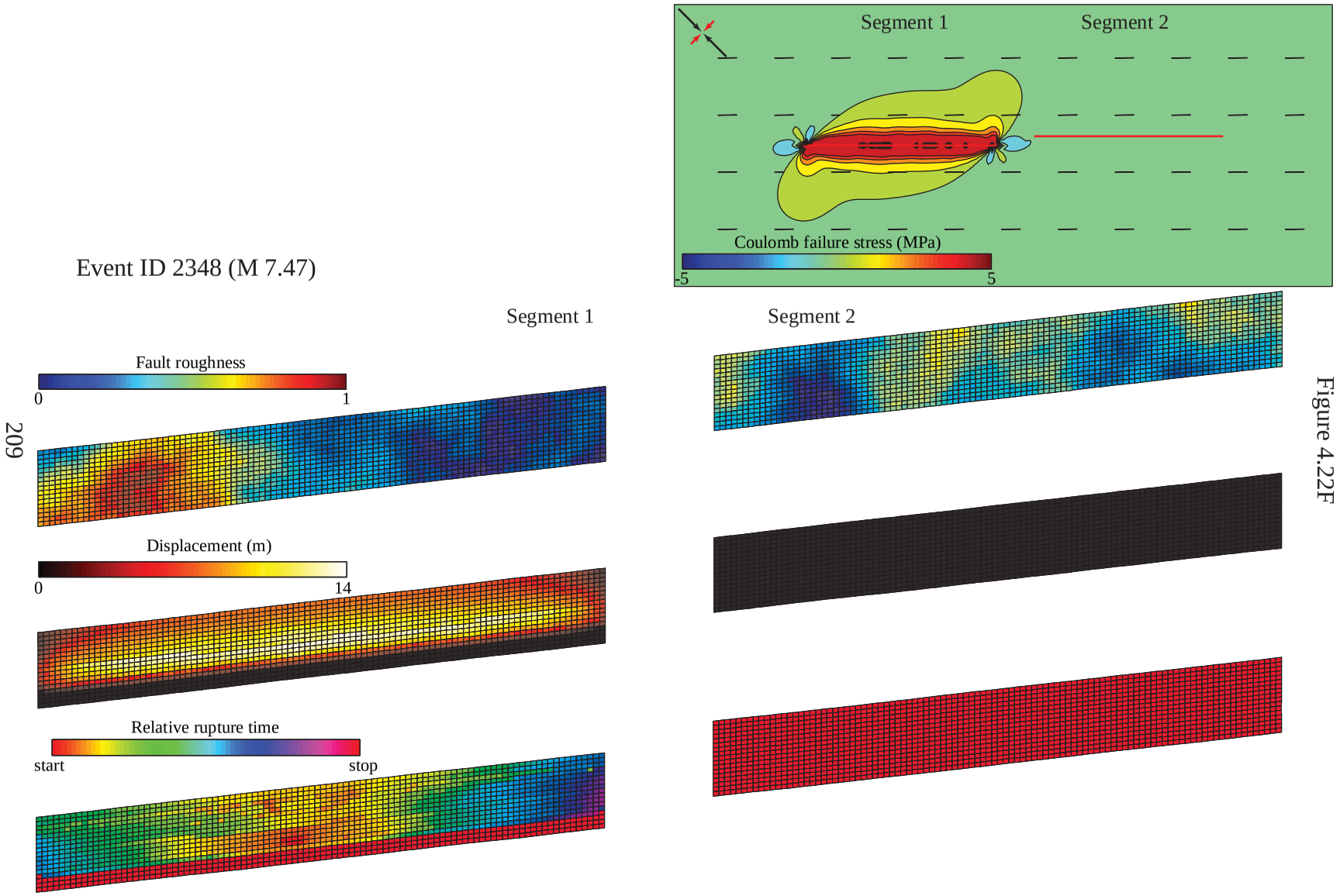
Segment 1
Segment 2
Coulomb failure stress (MPa)
-5
5
Event ID 2348 (M 7.47)
Segment 1
Segment 2
Fault roughness
0
1
Displacement (m)
0
14
Relative rupture time
start
stop

Figure 4.22F

Figure 4.22G

50 km overlap, 5 km stepover

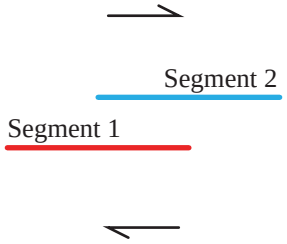

Smooth faults

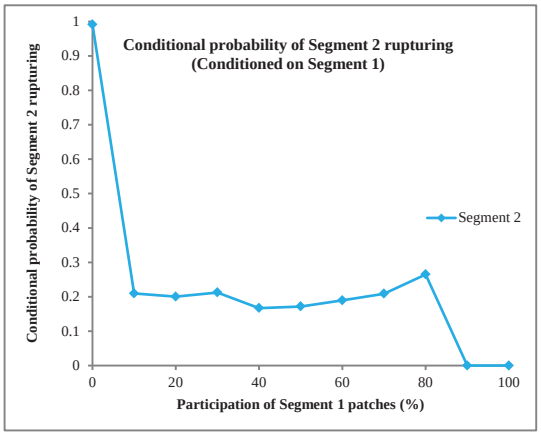

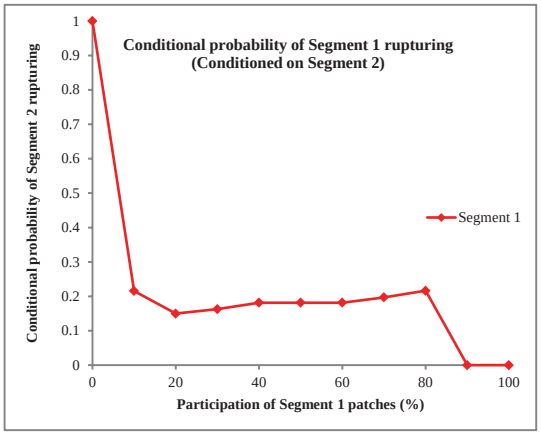

Rough faults

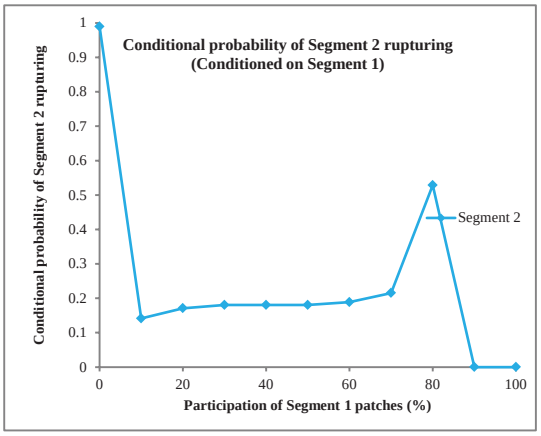

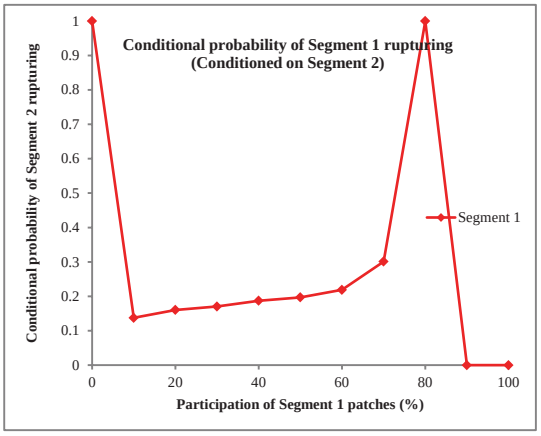

Figure 4.22H

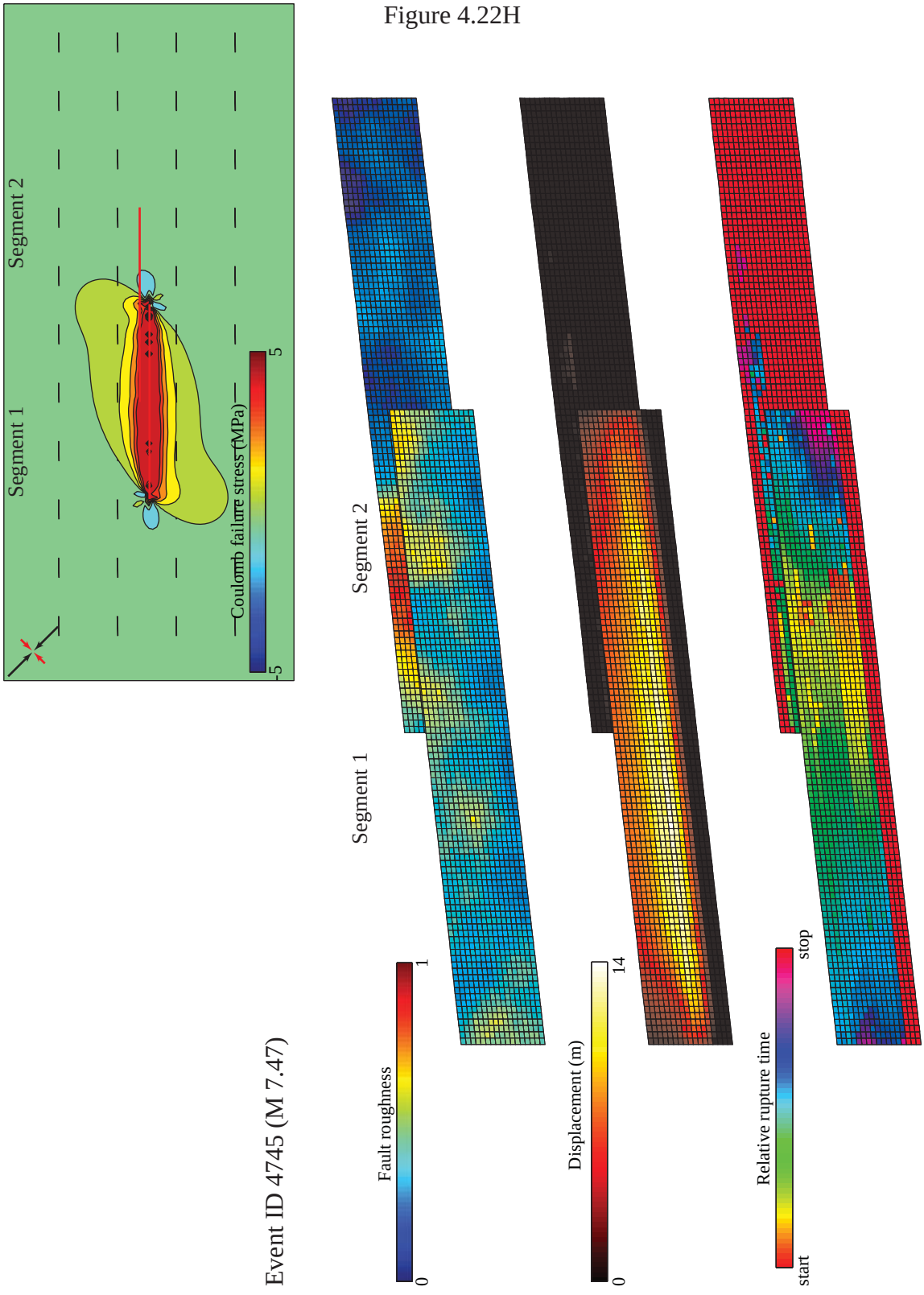
Segment 1
Segment 2
Coulomb failure stress (MPa)
5
-5
Event ID 4745 (M 7.47)
Segment 1
Segment 2
Fault roughness
1
0
Displacement (m)
14
0
Relative rupture time
stop
start

Figure 4.22I

20 km underlap, 2 km stepover

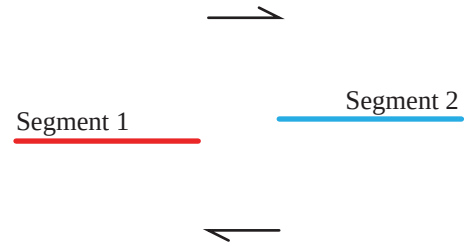

Smooth faults

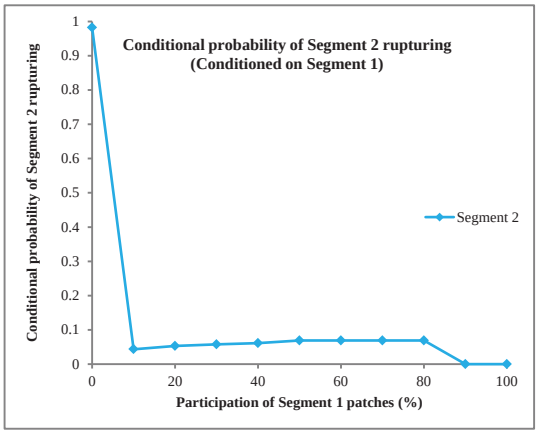

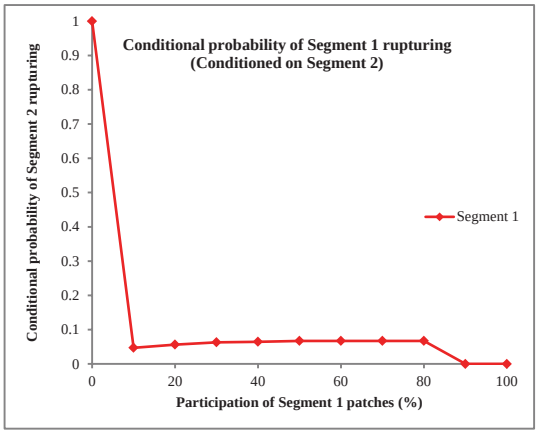

Rough faults

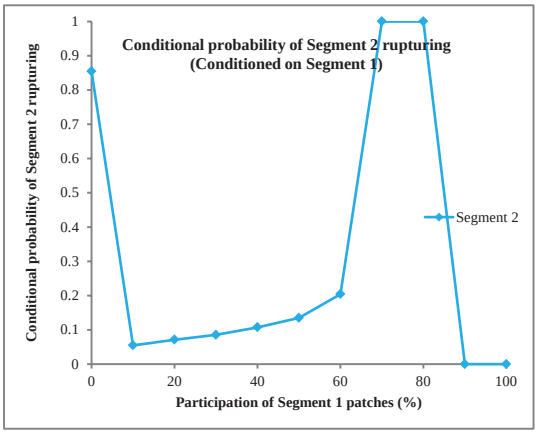

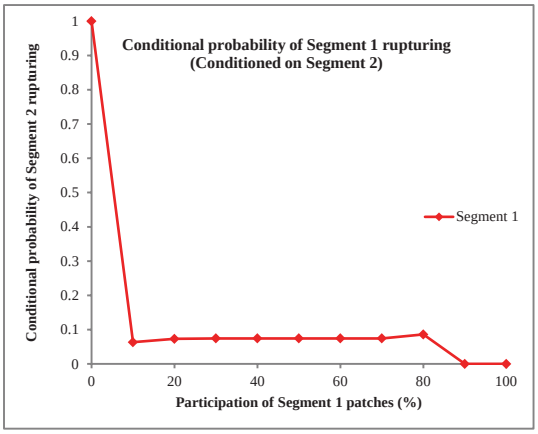

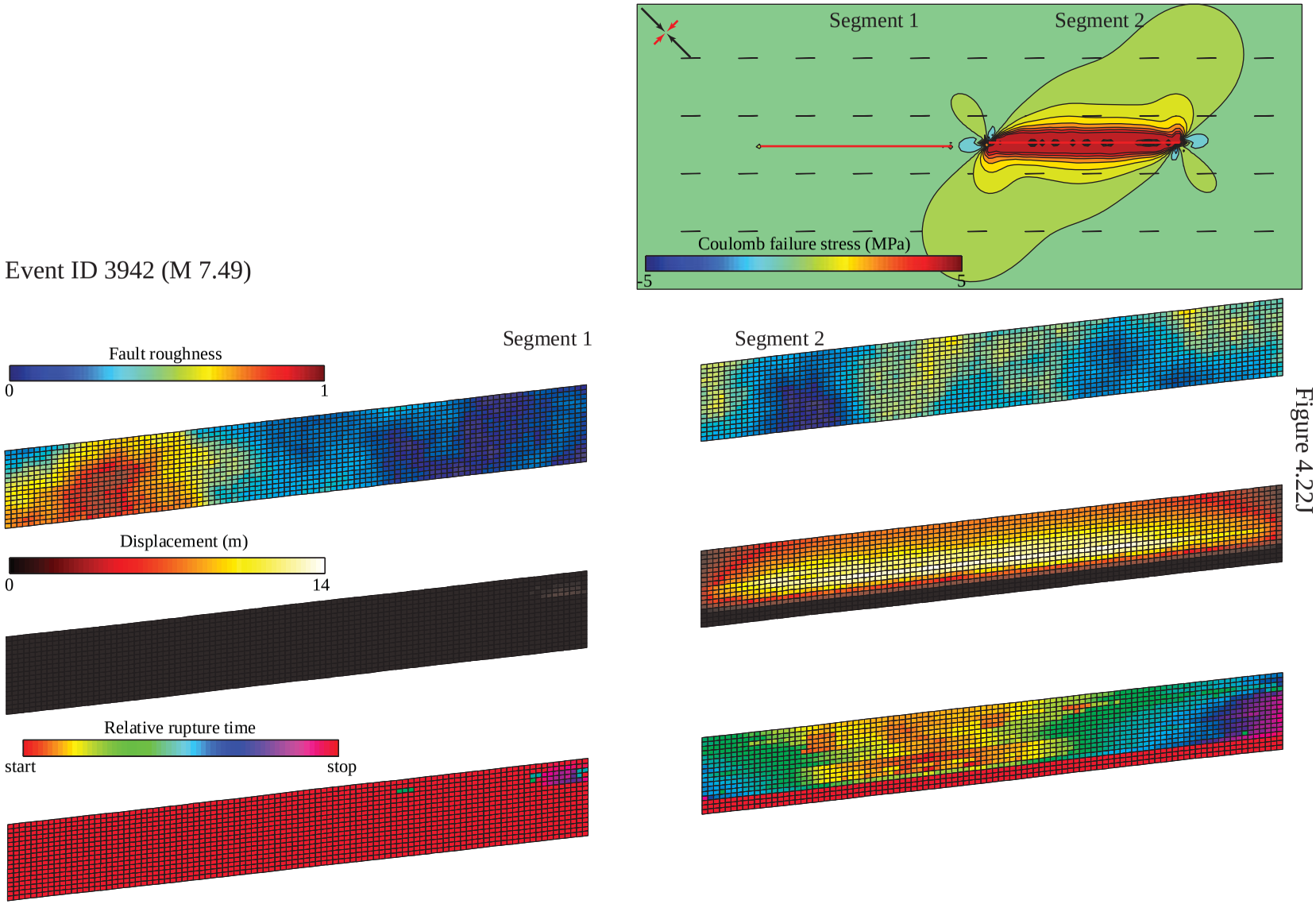
Segment 1
Segment 2
Coulomb failure stress (MPa)
-5
5
Event ID 3942 (M 7.49)
Segment 1
Segment 2
Fault roughness
0
1
Displacement (m)
0
14
Relative rupture time
start
stop

Figure 4.22J

Figure 4.22K

50 km underlap, 2 km stepover

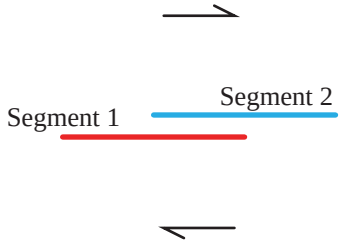

Smooth faults

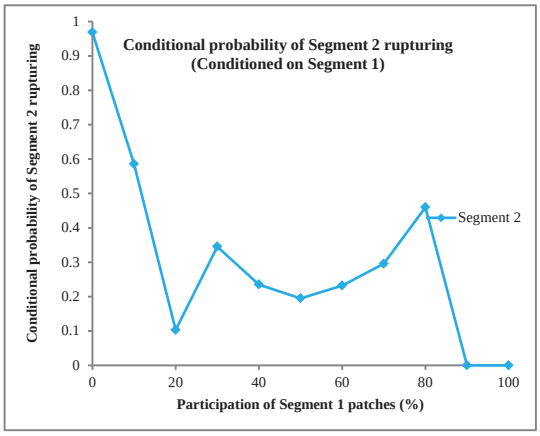

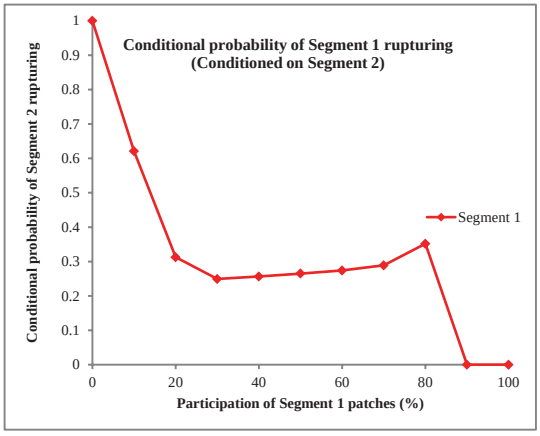

Rough faults

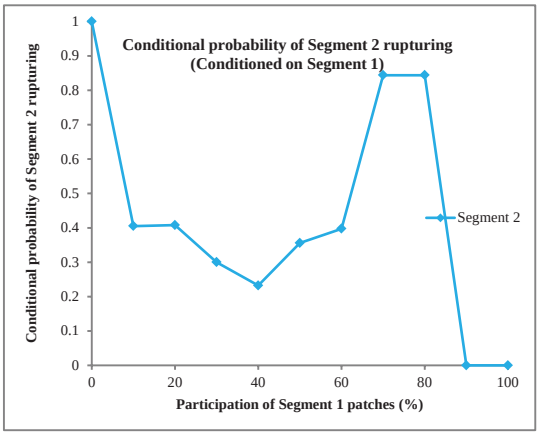

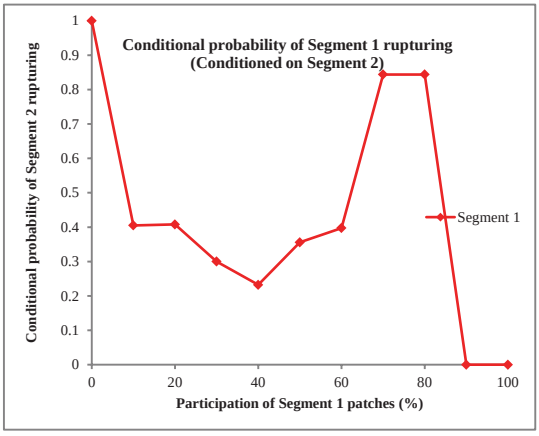

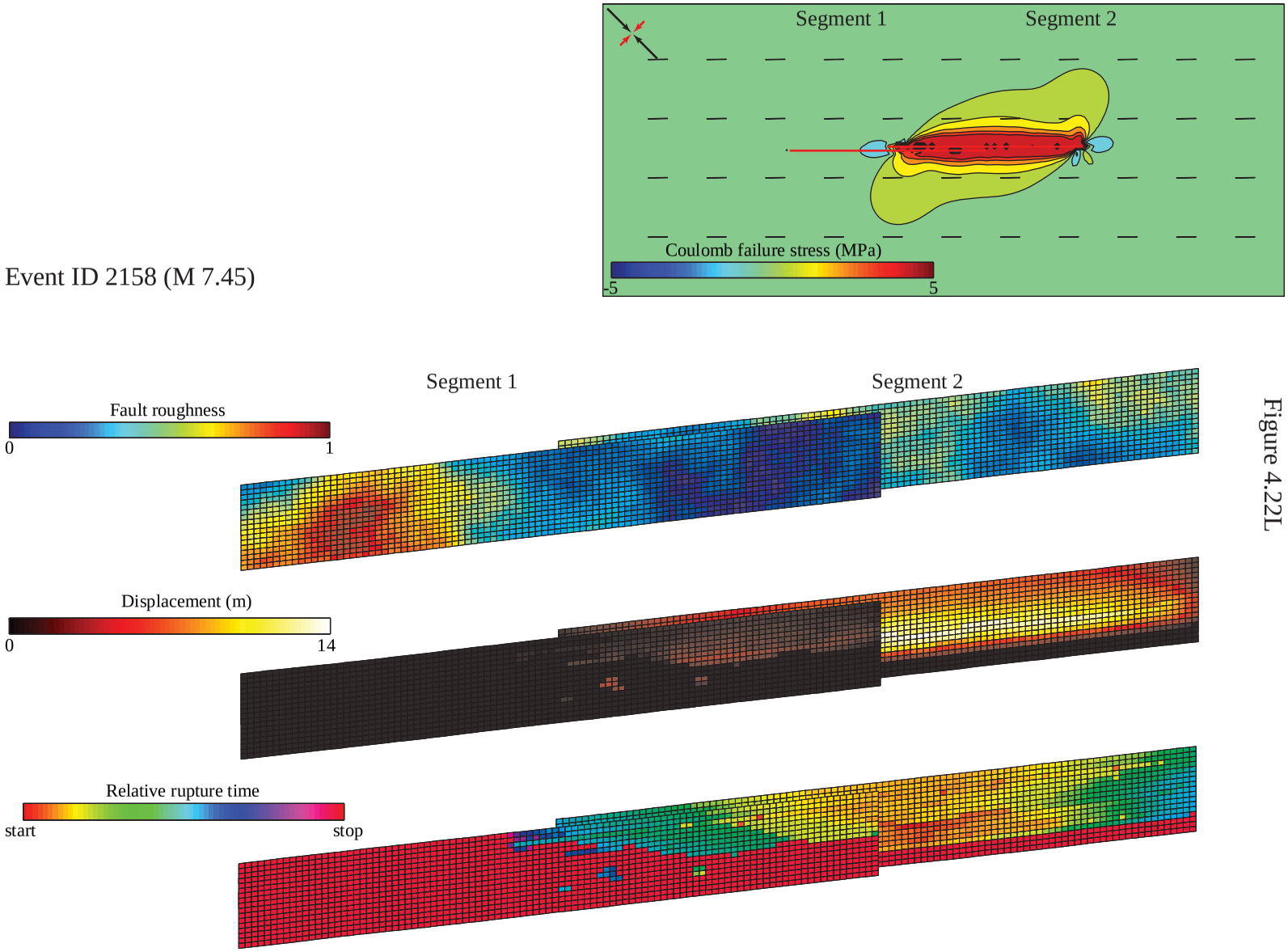
Segment 1
Segment 2
Coulomb failure stress (MPa)
-5
5
Event ID 2158 (M 7.45)
Segment 1
Segment 2
Fault roughness
0
1
Displacement (m)
0
14
Relative rupture time
start
stop

Figure 4.22L

Figure 4.23A

20 km underlap, 7 km stepover

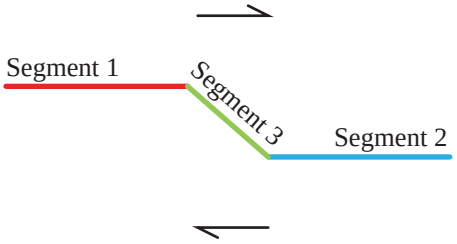

Smooth faults

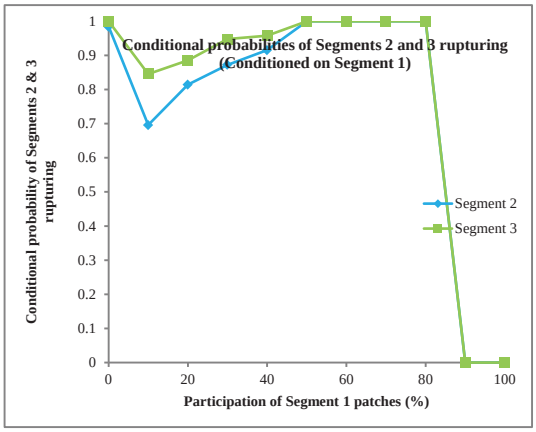

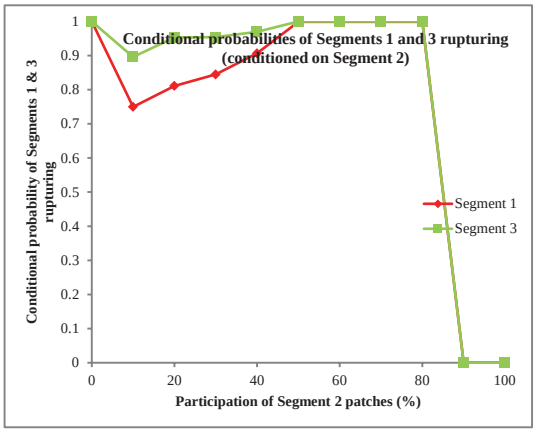

Rough faults

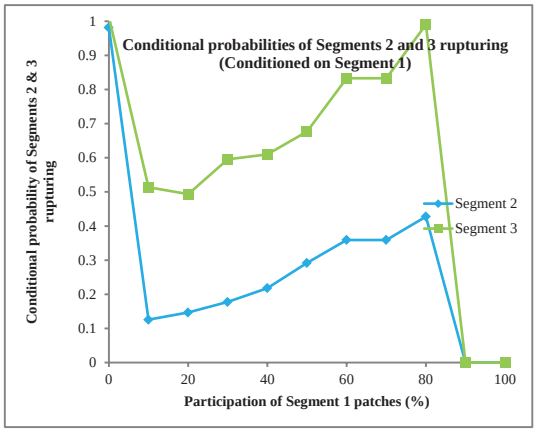

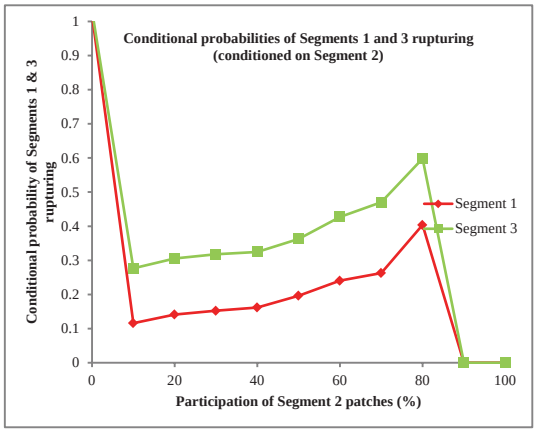

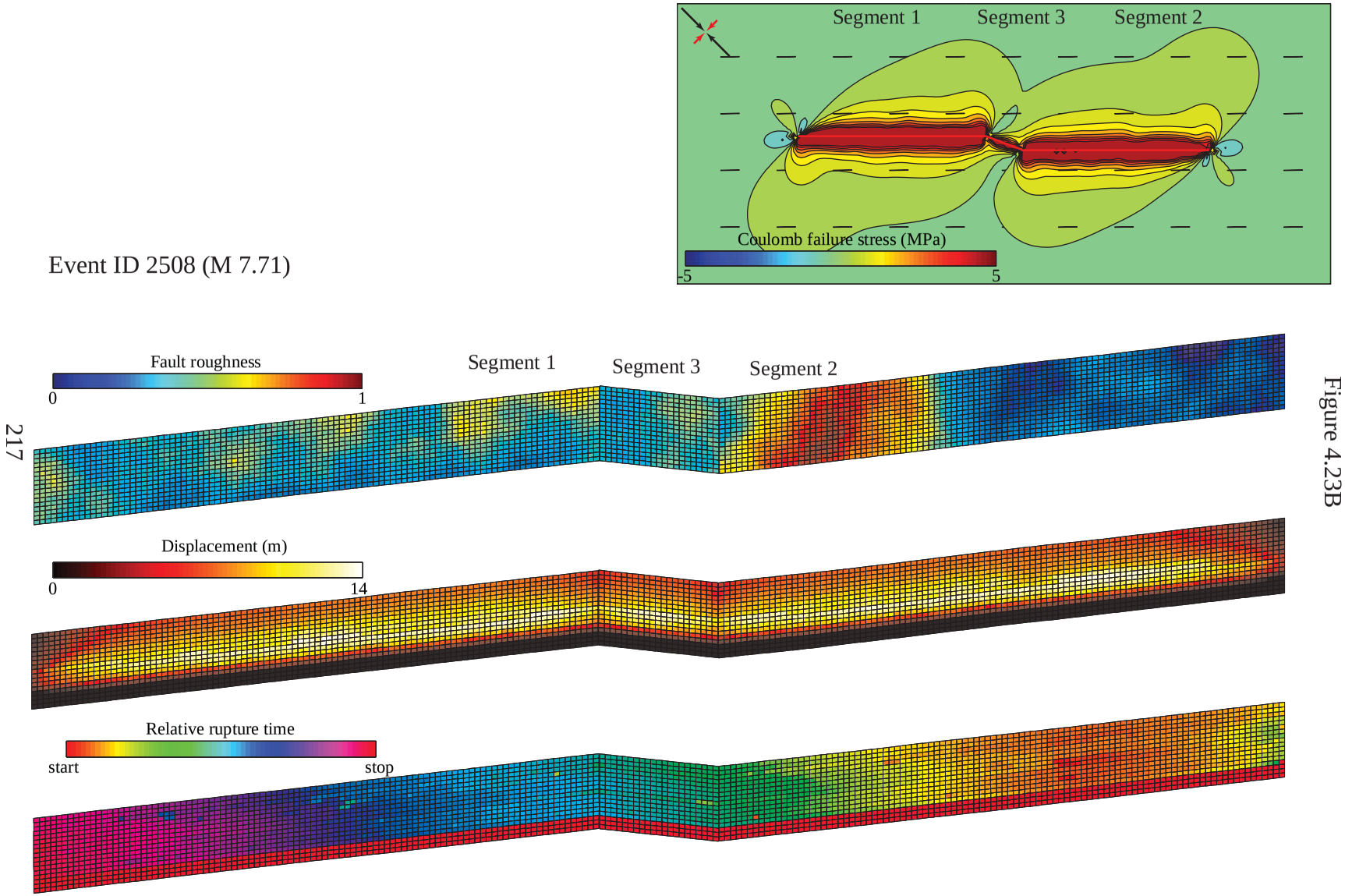
Segment 1
Segment 3
Segment 2
Coulomb failure stress (MPa)
-5
5
Event ID 2508 (M 7.71)
Fault roughness
0
1
Segment 1
Segment 3
Segment 2
Displacement (m)
0
14
Relative rupture time
start
stop

Figure 4.23B

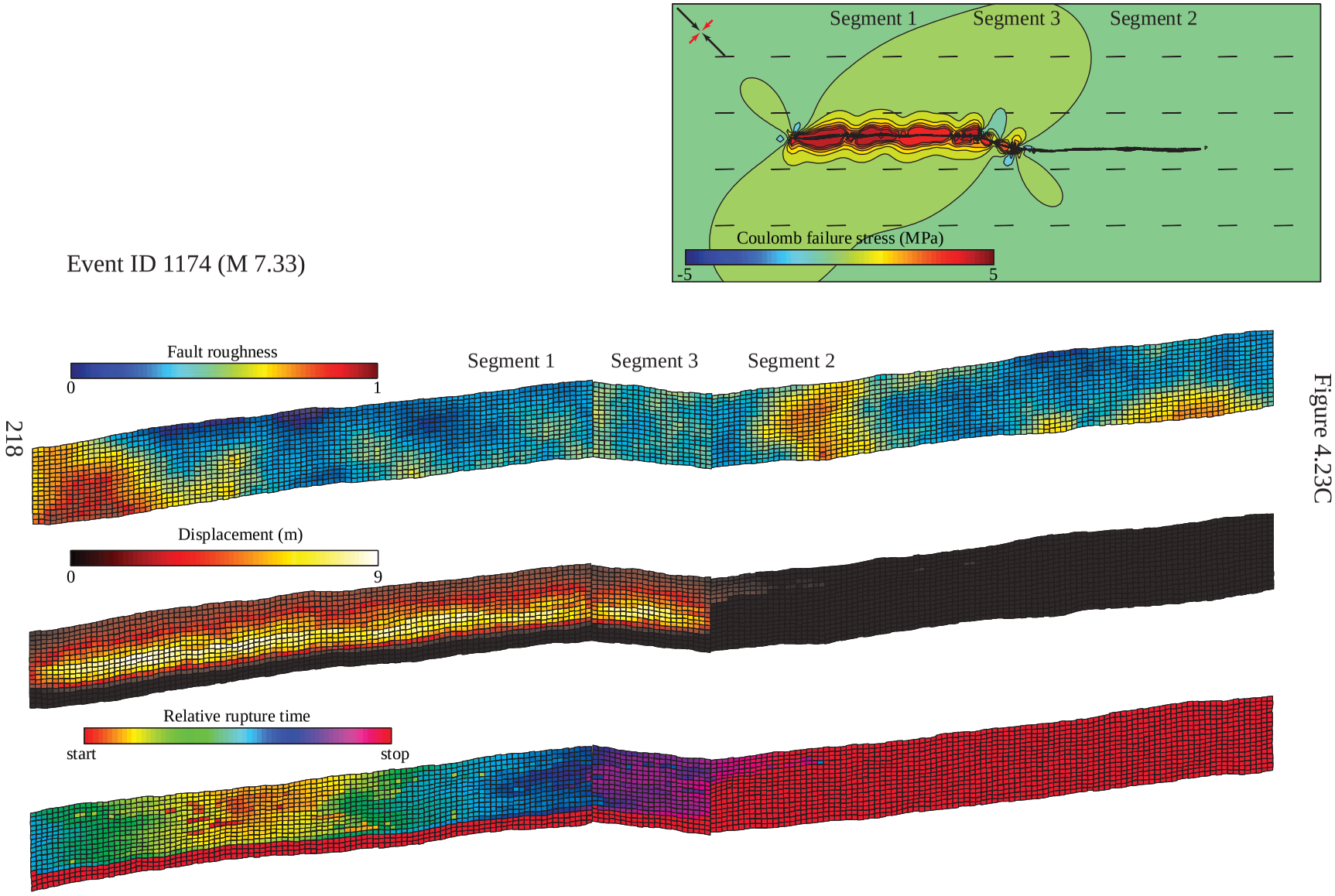
Segment 1
Segment 3
Segment 2
Coulomb failure stress (MPa)
-5
5
Event ID 1174 (M 7.33)
Fault roughness
0
1
Segment 1
Segment 3
Segment 2
Displacement (m)
0
9
Relative rupture time
start
stop

Figure 4.23C

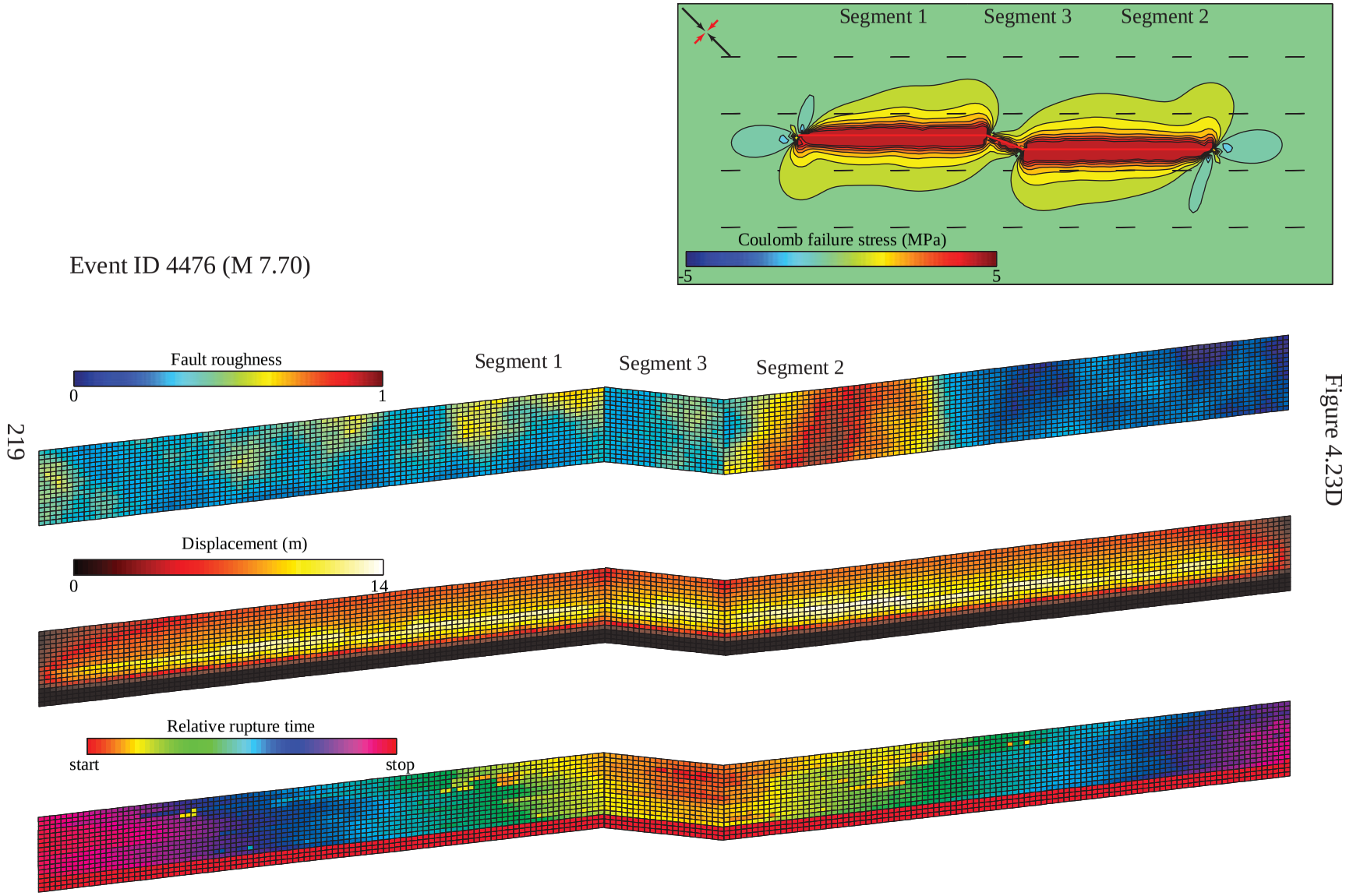
Segment 1
Segment 3
Segment 2
Coulomb failure stress (MPa)
-5
5
Event ID 4476 (M 7.70)
Fault roughness
0
1
Segment 1
Segment 3
Segment 2
Displacement (m)
0
14
Relative rupture time
start
stop

Figure 4.23D

Figure 4.23E

20 km underlap, 5 km stepover

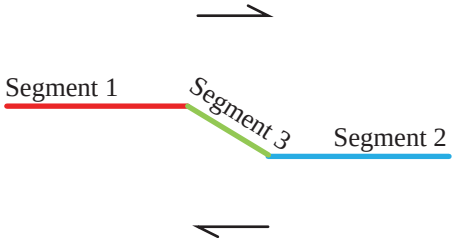

Smooth faults

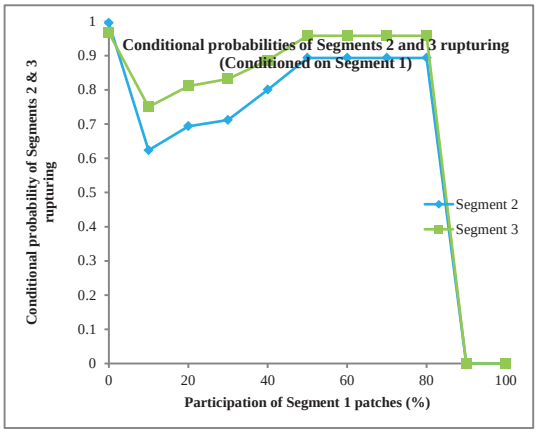

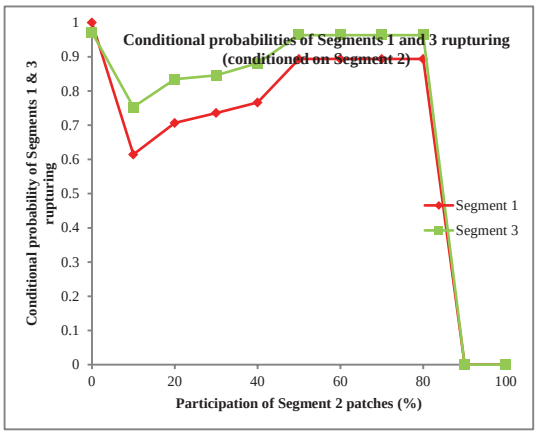

Rough faults

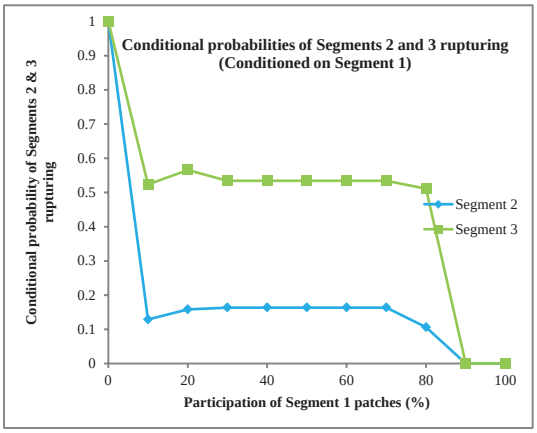

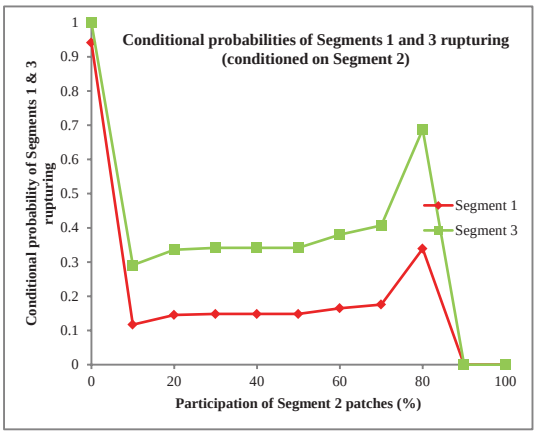

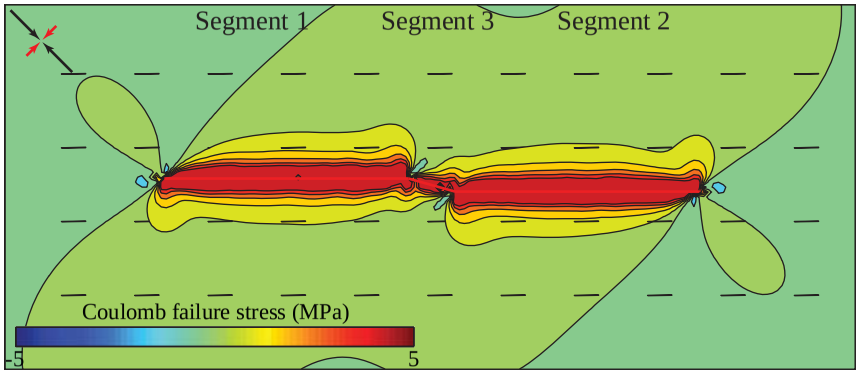

Event ID 3677 (M 7.69)

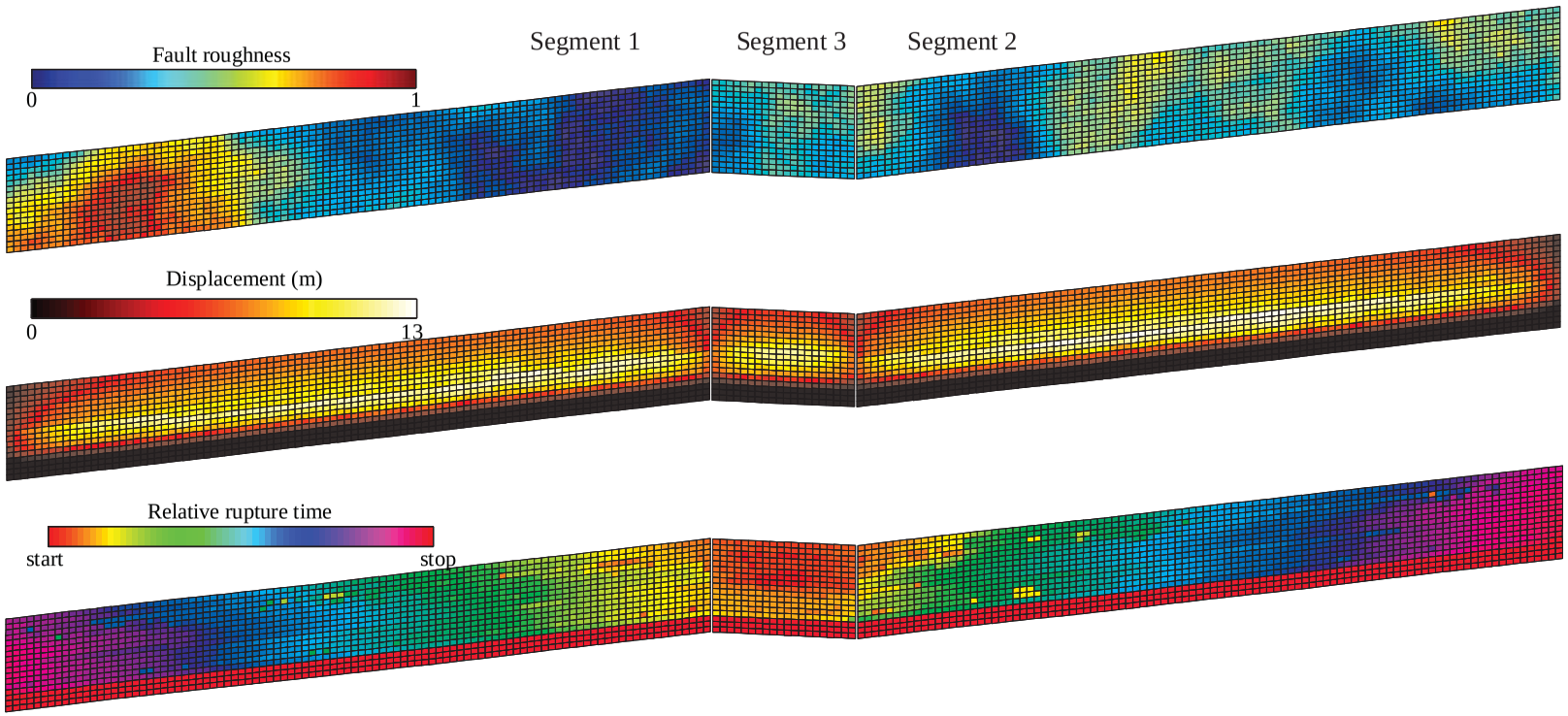

Figure 4.23F

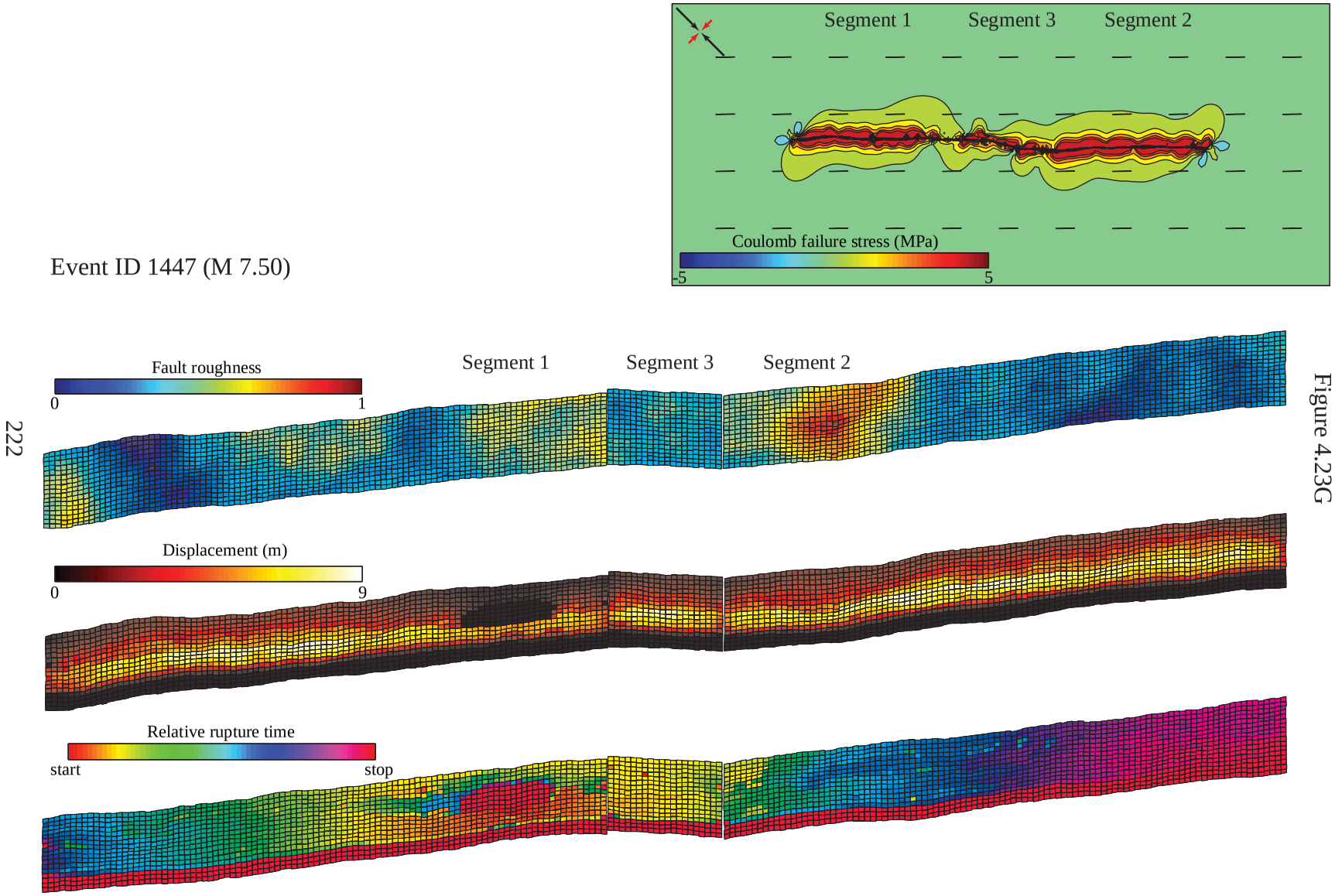
Segment 1
Segment 3
Segment 2
Coulomb failure stress (MPa)
-5
5
Event ID 1447 (M 7.50)
Fault roughness
0
1
Segment 1
Segment 3
Segment 2
Displacement (m)
0
9
Relative rupture time
start
stop

Figure 4.23G

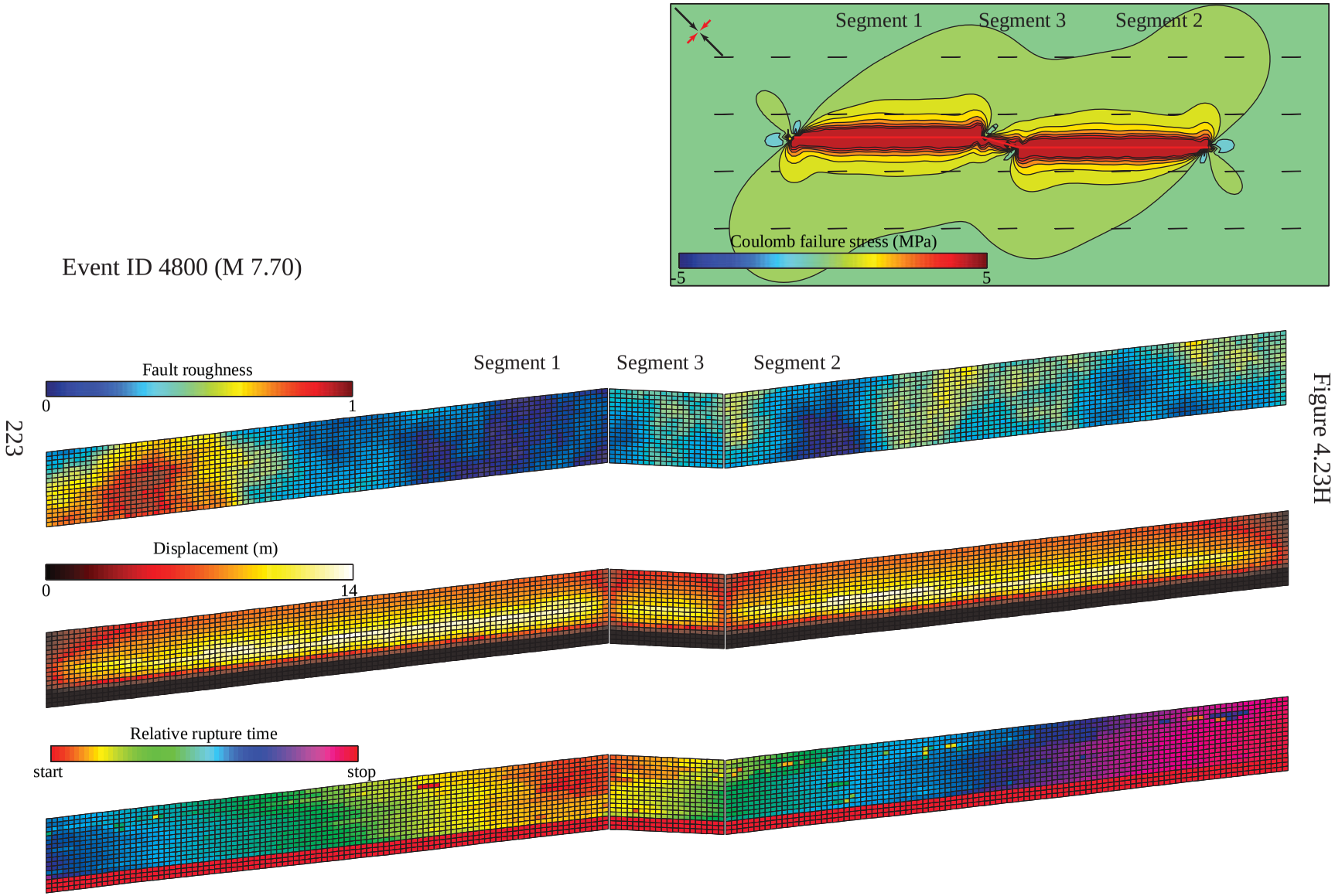
Segment 1
Segment 3
Segment 2
Coulomb failure stress (MPa)
-5
5
Event ID 4800 (M 7.70)
Fault roughness
0
1
Segment 1
Segment 3
Segment 2
Displacement (m)
0
14
Relative rupture time
start
stop

Figure 4.23H

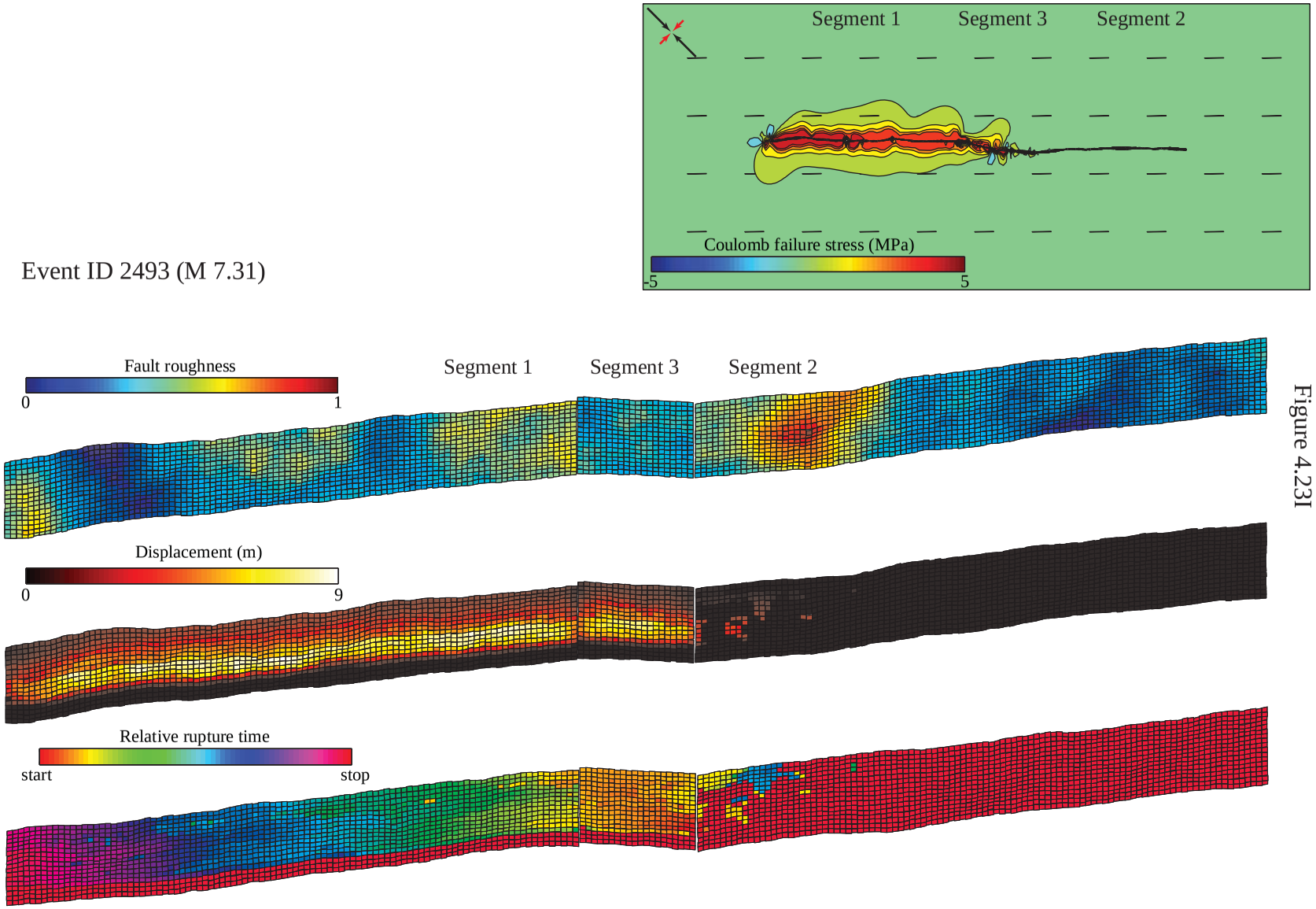
Segment 1
Segment 3
Segment 2
Coulomb failure stress (MPa)
-5
5
Event ID 2493 (M 7.31)
Fault roughness
0
1
Segment 1
Segment 3
Segment 2
Displacement (m)
0
9
Relative rupture time
start
stop

Figure 4.23I

Figure 4.23J

20 km underlap, 2 km stepover

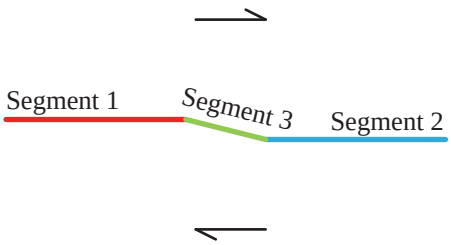

Smooth faults

Rough faults

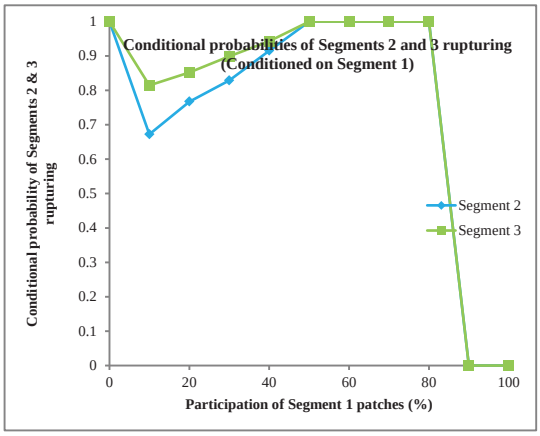

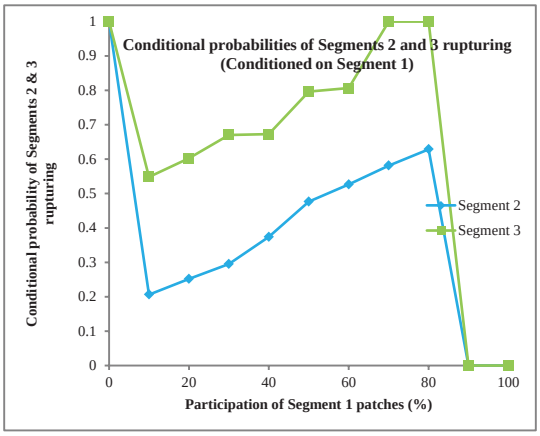

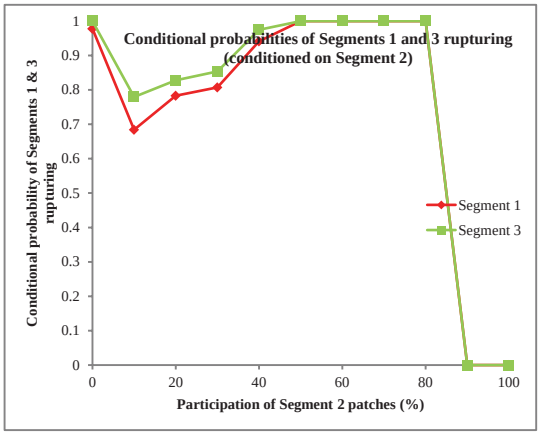

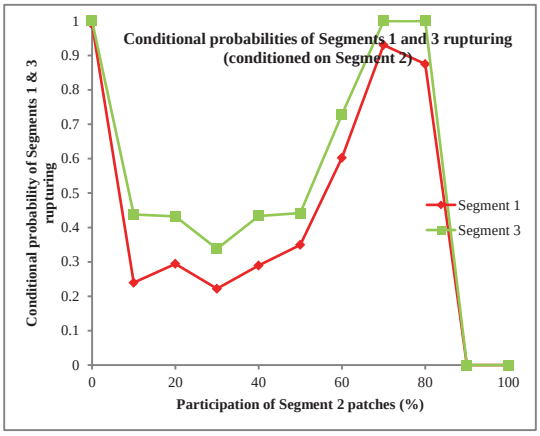

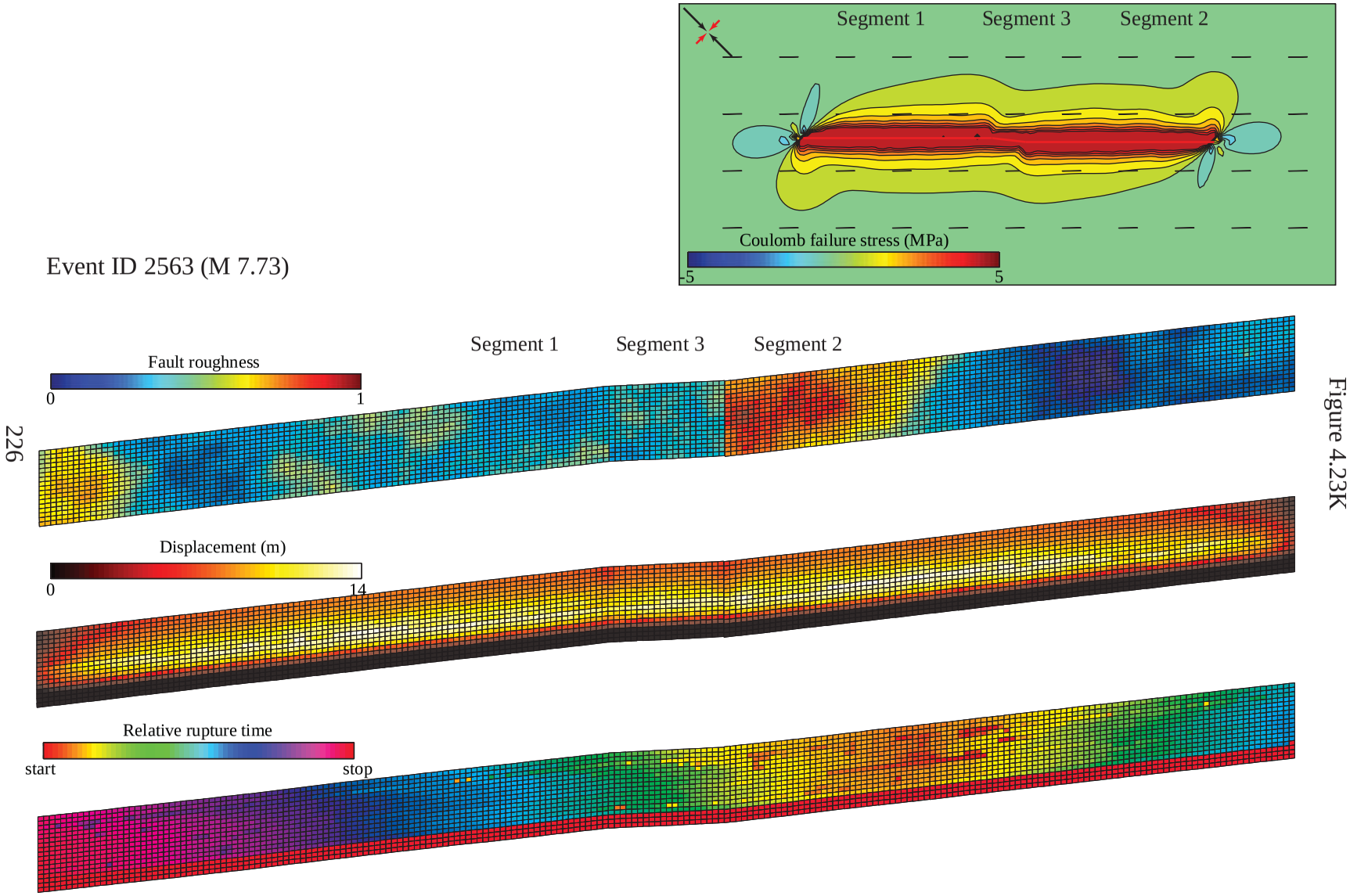
Segment 1
Segment 3
Segment 2
Coulomb failure stress (MPa)
-5
5
Event ID 2563 (M 7.73)
Segment 1
Segment 3
Segment 2
Fault roughness
0
1
Displacement (m)
0
14
Relative rupture time
start
stop

Figure 4.23K

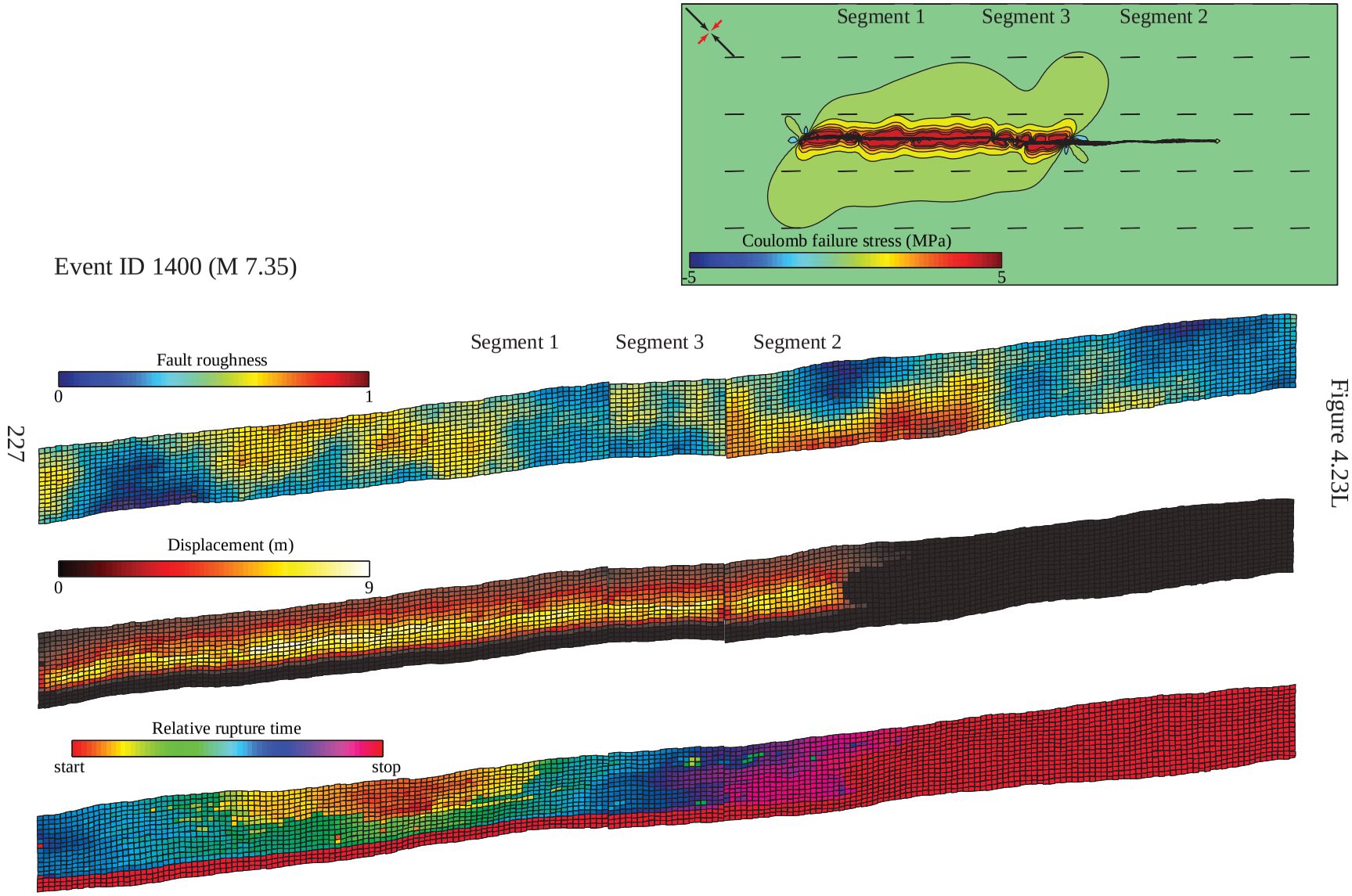
Segment 1
Segment 3
Segment 2
Coulomb failure stress (MPa)
-5
5
Event ID 1400 (M 7.35)
Segment 1
Segment 3
Segment 2
Fault roughness
0
1
Displacement (m)
0
9
Relative rupture time
start
stop

Figure 4.23L

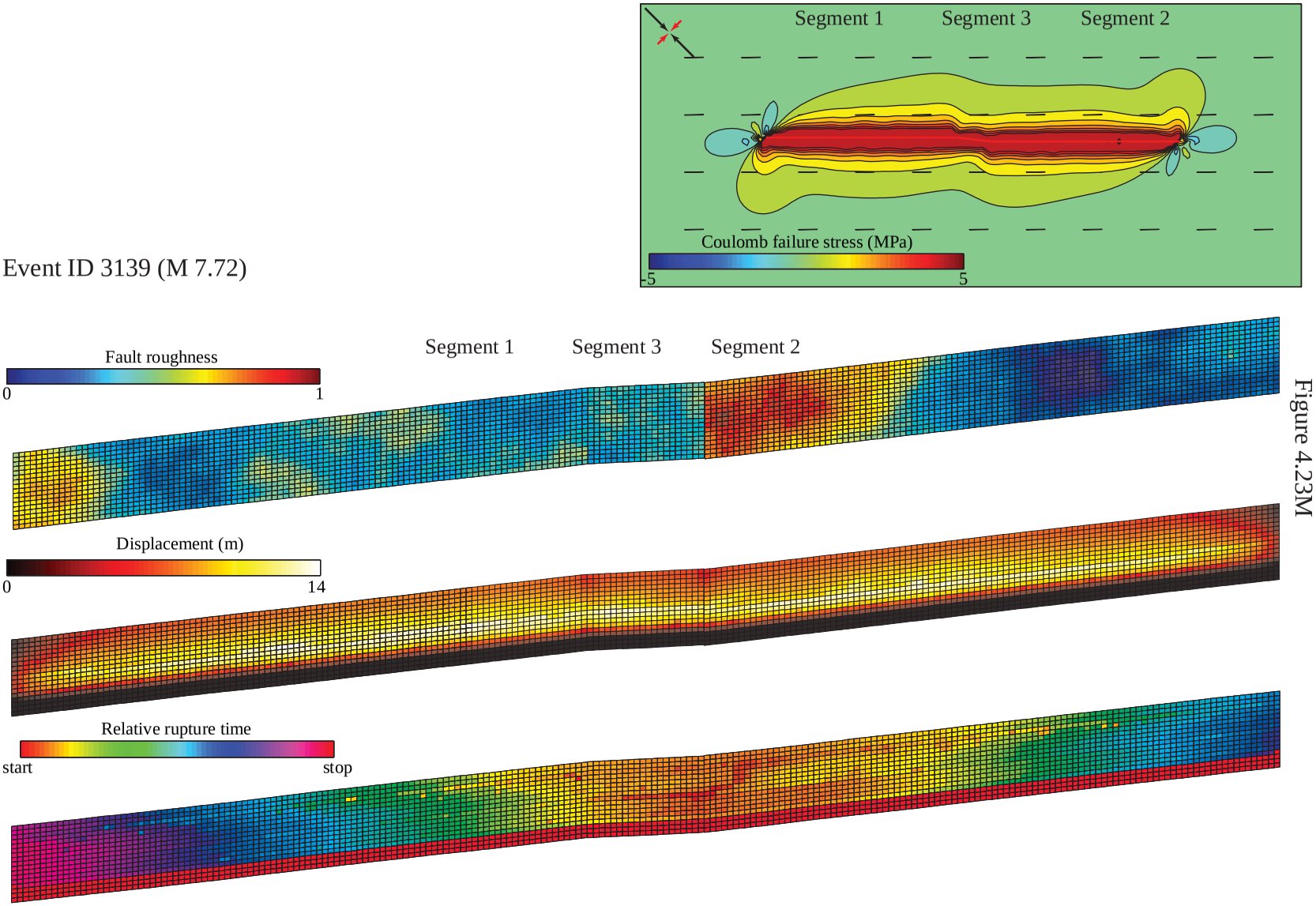
Segment 1
Segment 3
Segment 2
Coulomb failure stress (MPa)
-5
5
Event ID 3139 (M 7.72)
Segment 1
Segment 3
Segment 2
Fault roughness
0
1
Displacement (m)
0
14
Relative rupture time
start
stop

Figure 4.23M

Figure 4.24A

20 km underlap, 7 km stepover

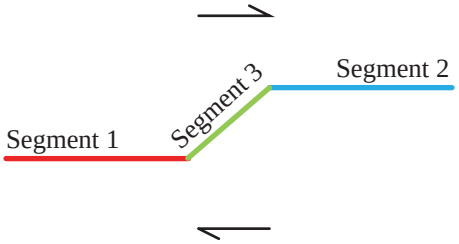

Smooth faults

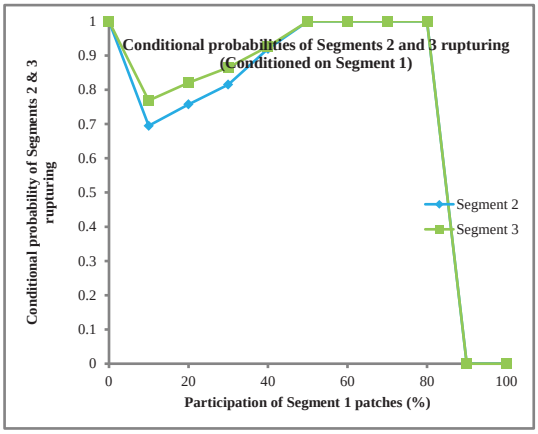

Rough faults

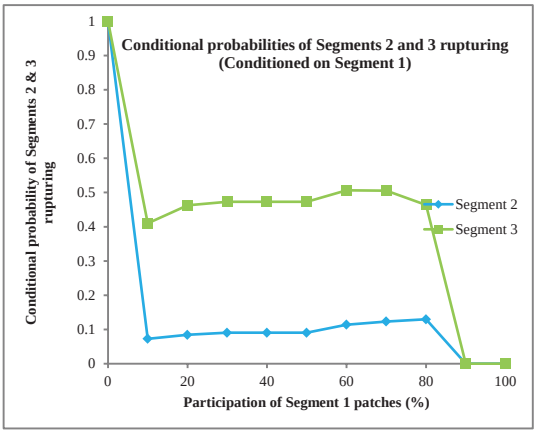

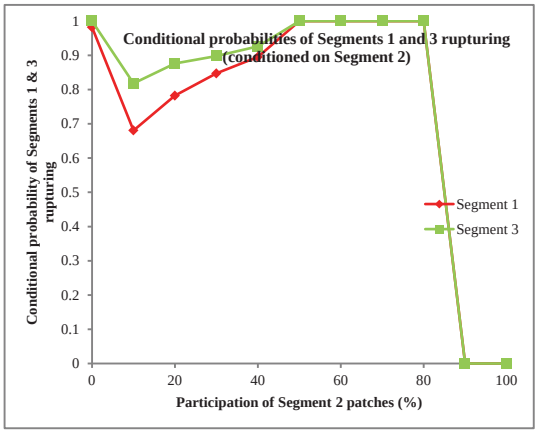

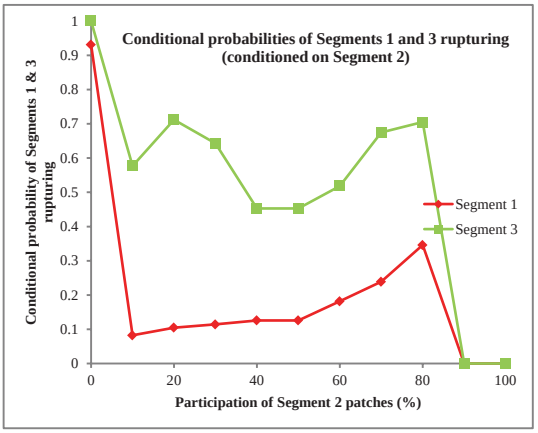

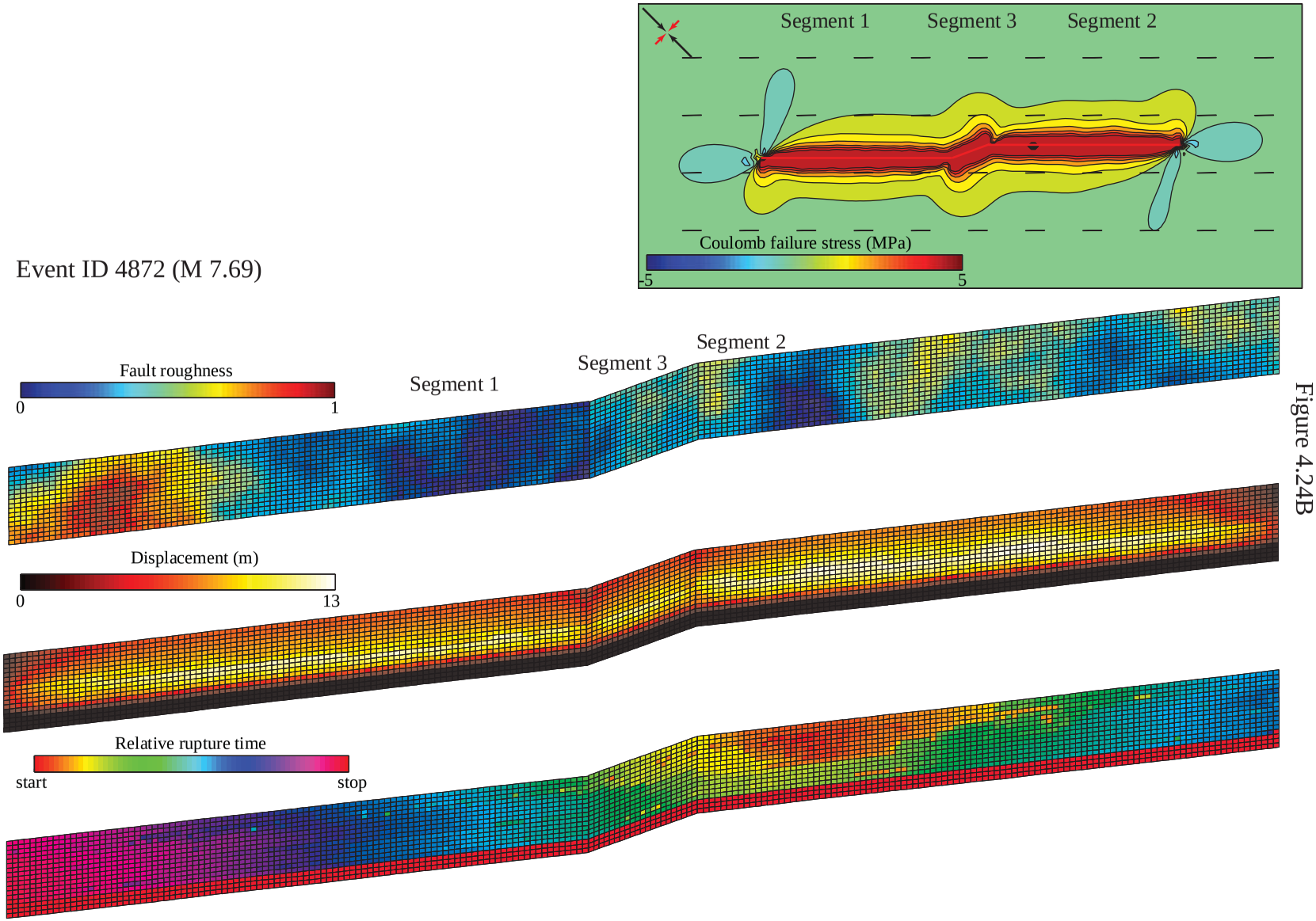
Segment 1
Segment 3
Segment 2
Coulomb failure stress (MPa)
-5
5
Event ID 4872 (M 7.69)
Fault roughness
0
1
Segment 1
Segment 3
Segment 2
Displacement (m)
0
13
Relative rupture time
start
stop

Figure 4.24B

Figure 4.24C

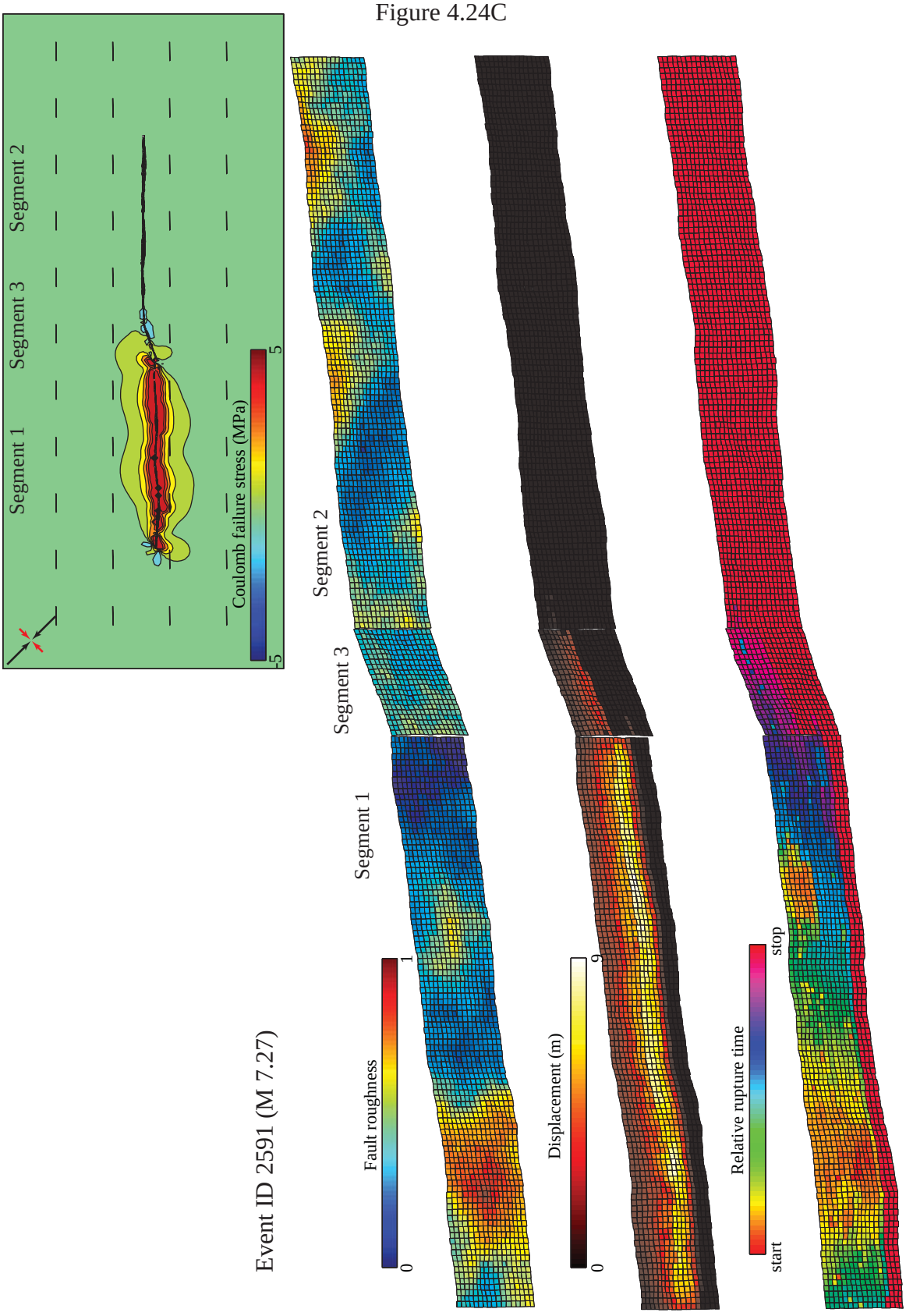
Segment 1
Segment 3
Segment 2
Coulomb failure stress (MPa)
5
-5
Segment 2
Segment 3
Segment 1
Fault roughness
1
0
Displacement (m)
9
0
Relative rupture time
stop
start
Event ID 2591 (M 7.27)

Figure 4.24D

20 km underlap, 5 km stepover

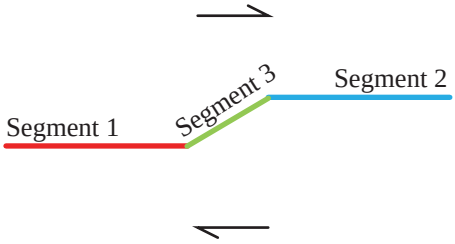

Smooth faults

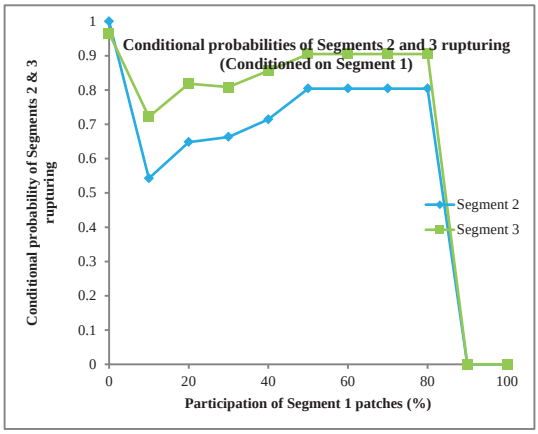

Rough faults

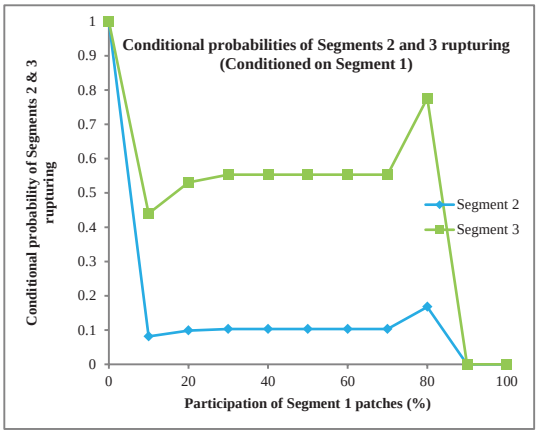

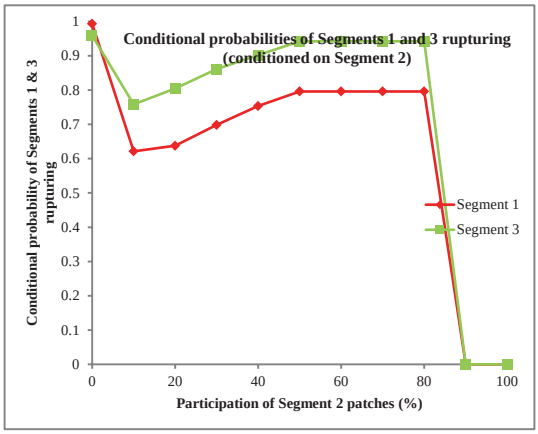

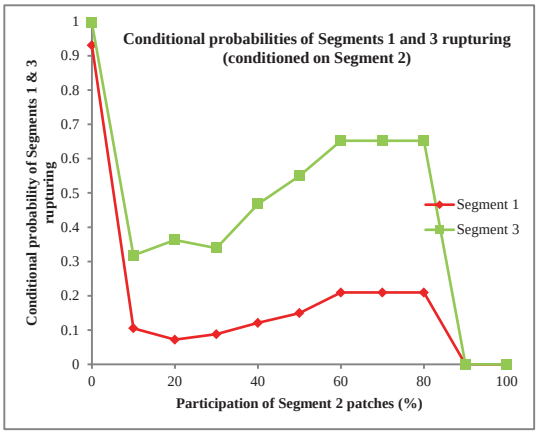

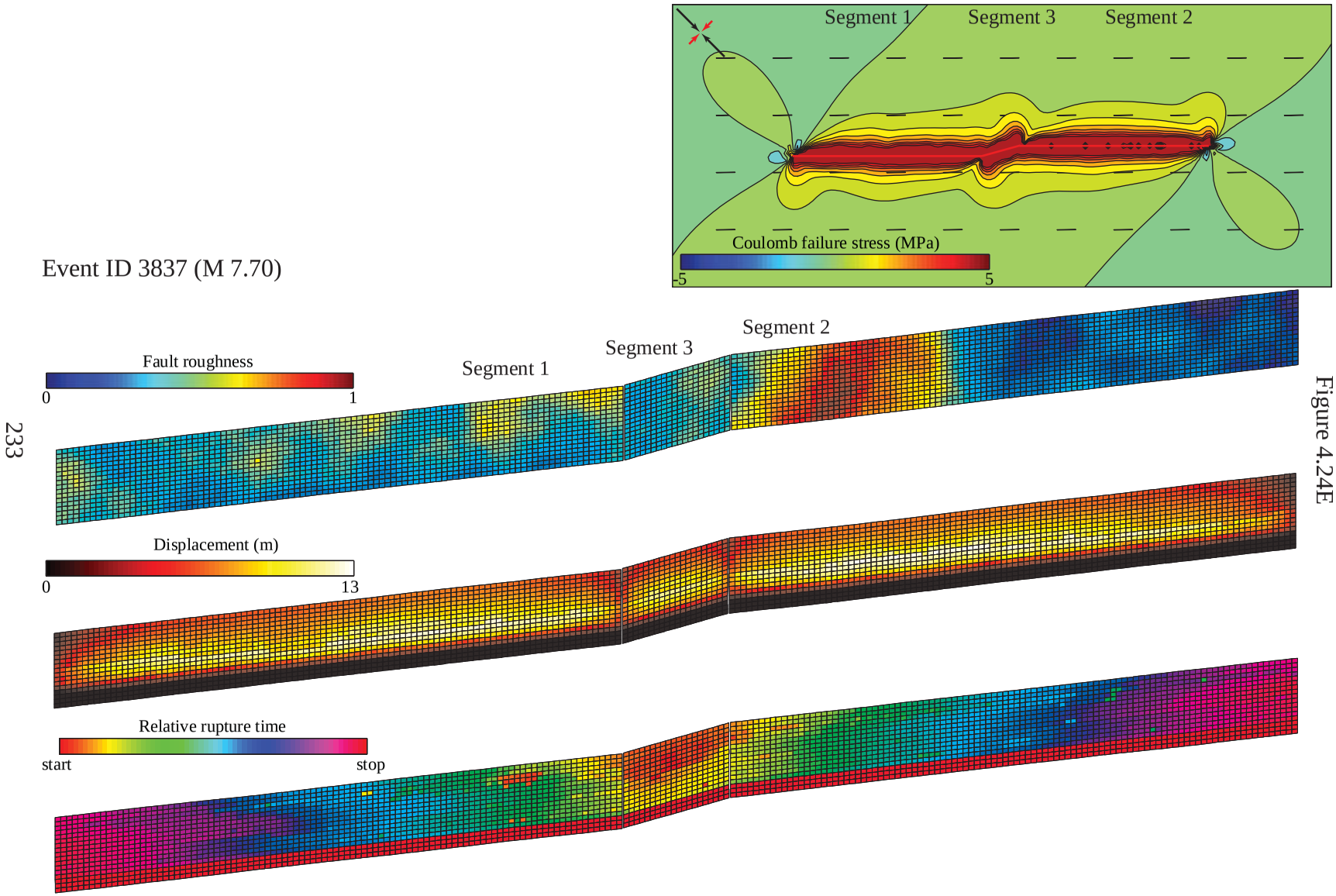
Segment 1
Segment 3
Segment 2
Coulomb failure stress (MPa)
-5
5
Event ID 3837 (M 7.70)
Fault roughness
0
1
Segment 1
Segment 3
Segment 2
Displacement (m)
0
13
Relative rupture time
start
stop

Figure 4.24E

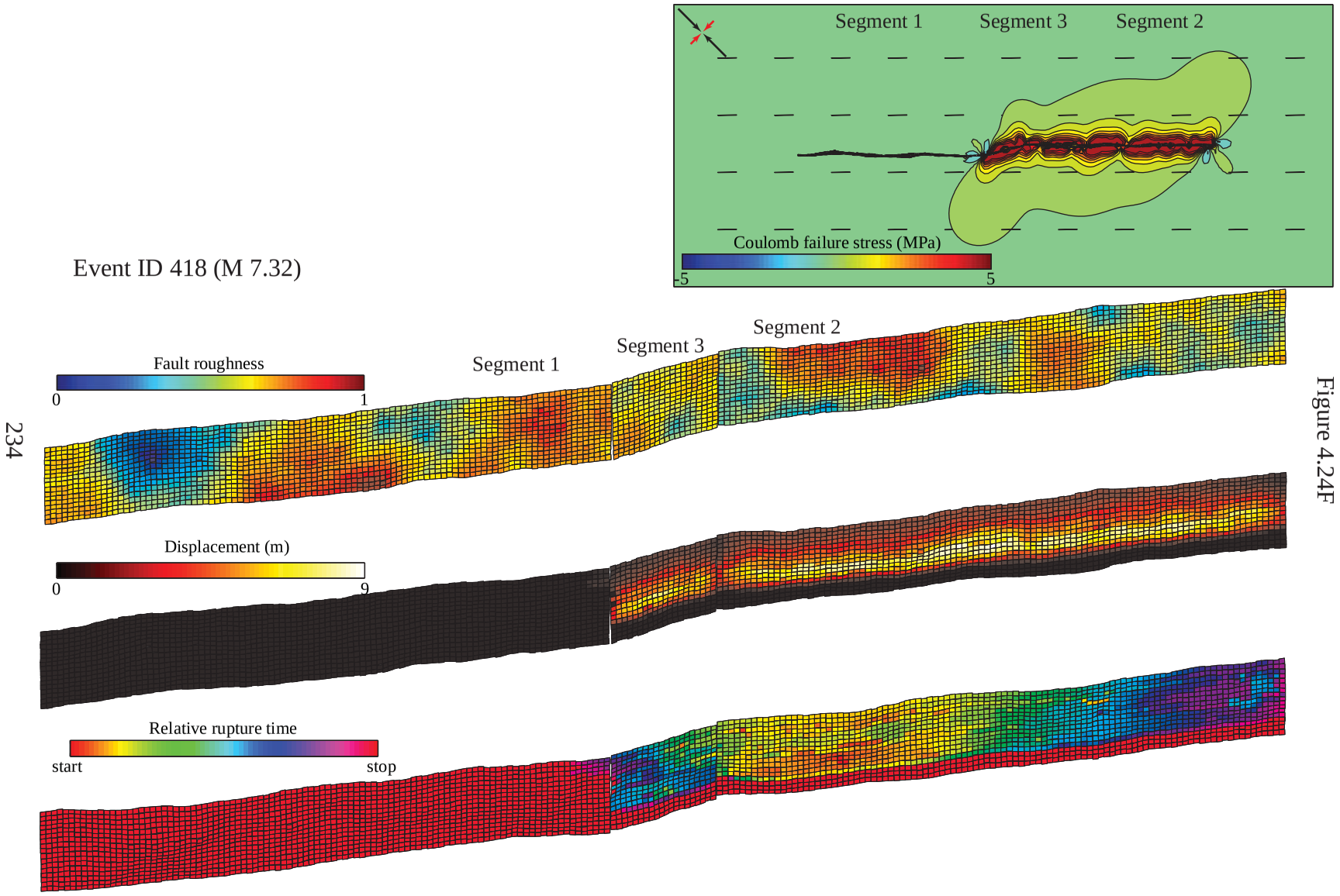
Segment 1
Segment 3
Segment 2
Coulomb failure stress (MPa)
-5
5
Event ID 418 (M 7.32)
Fault roughness
0
1
Segment 1
Segment 3
Segment 2
Displacement (m)
0
9
Relative rupture time
start
stop

Figure 4.24F

Figure 4.24G

20 km underlap, 2 km stepover

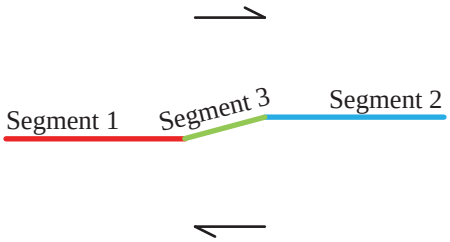

Smooth faults

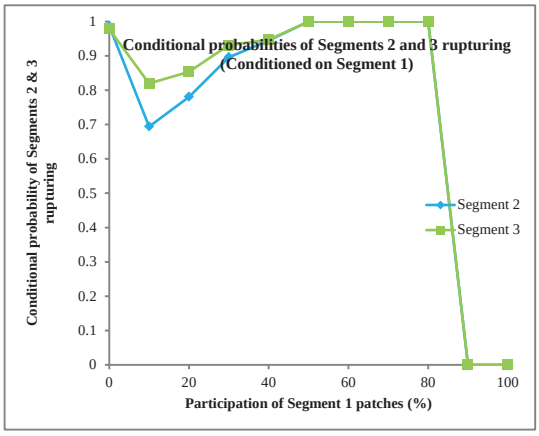

Rough faults

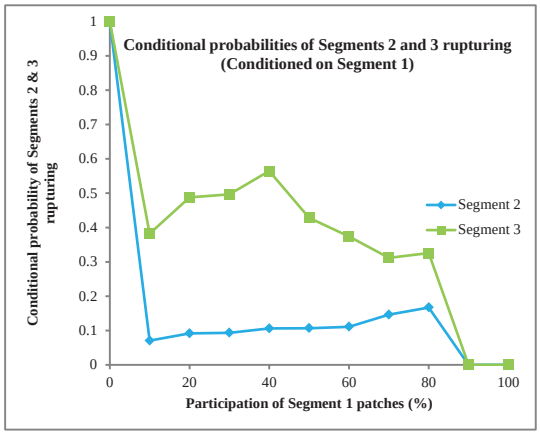

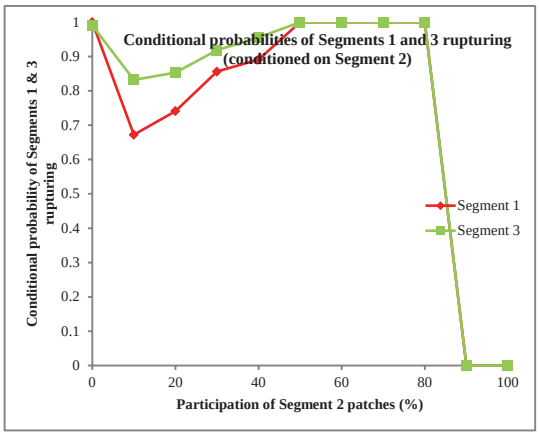

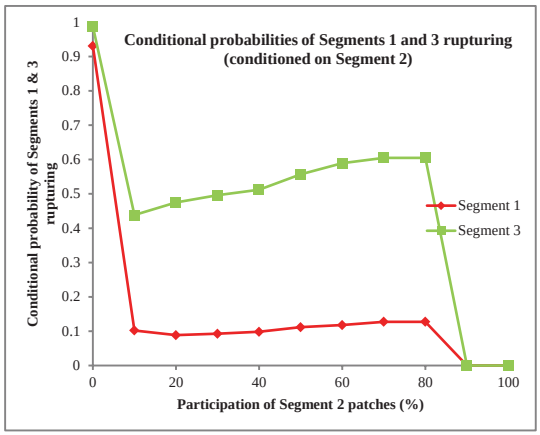

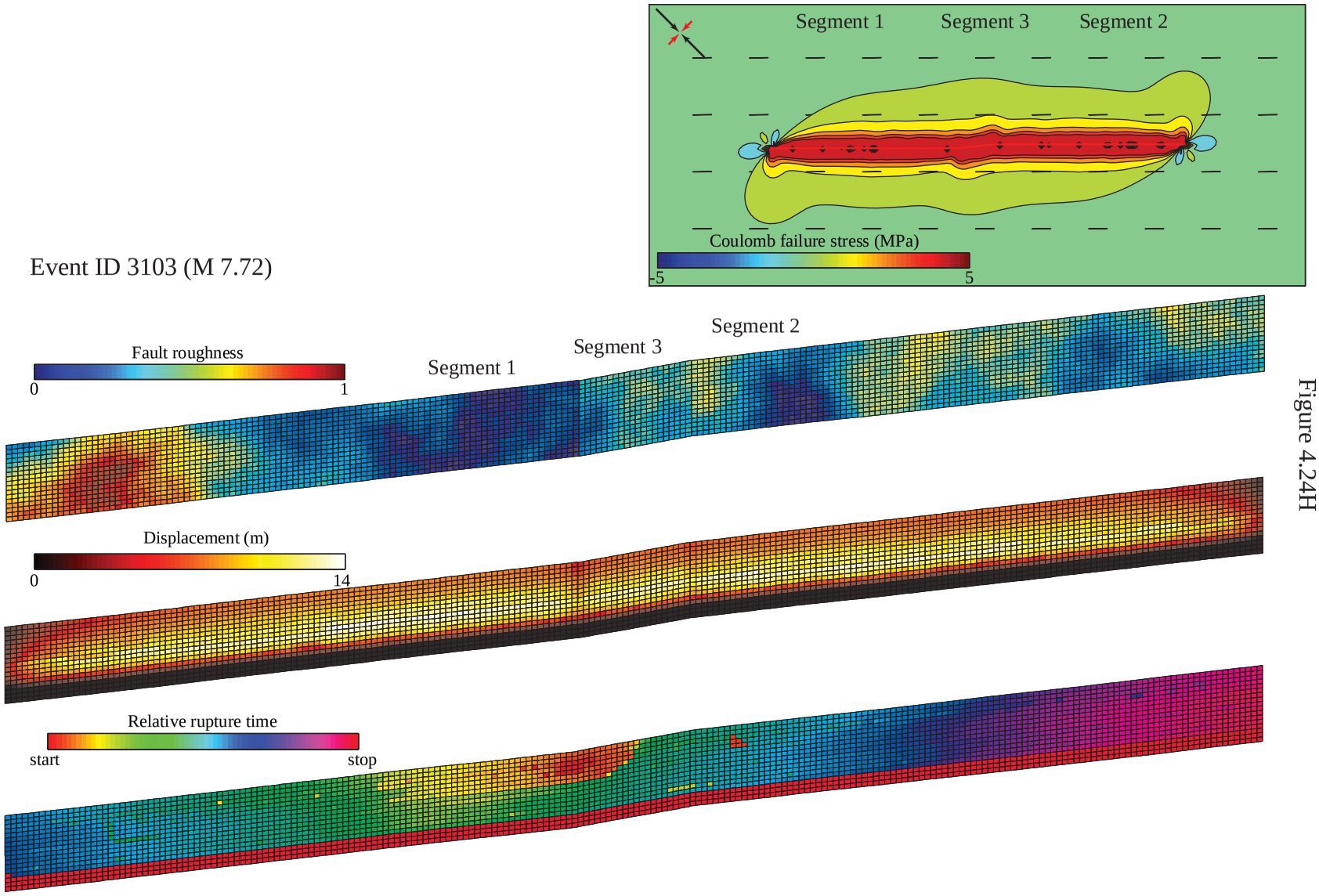
Segment 1
Segment 3
Segment 2
Coulomb failure stress (MPa)
-5
5
Event ID 3103 (M 7.72)
Fault roughness
0
1
Segment 1
Segment 3
Segment 2
Displacement (m)
0
14
Relative rupture time
start
stop

Figure 4.24H

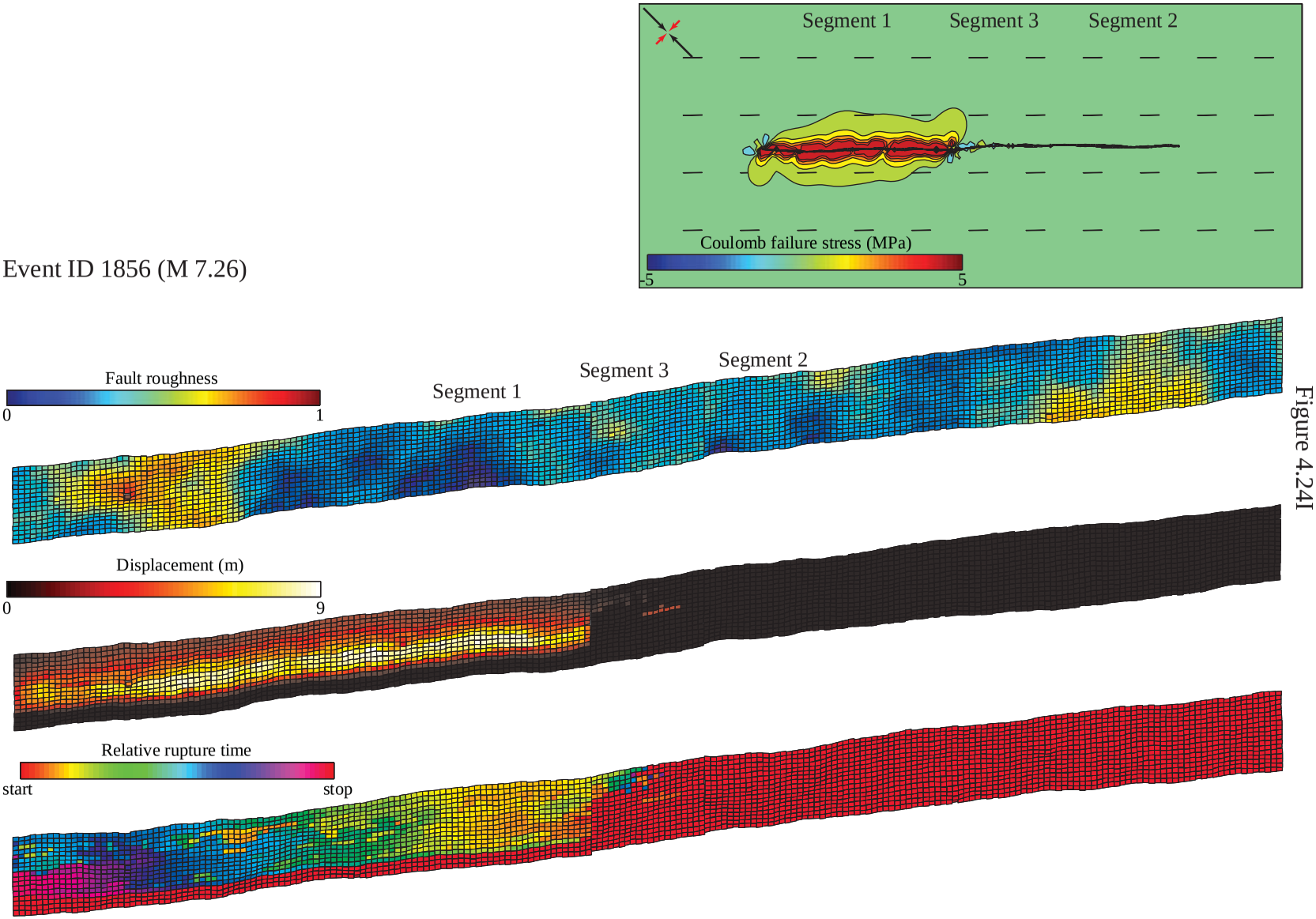
Segment 1
Segment 3
Segment 2
Coulomb failure stress (MPa)
-5
5
Event ID 1856 (M 7.26)
Fault roughness
0
1
Segment 1
Segment 3
Segment 2
Displacement (m)
0
9
Relative rupture time
start
stop

Figure 4.24l

Figure 4.25A

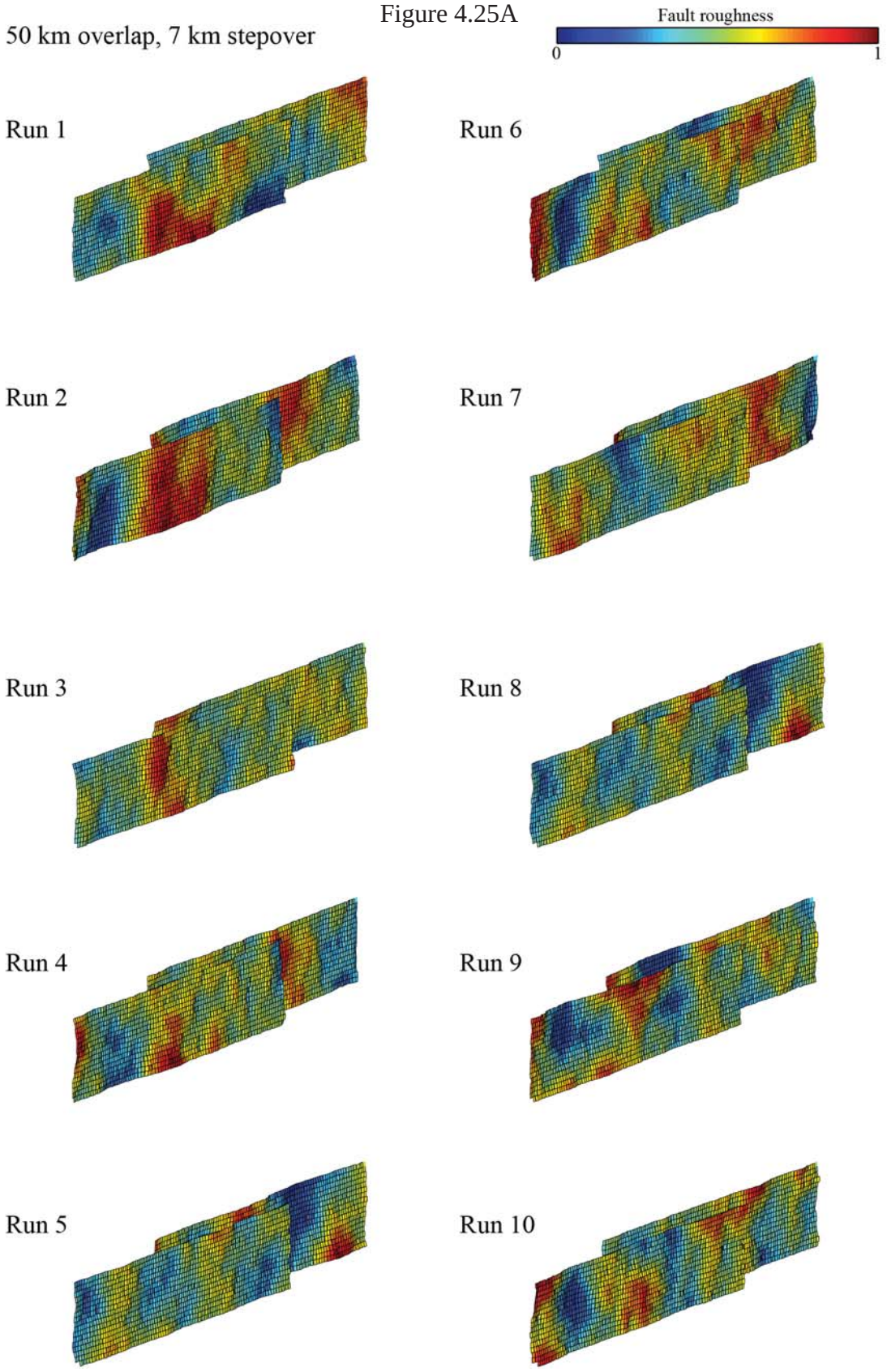
50 km overlap, 7 km stepover
Fault roughness
0
1
Run 1
Run 6
Run 2
Run 7
Run 3
Run 8
Run 4
Run 9
Run 5
Run 10

Figure 4.25B

50 km overlap, 7 km stepover

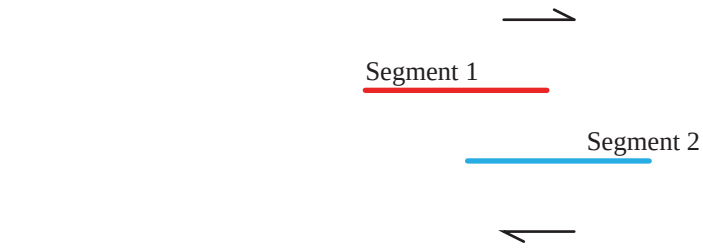

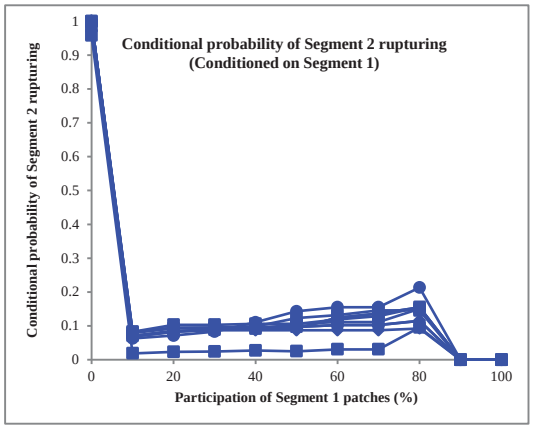

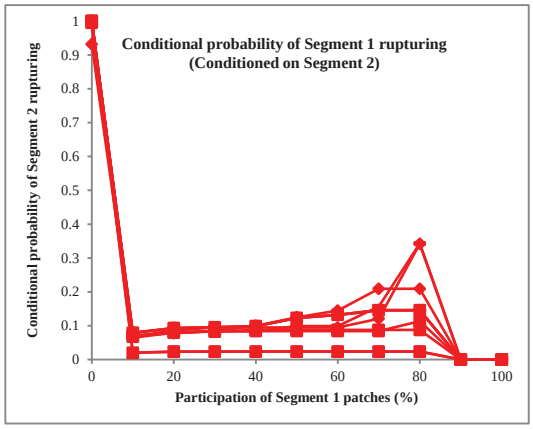

Figure 4.25C

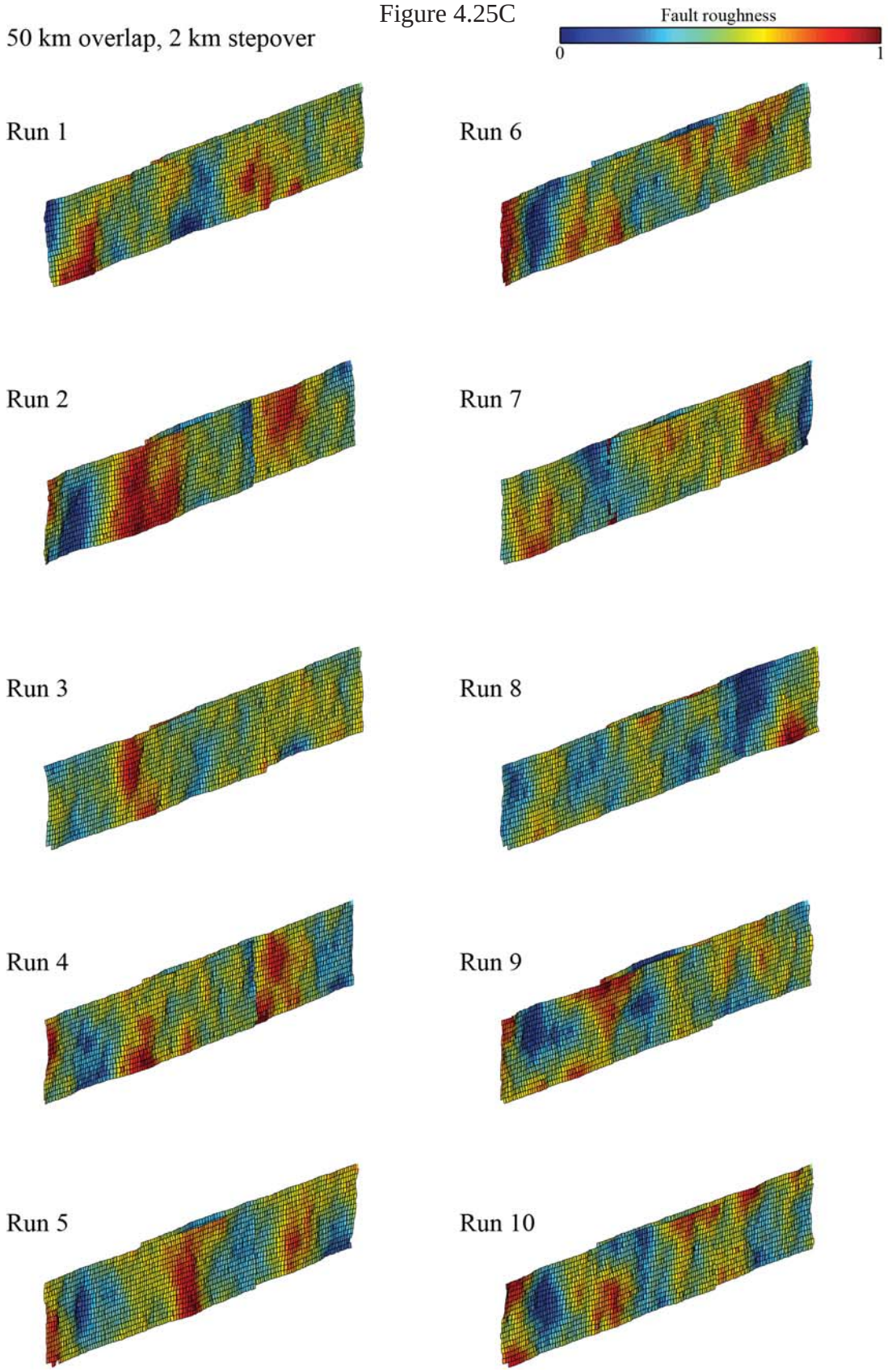
50 km overlap, 2 km stepover
Fault roughness
0
1
Run 1
Run 6
Run 2
Run 7
Run 3
Run 8
Run 4
Run 9
Run 5
Run 10

Figure 4.25D

50 km underlap, 2 km stepover

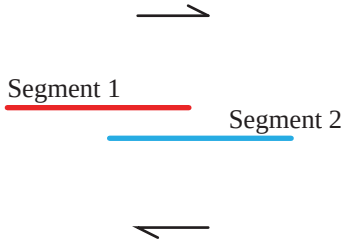

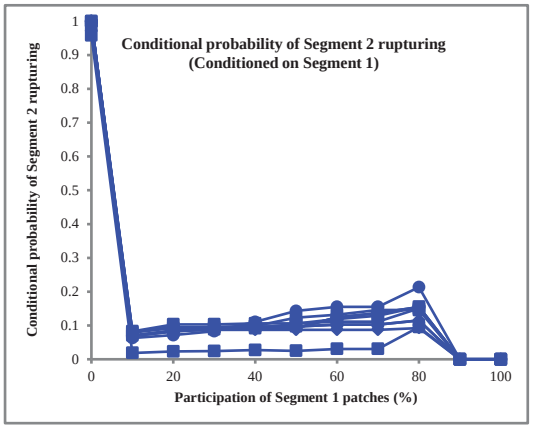

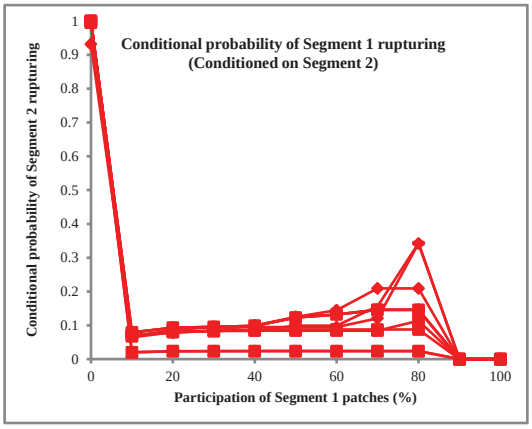

Figure 4.26A

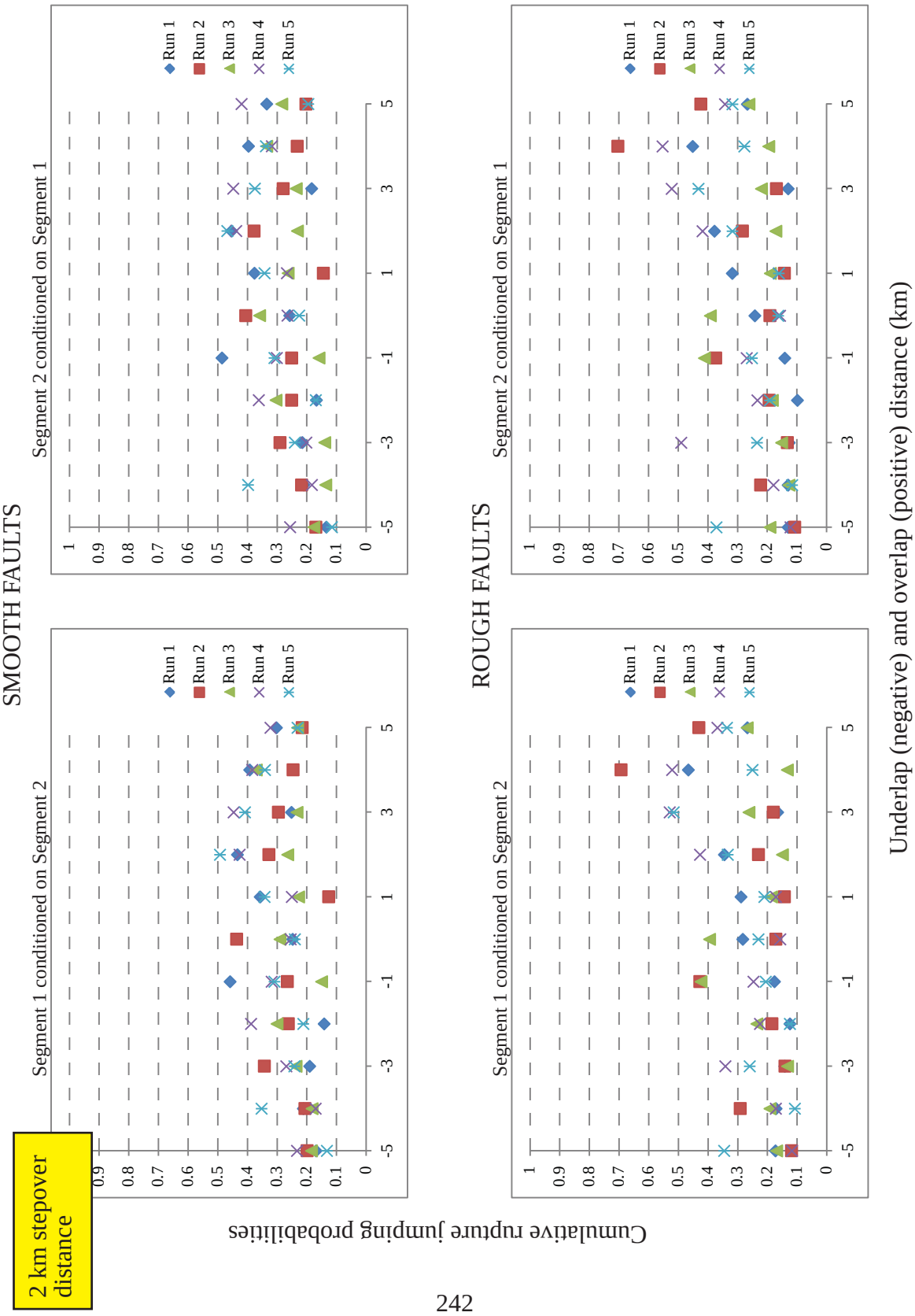
2 km stepover distance
SMOOTH FAULTS
ROUGH FAULTS
Segment 1 conditioned on Segment 2
Segment 2 conditioned on Segment 1
Run 1
Run 2
Run 3
Run 4
Run 5
Cumulative rupture jumping probabilities
Underlap (negative) and overlap (positive) distance (km)

Figure 4.26B

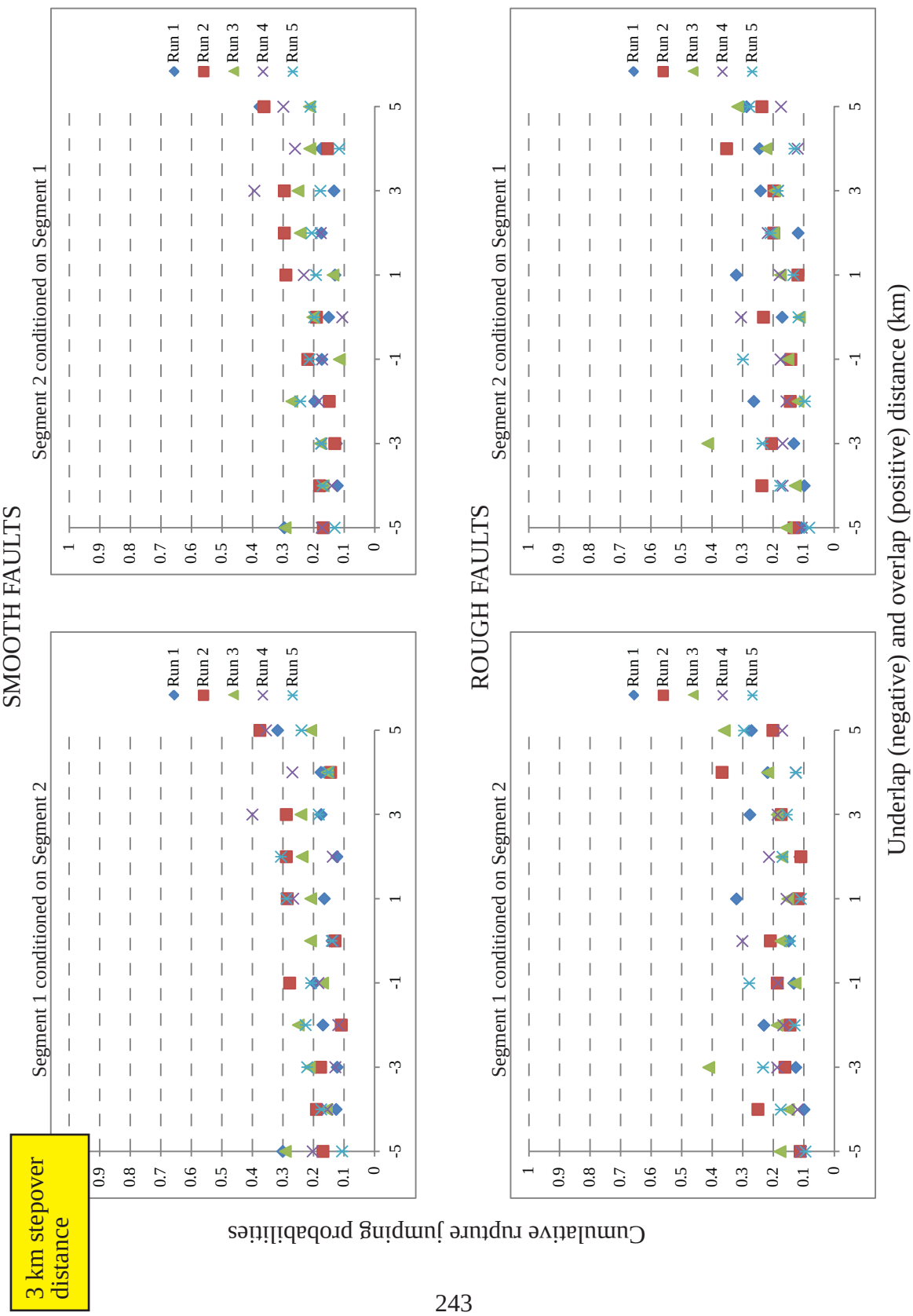
3 km stepover distance
SMOOTH FAULTS
ROUGH FAULTS
Segment 1 conditioned on Segment 2
Segment 2 conditioned on Segment 1
Run 1
Run 2
Run 3
Run 4
Run 5
Cumulative rupture jumping probabilities
Underlap (negative) and overlap (positive) distance (km)

4 km stepover distance

SMOOTH FAULTS

Segment 1 conditioned on Segment 2

Segment 2 conditioned on Segment 1

ROUGH FAULTS

Segment 1 conditioned on Segment 2

Segment 2 conditioned on Segment 1

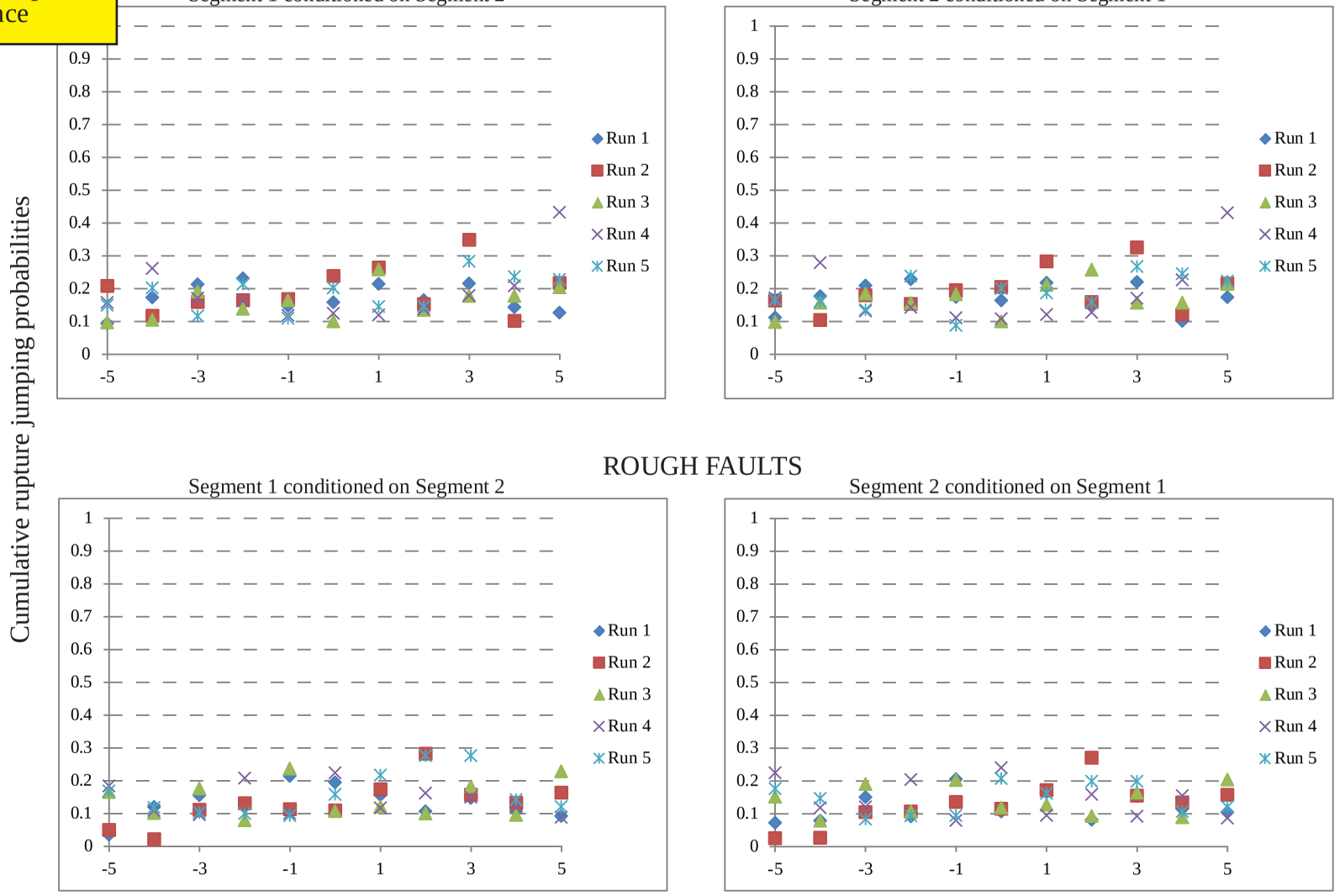

Figure 4.26C

Figure 4.27

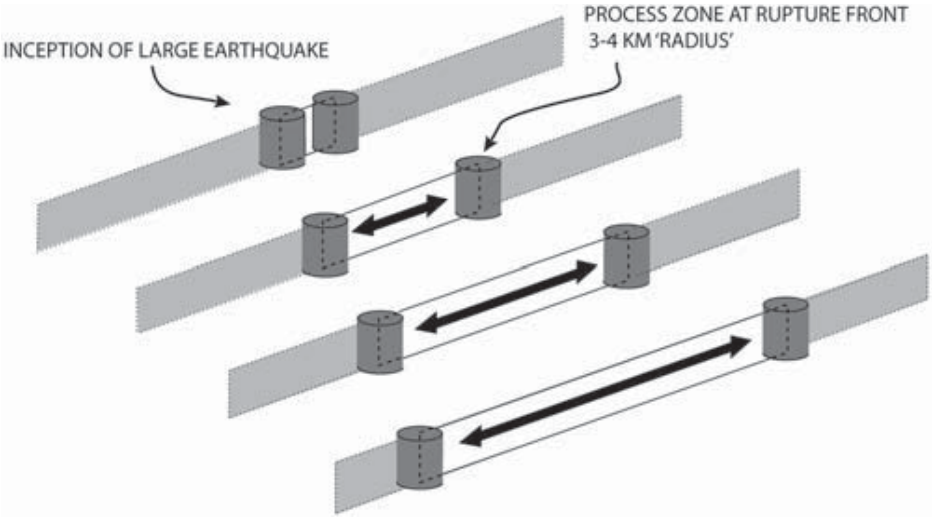
INCEPTION OF LARGE EARTHQUAKE
PROCESS ZONE AT RUPTURE FRONT
3-4 KM 'RADIUS'

Figure 4.28

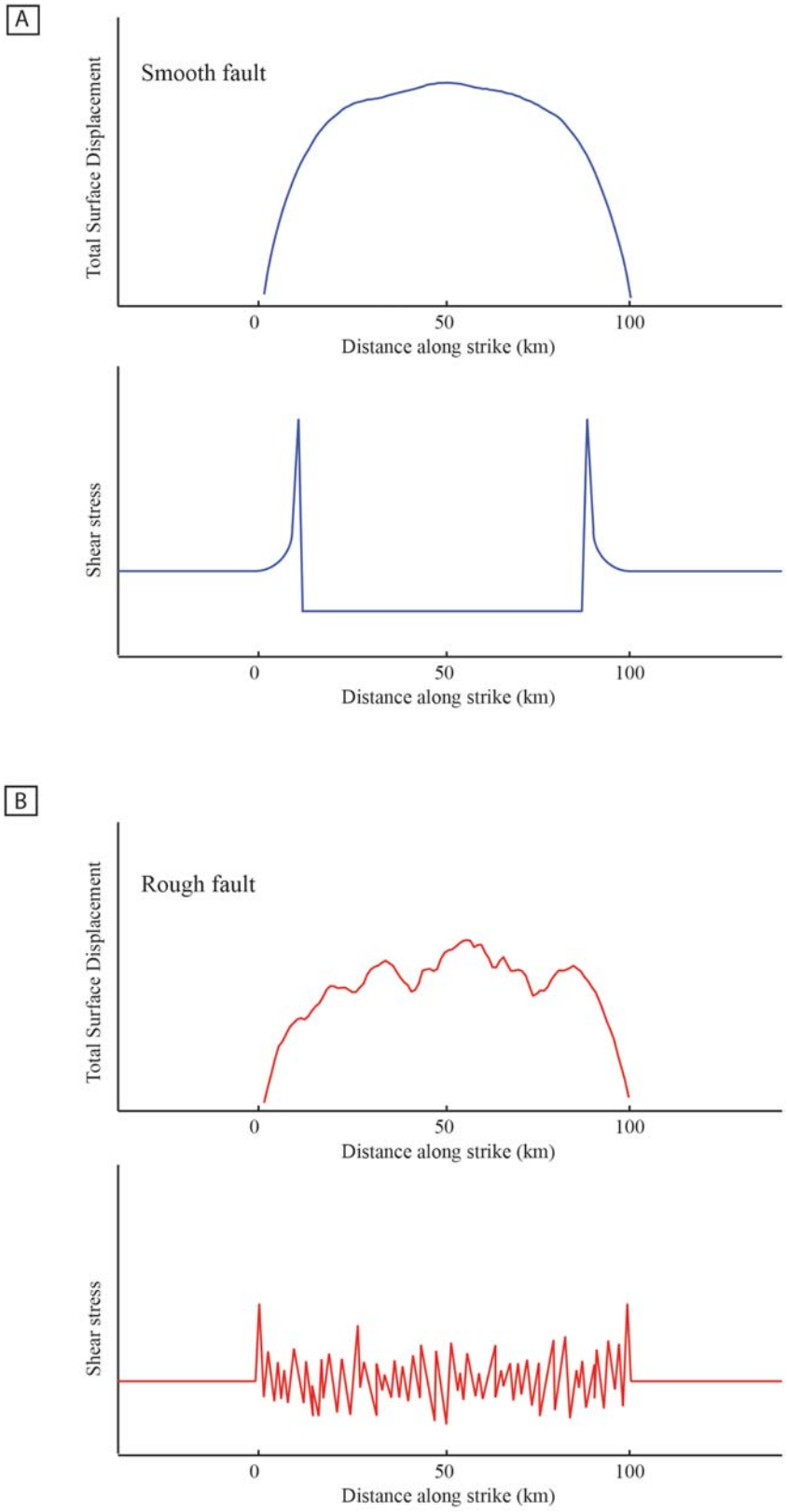
A
Smooth fault
Total Surface Displacement
0
50
100
Distance along strike (km)
Shear stress
0
50
100
Distance along strike (km)
B
Rough fault
Total Surface Displacement
0
50
100
Distance along strike (km)
Shear stress
0
50
100
Distance along strike (km)

Figure 4.29

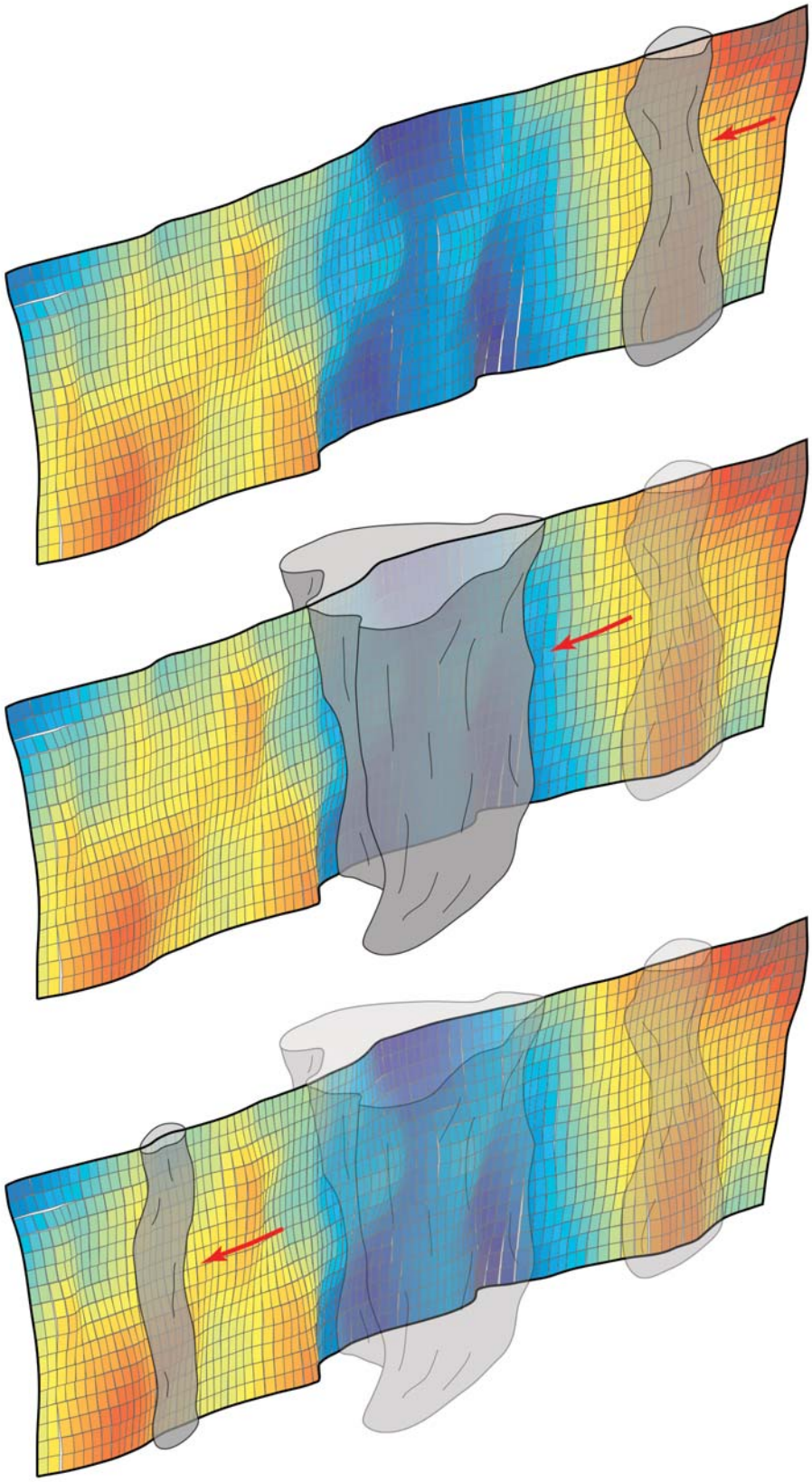

TABLES

Rupture probability conditioned on Segment 1

Minimum participation level of Segment 1: 70% of seismogenic patches

Event ID	Participation probability of Segment 1	Participation probability of Segment 2
1	0.73	0.30
2	0.93	0.12
3	0.78	0.75
4	0.81	0.53
5	0.96	0.23
...	...	...
Sum of participation probabilities for entire earthquake record	4.21	1.93
Normalized participation probability (conditioned on Segment 1)	1.00	0.46

This means that every time a rupture occurs on Segment 1 that activates at least 70% of its patches, Segment 2 has a 46% chance of participating in the same rupture.

Rupture probability conditioned on Segment 2

Minimum participation level of Segment 2: 70% of seismogenic patches

Event ID	Participation probability of Segment 1	Participation probability of Segment 2
1	0.42	0.90
2	0.20	0.76
3	0.71	0.82
4	0.30	0.71
5	0.27	0.77
...	...	...
Sum of participation probabilities for entire earthquake record	1.90	3.96
Normalized participation probability (conditioned on Segment 2)	0.48	1.00

This means that every time a rupture occurs on Segment 2 that activates at least 70% of its patches, Segment 1 has a 48% chance of participating in the same rupture.

Table 4.1. A worked example of how rupture jumping probabilities are calculated. Rupture jumping probabilities in the left table are conditioned on Segment 1 and mean that every time a rupture occurs on Segment 1 that activates at least 70% of its patches, Segment 2 has a 46% chance of participating in the same rupture. The right table shows rupture jumping probabilities that are conditioned on Segment two and mean that every time a rupture occurs on Segment 2 that activates at least 70% of its patches, the rupture has a 48% chance of jumping to Segment 1.

REFERENCES

Aochi, H., Madariaga, R., and Fukuyama, F., 2002, Effect of normal stress during rupture propagation along nonplanar faults: Journal of Geophysical Research - Solid Earth, v. 107, no. B2, p. 2038.

Beeler, N. M., Tullis, T. E., and Weeks, J. D., 1994, The roles of time and displacement in the evolution effect in rock friction: Geophysical Research Letters, v. 21, p. 1987-1990.

Biasi, G. P., and Weldon, R. J., 2006, Estimating surface rupture length and magnitude of paleoearthquakes from point measurements of rupture displacement: Bulletin of the Seismological Society of America, v. 96, no. 5, p. 1612-1623.

Bistacchi, A., Griffith, W. A., Smith, S. A. F., Di Toro, G., Jones, R., and Nielsen, S., 2011, Fault Roughness at Seismogenic Depths from LIDAR and Photogrammetric Analysis: Pure and Applied Geophysics, v. 168, no. 12, p. 2345-2363.

Blanpied, M. L., Lockner, D. A., and Byerlee, J. D., 1991, Fault stability inferred from granite sliding experiments at hydrothermal conditions: Geophysical Research Letters, v. 18, no. 4, p. 609-612.

Burbank, D. W., and Anderson, R. S., 2001, Tectonic geomorphology, Malden, Mass, Blackwell Science, v. Book, Whole.

Burgmann, R., Pollard, D. D., and Martel, S. J., 1994, Slip distributions on faults: effects of stress gradients, inelastic deformation, heterogeneous host-rock stiffness, and fault interaction: Journal of Structural Geology, v. 16, p. 1675-1690.

Chang, S., Avouac, J., Barbot, S., and Lee, J., 2013, Spatially variable fault friction derived from dynamic modeling of aseismic afterslip due to the 2004 Parkfield earthquake: Journal of Geophysical Research, v. 118, p. 1-17.

Chang, W. L., and Smith, R. B., 2002, Integrated seismic-hazard analysis of the Wasatch Front, Utah: Bulletin of the Seismological Society of America, v. 92, p. 1902-1922.

Densmore, A. L., Ellis, M. A., and Anderson, R. S., 1998, Landsliding and the evolution of normal-fault-bounded mountains: Journal of Geophysical Research-Solid Earth, v. 103, no. B7, p. 15203-15219.

Dieterich, J. H., and Kilgore, B. D., 1994, Direct observation of frictional contacts: new insights for state dependent properties: Pure and Applied Geophysics, v. 143, p. 283-302.

Dieterich, J. H., and Smith, D. E., 2009, Nonplanar Faults: Mechanics of Slip and Off-fault Damage: Pure and Applied Geophysics, v. 166, p. 1799-1815.

Duan, B., and Oglesby, D. D., 2006, Heterogeneous fault stresses from previous earthquakes and the effect on dynamics of parallel strike-slip faults: Journal of Geophysical Research - Solid Earth, v. 111, no. B5, p. B05309.

Dunham, E. M., Belanger, D., Cong, L., and Kozdon, J. E., 2011, Earthquake Ruptures with Strongly Rate-Weakening Friction and Off-Fault Plasticity, Part 2: Nonplanar Faults: Bulletin of the Seismological Society of America, v. 101, no. 5, p. 2308-2322.

Ferrill, D. A., and Morris, A. P., 2001, Displacement gradient and deformation in normal fault systems: Journal of Structural Geology, v. 23, p. 619-638.

Field, E. H., Biasi, G. P., Bird, P., Dawson, T. E., Felzer, K. R., Jackson, D. D., Johnson, K. M., Jordan, T. H., Madden, C., Michael, A. J., Milner, K. R., Page, M. T., Parsons, T., Powers, P. M., Shaw, B. E., Thatcher, W. R., Weldon, R. J., and Zeng, Y., 2013, Uniform California Earthquake Rupture Forecast, Version 3 (UCERF3)—The Time-Independent Model: U.S. Geological Survey Open-File Report 2013-1165.

Gualandi, A., Serpelloni, E., and Belardinelli, M., 2014, Space–time evolution of crustal deformation related to the Mw 6.3, 2009 L'Aquila earthquake (central Italy) from principal component analysis inversion of GPS position time-series: Geophysical Journal International.

Haddad, D. E., Madden, C. M., Salisbury, J. B., Arrowsmith, J. R., and Weldon, R. J., 2011, LiDAR-derived measurements of slip in the most recent ground-rupturing earthquakes along elements of the San Andreas fault system: SCEC Proceedings and Abstracts, v. 21.

Harris, R. A., Archuleta, R. J., and Day, S. M., 1991, Fault steps and the dynamic rupture process -- 2-D numerical simulations of a spontaneously propagating shear fracture: Geophysical Research Letters, v. 18, no. 5, p. 893-896.

Harris, R. A., and Day, S. M., 1993, Dynamics of fault interaction: Parallel strike-slip faults: Journal of Geophysical Research-Solid Earth, v. 98, no. B3, p. 4461-4472.

Jaeger, J. C., Cook, N. G. W., and Zimmerman, R. W., 2007, Fundamentals of rock mechanics, Malden, Wiley-Blackwell, 488 p.

Kame, N., Rice, J. R., and Dmowska, R., 2003, Effects of prestress state and rupture velocity on dynamic fault branching: Journal of Geophysical Research - Solid Earth, v. 108, no. B5, p. 2265.

Kaneko, Y., Fialko, Y., Sandwell, D., Tong, X., and Furuya, M., 2013, Interseismic deformation and creep along the central section of the North Anatolian Fault (Turkey): InSAR observations and implications for rate-and-state friction properties: Journal of Geophysical Research, v. 118, p. 1-15.

Kase, Y., and Day, S. M., 2006, Spontaneous rupture processes on a bending fault: Geophysical Research Letters, v. 33, no. 10, p. L10302.

Lozos, J. C., Oglesby, D. D., Brune, J. N., and Olsen, K. B., 2012, Small intermediate fault segments can either aid or hinder rupture propagation at stepovers: Geophysical Research Letters, v. 39, no. L18305.

Madden, C. M., Arrowsmith, J. R., Haddad, D. E., Salisbury, J. B., and Weldon, R. J., 2011, Compilation of slip in the last earthquake data for high slip rate faults in California for input into slip-dependent rupture forecast: SCEC Proceedings and Abstracts, v. 21.

Marone, C., Raleigh, C. B., and Scholz, C. H., 1990, Frictional behavior and constitutive modelling of simulated fault gouge: Journal of Geophysical Research, v. 95, p. 7007-7025.

Moss, R. E., Stanton, K. V., and Buelna, M. I., 2013, The Impact of Material Stiffness on the Likelihood of Fault Rupture Propagating to the Ground Surface: Seismological Research Letters, v. 84, no. 3, p. 485-488.

Oglesby, D. D., 2008, Rupture termination and jump on parallel offset faults: Bulletin of the Seismological Society of America, v. 98, p. 440-447.

Oglesby, D. D., Day, S. M., Li, Y., and Vidale, J. E., 2003, The 1999 Hector Mine earthquake: The dynamics of a branched fault system: Bulletin of the Seismological Society of America, v. 93, p. 2459-2476.

Okada, Y., 1992, Internal deformation due to shear and tensile faults in a half-space: Bulletin of the Seismological Society of America, v. 82, no. 2, p. 1018-1040.

Oskin, M. E., Arrowsmith, J. R., Hinojosa, A. C., Elliott, A. J., Fletcher, J. M., Fielding, E. J., Gold, P. O., Garcia, J. J. G., Hudnut, K. W., Liu-Zheng, J., and Teran, O. J., 2012, Near-field deformation from the El Mayor-Cucupah earthquake revealed by differential LiDAR: Science, v. 335, no. 702.

Parsons, T., Field, E. H., Page, M. T., and Milner, K., 2012, Possible Earthquake Rupture Connections on Mapped California Faults Ranked by Calculated Coulomb Linking Stresses: Bulletin of the Seismological Society of America, v. 102, no. 6, p. 2667-2676.

Pollard, D. D., and Fletcher, R. C., 2005, Fundamentals of structural geology, Cambridge, UK, Cambridge University Press, v. Book, Whole.

Pollitz, F. F., 2012, ViscoSim Earthquake Simulator: Seismological Research Letters, v. 83, no. 6, p. 979-982.

Power, W., and Tullis, T., 1991, Euclidean and fractal models for the description of rock surface roughness J Geophys Res V96, NB1, Jan 1991, P415–424: International Journal of Rock Mechanics and Mining Sciences & Geomechanics Abstracts, v. 28, no. 6, p. A344-A344.

Richards-Dinger, K., and Dieterich, J. H., 2012, RSQSim Earthquake Simulator: Seismological Research Letters, v. 83, no. 6, p. 983-990.

Ruina, A. L., 1983, Slip instability and state variable friction laws: Journal of Geophysical Research, v. 88, p. 10359-10370.

Sachs, M. K., Heien, E. M., Turcotte, D. L., Yikilmaz, M. B., Rundle, J. B., and Kellogg, L. H., 2012, Virtual California Earthquake Simulator: Seismological Research Letters, v. 83, no. 6, p. 973-978.

Salyards, S. L., Sieh, K., and Kirschvink, J. L., 1992, Paleomagnetic measurement of nonbrittle coseismic deformation across the San Andreas fault at Pallett Creek: Journal of Geophysical Research, v. 97, no. B9, p. 12457-12470.

Saucier, F., Humphreys, E., and Weldon, R., 1992, Stress near geometrically complex strike-slip faults: Application to the San Andreas fault at Cajon Pass, southern California: Journal of Geophysical Research-Solid Earth, v. 97, no. B4, p. 5081-5094.

Scholz, C. H., 2002, The mechanics of earthquakes and faulting, Cambridge, Cambridge Universiry Press, 496 p.

-, 2010, Large Earthquake Triggering, Clustering, and the Synchronization of Faults: Bulletin of the Seismological Society of America, v. 100, no. 3, p. 901-909.

Segall, P., 2010, Earthquake and volcano deformation, Princeton, Princeton University Press, v. Book, Whole.

Segall, P., and Pollard, D. D., 1980, Mechanics of discontinuous faults: Journal of Geophysical Research, v. 85, no. B8, p. 4337-4350.

Sibson, R. H., 1984, Roughness at the base of the seismogenic zone: contributing factors: Journal of Geophysical Research, v. 89, no. B7, p. 5791-5799.

Sylvester, A. G., 1999, Rifting, transpression, and neotectonics in the Central Mecca Hills, Salton Trough, Santa Barbara, University of California, Santa Barbara, 52 p.

Toda, S., Stein, R. S., Sevilgen, V., and Lin, J., 2011, Coulomb 3.3 Graphic-rich deformation and stress-change software for earthquake, tectonic, and volcano research and teaching—user guide: U.S. Geological Survey Open-File Report 2011-1060, p. 63.

Tullis, T. E., Sachs, M. K., Turcotte, D. L., Ward, S. N., Yikilmaz, M. B., Richards-Dinger, K., Barall, M., Dieterich, J. H., Field, E. H., Heien, E. M., Kellogg, L. H., Pollitz, F. F., and Rundle, J. B., 2012, Generic Earthquake Simulator: Seismological Research Letters, v. 83, no. 6, p. 959-963.

Vedder, J. G., and Wallace, R. E., 1970, The San Andreas fault in the Carrizo Plain–Temblor Range region, California, in Crowell, J. C., ed., San Andreas Fault in Southern California: A Guide to San Andreas Fault from Mexico to Carrizo Plain, Volume 118, California Division of Mines and Geology Special Report, p. 241-250.

Ward, S. N., 2012, ALLCAL Earthquake Simulator: Seismological Research Letters, v. 83, no. 6, p. 964-972.

Wesnousky, S. G., 1988, Seismological and structural evolution of strike-slip faults: Nature, v. 335, no. 6188, p. 340-342.

-, 2006, Predicting the endpoints of earthquake ruptures: Nature, v. 444, no. 7117, p. 358-360.

Wesnousky, S. G., 2008, Displacement and Geometrical Characteristics of Earthquake Surface Ruptures: Issues and Implications for Seismic-Hazard Analysis and the Process of Earthquake Rupture: Bulletin of the Seismological Society of America, v. 98, no. 4, p. 1609-1632.

Willemse, E. J. M., 1997, Segmented normal faults: Correspondence between three dimensional mechanical models and field data: Journal of Geophysical Research-Solid Earth, v. 102, no. B1, p. 675-692.

Willemse, E. J. M., Pollard, D. D., and Aydin, A., 1996, Three-dimensional analyses of slip distributions on normal fault arrays with consequences for fault scaling: Journal of Structural Geology, v. 18, no. 2, p. 295-309.

Zielke, O., 2009, How fault geometric complexity and frictional properties affect seismic fault behavior and accumulation of slip along strike-slip faults, PhD: Arizona State University, 315 p.

Zielke, O., and Arrowsmith, J. R., 2008, Depth variation of coseismic stress drop explains bimodal earthquake magnitude-frequency distribution: Geophysical Research Letters, v. 35, no. 24.

Chapter 5

FAULT ROUGHNESS AND FRICTIONAL CONTROLS ON SURFACE SLIP: IMPLICATIONS FOR FAULT STRENGTH AND PALEOSEISMIC INTERPRETATIONS

ABSTRACT

Variations in geologic slip rates determined by paleoseismic means can have profound impacts on the seismic hazards estimated for seismogenic faults. The analysis of slip rates and slip per event in an aggregate manner is commonly used to infer fault interaction and its control on earthquake recurrence and spatiotemporal clustering. Furthermore, this approach is used to explain discrepancies between geodetic and geologic observations of crustal deformation rates. What is commonly ignored by this aggregate approach are the effects of the physical properties of faults such as deviation from planarity and complex frictional behavior, both of which are related to the fault's structural maturity. In this chapter, I use the earthquake simulator FIMozFric (Zielke and Arrowsmith, 2008) to explore the effects of fault roughness and friction on surface slip distributions, slip at a point, and earthquake clustering. I take two examples from California: the Hayward-Calaveras fault system and the Garlock fault zone. Simulations of the Hayward-Calaveras faults incorporated complex distributions of velocity-strengthening/weakening friction to model the effects of heterogeneous fault creep on surface deformation and rupture jumping probabilities. For the Garlock fault, lidar-derived offset measurements were made and analyzed to investigate variations in slip magnitude along strike. Additionally, two simulations were carried out on the Garlock fault to investigate the effects of fault roughness and variable tectonic loading rates on

slip per event and earthquake clustering. Earthquake simulations for the Hayward-Calaveras faults showed that irregular surface slip distributions are directly related to the distribution of creep along both faults. Furthermore, the Hayward and Calaveras faults behaved as an interacting system where the coseismic participation of one fault was controlled by events that occurred along the other. Simulated surface slip distributions for the Garlock fault were complex due to local asperities along the fault surface. Spatiotemporal clustering of slip magnitudes at select points along the Garlock fault indicate that fault roughness plays a role in controlling the local slip rate. This may explain discrepancies between geodetically and geologically derived slip rates along with other explanations such as phase locking of earthquake cycles. My results caution against the aggregate interpretation of paleoseismically derived slip rates or surface slip distributions without first understanding the structural complexity that is inherent to any fault under investigation.

INTRODUCTION

Earthquakes that are large enough ($M_w \geq 7$) to break the topographic surface provide important insights into coseismic processes that occur at seismogenic depths and thus seismic hazards associated with active faults. As part of our efforts to understand these seismic hazards, it is now standard practice to quantify on-fault coseismic deformation and link individual earthquake events to their temporal expression via paleoseismic trenching (McCalpin, 2009). These datasets provide the fundamental building blocks for earthquake recurrence models (e.g., variable slip vs. uniform slip vs. characteristic earthquakes), which are commonly looked upon as models of fault behavior (e.g., Schwartz and Coppersmith, 1984). With enough of such datasets available for fault systems, a general understanding of the spatiotemporal patterns of strain accumulation and release rates can be achieved (e.g., Dolan et al., 2007; Scholz, 2010). However, when considering the available paleoseismically derived slip rates for some of the best-studied active faults, there exist discrepancies between slip rates determined at instrumental time scales (e.g., GPS, InSAR) and geologic timescales (e.g., the Holocene). Setting aside the possibility of misidentification of event horizons or dating errors at paleoseismic sites, several reasons have been used to explain this discrepancy. These include changes in flow rates of the upper mantle over millennial timescales (e.g., Pollitz et al., 2001; Savage et al., 2003), whether the stress states of faults are either in or out of phase with each other (Scholz, 2010). Kinematically based explanations suggest earthquake occurrence as a function of mechanical fault interaction at regional scales (e.g., Dolan et al., 2007). Other explanations imply a feedback mechanism between seismic and aseismic portions of faults whereby large earthquakes that punch through the velocity-

strengthening base of the seismogenic zone increase basal creep rates, which increases interseismic stress loading rates updip (e.g., Oskin et al., 2008).

In Chapter 4 I showed how the spatiotemporal clustering of earthquakes and thus slip rates are controlled by complex fault frictional properties. In this chapter, I expand upon this by showing that the discrepancy between geologic and geodetic crustal deformation rates can be simply explained by natural variations in fault roughness and the frictional complexities along faults. I apply the insights gained from Chapter 4 to two fault scenarios in California (Fig. 5.1). The first scenario explores the effects of fault strength and frictional complexities on the surface manifestation of earthquakes along the Hayward-Calaveras fault systems in northern California. The second scenario investigates the discrepancy between geologically and geodetically derived slip rates for the Garlock fault. I conclude this chapter by discussing the various implications that fault roughness and complex friction have on interpreting the paleoseismic records of seismogenic faults, and what this means in terms of estimating their associated seismic hazards.

METHODS

FIMozFric Earthquake Simulator

I use FIMozFric (Zielke and Arrowsmith, 2008; Zielke, 2009), which is a quasi-static earthquake simulator that incorporates the interaction of faults that are governed by complex friction laws. FIMozFric employs the 3D boundary element method and numerically resolves stresses and calculates strains due to slip along rectangular displacement discontinuities (faults). Faults are embedded in a mechanically homogeneous, isotropic, and linear-elastic halfspace (e.g., Okada, 1992; Toda et al.,

2011). Faults are discretized into 2 km x 2 km patches and assigned varying strikes and dips to simulate non planar surfaces. Each patch is also assigned dynamic and static coefficients of friction. The difference between these coefficients varies with depth in order to simulate laboratory-derived fault friction behavior. This is done by expanding upon the Coulomb friction law and implementing the depth/temperature dependency effects on fault friction. Laboratory friction experiments show that friction varies with slip velocity (rate dependence) and holding time (time since the last slip occurred on the slip interface) (e.g., Marone et al., 1990; Blanpied et al., 1991; Beeler et al., 1994; Dieterich and Kilgore, 1994). This resulted in the formulation of the rate- and state-friction law (Ruina, 1983),

$$\tau = \sigma_n \left[\mu_0 + a \ln \frac{V}{V_0} + b \ln \frac{V_0 \theta}{D_c}\right], \tag{4.1}$$

where τ is the shear stress, σ_n is the normal stress, μ_0 is the initial coefficient of friction, V is the sliding velocity, V_0 is the initial sliding velocity, θ is the state variable, D_c is the critical slip distance, and a, b are experimentally determined constants. Velocity-weakening frictional behavior occurs when $[a - b] < 0$ and promotes unstable sliding (earthquakes) whereas velocity-strengthening behavior promotes stable sliding (creep) and occurs when $[a - b] > 0$. In FIMozFric, each fault patch is assigned a $[a - b]$ value to determine its frictional behavior during simulations (Zielke and Arrowsmith, 2008; Zielke, 2009). FIMozFric also allows the distribution of velocity-strengthening and velocity-weakening patches to be customized so that the effects of realistic fault properties can be investigated (e.g., shallow fault creep).

The seismic cycle in FIMozFric is divded into interseismic and coseismic stages by iteratively evaluating the current state of stress on all patches given their friction

coefficients and the tectonic loading rate (Zielke and Arrowsmith, 2008; Zielke, 2009). During the interseismic stage, the tectonic loading mechanism incrementally increases shear tractions until they exceed the static friction strength of a patch. The shear traction and friction strength of each patch is calculated at every interseismic time increment. FIMozFric enters the coseismic stage if shear tractions exceed the frictional strength of at least one patch. When this happens, the tectonic loading mechanism is halted and the static friction coefficients of all patches that failed are converted to dynamic friction coefficients. Shear tractions are then released via in-plane slip. Displacements due to slip along patches are calculated using Okada's (1992) formulations, which alter the local stresses in the volume surrounding the failed patches. These altered stresses may induce further coseismic stresses on neighboring patches and may cause them to fail too. Thus an earthquake is born and propagates along the fault until all shear tractions are released and fall below the dynamic strength of activated patches. Once this happens, FIMozFric enters the interseismic stage where static friction coefficients are reapplied to all patches and the tectonic loading mechanism is resumed.

Rough faults are constructed by deviating the midpoint of each fault patch from a central fault plane (Fig. 5.2). The strike and dip of each patch are varied along strike and with depth so that a continuous self-similar fault surface is constructed (e.g., Power and Tullis, 1991).

Hayward and Calaveras Faults

Geologic Setting

Accommodation of deformation along the Pacific and North American plates in the San Francisco Bay Area takes the form of an intricate system of faults and folds (Fig.

5.3). The dextral Hayward (HF), Calaveras (CF) and San Andreas (SAF) faults are the primary faults along which this deformation takes place. The HF and CF are separated by a ~5 – 15 km-wide stepover and a ~60 km-long overlap distance, forming a restraining step that is accommodated by contractional structures and manifest as the East Bay Hills (Lawson, 1908). Both faults accommodate plate motions by a combination of large coseismic ruptures, frequent microseismic events, and creep (e.g., Lienkaemper et al., 1991; Toppozada and Borchardt, 1998; Waldhauser and Ellsworth, 2002). Several studies were carried out to understand this complex behavior and explain variations in along strike creep rates, in particular for the HF (e.g., Lienkaemper et al., 1991; Shirzaei and Burgmann, 2013). These variations were attributed to several reasons, including a variable depth of creep (Simpson et al., 2001), a heterogeneous distribution of locked versus creeping sections (Malservisi et al., 2003), and the effects of past earthquakes on the regional stress field (e.g., Lienkaemper et al., 1997; Lienkaemper et al., 2012). Here I explore these relationships and their effects on the surface manifestation of locked/creeping sections of the HF, CF, and SAF.

Model Setup

This simulation uses a 30 mm/yr regional tectonic loading rate over a 5,000-year period, a Young's modulus of 40 GPa, Poisson's ratio of 0.25, shear modulus of 16 GPa, and a density of 2700 kg/m^3. The HF is modeled as a 76-km long fault and has an average strike of 340. I divide the CF into northern and southern sections. The northern section is 90 km long and strikes ~170. The southern section of the CF is 100 km long and strikes ~160. All faults dip vertically, are 16 km wide, and are assigned a roughness value of 0.1 (Fig. 5.2). The distribution of creeping (velocity-strengthening) and locked

(velocity-weakening) regions within the HF and CF are implemented as fault areas with positive and negative [$a - b$] regions, respectively. The degree to which velocity-weakening regions are locked varies with depth as a function of temperature (25 °C/km geothermal gradient). For the HF, creeping sections have variable magnitudes of positive [$a - b$] values so as to simulate spatially non-uniform creep rates. Although no estimates of [$a - b$] exist for the HF, the spatial extent of creep and creep rates were determined by Shirzaei and Burgmann (2013) using joint inversion of an 18-year record of InSAR and surface creep data. I use Shirzaei and Burgmann's (2013) geodetically derived fault creep model as a template onto which the [$a - b$] friction distribution is assumed for the HF in FIMozFric (Fig. 5.4). Unfortunately, insufficient information exists that delineates the extent to which the CF creeps at depth (e.g., Kondo et al., 2008). Therefore, I assume a creeping depth of 8 km above which a moderately velocity-strengthening region ([$a - b$] = 0.005) spans the southern half of the northern section and the entire southern section of the CF. For the SAF, I assume a regular depth-dependent distribution of [$a - b$] that defines a velocity-weakening section that is bound by upper and lower velocity-strengthening zones (Scholz, 1988).

Calculating Rupture Jumping Probabilities

In Chapter 4, I showed how FIMozFric calculates rupture jumping probabilities that are conditioned on the failure of a particular fault in an earthquake record. I refer the reader to Chapter 4 for the details of this method. For the HF-CF-SAF system that I model here, I condition the rupture jumping probabilities on all fault segments individually. I use a minimum patch participation level of 70%. For example, suppose I

condition the rupture jumping probabilities on the SAF, I calculate the probability of a rupture occurring on the HF and CF if 70% of the patches in the SAF fail.

Garlock fault

Geologic Setting

The Garlock fault (GF) is a ~250 km-long sinistral fault that forms a major tectonic boundary between the Mojave block to the south and the Basin and Range province to the north in California (Davis and Burchfiel, 1973). It extends westward from the SAF to the southern edge of Death Valley (Fig. 5.5) and accommodated ~48-64 km of sinistral displacement in the last 17 – 7 million years (Smith, 1962; Davis and Burchfiel, 1973; Carr et al., 1993). No large earthquakes ruptured the GF during historic times (McGill and Rockwell, 1998). Three models are used to explain the discordant strike of the GF relative to the strike of other faults in the eastern California shear zone (ECSZ; Fig. 5.5): (1) a transform fault that accommodates differential deformation between the ECSZ to the south and extension along the Basin and Range province to the north (Davis and Burchfiel, 1973); (2) a fault that accommodates clockwise rotation of the Mojave block with the dextral SAF (Humphreys and Weldon, 1994); or (3) a conjugate fault to the SAF that accommodates transpression in the Big Bend (Hill and Dibblee, 1953; McGill et al., 2009).

Several paleoseismic studies have been carried out along the GF (Fig. 5.5). Table 5.1 summarizes all slip rates determined from paleoseismic events and offset geomorphic features that were dated using a variety of methods. In contrast, geodetically derived slip rates determined using elastic block models by (Meade and Hager, 2005) resolved 3.2 +/- 1.5 mm/yr, 1.8 +/- 1.5 mm/yr, and 1.1 +/- 1.9 mm/yr on the western, central, and eastern

sections of the GF, respectively. The range in slip rates both in space (along strike) and time (from the late Pleistocene to the present) is quite large and motivated various work to try to explain the discrepancy between geodetic and geologic slip rates. Most of these studies (e.g., Wallace, 1975; Wallace and Schulz, 1983; Wallace, 1991; Salyards et al., 1992) attribute the variation in GF slip rates to its interaction with the southern and northern portions of the ECSZ. The only existing study that uses a mechanical basis to explain the interaction of ruptures between the central GF and Panamint Valley fault (Haugerud et al., 2003) applies simple Coulomb modeling of single earthquakes with rudimentary friction assumptions. These investigations may be missing a fundamental physical process that is responsible for the slip rate variability along the GF.

Model Setup

I model the Garlock fault as a vertically dipping sinistral fault that is divided into three 16 km-wide sections (e.g., McGill and Sieh, 1991). The western section is 86 km long with an average strike of 060. The central section is divided into two segments. The first segment is 36 km long (average strike 060) and is separated from the western section by a 2 km releasing step with no overlap. The second segment is 72-km long with an average strike of 075. The eastern section of the GF is 52 km long and has an average strike of 090. All faults are assigned a roughness value of 0.1 (Fig. 5.2). The elastic halfspace is assigned a Young's modulus of 40 GPa, Poisson's ratio of 0.25, shear modulus of 16 GPa, and a density of 2700 kg/m^3. The rupture velocity is assumed to be 2.20 km/s. Simulation runs are limited to 10,000 years.

I ran simulations using geologically and geodetically derived sinistral slip rates for the GF. The first simulation uses geologically derived slip rates of 7 mm/yr, 5 mm/yr,

and 6.5 mm/yr for the western, central and eastern sections of the GF, respectively. I selected these slip rates as representative values of GF slip rates that have been determined by paleoseismic work for the Holocene (e.g., Clark and Lajoie, 1974; Wallace, 1975; LaViolette et al., 1980; Wallace and Schulz, 1983; Wallace, 1991; Salyards et al., 1992; McGill et al., 2009). The second simulation uses an average slip rate of 11 mm/yr that was derived from present-day GPS velocity fields (e.g., Chuang and Johnson, 2011) and resolved on all three sections of the GF. In both simulations, slip histories of surface patches (i.e. patches that intersect the surface of the halfspace) are reconstructed for various locations along the GF. In essence, these patch slip histories serve as a proxy for slip-per-event and slip-at-a-point that are normally recorded in the field (from paleoseismic studies, offset geomorphic features, etc).

Lidar-Derived Offset Measurements

I measured laterally displaced geomorphic markers such as offset ridges, stream channels, and terraces along the GF using lidar-derived digital elevation models (DEMs) and the lateral displacement calculator LaDiCaoz (Zielke and Arrowsmith, 2012). Lidar data for the GF were collected by the National Center for Airborne Laser Mapping in 2007 and are available from the OpenTopography lidar facility (www.OpenTopography.org). Appendix A details the workflow for accessing/processing lidar data in OpenTopography and using LaDiCaoz to measure lateral offsets. Offsets are rated using the UCERF3 offset rating scheme (Appendix D). To validate my lidar-derived measurements with those made in the field, I reoccupy 129 offset features that were measured in the field by McGill and Sieh (1991) using LaDiCaoz.

RESULTS

Hayward and Calaveras Faults

Surface Slip Distributions

The modeled surface slip distributions shown in Figure 5.6 illustrate the effects of fault strength and interactions on the propensity for large earthquakes to break the ground surface. The velocity-strengthening nature of the upper part of the CF subdued the magnitude of surface slip, particularly in the southern half of the northern CF. The variable fault strength of the HF resulted in complex surface slip distributions. Ruptures preferentially had greater surface slip magnitudes in the predominantly velocity-weakening regions of the HF than the creeping sections (compare the HF slip distributions in Fig. 5.6 to the distribution and degree of creep in Fig. 5.4). For the SAF, slip distributions for large earthquakes were generally uniform in this modeled section.

Rupture Jumping Probabilities

Table 5.2 summarizes the calculated rupture jumping probabilities for the SAF-CF-HF system. Given the model set up and assigned tectonic loading rate, for every rupture that activates at least 70% of the northern section of the Calaveras fault, the southern section of the Calaveras fault and the Hayward fault have a 66.9% and 4.18% chance of rupturing, respectively. Similarly, for every rupture where at least 70% of the southern section of the Calaveras fault ruptures, the northern section of the Calaveras fault and the Hayward fault have a 76.4% and 4.48% chance of rupturing. When conditioned on the Hayward fault, the southern section of the Calaveras fault has a 0.6% chance of rupturing.

Garlock Fault

Surface Offsets

Figure 5.7 (see also Appendix C) shows the locations of the 129 sinistral offsets that were measured by McGill and Sieh (1991) in the field and reoccupied in this study using lidar-derived DEMs. Measurements made using the lidar approach compared well with those determined in the field (R^2 of 0.9; Fig. 5.8). Although this analysis was limited to the resolution of the DEM (0.5 m) and centimeter-scale artifacts in the lidar data of the central section of the GF, this validation demonstrated that the lidar-derived offset measurements serve as reliable indicators of coseismic slip. This is especially useful in the western section of the GF where few field offset measurements exist.

I measured 528 sinistral offsets along the entire length of the GF. These are presented in Figure 5.9, which shows histograms and probability density functions (PDF) for each section. The western section of the GF contains at least five groups of offsets that cluster around 2.93 m, 6.69 m, 9.73 m, 13.19 m, and 16.91 m (Fig. 5.9A). The central section of the GF has six groups of offsets at 2.89 m, 5.56 m, 9.23 m, 11.88 m, 15.02 m, and 18.01 m (Fig. 5.9B). The eastern section contains three offset families at 2.88 m, 5.13 m, and 10.81 m (Fig. 5.9C). All of these measurements are also reported in Appendix R of the UCERF3 report (Madden et al., 2013).

Figure 5.10 shows surface slip distributions of the first ten surface-rupturing earthquakes along the GF using geologically and geodetically derived slip rates. Both simulations resulted in similar slip distribution shapes. Local irregularities in the slip distributions corresponded to asperities along each fault section. The main difference between the two sets of slip distributions was a region of slip deficit that persisted near

the center of the western section in the simulation that used the constant geodetically derived loading rate (middle panel in Fig. 5.10). Irregularities in the slip distribution shapes and slip magnitudes are concentrated in regions where the GF bends (e.g., the boundary between the central and eastern sections in Fig. 5.10).

Surface Slip at a Point

Figure 5.11 presents the modeled slip histories for the selected surface patches along the GF using the geodetically and geologically derived loading rates. In both simulations, slip magnitudes showed significant clustering along strike. Clusters of partial ruptures (blue dots in Fig. 5.11) were generally separated by long interseismic periods, which in turn were punctuated by full ruptures (red dots in Fig. 5.11). Furthermore, individual surface-rupturing earthquakes can be correlated with ease between a few of the selected patches. For example, the first four earthquakes in patch 56 can be tracked to the first four ruptures recorded in patch 168 in Fig. 5.11A). Most ruptures, however, cannot be correlated as easily. Compare the slip histories of patches 432 and 600 in the central section of the GF in Figure 5.11B. No synchronization in the timing or magnitude of any of the events recorded at these locations is apparent.

DISCUSSION

Hayward and Calaveras Faults

The effects of fault roughness along the HF, CF, and SAF are reflected in their modeled surface slip distributions in that they are not smooth in shape. Instead, local asperities along each fault either enhance or reduce local slip magnitudes (Fig. 5.6). For the CF and especially the HF, this effect is further overprinted by the effect of fault strength. The reduced surface slip magnitudes along the creeping sections of the CF and

HF are due to the consumption of elastic strain energy of large ruptures by the creeping zones (e.g., highly positive [$a - b$] regions along the HF in Fig. 5.4), resulting in a slip deficit that is manifested by small slip events at the surface. This was shown by Shirzaei et al. (2013) where they investigated the relationship between repeating seismic events along locked regions amidst the variably creeping HF. They posited that these seismic events, which occurred on local asperities on the HF, altered the short-term aseismic deformation rates along creeping regions of the HF, thereby changing the short-term probabilities of large ruptures.

The computed rupture probabilities for the modeled HF-CF-SAF system indicates that that SAF does not contribute to rupture probabilities along the HF and CF. Instead, the HF and CF behave as an interacting system where the coseismic participation of one fault was controlled by events that occurred along the other. This is expected given their close proximity to each other (e.g., Chapter 4). However, the assumption of spatially constant creep fronts along the modeled HF and CF is limiting and indicates that the computed rupture probabilities are not absolute. It has been shown by dynamic earthquake models that the depth and along-strike extent of creeping sections can vary during interseismic periods of the earthquake cycle (e.g., Kaneko et al., 2013). Shirzaei et al. (2013) documented this change over the timespan of 18 years. Therefore, a significant complication arises in interpreting the computed participation probabilities in that the distribution of [$a - b$] along the HF can vary in space and time over the duration of the earthquake catalog. As a result, my computed rupture jumping probabilities for the HF and CF are not absolute and do not account for the fundamental process of aseismic creep that undoubtedly occurs along these faults.

Another assumption used in simulating earthquakes along the HF-CF-SAF system is that they are stand-alone faults. These faults are indeed the dominating structures in this part of the Bay Area. However, there exists several tens of smaller faults that branch off along strike and with depth from the HF and CF. While the exact roles that these faults play in accommodating coseismic and interseismic deformation is unknown, these faults could participate in accommodating deformation during coseismic events on any of the three faults modeled here. This is not considered in my models, but constructing a more structurally detailed model for the HF-CF-SAF system can readily be done in FIMozFric.

In this chapter, I have considered only on-fault coseismic deformation. Given the quasi-static nature of FIMozFric and its assumption of a linear-elastic halfspace, it is not possible to account for the effects of time-dependent afterslip caused by viscoelastic relaxation following large earthquakes. Secondary deformation caused by postseismic deformation could significantly add to the total magnitude of slip preserved in the simulated earthquake record.

Garlock Fault

Implications for Interpreting Paleoseismic Slip Rates

The lidar-derived offset measurements showed that earthquakes that rupture along the GF generally transmit coseismic slip at regular magnitudes. The range of slip per event along the western section is between 3.04 – 3.76 m, while the respective ranges of slip per event for the central and eastern sections are 2.65 – 3.14 m and 2.25 – 2.88 m. Assuming that each section ruptures individually, upper and lower moment magnitude ranges of possible earthquakes along the GF can be computed using seismic moment M_0

= μAS and moment magnitude M_w = 0.667 log M_0 – 10.7 relationships (Hanks and Kanamori, 1979). This corresponds to possible earthquake magnitude ranges between M_w 7.37 – 7.44, M_w 7.40 – 7.45, and M_w 7.14 – 7.21 for the western, central and eastern section of the GF, respectively, assuming a 16 km rupture width. These ranges are consistent with values determined by other workers (e.g., Wallace, 1975; McGill and Sieh, 1991). I must note that, although each measured offset was given a quality rating, the ratings were not used to compute cumulative offset probability densities in Figure 5.9. This can and should be done in the future to refine families of offset magnitudes (e.g., Zielke and Arrowsmith, 2012).

The above analysis has a major limitation in that it assumes that each section of the GF ruptures individually and in essence behaves as an individual segment. We can see from both the surface slip distributions and patch slip histories (Fig. 5.10 and Fig. 5.11) that segmentation in the GF is not present, even when section-specific loading rates were used. Whatever signal of fault segmentation that may have been present in the slip distributions could have been overprinted by the roughness effects of individual sections. As a result, interpreting surface offsets at individual points along the GF or in an aggregate manner (e.g., Fig. 5.9) will produce significant uncertainties.

I note that the following discussion does not attempt to compare absolute slip magnitudes of the simulated slip per event with those determined geologically/geodetically. Obviously, the absolute values of slip magnitude, earthquake clustering, and recurrence are a function of the geometry of the particular fault under investigation and the chosen slip rates for that simulation. However, regardless of which tectonic loading rate was used (i.e. geodetically derived constant rate or geologically

derived section-specific rates), it is clear that spatiotemporal clustering of earthquakes exists along the GF. The implication of this observation is that whatever tectonic loading mechanism is accommodated by the GF may not control earthquake clustering. Instead, discrepancies in short- and long-term slip rates may be controlled by the self-similar nature of the fault surface (i.e. roughness). As demonstrated in Chapter 4, spatiotemporal variations in earthquake recurrence and magnitude are controlled by structural complexities and fault roughness. This can be seen in the surface record of the simulated earthquakes near Koehn Lake (patches 296 and 360 in Fig. 5.11A) and I explained this in Chapter 4 in terms of elastic strain energy expended by ruptures to overcome asperities. As a result, rough faults may exhibit rupture synchronization

Let us imagine that the simulated patch slip histories in Figure 5.11 are paleoseismic sites along the GF (or any other fault for that matter). Any computed slip rates at individual points along the GF will inherently vary along strike and through time simply due to the natural variation in the fault's roughness. From a paleoseismic perspective, slip rates determined at individual sites must factor in this major uncertainty, especially if correlating large earthquakes across multiple faults or even along the same fault. This raises significant issues with paleoseismically derived slip rates used to constrain fault synchronization (Scholz, 2010), explain slip-rate constancy (e.g., Dolan et al., 2007) or plate reorganization (e.g., Shelef and Oskin, 2010). As a result, the analysis of aggregate paleoseismic slip rates should not be made without first accounting for the structural geometry and roughness of every fault under investigation. For example, geologically determined slip rates of structurally mature/smooth faults may be representative of actual slip rates because all of the strain is resolved on them.

Conversely, for structurally immature/young faults, apparently low slip rates will not be representative of the “true” slip rate.

The above has important implications for seismic hazard estimations. Consider the Uniform California Earthquake Rupture Forecast (UCERF3) deformation model as an example (e.g., Field et al., 2013). The UCERF3 deformation model employs geologically determined slip rates and surface slip distributions to drive the tectonic loading mechanism, which in turn determines the rates at which earthquakes occur along the UCERF3 fault model. If we consider geologic slip rates of structurally rough faults as minima, then the UCERF3 deformation model will underestimate the earthquake rates along young/rough faults. The same can be said for estimates of paleoearthquake magnitudes based on point measurements of surface slip distributions (e.g., Biasi and Weldon, 2006) for rough/young faults. Using the underestimated on-fault record of deformation (surface slip distributions and slip rates) from these faults would result in the underestimation of the magnitudes of paleoearthquakes. Therefore, seismic hazards computed for rough/young faults will include large errors and thus severely underestimate the hazards associated by these faults in the UCERF3 model.

The degree to which faults are discretized in deformation models could play an important role in deformation resulting from slip along dislocations. In Chapter 4 I discretized faults into 1 km by 1 km patches. In this chapter I discretized faults into 2 km by 2 km patches. While these dimensions might be appropriate to investigate surface slip at the kilometer scale, larger dislocations might prove otherwise. Take the current fault model used in the UCERF3 as an example. In this fault model, fault patches are 7 km long along strike, which corresponds to approximately half of the seismogenic width. Yet

the paleoseismic studies used to derive the geologic deformation rates are spaced on the order of a few kilometers along strike at best. The mismatch between the spatial scales of the geologic slip rates that are resolved on such large dislocations might yield unrealistic deformation and rupture jumping plausibilities (e.g., Parsons et al., 2012). While not explored in this chapter, the effect of patch size on the surface manifestation of simulated deformation could easily be investigated in FIMozFric.

Implications for Fault Zone Evolution

As seen in Chapter 4 and here, the consistency of the correlation between fault roughness and irregular slip rates/slip distributions suggests that the age of faults plays a role in the constancy of strain rate accommodation. Rough faults with low total fault displacement may be considered structurally immature and young. Therefore, I expect the slip rates for such faults to be low and inconsistent along strike. Field (e.g., Ferrill et al., 2011) and seismologic (e.g., Cochran et al., 2009) observations show that faults are comprised of mechanically compliant damage zones. Depending on the ages of these faults, deformation within the damage zones causes an increase in the density of smaller-scale faults. With repeated slip events, deformation progressively localizes (Segall and Pollard, 1983) such that enough stress is resolved on fewer and fewer fault surfaces without exceeding the differential stresses needed to form new faults. This form of strain softening (Jaeger et al., 2007) likely occurs in the upper few kilometers of faults that contain mechanically compliant damage zones ranging from a few meters (Ferrill et al., 2011) to several kilometers (Cochran et al., 2009) in width. With this in mind, I posit that the temporal persistence of local asperities along young/rough faults gives way to a smoother fault surface with repeating earthquakes. At timescales on which earthquakes

occur, fault activity varies such that individual faults may have low slip rates until deformation is localized onto a single fault with a higher slip rate. This would eventually lead to constant along-strike slip rates that reach a steady state reflected by “regular” stick-slip behavior. Conversely,the mechanically compliant damage zones may behave differently in fault sections that creep aseismically. For example, the southern edge of the creeping section of the SAF (near Parkfield) contains several fault-bounded oblate blocks that define the SAF (Thayer, 2006). Detailed analyses of these blocks revealed their subsurface as resembling a ship’s keel where the bounding faults merge at depth into a single fault zone. In this case, these faults accommodate deformation by sliding the blocks past each other, essentially behaving as a shear zone where slip does not progressively localize onto a single fault surface. As a result, large ruptures that are able to punch through the velocity-strengthening creeping region of the SAF may activate different fault strands at a time.

Unfortunately, the above process cannot be simulated using FIMozFric for several reasons. First, FIMozFric does not allow fault surfaces to change shape or roughness through time. Therefore, local asperities persist throughout the entire earthquake simulation. Second, the rudimentary assumption of linear elasticity does not allow new faults to form where the elastic strength of the halfspace is exceeded. While the elastic dislocation modeling approach replicates many of the first-order features associated with tectonic deformation (e.g., Stein et al., 1988; Massonnet et al., 1993; Gomberg and Ellis, 1994; Landgraf et al., 2013), rock deformation in the form of large strains accumulated over geologic time is not elastic. Permanent rock deformation takes the form of faulting, fracturing, pore space collapse, dissolution/precipitation, or granular flow (Pollard and

Fletcher, 2005; Scholz, 2010). Thus, strain softening by definition cannot be modeled using the assumption of linear elasticity. This by no means takes away from the value of FIMozFric (or any other earthquake simulator) because inherently it was not designed to model fault evolution. However, using a combination of FIMozFric and Coulomb failure stress analysis in FIMoz (see Chapter 4) could serve as a quasi-static predictor of where new faults are expected to form when the elastic strength of the halfspace is exceeded. Alternatively, one could apply the elasto-plastic von Mises failure stress analysis to evaluate areas where the maximum distortional strain energy of the halfspace is exceeded due to slip along faults. The combination of elastic (prior to failure) and plastic (following failure) deformation could explain ground deformation where faulting and folding occur coseismically (e.g., Oskin et al., 2012; Quigley et al., 2012). A more advanced approach would be to employ principals of continuum damage mechanics that mimic real rock behavior and allow for the simultaneous brittle and plastic deformation during fault zone evolution (e.g., Busetti et al., 2012).

CONCLUSIONS

In this chapter, I explored the effects of fault roughness and strength on the surface slip distributions of large earthquakes and slip magnitudes at various points along crustal-scale faults. I used the FIMozFric earthquake simulator to simulate long earthquake records along the Garlock fault and the Hayward-Calaveras-San Andreas fault systems. While many studies attribute the spatiotemporal clustering of earthquakes to regional-scale fault interactions, my results presented a clear connection between fault roughness and the spatiotemporal clustering of slip rates and slip magnitudes. My results suggest that rough faults (i.e. structurally immature faults) tend to have lower apparent

slip rates along strike. These faults progressively smoothen with time such that their apparent slip rates converge to the “true” slip rate that matches the tectonic loading rate. Therefore, the degree to which faults are rough/smooth/young/old has important controls on paleoseismically derived slip rates and surface slip distributions of large earthquakes. This adds to the challenges that are faced when correlating earthquakes along single or multiple faults that contain complex structural geometries or strength/frictional properties, which in turn has profound implications for constructing earthquake recurrence models to be used in earthquake rupture forecasts.

ACKNOWLEDGMENTS

I thank Sally McGill for providing her offset locations for the Garlock fault. Thank you to Olaf Zielke for making his code for FIMozFric available to me and especially for his technical support in running his code. High-performance computing support is greatly appreciated and was provided by the Arizona State University Advanced Computing Center which allowed me to run the earthquake simulations presented in this chapter.

FIGURES

Figure 5.1. Regional map showing the location of faults studied in this chapter. Faults are colored by the Quaternary slip rates from the USGS Active Faults and Folds database. SAF – San Andreas fault, GF – Garlock fault, CF – Calaveras fault, HF – Hayward fault, SD – San Diego, LA – Los Angeles, SF – San Francisco.

Figure 5.2. Examples of a smooth and a rough fault. Faults are discretized into 2 km by 2 km patches. Strikes and dips of patches in smooth faults have little deviation from each other. Conversely, patches in rough faults have variable strikes and dips, which results in an overall rougher fault geometry.

Figure 5.3. Map of the northern San Andreas fault system in the Bay Area, California. SF – San Francisco. Faults are colored by the Quaternary slip rates from the USGS Active Faults and Folds database.

Figure 5.4. Implementation of creep for the Hayward fault. Top panel shows average right-lateral creep rate along the Hayward fault from joint inversion of InSAR and surface creep measurements. Black dots represent microseismicity and magenta dots represent locations of repeating earthquakes. Modified from Shirzaei and Burgmann (2013). Lower panel shows the implementation of creep along the Hayward fault in FIMozFric as velocity-strengthening (positive [$a - b$]) regions.

Figure 5.5. Map of the Garlock fault and nearby fault systems. Faults are colored by the Quaternary slip rates from the USGS Active Faults and Folds database. Black stars indicate locations where sinistral slip rates (in mm/yr) were determined by paleoseismic studies.

Figure 5.6. Simulation results for surface slip distributions of the first ten surface-rupturing earthquakes along the Calaveras, Hayward, and San Andreas faults. Top panel is an oblique view of this fault system. Fault patches are 2 km x 2 km and colored by their roughness.

Figure 5.7. Locations of displaced features along the Garlock fault that were measured in this study.

Figure 5.8. Comparison between lidar- and field-derived sinistral offsets along the Garlock fault. Field-derived measurements were made by McGill and Sieh (1991). Lidar-derived offsets were made by reoccupying McGill and Sieh's (1991) displaced features. Error bars represent ranges in each offset magnitude using the field (vertical bars) and lidar (horizontal bars) methods.

Figure 5.9. Slip magnitudes measured from offset geomorphic markers along the (A) western, (B) central, and (C) eastern sections of the Garlock fault. Top panels in A, B, and C are sections of my lidar-derived fault trace map plotted on top of a 0.5 m DEM.

Lower panels show the along-strike slip measurements of offset features. The histograms in the left panels group offset magnitudes into 50 bins.

Figure 5.10. Simulation results for surface slip distributions of the first ten surface-rupturing earthquakes along the Garlock fault. Top panel is an oblique view of this fault system. Fault patches are 2 km x 2 km and colored by their roughness. Middle panel shows slip distributions along the Garlock fault using the geodetically determined slip rate of 11 mm/yr. Lower panel shows the modeled surface slip distributions that were determined paleoseismically.

Figure 5.11. Surface patch slip histories for select locations along the Garlock fault using (A) a geodetically derived slip rate of 11 mm/yr, and (B) geologically derived slip rates of 7 mm/yr, 5 mm/yr, and 6.5 mm/yr for the western, central and eastern sections of the Garlock fault, respectively. Fault traces (red lines) were mapped using lidar-derived DEMs and DEM products (see Chapter 3 for the details of this method). Red dots represent surface slip for full ruptures that propagated through the entire seismogenic zone. Blue dots represent surface slip for earthquakes that partially ruptured the seismogenic zone.

Figure 5.1

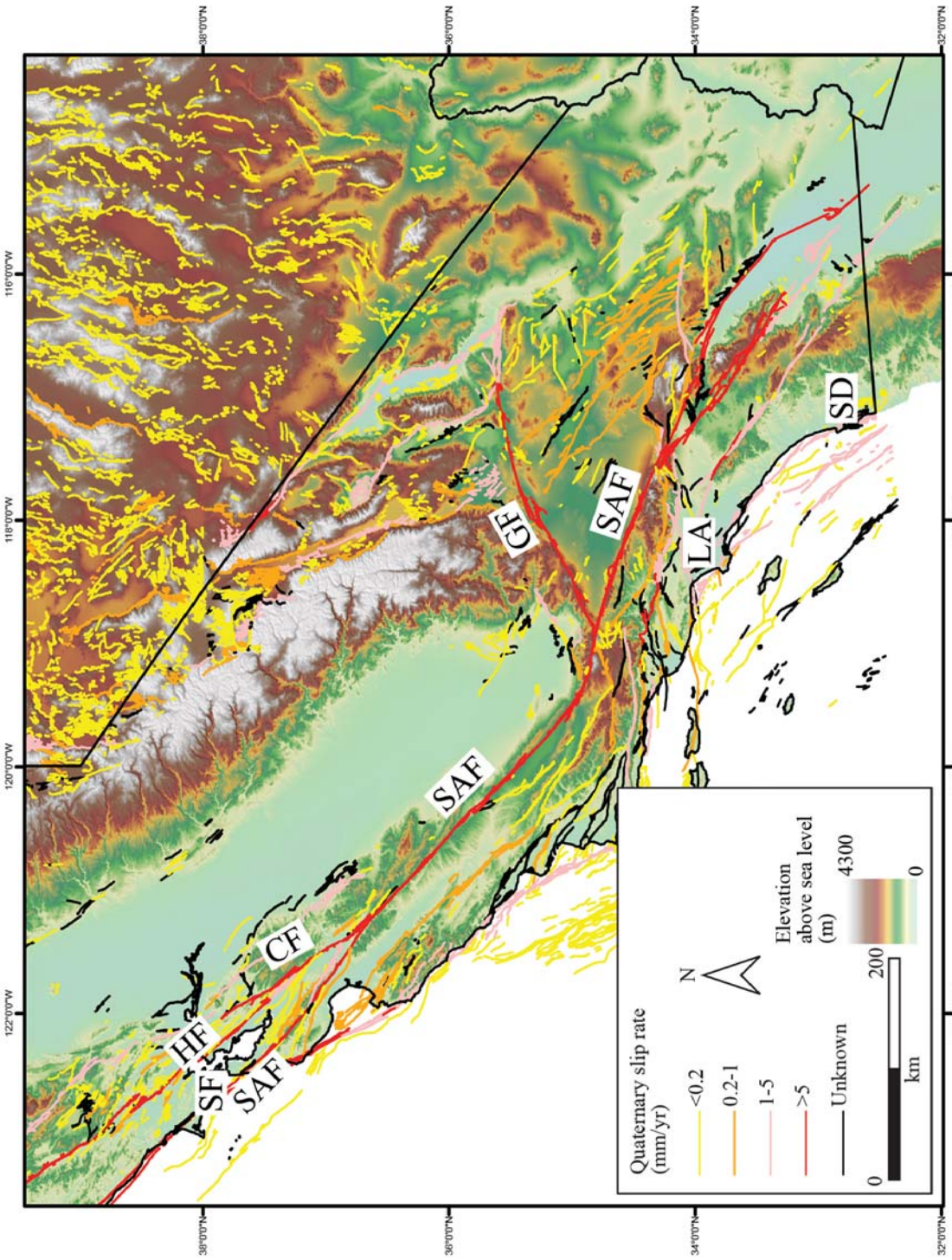
38°0'0"N
36°0'0"N
34°0'0"N
32°0'0"N
116°0'0"W
118°0'0"W
120°0'0"W
122°0'0"W
SAF
GF
SAF
LA
SD
SAF
CF
HF
SF
Quaternary slip rate (mm/yr)
<0.2
0.2-1
1-5
>5
Unknown
N
Elevation above sea level (m)
4300
0
0
200
km

Figure 5.2

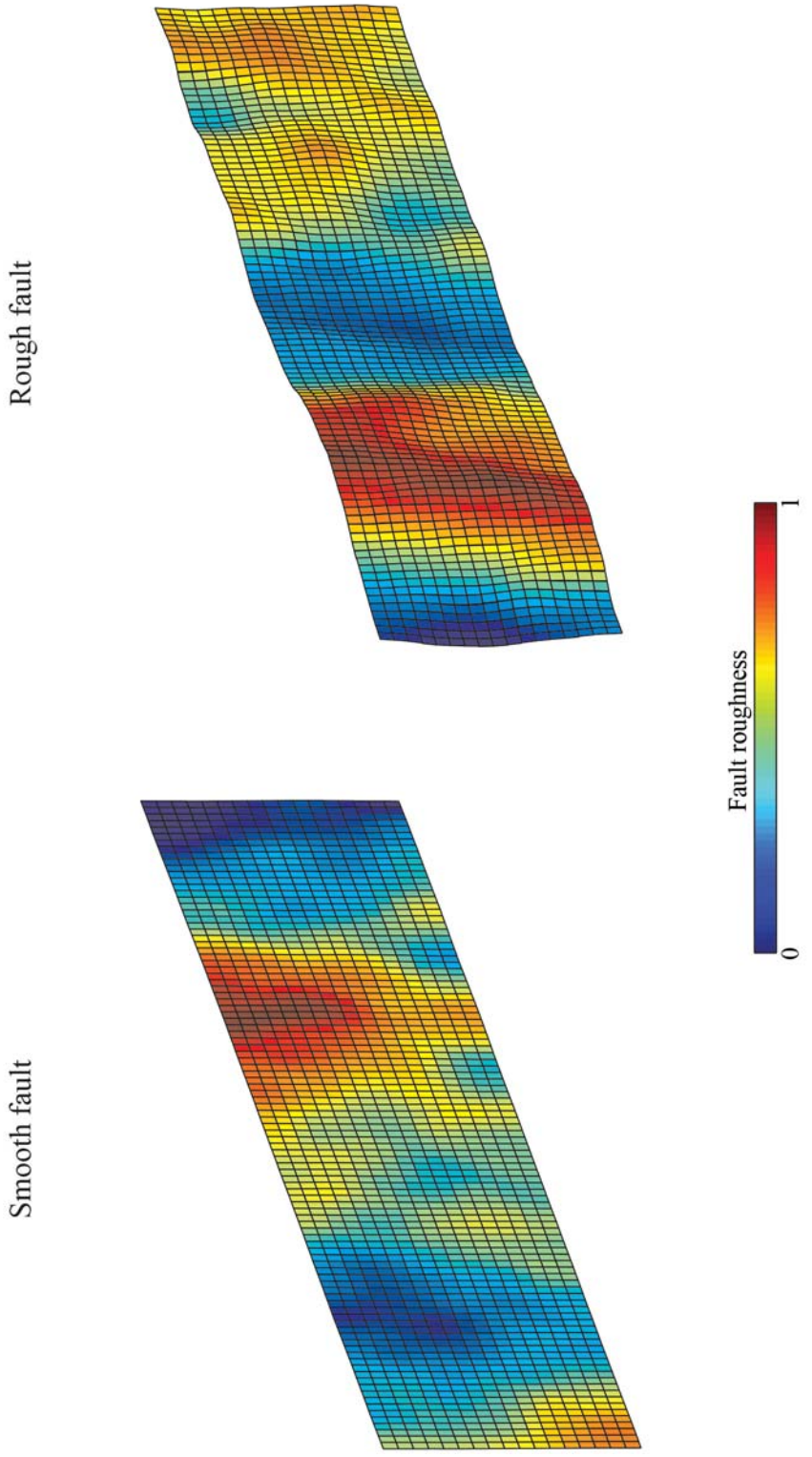

Figure 5.3

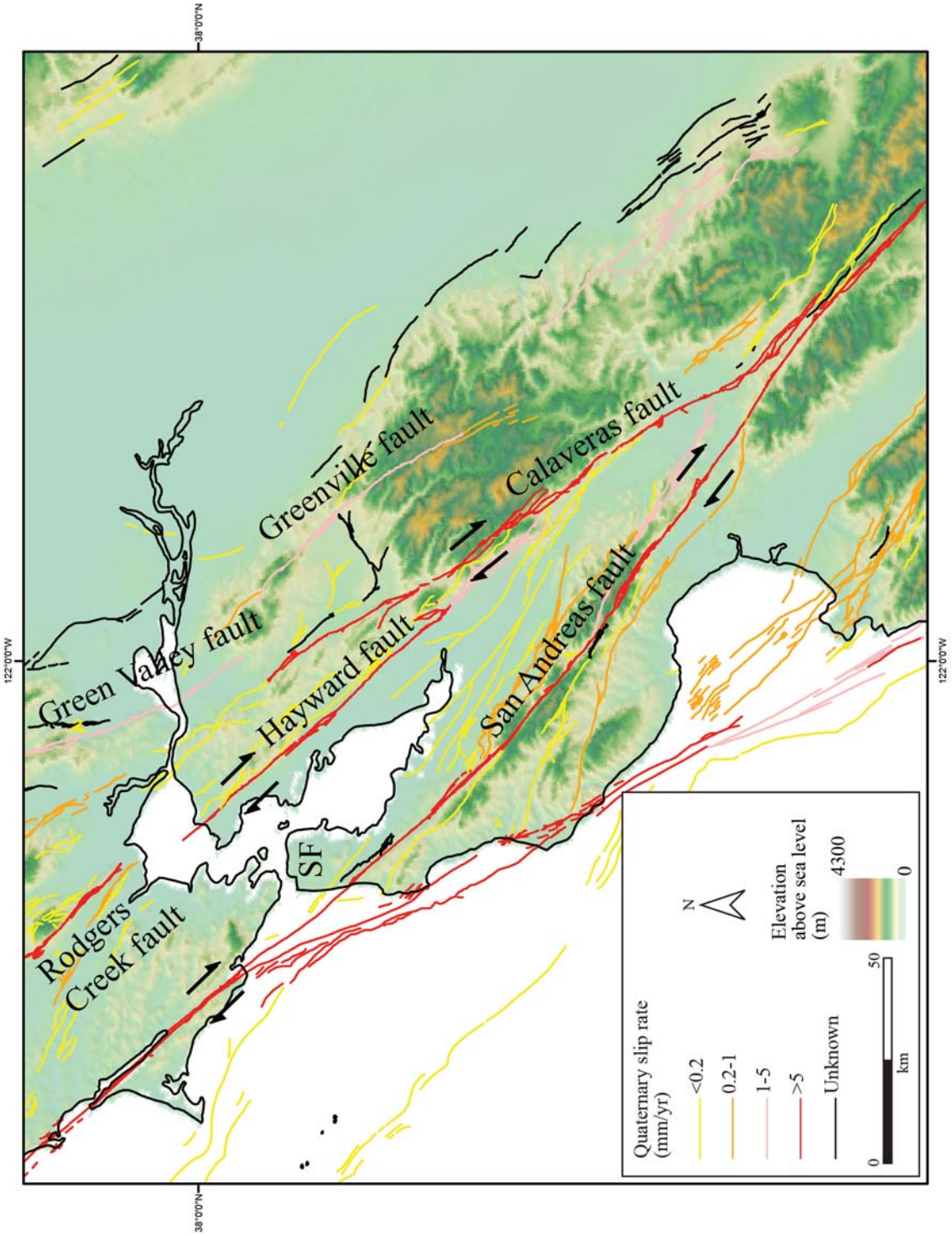
38°00'N
122°00'W
Greenville fault
Calaveras fault
Green Valley fault
Hayward fault
San Andreas fault
SF
Rodgers Creek fault
Quaternary slip rate (mm/yr)
<0.2
0.2-1
1-5
>5
Unknown
N
Elevation above sea level (m)
4300
0
50
0
km

Figure 5.4

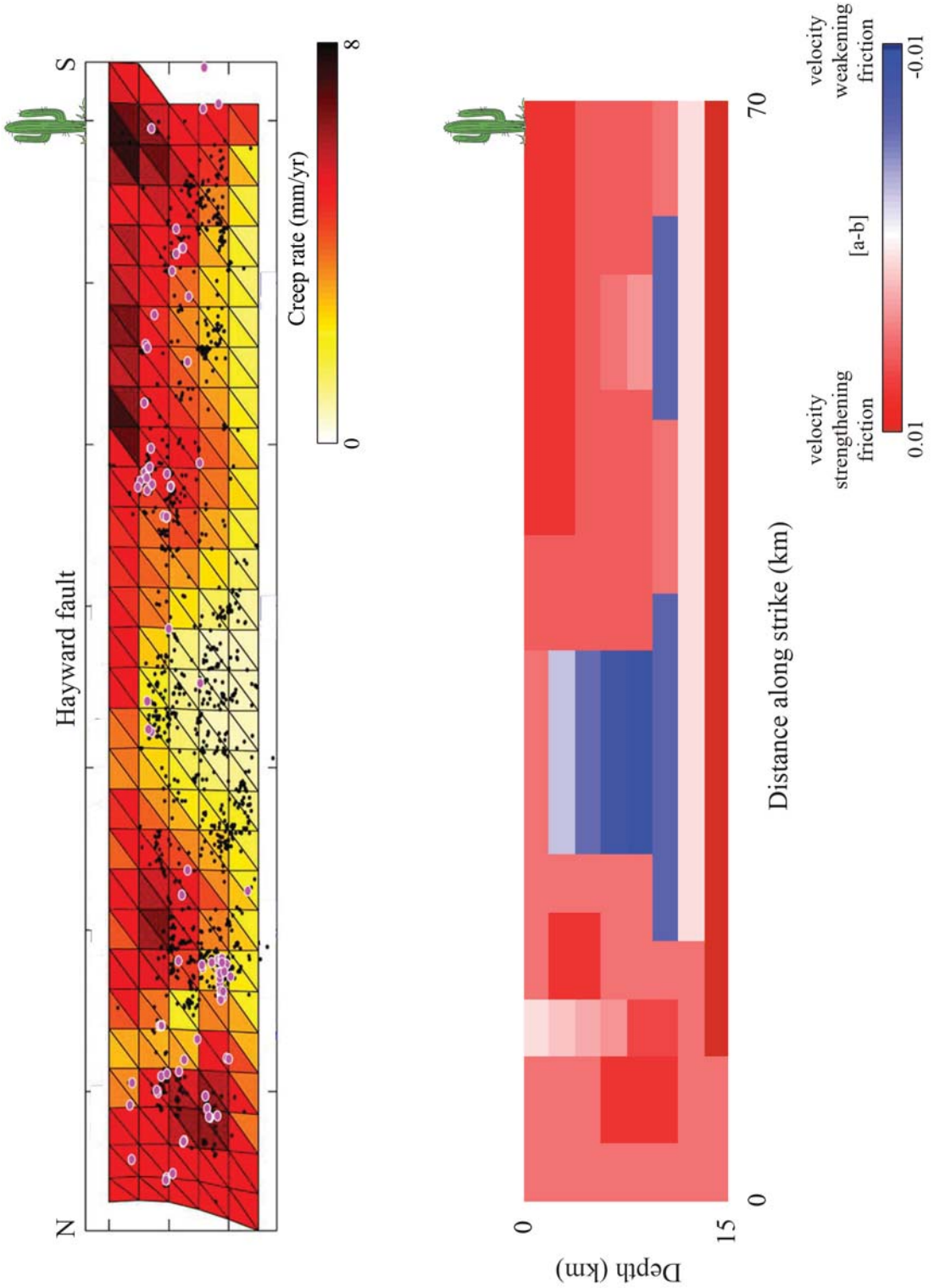
S
N
Hayward fault
Creep rate (mm/yr)
8
0
Depth (km)
0
15
0
70
Distance along strike (km)
velocity
strengthening
friction
[a-b]
velocity
weakening
friction
0.01
-0.01

Figure 5.5

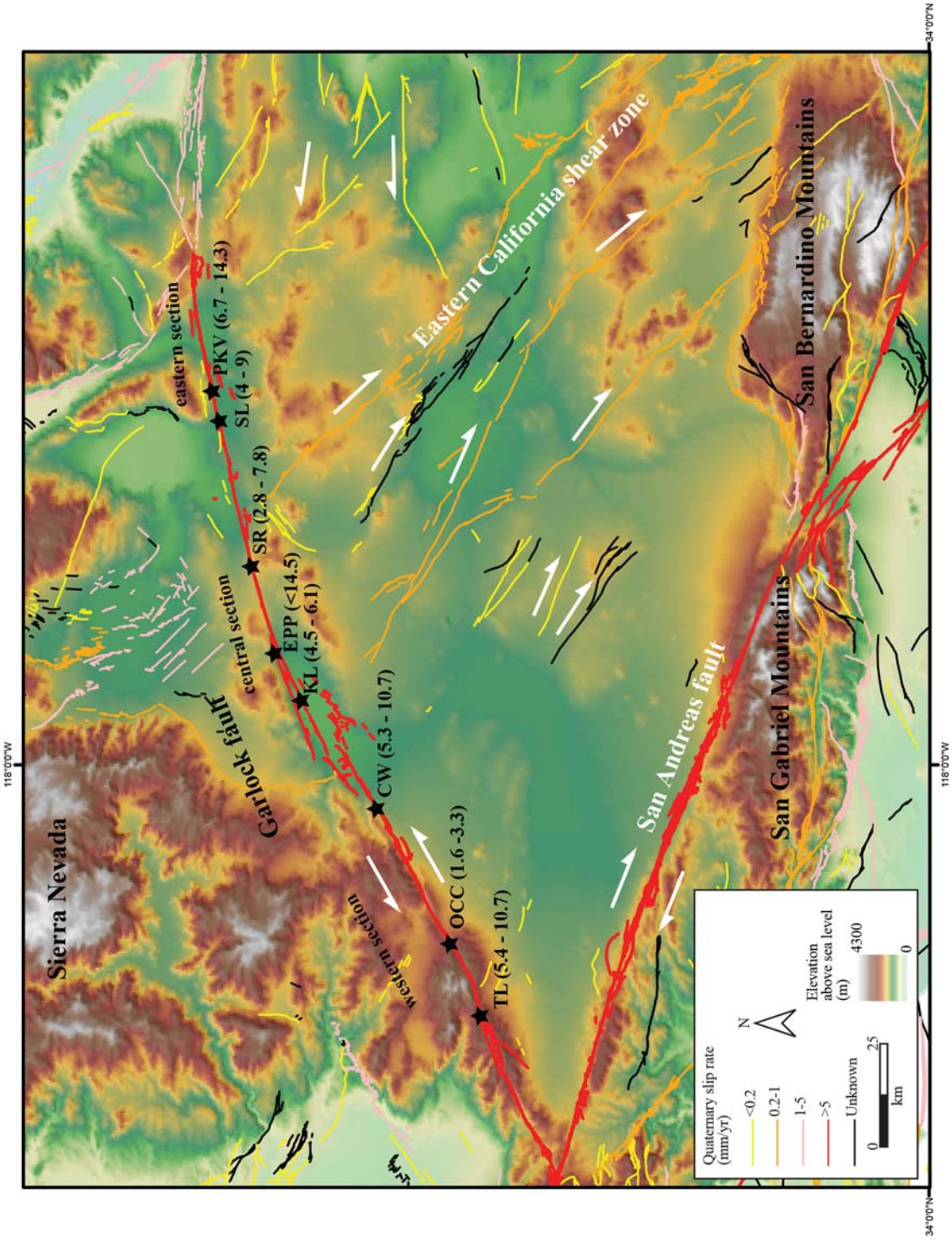
Sierra Nevada
Garlock fault
eastern section
central section
western section
Eastern California shear zone
San Andreas fault
San Gabriel Mountains
San Bernardino Mountains
PKV (6.7 - 14.3)
SL (4 - 9)
SR (2.8 - 7.8)
EPP (<14.5)
KL (4.5 - 6.1)
CW (5.3 - 10.7)
OCC (1.6 -3.3)
TL (5.4 - 10.7)
118°0'0"W
34°0'0"N
Quaternary slip rate (mm/yr)
<0.2
0.2-1
1-5
>5
Unknown
N
Elevation above sea level (m)
4300
0
0
25
km

Figure 5.6

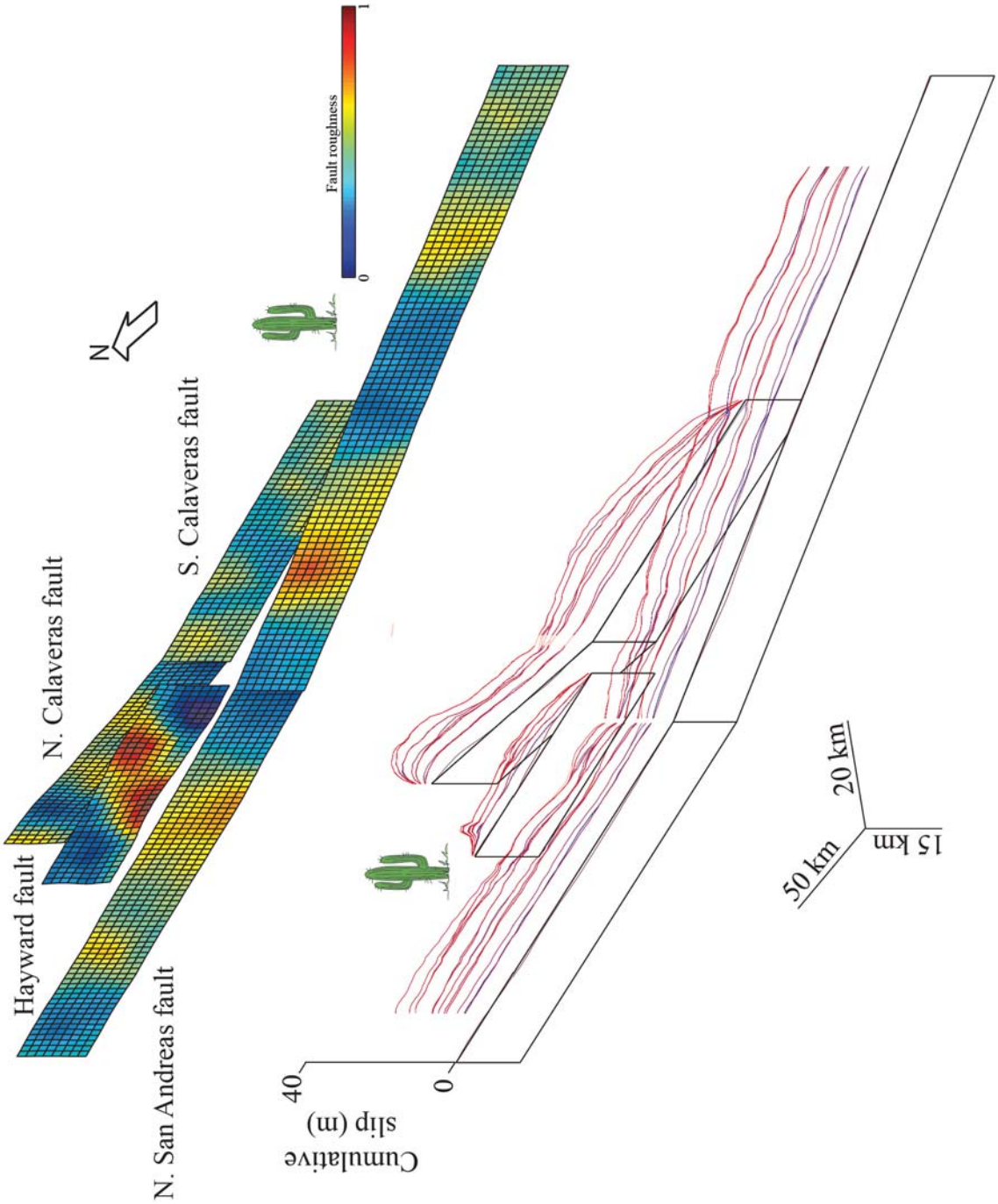
Fault roughness
1
0
N
Hayward fault
N. Calaveras fault
S. Calaveras fault
N. San Andreas fault
Cumulative slip (m)
40
0
50 km
20 km
15 km

Figure 5.7

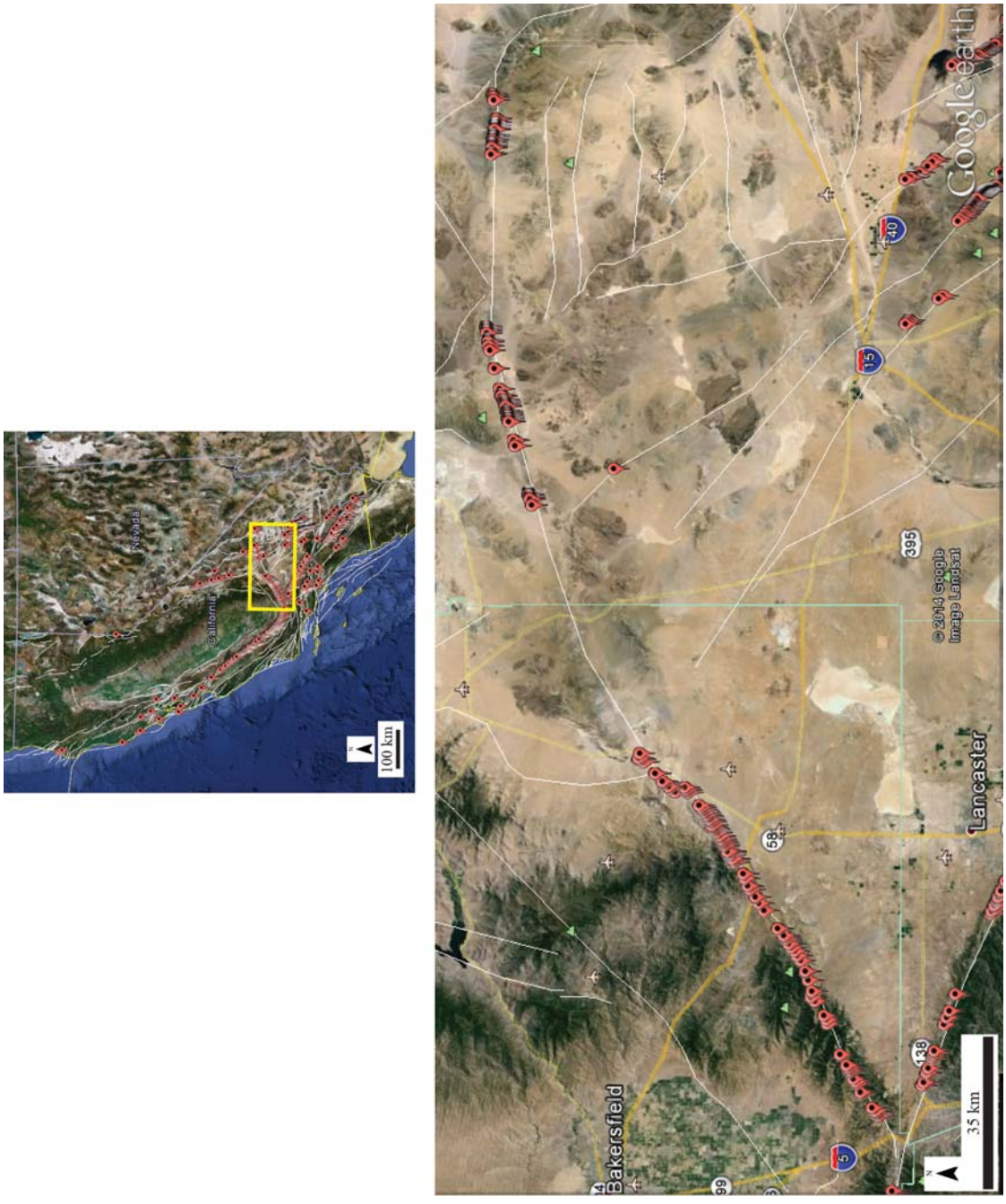
Nevada
California
100 km
Google earth
© 2014 Google
Image Landsat
Bakersfield
Lancaster
35 km

Figure 5.8

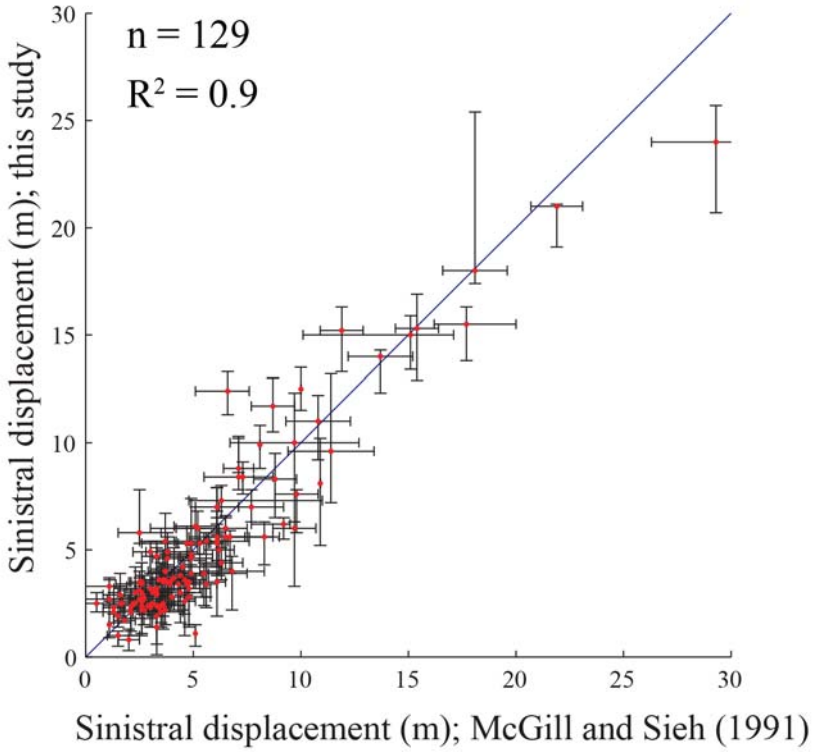
n = 129
R² = 0.9
Sinistral displacement (m); this study
Sinistral displacement (m); McGill and Sieh (1991)
0
5
10
15
20
25
30

Figure 5.9A

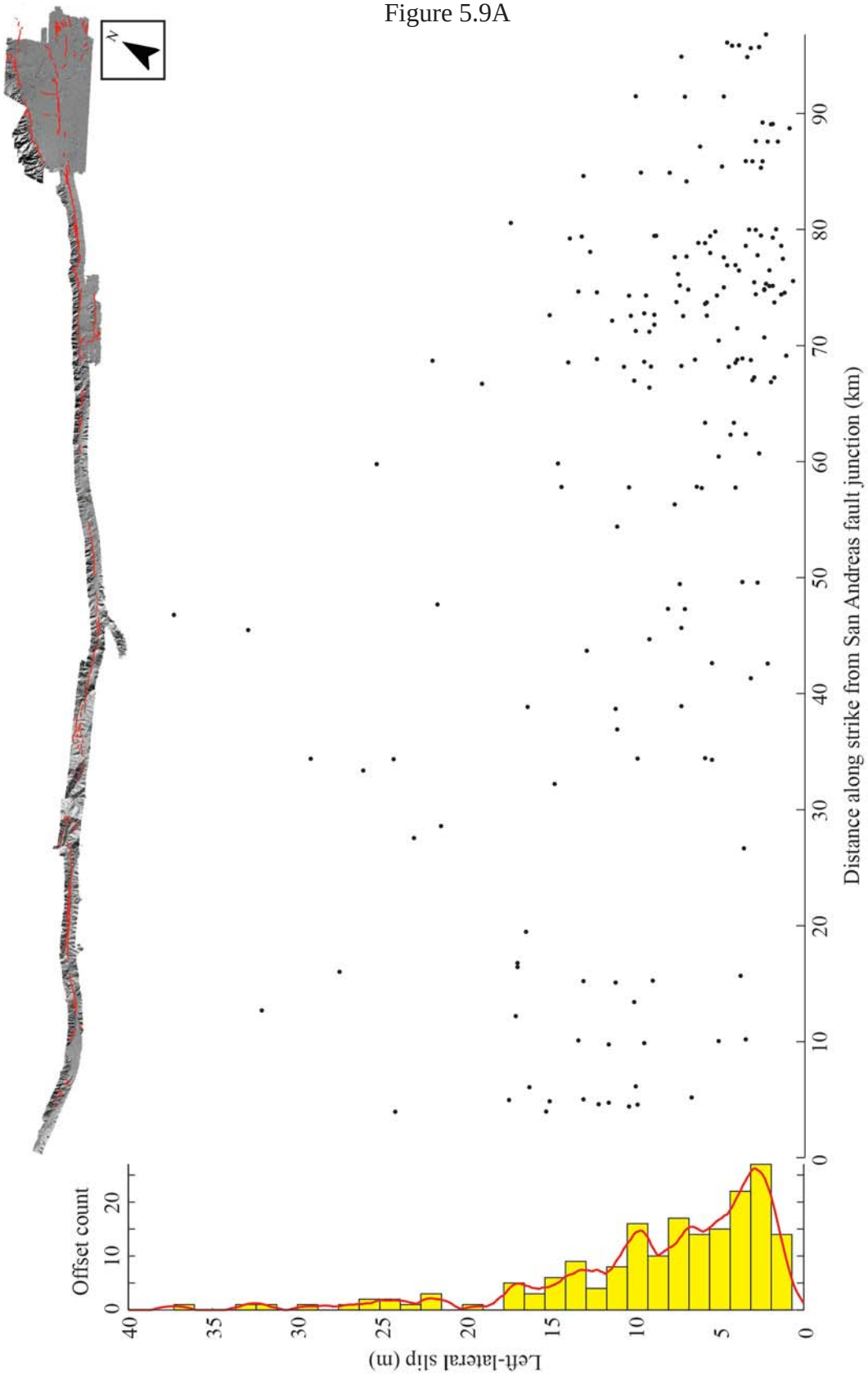
N
Offset count
0
10
20
Left-lateral slip (m)
40
35
30
25
20
15
10
5
0
Distance along strike from San Andreas fault junction (km)
0
10
20
30
40
50
60
70
80
90

Figure 5.9B

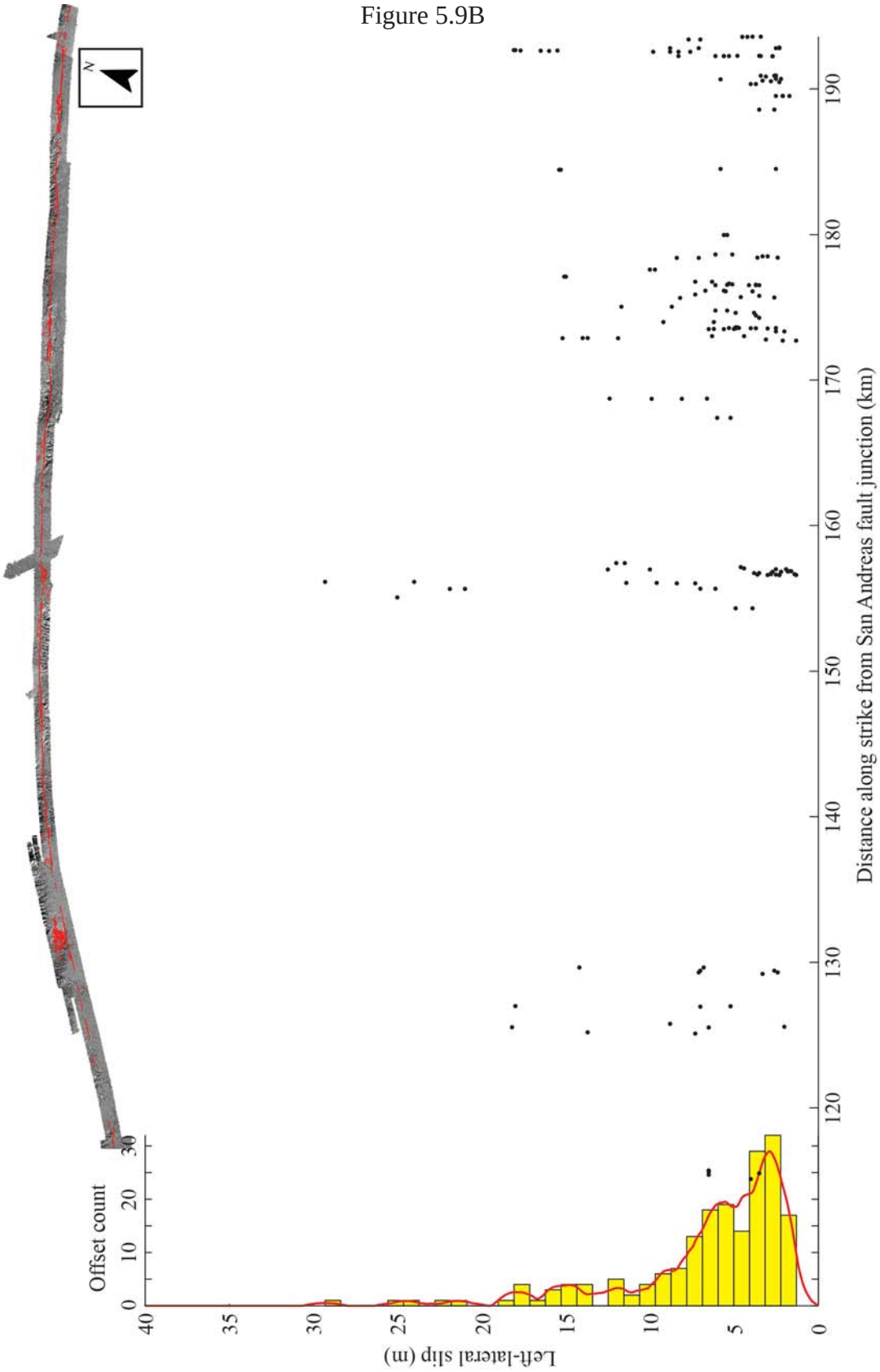
N
Offset count
0
10
20
30
40
35
30
25
20
15
10
5
0
Left-lateral slip (m)
120
130
140
150
160
170
180
190
Distance along strike from San Andreas fault junction (km)

Figure 5.9C

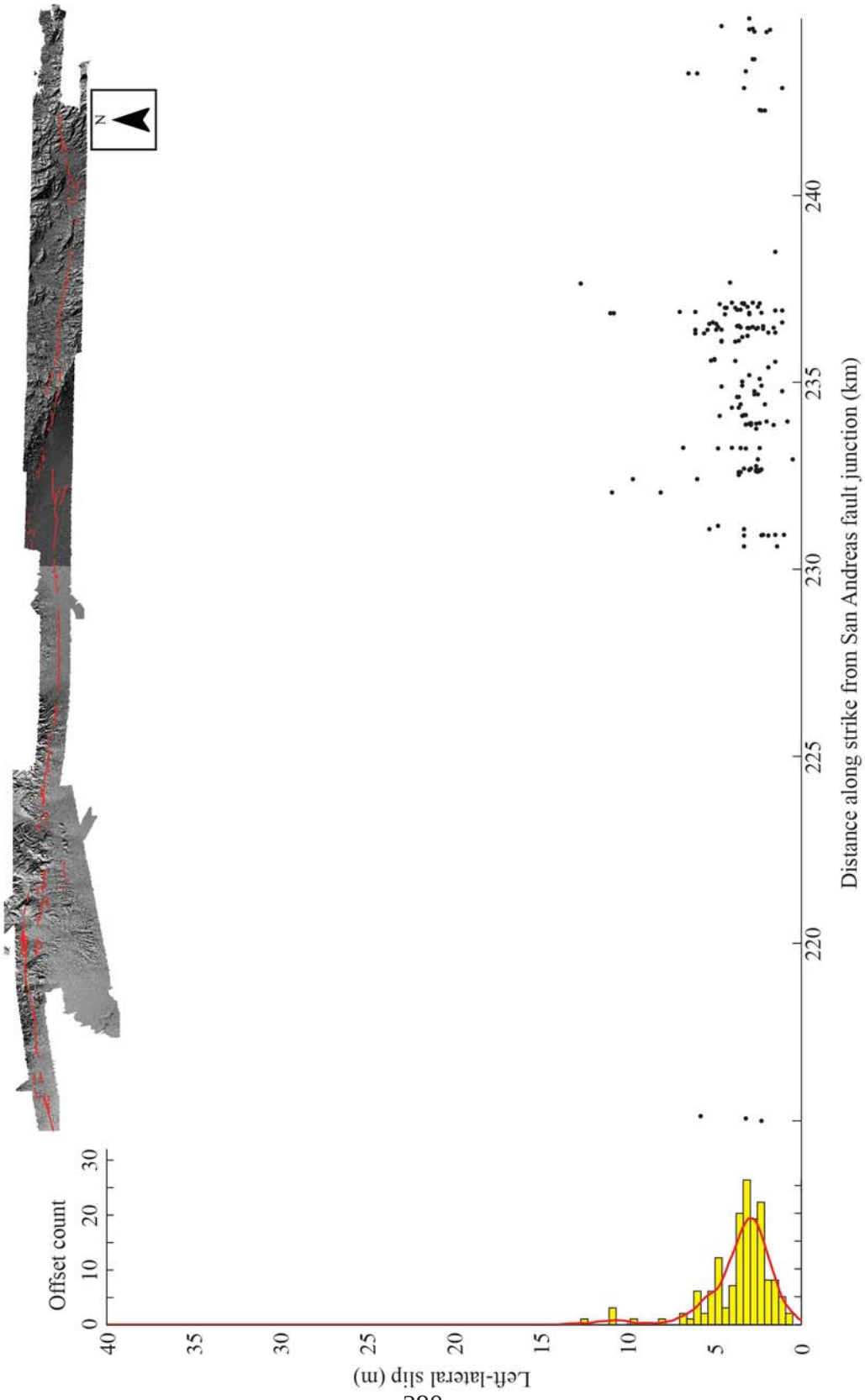
N
Offset count
0
10
20
30
Left-lateral slip (m)
40
35
30
25
20
15
10
5
0
220
225
230
235
240
Distance along strike from San Andreas fault junction (km)

Figure 5.10

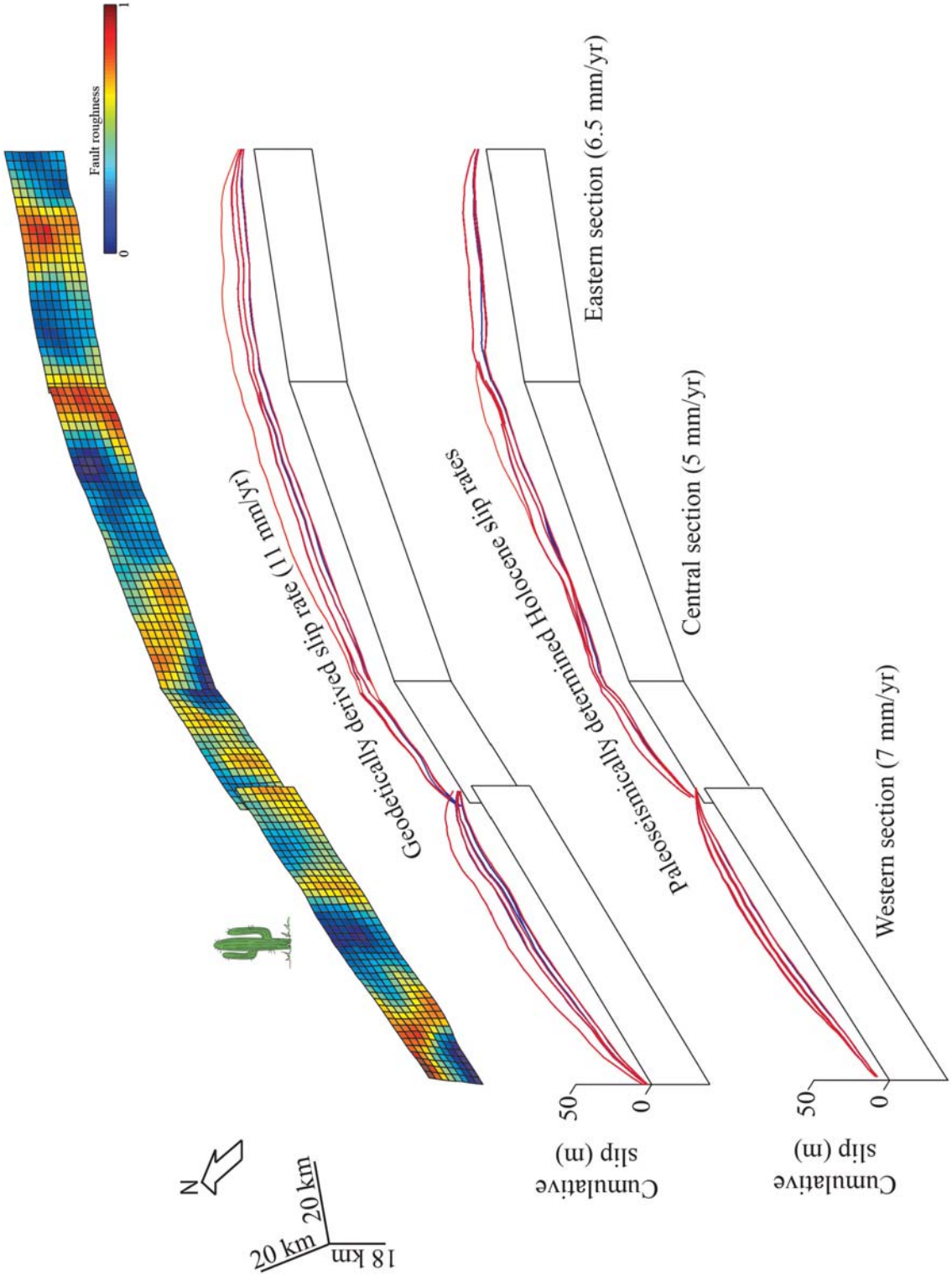
Fault roughness
1
0
Geodetically derived slip rate (11 mm/yr)
Paleoseismically determined Holocene slip rates
Eastern section (6.5 mm/yr)
Central section (5 mm/yr)
Western section (7 mm/yr)
Cumulative slip (m)
50
0
Cumulative slip (m)
50
0
N
20 km
20 km
18 km

Figure 5.11A

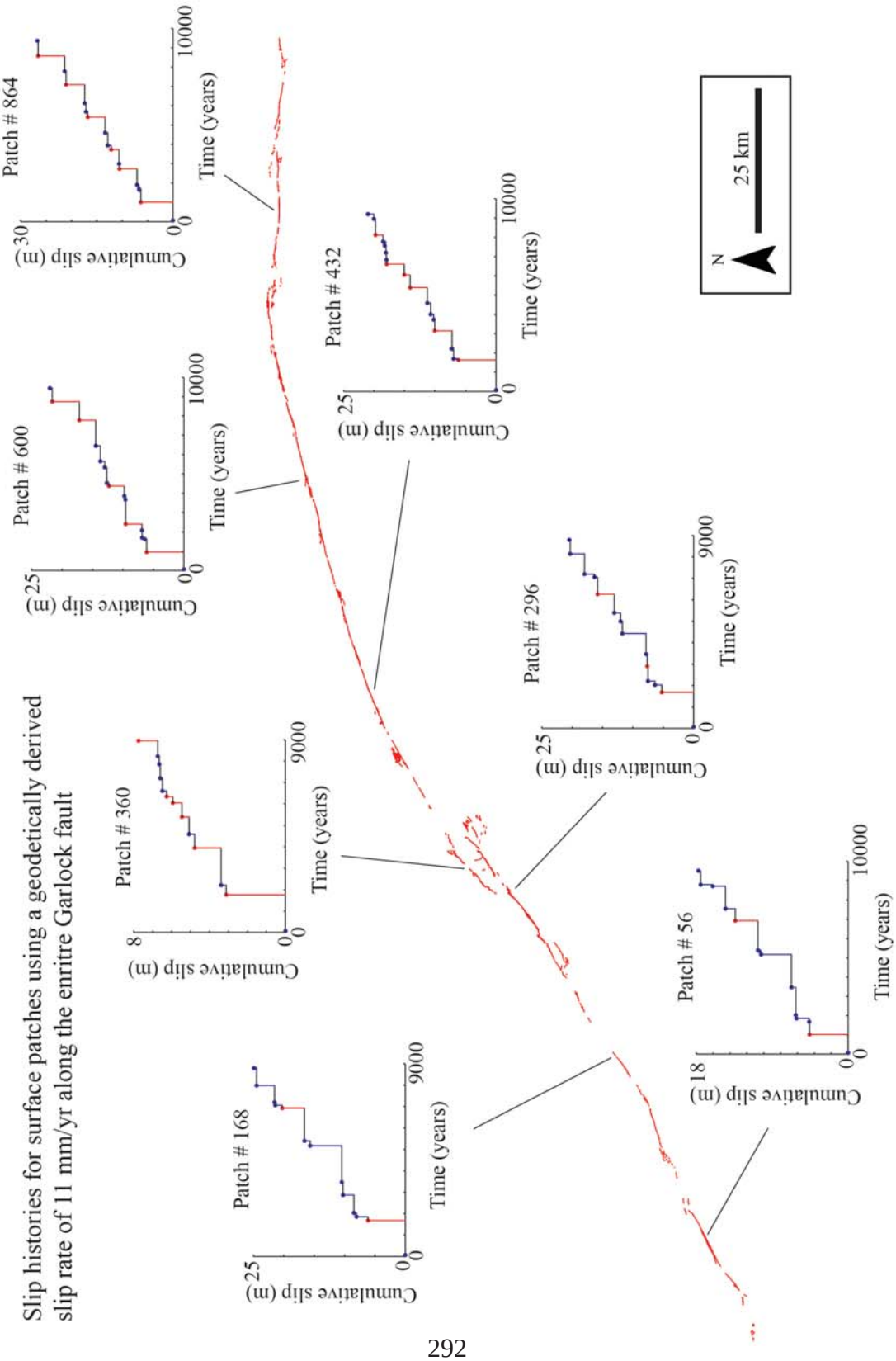
Slip histories for surface patches using a geodetically derived slip rate of 11 mm/yr along the enritre Garlock fault
Patch # 864
Patch # 600
Patch # 432
Patch # 360
Patch # 296
Patch # 168
Patch # 56
Cumulative slip (m)
Time (years)
N
25 km

Figure 5.11B

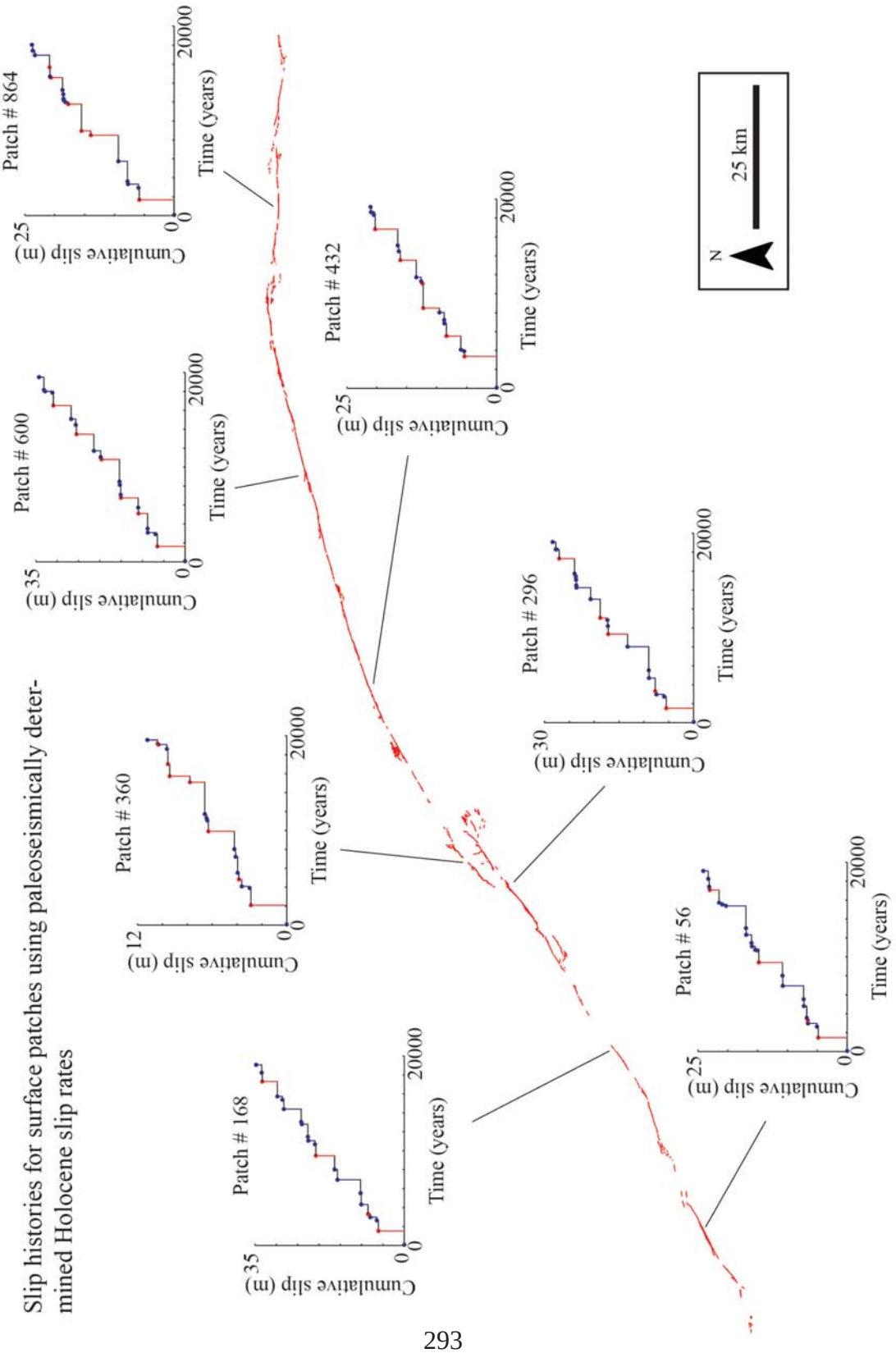
Slip histories for surface patches using paleoseismically determined Holocene slip rates
Patch # 864
Patch # 600
Patch # 432
Patch # 360
Patch # 296
Patch # 168
Patch # 56
Cumulative slip (m)
Time (years)
0
20000
N
25 km

TABLES

	Site name	Slip rate (mm/yr)	Offset dating method	Reference
Western section	Twin Lakes	5.4 – 10.7	^{14}C	Madugo et al., 2012
	Oak Creek Canyon	1.6 – 3.3	soil profile	LaViolette et al., 1980
	Clark Wash	5.3 – 10.7	^{14}C	McGill et al., 2009
Central section	Koehn Lake	4.5 – 6.1	^{14}C	Clark and Lajoie, 1974
	El Paso Peaks	≤14.5	^{14}C	Dawson et al., 2003
	Summit Range	2.8 – 7.8	^{10}Be	Ganev et al., 2012
Eastern section	Searles Lake	4 – 9	^{14}C	McGill and Sieh, 1993
	Pilot Knob Valley	6.7 – 14.3	OSL	Ritasse et al., 2014

Table 5.1. Compilation of slip rates determined by paleoseismic studies along the Garlock fault to date. OSL – optically stimulated luminescence.

Minimum patch participation level: 70%					
Conditioned on	N. SAF	S. SAF	N. Calaveras	S. Calaveras	Hayward
N. San Andreas	100	50	0	0	0
S. San Andreas	50	100	0	0.1	0
N. Calaveras fault	0	0	100	69	4
S. Calaveras fault	0	0.1	76.3	100	45
Hayward fault	0	0	0	0.6	100

Table 5.2. Summary of rupture jumping probabilities for the Hayward-Calaveras-San Andreas fault system conditioned on each fault segment. All probabilities are reported as percentages.

REFERENCES

Beeler, N. M., Tullis, T. E., and Weeks, J. D., 1994, The roles of time and displacement in the evolution effect in rock friction: Geophysical Research Letters, v. 21, p. 1987-1990.

Biasi, G. P., and Weldon, R. J., 2006, Estimating surface rupture length and magnitude of paleoearthquakes from point measurements of rupture displacement: Bulletin of the Seismological Society of America, v. 96, no. 5, p. 1612-1623.

Blanpied, M. L., Lockner, D. A., and Byerlee, J. D., 1991, Fault stability inferred from granite sliding experiments at hydrothermal conditions: Geophysical Research Letters, v. 18, no. 4, p. 609-612.

Busetti, S., Mish, K., and Reches, Z., 2012, Damage and plastic deformation of reservoir rocks: Part 1. Damage fracturing: American Association of Petroleum Geologists Bulletin, v. 96, no. 9, p. 1687-1709.

Carr, M. D., harris, A. G., Poole, F. G., and Fleck, R. J., 1993, Stratigraphy and structure of Paleozoic outer continental margin rocks in PilotKnobValley, north central Mojave Desert, California: U.S. Geological Survey Bulletin, v. 2015, p. 33.

Chuang, R. Y., and Johnson, K. M., 2011, Reconciling geologic and geodetic model fault slip-rate discrepancies in Southern California: Consideration of nonsteady mantle flow and lower crustal fault creep: Geology, v. 39, p. 627-630.

Clark, M. M., and Lajoie, K. R., 1974, Holocene behavior of the Garlock fault: Geological Society of America Abstracts with Programs, v. 6, p. 156-157.

Cochran, E. S., Li, Y., Shearer, P. M., Barbot, S., Fialko, Y., and Vidale, J. E., 2009, Seismic and geodetic evidence for extensive, long-lived fault damage zones: Geology, v. 37, no. 4, p. 315-318.

Davis, G. A., and Burchfiel, B. C., 1973, Garlock fault: an intracontinental transform structure, southern California: Geological Society of America Bulletin, v. 84, p. 1407-1422.

Dieterich, J. H., and Kilgore, B. D., 1994, Direct observation of frictional contacts: new insights for state dependent properties: Pure and Applied Geophysics, v. 143, p. 283-302.

Dolan, J. F., Bowman, D. D., and Sammis, C. G., 2007, Long-range and long-term fault interactions in Southern California: Geology, v. 35, no. 9, p. 855-858.

Ferrill, D. A., Morris, A. P., McGinnis, R., Smart, K. J., and Ward, W. C., 2011, Fault zone deformation and displacement partitioning in mechanically layered

carbonates: The Hidden Valley fault, central Texas: American Association of Petroleum Geologists Bulletin, v. 95, no. 8, p. 1383-1397.

Field, E. H., Biasi, G. P., Bird, P., Dawson, T. E., Felzer, K. R., Jackson, D. D., Johnson, K. M., Jordan, T. H., Madden, C., Michael, A. J., Milner, K. R., Page, M. T., Parsons, T., Powers, P. M., Shaw, B. E., Thatcher, W. R., Weldon, R. J., and Zeng, Y., 2013, Uniform California Earthquake Rupture Forecast, Version 3 (UCERF3)—The Time-Independent Model: U.S. Geological Survey Open-File Report 2013-1165.

Gomberg, J., and Ellis, M. A., 1994, Topography and tectonics of the central New Madrid seismic zone: Results of numerical experiments using a three-dimensional boundary element program: Journal of Geophysical Research, v. 99, no. b10, p. 20299-20310.

Hanks, T. C., and Kanamori, H., 1979, A moment magnitude scale: Journal of Geophysical Research, v. 84, no. B5, p. 2348-2350.

Haugerud, R. A., harding, D. J., Johnson, S. Y., Harless, j. L., Weaver, C. S., and Sherrod, B. L., 2003, High-resolution Lidar topography of the Puget Lowland, Washington—a bonanza for earth science: Geology, v. 13, no. 6, p. 4-10.

Hill, M. L., and Dibblee, T. W., 1953, San Andreas, Garlock, and Big Pine faults, California: a study of the character, history, and tectonic significance of their displacements: Geological Society of America Bulletin, v. 64, p. 443-458.

Humphreys, E. D., and Weldon, R., 1994, Deformation across the western United States: a local estimate of Pacific-North America transform deformation: Journal of Geophysical Research, v. 99, p. 19975-20010.

Jaeger, J. C., Cook, N. G. W., and Zimmerman, R. W., 2007, Fundamentals of rock mechanics, Malden, Wiley-Blackwell, 488 p.

Kaneko, Y., Fialko, Y., Sandwell, D., Tong, X., and Furuya, M., 2013, Interseismic deformation and creep along the central section of the North Anatolian Fault (Turkey): InSAR observations and implications for rate-and-state friction properties: Journal of Geophysical Research, v. 118, p. 1-15.

Kondo, H., Toda, S., Okamura, K., and Chiba, T., 2008, A fault scarp in an urban area identified by LiDAR survey: a Case study on the Itoigawa–Shizuoka Tectonic Line: Geomorphology, v. 101, p. 731-739.

Landgraf, A., Zielke, O., Arrowsmith, J. R., Ballato, P., Strecker, M. R., Schildgen, T. F., Friedrich, A. M., and Tabatabaei, 2013, Differentiating simple and composite tectonic landscapes using numerical fault slip modeling with an example from the south central Alborz Mountains, Iran: Journal of Geophysical Research, v. 118, p. 1792-1805.

LaViolette, J. W., Christensen, G. E., and Stepp, J. C., 1980, Quaternary displacement on the western Garlock fault, southern California, South Coast Geological Society, Geology and Mineral Wealth of the California Desert, Santa Ana, California.

Lawson, A., 1908, Report of the Earthquake Investigation Commission upon the California Earthquake of April 18, 1906: Carnegie Institution.

Lienkaemper, J. J., Borchardt, G., and Lisowski, M., 1991, Historic creep rate and potential for seismic slip along the Hayward Fault, California: Journal of Geophysical Research, v. 97, p. 18261–18283.

Lienkaemper, J. J., Galehouse, J. S., and Simpson, R. W., 1997, Creep response of the Hayward fault to stress changes caused by the Loma Prieta earthquake: Science, v. 276, no. 5321, p. 2014-2016.

Lienkaemper, J. J., McFarland, F. S., Simpson, R. W., Bilham, R. G., Ponce, D. A., Boatwright, J. J., and Caskey, S. J., 2012, Long-term creep rates on the Hayward fault: Evidence for controls on the size and frequency of large earthquakes: Bulletin of the Seismological Society of America, v. 102.

Malservisi, R., Gans, C., and Furlong, K., 2003, Numerical modeling of strike-slip creeping faults and implications for the Hayward fault, California: Tectonophysics, v. 361, no. 1-2.

Marone, C., Raleigh, C. B., and Scholz, C. H., 1990, Frictional behavior and constitutive modelling of simulated fault gouge: Journal of Geophysical Research, v. 95, p. 7007-7025.

Massonnet, D., Rossi, M., Carmona, C., Adragna, F., G., P., Feigl, K., and Rabaute, T., 1993, The displacement field of the Landers earthquake mapped by radar interferometry: Nature, v. 364, p. 138-142.

McCalpin, J. P., 2009, Paleoseismology, International Geophysics Series: San Diego, Academic Press, p. 613.

McGill, S. F., and Rockwell, T., 1998, Ages of late Holocene earthquakes on the central Garlock fault near El Paso Peaks, California: Journal of Geophysical Research, v. 103, no. B4, p. 7265–7279.

McGill, S. F., and Sieh, K., 1991, Surficial offsets on the central and eastern Garlock fault associated with prehistoric earthquakes: Journal of Geophysical Research, v. 96, no. B13, p. 21,597-521,621.

McGill, S. F., Wells, S. G., Fortner, S. K., Kuzma, H. A., and McGill, J. D., 2009, Slip rate of the western Garlock fault, at Clark Wash, near Lone Tree Canyon, Mojave Desert, California: Geological Society of America Bulletin, v. 121, no. 3/4, p. 536-554.

Meade, B. J., and Hager, B. H., 2005, Block models of crustal motion in southern California constrained by GPS measurements: Journal of Geophysical Research-Solid Earth, v. 110, no. B3.

Okada, Y., 1992, Internal deformation due to shear and tensile faults in a half-space: Bulletin of the Seismological Society of America, v. 82, no. 2, p. 1018-1040.

Oskin, M., Perg, L., Shelef, E., Strane, M., Gurney, E., Singer, B., and Zhang, X., 2008, Elevated shear zone loading rate during an earthquake cluster in eastern California: Geology, v. 36, no. 6, p. 507-510.

Oskin, M. E., Arrowsmith, J. R., Hinojosa, A. C., Elliott, A. J., Fletcher, J. M., Fielding, E. J., Gold, P. O., Garcia, J. J. G., Hudnut, K. W., Liu-Zheng, J., and Teran, O. J., 2012, Near-field deformation from the El Mayor-Cucupah earthquake revealed by differential LiDAR: Science, v. 335, no. 702.

Parsons, T., Field, E. H., Page, M. T., and Milner, K., 2012, Possible Earthquake Rupture Connections on Mapped California Faults Ranked by Calculated Coulomb Linking Stresses: Bulletin of the Seismological Society of America, v. 102, no. 6, p. 2667-2676.

Pollard, D. D., and Fletcher, R. C., 2005, Fundamentals of structural geology, Cambridge, UK, Cambridge University Press, v. Book, Whole.

Pollitz, F. F., Wicks, C., and Thatcher, W., 2001, Mantle flow beneath a continental strike-slip fault: postseismic deformation after the 1999 Hector Mine earthquake: Science, v. 293, p. 1814-1818.

Power, W., and Tullis, T., 1991, Euclidean and fractal models for the description of rock surface roughness J Geophys Res V96, NB1, Jan 1991, P415–424: International Journal of Rock Mechanics and Mining Sciences & Geomechanics Abstracts, v. 28, no. 6, p. A344-A344.

Quigley, M., Van Dissen, R., Litchfield, N., Duffy, B., Barrell, D., Furlong, K., Stahl, T., Bilderback, E., and Noble, D., 2012, Surface rupture during the 2010 Mw 7.1 Darfield (Canterbury) earthquake: implications for fault rupture dynamics and seismic-hazard analysis: Geology, v. 40, no. 1, p. 55-58.

Ruina, A. L., 1983, Slip instability and state variable friction laws: Journal of Geophysical Research, v. 88, p. 10359-10370.

Salyards, S. L., Sieh, K., and Kirschvink, J. L., 1992, Paleomagnetic measurement of nonbrittle coseismic deformation across the San Andreas fault at Pallett Creek: Journal of Geophysical Research, v. 97, no. B9, p. 12457-12470.

Savage, J. C., Svarc, J. L., and Prescott, W. H., 2003, Near-field postseismic deformation associated with the 1992 Landers and 1999 Hector Mine, California earthquakes: Journal of Geophysical Research, v. 108, no. B9.

Scholz, C. H., 1988, The brittle-plastic transition and the depth of seismic faulting: Geologische Rundschau, v. 77, no. 1, p. 319-328.

-, 2010, Large Earthquake Triggering, Clustering, and the Synchronization of Faults: Bulletin of the Seismological Society of America, v. 100, no. 3, p. 901-909.

Schwartz, D. P., and Coppersmith, K. J., 1984, Fault behavior and characteristic earthquakes; examples from the Wasatch and San Andreas fault zones: Journal of Geophysical Research, v. 89, p. 5681-5698.

Segall, P., and Pollard, D. D., 1983, Nucleation and growth of strike slip faults in granite: Journal of Geophysical Research, v. 88, no. B1, p. 555-568.

Shelef, E., and Oskin, M., 2010, Deformation processes adjacent to active faults: Examples from eastern California: Journal of Geophysical Research-Solid Earth, v. 115.

Shirzaei, M., and Burgmann, R., 2013, Time-dependent model of creep on the Hayward fault from joint inversion of 18 years of InSAR and surface creep data: Journal of Geophysical Research, v. 118, p. 1733-1746.

Shirzaei, M., Burgmann, R., and Taira, T., 2013, Implications of recent asperity failures and aseismic creep for time-dependent earthquake hazard on the Hayward fault: Earth and Planetary Science Letters, v. 371, p. 59-66.

Simpson, R. W., Lienkaemper, J. J., and Galehouse, J. S., 2001, Variations in creep rate along the Hayward Fault, California, interpreted as changes in depth of creep: Geophysical Research Letters, v. 28, no. 11.

Smith, G. I., 1962, Large lateral displacement on Garlock fault, as measured from offset dyke swarm: American Association of Petroleum Geologists Bulletin, v. 46, p. 85-104.

Stein, R. S., King, G., and Rundle, J. B., 1988, The growth of geological structures by repeated earthquakes, 2, Field examples of continental dip-slip faults: Journal of Geophysical Research, v. 95, p. 13319-13331.

Toda, S., Stein, R. S., Sevilgen, V., and Lin, J., 2011, Coulomb 3.3 Graphic-rich deformation and stress-change software for earthquake, tectonic, and volcano research and teaching—user guide: U.S. Geological Survey Open-File Report 2011-1060, p. 63.

Toppozada, T. R., and Borchardt, G., 1998, Re-evaluation of the 1836 “Hayward fault” and the 1838 San Andreas fault earthquakes: Bulletin of the Seismological Society of America, v. 88, no. 1, p. 140-159.

Waldhauser, F., and Ellsworth, W. L., 2002, Fault structure and mechanics of the Hayward Fault, California, from double-difference earthquake locations: journal of Geophysical Research, v. 107, no. 3.

Wallace, R. E., 1975, The San Andreas fault in the Carrizo Plain–Temblor Range region, California, in Crowell, J. C., ed., San Andreas Fault in Southern California: A Guide to San Andreas Fault from Mexico to Carrizo Plain, Volume 118, California Division of Mines and Geology Special Report, p. 241-250.

-, 1991, The San Andreas Fault System, California: U.S. Geological Survey Open File Report.

Wallace, R. E., and Schulz, S. S., 1983, Aerial views in color of the San Andreas fault, California: U S Geological Survey Open File Report.

Zielke, O., 2009, How fault geometric complexity and frictional properties affect seismic fault behavior and accumulation of slip along strike-slip faults, PhD: Arizona State University, 315 p.

Zielke, O., and Arrowsmith, J. R., 2008, Depth variation of coseismic stress drop explains bimodal earthquake magnitude-frequency distribution: Geophysical Research Letters, v. 35, no. 24.

-, 2012, LaDiCaoz and LiDARimager - MATLAB GUIs for LiDAR data handling and lateral displacement measurement: Geosphere, v. 8, p. 206-221.

Chapter 6

EARTH SCIENCE MEETS THE SPECIAL EDUCATION CLASSROOM

ABSTRACT

Mainstream classrooms have difficulty accommodating students with special learning needs while achieving state-mandated standards in reading, writing, math, and science. These students with learning disabilities (LD) are subsequently grouped into special education (SE) classrooms where they receive specialized instruction. Few science lesson plans and teaching activities exist to help SE teachers guide their students toward meeting the state-mandated academic standards, especially for Earth science curricula. I introduce a set of Earth science-themed lesson plans designed and implemented for elementary-level students with LD. I document the lessons' effectiveness in helping students retain Earth science concepts. All lessons used tactile and interactive learning activities to teach Earth science (e.g., tectonic boundaries, Earth structure, and natural hazards) and science inquiry concepts outlined in the Arizona Department of Education curriculum standards. All lessons were administered by a SE teacher to a class of 8-10 students over the course of two weeks. Student responses were coded semi-quantitatively to assess the effectiveness of the lessons and the various instruction methods. Pre- and post-assessments of each student's state of knowledge showed increased retention of Earth science concepts after implementing the new lesson plans. The two primary findings of this chapter include: (1) Earth science provides a highly engaging learning environment for students with LD, and (2) hands-on, student-led learning activities are paramount to enhancing the retention of Earth science concept by students with LD.

INTRODUCTION

Students with learning disabilities (LD) that require special classroom accommodations are gaining recognition as a severely underrepresented group within the Broader Impacts of the National Science Foundation's educational directives (Clewell and Fortenberry, 2009). Students with LD are commonly put into self-contained classrooms and given sets of educational goals and objectives that are customized to their individual academic abilities and disabilities, thereby requiring all special education teachers to accommodate the special needs of every student (Cawley et al., 2002). This challenge is amplified by the paucity of educational resources available to special education teachers to help students with LD meet the state-mandated curriculum standards that were set in motion by the No Child Left Behind Act of 2001 (Browder et al., 2010). This is especially true for science education in the special education classroom. Educational curricula and lesson plans that engage mainstream K-12 students in science are multiplying on a daily basis, but they unfortunately lack the adaptability to meet the special learning needs of students with LD (Haddad et al., 2012). In fact, science in general has been neglected in the special education curricula for decades (Holahan et al., 1994), even though "many science educators feel that science as a process approach offers a vast resource to the special education curriculum" (Anderson et al., 1970). As a result, students with LD consistently score an average of one standard deviation lower in science and other disciplines (Anderman, 1998) and are subsequently excluded from the enhanced learning environment that cutting-edge research brings to K-12 classrooms (Haddad et al., 2012).

Students with LD students struggle with the deductive and inductive reasoning of the science curriculum (e.g., Mastropieri et al., 2001) but they excel when science concepts are adapted to their learning level (Mastropieri et al., 2006 and references therein). For instance, textbook reading is not effective in teaching science to students with LD (e.g., Parmar et al., 2004) however several existing models for teaching science to students with LD include peer-mediation (e.g., Mastropieri et al., 2006; Simpkins et al., 2009), modifications to textbook content (e.g., Lovitt et al., 1986; e.g., Lovitt and Horton, 1994), allowing more time for vocabulary recognition (e.g., Browder et al., 2010), and adapting the mode of response to the student abilities (e.g., Mastropieri et al., 2001). Furthermore, there exists only one study to our knowledge that utilizes tactile activities to explore Earth science (Haddad et al., 2012). It is important to provide students with LD with lessons and tactile activities that strengthen their inductive and deductive reasoning skills, as well as expose them to Earth science processes that operate in the world within which they reside. The motivation for this study and for future work planned was and is to provide special education teachers much-needed Earth science material that is adaptable for each of their student's learning needs.

I present a series of Earth science lesson plans that engage students with LD in the scientific method and expose them to Earth science concepts while helping them meet state-mandated Earth science curriculum standards. All lessons were developed with the sole purpose of adapting key Earth science concepts to the learning abilities of elementary school students with LD. Our study spans two weeks of observing and recording the behavior of eight students and chronicles the effect of tactile lesson plans on the retention of Earth science concepts. I present results from student pre- and post-

tests, and then present quantitative analyses of student behavior and reactions to the adapted lessons.

METHODS

Classroom Setting and Observational Procedures

Eight 8th grade students with 2nd to 3rd grade cognitive levels in reading, writing, mathematics, and science were seated at his/her desk to which they were assigned since the beginning of the school year, with 2-3 students seated per table. In order to preserve their regular learning environment and minimize any possible effects of external distractions on their performance or behavior during the study period, no alterations were made to the usual classroom layout or appearance, or the students' seating arrangements. Two weeks prior to the study, two researchers visited the classroom and interacted with the students via informal introductions, general information about the study, career discussions (e.g., what does a geologist do?), and school/career advice with the intention of familiarizing them students with the researchers and their research goals. Also during this visit, each of the two researchers sat in a predetermined observation location and silently observed their science lesson of the day to acclimate the students to our presence in their classroom.

Lesson Plan Description

Three lesson plans were developed to evaluate the effectiveness of several concept delivery methods: (1) conventional PowerPoint-style lecture, (2) cooperative learning (i.e. "jigsaw" exercise), (3) hands-on learning using manipulatives, and (4) use of concept sketches (e.g., Johnson and Reynolds, 2005). All lessons were designed to be adaptable, offering the teacher a bank of questions ranging in cognitive level thus making

the lessons highly customizable by the teacher for each student. The lessons were designed to cover ~80 minutes, which is the students' allotted time for science per day.

Pre- and Post-Tests

Pre- and post-lesson tests were administered to each student to quantify the effectiveness of the adaptive lesson plans. Each test consisted of five multiple-choice or fill-in-the-blank questions that were related to the lessons' topics (Fig. 6.1). Questions were read aloud by the teacher to accommodate those students with reading difficulties. No answers were revealed to the students at the end of the pre-test. At the conclusion of each lesson, the same test questions were distributed as post-tests and again read aloud by the teacher. Only after each student handed in his/her post-test were the questions discussed among the teacher and students, and the correct answers verbally given to the students.

Student Behavioral Observations

Direct observations of student behavior and reactions to each lesson followed methods similar to those developed by Williams and Semken (2011). During each lesson, three observers were seated along the outer edges of the classroom and were assigned two to three students each. The behavior of each student was instantaneously spot sampled and recorded in an ethogram at one-minute intervals. Observations were pre-divided into five behavioral and physical characteristics (Fig. 6.2). Body position was divided into the three subcategories of leaning forward, relaxed, or slumped. These divisions were based on the interpretation that a leaning forward body position represented positive engagement with the material, a relaxed position represented neutral engagement with the material, and a slumped position represented disengagement from or disinterest in the

material Williams and Semken (2011). Similarly, student gaze was divided into two subcategories that included gazing toward the teacher/activity (positive engagement) or gazing away from the teacher/activity (negative engagement). Verbalization instances included verbalizing with the teacher or fellow students, and either on or off topic, while writing activities were categorized by the level of independence each student exhibited and the relevance of the written material to the assigned written tasks. Finally, the use of manipulatives was coded as either appropriate for their intended purpose or inappropriate and thus a distraction from the lesson. These categories were primarily used as a means to assess the level of engagement exhibited by each student throughout the duration of the lesson, and thus the degree to which each concept delivery method was effective. Following each lesson, these behavioral observations were calibrated byinput from the teacheron the students' "normal" behavior before a final assessment was made. This final step was necessary to constrain the interpretation that a student leaning forward was indeed engaged in the material during the lesson, for example, and not due to an inherent behavioral or cognitive condition.

RESULTS

Pre- and Post-Tests

Results from pre- and post-lesson tests showed that, on average, student test scores increased by approximately 21% for all lessons (Table 6.1). Some students increased their post-test scores by as much as 100%. However, 25% of the students scored lower on the post-tests relative to their pre-tests by as much as 60% of the perfect test score (Fig. 6.3). I must note, however, that these results are preliminary and it is uncertain how representative they are of pre-/post-test scores if administered to a more

statistically significant number of student participants (i.e. >30 students). Furthermore, our pre-test/post-test approach may contain the possible limitation that not all students with LD are comfortable in written exercises, especially those that require aid from the teacher or the teaching assistant in reading test questions and writing down the answers. One possible solution would be to adapt pre- and post-test evaluations by incorporating verbal student-teacher responses (e.g., one-on-one questionnaires) or by using manipulatives to assess the how well each student retained the Earth science concepts covered during the lesson.

Student Body Behavior and Verbalization

Observations recorded of student body and verbalization behaviors demonstrate obvious differences in student behavior throughout the duration of the lesson (Fig. 6.4). This was exemplified in the "Tectonic Boundaries" lesson, the data for which I discuss here. Almost every student was engaged in the pre- and post-tests, as expected. As the lesson progressed into the PowerPoint presentation, the majority of students alternated between leaning forward and remaining in a relaxed body position. Similarly, student gaze alternated between the teacher and off-topic distracters such as classmates, classroom walls, and books/toys. Within 15 minutes of the beginning of the PowerPoint presentation, nearly every student transitioned to a slumped position and gazed away from the teacher and slide show (Fig. 6.4).

In the first part of the jigsaw exercise (group discussion and student-led teaching), on-topic student-student and student-teacher verbalizations increased as each plate boundary type was distributed to the three student groups. Similarly, student on-topic writing activity increased as each group participated in drafting the concept sketch for its

assigned plate boundary with the aid of the teacher. During the second part of the jigsaw exercise (group presentations), the majority of students leaned forwarded and gazed at each student-led presentation.

DISCUSSION

Given the inherent variability in the learning needs of our student participants, our results show that there is no single effective delivery method of Earth science concepts that will reach all students with LD in the same classroom. However, similar to previous studies involving marine science education (Haddad et al., 2012) our data strongly suggest that the most effective approach to material delivery is multifaceted and should incorporate a combination of delivery techniques to help students with LD grasp and retain Earth science concepts. Broadly, these techniques include interactive slide presentations (not longer than 15 minutes), the use of manipulatives as teaching aids, the use of teacher-assisted concept sketches, student-led teaching, limiting the number of concepts covered per lesson, and reducing the readability of the level of lesson texts. This study demonstrates that lecture-style delivery of Earth science concepts is effective to a certain degree within the first 10-15 minutes at which time students with LD disengage from the lesson. This may be due to either time-dependent loss of interest in the material or cognitive conditions specific to each student. Conversely, hands-on, interactive, and student-led learning activities such as the jigsaw exercise appear to enhance the engagement of all students with LD in the classroom. This is consistent with the many findings of other studies on hands-on learning as a more effective delivery method than traditional instruction methods (see Haury and Rillero, 1994 for a complete review). However, these instructional approaches and learning activities are usually modified from

pre-existing mainstream lesson plans by the teacher in order to meet the individual cognitive and learning need of every student in the classroom. Adaptable lessons like these provided to the special education teacher saves the teacher preparation time and ultimately results in the increased use of effective lesson plans for their students.

FUTURE DIRECTIONS

The analyses and results presented in this paper can be considered as a pilot study in teaching Earth science concepts to students with LD. However, there remains a significant amount of work to further test the methods described here and develop the best customizable lesson plans that will most effectively deliver Earth science concepts to students with LD. One approach to improving the direct observational method is to validate it against continuous video-enabled student observations and coding. In an ideal classroom setting and given unlimited amount of data processing time, each lesson would be filmed in its entirety and each student would be coded continuously. However, this approach is not always practical, especially for the analysis of large numbers of students, given its time-intensive nature. Therefore, future work will involve direct comparisons of an instantaneously sampled ethogram with a continuously (from video) sampled ethogram as a way of calibrating the method described here. Additionally, one possible source of epistemic uncertainty in our direct observation method includes differences between the coding made by the different observers. To explore for the nature of this uncertainty, and to account for it in future analyses, observer-observer and observer-video comparisons need to be performed.

Another possible source of epistemic uncertainty in our results stems from the fact that our study included only eight student participants. This is not a statistically

significant sample size, and therefore may not judiciously represent the effectiveness or ineffectiveness of our lesson plans. Therefore, our results may be amplifying high-frequency signals or bias in our student behavior observations that would otherwise be reduced if our sample size were increased to more than 30 students. Finally, a significant source of uncertainty in our analyses is the lack of a control group. Future work will include direct observations of a group of students with LD that participate in an unaltered special education classroom lesson. This group should provide the control observations necessary to calibrate our observations and lesson plan effectiveness.

Future work will also include extended and standardized interviews with the special education teachers and their students. Interviews with specific and consistent questions will be conducted with the teachers after each lesson (and in the absence of the students) with regards to each student's performance during the lesson will provide systematic feedback about the effectiveness of the lesson and will refine our interpretations of each student's behavior. For example, a student might have difficulty remaining seated throughout the lesson even though he/she is engaged in the lesson and had a significant improvement in his/her post-test score. Therefore, his/her ethogram of body position may not provide a fair assessment of his/her level of engagement in the lesson and retention of concepts. Similarly, standardized interviews with each student at the end of the lesson will provide us with a more detailed assessment of their level of engagement.

ACKNOWLEDGEMENTS

I thank the parents and students of Challenger Middle School for their participation in this study, and the Glendale Elementary School District and Principal

Tiffany Molina for providing permission to conduct this study. Thank you to Professor Steven Semken and Deborah Williams for insightful discussions about our observation and data analysis methodologies. This project was partially funded by the Arizona State University (ASU) Active Tectonics, Quantitative Structural Geology, and Geomorphology Laboratory, and the ASU Graduate and Professional Student Association.

FIGURES

Figure 6.1. Sample pre-/post-test handout given to students before and after each lesson. The questions were primarily closed form and were read aloud by the teacher to accommodate students with reading difficulties. The example shown here is from the "Tectonic Boundaries" lesson plan.

Figure 6.2. Sample ethogram used in this analysis. The ethogram is divided horizontally into one-minute observation intervals where observations of several behavioral characteristics were made for the 2-3 students assigned to each observer. Each ethogram was then converted to a density plot of student behaviors (e.g., Fig. 6.4).

Figure 6.3. Examples of pre- and post-tests completed by two students. (A) In the case of the "Structure of the Earth" lesson plan, some student scores improved by up to 100% after participating in the lessons, while (B) other student scores decreased.

Figure 6.4. Density timeline illustrating observed student behavior during a ~80-minute lesson. The example shown here is from the "Tectonic Boundaries" lesson plan. *x*- and *y*-axes represent lesson time and various student behavioral indicators as coded into the ethogram (Fig. 6.2), respectively.

Figure 6.1

Name: _____

Lesson 2 – Plate Tectonics

Please answer the following questions on your own.

1) Earth's crust is divided into blocks that are called tectonic _____.

Volcanoes Plates Oceans Seafloors

2) What happens between tectonic plates?

Earthquakes and volcanoes Weather and climate Landslides

3) Earth's plates can move in many directions, such as ***up***, ***down***, ***sideways***, and _____.

Away Toward the moon Toward the core

4) Using the map below, draw a circle where earthquakes can happen.

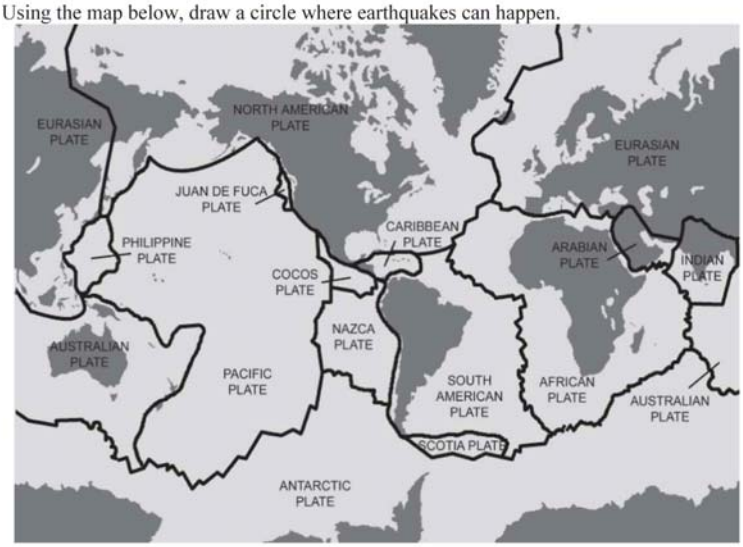

Pre-test

Figure 6.2

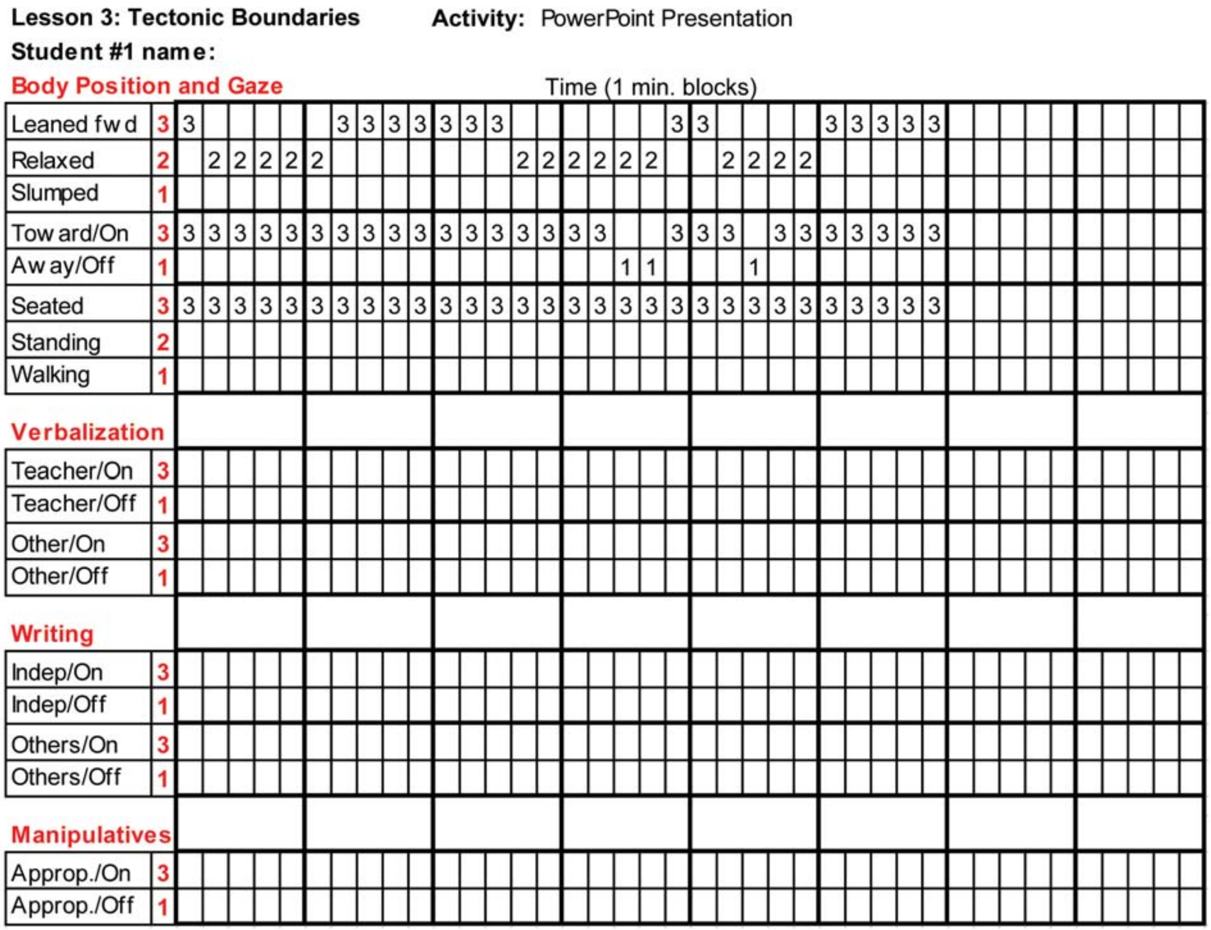

Lesson 3: Tectonic Boundaries **Activity:** PowerPoint Presentation

Student #1 name:

Body Position and Gaze Time (1 min. blocks)

Leaned fwd	3	3						3	3	3	3	3	3	3							3	3					3	3	3	3	3										
Relaxed	2		2	2	2	2	2								2	2	2	2	2	2			2	2	2	2															
Slumped	1																																								
Toward/On	3	3	3	3	3	3	3	3	3	3	3	3	3	3	3	3	3	3			3	3	3		3	3	3	3	3	3	3										
Away/Off	1																		1	1				1																	
Seated	3	3	3	3	3	3	3	3	3	3	3	3	3	3	3	3	3	3	3	3	3	3	3	3	3	3	3	3	3	3	3										
Standing	2																																								
Walking	1																																								
Verbalization																																									
Teacher/On	3																																								
Teacher/Off	1																																								
Other/On	3																																								
Other/Off	1																																								
Writing																																									
Indep/On	3																																								
Indep/Off	1																																								
Others/On	3																																								
Others/Off	1																																								
Manipulatives																																									
Approp./On	3																																								
Approp./Off	1																																								

Figure 6.3

A

Pre-test (0/5)

Post-test (5/5)

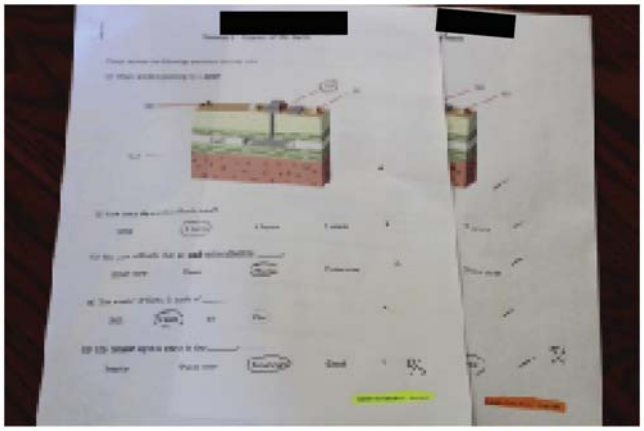

B

Pre-test (3/5)

Post-test (0/5)

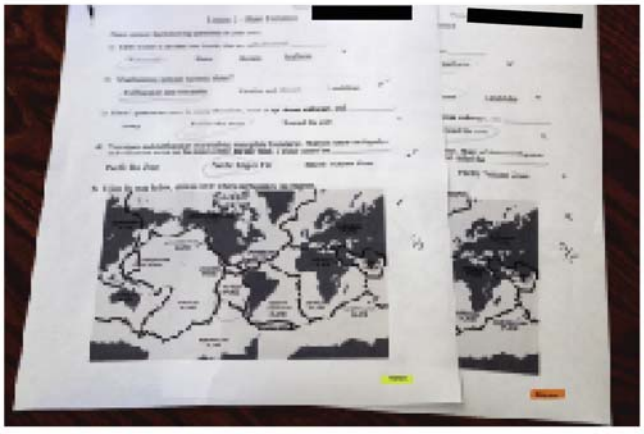

Figure 6.4

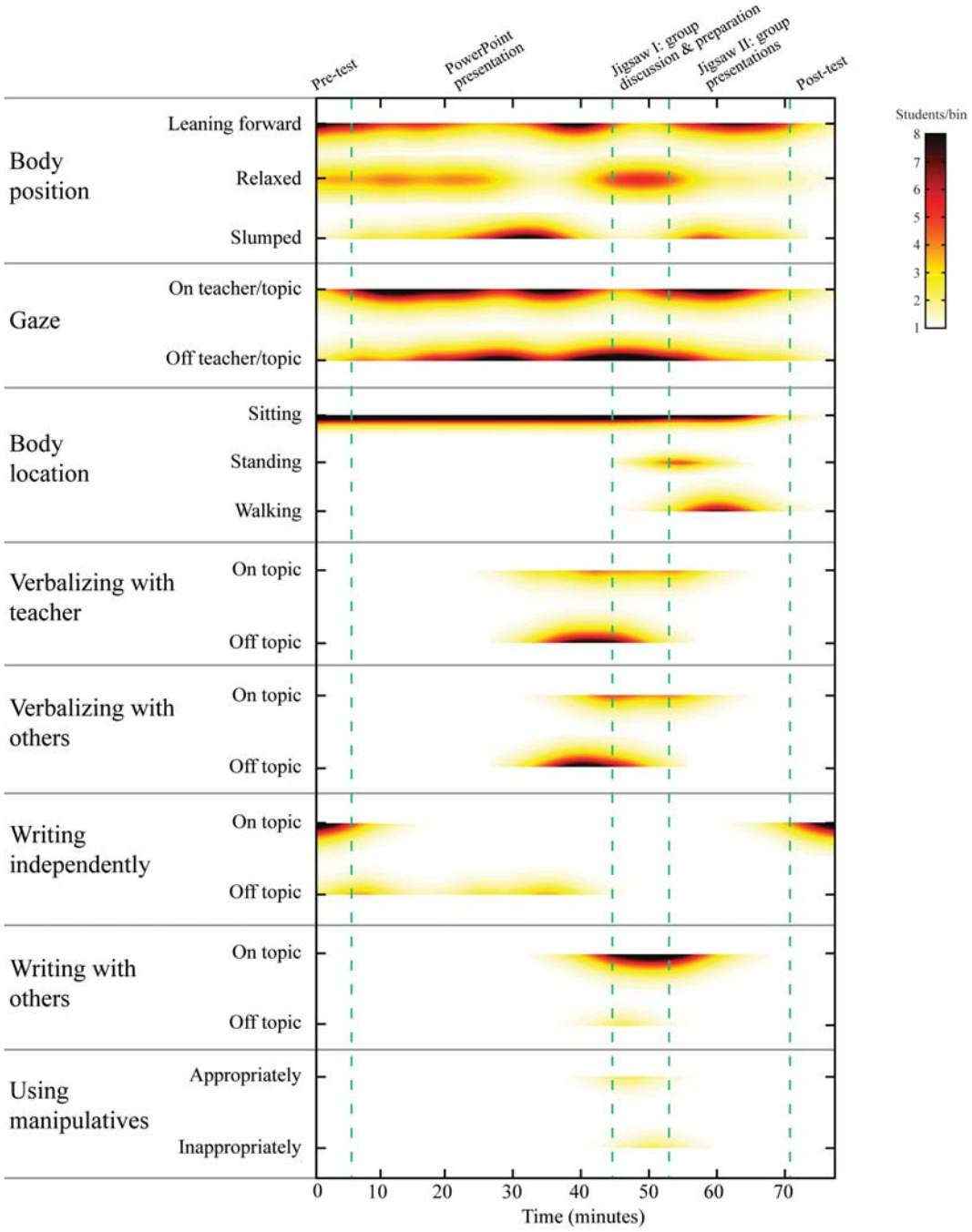
Pre-test
PowerPoint presentation
Jigsaw I: group discussion & preparation
Jigsaw II: group presentations
Post-test
Students/bin
8
7
6
5
4
3
2
1
Body position
Leaning forward
Relaxed
Slumped
Gaze
On teacher/topic
Off teacher/topic
Body location
Sitting
Standing
Walking
Verbalizing with teacher
On topic
Off topic
Verbalizing with others
On topic
Off topic
Writing independently
On topic
Off topic
Writing with others
On topic
Off topic
Using manipulatives
Appropriately
Inappropriately
0
10
20
30
40
50
60
70
Time (minutes)

TABLES

	Lesson 1 - Earth Structure			Lesson 2 - Plate tectonics			Lesson 3 - Tectonic margins		
Student #	Pre-test	Post-test	% change	Pre-test	Post-test	% change	Pre-test	Post-test	% change
1	2.00	3.00	**20.00**	3.00	3.00	**0.00**	2.00	0.00	**-50.00**
2	2.00	4.00	**40.00**	3.00	0.00	**-60.00**	0.00	2.00	**50.00**
3	2.00	3.00	**20.00**	3.00	4.00	**20.00**	2.00	0.00	**-50.00**
4	1.00	4.00	**60.00**	4.00	4.00	**0.00**	2.00	3.00	**25.00**
5	1.00	2.00	**20.00**	1.00	2.00	**20.00**	1.00	3.00	**50.00**
6	0.00	5.00	**100.00**	2.00	3.00	**20.00**	2.00	2.00	**0.00**
7	1.00	1.00	**0.00**	2.00	3.00	**20.00**	3.00	3.00	**0.00**
8	0.00	2.00	**40.00**	3.00	2.00	**-20.00**	2.00	2.00	**0.00**
Mean % change			**37.50**			**13.33**			**10.71**

Mean % change for ALL lessons (3 so far)	**20.52 % change**

Table 6.1. Pre- and post-test results obtained from the new lesson plans.

REFERENCES

Anderman, E. M., 1998, The middle school experience: effects on the math and science achievement of adolescents with LD: Journal of Learning Disabilities, v. 31, p. 128-138.

Anderson, R. C., Spiro, R. J., and Anderson, M. C., 1970, Schemata as scaffolding for the representation of information in connected disclosure: American Educational Research Journal, v. 15, p. 433-440.

Browder, D. M., Trela, K., Courtade, G. R., Jimenez, B. A., Knight, V., and Flowers, C., 2010, Teaching mathematics and science standards to students with moderate and severe developmental disabilities: Journal of Special Education, no. doi:10.1177/0022466910369942.

Cawley, J. F., Hayden, S., Cade, E., and Baker-Krooczynski, S., 2002, Including students with disabilities into the general education science classroom: Exceptional Children, v. 68, p. 423-435.

Clewell, B. C., and Fortenberry, N., 2009, Framework for Evaluating Impacts of Broadening Participation Projects: Report from a National Science Foundation Workshop, National Science Foundation, p. 89.

Haury, D. L., and Rillero, P., 1994, Perspectives of Hands-On Science Teaching, Columbus, Ohio, ERIC Clearinghouse for Science, Mathematics, and Environmental Education, 151 p.:

Holahan, G. G., McFarland, J., and Piccillo, B. A., 1994, Elementary school science for students with disabilities: Remedial and Special Education, v. 15, no. 2, p. 86-93.

Johnson, J. K., and Reynolds, S. J., 2005, Concept sketches - using student- and instructor-generated, annotated sketches for learning, teaching, and assessment in geology courses: Journal of Geoscience Education, v. 53, no. 1, p. 85-95.

Lovitt, T., Rudsit, J., Jenkins, J., Pious, C., and Benedetti, D., 1986, Adapting science materials for regular and learning disabled seventh graders: Remedial and Special Education, v. 7, no. 1, p. 31-39.

Lovitt, T. C., and Horton, S. V., 1994, Strategies for adapting science textbooks for youth with learning disabilities: Remedial and Special Education, v. 15, no. 2, p. 105-116.

Mastropieri, M. A., Scruggs, T. E., Boon, R., and Carter, K. B., 2001, Correlates of inquiry learning in science: constructing concepts of density and buoyancy: Remedial and Special Education, v. 22, p. 130-138.

Mastropieri, M. A., Scruggs, T. E., Norland, J. J., Berkeley, S., McDuffie, K., Tornquist, E. H., and Conners, N., 2006, Differentiated curriculum enhancement in inclusive middle school science: effects on classroom and high-stakes tests: Journal of Special Education, v. 40, p. 130-137.

Parmar, R. S., Deluca, C. B., and Jaczak, T. M., 2004, Investigations into the relationship between science and language abilities of students with mild disabilities: Remedial and Special Education, v. 15, p. 117-126.

Simpkins, P. M., Mastropieri, M. A., and Scruggs, T. E., 2009, Differentiated curriculum enhancements in inclusive fifth-grade science classes: Remedial and Special Education, v. 30, p. 300-308.

Williams, D., and Semken, S., 2011, Ethnographic methods in analysis of place-based geoscience curriculum and pedagogy, in Fieg, A. D., and Stokes, A., eds., Qualitative Inquiry in Geoscience Education Research: Geological Society of America Special Paper 474, p. 49-62.

Chapter 7

CONCLUSIONS

DIRECTIONS FOR FUTURE RESEARCH

The work presented in this dissertation documents earthquake-generated deformation as seen from the lenses of paleoseismology, geomorphology, and numerical modeling. While it provides an initial framework onto which future efforts may be constructed, my work highlights several areas that need improvement. Given a large amount of time, funding, and graduate students, I recommend the following directions for future research be taken.

First, the monitoring of the geomorphic degradation of the Landers fault scarp that was presented in Chapter 2 should be continued. A critical tool that I recommend be used to ensure the success of such monitoring is structure from motion (SfM). Gone are the days of dragging a 100+ lb terrestrial laser scanner halfway to Montana and spending days scanning a few square kilometers of some interesting landform. The ease with which centimeter-scale digital elevation models can be generated from SfM photographs, which can be taken by balloon aerial photography, will ensure the persistent monitoring of the Landers fault scarp for years to come. We must not forget that the geomorphic monitoring of the Landers fault scarp was initiated by Arrowsmith and Rhodes (1994) only days following the Landers earthquake 22 years ago. While recent work using terrestrial lidar documents fault scarps generated by recent earthquakes (e.g., Gold et al., 2012), Chapter 2 presents the longest quantitative record of fault scarp degradation (Haddad et al., 2012; Johnson et al., in review). SfM provides us with a unique opportunity to continue this monitoring efficiently and cost effectively. Such an effort

will be of immense use to us for several reasons. The quantification of continued scarp degradation will allow us to calibrate numerical scarp evolution models (e.g., Hanks et al., 1984; Hanks, 2000) and analog models of offset channel degradation (i.e. in a sand table/flume). The use of SfM in such experimental setups will be critical in documenting topographic deformation/modification following simulated earthquakes and rainfall events. Geomorphic degradation rates can then be computed in 3D using similar methods employed to quantify real earthquake deformation fields (e.g., Chapter 3 and Nissen et al. (2012)). These rates can subsequently be used to calibrate scarp diffusion models and reevaluate the timing of prehistoric earthquakes that are recorded by older fault scarps. Another application of SfM should take place in paleoseismic trenches to accurately document piercing points in 3D. This will prove invaluable to the quantification of paleoearthquake-related topographic deformation several meters away from the principal displacement zone. The opportunities for SfM are endless.

Second, future work should further expand upon numerical simulations of earthquake ruptures and their associated crustal deformation. It is clear that the methods I used in Chapters 4 and 5 oversimplify the physical processes that govern the physics of the earthquake cycle. We know that the upper lithosphere behaves in a much more complex manner than how it is modeled in my dissertation. If the research problem is focused on a few earthquake cycles, then the assumptions used in Chapters 4 and 5 may suffice. However, earthquake physics is far from static, and the paleoseismic record preserves the cumulative effects of coseismic, postseismic, and interseismic phenomena. We know that dynamic rupture processes control coseismic and postseismic deformation during the earthquake cycle, as demonstrated by dynamic simulations of single ruptures

and by geodetic documentation of modern earthquakes (e.g., Oglesby et al., 2003; Dunham et al., 2011; Kaneko and Fialko, 2011; Lozos et al., 2011; Kaneko et al., 2013; Shirzaei and Burgmann, 2013; Shirzaei et al., 2013). Present-day computing capabilities inhibit the dynamic simulation of ruptures over thousands of earthquake cycles. But continued acceleration of computing power should soon allow us to explore how much dynamic earthquake processes contribute to topographic deformation at paleoseismic timescales. These dynamic models should eventually be incorporated into earthquake hazard assessments such as the Uniform California Earthquake Rupture Forecast (UCERF). Of course, this will depend on the spatial and temporal scales in which we are interested. If we are interested in geologic timescales (thousands to millions of years – to understand long-term fault interactions, for example), then obviously a different set of modeling tools is needed that will allow for the evolution/interaction of faults and geodynamic processes. Future work should bring lithospheric deformation models closer to reality by allowing spatiotemporal variations in fault geometry, roughness, depth-dependent friction, and lithospheric strength. How can we formulate crustal deformation models that emphasize the earthquake cycle over single/multiple events? How can we use geodetic datasets (e.g., InSAR and GPS) to understand the nature of crust-mantle coupling and in turn say something about earthquake interactions in space and time? This is an age-old conundrum with which geologists have been dealing since accepting the theory of plate tectonics. So, it should be no surprise to us that it exists in the context of reconciling geodetically vs. geologically determined fault slip rates.

I close this dissertation with the notion that the inevitability of earthquake occurrence in densely populated areas underlines the importance of integrating insights

from geomorphic, geologic, geodetic, and numerical observations to improve seismic hazard analyses. It is the responsibility of earthquake scientists to make sure this integration remains a topmost priority in guiding earthquake-mitigation policies. The efforts of the multidisciplinary groups involved in UCERF serve as a fine example of how these observations converge to a tangible product of which policy makers can make use to ensure the safety of the general public.

REFERENCES

Arrowsmith, J. R., and Rhodes, D. D., 1994, Original forms and initial modifications of the Galway Lake Road scarp formed along the Emerson Fault during the 28 June 1992 Landers, California, Earthquake: Bulletin of the Seismological Society of America, v. 84, no. 3, p. 511-527.

Dunham, E. M., Belanger, D., Cong, L., and Kozdon, J. E., 2011, Earthquake Ruptures with Strongly Rate-Weakening Friction and Off-Fault Plasticity, Part 2: Nonplanar Faults: Bulletin of the Seismological Society of America, v. 101, no. 5, p. 2308-2322.

Gold, P. O., Cowgill, E., Kreylos, O., and Gold, R. D., 2012, A terrestrial lidar-based workflow for determining three-dimensional slip vectors and associated uncertainties: Geosphere, v. 8, no. 2, p. 431-442.

Haddad, D. E., Akciz, S. O., Arrowsmith, J. R., Rhodes, D. D., Oldow, J. S., Zielke, O., Toké, N. A., Haddad, A. G., Mauer, J., and Shilpakar, P., 2012, Applications of airborne and terrestrial laser scanning to paleoseismology: Geosphere, v. 8, no. 4, p. 771-786.

Hanks, T. C., 2000, The age of scarplike landforms from diffusion-equation analysis, in Noller, J. S., Sowers, J. M., and Lettis, W. R., eds., Quaternary Geochronology, AGU Reference Shelf, p. 313-338.

Hanks, T. C., Bucknam, R. C., Lajoie, K. R., and Wallace, R. E., 1984, Modification of wave-cut and faulting-controlled landforms: Journal of Geophysical Research, v. 89, no. B7, p. 5771-5790.

Johnson, K., Nissen, E., Saripalli, S., Arrowsmith, J. R., McGarey, P., Scharer, K. M., Williams, P., and Blisniuk, K., in review, Rapid mapping of ultra-fine fault zone topography with Structure from Motion: Geosphere.

Kaneko, Y., and Fialko, Y., 2011, Shallow slip deficit due to large strike-slip earthquakes in dynamic rupture simulations with elasto-plastic off-fault response: Geophysical Journal International, v. 186, p. 1389-1403.

Kaneko, Y., Fialko, Y., Sandwell, D., Tong, X., and Furuya, M., 2013, Interseismic deformation and creep along the central section of the North Anatolian Fault (Turkey): InSAR observations and implications for rate-and-state friction properties: Journal of Geophysical Research, v. 118, p. 1-15.

Lozos, J. C., Oglesby, D. D., Duan, B., and Wesnousky, S. G., 2011, The Effects of Double Fault Bends on Rupture Propagation: A Geometrical Parameter Study: Bulletin of the Seismological Society of America, v. 101, no. 1, p. 385-398.

Nissen, E., Krishnan, A. K., Arrowsmith, J. R., and Saripalli, S., 2012, Three-dimensional surface displacements and rotations from differencing pre- and post-earthquake LiDAR point clouds: Geophysical Research Letters, v. 39, no. L16301.

Oglesby, D. D., Day, S. M., Li, Y., and Vidale, J. E., 2003, The 1999 Hector Mine earthquake: The dynamics of a branched fault system: Bulletin of the Seismological Society of America, v. 93, p. 2459-2476.

Shirzaei, M., and Burgmann, R., 2013, Time-dependent model of creep on the Hayward fault from joint inversion of 18 years of InSAR and surface creep data: Journal of Geophysical Research, v. 118, p. 1733-1746.

Shirzaei, M., Burgmann, R., and Taira, T., 2013, Implications of recent asperity failures and aseismic creep for time-dependent earthquake hazard on the Hayward fault: Earth and Planetary Science Letters, v. 371, p. 59-66.

Dissertation References

Akçiz, S. O., Grant Ludwig, L., and Arrowsmith, J. R., 2009, Revised dates of large earthquakes along the Carrizo section of the San Andreas fault, California, since A.D. 1310 ± 30: Journal of Geophysical Research, v. 114, no. B01313.

Akçiz, S. O., Grant Ludwig, L., Arrowsmith, J. R., and Zielke, O., 2010, Century-long average time intervals between earthquake ruptures of the San Andreas fault in the Carrizo Plain, California: Geology, v. 38, no. 9, p. 787-790.

Anderson, R. C., Spiro, R. J., and Anderson, M. C., 1970, Schemata as scaffolding for the representation of information in connected disclosure: American Educational Research Journal, v. 15, p. 433-440.

Anderman, E. M., 1998, The middle school experience: effects on the math and science achievement of adolescents with LD: Journal of Learning Disabilities, v. 31, p. 128-138.

Anooshehpoor, A., Brune, J. N., and Purvance, M. D., 2009, Field-test of precariously balanced rocks near Yucca Valley, California: seismic hazard ramifications (proceedings and abstracts): SCEC Annual Meeting, Palm Springs, California, September 12-16, 2009, 19.

Anooshehpoor, A., Purvance, M., Brune, J., and Rennie, T., 2007, Reduction in the uncertainties in the ground motion constraints by improved field testing techniques of precariously balanced rocks (proceedings and abstracts): SCEC Annual Meeting, Palm Springs, California, September 9-12, 2007, 17.

Aochi, H., Madariaga, R., and Fukuyama, F., 2002, Effect of normal stress during rupture propagation along nonplanar faults: Journal of Geophysical Research - Solid Earth, v. 107, no. B2, p. 2038.

Arrowsmith, J. R., Madden, C. M., Haddad, D. E., Salisbury, J. B., and Weldon, R. J., 2011, Compilation of slip in the last event data for high slip rate faults in California for input into slip-dependent rupture forecast: Eos Trans., no. AGU, S13B-06.

Arrowsmith, J. R., Pollard, D. D., and Rhodes, D. D., 1996, Hillslope development in areas of active tectonics: Journal of Geophysical Research, v. 101, p. 6255-6275.

Arrowsmith, J. R., and Rhodes, D. D., 1994, Original forms and initial modifications of the Galway Lake Road scarp formed along the Emerson Fault during the 28 June 1992 Landers, California, Earthquake: Bulletin of the Seismological Society of America, v. 84, no. 3, p. 511-527.

Arrowsmith, J. R., and Rhodes, D. D., 2000, A 3-stage model for erosional modification of the Emerson fault (Landers, California earthquake) scarp, June 1992-January 2000: GSA Abstracts with Programs, v. 7, no. A-366.

Arrowsmith, J. R., Rhodes, D. D., and Pollard, D. D., 1998, Morphologic dating of scarps formed by repeated slip events along the San Andreas fault, Carrizo Plain, California: Journal of Geophysical Research, v. 103, no. B5, p. 10,141-110,160.

Arrowsmith, J. R., and Zielke, O., 2009, Tectonic geomorphology of the San Andreas Fault zone from high resolution topography: An example from the Cholame segment: Geomorphology, v. 113, p. 70-81.

Beeler, N. M., Tullis, T. E., and Weeks, J. D., 1994, The roles of time and displacement in the evolution effect in rock friction: Geophysical Research Letters, v. 21, p. 1987-1990.

Bell, J. W., Brune, J. N., Liu, T., Zreda, M., and Yount, J. C., 1998, Dating precariously balanced rocks in seismically active parts of California and Nevada: Geology, v. 26, no. 6, p. 495-498.

Bevis, M., Hudnut, K., Sanchez, R., Toth, C., Grejner-Brzezinska, D., Kendrick, E., Caccamise, D., Raleigh, D., Zhou, H., Shan, S., Shindle, W., Yong, A., Harvey, J., Borsa, A., Ayoub, F., Elliot, B., Shrestha, R., Carter, B., Sartori, M., Phillips, D., Coloma, F., and Stark, K., 2005, The B4 Project: scanning the San Andreas and San Jacinto fault zones: Eos Trans. AGU 86(52), Fall Meet. Suppl., Abstract H34B-01.

Biasi, G. P., and Weldon, R. J., 2006, Estimating surface rupture length and magnitude of paleoearthquakes from point measurements of rupture displacement: Bulletin of the Seismological Society of America, v. 96, no. 5, p. 1612-1623.

Bistacchi, A., Griffith, W. A., Smith, S. A. F., Di Toro, G., Jones, R., and Nielsen, S., 2011, Fault Roughness at Seismogenic Depths from LIDAR and Photogrammetric Analysis: Pure and Applied Geophysics, v. 168, no. 12, p. 2345-2363.

Blanpied, M. L., Lockner, D. A., and Byerlee, J. D., 1991, Fault stability inferred from granite sliding experiments at hydrothermal conditions: Geophysical Research Letters, v. 18, no. 4, p. 609-612.

Borsa, A., and Minster, J. B., in press, Rapid determination of near-fault earthquake deformation using differential LiDAR: Bulletin of the Seismological Society of America.

Browder, D. M., Trela, K., Courtade, G. R., Jimenez, B. A., Knight, V., and Flowers, C., 2010, Teaching mathematics and science standards to students with moderate and severe developmental disabilities: Journal of Special Education, no. doi:10.1177/0022466910369942.

Brune, J. N., 1993a, Distribution of precariously balanced rocks in Nevada and California - correlation with probability maps for strong ground motion: Eos, v. 73, no. 43, p. 351.

Brune, J. N., 1993b, Precariously balanced rocks in Nevada and California - implications for earthquake hazard in Nevada, particularly at Yucca Mountain: Geological Society of America Abstracts with Programs, v. 25, no. 5, p. 15.

Brune, J. N., 1994, Constraints on ground motion from great earthquakes provided by groups of precarious rocks: Seismological Research Letters, v. 65, no. 1, p. 64.

Brune, J. N., 1996, Precariously balanced rocks and ground-motion maps for Southern California: Bulletin of the Seismological Society of America, v. 86, no. 1A, p. 43-54.

Brune, J. N., Anooshehpoor, A., Purvance, M. D., and Brune, R. J., 2006, Band of precariously balanced rocks between the Elsinore and San Jacinto, California, fault zones: Constraints on ground motion for large earthquakes: Geology, v. 34, no. 3, p. 137-140.

Brune, J. N., and Whitney, J. W., 2000, Precarious rocks and seismic shaking at Yucca Mountain, Nevada: US Geological Survey Digital Data Series 058, p. 1-19.

Burbank, D. W., and Anderson, R. S., 2001, Tectonic geomorphology, Malden, Mass, Blackwell Science, v. Book, Whole.

Burgmann, R., Pollard, D. D., and Martel, S. J., 1994, Slip distributions on faults: effects of stress gradients, inelastic deformation, heterogeneous host-rock stiffness, and fault interaction: Journal of Structural Geology, v. 16, p. 1675-1690.

Busetti, S., Mish, K., and Reches, Z., 2012, Damage and plastic deformation of reservoir rocks: Part 1. Damage fracturing: American Association of Petroleum Geologists Bulletin, v. 96, no. 9, p. 1687-1709.

Carr, M. D., Harris, A. G., Poole, F. G., and Fleck, R. J., 1993, Stratigraphy and structure of Paleozoic outer continental margin rocks in PilotKnobValley, north central Mojave Desert, California: U.S. Geological Survey Bulletin, v. 2015, p. 33.

Carter, W. E., Shrestha, R. L., and Slatton, K. C., 2007, Geodetic laser scanning: Physics Today, v. 60, no. 12, p. 41-47.

Cawley, J. F., Hayden, S., Cade, E., and Baker-Krooczynski, S., 2002, Including students with disabilities into the general education science classroom: Exceptional Children, v. 68, p. 423-435.

Chang, S., Avouac, J., Barbot, S., and Lee, J., 2013, Spatially variable fault friction derived from dynamic modeling of aseismic afterslip due to the 2004 Parkfield earthquake: Journal of Geophysical Research, v. 118, p. 1-17.

Chang, W. L., and Smith, R. B., 2002, Integrated seismic-hazard analysis of the Wasatch Front, Utah: Bulletin of the Seismological Society of America, v. 92, p. 1902-1922.

Chuang, R. Y., and Johnson, K. M., 2011, Reconciling geologic and geodetic model fault slip-rate discrepancies in Southern California: Consideration of nonsteady mantle flow and lower crustal fault creep: Geology, v. 39, p. 627-630.

Clark, M. M., and Lajoie, K. R., 1974, Holocene behavior of the Garlock fault: Geological Society of America Abstracts with Programs, v. 6, p. 156-157.

Clewell, B. C., and Fortenberry, N., 2009, Framework for Evaluating Impacts of Broadening Participation Projects: Report from a National Science Foundation Workshop, National Science Foundation, p. 89.

Cochran, E. S., Li, Y., Shearer, P. M., Barbot, S., Fialko, Y., and Vidale, J. E., 2009, Seismic and geodetic evidence for extensive, long-lived fault damage zones: Geology, v. 37, no. 4, p. 315-318.

Cooke, M. L., and Dair, L. C., 2011, Simulating the recent evolution of the southern big bend of the San Andreas fault, Southern California: Journal of Geophysical Research, v. 116, no. B04405, p. 20.

Davis, W. M., 1892, The convex profile of badland divides: Science, v. 20, p. 245.

Davis, W. M., 1899, The geographical cycle: The Geographical Journal, v. 14, p. 481-504.

Davis, G. A., and Burchfiel, B. C., 1973, Garlock fault: an intracontinental transform structure, southern California: Geological Society of America Bulletin, v. 84, p. 1407-1422.

DeLong, S. B., Hilley, G. E., Rymer, M. J., and Prentice, C., 2010, Fault zone structure from topography: Signatures of en echelon fault slip at Mustang Ridge on the San Andreas Fault, Monterey County, California: Tectonics, v. 29, no. TC5003, doi: 10.1029/2010TC002673.

DeMers, 2002, Fundamentals of Geographic Information Systems, Hoboken, John Wiley & Sons, 480 p.

Densmore, A. L., Ellis, M. A., and Anderson, R. S., 1998, Landsliding and the evolution of normal-fault-bounded mountains: Journal of Geophysical Research-Solid Earth, v. 103, no. B7, p. 15203-15219.

DeWitt, E., Langenheim, V., Force, E., Vance, R. K., Lindberg, P. A., and Driscoll, R. L., 2008, Geologic map of the Prescott National Forest and the headwaters of the Verde River, Yavapai and Coconino Counties, Arizona: US Geological Survey Scientific Investigations Map 2996, scale 1:100,000, p. 100.

Dieterich, J. H., and Kilgore, B. D., 1994, Direct observation of frictional contacts: new insights for state dependent properties: Pure and Applied Geophysics, v. 143, p. 283-302.

Dieterich, J. H., and Smith, D. E., 2009, Nonplanar Faults: Mechanics of Slip and Off-fault Damage: Pure and Applied Geophysics, v. 166, p. 1799-1815.

Dietrich, W. E., Wilson, C. J., Montgomery, D. R., McKean, J., and Bauer, R., 1992, Erosion thresholds and land surface morphology: Geology, v. 20, p. 675-679.

Dolan, J. F., Bowman, D. D., and Sammis, C. G., 2007, Long-range and long-term fault interactions in Southern California: Geology, v. 35, no. 9, p. 855-858.

Duan, B., and Oglesby, D. D., 2006, Heterogeneous fault stresses from previous earthquakes and the effect on dynamics of parallel strike-slip faults: Journal of Geophysical Research - Solid Earth, v. 111, no. B5, p. B05309.

Dunham, E. M., Belanger, D., Cong, L., and Kozdon, J. E., 2011, Earthquake Ruptures with Strongly Rate-Weakening Friction and Off-Fault Plasticity, Part 2: Nonplanar Faults: Bulletin of the Seismological Society of America, v. 101, no. 5, p. 2308-2322.

El-Sheimy, N., Valeo, C., and Habib, A., 2005, Digital terrain modeling: acquisition, manipulation, and applications, Boston, MA, Artech House, 257 p.

Ferrill, D. A., and Morris, A. P., 2001, Displacement gradient and deformation in normal fault systems: Journal of Structural Geology, v. 23, p. 619-638.

Ferrill, D. A., Morris, A. P., McGinnis, R., Smart, K. J., and Ward, W. C., 2011, Fault zone deformation and displacement partitioning in mechanically layered carbonates: The Hidden Valley fault, central Texas: American Association of Petroleum Geologists Bulletin, v. 95, no. 8, p. 1383-1397.

Field, E. H., Biasi, G. P., Bird, P., Dawson, T. E., Felzer, K. R., Jackson, D. D., Johnson, K. M., Jordan, T. H., Madden, C., Michael, A. J., Milner, K. R., Page, M. T., Parsons, T., Powers, P. M., Shaw, B. E., Thatcher, W. R., Weldon, R. J., and Zeng, Y., 2013, Uniform California Earthquake Rupture Forecast, Version 3 (UCERF3)—The Time-Independent Model: U.S. Geological Survey Open-File Report 2013-1165.

Frankel, K. L., Dolan, J. F., Owen, L. A., Ganev, P., and Finkel, R. C., 2011, Spatial and temporal constancy of seismic strain release along an evolving segment of the

Pacific-North America plate boundary: Earth and Planetary Science Letters, v. 304, no. 3-4, p. 565-576.

Gardner, T. W., 1983, Experimental study of knickpoint and longitudinal profile evolution in cohesive, homogenous material: Geological Society of America Bulletin, v. 94, p. 664-672.

Giardini, D., Grunthal, G., Shedlock, K., and Zhang, P., 1999, The Global Seismic Hazard Map.

Gilbert, G. K., 1877, Report on the geology of the Henry Mountains (Utah), Washington, D.C., U.S. Geographical and Geological Survey of the Rocky Mountain Region, Government Printing Office, 160 p.

Gilbert, G. K., 1909, The convexity of hilltops: Journal of Geology, v. 17, p. 344-350.

Gold, P. O., Cowgill, E., Kreylos, O., and Gold, R. D., 2012, A terrestrial lidar-based workflow for determining three-dimensional slip vectors and associated uncertainties: Geosphere, v. 8, no. 2, p. 431-442.

Gomberg, J., and Ellis, M. A., 1994, Topography and tectonics of the central New Madrid seismic zone: Results of numerical experiments using a three-dimensional boundary element program: Journal of Geophysical Research, v. 99, no. b10, p. 20299-20310.

Grant, L. B., and Sieh, K., 1994, Paleoseismic evidence of clustered earthquakes on the San Andreas fault in the Carrizo Plain, California: Journal of Geophysical Research, v. 99, no. B4, p. 6819-6841.

Grant Ludwig, L., Akçiz, S. O., Noriega, G. R., Zielke, O., and Arrowsmith, J. R., 2010, Climate-modulated channel incision and rupture history of the San Andreas fault in the Carrizo Plain: Science, v. 327, p. 1117-1119.

Gualandi, A., Serpelloni, E., and Belardinelli, M., 2014, Space–time evolution of crustal deformation related to the Mw 6.3, 2009 L'Aquila earthquake (central Italy) from principal component analysis inversion of GPS position time-series: Geophysical Journal International.

Haddad, D. E., 2010, Geologic and geomorphic characterization of precariously balanced rocks, MS Thesis: Arizona State University, 207 p.

Haddad, D. E., Akciz, S. O., Arrowsmith, J. R., Rhodes, D. D., Oldow, J. S., Zielke, O., Toké, N. A., Haddad, A. G., Mauer, J., and Shilpakar, P., 2012, Applications of airborne and terrestrial laser scanning to paleoseismology: Geosphere, v. 8, no. 4, p. 771-786.

Haddad, D. E., Madden, C. M., Salisbury, J. B., Arrowsmith, J. R., and Weldon, R. J., 2011, LiDAR-derived measurements of slip in the most recent ground-rupturing earthquakes along elements of the San Andreas fault system: SCEC Proceedings and Abstracts, v. 21.

Hanks, T. C., 2000, The age of scarplike landforms from diffusion-equation analysis, in Noller, J. S., Sowers, J. M., and Lettis, W. R., eds., Quaternary Geochronology, AGU Reference Shelf, p. 313-338.

Hanks, T. C., Bucknam, R. C., Lajoie, K. R., and Wallace, R. E., 1984, Modification of wave-cut and faulting-controlled landforms: Journal of Geophysical Research, v. 89, no. B7, p. 5771-5790.

Hanks, T. C., and Kanamori, H., 1979, A moment magnitude scale: Journal of Geophysical Research, v. 84, no. B5, p. 2348-2350.

Harris, R. A., Archuleta, R. J., and Day, S. M., 1991, Fault steps and the dynamic rupture process -- 2-D numerical simulations of a spontaneously propagating shear fracture: Geophysical Research Letters, v. 18, no. 5, p. 893-896.

Harris, R. A., and Day, S. M., 1993, Dynamics of fault interaction: Parallel strike-slip faults: Journal of Geophysical Research-Solid Earth, v. 98, no. B3, p. 4461-4472.

Haugerud, R. A., Harding, D. J., Johnson, S. Y., Harless, J. L., Weaver, C. S., and Sherrod, B. L., 2003, High-resolution Lidar topography of the Puget Lowland, Washington—a bonanza for earth science: GSA Today, v. 13, no. 6, p. 4-10.

Haury, D. L., and Rillero, P., 1994, Perspectives of Hands-On Science Teaching, Columbus, Ohio, ERIC Clearinghouse for Science, Mathematics, and Environmental Education, 151 p.:

Heimsath, A. M., Chappell, J., Dietrich, W. E., Nishiizumi, K., and Finkel, R., 2001, Late Quaternary erosion in southeastern Australia: a field example using cosmogenic nuclides: Quaternary International, v. 83-85, p. 169-185.

Hill, M. L., and Dibblee, T. W., 1953, San Andreas, Garlock, and Big Pine faults, California: a study of the character, history, and tectonic significance of their displacements: Geological Society of America Bulletin, v. 64, p. 443-458.

Hilley, G. E., and Arrowsmith, J. R., 2001, Penck1D: Transport- and production-limited fault scarp simulation software: GSA Special Short Course Manual, p. 44.

Hilley, G. E., and Arrowsmith, J. R., 2003, Scarp dater software: Scarp diffusion exercise from the International Quality Network Workshop: Potsdam, Germany, Potsdam University.

Hilley, G. E., and Arrowsmith, J. R., 2008, Geomorphic response to uplift along the Dragon's Back pressure ridge, Carrizo Plain, California: Geology, v. 36, no. 5, p. 367-370.

Hilley, G. E., DeLong, S., Prentice, C., Blisniuk, K., and Arrowsmith, J., 2010, Morphologic dating of fault scarps using airborne laser swath mapping (ALSM) data: Geophysical Research Letters, v. 37.

Holahan, G. G., McFarland, J., and Piccillo, B. A., 1994, Elementary school science for students with disabilities: Remedial and Special Education, v. 15, no. 2, p. 86-93.

Hudnut, K., Amidon, W., Bawden, G., Brune, J., Bond, S., Graves, R., Haddad, D. E., Limaye, A., Lynch, D. K., Phillips, D. A., Pounders, E., Rood, D., and Weiser, D., 2009a, The Echo Cliffs precariously balanced rock; discovery and description by terrestrial laser scanning (proceedings and abstracts): Southern California Earthquake Center Annual Meeting, Palm Springs, California, September 12-16, 2009, 19.

Hudnut, K., Amidon, W., Bawden, G., Brune, J., Graves, R., Haddad, D. E., Limaye, A., Lynch, D. K., Phillips, D. A., Pounders, E., and Rood, D., 2009b, The Echo Cliffs precariously balanced rock: discovery and description by terrestrial laser scanning: Eos Trans. AGU 90(52), Fall Meet. Suppl., Abstract G51B-0657.

Hudnut, K. W., Borsa, A., Glennie, C., and Minster, J.-B., 2002, High-resolution topography along surface rupture of the 16 October 1999 Hector Mine, California, earthquake (Mw 7.1) from airborne laser swath mapping: Bulletin of the Seismological Society of America, v. 92, no. 4, p. 1570-1576.

Humphreys, E. D., and Weldon, R., 1994, Deformation across the western United States: a local estimate of Pacific-North America transform deformation: Journal of Geophysical Research, v. 99, p. 19975-20010.

Jaeger, J. C., Cook, N. G. W., and Zimmerman, R. W., 2007, Fundamentals of rock mechanics, Malden, Wiley-Blackwell, 488 p.

Jordan, T. H., Chen, Y., Gasparini, P., Madariaga, R., Main, I., Marzocchi, W., Papadopoulos, G., Sobolev, G., Yamaoka, K., and Zschau, J., 2011, Operational earthquake forecasting: state of knowledge and guidelines for utilization: Annals of Geophysics, v. 54, no. 4, p. 316-391.

Johnson, A. M., Fleming, R. W., Cruikshank, K. M., Martosudarmo, S. Y., Johnson, N. A., Johnson, K. M., and Wei, W., 1997, Analecta of structures formed during the 28 June 1992 Landers-Big Bear, California earthquake sequence: U.S. Geological Survey.

Johnson, K., Nissen, E., Saripalli, S., Arrowsmith, J. R., McGarey, P., Scharer, K. M., Williams, P., and Blisniuk, K., in review, Rapid mapping of ultra-fine fault zone topography with Structure from Motion: Geosphere.

Johnson, J. K., and Reynolds, S. J., 2005, Concept sketches - using student- and instructor-generated, annotated sketches for learning, teaching, and assessment in geology courses: Journal of Geoscience Education, v. 53, no. 1, p. 85-95.

Kaneko, Y., and Fialko, Y., 2011, Shallow slip deficit due to large strike-slip earthquakes in dynamic rupture simulations with elasto-plastic off-fault response: Geophysical Journal International, v. 186, p. 1389-1403.

Kaneko, Y., Fialko, Y., Sandwell, D., Tong, X., and Furuya, M., 2013, Interseismic deformation and creep along the central section of the North Anatolian Fault (Turkey): InSAR observations and implications for rate-and-state friction properties: Journal of Geophysical Research, v. 118, p. 1-15.

Kame, N., Rice, J. R., and Dmowska, R., 2003, Effects of prestress state and rupture velocity on dynamic fault branching: Journal of Geophysical Research - Solid Earth, v. 108, no. B5, p. 2265.

Kase, Y., and Day, S. M., 2006, Spontaneous rupture processes on a bending fault: Geophysical Research Letters, v. 33, no. 10, p. L10302.

Kirkby, M. J., 1971, Hillslope process-response models based on the continuity equation: Institute of British Geographers, Special Publication, v. 3, p. 15-30.

Kondo, H., Toda, S., Okamura, K., and Chiba, T., 2008, A fault scarp in an urban area identified by LiDAR survey: a Case study on the Itoigawa–Shizuoka Tectonic Line, central Japan: Geomorphology, v. 101, p. 731-739.

Krishnan, S., Crosby, C., Nandigam, V., Phan, M., Cowart, C., Baru, C., Arrowsmith, J. R., and OpenTopography, 2011, A services oriented architechture for community access to LiDAR topogaphy: Proceedings of the 2nd International Conference on Computing for Geospatial Research and Applications.

Landgraf, A., Zielke, O., Arrowsmith, J. R., Ballato, P., Strecker, M. R., Schildgen, T. F., Friedrich, A. M., and Tabatabaei, 2013, Differentiating simple and composite tectonic landscapes using numerical fault slip modeling with an example from the south central Alborz Mountains, Iran: Journal of Geophysical Research, v. 118, p. 1792-1805.

LaViolette, J. W., Christensen, G. E., and Stepp, J. C., 1980, Quaternary displacement on the western Garlock fault, southern California, South Coast Geological Society, Geology and Mineral Wealth of the California Desert, Santa Ana, California.

Lawson, A., 1908, Report of the Earthquake Investigation Commission upon the California Earthquake of April 18, 1906: Carnegie Institution.

Leprince, S., Hudnut, K. W., Akciz, S., Hinojosa-Corona, A., and Fletcher, J. M., 2011, Surface rupture and slip variation induced by the 2010 El Mayor-Cucupah earthquake, Baja California, quantified using COSI-Corr analysis on pre- and post-earthquake LiDAR acquitions: AGU Fall Meeting Abstracts, EP41A-0596.

Lienkaemper, J. J., Borchardt, G., and Lisowski, M., 1991, Historic creep rate and potential for seismic slip along the Hayward Fault, California: Journal of Geophysical Research, v. 97, p. 18261–18283.

Lienkaemper, J. J., Galehouse, J. S., and Simpson, R. W., 1997, Creep response of the Hayward fault to stress changes caused by the Loma Prieta earthquake: Science, v. 276, no. 5321, p. 2014-2016.

Lienkaemper, J. J., McFarland, F. S., Simpson, R. W., Bilham, R. G., Ponce, D. A., Boatwright, J. J., and Caskey, S. J., 2012, Long-term creep rates on the Hayward fault: Evidence for controls on the size and frequency of large earthquakes: Bulletin of the Seismological Society of America, v. 102.

Lovitt, T. C., and Horton, S. V., 1994, Strategies for adapting science textbooks for youth with learning disabilities: Remedial and Special Education, v. 15, no. 2, p. 105-116.

Lovitt, T., Rudsit, J., Jenkins, J., Pious, C., and Benedetti, D., 1986, Adapting science materials for regular and learning disabled seventh graders: Remedial and Special Education, v. 7, no. 1, p. 31-39.

Lozos, J. C., Oglesby, D. D., Brune, J. N., and Olsen, K. B., 2012, Small intermediate fault segments can either aid or hinder rupture propagation at stepovers: Geophysical Research Letters, v. 39, no. L18305.

Lozos, J. C., Oglesby, D. D., Duan, B., and Wesnousky, S. G., 2011, The Effects of Double Fault Bends on Rupture Propagation: A Geometrical Parameter Study: Bulletin of the Seismological Society of America, v. 101, no. 1, p. 385-398.

Ludington, S., Moring, B. C., Miller, R. J., Stone, P. A., Bookstrom, A. A., Bedford, D. R., Evans, J. G., Haxel, G. A., Nutt, C. J., Flyn, K. S., and Hopkins, M. J., 2007, Preliminary integrated geologic map databases for the United States - Western States: California, Nevada, Arizona, Washington, Oregon, Idaho, and Utah: U.S. Geological Survey Open-File Report 2005-1305.

Madden, C. M., Arrowsmith, J. R., Haddad, D. E., Salisbury, J. B., and Weldon, R. J., 2011, Compilation of slip in the last earthquake data for high slip rate faults in California for input into slip-dependent rupture forecast: SCEC Proceedings and Abstracts, v. 21.

Marone, C., and Richardson, E., 2010, Learning to read fault-slip behavior from fault-zone structure: Geology, v. 38, no. 8, p. 767-768.

Malservisi, R., Gans, C., and Furlong, K., 2003, Numerical modeling of strike-slip creeping faults and implications for the Hayward fault, California: Tectonophysics, v. 361, no. 1-2.

Massonnet, D., Rossi, M., Carmona, C., Adragna, F., G., P., Feigl, K., and Rabaute, T., 1993, The displacement field of the Landers earthquake mapped by radar interferometry: Nature, v. 364, p. 138-142.

Mastropieri, M. A., Scruggs, T. E., Boon, R., and Carter, K. B., 2001, Correlates of inquiry learning in science: constructing concepts of density and buoyancy: Remedial and Special Education, v. 22, p. 130-138.

Mastropieri, M. A., Scruggs, T. E., Norland, J. J., Berkeley, S., McDuffie, K., Tornquist, E. H., and Conners, N., 2006, Differentiated curriculum enhancement in inclusive middle school science: effects on classroom and high-stakes tests: Journal of Special Education, v. 40, p. 130-137.

Marone, C., Raleigh, C. B., and Scholz, C. H., 1990, Frictional behavior and constitutive modelling of simulated fault gouge: Journal of Geophysical Research, v. 95, p. 7007-7025.

McCalpin, J. P., 2009, Paleoseismology, International Geophysics Series: San Diego, Academic Press, p. 613.

McGill, S. F., and Sieh, K., 1991, Surficial offsets on the central and eastern Garlock fault associated with prehistoric earthquakes: Journal of Geophysical Research, v. 96, no. B13, p. 21,597-521,621.

McGill, S. F., Wells, S. G., Fortner, S. K., Kuzma, H. A., and McGill, J. D., 2009, Slip rate of the western Garlock fault, at Clark Wash, near Lone Tree Canyon, Mojave Desert, California: Geological Society of America Bulletin, v. 121, no. 3/4, p. 536-554.

Meade, B. J., and Hager, B. H., 2005, Block models of crustal motion in southern California constrained by GPS measurements: Journal of Geophysical Research-Solid Earth, v. 110, no. B3.

Moss, R. E., Stanton, K. V., and Buelna, M. I., 2013, The Impact of Material Stiffness on the Likelihood of Fault Rupture Propagating to the Ground Surface: Seismological Research Letters, v. 84, no. 3, p. 485-488.

Nash, D. B., 1980, Morphologic dating of degraded normal fault scarps: Journal of Geology, v. 88, p. 353-360.

Nissen, E., Krishnan, A. K., Arrowsmith, J. R., and Saripalli, S., 2012, Three-dimensional surface displacements and rotations from differencing pre- and post-earthquake LiDAR point clouds: Geophysical Research Letters, v. 39.

Oglesby, D. D., 2008, Rupture termination and jump on parallel offset faults: Bulletin of the Seismological Society of America, v. 98, p. 440-447.

Oglesby, D. D., Day, S. M., Li, Y., and Vidale, J. E., 2003, The 1999 Hector Mine earthquake: The dynamics of a branched fault system: Bulletin of the Seismological Society of America, v. 93, p. 2459-2476.

Okada, Y., 1992, Internal deformation due to shear and tensile faults in a half-space: Bulletin of the Seismological Society of America, v. 82, no. 2, p. 1018-1040.

Oskin, M., Arrowsmith, R., Hinojosa, A., Gonzalez, J., Gonzalez, A., Sartori, M., Fernandez, J., Fialko, Y., Floyd, M., Galetzka, J., and Sandwell, D., 2010a, Airborne lidar survey of the 4 April 2010 El Mayor-Cucupah earthquake rupture: (proceedings and abstracts): Southern California Earthquake Center Annual Meeting, Palm Springs, California, September 12-16, 2009, 19.

Oskin, M. E., Arrowsmith, J. R., Hinojosa, A. C., Elliott, A. J., Fletcher, J. M., Fielding, E. J., Gold, P. O., Garcia, J. J. G., Hudnut, K. W., Liu-Zheng, J., and Teran, O. J., 2012, Near-field deformation from the El Mayor-Cucupah earthquake revealed by differential LiDAR: Science, v. 335, no. 702.

Oskin, M. E., Gold, P. O., Hinojosa, A., Arrowsmith, J. R., Elliott, A. J., Taylor, M. H., Herrs, A. J., Sartori, M., Gonzalez-Garcia, J. J., Gonzalez, A., Kreylos, O., and Cowgill, E., 2010b, Airborne and terrestrial lidar imaging and analysis of the 4 April 2010 El Mayor-Cucupah earthquake rupture: Abstract T35B-2135 presented at 2010 Fall Meeting, AGU, San Francisco, Calif. 13-17 Dec.

Oskin, M. E., Le, K., and Strane, M. D., 2007, Quantifying fault-zone activity in arid environments with high-resolution topography: Geophysical Research Letters, v. 34, no. L23S05, doi: 10.1029/2007GL031295.

Oskin, M., Perg, L., Shelef, E., Strane, M., Gurney, E., Singer, B., and Zhang, X., 2008, Elevated shear zone loading rate during an earthquake cluster in eastern California: Geology, v. 36, no. 6, p. 507-510.

Parmar, R. S., Deluca, C. B., and Jaczak, T. M., 2004, Investigations into the relationship between science and language abilities of students with mild disabilities: Remedial and Special Education, v. 15, p. 117-126.

Parsons, T., Field, E. H., Page, M. T., and Milner, K., 2012, Possible Earthquake Rupture Connections on Mapped California Faults Ranked by Calculated Coulomb Linking Stresses: Bulletin of the Seismological Society of America, v. 102, no. 6, p. 2667-2676.

Penck, W., 1953, Morphological analysis of land forms, London, MacMillan and Co., Limited.

Pierce, K. L., and Colman, S. M., 1986, Effect of height and orientation (microclimate) on geomorphic degradation rates and processes, late-glacial terrace scarps in central Idaho: Geological Society of America Bulletin, v. 97, p. 869-885.

Pollard, D. D., and Fletcher, R. C., 2005, Fundamentals of structural geology, Cambridge, UK, Cambridge University Press, v. Book, Whole.

Pollitz, F. F., 2012, ViscoSim Earthquake Simulator: Seismological Research Letters, v. 83, no. 6, p. 979-982.

Pollitz, F. F., Wicks, C., and Thatcher, W., 2001, Mantle flow beneath a continental strike-slip fault: postseismic deformation after the 1999 Hector Mine earthquake: Science, v. 293, p. 1814-1818.

Power, W., and Tullis, T., 1991, Euclidean and fractal models for the description of rock surface roughness J Geophys Res V96, NB1, Jan 1991, P415–424: International Journal of Rock Mechanics and Mining Sciences & Geomechanics Abstracts, v. 28, no. 6, p. A344-A344.

Prentice, C. S., Crosby, C. J., Whitehill, C. S., Arrowsmith, J. R., Furlong, K. P., and Phillips, D. A., 2009, Illuminating northern California's active faults: Eos, v. 90, no. 7, p. 55-56.

Purvance, M., 2005, Overturning of slender blocks: numerical investigation and application to precariously balanced rocks in southern California, PhD Dissertation: University of Nevada, Reno, 233 p.

Purvance, M. D., Abdolrasool, A., and Brune, J. N., 2008a, Freestanding block overturning fragilities: Numerical simulation and experimental validation: Earthquake Engineering and Structural Dynamics, v. 37, p. 791-808.

Purvance, M. D., Brune, J. N., Abrahamson, N. A., and Anderson, J. G., 2008b, Consistency of precariously balanced rocks with probabilistic seismic hazard estimates in Southern California: Bulletin of the Seismological Society of America, v. 98, no. 6, p. 2629-2640.

Quigley, M., Van Dissen, R., Litchfield, N., Duffy, B., Barrell, D., Furlong, K., Stahl, T., Bilderback, E., and Noble, D., 2012, Surface rupture during the 2010 Mw 7.1 Darfield (Canterbury) earthquake: implications for fault rupture dynamics and seismic-hazard analysis: Geology, v. 40, no. 1, p. 55-58.

Ragona, D., Minster, B., Rockwell, T., and Jussila, J., 2006, Field imaging spectroscopy: A new methodology to assist the description, interpretation, and archiving of

paleoseismological information from faulted exposures: Journal of Geophysical Research, v. 111, no. B10309, doi: 10.1029/2006JB004267.

Richards-Dinger, K., and Dieterich, J. H., 2012, RSQSim Earthquake Simulator: Seismological Research Letters, v. 83, no. 6, p. 983-990.

Rockwell, T. K., and Ben-Zion, Y., 2007, High localization of primary slip zones in large earthquakes from paleoseismic trenches: Observations and implications for earthquake physics: Journal of Geophysical Research-Solid Earth, v. 112, no. B10.

Roering, J. J., Kirchner, J. W., and Dietrich, W. E., 1999, Evidence for nonlinear, diffusive sediment transport on hillslopes and implications for landscape morphology: Water Resources Research, v. 35, no. 3, p. 853-870.

Rood, D., Brune, J., Kendrick, K., Purvance, M., Anooshehpoor, R., Grant-Ludwig, L., and Balco, G., 2008, How do we date a PBR?: testing geomorphic models using surface-exposure dating and numerical methods: ExGM Workshop, SCEC Annual Meeting, Palm Springs, California, September 6-11, 2009, 18.

Rood, D. H., Balco, G. A., Purvance, M. D., Anooshehpoor, A., Brune, J. N., Grant-Ludwig, L. B., and Kendrick, K., 2009, How do we date a PBR?: a robust method using BE-10 surface exposure dating with numerical models: SCEC Annual Meeting, Palm Springs, California, September 12-16, 2009, 19.

Ruina, A. L., 1983, Slip instability and state variable friction laws: Journal of Geophysical Research, v. 88, p. 10359-10370.

Sachs, M. K., Heien, E. M., Turcotte, D. L., Yikilmaz, M. B., Rundle, J. B., and Kellogg, L. H., 2012, Virtual California Earthquake Simulator: Seismological Research Letters, v. 83, no. 6, p. 973-978.

Salyards, S. L., Sieh, K., and Kirschvink, J. L., 1992, Paleomagnetic measurement of nonbrittle coseismic deformation across the San Andreas fault at Pallett Creek: Journal of Geophysical Research, v. 97, no. B9, p. 12457-12470.

Saucier, F., Humphreys, E., and Weldon, R., 1992, Stress near geometrically complex strike-slip faults: Application to the San Andreas fault at Cajon Pass, southern California: Journal of Geophysical Research-Solid Earth, v. 97, no. B4, p. 5081-5094.

Savage, J. C., Svarc, J. L., and Prescott, W. H., 2003, Near-field postseismic deformation associated with the 1992 Landers and 1999 Hector Mine, California earthquakes: Journal of Geophysical Research, v. 108, no. B9.

Scholz, C. H., 2010, Large Earthquake Triggering, Clustering, and the Synchronization of Faults: Bulletin of the Seismological Society of America, v. 100, no. 3, p. 901-909.

Scholz, C. H., 1988, The brittle-plastic transition and the depth of seismic faulting: Geologische Rundschau, v. 77, no. 1, p. 319-328.

Scholz, C. H., 2002, The mechanics of earthquakes and faulting, Cambridge, Cambridge Universiry Press, 496 p.:

Schumm, S. A., 1967, Rates of surficial rock creep on hillslopes in western Colorado: Science, v. 155, no. 3762, p. 560-562.

Schwartz, D. P., and Coppersmith, K. J., 1984, Fault behavior and characteristic earthquakes; examples from the Wasatch and San Andreas fault zones: Journal of Geophysical Research, v. 89, p. 5681-5698.

Segall, P., and Pollard, D. D., 1983, Nucleation and growth of strike slip faults in granite: Journal of Geophysical Research, v. 88, no. B1, p. 555-568.

Segall, P., 2010, Earthquake and volcano deformation, Princeton, Princeton University Press, v. Book, Whole.

Segall, P., and Pollard, D. D., 1980, Mechanics of discontinuous faults: Journal of Geophysical Research, v. 85, no. B8, p. 4337-4350.

Shan, S., Bevis, M., Kendrick, E., Mader, G. L., Raleigh, D., Hudnut, K., Sartori, M., and Phillips, D., 2007, Kinematic GPS solutions for aircraft trajectories: Identifying and minimizing systematic height errors associated with atmospheric propagation delays: Geophysical Research Letters, v. 34, no. 23.

Sherrod, B. L., Brocher, T. M., Weaver, C. S., Bucknam, R. C., Blakely, R. J., Kelsey, H. M., Nelson, A. R., and Haugerud, R. A., 2004, Holocene fault scarps near Tacoma, Washington, USA: Geology, v. 32, p. 9-12.

Shelef, E., and Oskin, M., 2010, Deformation processes adjacent to active faults: Examples from eastern California: Journal of Geophysical Research-Solid Earth, v. 115.

Shi, B., Abdolrasool, A., Zeng, Y., and and Brune, J. N., 1996, Rocking and overturning of precariously balanced rocks by earthquakes: Bulletin of the Seismological Society of America, v. 86, no. 5, p. 1364-1371.

Shi, Z. Q., and Ben-Zion, Y., 2006, Dynamic rupture on a bimaterial interface governed by slip-weakening friction: Geophysical Journal International, v. 165, no. 2, p. 469-484.

Shirzaei, M., and Burgmann, R., 2013, Time-dependent model of creep on the Hayward fault from joint inversion of 18 years of InSAR and surface creep data: Journal of Geophysical Research, v. 118, p. 1733-1746.

Shirzaei, M., Burgmann, R., and Taira, T., 2013, Implications of recent asperity failures and aseismic creep for time-dependent earthquake hazard on the Hayward fault: Earth and Planetary Science Letters, v. 371, p. 59-66.

Sibson, R. H., 1977, Fault rocks and fault mechanisms: Journal of the Geological Society of London, v. 133, p. 191-213.

Sibson, R. H., 1984, Roughness at the base of the seismogenic zone: contributing factors: Journal of Geophysical Research, v. 89, no. B7, p. 5791-5799.

Sibson, R. H., 1982, Fault zone models, heat flow, and the depth distribution of earthquakes in the continental crust of the United States: Bulletin of the Seismological Society of America, v. 72, no. 1, p. 151-163.

Sibson, R. H., 1986, Earthquakes and rock deformation in crustal fault zones: Annual Reviews of Earth and Planetary Sciences, v. 14, p. 149-175.

Sibson, R. H., 2003, Thickness of the seismic slip zone: Bulletin of the Seismological Society of America, v. 93, no. 3, p. 1169-1178.

Sieh, K. E., and Jahns, R. H., 1984, Holocene activity of the San Andreas fault at Wallace Creek, California: Geological Society of America Bulletin, v. 95, p. 883-896.

Simpson, R. W., Lienkaemper, J. J., and Galehouse, J. S., 2001, Variations in creep rate along the Hayward Fault, California, interpreted as changes in depth of creep: Geophysical Research Letters, v. 28, no. 11.

Simpkins, P. M., Mastropieri, M. A., and Scruggs, T. E., 2009, Differentiated curriculum enhancements in inclusive fifth-grade science classes: Remedial and Special Education, v. 30, p. 300-308.

Smith, G. I., 1962, Large lateral displacement on Garlock fault, as measured from offset dyke swarm: American Association of Petroleum Geologists Bulletin, v. 46, p. 85-104.

Stein, R. S., King, G., and Rundle, J. B., 1988, The growth of geological structures by repeated earthquakes, 2, Field examples of continental dip-slip faults: Journal of Geophysical Research, v. 95, p. 13319-13331.

Stewart, I. S., and Hancock, P. L., 1990, What is a fault scarp?: Episodes, v. 13, no. 4, p. 256-263.

Stirling, M., 2008, Cosmogenic and soil age constraints on PBRs in New Zealand: ExGM Workshop, SCEC Annual Meeting, Palm Springs, California, September 6-11, 2009, 18.

Stirling, M. W., Anooshehpoor, A., Brune, J. N., Biasi, G. P., and Wesnousky, G., 2002, Assessment of the site conditions of precariously balanced rocks in the Mojave Desert, Southern California: Bulletin of the Seismological Society of America, v. 92, p. 2139-2144.

Stirling, M. W., and Anooshehpoor, R., 2006, Constraints on probabilistic seismic-hazard models from unstable landform features in New Zealand: Bulletin of the Seismological Society of America, v. 96, no. 2, p. 404-414.

Sylvester, A. G., 1999, Rifting, transpression, and neotectonics in the Central Mecca Hills, Salton Trough, Santa Barbara, University of California, Santa Barbara, 52 p.

Tarboton, D. G., 1997, A new method for the determination of flow directions and upslope areas in grid digital elevation models: Water Resources Research, v. 33, no. 2, p. 309-319.

Terza, G., Galgaro, A., Zaltron, N., and Genevois, R., 2007, Terrestrial laser scanner to detect landslide displacement fields: a new approach: International Journal of Remote Sensing, v. 28, no. 16, p. 3425-3446.

Titus, S. J., Dyson, M., DeMets, C., Tikoff, B., Rolandone, F., and Buergmann, R., 2011, Geologic versus geodetic deformation adjacent to the San Andreas fault, central California: Geological Society of America Bulletin, v. 123, no. 5-6, p. 794-820.

Toda, S., Stein, R. S., Sevilgen, V., and Lin, J., 2011, Coulomb 3.3 Graphic-rich deformation and stress-change software for earthquake, tectonic, and volcano research and teaching—user guide: U.S. Geological Survey Open-File Report 2011-1060, p. 63.

Toké, N. A., Arrowsmith, J. R., Rymer, M. J., Landgraf, A., Haddad, D. E., Busch, M., Coyan, J., and Hannah, A., 2011, Late Holocene slip rate of the San Andreas fault and its accommodation by creep and moderate-magnitude earthquakes at Parkfield, California: Geology, v. 39, no. 3, p. 243-246.

Toppozada, T. R., and Borchardt, G., 1998, Re-evaluation of the 1836 “Hayward fault” and the 1838 San Andreas fault earthquakes: Bulletin of the Seismological Society of America, v. 88, no. 1, p. 140-159.

Tullis, T. E., Sachs, M. K., Turcotte, D. L., Ward, S. N., Yikilmaz, M. B., Richards-Dinger, K., Barall, M., Dieterich, J. H., Field, E. H., Heien, E. M., Kellogg, L. H., Pollitz, F. F., and Rundle, J. B., 2012, Generic Earthquake Simulator: Seismological Research Letters, v. 83, no. 6, p. 959-963.

Twidale, C. R., 1982, Granitic Landforms, Amsterdam, Elsevier, 372 p.

Vedder, J. G., and Wallace, R. E., 1970, Recent active breaks along the San Andreas fault between Cholame Valley and Tejon Pass, California: U.S. Geological Survey Miscellaneous Geological Investigations Map I-741, scale 1:24,000, 3 sheets.

Vedder, J. G., and Wallace, R. E., 1970, The San Andreas fault in the Carrizo Plain–Temblor Range region, California, in Crowell, J. C., ed., San Andreas Fault in Southern California: A Guide to San Andreas Fault from Mexico to Carrizo Plain, Volume 118, California Division of Mines and Geology Special Report, p. 241-250.

Waldhauser, F., and Ellsworth, W. L., 2002, Fault structure and mechanics of the Hayward Fault, California, from double-difference earthquake locations: journal of Geophysical Research, v. 107, no. 3.

Wallace, R. E., 1975, The San Andreas fault in the Carrizo Plain–Temblor Range region, California, in Crowell, J. C., ed., San Andreas Fault in Southern California: A Guide to San Andreas Fault from Mexico to Carrizo Plain, Volume 118, California Division of Mines and Geology Special Report, p. 241-250.

Wallace, R. E., 1977, Profiles and ages of young fault scarps, north-central Nevada: Geological Society of America Bulletin, v. 88, p. 1267-1281.

Wallace, R. E., 1991, The San Andreas Fault System, California: U.S. Geological Survey Open File Report.

Wallace, R. E., and Schulz, S. S., 1983, Aerial views in color of the San Andreas fault, California: U S Geological Survey Open File Report.

Ward, S. N., 2012, ALLCAL Earthquake Simulator: Seismological Research Letters, v. 83, no. 6, p. 964-972.

Wesnousky, S. G., 1988, Seismological and structural evolution of strike-slip faults: Nature, v. 335, no. 6188, p. 340-342.

Wesnousky, S. G., 2008, Displacement and Geometrical Characteristics of Earthquake Surface Ruptures: Issues and Implications for Seismic-Hazard Analysis and the Process of Earthquake Rupture: Bulletin of the Seismological Society of America, v. 98, no. 4, p. 1609-1632.

Wesnousky, S. G., 2006, Predicting the endpoints of earthquake ruptures: Nature, v. 444, no. 7117, p. 358-360.

WGCEP, 2008, The uniform California earthquake rupture forecast, Version 2 (UCERF 2): U.S. Geological Survey Open File Report 2007-1437, p. 104.

Wilkinson, M., McCaffrey, K. J. W., Roberts, G., Cowie, P. A., Phillips, R. J., Michetti, A. M., Vittori, E., Guerrieri, L., Blumetti, A. M., Bubeck, A., Yates, A., and Sileo, G., 2010, Partitioned postseismic deformation associated with the 2009 Mw 6.3 L'Aquila earthquake surface rupture measured using a terrestrial laser scanner: Geophysical Research Letters, v. 37, no. L10309, doi:10.1029/2010GL043099.

Willemse, E. J. M., 1997, Segmented normal faults: Correspondence between three dimensional mechanical models and field data: Journal of Geophysical Research-Solid Earth, v. 102, no. B1, p. 675-692.

Willemse, E. J. M., Pollard, D. D., and Aydin, A., 1996, Three-dimensional analyses of slip distributions on normal fault arrays with consequences for fault scaling: Journal of Structural Geology, v. 18, no. 2, p. 295-309.

Williams, D., and Semken, S., 2011, Ethnographic methods in analysis of place-based geoscience curriculum and pedagogy, in Fieg, A. D., and Stokes, A., eds., Qualitative Inquiry in Geoscience Education Research: Geological Society of America Special Paper 474, p. 49-62.

Xu, X., 2000, Three-dimensional virtual geology: photorealistic outcrops, and their acquisition, visualization and analysis: PhD Dissertation, University of Texas, Dallas, Dallas, TX.

Zielke, O., 2009, How fault geometric complexity and frictional properties affect seismic fault behavior and accumulation of slip along strike-slip faults, PhD: Arizona State University, 315 p.

Zielke, O., and Arrowsmith, J. R., 2008, Depth variation of coseismic stress drop explains bimodal earthquake magnitude-frequency distribution: Geophysical Research Letters, v. 35, no. 24.

Zielke, O., and Arrowsmith, J. R., 2012, LaDiCaoz and LiDARimager - MATLAB GUIs for LiDAR data handling and lateral displacement measurement: Geosphere, v. 8, p. 206-221.

Zielke, O., Arrowsmith, J. R., Ludwig, L. G., and Akciz, S. O., 2010, Slip in the 1857 and earlier large earthquakes along the Carrizo Plain, San Andreas Fault (vol 327, pg 1119, 2010): Science, v. 329, no. 5990, p. 390-390.

APPENDIX A

MEASURING EARTHQUAKE-GENERATED SURFACE OFFSETS USING LIDAR

INTRODUCTION

High-resolution digital topographic data products such as LiDAR-derived digital elevation models (DEMs) provide unprecedented insights into the geomorphic response of earthquake-induced surface deformation. By measuring m-scale offsets of geologic and geomorphic markers, we can understand the surface slip history associated with recent earthquake ruptures, their spatiotemporal distributions, magnitudes, and recurrences. Surface offsets also facilitate physical constraints for surface slip distributions, thus providing physical guides to earthquake forecast models such as the Working Group on California Earthquake Probabilities' (WGCEP) Uniform California Earthquake Rupture Forecasts (UCERF; http://www.wgcep.org/goals).

The goal of this document is to provide an overview of the workflow involved in calculating surface slip offsets using LiDAR-derived DEMs. The workflow is comprised of modules that use different software suites, and so it is not intended to replace the already comprehensive documentation available for each software suite. Where appropriate, we provide information on how to access the documentation that typically accompanies each software.

COMPUTING CONSIDERATIONS

The workflow presented herein requires the following computing considerations and software:

1. High-speed Internet access and a Web browser.
2. Access to the ArcGIS suite (ArcMap, ArcToolbox, and ArcCatalog), or alternatively...
3. ...access to the paid version of Global Mapper.
4. MATLAB numerical computing environment.
5. LaDiCaoz lateral displacement calculator and LiDARimager (Zielke et al., 2010; Zielke and Arrowsmith, 2012).
6. Access to a spreadsheet software (e.g., MS Excel).
7. Google Earth (optional).

WORKFLOW OVERVIEW

The following is a brief overview of the workflow that goes through the steps of generating DEMs and computing surface offsets. Each screenshot is representative of the software/website application. A more detailed graphical workflow is presented in the following section of this document.

1. Generate and download DEMs from OpenTopography.

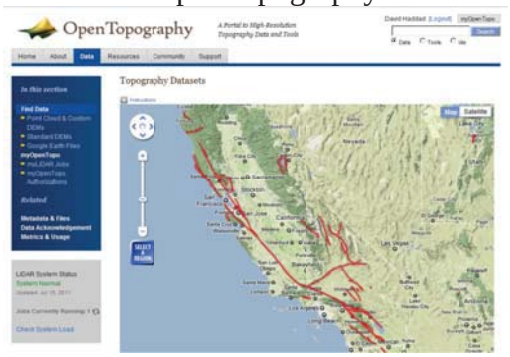

2. Convert the DEMs from Arc ASCII to Arc raster formats in ArcMap. Alternatively, load the DEMs directly into Global Mapper.

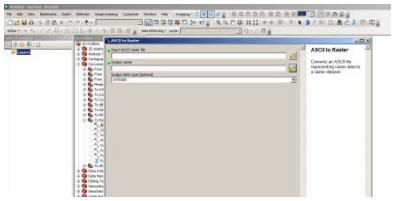

3. Map traces of fault surface ruptures using hillshades, slope maps, and other imagery as aids.

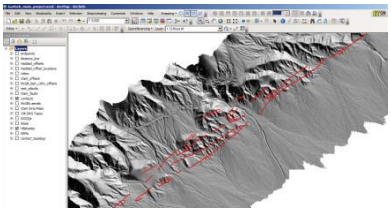

4. Visually inspect fault traces and search for channel offsets, pressure ridges, shutter ridges, or other tectonogeomorphic features where surface offset is manifest.

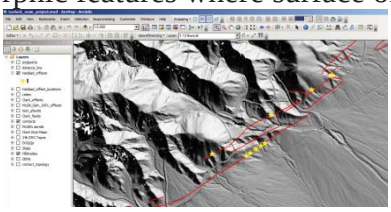

5. Calculate lateral displacements using LaDiCaoz.

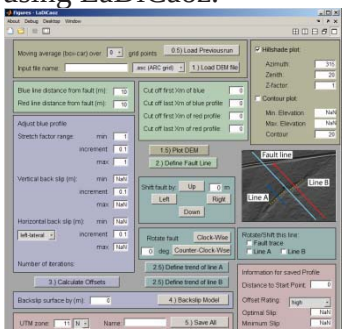

6. Record offset measurement in a local spreadsheet. These data will ultimately be combined into the UCERF Master Database.

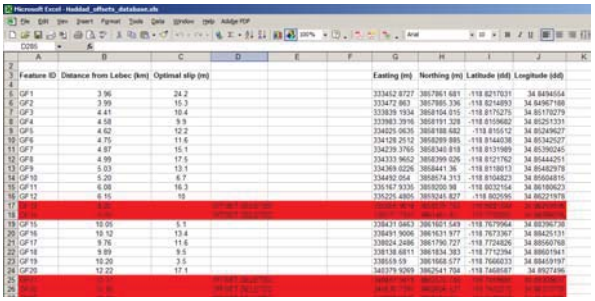

DETAILED WORKFLOW

This section describes, in detail, the workflow associated with calculating an offset measurement.

Step 1: Generate a DEM in OpenTopography

Go to http://opentopography.org. If you are a new user to OpenTopography, click the "myOpenTopo" button and request a new account. This will allow you to process larger DEMs and have a custom interface from which you can access previously submitted DEM jobs. Registration is free. New account requests are typically granted in less than a day. Once your request has been granted, sign into your account and click the "Find Data" button.

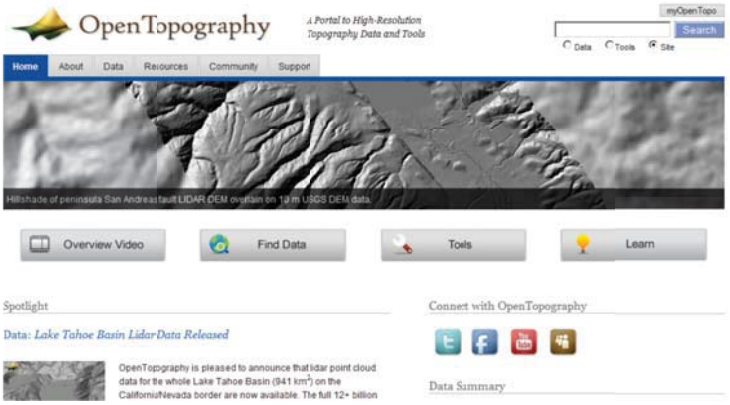

Click "Point Cloud & Custom DEMs" from the left-hand menu. OpenTopography uses the Google Maps navigation interface.

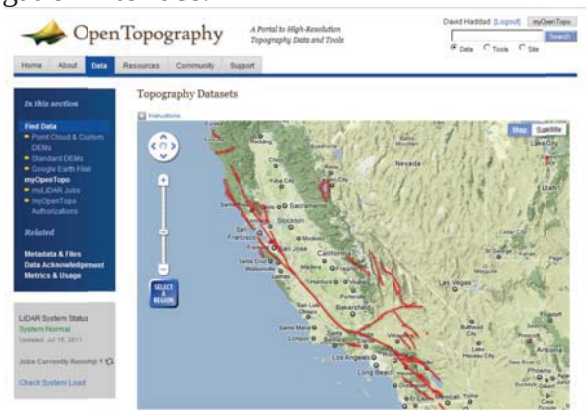

Select a dataset from the list and navigate to the area from which you want to create a DEM. Click the "Select a region" button and draw a polygon that defines the extent of the DEM you wish to create. The DEM's processing time depends on the size of this polygon. The user is advised to select small regions of which to create DEMs as opposed to selecting one large region to facilitate the subsequent processing of DEMs on the user's local machine in "bite-sized" pieces versus large DEM tiles.

Set the DEM parameters. These parameters depend on the quality of the original LiDAR dataset. Measures such as shot density (the number of laser returns per area) and point cloud classification schemes are factors that control the quality of the final DEM. In general, airborne LiDAR data hosted on OpenTopography can produce DEMs of resolutions as high as 0.25 m per pixel. For more information on these factors and the science (and sometimes art) of finding the best DEM parameters, see the OpenTopography resource pages and http://lidar.asu.edu.

For the purposes of this document, set the DEM parameters to the following:

- *DEM Generation:* select the "**Calculate Zidw grid**" option. Set the "**Grid Resolution**" to 0.25 (meters) and the "**Radius**" to 2 (meters).
- *Derivative Products:* uncheck this option if you prefer to create your own hillshades and slope maps in ArcMap. Checking this option increases the DEM processing time. Note that Global Mapper automatically creates slope maps and hillshades of DEMs from the ASCII files that OpenTopography generates.
- *Visualization:* optional if you wish to visualize the DEM in Google Earth.
- *Job Description:* Enter a Job title (e.g., dem_1) and a brief description (optional). The user is highly advised to provide each DEM with a unique job title. This will greatly facilitate management of the DEMs in the future.
- *Email address:* If you are signed into your OpenTopography account, you email address should automatically appear in this field. If not, then you are visiting OpenTopography as a guest (with limited access). The user is highly advised to use OpenTopography as a registered user so as to keep track of the submitted DEM jobs and have access to larger LiDAR dataset processing power. Once you are satisfied with the parameters and signed into your OpenTopography account, hit the "Submit" button.

Horizontal Coordinates: UTM Zone 11 N WGS84 Meters - **Vertical Coordinates**: Ellipsoid
Data Selection Coordinates: ☐ Manually enter selection coordinates

X_{min} = 427409.521 Y_{min} = 3917238.438 X_{max} = 427904.501 Y_{max} = 3917731.246

The selection area contains approximately 190,000 points.

1b. Choose return classification: ◉ Ground ○ Unclassified (Vegetation & Structures) ○ All

2. Point Cloud Data Download:

☐ Download point cloud data in ASCII format
☐ Download point cloud data in LAS format

3a. DEM Generation (Local Gridding):

Gridding Method
☐ Calculate Zmin grid
☐ Calculate Zmax grid
☐ Calculate Zmean grid
☑ Calculate Zidw grid
☐ Calculate point count grid

Gridding Paramters
Grid Resolution (Default = 1 meter): 0.25
Radius value (Default = 1 meter): 2

Grid Format Arc ASCII Grid **Null Filling** None

3b. DEM Generation (TIN):

Gridding Method
☐ Calculate TIN

Gridding Paramters
Grid Resolution (Default = 1 meter): 1
Max. triangle size(Default 50 units): 50

Grid Format Arc ASCII Grid

Gridding Method
☐ Calculate TIN

Gridding Paramters
Grid Resolution (Default = 1 meter): 1
Max. triangle size(Default 50 units): 50

Grid Format Arc ASCII Grid

4. Derivative Products:

☐ Generate Hillshade & Slope

Job Description

These options allow users to describe and keep track of their jobs. Information entered below is recorded along with other job parameters in your personal LiDAR Job archive accessed via myOpenTopo (available only to registered OpenTopography users).

Job title: (up to 100 characters) demo_DEM

Job description: (up to 500 characters) This is a demonstration DEM.

Email Address:

Enter your e-mail address for notification upon completion of processing * david.e.haddad@asu.

Submit Clear All

By submitting an OpenTopography point cloud processing job you agree to acknowledge OpenTopography and the dataset source as specified here in publications, presentations, and other materials produced using these data.

Step 2: Download the DEM from OpenTopography

OpenTopography creates several products that accompany the DEM. For the purposes of this document, we are only interested in the DEM. Click the "dems.tar.gz" link (exact link name may vary) to download the DEM in zipped form. Extract the DEM once the download is complete. The extension of the extracted DEM file is .asc. This is the raw DEM file in ASCII format.

Step 3: DEM visualization

Global Mapper can import the .asc file and visualize the DEM very efficiently:

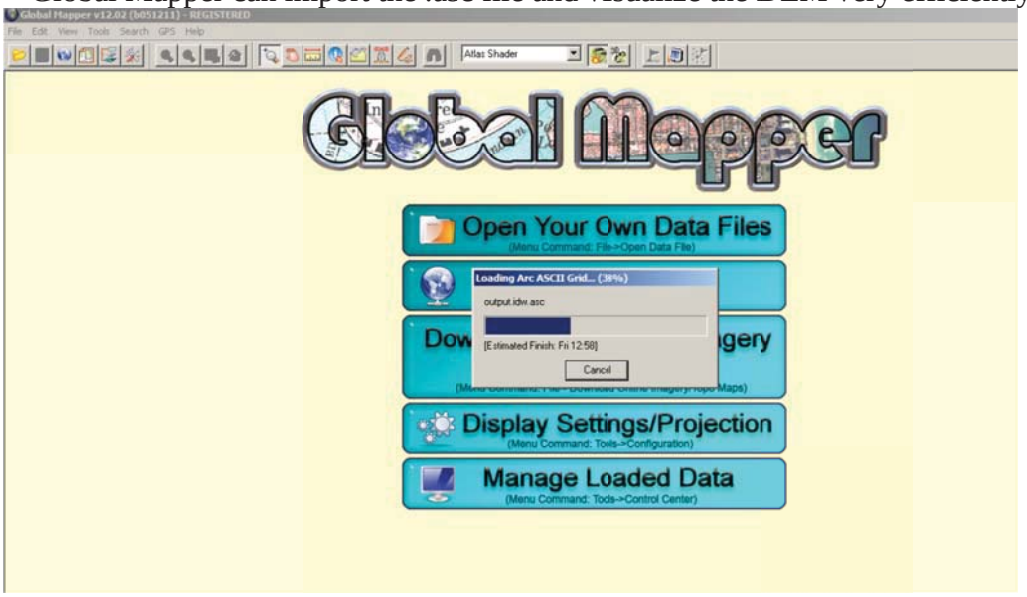

Global Mapper automatically creates a hillshade and slope map from the .asc file.

If using ArcMap, the .asc file needs to be converted to an Arc raster using ArcToolbox. In ArcMap, start ArcToolbox and go to Conversion Tools >> To Raster >> ASCII to Raster. Follow the directions from there. **NB: make sure to change the output data type to FLOAT.**

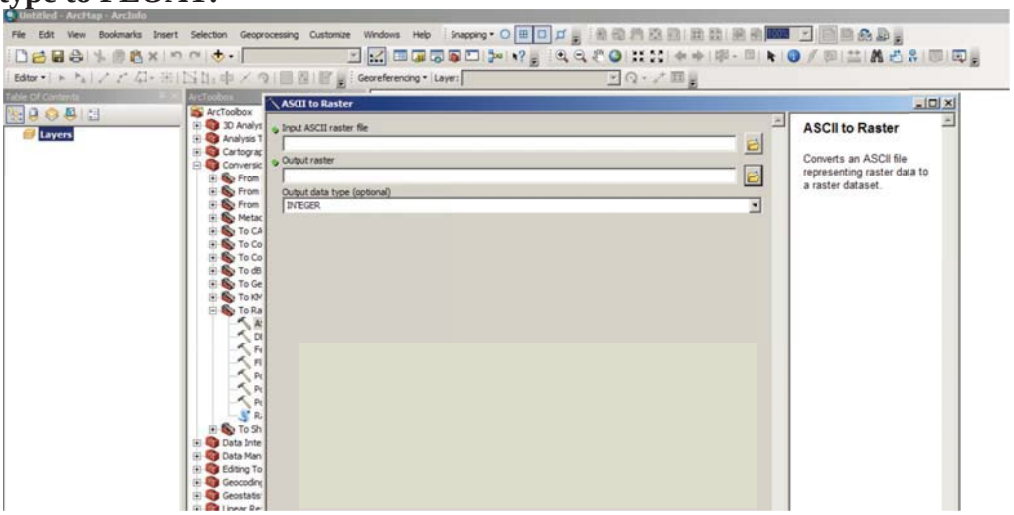

Step 4: Map fault traces

For Global Mapper and ArcMap users: create a line shapefile (polyline) and begin digitizing fault traces. This should be done at a scale of 1:2,000 or larger. Use aerial imagery (DOQQs/Google Earth/aerial photographs) to aid your mapping (and to make sure you are actually mapping faults). Slope maps can be very handy in illuminating subtle tectonogeomorphic features such as very low-relief fault scarps or offset channels. In general, for scarps that exhibit vertical displacement, the user has three placement options for the linework: (1) at the top of the scarp, (2) at the bottom of the scarp, or (3) in the middle of the scarp. For the purposes of this document, we place our linework in the middle of the fault scarp.

The user is advised to go over their linework at least twice to ensure all fault traces have been mapped and double check the existing linework indeed represents fault traces.

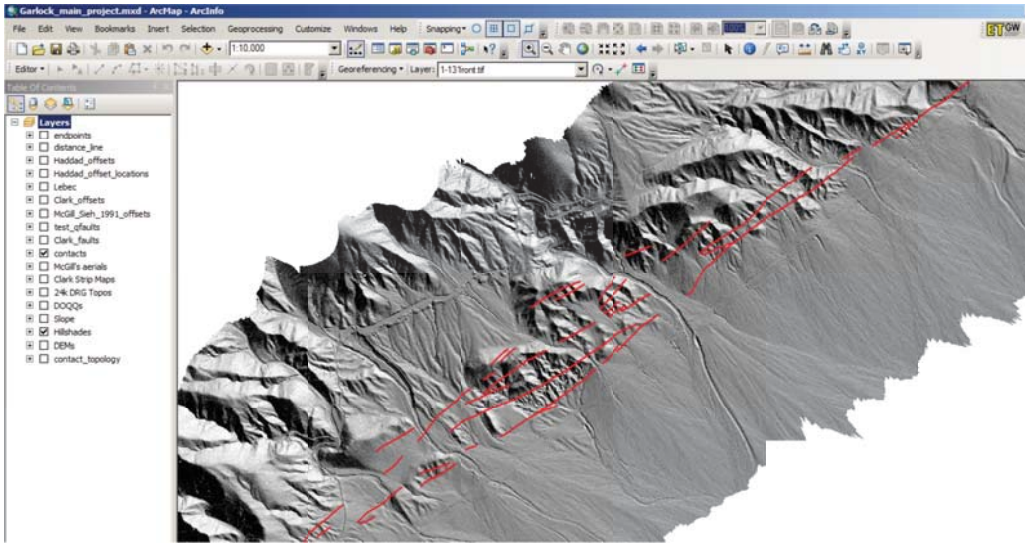

Step 5: Mark offset locations

For Global Mapper and ArcMap users, create a point shapefile and digitize the locations of offset geologic/geomorphic features. Depending on the resolution and quality of the DEM, this should be done at a scale between 1:500 and 1:1,000. The user is advised to perform this procedure at least twice to ensure that all offsets have been marked. Assign a unique offset name (e.g. "GF_1") to the offset marker and enter it into the attributes table of the shapefile and your Excel spreadsheet (where the offset data will eventually go).

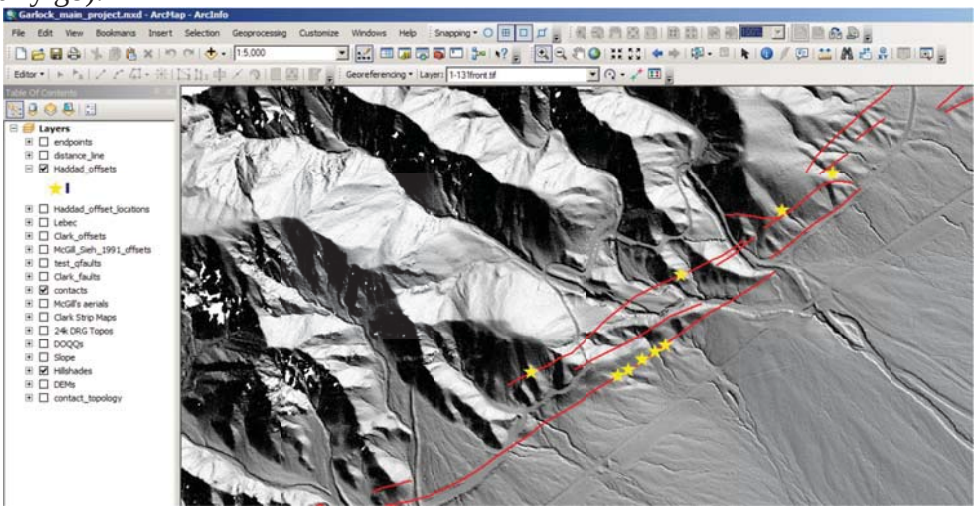

Step 6: Calculate lateral offsets

The user is highly advised to review the following comprehensive videos and instructions that go through preparing DEMs using LiDARimager and calculating lateral offsets using LaDiCaoz here: http://stockdale.sese.asu.edu/Geosphere_SOM/. The following section provides a very brief overview of the workflow.

Step 6a: Download the software

Go to http://stockdale.sese.asu.edu/Geosphere_SOM/ and download the LiDARview.p and LaDiCaoz.p files into the directory that contains the .asc DEM files. **NB: these files must all be in the same directory!**

Step 6b: Prepare the DEM using LiDARimager

To improve processing efficiency in LaDiCaoz, the user will need to crop the DEM file to the extent that displays the offset feature(s). LiDARimager is a MATLAB-based GUI that loads the .asc file, creates a hillshade of the DEM using user-defined illumination parameters, and allows the user to create smaller .asc files at user-defined spatial extents (Zielke et al., 2010)

Start MATLAB and navigate to the directory that contains LiDARimager and the .asc files. In the Current Folder list to the left of the Command Window, right click on LiDARimager and select "Run File". This will load the LiDARimager GUI. Follow the instructions in the LiDARimager video (see above link).

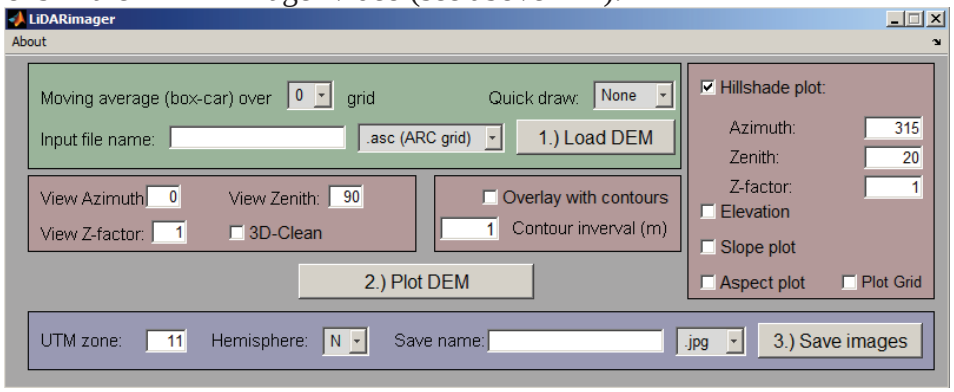

Step 6c: Calculate lateral offsets using LaDiCaoz

LaDiCaoz is a MATLAB-based GUI that calculates lateral displacements from high-resolution digital topography using a goodness-of-fit approach (Zielke et al., 2010). Start MATLAB and navigate to the directory that contains the .asc and LaDiCaoz files. In the Current Folder list to the left of the Command Window, right click on LaDiCaoz and select "Run File". This will load the LaDiCaoz GUI. Follow the instructions in the LaDiCaoz video (see above link).

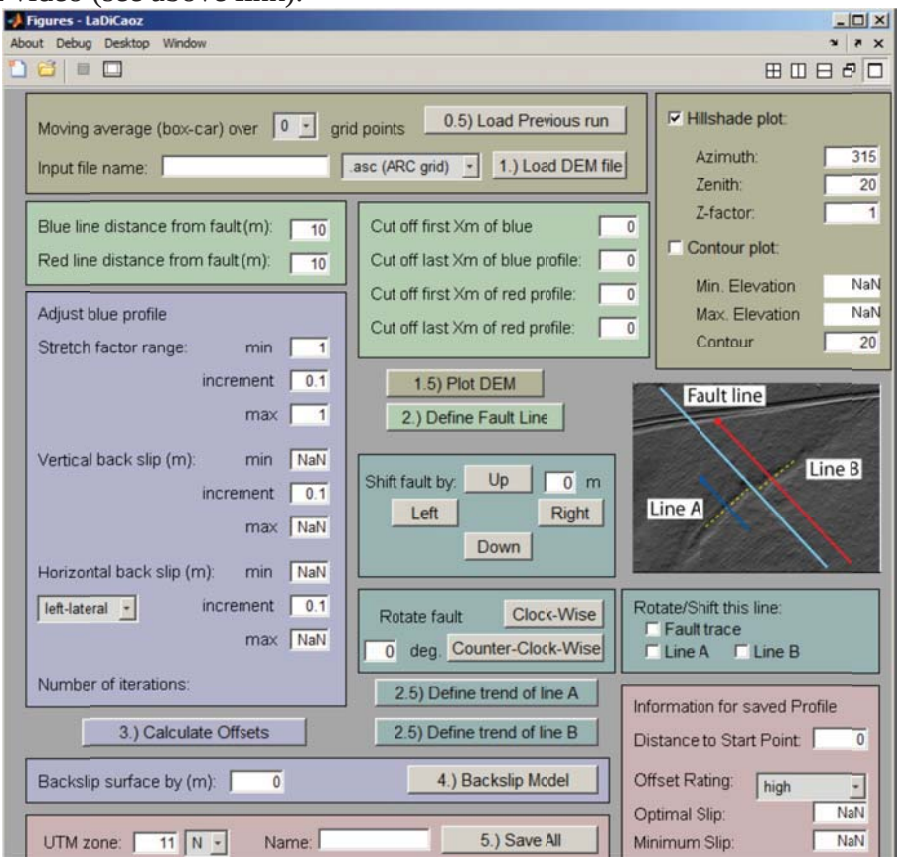

REFERENCES

Zielke, O., Arrowsmith, J R., Grant-Ludwig, L. B., Akciz, S. O., 2010. Slip in the 1857 and earlier large earthquakes along the Carrizo Plain, San Andreas fault, *Science*, v. 327, p. 1119-1121.

Zielke, O., Arrowsmith, J R., 2012. LaDiCaoz and LiDARimager – MATLAB GUIs for LiDAR data handling and lateral displacement measurement, *Geosphere*, v. 8, p. 206-221.

APPENDIX B

DISPLACEMENT MEASUREMENTS FOR THE GARLOCK AND OWENS VALLEY FAULT ZONES

The following tables are lidar-derived measurements of offset geomorphic features along the Garlock and Owens Valley fault zones (California). These data are available in the Madden et al. (2013) appendix J of the Uniform California Earthquake Rupture Forecast (UCERF3) report (Field et al., 2013). The maps below show the locations of offsets measured along both fault zones.

Garlock fault zone

Owens Valley fault zone (oblique view facing northeast)

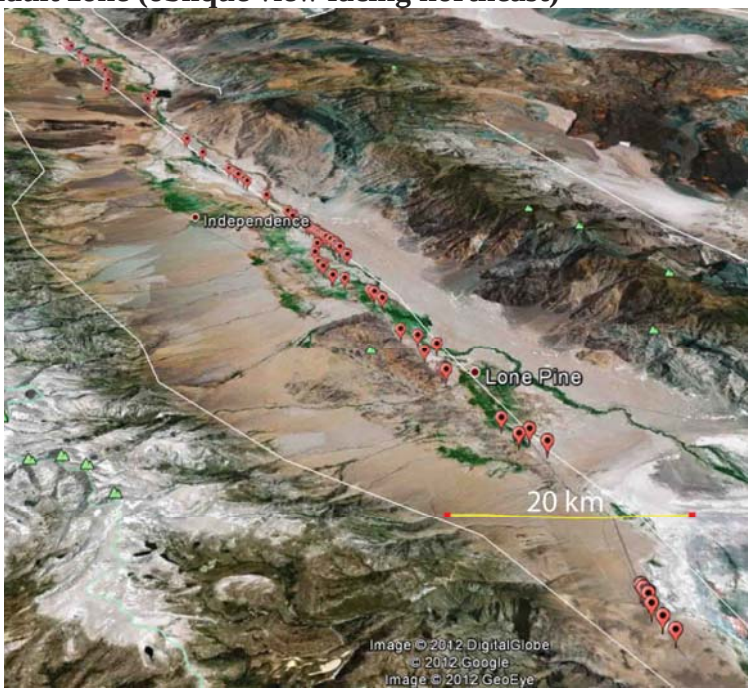

GARLOCK FAULT OFFSET MEASUREMENTS

Feature ID	Distance along strike (km)	Optimal slip (m)	Max slip (+)	Min slip (-)	Slip (+)	Slip (-)	Slip range (m)	Quality rating	Easting (m)	Northing (m)
GF1	3.96	24.2	27	22	2.8	2.2	22 - 27	Moderate	333452.9	3857861.7
GF2	3.99	15.3	17	15	1.7	0.3	15 - 17	Low	333472.9	3857885.3
GF3	4.41	10.4	13	9	2.6	1.4	9 - 13	Low	333839.2	3858104
GF4	4.58	9.9	12	7	2.1	2.9	7 - 12	Moderate-low	333983.4	3858191.3
GF5	4.62	12.2	16	10	3.8	2.2	10 - 16	Moderate-low	334025.1	3858188.7
GF6	4.75	11.6	13	10	1.4	1.6	10 - 13	High-moderate	334128.3	3858289.9
GF7	4.87	15.1	16.5	12	1.4	3.1	12 - 16.5	Moderate	334239.4	3858340.8
GF8	4.99	17.5	19	12	1.5	5.5	12 - 19	Moderate	334334	3858399
GF9	5.03	13.1	14	10	0.9	3.1	10 - 14	High-moderate	334369	3858441.4
GF10	5.20	6.7	10	5	3.3	1.7	5 - 10	High-moderate	334492.1	3858574.3
GF11	6.08	16.3	18	14	1.7	2.3	14 - 18	Moderate	335167.9	3859201
GF12	6.15	10	12	6.5	2	3.5	6.5 - 12	Moderate	335225.5	3859245.8
GF15	10.05	5.1	6	4	0.9	1.1	4 - 6	Moderate	338431	3861601.5
GF16	10.12	13.4	14.5	10	1.1	3.4	10 - 14.5	Moderate-low	338491.9	3861632
GF17	9.76	11.6	15	10	3.4	1.6	10 - 15	Moderate	338024.2	3861790.7
GF18	9.89	9.5	12	8.5	2.5	1	8.5 - 12	Moderate	338138.7	3861834.4
GF19	10.20	3.5	6	3	2.5	0.5	3 - 6	Low	338559.6	3861668.6
GF20	12.22	17.1	19	16	1.9	1.1	16 - 19	High-moderate	340379.9	3862541.7
GF24	12.70	32.1	35	30	2.9	2.1	30 - 35	Moderate	340824.4	3862742.8
GF26	13.42	10.1	12	8	1.9	2.1	8 - 12	Moderate	341407.3	3863180.7
GF28	15.10	11.2	12	7	0.8	4.2	7 - 12	Moderate	342958.3	3863849.5
GF29	15.22	13.1	15	10	1.9	3.1	10 - 15	High-moderate	343055.7	3863913
GF30	15.26	9	12	7	3	2	7 - 12	High	343091.6	3863940.6
GF32	15.68	3.8	5	2	1.2	1.8	2 - 5	Moderate-low	343463.9	3864123.9
GF33	16.03	27.5	30	24	2.5	3.5	24 - 30	Moderate-low	343768.2	3864299.9
GF37	16.43	17	20	15	3	2	15 - 20	Moderate	344129.3	3864482.4
GF38	16.79	17	20	15	3	2	15 - 20	Moderate-low	344450.8	3864631.9
GF39	19.47	16.5	18	14	1.5	2.5	14 - 18	Moderate-low	346769.9	3866002.5
GF42	26.67	3.6	6	2	2.4	1.6	2 - 6	Low	353442.4	3868737.9
GF43	27.55	23.1	24.5	20	1.4	3.1	20 - 24.5	Moderate	354321.9	3868926.8
GF44	28.59	21.5	26.5	23	5	-1.5	23 - 26.5	Moderate-low	355232.1	3869425.4
GF45	32.21	14.8	16	13	1.2	1.8	13 - 16	Moderate-low	358335.2	3871345.7
GF46	34.30	5.5	6	5	0.5	0.5	5 - 6	Moderate	360377.5	3871917.2
GF47	34.35	24.3	26	22	1.7	2.3	22 - 26	High-moderate	360421.9	3871933.9
GF48	34.39	29.2	31.5	27	2.3	2.2	27 - 31.5	Moderate	360457.7	3871947.4

GF49	34.41	9.9	10.5	8	0.6	1.9	8 - 10.5	Moderate	360478.3	3871959.3
GF50	34.43	5.9	7	5	1.1	0.9	5 - 7	High-moderate	360498.1	3871964.9
GF52	33.37	26.1	27	25	0.9	1.1	25 - 27	Moderate	359231.3	3872174.4
GF54	36.92	11.1	14	9	2.9	2.1	9 - 14	Moderate-low	362873	3872753.9
GF56	38.69	11.2	14	9	2.8	2.2	9 - 14	High-moderate	364578	3873290.4
GF58	38.85	16.4	17.5	15.5	1.1	0.9	15.5 - 17.5	Moderate	364735.2	3873326.9
GF59	38.92	7.3	8.5	6.5	1.2	0.8	6.5 - 8.5	Moderate	364809.8	3873347.6
GF60	41.33	3.2	4.5	6.5	1.3	-3.3	6.5 - 4.5	Moderate-low	367048.2	3874319.1
GF61	42.59	2.2	4	1	1.8	1.2	1 - 4	Low	368061.5	3875083.5
GF62	42.62	5.5	6.5	4.5	1	1	4.5 - 6.5	High-moderate	368085.9	3875095.2
GF63	43.69	12.9	15	11	2.1	1.9	11 - 15	Low	369047.4	3875585.2
GF64	44.69	9.2	15.5	7.5	6.3	1.7	7.5 - 15.5	Moderate	369763.9	3876311.2
GF65	45.48	32.9	35	30	2.1	2.9	30 - 35	High-moderate	370478.2	3876663.6
GF66	45.66	7.3	8.5	6	1.2	1.3	6 - 8.5	Moderate	370588.3	3876819.2
GF68	46.79	37.3	40	35	2.7	2.3	35 - 40	Moderate	371555.6	3877414
GF69	47.30	8.1	11.5	6.5	3.4	1.6	6.5 - 11.5	Moderate-low	372018.1	3877641.5
GF70	47.30	7.1	8	6.5	0.9	0.6	6.5 - 8	Moderate	371961	3877718.8
GF72	47.69	21.7	25	19	3.3	2.7	19 - 25	Moderate-low	372347.3	3877851.1
GF73	49.44	7.4	8.5	5	1.1	2.4	5 - 8.5	High-moderate	373759.9	3878875.7
GF74	49.56	2.8	3.5	2	0.7	0.8	2 - 3.5	High-moderate	373793.2	3879055.1
GF75	49.63	3.7	4.5	3	0.8	0.7	3 - 4.5	High-moderate	373838	3879106.4
GF76	54.40	11.1	15	9	3.9	2.1	9 - 15	Low	377675.1	3881959.7
GF78	56.31	7.7	9	6	1.3	1.7	6 - 9	Moderate	379233.5	3883072.6
GF80	57.76	4.1	6	2	1.9	2.1	2 - 6	Moderate-low	380503.4	3883775.4
GF82	57.80	14.4	16.5	12	2.1	2.4	12 - 16.5	Moderate-low	380545.2	3883783.3
GF83	57.83	6.4	8.5	5	2.1	1.4	5 - 8.5	Moderate-low	380574.9	3883787.5
GF84	57.73	6.1	7.5	5	1.4	1.1	5 - 7.5	Low	380401.8	3883865.9
GF85	57.77	10.4	12	9	1.6	1.4	9 - 12	Low	380441	3883890.2
GF90	59.78	25.3	27	24	1.7	1.3	24 - 27	Low	382145.6	3884958.6
GF91	59.84	14.6	17	11	2.4	3.6	11 - 17	Moderate-low	382195.3	3884983
GF94	60.44	5.1	6	4	0.9	1.1	4 - 6	High-moderate	382807.5	3885136.4
GF95	60.70	2.7	4.5	1	1.8	1.7	1 - 4.5	High-moderate	382953.6	3885387.8
GF96	62.32	4.4	5.5	3.5	1.1	0.9	3.5 - 5.5	Moderate-low	384489.3	3886004.8
GF97	62.36	3.5	5.5	2	2	1.5	2 - 5.5	Low	384533	3886021.5
GF99	63.33	4.2	5.5	3	1.3	1.2	3 - 5.5	Low	385489.9	3886325.5
GF100	63.35	5.9	7	4.5	1.1	1.4	4.5 - 7	Low	385503.6	3886330.8
GF107	66.38	9.2	10.5	8	1.3	1.2	8 - 10.5	Moderate-low	387861.6	3888270.5

GF108	66.71	19.1	21	17	1.9	2.1	17 - 21	Moderate-low	388214.2	3888329.7
GF111	66.96	10.1	11.5	9	1.4	1.1	9 - 11.5	Low	388420.5	3888481.5
GF112	66.84	2	2.5	1.5	0.5	0.5	1.5 - 2.5	Moderate	388569.6	3888021.5
GF114	67.00	3.1	4	2	0.9	1.1	2 - 4	Low	388726.8	3888083.8
GF144	68.78	6.5	8	4	1.5	2.5	4 - 8	Low	390317	3888897.1
GF145	68.74	3.2	4.5	2	1.3	1.2	2 - 4.5	Moderate-low	390273.6	3888886.5
GF146	68.59	9.5	11	8	1.5	1.5	8 - 11	Moderate	390065.1	3888943.7
GF148	68.51	4.1	5.5	2.5	1.4	1.6	2.5 - 5.5	Low	389965.6	3888941.6
GF149	68.16	10.7	11.5	9.5	0.8	1.2	9.5 - 11.5	Low	389552.9	3888931
GF150	67.24	1.8	2.5	0.5	0.7	1.3	0.5 - 2.5	Low	388654.3	3888636.3
GF151	67.27	3	4	2	1	1	2 - 4	Low	388675.2	3888647.1
GF152	68.16	4.5	5.5	3	1	1.5	3 - 5.5	Moderate-low	389444.7	3889106.2
GF154	68.19	9.1	11	7	1.9	2.1	7 - 11	Low	389487.2	3889083.2
GF155	68.24	7.3	8.5	6	1.2	1.3	6 - 8.5	Moderate	389534	3889101.8
GF156	68.54	14	15.5	13	1.5	1	13 - 15.5	Moderate	389791.3	3889260.1
GF157	68.70	22	23	21	1	1	21 - 23	Moderate-low	389913.7	3889362.6
GF159	68.79	4	5	3	1	1	3 - 5	Moderate-low	389983.8	3889418.2
GF160	68.84	12.3	13.5	11	1.2	1.3	11 - 13.5	Low	390030.1	3889442.6
GF161	68.89	3.7	4.5	2.5	0.8	1.2	2.5 - 4.5	Moderate	390073.1	3889479.7
GF162	69.13	1.1	2.5	0.5	1.4	0.6	0.5 - 2.5	Low	390233.4	3889665.7
GF166	70.42	5.1	6.5	3.5	1.4	1.6	3.5 - 6.5	Moderate-low	391371.8	3890289.9
GF168	70.70	2.4	3.5	1.5	1.1	0.9	1.5 - 3.5	Moderate-low	391638.5	3890391.5
GF169	71.19	9.2	11	8	1.8	1.2	8 - 11	High-moderate	392063.4	3890622.7
GF170	71.26	10	11.5	8	1.5	2	8 - 11.5	Moderate	392147.5	3890631.7
GF172	71.49	4	5	3	1	1	3 - 5	Moderate	392366.5	3890706.9
GF173	71.80	8.9	10.5	7.5	1.6	1.4	7.5 - 10.5	Moderate-low	392634.8	3890879.4
GF177	72.14	11.4	13	10.5	1.6	0.9	10.5 - 13	Low	392958.1	3890995.9
GF178	72.54	7.2	8	6.5	0.8	0.7	6.5 - 8	High-moderate	393347.6	3891125.5
GF179	72.55	10.3	11	9.5	0.7	0.8	9.5 - 11	Moderate	393365.1	3891130.3
GF180	72.57	5.8	7	5	1.2	0.8	5 - 7	Moderate	393381.5	3891139.3
GF181	72.61	15.1	16	14	0.9	1.1	14 - 16	Moderate	393428	3891139.8
GF182	72.64	8.9	10	8	1.1	0.9	8 - 10	Moderate-low	393448.1	3891170
GF183	72.78	9.5	11	8	1.5	1.5	8 - 11	Moderate-low	393543.9	3891273.1
GF189	73.59	5.9	7	5	1.1	0.9	5 - 7	High-moderate	394139	3891847
GF190	73.71	1.8	2.5	1	0.7	0.8	1 - 2.5	Moderate	394218.4	3891933.9
GF191	73.72	5.8	7	4.5	1.2	1.3	4.5 - 7	Moderate	394227.9	3891941.9
GF192	73.74	7.6	9	6.5	1.4	1.1	6.5 - 9	Moderate-low	394249.4	3891955
GF198	74.30	10.4	11.5	9.5	1.1	0.9	9.5 - 11.5	Moderate-low	394731.3	3892225.8

GF199	74.31	5.2	6.5	4	1.3	1.2	4 - 6.5	Moderate	394746.2	3892230.4
GF200	74.32	9.4	11	8	1.6	1.4	8 - 11	Moderate	394745.2	3892246.9
GF202	74.40	1.4	2.5	0.5	1.1	0.9	0.5 - 2.5	Low	394745.1	3892401.9
GF203	74.42	2.9	3.5	2	0.6	0.9	2 - 3.5	Low	394755.9	3892407.1
GF207	74.54	1.2	2	0.5	0.8	0.7	0.5 - 2	Low	394897.5	3892413
GF207a	74.55	1.4	2	0.5	0.6	0.9	0.5 - 2	Low	394905.6	3892430
GF208	74.57	12.3	14	11	1.7	1.3	11 - 14	Moderate	394927.6	3892434.7
GF209	74.65	13.4	15	12	1.6	1.4	12 - 15	High-moderate	394987.2	3892481.8
GF209a	74.73	1.8	2.5	1	0.7	0.8	1 - 2.5	High-moderate	395011.5	3892498.3
GF209b	74.76	3.8	5	3	1.2	0.8	3 - 5	Moderate-low	395026.3	3892500.4
GF212	74.78	2.4	3	1.5	0.6	0.9	1.5 - 3	Low	395088.2	3892568.3
GF213	74.82	6.9	8.5	6	1.6	0.9	6 - 8.5	Moderate	395116.3	3892598.7
GF214	74.85	2.4	3	1.5	0.6	0.9	1.5 - 3	Low	395135.1	3892627.8
GF215	75.02	4.8	6	4	1.2	0.8	4 - 6	High-moderate	395139.8	3892919.1
GF216	75.12	2.1	3	1.5	0.9	0.6	1.5 - 3	Low	395253.1	3892938.7
GF217	75.14	1.9	3	0.5	1.1	1.4	0.5 - 3	Moderate-low	395265.8	3892945.6
GF218	75.17	7.4	9	6	1.6	1.4	6 - 9	Moderate-low	395299.6	3892961.4
GF219	75.32	2.3	3	1.5	0.7	0.8	1.5 - 3	Low	395558.2	3892829.4
GF221	75.56	0.7	1.5	0.1	0.8	0.6	0.1 - 1.5	Low	395824.4	3892860.2
GF224	75.45	3	4.5	1	1.5	2	1 - 4.5	Low	395502.3	3893157.6
GF225	76.15	7.5	9	6.5	1.5	1	6.5 - 9	Low	396475.4	3892949.1
GF226	76.47	3.9	5	3	1.1	0.9	3 - 5	Low	396694.7	3893187.3
GF227	76.48	2.1	2.8	1.5	0.7	0.6	1.5 - 2.8	Moderate-low	396706.3	3893197.7
GF230	76.91	4.6	5.5	4	0.9	0.6	4 - 5.5	Moderate	397025.7	3893499.8
GF231	76.92	4.1	5.5	3	1.4	1.1	3 - 5.5	Low	397041.9	3893494.5
GF233	77.47	1.3	2	0.5	0.7	0.8	0.5 - 2	Low	397525.2	3893759.3
GF235	77.59	4.8	6	4	1.2	0.8	4 - 6	Low	397672.7	3893754.7
GF236	77.61	7.7	8.5	6.5	0.8	1.2	6.5 - 8.5	Low	397689	3893764
GF236a	77.64		3.5	1.5	3.5	-1.5	1.5 - 3.5	Low	397711.7	3893780.1
GF237	77.67	7	8	6.5	1	0.5	6.5 - 8	High	397733.4	3893794
GF237a	77.69	5.7	7	5	1.3	0.7	5 - 7	Moderate-low	397750.3	3893804.6
GF239	77.77	2.8	3.5	2.3	0.7	0.5	2.3 - 3.5	Low	397775.5	3893922.6
GF241	77.97	5.6	6.5	5	0.9	0.6	5 - 6.5	High-moderate	397944.6	3894029.5
GF243	78.08	12.7	13.5	11.5	0.8	1.2	11.5 - 13.5	Moderate	398027.4	3894091.1
GF246	78.59	1.4	2	0.5	0.6	0.9	0.5 - 2	Low	398450.2	3894378.5
GF247	78.60	3.5	4	3	0.5	0.5	3 - 4	Low	398463.1	3894380.9
GF250	78.83	5.9	7.5	4	1.6	1.9	4 - 7.5	Low	398613.6	3894568.4
GF251	78.85	6.3	8	5	1.7	1.3	5 - 8	Low	398629.5	3894576.6
GF252	79.22	13.9	15	13	1.1	0.9	13 - 15	Moderate	398911	3894827.7

GF253	79.30	1.9	2.5	0.5	0.6	1.4	0.5 - 2.5	High-moderate	398980.1	3894863.4
GF255	79.40	13.2	14	12	0.8	1.2	12 - 14	Moderate	399030.3	3894971.2
GF256	79.46	8.8	10	8	1.2	0.8	8 - 10	Moderate	399092.9	3894989.4
GF257	79.43	5.6	6.5	4.5	0.9	1.1	4.5 - 6.5	High-moderate	399070	3894969.9
GF259	79.44	8.9	10	8	1.1	0.9	8 - 10	Moderate-low	399103.1	3894940.8
GF260	79.48	2.6	3.5	2	0.9	0.6	2 - 3.5	Moderate	399146.1	3894940.1
GF262	79.82	5.3	6.5	4	1.2	1.3	4 - 6.5	Moderate	399424.1	3895147.5
GF263	79.97	2.9	4	2	1.1	0.9	2 - 4	Moderate-low	399542.5	3895242.7
GF264	79.99	3.3	4	2	0.7	1.3	2 - 4	Moderate-low	399544.5	3895261.9
GF265	80.02	1.7	2.3	1	0.6	0.7	1 - 2.3	Low	399597.1	3895237.8
GF266	80.56	17.4	18.5	16.5	1.1	0.9	16.5 - 18.5	Moderate-low	400047.7	3895537.9
GF270	84.14	7	8	6	1	1	6 - 8	Low	402737.8	3897961.9
GF271	84.61	13.1	15.5	11	2.4	2.1	11 - 15.5	Low	403148.6	3898195.8
GF271a	84.65	7.7	9	6.5	1.3	1.2	6.5 - 9	Low	403189.5	3898221.2
GF272	84.88	8	9	7	1	1	7 - 9	Moderate-low	403347.1	3898388.3
GF273	84.91	9.7	10.5	9	0.8	0.7	9 - 10.5	Moderate-low	403372.9	3898400.2
GF274	85.33	2.6	3.3	2	0.7	0.6	2 - 3.3	Low	403806.8	3898502.8
GF275	85.42	4.9	6.5	3	1.6	1.9	3 - 6.5	Low	403878.2	3898572.9
GF276	85.87	2.5	4	1	1.5	1.5	1 - 4	Low	402919.6	3900586.6
GF277	85.88	3.1	3.8	2.5	0.7	0.6	2.5 - 3.8	Low	402929.2	3900598.1
GF278	85.90	3.5	4.3	2.8	0.8	0.7	2.8 - 4.3	Low	402940.1	3900614
GF283	87.15	6.2	7.5	5	1.3	1.2	5 - 7.5	Moderate-low	403731.8	3901682.8
GF285	87.58	2.2	2.8	1.8	0.6	0.4	1.8 - 2.8	Low	404060	3901956.1
GF286	87.58	1.6	2.3	1	0.7	0.6	1 - 2.3	Low	404060.8	3901961.2
GF287	87.62	2.9	4	2	1.1	0.9	2 - 4	Low	404033.2	3902079
GF288	88.71	0.9	1.2	0.1	0.3	0.8	0.1 - 1.2	Low	404728.8	3902996.6
GF290	89.06	2	2.5	1.5	0.5	0.5	1.5 - 2.5	Low	405024.1	3903185.8
GF291	89.09	1.9	2.5	1.5	0.6	0.4	1.5 - 2.5	Low	405040.5	3903209.1
GF292	89.22	2.5	3	2	0.5	0.5	2 - 3	Low	405161.2	3903269.7
GF301	91.45	7.1	8.5	6	1.4	1.1	6 - 8.5	Low	406854.1	3904755
GF302	91.46	4.8	6	4	1.2	0.8	4 - 6	Low	406862.1	3904765.6
GF303	91.48	10	11	9	1	1	9 - 11	Low	406871.6	3904781.1
GF306	94.87	3.4	4	2.8	0.6	0.6	2.8 - 4	Low	409311.7	3907228.7
GF306a	94.88	1.5	2	1	0.5	0.5	1 - 2	Low	409321.1	3907231.4
GF307	94.91	7.3	8.3	6.5	1	0.8	6.5 - 8.3	High	409332	3907267.1
GF312	96.80	2.3	2.8	1.5	0.5	0.8	1.5 - 2.8	Low	411131.7	3907987.5
GF312a	96.77	2.6	3	1.5	0.4	1.1	1.5 - 3	Low	411105.8	3907978.5
GF312b	96.82	4.8	5.5	3.5	0.7	1.3	3.5 - 5.5	Low	411154.1	3907993.7
GF319	95.65	3.2	4.3	2.5	1.1	0.7	2.5 - 4.3	Moderate-low	409876.2	3907784.1

GF320	95.71	2.7	3.3	2	0.6	0.7	2 - 3.3	Moderate-low	409907.3	3907850
GF321	95.73	2.7	3.5	2	0.8	0.7	2 - 3.5	Low	409916.5	3907884
GF322	95.83	4.3	5.5	3.5	1.2	0.8	3.5 - 5.5	Low	409796.4	3908240.1
GF323	95.87	3.9	5	3	1.1	0.9	3 - 5	Moderate-low	409805.1	3908303.1
GF325	96.12	4.6	5.5	3.5	0.9	1.1	3.5 - 5.5	Moderate-low	410129	3908253

OWENS VALLEY OFFSET MEASUREMENTS

Feature ID	Dist. along strike (km)	Optimal slip (m)	Max slip (+)	Min slip (-)	Slip (+)	Slip (-)	Slip range (m)	Quality rating	Easting	Northing
OVF1	2.66	8.8	10	8	1.2	0.8	8 - 1.2	Moderate-low	382905.03	4119511.6
OVF3	2.59	5.4	6	5	0.6	0.4	5 - 0.6	Moderate	382958.49	4119606.3
OVF4	2.64	1.6	3	0.5	1.4	1.1	0.5 - 1.4	Low	382913.02	4119540
OVF5	2.82	5	6.5	4	1.5	1	4 - 1.5	Low	382910.2	4119346.6
OVF6	2.84	0.4	1	0	0.6	0.4	0 - 0.6	Low	382933.31	4119334.3
OVF7	2.93	1.8	2.5	1	0.7	0.8	1 - 0.7	Moderate	382958.01	4119244.2
OVF8	2.91	8.6	9.5	8	0.9	0.6	8 - 0.9	Low	382951.25	4119258.6
OVF9	2.86	2.7	3.5	2	0.8	0.7	2 - 0.8	Moderate-low	382937.63	4119310.7
OVF12	3.16	1.9	3	0.5	1.1	1.4	0.5 - 1.1	Low	383005.75	4119021.8
OVF13	3.09	3.6	5	2	1.4	1.6	2 - 1.4	Low	383005.47	4119092.7
OVF14	3.19	10.7	12.5	9	1.8	1.7	9 - 1.8	Moderate-low	383001.28	4118989
OVF15	3.22	8.7	12	7.5	3.3	1.2	7.5 - 3.3	Moderate	383004.03	4118959
OVF16	3.27	8	9	7	1	1	7 - 1	Moderate-low	383018.33	4118910.1
OVF19	3.44	9.5	11	8	1.5	1.5	8 - 1.5	Moderate-high	383042.48	4118735.7
OVF20	3.65	8.9	10.5	7.5	1.6	1.4	7.5 - 1.6	Moderate	383018.63	4118511.1
OVF21	3.95	3.9	4.5	3	0.6	0.9	3 - 0.6	Moderate	383161.71	4118237.5
OVF22	3.99	1.9	2.5	1	0.6	0.9	1 - 0.6	High	383175.14	4118197.8
OVF23	4.06	4.2	5.5	3	1.3	1.2	3 - 1.3	High	383203.51	4118133
OVF24	4.17	2.3	3	1.5	0.7	0.8	1.5 - 0.7	Moderate-high	383235.25	4118026.3
OVF25	4.19	7.9	8.75	7.25	0.85	0.65	7.25 - 0.85	Moderate-high	383241.41	4118013.6
OVF26	4.10	3.4	4	3	0.6	0.4	3 - 0.6	High	383213.29	4118096.5
OVF27	4.24	4.5	5.25	3.75	0.75	0.75	3.75 - 0.75	Moderate-high	383257.06	4117963.5
OVF28	4.34	2.3	2.75	1.75	0.45	0.55	1.75 - 0.45	Moderate-low	383329.57	4117886.6
OVF29	4.44	8	8.5	7.5	0.5	0.5	7.5 - 0.5	Moderate	383375.22	4117792.8
OVF30	4.36	5.4	6.5	4.5	1.1	0.9	4.5 - 1.1	High	383344.55	4117863.1
OVF31	4.72	10.2	11.5	9	1.3	1.2	9 - 1.3	Low	383517.68	4117541.6
OVF33	4.82	6.6	8	5	1.4	1.6	5 - 1.4	High	383579.02	4117456.7
OVF35	7.79	2.4	3.75	1.5	1.35	0.9	1.5 - 1.35	Moderate-high	384380.24	4114591.5
OVF38	9.23	3.7	4.75	2	1.05	1.7	2 - 1.05	High	384577.93	4113146
OVF39	9.67	7.1	8	6	0.9	1.1	6 - 0.9	High	384632.42	4112705.3
OVF41	9.79	13.6	14.5	12.5	0.9	1.1	12.5 - 0.9	Moderate-high	384893.05	4112660.6
OVF42	9.84	8.1	9	7.5	0.9	0.6	7.5 - 0.9	Moderate	384908.81	4112616.3
OVF43	9.82	5.1	6.5	4	1.4	1.1	4 - 1.4	High	384902.95	4112631.1
OVF47	10.07	11.5	12.5	10.5	1	1	10.5 - 1	Low	385009.4	4112407
OVF48	10.04	3.5	4.25	3	0.75	0.5	3 - 0.75	Moderate-low	385007.88	4112430.7
OVF49	10.11	2.7	3.5	2	0.8	0.7	2 - 0.8	Low	384930.24	4112330.5
OVF50	10.12	6.4	7	5	0.6	1.4	5 - 0.6	Moderate-low	384909.24	4112319.9
OVF51	10.16	10.5	12.5	9	2	1.5	9 - 2	Moderate-high	384918.24	4112281.8
OVF52	10.34	3.7	4.5	3	0.8	0.7	3 - 0.8	Moderate-low	385003.09	4112118.9

OVF54	10.18	5.4	7	4	1.6	1.4	4 - 1.6	Moderate-low	384930.04	4112257.4
OVF55	10.44	1.6	2.5	0.5	0.9	1.1	0.5 - 0.9	Moderate	385047.27	4112030.7
OVF56	10.48	3.1	4	2.5	0.9	0.6	2.5 - 0.9	Moderate	385062	4111988.5
OVF57	10.50	3.5	4.25	3	0.75	0.5	3 - 0.75	Moderate-low	385065.71	4111969.5
OVF58	10.48	3.1	3.75	2.5	0.65	0.6	2.5 - 0.65	Moderate	385158.39	4112015.9
OVF59	10.62	3.1	4	2.25	0.9	0.85	2.25 - 0.9	High	385066.17	4111841.1
OVF60	11.03	3.7	4.5	2.75	0.8	0.95	2.75 - 0.8	Moderate-low	385245.46	4111471.9
OVF61	13.42	2.4	3.5	1	1.1	1.4	1 - 1.1	Moderate-low	386221.93	4109272.5
OVF62	13.51	2	3	1	1	1	1 - 1	Moderate-high	386227.26	4109179.6
OVF63	13.50	2.1	3	1	0.9	1.1	1 - 0.9	Moderate-low	386310.89	4109215.1
OVF65	13.90	10.4	11.5	9	1.1	1.4	9 - 1.1	Moderate-high	386362.57	4108818.4
OVF71	14.49	11.5	13	10.5	1.5	1	10.5 - 1.5	Low	386461.56	4108229.4
OVF72	14.79	8	8.5	7	0.5	1	7 - 0.5	High	386631.43	4107970.2
OVF73	15.33	11	12.5	9.5	1.5	1.5	9.5 - 1.5	Moderate-high	386838	4107465.6
OVF74	15.35	9.6	11	8.5	1.4	1.1	8.5 - 1.4	Moderate	386844.05	4107443.9
OVF75	16.64	4.4	5.5	3	1.1	1.4	3 - 1.1	Moderate-low	387102.88	4106178.2
OVF78	17.27	9.4	10.5	8.5	1.1	0.9	8.5 - 1.1	Low	387077.64	4105505.6
OVF81	17.83	2.4	4	1	1.6	1.4	1 - 1.6	Low	387125.48	4104936
OVF82	17.95	3	4.5	1	1.5	2	1 - 1.5	Low	387166.65	4104814.4
OVF90	19.16	1.9	4	0.5	2.1	1.4	0.5 - 2.1	Moderate	387054.41	4103513.6
OVF93	19.32	6.9	8.5	5.5	1.6	1.4	5.5 - 1.6	Moderate	387028.51	4103330.9
OVF95	19.43	3.1	4.25	2	1.15	1.1	2 - 1.15	Low	387164.87	4103266.5
OVF96	19.40	10.6	12	9	1.4	1.6	9 - 1.4	Moderate-high	387044.56	4103256.6
OVF99	20.05	7.3	9	6	1.7	1.3	6 - 1.7	Low	387102.36	4102593.3
OVF100	20.07	14.2	16	12.5	1.8	1.7	12.5 - 1.8	Low	387098.89	4102571.1
OVF101	20.39	12.9	15	11	2.1	1.9	11 - 2.1	Moderate-low	387065.02	4102223.6
OVF103	23.25	2.2	3.5	1	1.3	1.2	1 - 1.3	Low	390835.36	4100442.2
OVF104	23.92	7.9	9	6.5	1.1	1.4	6.5 - 1.1	High	390173.44	4099524.1
OVF106	24.66	4.5	6	3.5	1.5	1	3.5 - 1.5	Low	390327.64	4098788.8
OVF112	35.09	5	6.5	3.5	1.5	1.5	3.5 - 1.5	Low	392859.81	4088642.5
OVF114	35.48	2.9	3.75	2.25	0.85	0.65	2.25 - 0.85	Low	392998.77	4088277.6
OVF115	38.80	6.4	7	5.8	0.6	0.6	5.8 - 0.6	Low	393966.42	4085109.3
OVF118	43.33	3.6	4.5	3	0.9	0.6	3 - 0.9	Moderate-low	395519.13	4080851.7
OVF119	44.00	10.1	11.5	9	1.4	1.1	9 - 1.4	Moderate-low	395762.69	4080222.6
OVF121	44.20	13.9	15.5	12.5	1.6	1.4	12.5 - 1.6	Moderate	395826.42	4080027.7
OVF124	44.54	6.5	7	6	0.5	0.5	6 - 0.5	Moderate-low	395945.3	4079716.6
OVF125	44.55	5.2	6.5	4.5	1.3	0.7	4.5 - 1.3	Moderate	395950.88	4079701.1
OVF126	44.61	6.6	7.5	6	0.9	0.6	6 - 0.9	Low	395974.12	4079647.2
OVF127	44.77	2.7	3.75	2	1.05	0.7	2 - 1.05	Moderate-low	396030.4	4079502.5

OVF132	45.60	4.7	5.75	4	1.05	0.7	4 - 1.05	Low	396318.5	4078723.2
OVF133	46.11	2	2.75	1.25	0.75	0.75	1.25 - 0.75	Low	396503.47	4078247
OVF134	48.76	7.1	8.5	6	1.4	1.1	6 - 1.4	Moderate-low	397510.03	4075786
OVF135	51.87	5.4	6	5	0.6	0.4	5 - 0.6	Low	398533.77	4072842
OVF138	52.60	5.9	6.4	5.6	0.5	0.3	5.6 - 0.5	Low	398832.4	4072176.4
OVF139	52.77	14.5	15.5	13.75	1	0.75	13.75 - 1	Low	398725.54	4071959.4
OVF152	54.31	4.7	5.5	4.4	0.8	0.3	4.4 - 0.8	Low	399377.38	4070558.3
OVF155	54.61	6.3	7.5	5.5	1.2	0.8	5.5 - 1.2	High	399528.59	4070290.9
OVF156	55.27	9.8	11.5	8.5	1.7	1.3	8.5 - 1.7	Moderate-high	399782.73	4069677.3
OVF157	55.40	5.7	7	5	1.3	0.7	5 - 1.3	Moderate-high	399849.96	4069562.1
OVF158	55.44	4.2	5.5	3.5	1.3	0.7	3.5 - 1.3	Moderate-high	399820.74	4069512.6
OVF160	55.78	4.2	5	3.5	0.8	0.7	3.5 - 0.8	Moderate-high	399927.2	4069192
OVF161	56.17	6.6	7.25	5.75	0.65	0.85	5.75 - 0.65	High	400047.89	4068820
OVF163	56.29	2.9	4	2	1.1	0.9	2 - 1.1	Moderate-high	400092.88	4068703.2
OVF164	56.51	9.1	10.5	8	1.4	1.1	8 - 1.4	Moderate-high	400159.75	4068498.8
OVF165	56.73	3.7	5	1	1.3	2.7	1 - 1.3	Moderate-low	400290.25	4068303.6
OVF166	57.25	7.2	8.5	6	1.3	1.2	6 - 1.3	High	400470.14	4067823.4
OVF167	57.73	4.1	5.5	3	1.4	1.1	3 - 1.4	High	400664.3	4067379.5
OVF168	57.74	4.6	5.5	3.5	0.9	1.1	3.5 - 0.9	High	400668.4	4067363.7
OVF169	57.76	2.9	4	2	1.1	0.9	2 - 1.1	High	400672.42	4067352.3
OVF170	58.13	3.7	4.75	2.5	1.05	1.2	2.5 - 1.05	Low	400794.41	4066995.6
OVF171	58.27	4.1	4.75	3.5	0.65	0.6	3.5 - 0.65	High	400819.51	4066861.5
OVF172	58.33	3.5	4.5	2.5	1	1	2.5 - 1	Moderate-high	400853.54	4066808.3
OVF173	58.34	3.7	4.75	2.75	1.05	0.95	2.75 - 1.05	Moderate-high	400859.25	4066797.1
OVF174	59.30	4.5	5.25	3	0.75	1.5	3 - 0.75	Moderate	401081.55	4065864.5
OVF175	59.43	5.9	7	5	1.1	0.9	5 - 1.1	Moderate	401113.77	4065736.3
OVF182	57.16	3.8	4.75	3.25	0.95	0.55	3.25 - 0.95	High	399645.72	4067649
OVF184	58.15	2.1	3	1.5	0.9	0.6	1.5 - 0.9	Moderate-high	399367.07	4066519.2
OVF188	59.85	3.3	4	2.5	0.7	0.8	2.5 - 0.7	Moderate-low	399673.39	4064822
OVF189	59.42	3.1	4.5	2	1.4	1.1	2 - 1.4	Moderate	399386.2	4065180.7
OVF191	60.08	2.7	4	1.5	1.3	1.2	1.5 - 1.3	Low	399556.29	4064549.5
OVF192	61.39	9.2	10.5	8.5	1.3	0.7	8.5 - 1.3	Moderate-low	399906.12	4063282.2
OVF193	61.30	1.8	1.5	1	-0.3	0.8	1 - -0.3	Low	399852.8	4063356.5
OVF194	62.07	2.8	3.5	2.25	0.7	0.55	2.25 - 0.7	Low	400488.44	4062751.4
OVF201	64.05	7.2	8	6	0.8	1.2	6 - 0.8	Low	401573.2	4061023.6
OVF203	64.30	8	8.75	7.5	0.75	0.5	7.5 - 0.75	Low	401723.92	4060817.8
OVF204	64.39	7.8	8.5	7	0.7	0.8	7 - 0.7	Low	401770.9	4060735.8
OVF212	65.33	1.4	2	1	0.6	0.4	1 - 0.6	Moderate	401998.35	4059820.8
OVF213	65.41	2.1	2.5	1.5	0.4	0.6	1.5 - 0.4	Low	402020.59	4059744.9
OVF217	68.72	3.7	4.5	3	0.8	0.7	3 - 0.8	Low	402300.34	4056357.5

OVF220	69.70	3.5	4.5	1	1	2.5	1 - 1	Low	403007.11	4055557
OVF221	70.96	5.1	6.5	3.5	1.4	1.6	3.5 - 1.4	Moderate-low	403730.57	4054462.8
OVF222	71.28	4	5	3	1	1	3 - 1	Low	402972.37	4053878.6
OVF226	73.23	2.4	3.5	1	1.1	1.4	1 - 1.1	High	403388.87	4051961.4
OVF228	73.30	3.7	4.5	3	0.8	0.7	3 - 0.8	Low	403455.11	4051916.1
OVF231	73.35	3.4	3.75	3.25	0.35	0.15	3.25 - 0.35	Moderate	403529.55	4051883.1
OVF232	73.43	2.6	3.5	2	0.9	0.6	2 - 0.9	Moderate-low	403564.13	4051812.7
OVF235	78.13	1.6	3.5	2	1.9	-0.4	2 - 1.9	Low	404975.76	4047327.6
OVF236	79.56	3.9	4.5	3.5	0.6	0.4	3.5 - 0.6	Low	405370.15	4045947.3
OVF237	79.41	4.2	5.5	3	1.3	1.2	3 - 1.3	Low	405925.7	4046293.7
OVF238	79.43	2.4	3.5	1.5	1.1	0.9	1.5 - 1.1	Low	405932.08	4046274.5
OVF240	79.46	4.9	6	4	1.1	0.9	4 - 1.1	Moderate-low	405941.94	4046241.6
OVF242	80.58	2	2.75	1	0.75	1	1 - 0.75	Moderate-low	406401.38	4045211.5
OVF243	80.61	6.8	8	5.5	1.2	1.3	5.5 - 1.2	High	406412.03	4045188.5
OVF264	89.60	6.3	7.5	5.5	1.2	0.8	5.5 - 1.2	Moderate	406839.53	4035876.2
OVF265	89.65	11.5	13	10	1.5	1.5	10 - 1.5	Moderate-low	406861.82	4035825.1
OVF266	89.79	5.9	7	4	1.1	1.9	4 - 1.1	Moderate-low	406879.22	4035681
OVF269	90.01	5.3	7	4	1.7	1.3	4 - 1.7	Low	407005.48	4035498.6
OVF271	90.05	7.3	10	5	2.7	2.3	5 - 2.7	Low	406964.63	4035444
OVF273	90.07	4.4	7	3	2.6	1.4	3 - 2.6	Moderate-high	406964.64	4035414.7
OVF275	90.51	1.2	2	0.5	0.8	0.7	0.5 - 0.8	Low	406883.09	4034931.6
OVF276	91.18	2.7	4	1.5	1.3	1.2	1.5 - 1.3	Moderate-low	407026.22	4034275.7
OVF277	91.89	4.1	5	3.5	0.9	0.6	3.5 - 0.9	Moderate-high	407194.66	4033574.3
OVF284	111.65	3.7	4.5	3	0.8	0.7	3 - 0.8	Moderate	414675.42	4015230.1
OVF286	111.70	3	3.75	2.25	0.75	0.75	2.25 - 0.75	Moderate-low	414638.47	4015171.7
OVF290	111.54	1.8	3	1	1.2	0.8	1 - 1.2	Moderate-low	414887.15	4015417
OVF295	111.12	2.8	3.75	2.25	0.95	0.55	2.25 - 0.95	Moderate-low	414476.56	4015726.1

APPENDIX C

MATLAB CODE USED TO GENERATE KML FILES FOR THE UCERF3 OFFSET DATABASE

kml_writer.m

```
% David E. Haddad and Ramon Arrowsmith
% 05/18/2011

% This script takes in a text file that contains offset measurement
data
% stored in columns and makes KML file for Google Earth. Most of this
% script is borrowed from Ramon Arrowsmith's Computers in Geology class
notes:
% (http://http://arrowsmith410-598.asu.edu/Lectures/Lecture21/)

% Here we go...

% Load the text file that contains all offset measurement data.
% IMPORTANT NOTE: the first line of the text file must not have a text
% header! Otherwise, MATLAB's "load" function will not work!
%-------------------------------------------------------------------------
----
offset_data = load('SJF_offset_data_Lat_Long.txt');


% Define what each column represents.
%-------------------------------------------------------------------------
----
offset_number = offset_data(:,1);
longitude = offset_data(:,2);
latitude = offset_data(:,3);
distance_along_fault = offset_data(:,4);
offset_field = offset_data(:,5);
offset_field_plusminus = offset_data(:,6);
confidence_field = offset_data(:,7);
offset_QTM = offset_data(:,8);
offset_QTM_plusminus = offset_data(:,9);
confidence_QTM = offset_data(:,10);
offset_aerial_photos = offset_data(:,11);
aerial_photos_plusminus = offset_data(:,12);
offset_LaDiCaoz = offset_data(:,13);
LaDiCaoz_plusminus = offset_data(:,14);
confidence_LaDiCaoz = offset_data(:,15);


% Plot the locations of the offset measurements to make sure the
% locations are correct.
%-------------------------------------------------------------------------
----
% figure(1)
% clf
% plot(longitude,latitude,'k.')


% Write the kml file.
% First, open the output file to write the KML.
%-------------------------------------------------------------------------
----
```

```
fid =fopen('SJF_offset_data.kml','w+');


% Then, print the xml header and KML namespace declaration.
%-------------------------------------------------------------------------
----
fprintf(fid, '<?xml version="1.0" encoding="UTF-8"?>\n');
fprintf(fid, '<kml xmlns="http://www.opengis.net/kml/2.2">\n');
fprintf(fid, '<Document>\n');


% Now define the icon for the points.
%-------------------------------------------------------------------------
----
fprintf(fid, '<Style id="dot">\n');
fprintf(fid, '<IconStyle>\n');
fprintf(fid, '<scale>0.5</scale>\n');
fprintf(fid, '<Icon>\n');
fprintf(fid,
'<href>http://maps.google.com/mapfiles/kml/shapes/placemark_circle.png<
/href>\n');
fprintf(fid, '</Icon>\n');
fprintf(fid, '</IconStyle>\n');
fprintf(fid, '</Style>\n');


% Here begins the fun part. Write the KML for each point in the text
file.
%-------------------------------------------------------------------------
----
for i=1:length(longitude)
    fprintf(fid, '<Placemark>\n');
    fprintf(fid, '<name> %4.0f </name>\n',offset_number(i)); % Use the
offset number to name the placemark.
    fprintf(fid,...
        '<description><![CDATA[<h1>San Jacinto Fault Offsets</h1><table
border="1" cellpadding="3"><tr><th>Offset number</th><th>Longitude
(dd)</th><th>Latitude (dd)</th><th>Distance along fault
(m)</th><th>Field offset measurement (m)</th><th>+/- (m)</th><th>Field
offset confidence</th><th>QTM offset measurement (m)</th><th>+/-
(m)</th><th>QTM offset confidence</th><th>Aerial photo offset
measurement (m)</th><th>+/- (m)</th><th>LaDiCaoz offset measurement
(m)</th><th>+/- (m)</th><th>LaDiCaoz
confidence</th></tr><tr><td>%3.0f</td><td>
%10.8f</td><td>%10.8f</td><td>%3.2f</td><td>%3.2f</td><td>%3.2f</td><td
>%3.2f</td><td>%3.2f</td><td>%3.2f</td><td>%3.2f</td><td>%3.2f</td><td>
%3.2f</td><td>%3.2f</td><td>%3.2f</td><td>%3.2f</td></tr></table>]]></d
escription>\n',...
        offset_number(i),...
        longitude(i),...
        latitude(i),...
        distance_along_fault(i),...
        offset_field(i),...
        offset_field_plusminus(i),...
        confidence_field(i),...
        offset_QTM(i),...
```

```
        offset_QTM_plusminus(i),...
        confidence_QTM(i),...
        offset_aerial_photos(i),...
        aerial_photos_plusminus(i),...
        offset_LaDiCaoz(i),...
        LaDiCaoz_plusminus(i),...
        confidence_LaDiCaoz(i));

    fprintf(fid, '<styleUrl>#dot</styleUrl>\n');
    fprintf(fid, '<Point>\n');
    fprintf(fid,
'<coordinates>%20.10f,%20.10f,0</coordinates>\n',longitude(i),latitude(
i));
    fprintf(fid, '</Point>\n');
    fprintf(fid, '</Placemark>\n');
end


% Close the Document and KML tags.
%--------------------------------------------------------------------------
----
fprintf(fid, '</Document>\n');
fprintf(fid, '</kml>\n');


% Close the output file.
%--------------------------------------------------------------------------
----
fclose(fid);
```

APPENDIX D

A COMPOSITE QUALITY RATING SCHEME FOR THE UCERF3 OFFSET DATABASE

INTRODUCTION

Tectonically displaced markers such as offset stream channels, valleys, ridges, roads, and fences provide direct evidence of earthquake-produced surface slip (McCalpin, 2009). These offsets are measured are typically made in the field (e.g., Sieh, 1978; McGill and Sieh, 1991; Arrowsmith and Rhodes, 1994; McGill and Rubin, 1999; Lienkaemper, 2001) or using remote techniques (e.g., Arrowsmith and Zielke, 2009; Zielke et al., 2010; Haddad et al., in review).

Offset markers are often assigned a quality rating based on factors that evaluate the operator's confidence in the offset measurement as a reliable indicator of tectonic offset. These measurements feed into collaborative and multidisciplinary efforts (e.g., WGCEP/UCERF) to physically constrain earthquake-produced surface offsets, explain the recurrence behavior of earthquakes, and analyze the mechanical behavior of faults. Nearly all measurements of tectonically offset markers are reported with a quality rating that is assigned base on author

In this report, we compile and summarize existing quality rating schemes for tectonically offset geologic, geomorphic, and anthropogenic markers across active faults. We focus on published rating schemes. We then propose a new quality rating scheme for offsets that provides the framework for an objective assessment of offset markers.

EXISTING SCHEMES

Several quality rating schemes exist for offset measurements made using field and remote techniques. This section summarizes each scheme in chronological order of publication.

Sieh (1978)

Sieh (1978) assigned offset quality designations as "excellent", "excellent/good", "good", "good/fair", "fair", "fair/poor", and "poor". Figure 1 presents published graphical examples of each rating. The "excellent and good" quality markers had the "absence of complicating secondary faults, little or no indication of lateral warping, sharpness of offset expression, relatively simple or clearly interpretable geological and geomorphic features," (Sieh, 1978). No explicit descriptions were given for the "fair" and "poor" ratings. To standardize his rating scheme, we translated the descriptions of his offsets into discrete qualities based on key descriptive words that repeatedly appeared in each offset description.

Assigned rating	**Rating description**
Excellent	Well defined offset; sharp offset; fresh scarp; straight channels; beheaded channels; deeply incised channels.
Excellent/Good	Fresh fault trace; sharp offset; slight colluviation on abandoned channels.
Good	Fault zone characterized by multiple strands; channels intersect fault at low angle; shallow and wide channels; possible warping of channel; possible deflection of channel; different orientations of upstream and downstream channel segments.
Good/Fair	Broad fault zone; possible secondary faults; possibly deflected channels; similar channel widths and slope angles across fault; beheaded channels have similar widths and depths as their source.
Fair	Possible secondary faults; mircogeomorphology and alluvial deposits may obscure fault trace; broad and low-relief channels.
Fair/Poor	Fault trace not clear; fault trace geometry and position uncertain; complex fault

	traces; exact slip partitioning among multiple traces is not possible; possible warping of channels; upstream and downstream channel segments not parallel; very broad channels.
Poor	Poor fault location; secondary faults; channels may never have been aligned before MRE; channel possibly obscured by mass wasting processes; possible channel deflection; heavy alluviation in channels.

McGill and Sieh (1991)

McGill and Sieh (1991) assigned offset quality ratings to their measurements based on four categories: "excellent", "good", "fair", and "poor". Figure 2 presents published graphical examples of each rating. Although no explicit definition for each quality rating is given, offset measurements were assigned a rating as follows (McGill and Sieh, 1991):

"Each feature was given a quality rating that indicates the reliability and accuracy of the feature as an indicator of tectonic offset. For example, excellent and good ratings were given to geomorphic features that clearly have correlative features or deposits across the fault trace and that have clearly been separated by tectonic offset. Fair ratings were given to features that could possibly be separated by nontectonic means, of whose correlations across the fault are poor. Features that could easily have formed by nontectonic means (such as deflection around an uphill-facing scarp or stream capture), that have uncertain correlations across the fault, or that cross the fault zone in an area where the location of the fault trace(s) is uncertain were not used."

Lienkaemper (2001)

Leinkaemper (2001) rated his offset measurements using three qualities: "low", "medium", and "high". Figure 3 presents published graphical examples of each rating. There are no standardized descriptions for each rating. To standardize his rating scheme, we translated the descriptions of his offsets into discrete qualities based on key descriptive words that repeatedly appeared in each offset description. Note that the link to the supplementary online materials (SOM) for this paper is dead. We contacted James Lienkaemper to see if we may access the materials. He has provided the following links:
ftp://ehzftp.wr.usgs.gov/jlienk/archive/With_BSSA2001_Cholame1857/anaglyphs.htm
ftp://ehzftp.wr.usgs.gov/jlienk/archive/With_BSSA2001_Cholame1857/readme.htm

Assigned rating	**Rating description**
High	Distinct offset; offset channels straight and parallel to fault; deep incisions that are not significantly degraded; channel beheading is distinct; single fault trace narrow and well defined; channel head and tail easily matched across fault.
Medium	Presence of secondary fault traces with measurable offsets on both traces; offset present but obscured by mass wasting processes (e.g., slumping, landsliding); intense and irregular erosion; large width variation of offset channel; parallel upstream and downstream channel segments but heavy erosion at fault trace; minor curvature of channel at fault; possible anthropogenic-induced incision (e.g., cattle introduction, stock ponds, disking); low-angle intersection of piercing lines with fault; wide zone of faulting makes offset projection to fault inexact; channel capture/piracy on downstream side of fault.
Low	Fault location uncertain; concealed fault; offset feature too irregular; offset linear features at low angle to fault; possible existence of secondary fault trace; weakly incised channels; badly eroded; heavily eroded; offset obscured by surficial cover (e.g., colluvium); wide offset channel; high channel sinuosity; channel capture/piracy on downstream side of fault; offset obscured by anthropogenic

	activities (e.g., levee); possible deflection of drainage (as opposed to discrete offset).

Zielke (2009; 2010)

Zielke (2009; 2010) assigned a quality rating for each offset based on its reliability as an indicator for coseismic slip as follows: "high", "high-moderate", "moderate", "moderate-low", and "low". Figure 4 presents published graphical examples of each rating. The following table is extracted directly from Zielke's (2009) PhD dissertation (page 32) and the SOM (Zielke, 2010).

Assigned rating	**Rating description**
High	Channel is at high angle to fault; only little degradation; long and straight channel sections at both sides of fault.
High-moderate	Channel at high-moderate angle of more degraded (abandoned channel?); subparallel channels at both sides, but not very long (makes exact estimate of orientation difficult) or longer channel but with slight curvature.
Moderate	Channel at moderate angle and more degraded; channels may have slightly different angle (obliquity) on either side of the fault, or are not very long or may have distinct curvature when crossing the fault; still relatively long upstream/downstream segments.
Moderate-low	Channel at oblique angle to fault trace; degraded; may have clear break in orientation (flow direction) at fault; curvature when crossing the fault; still relatively long upstream/downstream segments.
Low	Channel at oblique angle to fault trace; degraded; break in flow direction, curvature when crossing the fault only small upstream/downstream extent; possible secondary fault trace may have been activate in 1857 earthquake – possibility of distributed deformation.

Salisbury (2012)

Salisbury et al. (2012) used a scheme that assigns a numerical value for each rating as follows: 0-5 = "poor", 5.25-6.75 = "fair", 7-8.75 = "good", 9-10 = "excellent". No explicit description is given for each rating. Also, the reason for the skewed quality assignment is not provided. For example, it is unclear why the "poor" rating is weighted greater than the other ratings. Salisbury et al. (2012) assigned field- and LiDAR-derived measurement uncertainties as follows:

"*Feature distinctiveness, the prominence of the fault trace, the average size of alluvial material, the degree to which features were projected into the fault trace, the degree of feature degradation, and the density of the surrounding vegetation (which limited visibility considerably in some areas).*"

Williams (in preparation)

Williams (in preparation) assigned two letter grades for each offset measurement based on "fault location" and "geomorphic fault offset" criteria. Each feature's letter grade is further subdivided into a +/- assignment (e.g., A-, B+). Figure 5 shows graphical examples of the different ratings used in Williams (in preparation). The following text was extracted from his manuscript on the recent slip-per-event history of the Coachella segment of the San Andreas fault (in preparation):

"*Fault location was graded 'A' if it is clear and simple with multiple consistent evidence. A- was given if evidence of location was good and consistent but required longer projections from areas of better*

expression. B+ and lower grades were assigned with increase of fault width or complexity. Lower grades were also attributed if fault location was found to be ambiguous. Sites with fault location lower than B+ were rarely used in the study."

The following tables present Williams' (in preparation) quality rating schemes.

Fault location:

Assigned rating	**Rating description**
A_F	Multiple, clear, local field evidence of fault motion; fault trace interpreted to be simple and narrow.
B_F	Field evidence strongly indicates location of fault, but exact location of active trace is interpreted from multiple permissive evidences; fault may be branching, bending, or wide.
C_F	Location permissive but not clear ("C_F" sites are not used in compiling slip curve).

Geomorphic fault offset:

Assigned rating	**Rating description**
A_G	Consistent with well-known fault location; good, uniform preservation; multiple consistent measurements; smaller reported uncertainties.
B_G	Clearly offset by fault; projection of piercing lines to fault are longer; interpreted across multiple traces; preservation moderate to non-uniform; preferred but non-unique interpretations are reported; reported uncertainties are larger.
C_G	Offset may be apparent or biased by stream deflection against uphill-facing scarp, side-slope, or stream processes ("C_G" sites are not used in compiling slip curve).

PROPOSED RATING SCHEME

Based on our compiled quality rating schemes, there appear to be three factors that control the assignment of ratings in each study: (1) the quality of the marker that is offset, (2) the degree to which the fault zone is defined, and (3) the quality of the offset itself. Even though the compiled schemes used some combination of these factors to assign a rating to each offset, no standardized definition of each quality rating is provided. Furthermore, the quality assignments were not consistently used. For example, what does an offset rating of "high" look like using the Zielke et al. (2010) scheme? How is the degree of geomorphic degradation of each offset systematically assessed and assigned a value? The current rating schemes do not address such questions explicitly and thus could include a large degree of subjectivity or bias. Furthermore, the current schemes do not allow for a systematic quantification of confidence levels for the offsets that are to be used in the UCERF 3 models.

To address these issues, we developed a new composite rating scheme that incorporates the three controlling factors and assigns a single rating to each offset measurement. Our scheme uses a combination of visual and quantitative assessments of offset markers that are built into a streamlined workflow. The quantitative nature of our scheme has the added value of being incorporated into displacement reconstruction calculators (e.g., Zielke et al., 2010), where lateral slip vectors and their orientations are computed (e.g., dot product) for the offset and automatically assigned a rating based on the angle made by the piercing lines and the fault.

FUTURE DIRECTIONS

- Using our newly compiled database, we will compute the frequency of each quality rating and see if there exists a relationship between rating frequency and reported measurement errors. This will test the performance of existing rating schemes and the consistency of the original raters.
- Based on results from the above task, we will refine the final number of quality categories for our proposed rating scheme.

ACKNOWLEDGMENTS

We wish to thank Olaf Zielke, Sally McGill, Patrick Williams, etc etc, for providing access to their offset data and graphics. Support for this project was provided by the Uniform California Earthquake Rupture Forecast (UCERF3) project of the Working Group on California Earthquake Probabilities (WGCEP), the United States Geological Survey (USGS), and the National Earthquake Hazards Reduction Program (NEHRP) and the Southern California Earthquake Center (SCEC).

REFERENCES CITED

Arrowsmith, J. R., and Rhodes, D. D., 1994, Original forms and initial modifications of the Galway Lake Road scarp formed along the Emerson Fault during the 28 June 1992 Landers, California, Earthquake: Bulletin of the Seismological Society of America, v. 84, no. 3, p. 511-527.

Arrowsmith, J. R., and Zielke, O., 2009, Tectonic geomorphology of the San Andreas Fault zone from high resolution topography: An example from the Cholame segment: Geomorphology, v. 113.

Haddad, D. E., Akciz, S. O., Arrowsmith, J. R., Oldow, J. S., Rhodes, D. D., Zielke, O., Toke, N. A., Haddad, A. G., and Mauer, J., in review, Applications of airborne and terrestrial laser scanning to paleoseismology: Geosphere.

Lienkaemper, J. J., 2001, 1857 slip on the San Andreas fault southeast of Cholame, California: Bulletin of the Seismological Society of America, v. 91, no. 6, p. 1659-1672.

McCalpin, J. P., 2009, Paleoseismology, International Geophysics Series: San Diego, Academic Press, p. 613.

McGill, S. F., and Rubin, C. M., 1999, Surficial slip distribution on the central Emerson fault during the June 28, 1992, Landers earthquake, California: Journal of Geophysical Research, v. 104, no. B3, p. 4811-4833.

McGill, S. F., and Sieh, K., 1991, Surficial offsets on the central and eastern Garlock fault associated with prehistoric earthquakes: Journal of Geophysical Research, v. 96, no. B13, p. 21,597-21,621.

Sieh, K. E., 1978, Slip along the San Andreas fault associated with the great 1857 earthquake: Bulletin of the Seismological Society of America, v. 68, no. 5, p. 1421-1448.

Zielke, O., Arrowsmith, J. R., Ludwig, L. G., and Akciz, S. O., 2010, Slip in the 1857 and earlier large earthquakes along the Carrizo Plain, San Andreas Fault: Science, v. 327, p. 1119-1122.

APPENDIX E

OPENTOPOGRAPHY TUTORIAL FOR CHAPTER 3

INTRODUCTION

The drive for understanding geologic phenomena at submeter-resolution scales has led to a rapid increase in the demand for high-resolution digital topographic datasets collected by light detection and ranging (lidar) systems. The richness of lidar datasets makes them highly valuable beyond the original application that drove their acquisition. However, lidar datasets and analyses tend to be project-specific, computationally intensive, and large, thus creating technical challenges in their processing and distribution to the geoscience community. Furthermore, the useful analysis of lidar datasets requires special computing resources that are unavailable to many geoscientists. To help alleviate these challenges, the Arizona State University School of Earth and Space Exploration (http://sese.asu.edu) and the University of California (San Diego) San Diego Supercomputer Center (http://www.sdsc.edu), with support from the U.S. National Science Foundation, have collaborated to create the OpenTopography Facility (http://opentopography.org). OpenTopography facilitates community Web access to high-resolution geoscience-oriented topographic data, related tools, and resources as a means to democratize Web-based access to lidar datasets.

The purpose of this tutorial is to demonstrate how to access publicly available lidar datasets using the OpenTopography Web facility. This tutorial is not meant to be a comprehensive documentation of advanced OpenTopography functionalities. Instead, we encourage the reader to explore OpenTopography on the Web via its extensive online documentation, video tutorials, and educational resources.

COMPUTING CONSIDERATIONS

There are certain computing requirements to consider when visualizing and analyzing lidar datasets depending on their intended use. For this tutorial, the basic computing needs include access to high-speed Internet, a Web browser, and the free edition of Google Earth. More advanced lidar data analysis will require access to a geographic information system (e.g., ArcInfo or Global Mapper).

WORKFLOW

Step 1: Set up a free OpenTopography account

Go to http://opentopography.org. Click the "Overview Video" to watch a brief video about the OpenTopography facility.

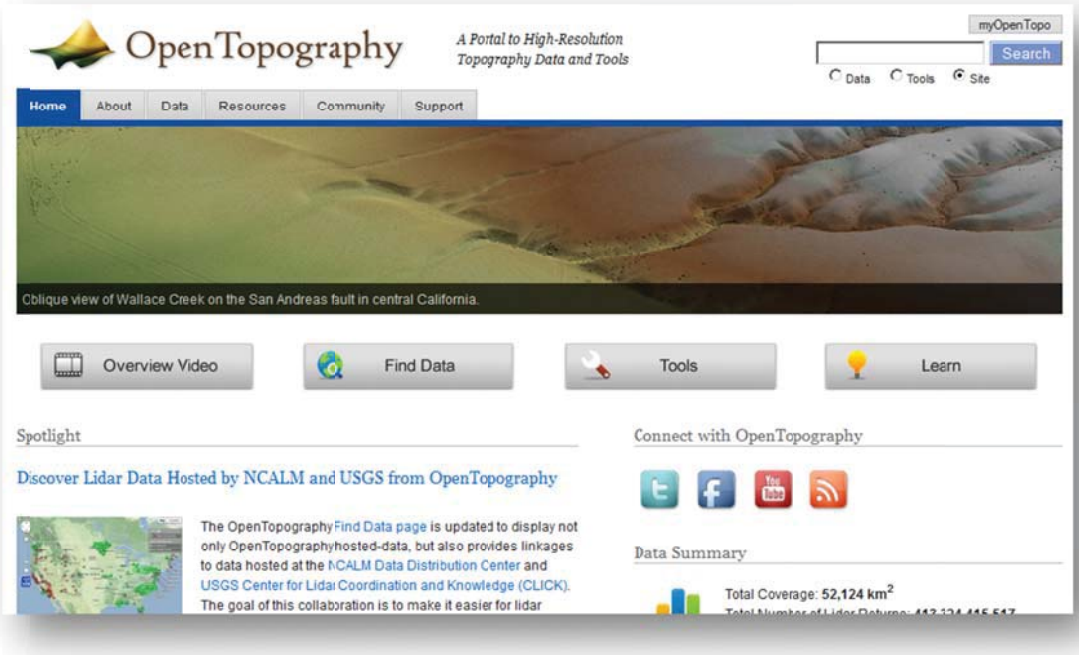

Click the "myOpenTopo" button on the top-right corner of the homepage and "Create new account." Fill out your user information.

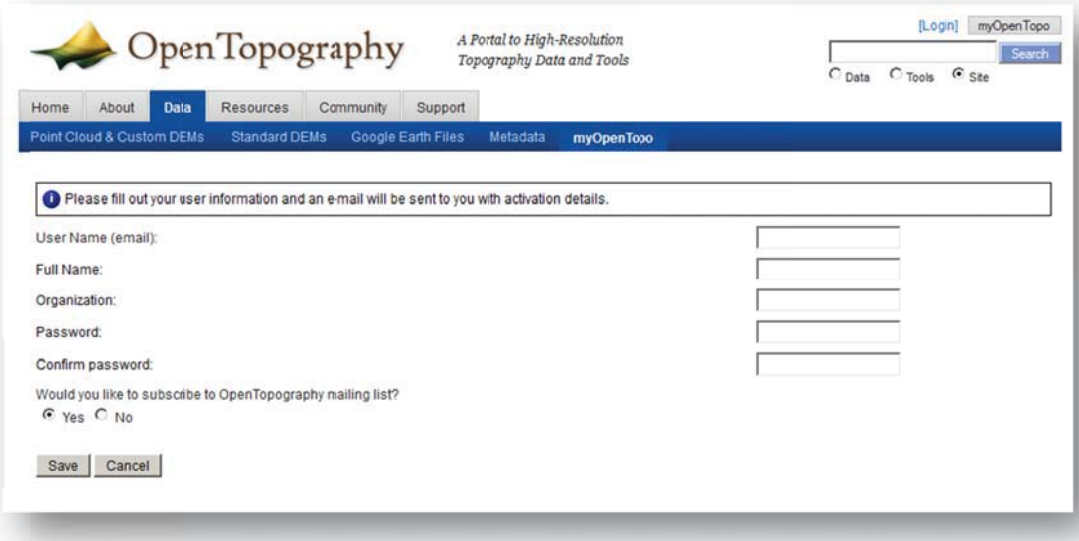

Once you activate your account, go back to the myOpenTopo log-in page and log into your account.

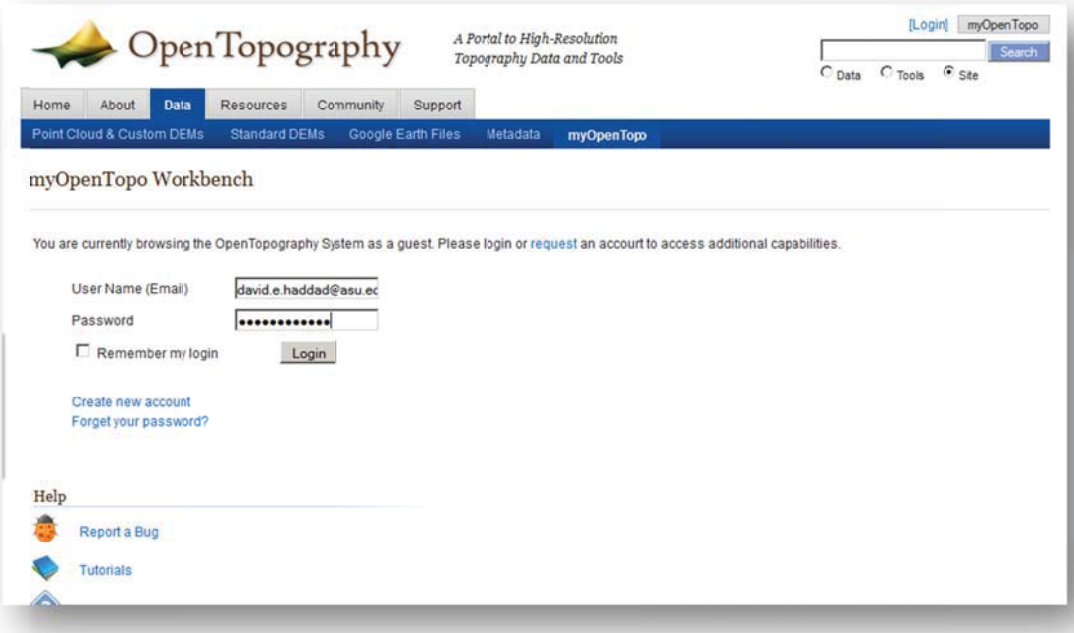

This page is divided into three main sections: (1) Data – where you can access past user-defined lidar job requests, (2) Contribute – where you can contribute lidar datasets or processing tools, and (3) User Account – where you can perform basic account management operations.

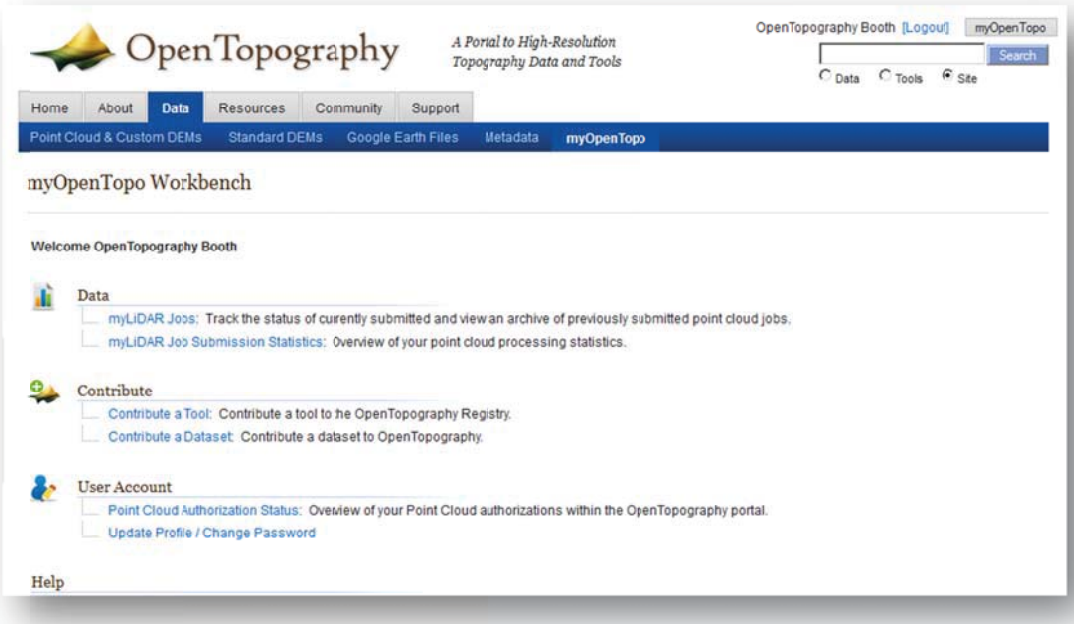

Step 2: Determine if lidar data exist for your area of interest

Click the "Data" tab near the top of the page. This will take you to a Google Maps interface that shows all publicly available lidar datasets. The datasets are color-coded by their data source. For example, red dots are datasets that are available directly via OpenTopography. Zoom to your area of interest to check the availability of lidar data. For this tutorial, we will access lidar data that are located within the OpenTopography facility.

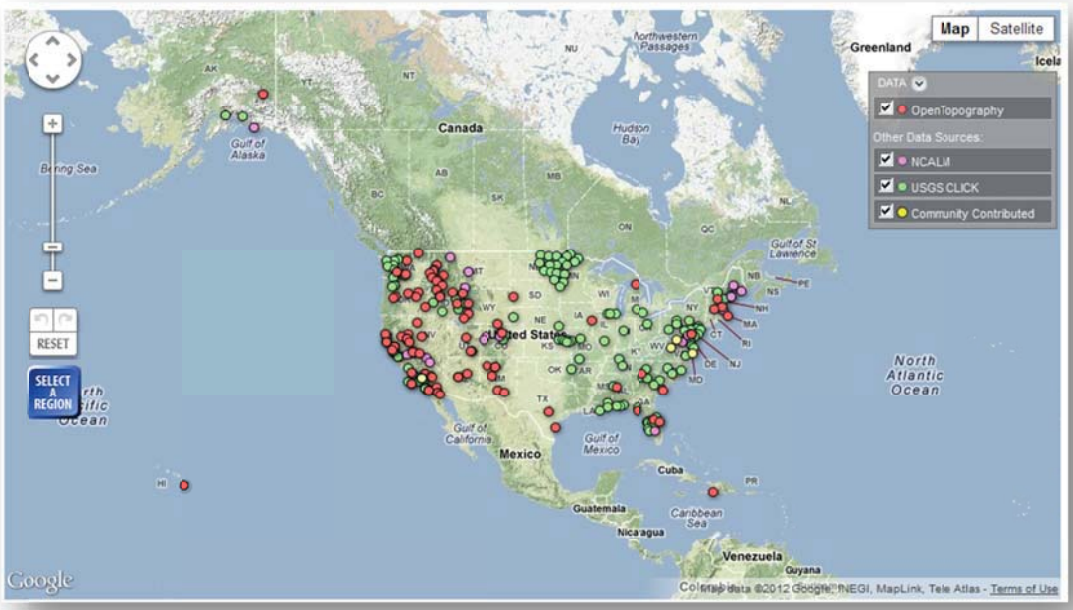

Zoom in to a portion of the Garlock fault in California, USA. Left-clicking once on the data extent will display a pop-up balloon with some basic information about that dataset. Take note of the name of the dataset (this example shows the "EarthScope Southern & Eastern California LiDAR Project") because we will use it to search for the actual data in OpenTopography.

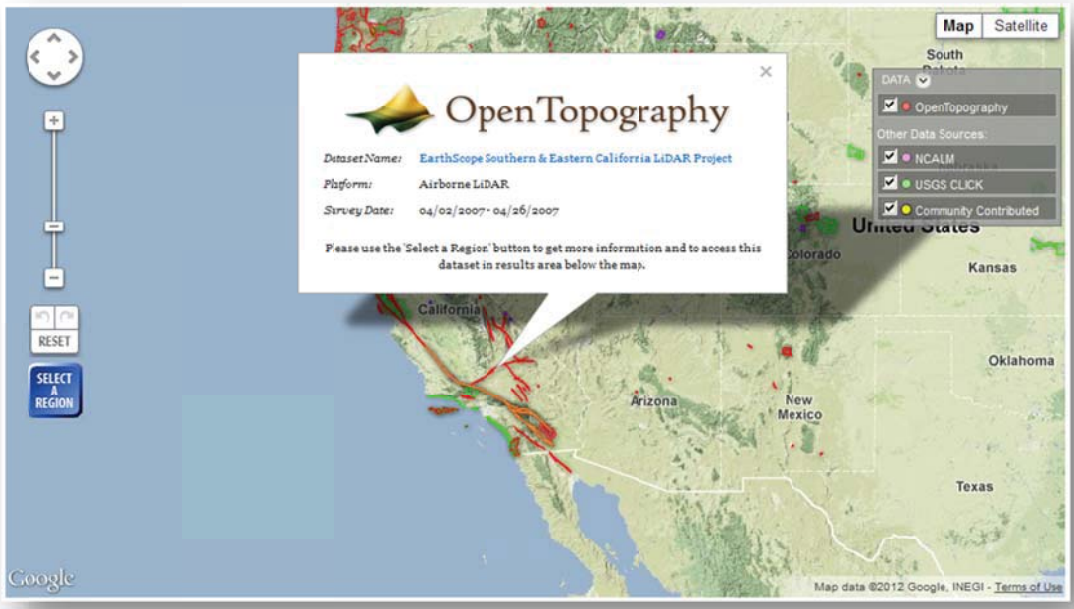

Step 3: Access lidar data for your area of interest

Click the "Point Cloud & Custom DEMs" link under the "Data" tab to go to the complete list of lidar datasets that are available in OpenTopography. Scroll down to the dataset of interest (in this example it is "EarthScope Southern & Eastern California LiDAR Project") and click the link.

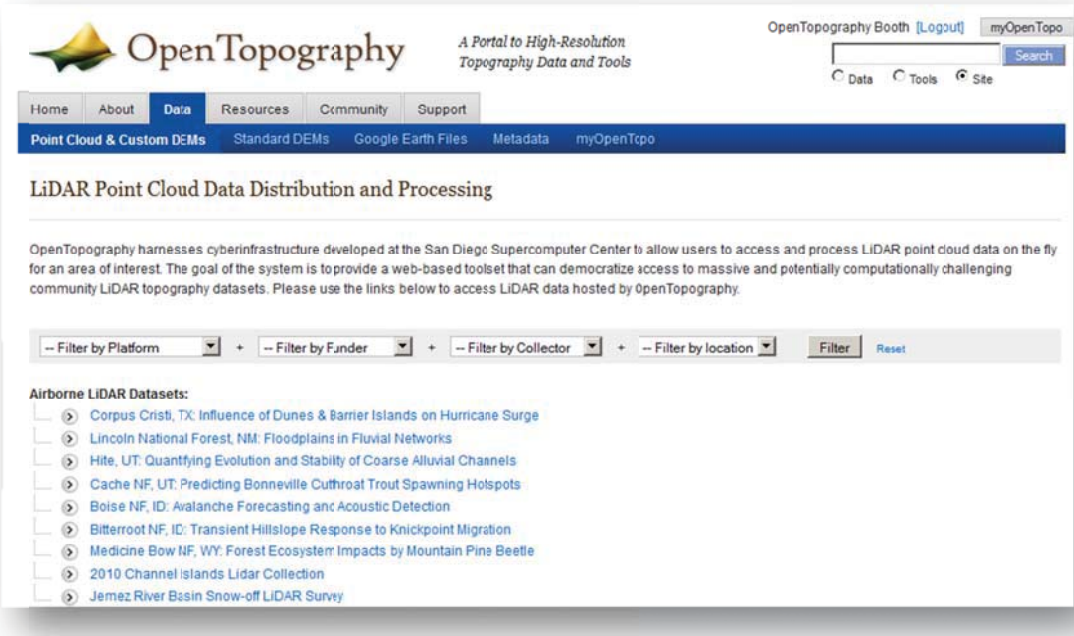

You will be taken to the dataset's page, which is divided into two sections. The top section contains general information about the dataset, the full metadata report that was generated by the data collector, information about the project funders, and DEM options. The contents of the lower section depend on which DEM option is selected.

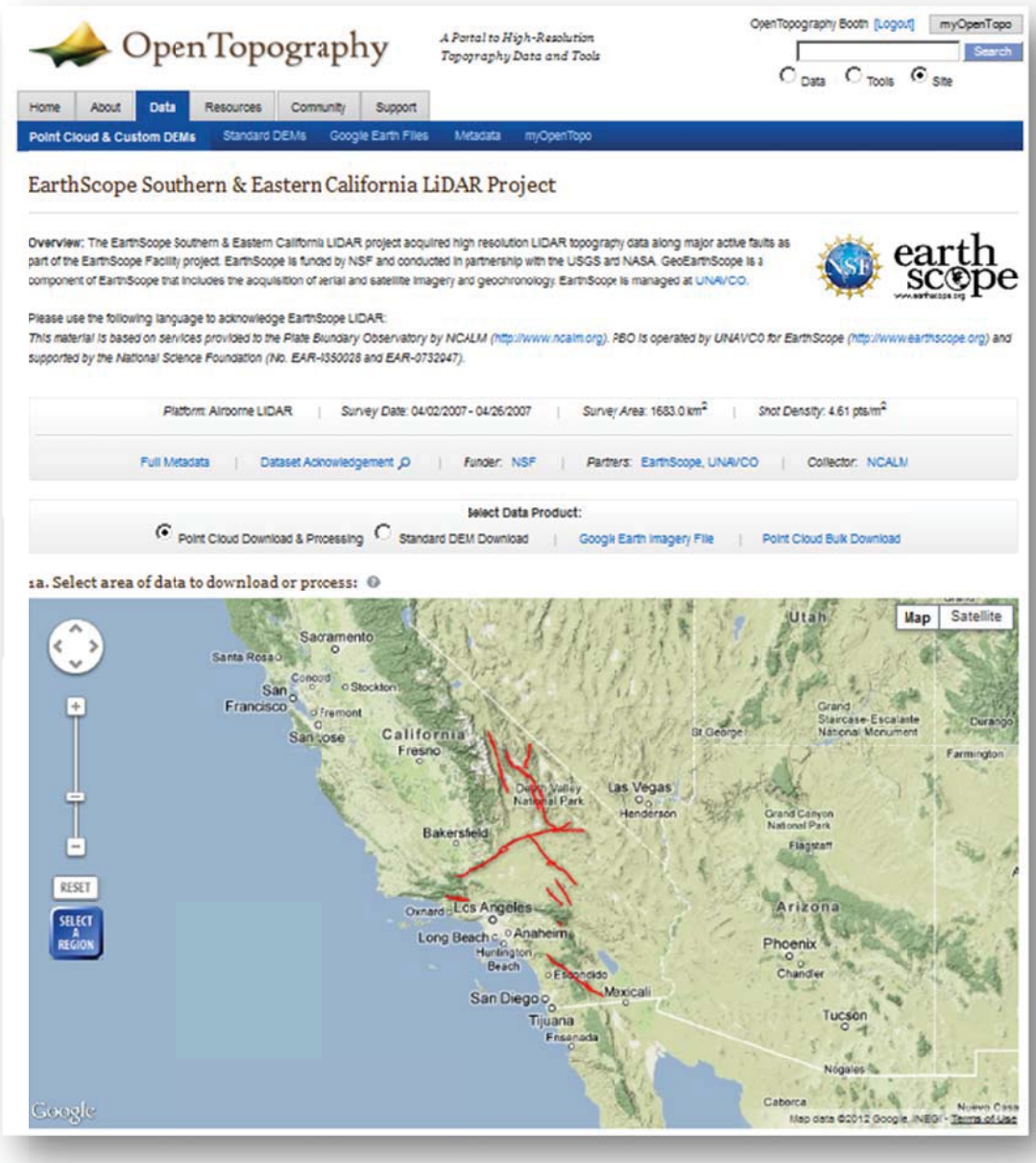

Step 4: Choose a method to create/download lidar-derived DEMs

Step 4: Choose a method to create/download lidar-derived DEMs

There are three ways to generate DEMs in OpenTopography.

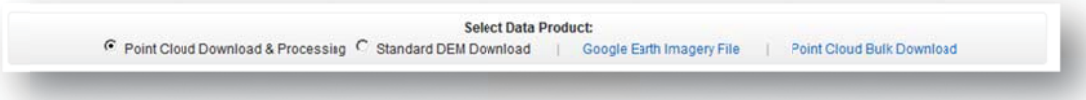

The first option (“Point Cloud Download & Processing”) is the most advanced and allows you to control the parameters that go into creating DEMs. The second option (“Standard DEM Download”) allows you to download DEMs that were already created by OpenTopography. Both of these options require a geographic information system to display and process the DEMs (e.g., ArcInfo or Global Mapper). See the supporting documents in the “Support” tab for details on how to do this. The third option (“Google Earth Imagery File”) allows the user to download DEM imagery that was created specifically for the Google Earth platform. The fourth option (“Point Cloud Bulk Download”) provides the user with the ability to download the raw lidar point data. For this tutorial, we use the third option of downloading DEM imagery that was created by OpenTopography to be displayed in Google Earth.

Step 5: Display DEM imagery in Google Earth

Click the “Google Earth Imagery File” link to download the Google Earth file. Once the download is complete, double click the Google Earth file and explore your area of interest.

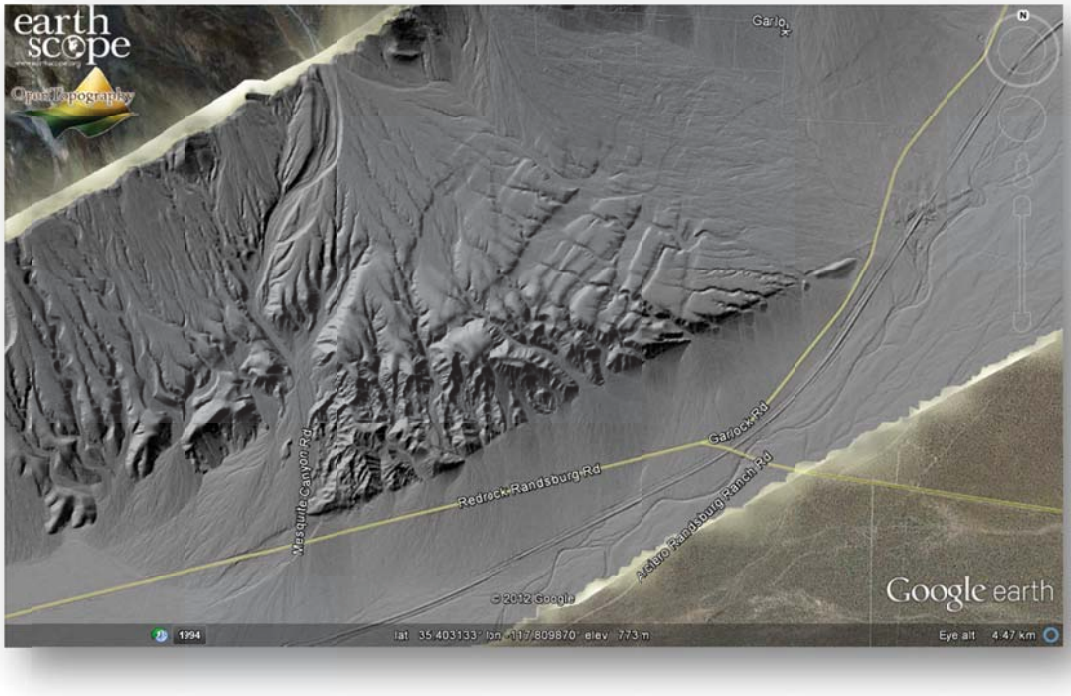

APPENDIX F

IRB APPROVAL FORMS AND MATERIALS FOR CHAPTER 6

ASU Knowledge Enterprise Development

Office of Research Integrity and Assurance

To:	Steven Semken PSF
From:	Mark Roosa, Chair Soc Beh IRB
Date:	09/09/2011
Committee Action:	**Exemption Granted**
IRB Action Date:	09/09/2011
IRB Protocol #:	1109006824
Study Title:	Earth Science Meets the Special Education Classroom

The above-referenced protocol is considered exempt after review by the Institutional Review Board pursuant to Federal regulations, 45 CFR Part 46.101(b)(1) .

This part of the federal regulations requires that the information be recorded by investigators in such a manner that subjects cannot be identified, directly or through identifiers linked to the subjects. It is necessary that the information obtained not be such that if disclosed outside the research, it could reasonably place the subjects at risk of criminal or civil liability, or be damaging to the subjects' financial standing, employability, or reputation.

You should retain a copy of this letter for your records.

State University Office of Research Integrity and Assurance 660 S. Mill Avenue Suite 315 Arizona State University Tempe AZ 85287-6111 (Mail Code 6111) Phone: 480-965-6788 Fax: (480) 965-7772		*For Office Use Only:* Date Received: HS Number:

SOCIAL BEHAVIORAL APPLICATION HUMAN SUBJECTS

PROTOCOL INFORMATION

Protocol Title:
Earth Science Meets the Special Education Classroom

Date: 09/01/2011

PRINCIPAL INVESTIGATOR (PI)

Please note that the PI's CV and human subject's protection training certification must be attached with this application.

Name and Degree(s):
Steven C. Semken, Ph.D.

Department/Center:
School of Earth and Space Exploration

Mailing Address:
Bateman Physical Sciences Center, F-Wing, Mail Code 1404

Email:	Phone:	Fax:
semken@asu.edu	480-965-7965	480-965-8102

University Affiliation:

- ☐ Professor
- ☒ Associate Professor
- ☐ Assistant Professor
- ☐ Instructor
- ☐ Other: Please specify. ("Other" categories may require prior approval. Students cannot serve as the PI)

CO-INVESTIGATORS (CO-I)

- A Co-I is anyone who has responsibility for the project's design, implementation, data collection, data analysis, or who has contact with study participants.
- If the project involves medical procedures or patient care that the PI is not certified or licensed to conduct, a responsible physician or other certified or licensed professional must be included as a Co-I. The application must include a copy of supporting documentation for this individual (CV, license, board certification etc).

Name	Study Role	Affiliation	Department	Email/Tel/Fax	Student (yes/no)
David E. Haddad	Protocol designer, data collector	ASU	School of Earth & Space Exploration	david.e.haddad@asu.edu T: 480-965-4053 F: 480-965-8102	Yes (Ph.D. track)

PROJECT FUNDING

1a)How is the research project funded? (A copy of the grant application **must** be provided prior to IRB approval)

☒ Research is **not funded** (Go to question 2)
☐ Funding decision is pending
☐ Research is **funded**

b) What is the source of funding or potential funding? (Check all that apply)

☐ Federal ☐ Private Foundation ☐ Department Funds
☐ Subcontract ☐ Fellowship ☐ Other

c) Please list the name(s) of the sponsor(s):

d) What is the grant number and title?

e) What is the ASU account number/project number?

f) Identify the institution(s) administering the grant(s):

PROJECT SUMMARY

2. Provide a **brief** description of the **background, purpose, and design** of your research. Avoid using technical terms and jargon. Describe all interactions with potential study participants (e.g., how identified, how recruited) including all of the **means you will use to collect data** (e.g. instruments, measures, tests, questionnaires, surveys, interview schedules, focus group questions, observations). Provide a short description of the tests, instruments, or measures. (If you need more than a few paragraphs, please attach additional sheets.) **Attach copies of all instruments and questionnaires. FOR ALL OF THE QUESTIONS, WRITE YOUR ANSWERS ON THE APPLICATION RATHER THAN SAYING "SEE ATTACHED".**

Background
Learning activities in the special education classroom have variable success rates. This is especially true for science- and mathematics-oriented subjects (e.g., Earth science, physics, chemistry), where mainstream classroom activities fail to meet the needs of students with special learning needs. Furthermore, few teaching aids and resources are available to special education teachers, thereby limiting the success of their students in meeting science and mathematics standards set at the state or federal level.

Purpose
The purpose of the proposed research is to design, implement, and evaluate new lesson plans for a special education classroom. Student reactions, level of engagement, and retention of the Earth science, science, and mathematics topics will be observed and documented. If proven to be effective, these lesson plans will be made available to special education teachers and curricula designers as a guide to helping their students meet state- and federally mandated Earth science, science, and mathematics educational standards.

Design
The design of the proposed research includes: (1) developing leaner-based lesson plans that are geared toward students with special learning needs, (2) implementing the lesson plans in a classroom setting under the instruction of a qualified special education teacher, (3) collecting data via direct, non-invasive observation of student reactions to the lesson plans, and (4) conducting pre- and post-evaluation tests to determine the effectiveness of the lesson plans.

Means by which data will be collected:
(1) Direct in-class observation. This will involve Co-I Haddad attending 80-minute classroom sessions over a period of 1-2 weeks. Haddad will observe and document the reactions exhibited by each student to the new lesson plans. Characteristics such as body posture, level of attention, and student-teacher interactions will be recorded in spreadsheet form (Williams and Semken, 2011; please see *Supplemental Material 1*).

(2) Pre-assessment tests. This will involve distributing a 4- to 5-question survey to students before each lesson to assess their current state of knowledge about the topic to be covered that day (please see *Supplemental Material 2*).

(3) Post-assessment tests. This will involve distributing a 4- to 5-question survey to students after each lesson to evaluate their understanding of the topic of the day and if the new lesson plan succeeded in helping them enhance their understanding of the concepts covered that day (please see *Supplemental Material 2*).

References Cited

Williams, D., Semken, S., 2011. Ethnographic methods in analysis of place-based geoscience curriculum and pedagogy. In A. P. Feig & Stokes (Eds.), *Qualitative research in geoscience education: Geological Society of America Special Paper 474* (pp. 49-62). Boulder, CO: Geological Society of America.

STUDY DURATION

3. What is the expected duration of the study through data analysis? (Include a timeline, if applicable).
10/10/2011 – 10/21/2011: Lesson plan design and preparation.
10/24/2011 – 11/11/2011: Lesson plan implementation, data collection via observations, pre-tests, and post-tests.
11/14/2011 – 12/09/2011: Data analysis and generation of preliminary results/interpretations. Presentation of preliminary results at the 2011 American Geophysical Union Fall Meeting.
01/02/2012 – April/2012: Further data analysis and preparation of report for Ph.D. candidacy exam (to be taken sometime in April 2012).

a. When is the expected date that you wish to begin research? (MM/DD/YY) 10/10/2011 (must be after submission date) Note: Protocols are approved for a maximum of 1 year. If a project is intended to last beyond the approval period, continuing review and reapproval are necessary. Research cannot begin until you have received an approval letter.

IRB APPROVAL

4. Has this project been reviewed by another IRB? ☐ Yes ☒ No (If yes, please complete the information below and attach a copy of the IRB approval materials).
a) What is the name of the institution?

b) What is the current IRB approval date/status of IRB application?

STUDY SITES

5. Where will the study be conducted? (Check all that apply)
☐ On campus (Please indicate building(s) and room number (s) when known)

☒ Off campus (Please provide location and letter of permission, where applicable)

Challenger Middle School
7301 N. 58th Ave
Glendale, AZ 85301

Please see permission agreement from the school principal in *Supplemental Material 3*.

SAMPLE SIZE/DURATION

6a) What is the expected number of individuals to be screened for enrollment? 10

b)What is the **MAXIMUM** number of subjects that you plan to enroll in the study? 10

c) What is the approximate number of: 5 Males 5 Females

d) Indicate the age range of the participants that you plan to enroll in your study. 12 to 14

e) What is the expected duration of participation for each subject? (at each contact session and total)
Each contact session: 80 minutes.
Total: 80 minutes x 10 days (maximum) = 800 minutes (maximum).

SUBJECTS

7. Will the study involve any of the following participants? (Please check all that apply if your study specifically targets these populations)

- ☒ Children (under 18)
- ☐ Pregnant women
- ☐ Prisoners or detainees
- ☐ Persons at high risk of becoming detained or imprisoned
- ☐ Decisionally impaired
- ☐ Patients- what is the status of their health?
- ☐ Fetuses
- ☐ Native Americans
- ☐ Non-English speakers (Include copy of all materials in language of participants and certification of the translation and back-translation: http://researchintegrity.asu.edu/humans/forms)

a) If **any** of the above categories have been checked, please state how you will protect the rights and privacy of these individuals.

Throughout the duration of the proposed research, we will not use any identifying information for any student. For example, no names, genders, race, ethnicity, or disability status will be exchanged that can uniquely identify individual participants. We will not ask about individual special needs, nor will we be privy to the types of disabilities each participant has. Similarly, the publication of any results in peer-reviewed journals or meetings/presentations will not use any of the above-mentioned identifiers. Instead, we will use semi-quantitative measures such as "There were X number of students in classrooms classified as "special education" or "special needs" that participated in this study. The new lesson plans were effective at improving the understanding of mandated curricula in X out of Y students," where "X" and "Y" represent numerical results from the proposed research.

b) Please provide the rationale for the choice of the subjects including any inclusion criteria.

We chose to include children under 18 (i.e., middle-school students) with special learning needs because few mathematics and science teaching resources are available to their teachers, thus limiting the success rates of special education students in public schools. By choosing special needs students under 18 as participants in our study, we have the potential to broaden their curriculum to include science.

c) Will any ethnic/racial or gender groups be excluded from this study? If so, provide the rationale for the exclusion criteria. No. We will not exclude any ethnic, racial, or gender groups because the special education classroom is inherently non-exclusive. This provides us with the most realistic study setting for the proposed research.

RECRUITMENT

8. Describe the process(es) you will use to **recruit participants** and inform them about their role in the study. (Attach copies of any recruitment materials.)

The parents of each participant will be informed of this study in a letter that describes the proposed research. The letter will have a parental consent section that requests parental consent of the participation of their child in the study (please see *Supplemental Material 4*). At the same time, we will hand out participant assent forms to each student in class that describes the study (please see *Supplemental Material 5*).

a) Will any of the following be used? (Check all that apply and attach copies)

- ☐ Internet/Email
- ☐ Newspapers/radio/television advertising
- ☒ Posters/brochures/letters
- ☐ Other

b) Does any member of the research team have a relationship (i.e., teacher, coach, physician, therapist, service provider, etc) with individuals who will be recruited for this study or with institutions that will be used to recruit for this study? If yes, describe this relationship in detail and explain how the research process will avoid any potential problems (e .g, coercion or appearance of possible coercion in recruiting) or conflicts of interest arising from this investigator's dual roles.

No.

DECEPTION

9. Does the proposed research require that you deceive participants in any way? ☐ Yes ☒ No

a) If your response is "yes," describe the type of **deception** you will use, indicate why it is necessary for this study, and provide a copy of the debriefing script.

COMPENSATION

10. Will any type of compensation be used? (e.g. money, gift, raffle, extra credit, etc)
a) ☐ Yes (Please describe what the compensation is) ☒ No (go to question 11)

b) Explain why the compensation is reasonable in relation to the experiences of and burden on participants.

c) Is compensation for participation in a study or completion of the study? (Note: participants must be free to quit at any time without penalty including loss of benefits).
☐ Participation ☐ Completion

d) If any of the participants are economically disadvantaged, describe the manner of compensation and explain why it is fair and not coercive.

INFORMED CONSENT

11. Describe the procedures you will use to **obtain and document informed consent and assent**. **Attach copies of the forms that you will use.** In the case of secondary data, please attach original informed consent or describe below why it has not been included. Fully justify a request for a waiver of written consent or parental consent for minors.
(The ASU IRB website has additional information and sample consent and assent forms.)
The parental consent form will be handed out by the classroom teacher and sent home with each student 1-2 weeks before the study start date to provide parents sufficient time to approve or deny the participation of their child. If we do not receive a consent form from a parent, we will consider it as a denied consent and will exclude their child from participation in the study. Non-participation in the study will not affect the results of any existing student evaluation measures that are normally employed in the classroom (i.e., their grade for the topic will not be affected if the student does not participate in the study; they will be given an alternate classroom activity). Assent forms will be distributed in class to each student. We have designed the assent form to be age appropriate by describing our proposed study in the simplest of terms. Each participant will have the choice to participate or opt out of participating in our study. We will make it clear to the students that non-participation will not affect their grade for the class.

RISKS

12. What are the potential risks of the research? (Check all that apply)
☐ Physical harm
☐ Psychological harm
☐ Release of confidential information
☒ Other We do not foresee any potential risks to the students.

a) Describe any potential risks to human subjects and the steps that will be taken to reduce the risks. Include any risks to the subject's well-being, privacy, emotions, employability, criminal, and legal status.
The proposed lessons will be administered in an every-day classroom setting that the students are already familiar with.

BENEFITS

13a) What are the potential benefits to the individual subject, if any, as a result of being in the study?
Potential benefits to each student include an enhanced learning experience via hands-on, learner-based classroom activities. If successful, our proposed lesson plans will help each student improve his/her understanding of basic mathematics and science concepts such that he/she can meet the state- and federally mandated curricula for his/her grade level.

b) What are the potential benefits, if any, to others from the study?
If the proposed lesson plans prove successful, they will be made available, free of charge, to special education teachers and curriculum designers. It is our hope that by making these lesson plans available, we will inspire more special education teachers and administrators to incorporate elements of our lessons and experiences into their own lesson plans to enhance their students' learning experiences.

DATA USE

14. How will the data be used? (Check all that apply)

- ☒ Dissertation
- ☐ Thesis
- ☐ Results released to participants/parents
- ☐ Results released to agency or organization
- ☐ Other *(please describe):*
- ☒ Publication/journal article
- ☐ Undergraduate honors project
- ☐ Results released to employer or school
- ☒ Conferences/presentations

PROTECTION OF CONFIDENTIALITY

15. Describe the steps you will take to ensure the confidentiality of the participants and data.
Neither primary data nor publications that may result from this study will include any identifying characteristics such as name, age, gender, type of disability, or cognitive abilities.

a) Indicate how you will safeguard data that includes identifying or potentially identifying information (e.g. coding).
Primary data will be locked in Co-I Haddad's office desk. Digital copies of the data will be stored on a password-protected ASU server that can only be accessed by the PI and Co-I.

b) Indicate when identifiers will be separated or removed from the data.
Not applicable because we will not use identifiers.

c) Will the study have a master list linking participants' identifying information with study ID codes, and thereby, their data? If so, provide a justification for having a master list. (Note: In many cases, the existence of a master list is the only part of a study that raises it above minimal risk, that is, places participants at risk.)
No.

d) If you have a master list and/or data with identifiers, where on campus will the list and/or data be kept? **(Data sets with identifiers and master lists, whether electronic or in hard copy, should be securely stored on an ASU campus except in unusual circumstances (e.g., research conducted out of the state or country).)**
Hard copies of the data will be secured in a drawer in Haddad's lab, located in the ASU Tempe Campus, Room INTDSA 121B. Haddad is the sole person that has access to the drawer keys. The lab has one entrance that has restricted access to 8 researchers. However, only Haddad has access to the drawer. The building within which the lab is located is open during business hours only (7:00 am -6:00 pm). After-hours access to the building is restricted to those that have keys (issued by ASU Tempe Police).

Digital copies of the data will be stored in Haddad's workspace on an ASU high-performance computing server and can be accessed by the PI and Co-I alone (using ASUrite ID and password). The data will not be transferred via email, unsecured FTP, or physical storage media (e.g., thumb drives, external hard drives). Electronic copies of the data will be transferred to the Co-I's ASU server space using the Co-I's password-protected lab computer.

e) If you have a master list, when will it be destroyed?
Not applicable because we will not use a master list.

f) How long do you plan to retain the data?
All primary data will be destroyed following the successful publication of this study's results, which is estimated to occur by May 2015 (Haddad's expected date of Ph.D. completion).

g) How will you dispose of the data?
The hard copy of the data will be shredded using an cross-cutting industrial-strength shredder that is located in the headquarters of the ASU School of Earth and Space Exploration (Physical Sciences F-wing, room 686).

The electronic copy of the data will be electronically shredded using the File Shredder software (http://www.fileshredder.org/) and the Guttman algorithm, which uses a 35-pass overwrite process to ensure that the data cannot be electronically recovered.

h) Where on campus will you store the signed consent, assent, and parental permission forms (If applicable)? (**Consent, assent, and parent permission forms should be securely stored on an ASU campus)**
Signed parental permission forms and signed participant assent forms will be stored in a locked drawer in the Co-I's lab space, located in room INTDSA 121B on the ASU Tempe campus.

INVESTIGATOR INTERESTS

16. Have all investigators filed a current annual conflict of interest questionnaire with the ASU Office of Research Integrity and Assurance? It is the COEUS module at: http://researchintegrity.asu.edu/coi ☒ Yes ☐ No

a) Do any of the researchers or their family members, have a financial interest in a business which owns a technology to be studied and/or is sponsoring the research? ☐ Yes ☒ No (If yes, please describe and disclose in the consent form.)

b) Are there any plans for commercial development related to the findings of this study?
☐ Yes (If yes, please describe.) ☒ No

c) Will the investigator or a member of the investigator's family financially benefit if the findings are commercialized?
☐ Yes (If yes, please describe.) ☒ No

d) Will participants financially benefit if the findings are commercialized?
☐ Yes (If yes, please describe.) ☒ No

BIOLOGICAL MATERIALS

17a) Will biological materials be collected from subjects or given to subjects? ☐ Yes ☒ No (If no, please skip to question 18)

b) Provide a description of the material (blood, tissue, vectors, antibodies, etc.) that will be used:

c) If the study involves human blood, do you have the required ASU Biosafety disclosure on file? ☐ Yes
☐ No(If yes, what is the Biosafety Disclosure number.)

d) Will any of the material being used in the study come from a third party? ☐ Yes ☐ No (If yes, attach copy of the Material Transfer Agreement if required.)

e) Does this study involve transfer of genetic material of animal tissue into humans? ☐ Yes ☐ No
(If yes, please cite the ASU Institutional Biosafety Disclosure number).

TRAINING

18. The research team must document completion of human subjects training from within the past 3 years.
(For more information see: http://researchintegrity.asu.edu/training/humans)

Please provide the date that the PI and co-investigators completed the training and attach the certificate.
PI's completion date: 06/03/2009 (PI has maintained certification since 2003)
Co-I's completion date: 02/15/2011

PRINCIPAL INVESTIGATOR

In making this application, I certify that I have read and understand the ASU Procedures for the Review of Human Subjects Research and that I intend to comply with the letter and spirit of the University Policy. Changes in to the study will be submitted to the IRB for written approval prior to these changes being put into practice. **I also agree and understand that informed consent/assent records of the participants will be kept for at least three (3) years after the completion of the research**. **Attach a copy of the PI's CV unless one is already on file with the Office of Research Integrity and Assurance.**
A copy is already on file but an updated copy is attached here.
Name (first, middle initial, last):
Steven C. Semken

Signature: Signed (hard copy) Date: 09/06/2011

FOR OFFICE USE:	This application has been reviewed by the Arizona State University IRB: ☐ Full Board Review ☐ Expedite Categories: ☐ Exempt Categories: ☐ Approved ☐ Deferred ☐ Disapproved ☐ Project requires review more often than annual Every months
	Signature of IRB Chair/Member: Date:

SUPPLEMENTAL MATERIAL 1
Data Collection Spreadsheet

Lesson _____ Instructor _____ Duration of lesson _____

Category _____ Coder _____

Student #2

	Body Position	Time (min)	**Make 1 tick mark for every minute
Leaned Fwd	+		Body leaning forward
Relaxed	0		
Slumped	-		
Toward/On	+		Body turned forward, on topic
Away/On	-		Body turned away, off topic
Away/Off			
Seated	0		
Standing	0		
Walking	0		**Indicate on or off topic**
	Gaze		
Forward	+		Turned toward teacher/screen, On topic
Away/On	+		Turned away from teacher/screen but on topic
Away/Off	-		Turned away and off topic
Away/ND	-		Non directed..wandering/gazing/daydreaming
	Verbalization		
Teacher/On	+		Directed toward teacher, on topic
Teacher/Off	-		Toward teacher, off topic
Other/On	+		Directed toward classmates or other, on topic
Other/Off	-		Toward classmates or other, off topic
	Writing		
Indep/On	+		Writing independently, on topic
Indep/Off	-		Writing independently, off topic
Others/On	+		Writing with others, on topic
Others/Off	-		Writing with others, off topic
	Manipulatives		
Approp./On	+		Uses manipulatives appropriately, on topic
Approp./Off	-		Uses manipulatives appropriately, off topic
Inapprop./Off	-		Uses manipulative inappropriately

SUPPLEMENTAL MATERIAL 2
Pre- and post-assessment tests

Topic of the Day: Earthquakes

Pre-test Assessment

(1) What do you know about earthquakes?

(2) What causes an earthquake?

(3) What are some effects of earthquakes?

(4) What can we do to prepare for an earthquake?

Topic of the Day: Earthquakes

Post-test Assessment

(1) What have we learned about earthquakes?

(2) What causes an earthquake?
- (a) Draw a picture and use the Word Bank to label your drawing.
- (b) Demonstrate using our earthquake model.
- (c) Write three complete sentences describing the causes of an earthquake.

(3) What are some effects of earthquakes?
- (a) Draw a picture and use the Word Bank to label your drawing.
- (b) Demonstrate using our earthquake model.
- (c) Write three complete sentences describing the effects of earthquakes.

(4) What can we do to prepare for an earthquake?
- (a) Draw a picture and use the Word Bank to label your drawing.
- (b) Demonstrate using the "Stop, drop, and hold on!" safety drill.
- (c) Describe what safety measures you would to stay safe during an earthquake.

SUPPLEMENTAL MATERIAL 3
School permission agreement

David Haddad <dehaddad@asu.edu>

Pilot study for the special education classroom

2 messages

David Haddad <dehaddad@asu.edu> **Tue, Aug 30, 2011 at 1:49 PM**
To: tmolina@gesd40.org

Dear Mrs. Molina,

My name is David Haddad and I'm a PhD student in geoscience education at Arizona State University (ASU). I'm writing to express my interest in conducting a pilot study with one of your teachers, Mrs. Mary Turner, as part of my PhD research on developing geoscience-themed lesson plans for the special education classroom. I have contacted Mrs. Turner regarding this and she recommended I contact you for approval.

My pilot study aims to evaluate the effectiveness of new lesson plans for the special education classroom. I am developing lessons that teach about the Earth sciences while incorporating elements from the Arizona mathematics and science curricula. The pilot study calls for the lessons to be carried out by a special education teacher (Mrs. Turner) while I evaluate their effectiveness using non-invasive observation. This involves me being present in the classroom and observing and noting the reactions of the students to the new lesson over a course of 1-2 weeks. To protect the students' identities, none of their names will be used in my study or any subsequent presentations/publications. Similarly, I will not take any photographs or videos that can potentially identify the students.

If my lesson plans prove to be effective in this pilot study, I plan to expand it to other schools and make the lessons freely available to other teachers. Of course, your school will be acknowledged in any presentations/publications that result from this study.

I am currently in the process of seeking permission from the ASU Institutional Review Board (IRB) to conduct my pilot study. Part of this process is to acquire approval from the teacher and the school. Mrs. Turner has agreed to participate in my pilot study and has provided me with a letter or approval. If approved by you, I kindly ask for a letter of support from you on behalf of Challenger Middle School. I will be requesting letters of consent from each student and their parents after acquiring approval from the ASU IRB, prior to conducting my pilot study.

Please feel free to let me know if you have any questions about the new lesson plans or any other aspect of my project.

Sincerely,

David E. Haddad
PhD Student
School of Earth and Space Exploration
Arizona State University
602-550-4076

Tiffany Molina <tmolina@gesd40.org> **Tue, Aug 30, 2011 at 3:09 PM**
To: David Haddad <dehaddad@asu.edu>

When you receive approval from ASU, you may conduct your study with Mrs. Turner.

Thank you,

Tiffany Molina
Principal
Challenger Middle School
tmolina@gesd40.org
623-237-4011

From: David Haddad [mailto:dehaddad@asu.edu]
Sent: Tuesday, August 30, 2011 1:49 PM
To: Tiffany Molina
Subject: Pilot study for the special education classroom

[Quoted text hidden]

PARENTAL CONSENT FORM:

By signing below, you are telling the researchers Yes, that you will allow your child to participate in this study. Please keep a copy of this form for your records.

Your child's name (please print): _____

Parent's name (please print): _____

Parent's signature: _____

Date: _____

SUPPLEMENTAL MATERIAL 5
Participant Assent Form

Earth Science Meets the Special Education Classroom

I have been told that my parents (mom or dad) have given permission (said it's okay) for me to take part in a study about learning Earth science using new classroom activities.

I will be learning about things like plate tectonics, earthquakes, and volcanoes by watching videos, doing experiments, and discussing Earth science with my classmates. I will do this for about two weeks.

I am taking part because I want to. I know that I can stop at any time if I want to and it will be okay if I want to stop. If I do not want to take part, or if I want to stop taking part at any time, I will continue with my usual classroom learning activities.

_____ _____
Sign Your Name Here Print Your Name Here

_____
Date